10 kHz PULSE REPETITION FREQUENCY CO_2 LASER FOR PROCESSING HIGH DAMAGE THRESHOLD MATERIALS

by

Donald Wilson McDonald BSc.

Thesis presented for the
Degree of Doctor of Philosophy
under general regulations

Department of Mechanical Engineering
Faculty of Engineering
University of Glasgow

October, 1989

ProQuest LLC.
789 East Eisenhower Parkway
P.O. Box 1346
Ann Arbor, MI 48106 – 1346

SYNOPSIS

Power intensities generated at the workpiece by continuous wave carbon dioxide lasers at 10.6 μm are insufficient to induce the non-conduction limited processes necessary for machining many of the refractory metals and ceramics employed in the manufacture of engineering components. Operated in a pulsed mode, analogous to solid state laser operation, the CO_2:N_2 laser can be designed to overcome these power intensity limitations. Nitrogen Carbon-dioxide mixtures can be pulse excited to give high output pulse intensities combined with a relatively low mean output power, thus, minimising thermal degradation of the optical system. Flat topped pulses with plateau powers controlled and matched to the processing requirements of metals and ceramics can be generated by proper choice of the input electrical pumping pulse, gas composition and design parameters of the optical resonator. Continuous machining is possible provided pulse repetition frequencies of up to 10 kHz can be achieved, since, at this frequency, a constantly evaporating liquid phase can be sustained.

A 10 kHz PRF CO_2:N_2 laser, with pulse powers matched to the requirements of non-conduction limited processing and a mean output power level in the range 2 - 5 kW, is reported. The laser comprises a 3 litre transverse flow discharge cavity which is pumped by a high voltage line type pulser. The gas flow required to convectively clear the discharge volume is provided by a high flow rate gas circulator, with two Root's blowers operating in parallel. Design of the 15000 m^3/hr gas circulator, gas cooling circuit and gas control system is reported, together with a transient thermodynamic analysis of the gas circulator and cooling circuit.

The transverse discharge cavity is excited by 10 μs duration rectangular voltage pulses. The excitation pulses are generated by a multi-section pulse forming network (PFN), which is resonantly charged from a 100 kW, 10 kV DC supply. CX1528 thyratrons were used for the PFN command charging circuit and discharge circuit. The major problem encountered during the development of the pulser circuit was the effect of thyratron grid-anode stray capacitance. Details are given of the thyratron trigger/control circuits which were designed to overcome these problems and permit continuous operation at 10 kHz PRF. Consideration is also given of system fault protection and control.

Results are reported of experimental work on gas discharge stability both for single shot and continuous pulse mode operation. Due to the low system operating pressure (100 - 200 torr) and low specific energy input (10 - 20 $J.l^{-1}atm^{-1}$), it was possible to attain clearing ratios below unity in continuous pulse excitation. The discharge was initiated by an auxiliary discharge from trigger-wires positioned above the cathode.

Experimental results showing the influence of trigger–wire parameters on discharge stability are presented; the development of the trigger–wire firing circuit is also discussed. A theoretical analysis of the discharge formative period is compared with the experimental results and the effective trigger–wire current calculated. The onset of arcing in the discharge was found to be due to the accumulated growth of instabilities over a sequence of pulses, resulting from ineffective clearing of the discharge volume in the inter–pulse period. Clearing was dominated by the presence of boundary layers, as discharge shock wave effects were found to be insignificant at these specific energy loadings. A maximum attainable PRF of 2 kHz was obtained with the trigger–wire initiated system. The limitations on discharge stability was found to be due to the non–uniform discharge current in the cavity, resulting from the position of the trigger–wires in the discharge. Electrode/preionization system modifications are proposed for extension of the stable discharge operating regime to a PRF of 10 kHz.

Results are reported of the output pulse characteristics from a multi–pass, stable optical resonator, with an 85% reflective ZnSe output window. The effect of controlled changes in gas mixture composition on output pulse characteristics is considered and experimental results compared with theoretical predictions from a laser kinetics code.

Finally, recommendations are made for future system development together with suggestions for research work in some critical areas.

To Matthew and Helen

ACKNOWLEDGEMENT

I would like to express my sincere gratitude to Professor B. F. Scott and Dr. C. R. Chatwin for their continuous encouragement and guidance during this work, and for the many useful discussions and ideas. Particular thanks is also due Ian Watson for assisting in the experimental work on the gas discharge and output pulse characteristics. I would also like to thank the technicians of the Mechanical Engineering Research Annexe: John Dunning, Bernard Hoey, Brian McAdams, John Davidson, Hamish McArthur, and Hugh Spence, for their invaluable contributions to the design and construction of the laser. Finally, I would like to thank Isobelle Lawson for the preparation of the drawings and appendix.

INDEX

APPENDIX.

PHOTOGRAPHS

LIST OF FIGURES.

CHAPTER 1.

Section (1.1)

Section (2.1)

CHAPTER 2.

Section (2.1)

Section (2.2)

Section (3.2)

Section (3.3)

Section (3.4)

Section (3.5)

Section (3.6)

CHAPTER 4.

Section (4.1)

Section (4.2)

Section (4.3)

Section (4.4)

Section (4.5)

CHAPTER 5.

Section (5.1)

Section (5.2)

Section (5.3)

NOTATION.

A	Area	m^2
A_{min}	Minimum gas flow area	m^2
A_p	Primary surface area	m^2
A_r	Root area	m^2
C	Head capacity ratio	
	Capacitance	F
C_{eff}	Effective capacitance	F
C_n	Network capacitance	F
C_p	Specific heat at constant pressure	$J.kg^{-1}\ K^{-1}$
Cp_w	Specific heat of water	$J.kg^{-1}\ K^{-1}$
C_s	Stray capacitance	F
C_v	Specific heat at constant volume	$J.kg^{-1}\ K^{-1}$
CR	Clearing ratio	
d	Inside diameter of tube	mm
	Electrode spacing	cm
D	Resonator length	m
	Outside diameter of tube	mm
D_e	Equivalent circular diameter	mm
e	Electronic charge	C
E	Electric field	$V\ m^{-1}$
E_i	Input energy to discharge	J
f_c	Cut-off frequency	Hz
f_{max}	Maximum PRF	Hz
h_f	Fin height	mm
h_i	Inside heat transfer coefficient	$kW\ m^{-2}\ K^{-1}$
h_o	Gas side heat transfer coefficient	$kW\ m^2\ K^{-1}$
h_{ot}	Gas side heat transfer coefficient	$kW\ m^{-2}\ K^{-1}$
i	Current	A
I	Current	A
I_f	Fault current	A
K	Thermal conductivity	$kW\ m^{-1}\ K^{-1}$
	Boltzmann's constant	$J\ K^{-1}$
K_a	Attachment coefficient	$cm^{-3}\ s^{-1}$
K_d	Detachment coefficient	$cm^{-3}\ s^{-1}$
K_i	Ionization coefficient	$cm^{-3}\ s^{-1}$
K_r^e	Recombination coefficient	$cm^{-3}\ s^{-1}$
K_i^*	Thermal conductivity component	$kW\ m^{-1}\ K^{-1}$
K_i^{**}	Thermal conductivity component	$kW\ m^{-1}\ K^{-1}$

l	Characteristic dimension	m
L	Inductance	H
L_c	Charging inductance	H
m	Mass flow rate	kg s^{-1}
m_w	Mass flow of water	kg s^{-1}
m_g	Mass flow of gas	kg s^{-1}
M	Molecular weight	kg mol^{-1}
M_g	Mass of gas in system	kg
M_w	Mass of water in tank	kg
M_{ij}	Coefficient defined by equation (2.9)	
n_e	Electron number density	cm^{-3}
n_{ek}	Electron number density perturbation	cm^{-3}
N	Number of transfer units	
	Neutral particle density	cm^{-3}
$Nu_{d,m}$	Nusselt number	
Nu_f	Nusselt number for fins	
P	Gas pressure	torr/mbar
	Electrical power	kW
P_o	Laser output power	kW
Pr_m	Prandtl number	
Q	Heat load	kW
Q_l	Cavity heat load	kW
Q_b	Blower heat load	kW
Q_{EX1}	Heat load exchanger 1	kW
Q_{EX2}	Heat load exchanger 2	kW
r	Radius of electron avalanche	m
R	Specific gas constant	$J.kg^{-1}$ K^{-1}
	Resistance	Ω
R_b	Back mirror radius of curvature	m
R_f	Front mirror reflectivity	%
$Re_{d,m}$	Reynolds number	
t	Water temperature	^0C
t_r	Rise time	s
T	Temperature of gas	K/^{o}C
T_e	Electron temperature	K
T_{ek}	Electron temperature perturbation	eV
T_v	Vibrational temperature	K
U	Overall heat transfer coefficient	kW m^{-2} K^{-1}

V	Volume	m^3
	Voltage	V
V_a	Anode voltage	V
V_d	Drift velocity	$m\ s^{-1}$
V_{dc}	DC voltage	V
V_i	Incident wave voltage	V
V_l	Load voltage	V
	Line voltage	V rms
V_{no}	PFN charge voltage	V
V_p	Phase voltage	V rms
V_r	Reflected wave voltage	V
V_{tw}	Trigger–wire voltage	V
y_f	Distance between fins	mm
W	Electrode width	m/cm
X	Transformer reactance	Ω
X_b	Base impedance	Ω
y_i	i^{th} component mole fraction	
Z	Impedance	Ω
	Avalanche track length	cm
Z_n	PFN impedance	Ω

Greek letters.

α	ionization coefficient	cm^{-1}
β	Area ratio	
γ	Ratio of specific heats	
	Townsend second coefficient	cm^{-1}
δ_f	Fin thickness	mm
ϵ	Exchanger effectiveness	
ϵ_c	Coil effectiveness	
ϵ_p	Effectiveness of each pass	
ζ	Damping coefficient	
η	Efficiency	
	Attachment coefficient	cm^{-1}
η_f	Fin efficiency	
λ	Wavelength of light	μm
λ_d	Debye length	m
μ	Dynamic viscosity	$kg\ m^{-1}\ s^{-1}$

v	Gas velocity	m s^{-1}
v_g	Disturbance growth rate	s^{-1}
v_m	Electron momentum transfer collision frequency	s^{-1}
v_u	Total electron energy exchange collision frequency	s^{-1}
ρ	Density	kg m^{-3}
τ	Pulse length	s
τ_{vt}	Mean relaxation rate	s^{-1}
φ	Fin effectiveness	
φ_{ij}	Coefficient in viscosity equation	
ω	Resonant frequency	rad s^{-1}
	Resonator mode radius	mm

$\wedge$ Denotes logarithmic differentiation with respect to electron temperature.

(1.0) INTRODUCTION.

From a manufacturing standpoint solid state and gas lasers are differentiated fundamentally by the heating mechanisms that can be induced in materials irradiated by them and their mean power capacity. When operated in the pulsed mode solid state devices can create heat transfer mechanisms propitious for process quality and control in a very wide range of materials. But their low efficiency precludes the attainment of pulse repetition frequencies (PRF) sufficient to permit heavy duty continuous processing.

In continuous wave (CW) operation gas lasers can operate at mean powers in the multi−kilowatt range and offer high processing rates. However, intensities generated at the workpiece are below the damage thresholds of many materials employed routinely in the manufacture of engineering components and of metals specifically. Successful applications depend upon means for enhancement of power release/absorption in the workpiece, e.g. reacting gas jets, electric arcs. These latter techniques are far from universally effective and are themselves attended by restrictive control and matching problems.

The power intensity distribution in the beam waist is controlled by two primary factors, viz: the physical aspects of the beam and the absorption characteristics of the optical elements. As the irradiance in the focal region of the focussing optics varies as the inverse square of wavelength, this militates against the relatively long wavelength of the CO_2 laser. In addition, handling of high power beams results in degraded performance arising from thermally induced distortion of the optical components. Particularly at 10.6 microns, the choice of materials combining acceptable thermal and optical properties is limited. An indication of the extent of this effect can be found in results reported by Ball *et al* [1.1], where an output power of 6 kW gave a spot−size of about 0.025" using F/7 optics. The corresponding mean power intensity is 1.9×10^{10} W/m^2; whereas an ideal F/7 system should achieve 1.6×10^{11} W/m^2. This problem is exacerbated at the higher laser mean powers; paradoxically a 20 kW CW laser may deliver a lower irradiance than a 1 kW system. In addition, the very high reflectivities exhibited by metals at 10.6 microns, limits the energy absorbed by the workpiece.

Operated in a pulsed mode, analogous to solid state laser operation, the CO_2 laser can be designed to overcome these power intensity limitations. Nitrogen Carbon−dioxide mixtures can be pulse excited to give high output pulse intensities combined with a relatively low mean output power, thus, minimising thermal degradation of the optical system. Flat topped pulses with plateau powers controlled

and matched to the processing requirements of metals and ceramics can be generated by proper choice of the input electrical pumping pulse, gas composition and design parameters of the optical resonator. Specifically, it has been found that with pulse powers (measured on the plateau) broadly in the range of 10 to 150 kW – depending upon the physical properties of the workpiece material – the high absorption, high reaction pressure heating regime encountered when machining with pulsed Nd:YAG lasers can be entered. Furthermore, continuous machining is possible provided pulse repetition frequencies of up to 10 kHz can be achieved. At or near this frequency a constantly evaporating liquid phase can be sustained in the workpiece, but the interpulse period remains of sufficient duration to allow the laser medium to be replaced and permit repetitive pulsing. In addition, micro–plasma transients necessary to the heating process – but which, if allowed to develop, could adversely affect the absorption – have sufficient time to decay.

(1.1) BEAM–WORKPIECE INTERACTION.

Metals are highly reflective at a wavelength of 10.6 microns; at ambient temperature the reflectivities of copper, aluminium and nickel are 98%, 96% and 94% respectively, making them unsuitable for CW CO_2 laser processing. It is estimated that the absorbed power intensities useful for laser machining lie between 10^{10} W/m^2 and 10^{11}W/m^2 [1.1]; below 10^{10} W/m^2 the surface temperature rise is insufficient to cause appreciable damage and above 10^{11} W/m^2 the absorption is significantly reduced by plasma emitted.

Fig. (1.1) as reported by Bakewell *et al* [1.2], shows the temporal response of aluminium to pulsed CO_2 laser heating vis–a–vis surface temperature, absorbed flux and incident flux. Elevation of the tail of the surface temperature profile, after the cessation of input pulse is explained by the transfer of energy from the sub–surface region. Aluminium is one of the most demanding materials to cut or weld, in terms of the pulse intensity and repetition frequency, hence the minimum pulse requirements for aluminium are considered sufficient for other metals. Fig. (1.1) shows that maximum absorption is approximately 40% of the incident flux at a surface temperature of about 4300 K. From Figures (1.2) and (1.3), taken from Bakewell *et al* [1.2], it is evident that to obtain this range of temperature a steady absorbed intensity of approximately 4.0 x 10^{10} W/m^2 for 4 μs is required. This means that a laser pulse with a steady power of about 50 kW (assuming a spot size of 0.5mm^2 and incident flux to be about 2.5 times the absorbed flux) for 4 μs is required. From results reported by Bakewell [1.2] it is noted that to achieve a much higher temperature than 4300 K the incident flux has to be increased by an order of

magnitude and thus cannot be justified.

Fig. (1.1) also shows that once the surface temperature has been raised it remains constant and the liquid phase persists for approximately 50−60 μs. If the pulse repetition frequency is close to 10 kHz successive pulses will encounter the high surface temperature produced by the previous pulse. Thus, a PRF of 10 kHz ensures that the metal surface remains liquid and in the enhanced absorbtion regime between pulses, permitting continuous processing.

Gain switching in pulsed lasers gives rise to an initial power spike, which if sufficiently large produces a highly absorbent blanking plasma, resulting in severe beam attenuation; this may defeat any attempt at machining. Without sufficient means of plasma control, emitted plasma develops into a laser−supported absorption (L.S.A.) wave that propagates back towards the laser [1.3] detaching itself from the material surface; almost complete decoupling of the beam from the workpiece results. A small initial spike − twice the plateau height − is desirable but ideally the processing laser pulse should be flat topped and of an intensity matched to the particular requirements of the material being processed. Fig. (1.3) shows the response time of different materials to step inputs of the incident intensity at a specified absorbed intensity; the influence of material properties on the intensity matching requirements is substantial. Fortunately the means for controlling the initial power spike and matching the pulse plateau height to the workpiece requirements are numerous, viz:

(i) The electrical pumping pulse.
(ii) The gas mixture total pressure.
(iii) The constituent partial pressures.
(iv) The mean photon decay time via the output coupling and resonator length.
(v) External injection of radiation.

(1.2) PREVIOUS WORK.

(1.2.1) Conceptual Desisign.

Fig. (1.4) shows the system selected by Khahra [1.4] for gas excitation, gas transport and output beam coupling. The transverse discharge arrangement was chosen because this allowed a high optimum working pressure with a large mode volume, hence high output powers. In addition, the short discharge length results in a relatively low voltage for a self−sustained discharge, thus, considerably simplifying the design of the pulsed power source. With the inclusion of a transverse flow gas circulator this arrangement also facilitates rapid removal of the discharge products between pulses,

even at moderate gas velocities, permitting high pulse repetition frequencies.

The difficulty associated with the development of the transverse discharge arrangement for pulse excitation is to ensure that a homogenous glow discharge is established throughout the volume. This can be achieved using a ballasted pin electrode system [1.5], however, significant I^2R losses are generated, reducing overall device efficiency. Moreover, the discharge produced is highly non−uniform and adversely affects laser mode development. Alternatively, it is possible to initiate a volume discharge by preionizing the discharge gap prior to application of the main voltage pulse. This prevents the discharge breaking down in the arc mode and has the additional advantage of reducing the static breakdown voltage [1.6]. The discharge operates in essentially a quasi−equilibrium regime, where the pulse energy is limited by the onset of discharge instabilities [1.7].

For an industrial laser, preionization must be cheap and robust, thus, a relatively simple scheme was chosen. Electron beam methods were resisted due to the high added cost and complexity. A double discharge system, similar to the system used by Dumanchin *et al* [1.8], was found to be suitable for this application. In this system dielectric coated trigger wires are positioned above the cathode; these are excited by a high voltage pulse prior to application of the main electrode voltage, producing sufficient preionization throughout the electrode gap to ensure homogenous discharge formation.

(1.2.2) Software tools.

In view of the need to reduce dependency on prototype developments, a range of software tools was developed to accelerate the design cycle. In addition to providing useful design data, the computer simulations have given profound insight into the processes occuring in the laser cavity and at the workpiece.

Prediction of the temporal characteristics of the laser output pulse involves solution of the rate equations that govern the molecular kinetic processes in the laser gas mixture [1.9]. This requires knowledge of the electron excitation and de−excitation rates for each of the vibrational levels of the CO_2 and N_2 molecules. The first step in the modelling process is the determination of the electron energy distribution function (EEDF) from the Boltzmann transport equation. Khahra [1.4] obtained a solution of the time−independent Boltzmann equation, however, this neglected many of the important kinetic processes due to the lack of reliable rate coefficient data at that time. Recently Hasan [1.10] has obtained accurate predictions of the EEDF using a

version of the BOLTZ code [4.9]; the results obtained include the effects of all the dominant kinetic processes, including super−elastic collisions. The

BOLTZ code was employed to obtain the EEDF for the laser gas mixture and calculate the mean exitation rates for the $CO_2(00^01)$ and $N_2(\nu=1-8)$ energy levels. The code was modified to provide additional plasma data e.g. attachment coefficient, ionization coefficient, electron mobility and diffusion coefficients.

A code (LASERSIM) was developed by Chatwin [1.11] to solve the molecular rate equations under conditions of pulse excitation. This was a refinement of Moore's [1.12] model and consists of a six level model of the excitation/relaxation processes. This code uses the mean excitation rates obtained from BOLTZ, together with specifications for the input pulse profile and resonator configuration to predict the temporal characteristics of the output pulse. This code was later modified by Bayabagambi [1.13] to include the effects of gas flow and heat transfer.

(1.2.3) Laser Cavity Design.

The software tools described above were used extensively in the design and optimization of the laser cavity. Although the simulation codes give valuable information, it was not possible to achieve a satisfactory design solution without considering the more practical aspects of the design. In particular, data was required on the V−I characteristics of the gas discharge under conditions of pulse excitation, since these govern the molecular excitation rates and dictate the design parameters of the pulsed power source. Moreover, consideration must be given to the allowable power density that can be sustained in the cavity; this being limited by the onset of arcing. The present understanding of the instability mechanisms which lead to a glow to arc transition is still far from complete and no general design guides can be given. The complexity of the physical phenomena that lead to arcing in the laser cavity preclude the use of computer models in all but the simplest of cases. It is therefore necessary to obtain this design information from experimental prototypes.

Khahra [1.4] built a prototype transverse discharge laser cavity, as shown in plate (1), to confirm theoretical predictions and study the characteristics of the gas discharge. This comprised two planar brass electrodes (100 cm x6 cm) with profiled edges; the discharge gap could be varied in the range 35−45mm. The pulse power supply comprised a resistively charged, high voltage, multi−section pulse forming network (PFN). Electrical pulse characteristics were controlled by varying the PFN charging voltage and the design parameters of the PFN. A stable optical resonator with a 10

meter radius gold−coated rear mirror and a 90% reflective germanium output window was used. The output power was measured by focussing the beam onto a photon drag detector.

Initial experiments were conducted with excitation pulses of up to 10 μs duration. It was observed that following a short discharge formation time (approximately 1 μs), the discharge voltage collapsed to a steady value, which for a given mixture was found to be independent of discharge current. It is well known that for pulsed, self−sustained glow discharges in CO_2:N_2:H_e gas mixtures, that the quasi−steady value of (E/P) depends only on the gas mixture composition and is independent of discharge current, total pressure and electrode spacing [1.14]. This occurs when attachment is the main electron loss mechanism, with the quasi−steady value of (E/P) being given by the intersection of attachment and ionization curves obtained from the BOLTZ. Good agreement was found between the experimental value of (E/P) and the value derived from the EEDF [1.10].

In determining the design conditions for the laser cavity, the EEDF was first obtained for a range of gas mixtures at the experimentally measured quasi−steady value of (E/P) and the coupling efficiencies for the $CO_2(00^01)$ and N_2 (ν=1−8) levels calculated. LASERSIM [1.11] was then used to simulate the output pulse from the laser. It was found that for a given mixture, the total efficiency varied as a function of the input power, however, the efficiency remained substantially constant at power densities above 50×10^{-6} J/cc.torr. The simulations were confined to the operating conditions which could be demonstrated in the prototype laser cavity.

Fig. (1.5) shows the EEDF for a 1:1:4 mixture at the quasi−steady (E/P)= 11.78 V/cm.torr. The fractional power coupled into the CO_2 (00^01) and N_2 (ν=1−8) vibrational levels is 9.36% and 41.8%, respectively, giving a maximum theoretical laser efficiency of 20.5%. As the coupling efficiencies are controlled by the actual experimental value of (E/P), which is dependant only on mixture composition, it is important to investigate the effects arising from controlled changes in mixture composition.

Fig. (1.6) shows the variation of the coupling efficiencies for the CO_2 (00^01) and N_2 (ν=1−8) vibrational levels as a function of the normalised CO_2 partial pressure, for a helium free mixture with a constant CO_2+N_2 pressure of 40 torr. The excitation efficiency of the N_2 (ν=1−8) energy levels shows a marked increase with the addition of N_2 to the mixture. This is due to both the availability of more ground state molecules and a shift in the mean electron energy to a lower value, where the excitation cross section is larger. The excitation efficiency of the CO_2 (00^01) laser

level shows a gradual increase throughout the range γ = 0.25–0.4, levelling off at high proportions of CO_2. The initial increase in the coupling efficiency for this level is again attributed to an increase in the availability of ground state molecules, however, as the CO_2 content is increased further, the (E/P) increases, shifting the mean electron energy away from the optimum value (approximately 1 eV).

The addition of helium to the gas mixture also has a significant effect on the coupling efficiencies, with optimum compositions being found in the range $He/(CO_2+N_2)$ = 3–4, depending on the CO_2:N_2 ratio. In spite of helium lowering the operating value of (E/P), the addition of helium raises the mean electron energy of the discharge, hence, shifts the optimum (E/P) to a lower value.

Although the excitation efficiencies are determined by the EEDF, it is not possible to relate these in a simple way to the actual laser conversion efficiency, due to the inherent complexities of the molecular excitation/relaxation processes. A final judgement must therefore be based on the overall efficiency as calculated from the laser output pulse. Fig. (1.7) shows the output from LASERSIM for three gas mixtures at a constant input pulse power of 823 kW for 10 μs. These results illustrate the effects of increasing the N_2 and helium content of the mixture.

It was found that although higher conversion efficiencies could be obtained by increasing the N_2 content, and this was also effective in reducing the initial spike, most of the increased energy was being released in a long pulse tail. This was due to the relatively slow transfer from the vibrationally excited N_2 to the $CO_2(00^01)$ vibrational level. As the output power in the the tail of the pulse was below the level required for enhanced machining, it was not possible to take advantage of the increased efficiency.

Fig. (1.7) also illustrates the effects of increasing helium content. It was found that although the efficiency increased with the addition of helium, this was at the expense of increased oscillations on the output pulse [1.11]. The addition of helium also significantly increases the magnitude of the gain switched spike as it reduces gain; this is a result of the line broadening effect of helium which significantly reduces the stimulated emission cross–section.

In conclusion, the laser gas mixture was optimised to give the required pulse profile i.e. a small initial spike, approximately twice the plateau height, followed by a relatively constant plateau of approximately 4μs duration. In terms of efficiency, plateau characteristics and experimental performance, a 1:1:4 mixture at a total pressure of 120 torr was identified as being broadly suitable for a wide range of

materials processing applications [1.4]. Nevertheless, gas mixture composition is a significant control parameter whereby the laser output pulse can be optimised for each particular processing task and should therefore be considered as a variable control parameter

(1.2.4) Gas Circulator.

The attainment of high mean powers in the transverse discharge system is dependant critically upon the removal of gas from the discharge volume [1.15]. Under conditions of pulse excitation the gas flow must be sufficient to ensure that the power loading is below the threshold for arc formation. For high PRF operation it is also necessary to clear the discharge products from the laser cavity during the inter-pulse period: on this basis a minimum clearing ratio of 1:1 is required. However, at the low specific energy loading of this device, it is possible to satisfy the above stability criteria at a much lower clearing ratio [1.16]. This permits a relatively low volume flow rate gas circulator system to be designed to meet the specifications for 10 kHz PRF.

The major design effort in previous work [1.11] has been to establish a commercially viable gas recirculation system. The critical component in the circulator is the compressor; this was the subject of an extensive investigation by Chatwin [1.11], from which the following conclusions were drawn: Specific speed calculations indicated a mixed-flow compressor to be an ideal choice for the required duty, however, a compressor fulfilling the performance specification was unavailable at a realistic price. The compressor selection was therefore dictated by commercial considerations.

Fig. (1.8) illustrates the design proposed by Chatwin [1.11] based on an Elliot 50P centrifugal compressor. This design featured fully aerodynamic flow transitions in order to minimise circuit pressure losses.

(1.2.5) Pulser Developments.

The experimental work conducted on the prototype cavity confirmed that under pulse excitation – with pulse lengths in the range 5–10 μs – the gas discharge operates at a quasi-steady value of (E/P); this is found to be dependant only on mixture composition. For the range of cavity operating conditions a maximum input electrical pulse power of 1 MW for 10 μs, at a maximum PRF of 10 kHz, is required. In addition, the electrical pulse must be generated at the correct voltage and impedance level for optimum excitation of the active volume: results from the prototype cavity indicated a pulse voltage in the range 5–10 kV was required. Of the alternative pulse

power systems available, a line type modulator [1.17] was selected for development. Although a hard tube switched modulator offered distinct pulse control advantages, coupled with extremely high operating frequency, this type of pulser was found to be usuitable on the grounds of power transfer efficiency.

Fig. (1.9) illustrates the main components of the high frequency line type modulator circuit [1.18]. This comprises a multi-section PFN, which is resonantly charged from a high voltage direct current supply. The circuit incorporates three EEV-CX1528 tetrodes, viz: triggered charging diode, discharge switch and tailbiter. The output pulse characteristics are controlled by the design parameters of the PFN and by its charging voltage. For high electrical transfer efficiency the pulser must be matched to the characteristics of the gas discharge. Due to the quasi-steady operating discharge voltage, the pulser can be matched to the load simply by charging the PFN to twice the quasi-steady discharge voltage. Although the design parameters of the PFN do not affect power transfer efficiency, the PFN must be matched to the specific pulse power requirements of the discharge. For a particular pulse length the impedance of the discharge is fixed by the maximum allowable specific input power. It should be noted that with this pulser system a mismatch of up to 30% results in only a 3% drop in power transfer efficiency.

For this particular application a 10 μs type-E pulse forming network was designed with an impedance of 100 Ω. This comprised 14 resonant LC meshes with a total capacitance of 0.05 μF. The PFN was constructed to allow any number of meshes to be connected, permitting the output pulse duration to be varied in the range 2-10 μs. The PFN charging circuit was designed with a variable high voltage charging circuit to allow the pulser to be matched to the full range of laser gas compositions. At a peak charging voltage of 20 kV, the pulser can deliver 1 MW pulses of 10 μs duration at a maximum pulse repetition frequency of 10 kHz.

(1.3) SCOPE OF PRESENT WORK.

The principle objective of this work was to design and develop a 10 kHz PRF CO_2 laser, capable of continuous operation at a mean output power of approximately 2 kW, with pulse powers broadly in the range 10 - 150 kW. The laser system design was founded on the earlier work of Khahra [1.4], Spall [1.18] and Chatwin [1.11], some details of which have already been considered above. The present work can be split into two areas, one concerning the laser system design and development, the other concerning the pulser development.

Laser System Development.

Khahra [1.4] has shown that the laser output characteristics required for enhanced machining of non-ferrous metals can be produced by suitably exciting the N_2:CO_2 gas system. The transverse discharge cavity developed by Khahra was suitable for single shot and burst mode only, as no facilities were incorporated for transverse gas flow. It was therefore not possible to establish the gas conditioning requirements necessary for sustained operation at the design PRF, nor was it possible the assess the full matarials processing potential of the device. Nevertheless, this work did establish suitable discharge cavity and optical resonator designs, and identified suitable gas mixture compositions. This work was complemented by the output pulse simulations obtained by Chatwin [1.11], with the conclusion that to obtain the desired temporal laser pulse characteristics - low spike power, constant plateau power - a long cavity photon decay time was required.

The laser cavity developed by Khahra was essentially an experimental device which was constructed in a short timescale. This satisfied the objectives at that time, however, the present development called for a cavity design which could incorporate almost any transverse electrode arrangement, thus providing the necessary flexibility for experimentation with electrode geometries, preionization and gas flow-shaping. A prime objective of this work was therefore to establish a suitable cavity design, together with a high volumetric flowrate gas circulator, including gas cooling and control. In addition to this, new designs were established for the optical resonator and beam delivery system. This development was undertaken in order to improve resonator coupling efficiency. In view of the complexity of the complete laser system, a control system was designed and built to integrate the control of all the sub-systems. This included the necessary links for future expansion into a computer controlled manufacturing environment. Details of system design and development are given in chapter (2).

Pulser Design and Development.

The high voltage pulser developed by Spall [1.17] was tested at the full 10 kHz PRF only in burst mode into a dummy load. Experience with the pulser during Khahra's experimental work highlighted several problems, including fire-throughs (two thyratrons conducting simultaneously), fault protection and power supply control. A major portion of the work reported here concerns the development work on the pulser circuit which was required to extend operation to the full design specification. This involved re-designing all thyratron trigger and control circuits and upgrading system fault protection. This work is reported in chapter (3).

On completeion of the laser system, a series of experimental tests were undertaken to establish device performance characteristics. Chapter (4) details the results of investigations into the critical aspects of the gas discharge, particularly, discharge formation, stability and gas conditioning requirements. Chapter (5) covers the assesment of the output beam characteristics, including a comparison with the theoretical predictions from LASERSIM. General conclusions and recommendations are considered in chapter (6).

REFERENCES FOR CHAPTER (1)

[1.1] Ball, W.C.; Bonnas, C.M., "Welding with high power CO_2 lasers." Soc. Auto. Eng. Inc., Report No. 740863 (1974).

[1.2] Bakewell, B.A.; Scott, B.F., "Journal of Heat and Mass Transfer" (to be published)

[1.3] Stegman R.L.; Schriempf J.T.; Hettche L.R., J. Appl. Phys. Vol. 44, 3675 (1973)

[1.4] Khahra J.H., "Optimisation of the output characteristics of a pulsed carbon-dioxide laser for processing of materials." Ph.D. Thesis Univ. Birmingham, Dec 1976.

[1.5] Beaulieu A.J., "Transversely excited atmospheric pressure CO_2 lasers." Appl. Phy. Lett., Vol 16, No.12, 1971 pp 708-709.

[1.6] Kuffel E., Zaengl W. S. "High Voltage Engineering Fundamantals." Pergamon Press.

[1.7] Nighand W. L., Weigand W. J. "Causes of arcing in CO_2 convection laser discharges." App. Phys. Lett., Vol. 25, No. 11, 1974

[1.8] Dumanchin R.; Michon M.; Farcy J.C.; Boudinet G.; Rocca-Serra J., " extension of TEA CO_2 laser capabilities." I.E.E.E. J. Q.E. Q.E.8, No.2 pp. 1663. 1972.

[1.9] Thomson R.M.; Smith K., "Computer Modelling of Gas Lasers." Plenum Press.

[1.10] Hasan M. A. "Thermodynamics of a transiently pumped CO_2 gas laser plasma." Ph.D Thesis, Department of Mech. Eng. Univ. Of Glasgow, 1989.

[1.11] Chatwin C.R., "Thermodynamics of a pulsed carbon-dioxide laser for machining metals." Ph.D. Thesis Univ. Birmingham. U.K. 1979.

[1.12] Moore C.B.; Wood R.E.; Bei-Lok Hu; Yardley J.T., "Vibrational energy transfer in CO_2 lasers." J. Chem. Phy. pp 4222, Vol. 46, No. 11 1976.

[1.13] Bayabagambi C. A. "Surface heating in metals irradiated by fast I.R. laser pulses." Ph.D. Thesis, Univ. Glasgow, 1987.

[1.14] Denes L.J.; Lowke J.J., "V-I characteristics of pulsed CO_2 laser discharges." Appl. Phy. Lett. Vol 23 No.3 Aug 1973.

[1.15] Baranov V. Yu., Kazsakov S. A. *et al* "Average power limitations in high repetition-rate pulsed gas lasers at 10.6 and 16 μm." Applied Optics, Vol. 19, No. 6 1980.

[1.16] Chatwin C.R., McDonald D. W., Scott B.F., "Design of a high PRF Carbon- Dioxide laser for processing high damage threshold materials." SPIE Vol. 1042 CO_2 Lasers and Applications, 1989.

[1.17] Spall R. "Pulsed power supply for an unstable resonator." Ph.D thesis, Department of Mech. Eng., Univ. Of Birmingham, 1979.

[1.18] McDonald D. W. Chatwin C. R., Scott B. F. " A 100 kW, 10 kHz PRF line type pulser for gas laser pumping." SPIE Vol. 1046. Pulse Power for Lasers II, 1989.

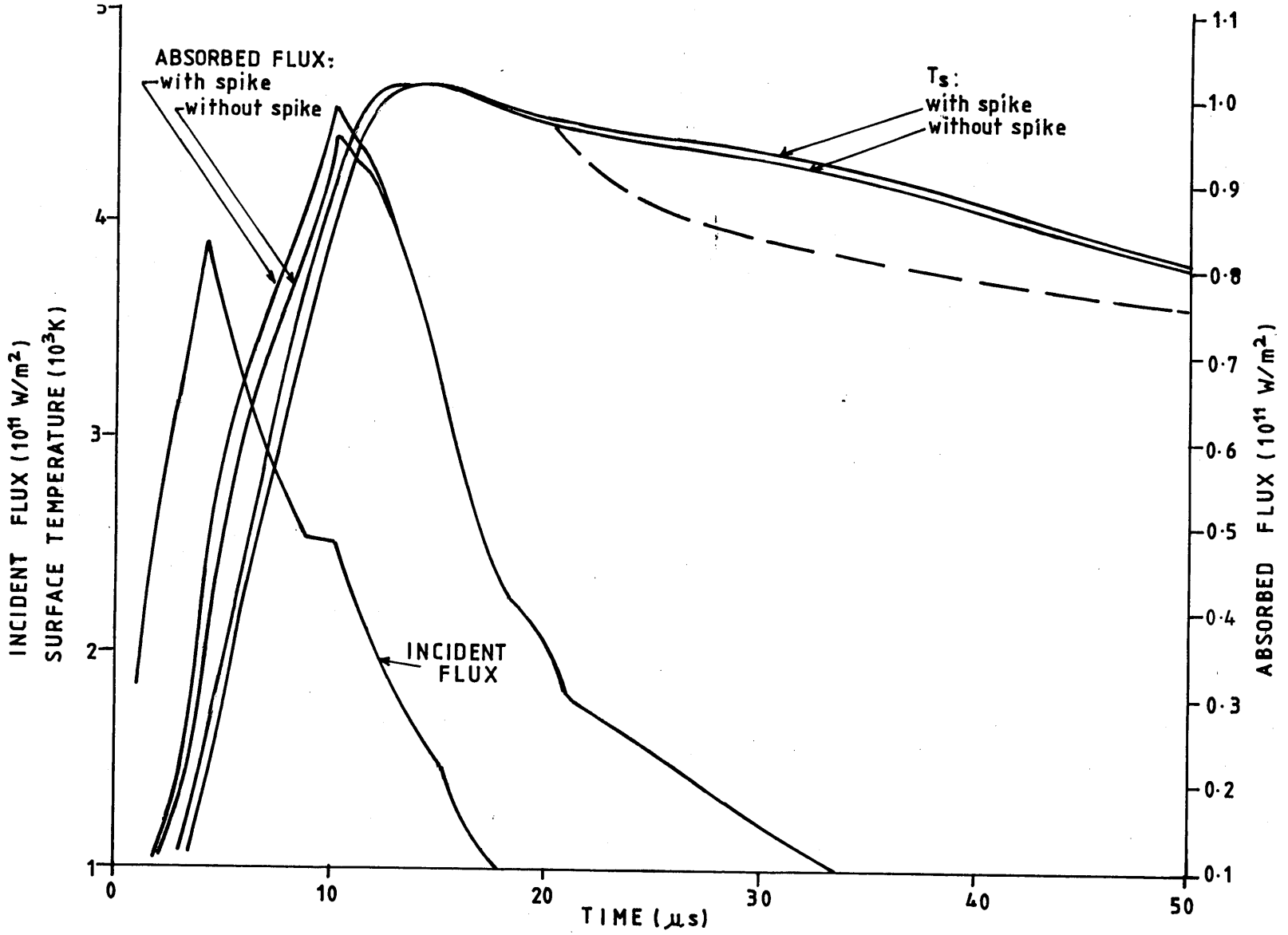

FIGURE 1.1 RESPONSE OF ALUMINIUM TO PULSED CO_2 LASER HEATING

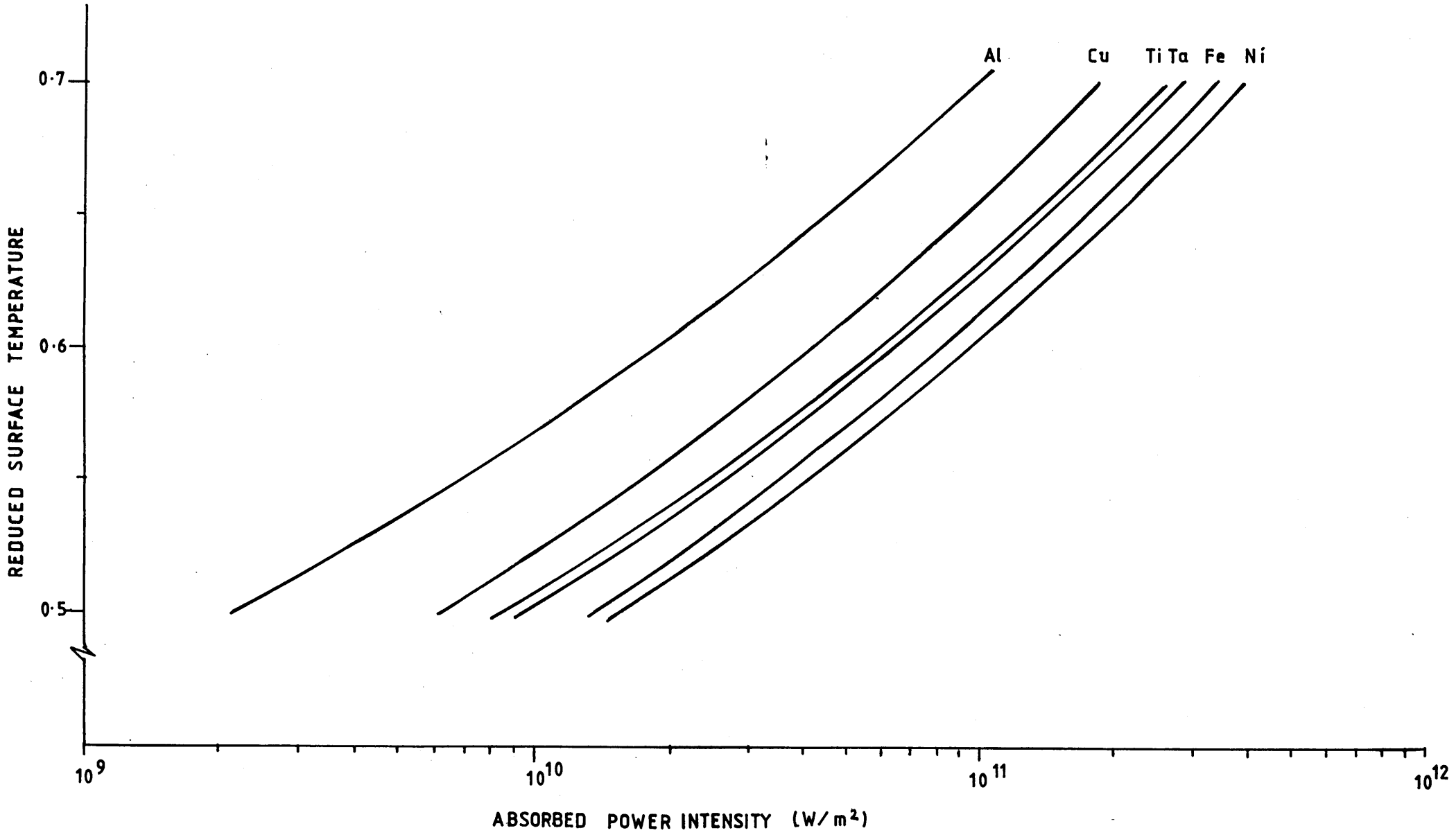

FIGURE 1.2 STEADY STATE SURFACE TEMPERATURE RESPONSE

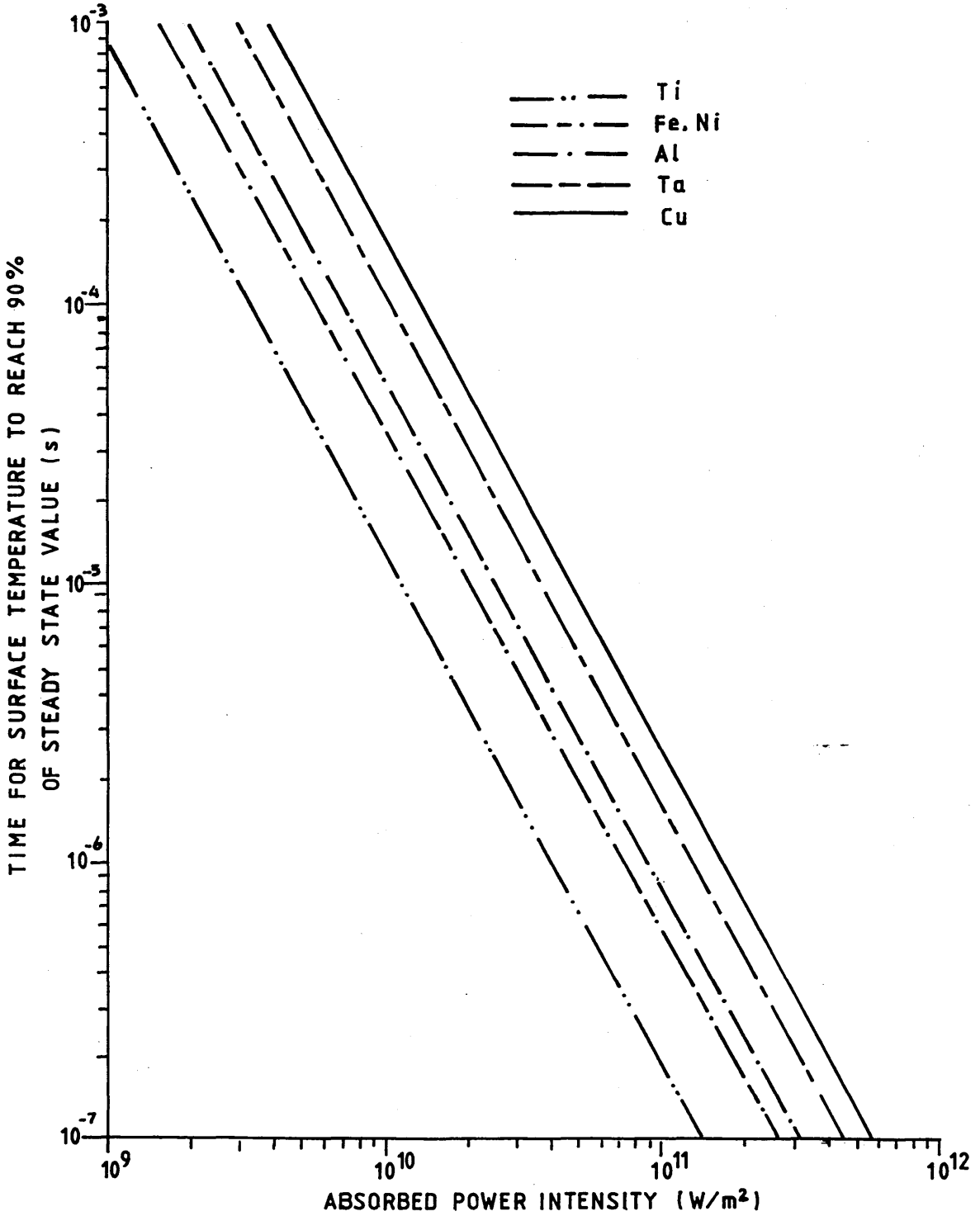

FIGURE 1.3 TIME TO REACH STEADY STATE RELATED TO POWER INTENSITY

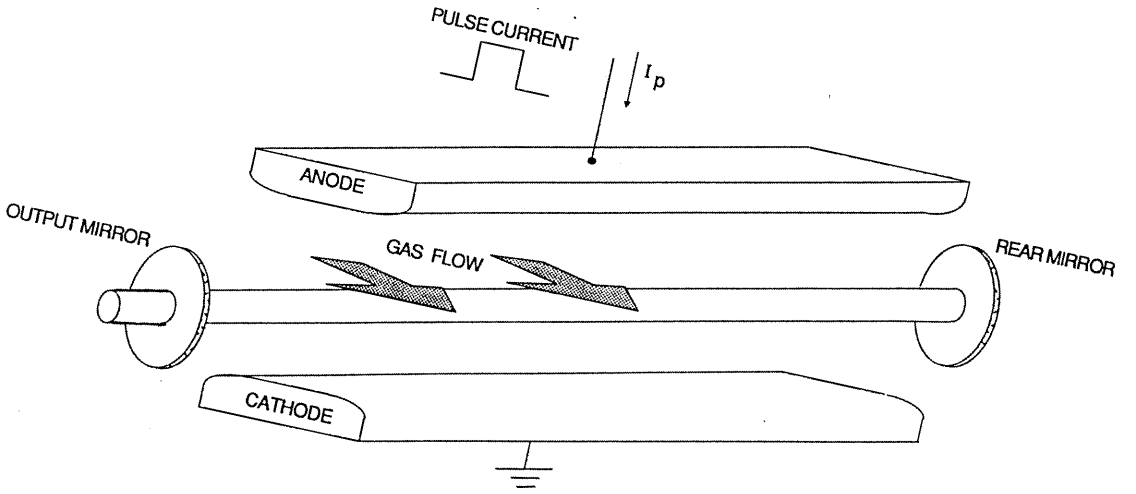

FIGURE 1.4 TRANSVERSE DISCHARGE SYSTEM

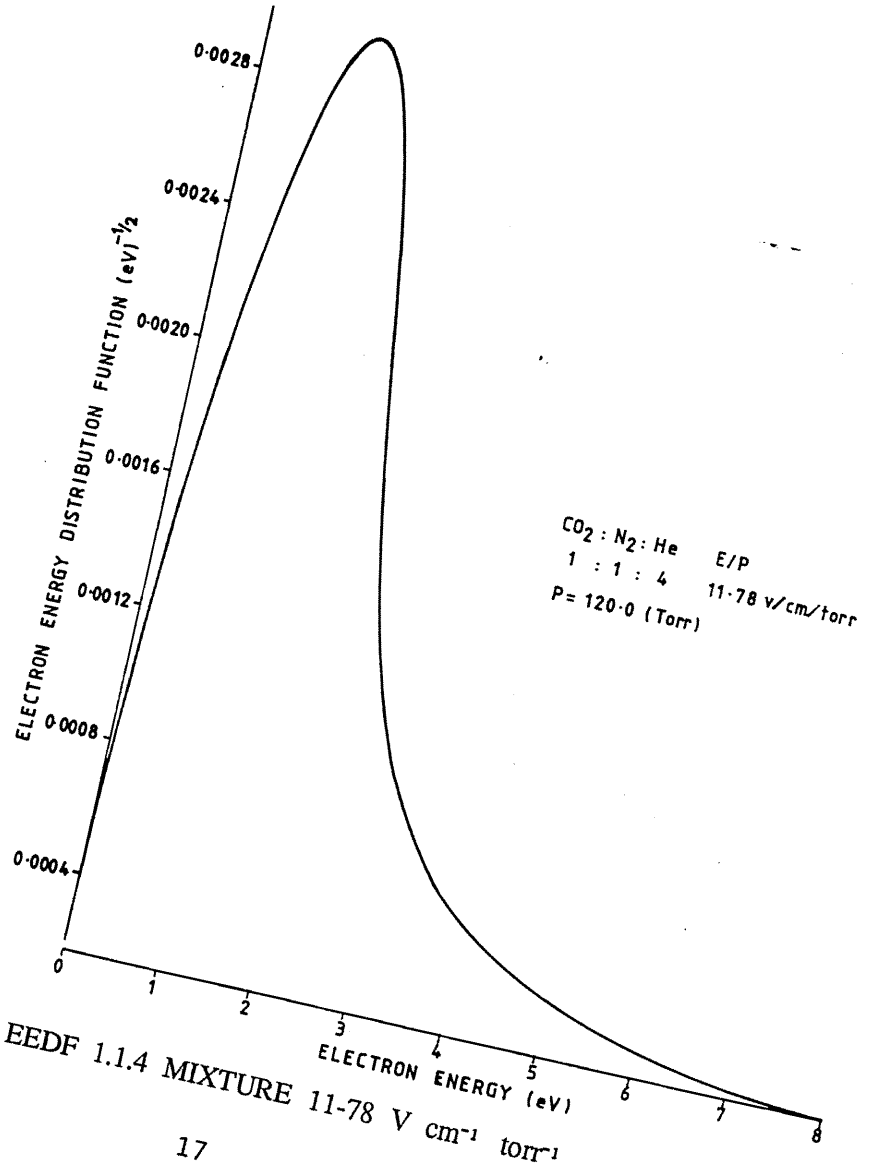

FIGURE 1.5 EEDF 1.1.4 MIXTURE 11-78 V cm^{-1} $torr^{-1}$

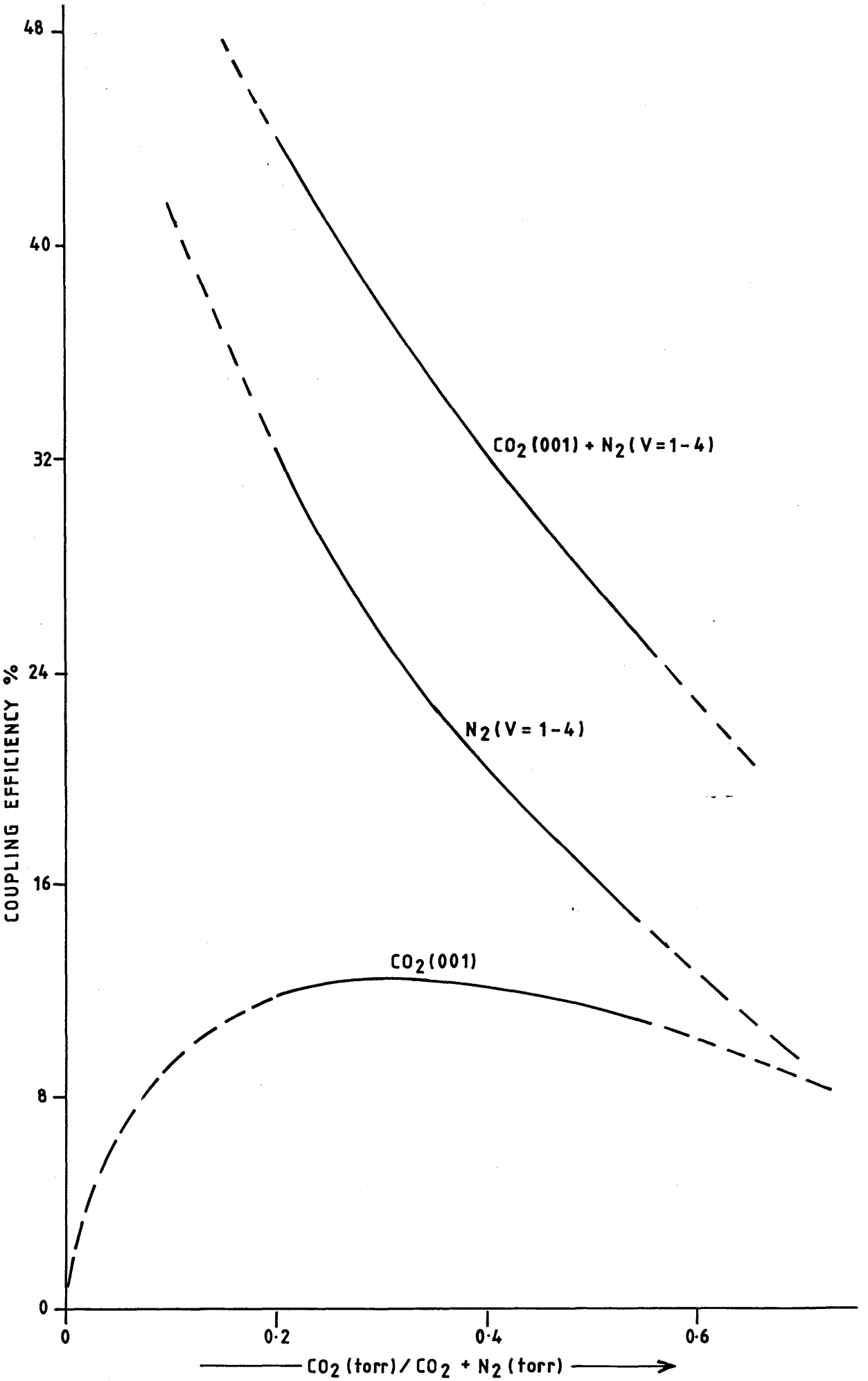

FIGURE 1.6 COUPLING EFFICIENCY VERSUS MIXTURE COMPOSITION

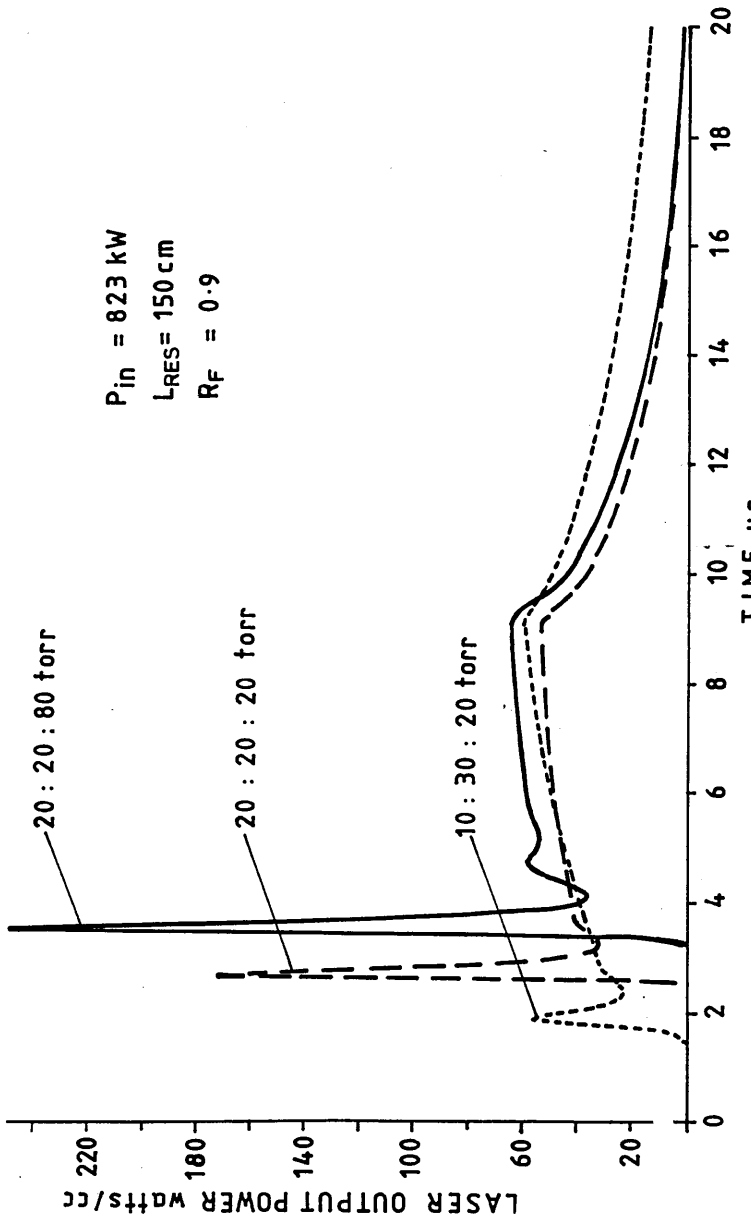

FIGURE 1.7 LASER OUTPUT PULSE CHARACTERISTICS

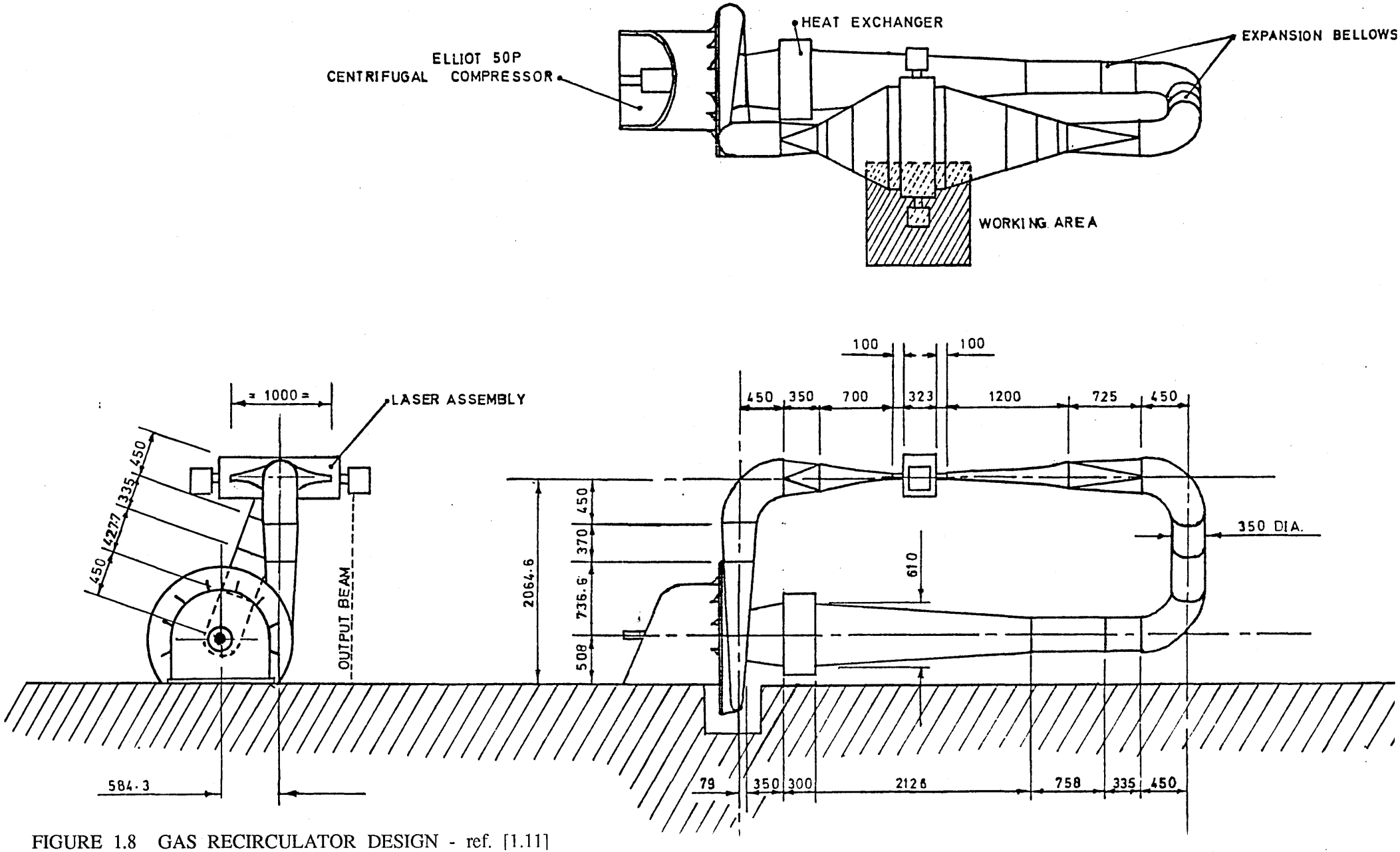

FIGURE 1.8 GAS RECIRCULATOR DESIGN - ref. [1.11]

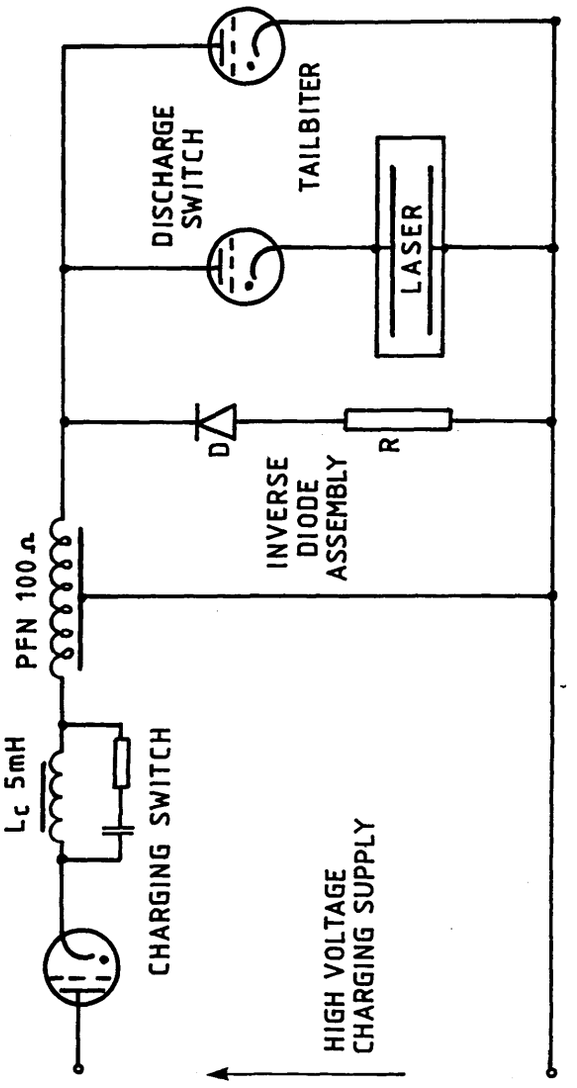

FIGURE 1.9 SCHEMATIC OF PULSER CIRCUIT

(2.0) LASER SYSTEM DESIGN AND DEVELOPMENT.

The prototype laser cavity developed by Khahra [2.1] demonstarated the feasibility of generating laser pulses with the characteristics required for enhanced machining of non−ferrous metals. This prototype was however only capable of running in single shot and short burst mode and as such could not be used to demonstrate the true machining potential of the device. The problem of extending operation of the laser to full continuous pulse mode is primarily associated with gas conditioning. It is well known that stable operation of the discharge depends critically on the removal of the gas from the electrode region in the inter−pulse period [2.2]. It is therefore necessary to ensure a sufficiently high gas flow to convectively clear the discharge volume. One of the main activities in the present work has been to design and construct a high volume flow−rate gas circulator. The design chosen for the circulator reflects the constraints imposed on the project by budget limitations and equipment availability, together with the requirements for "in house" manufacture. Advantage was taken of the department design facilities and where practicable part and assembly drawings were generated on the Ferranti CAMX CAD system. The use of CAD substantially reduced system development time by allowing design modifications to be accomplished with minimal delay.

(2.1) DISCHARGE CAVITY DESIGN.

The experimental work undertaken by Khahra optimised the electrode geometry, electrode material, electrode surface finish and the configuration of the trigger−wires. The main conclusions from this study were:−

(1) The electrodes should be flat along the length with tapered ends to minimise electric field distortion. All edges should have a minimum raduis of $\frac{1}{4}$".

(2) Both electrode material and surface finish appeared to have no influence on the stability of the discharge: shot blasted electrodes performed equally as well as polished ones.

(3) The cathode should have serrations running along the length to create a high intensity electric field for the production of preionization. The depth of the serrations was found to be unimportant.

(4) The trigger−wires should be encapsulated in glass and mounted at a height of approximately 2 mm above the surface of the cathode. The capacitance coupling

the trigger−wires to the anode should be approximately 0.02 μF.

(5) The discharge was found to be sensitive to electrode alignment, with a tendency for arcing at the narrowest point. An alignment tolerance of ± 0.5% was generally required for arc free discharge operation.

Based on these findings Chatwin [2.3] established laser system designs for a 5 kW mean power device; fig. (2.1) shows the proposed laser cavity design. The major innovation with this design is the selection of an epoxy composite for the structural components of the laser cavity, i.e. anode and cathode support beams. It can also be seen that the brass cathode is thermally insulated from the epoxy support beam by ground glass spacers and secured in position by four vacuum sealed brass bolts; these also double as the electrical connection. The anode is aligned by four push−pull mechanisms. For major adjustments of the electrode gap the service sections must be removed and the nozzle and diffuser fixing bolts slackened. The ceramic nozzle and diffuser are spring−loaded giving them the capability of following the anode when fine adjustment is required. The glass insulated trigger−wires are supported through the cathode by glass coated supports which are bonded to the trigger−wires.

The work undertaken by Chatwin identified suitable materials and in addition established designs for vacuum seals, electrode supports and gas flow−shaping. At the start of the present phase of work these designs were reviewed and suitable modifications incorporated reflecting current materials availability and cost. The major design modification was to use a stainless steel vacuum chamber as the structural element of the laser cavity, as shown in fig. (2.2). This permitted great flexibility in the design of the electrodes and gas flow−shaping, allowing almost any transverse electrode configuration to be assembled in the cavity and tested. Fig. (2.3) shows the main components of the re−designed electrode assembly. The complete electrode assembly prior to installation in the cavity is shown in plate (2). The important features of this design will now be considered.

(2.2.1) Electrode Assembly.

The brass anode (74mm x 1165mm) is supported by six epoxy mounts, these being fixed to a $\frac{1}{2}$" aluminium base plate which slides into the cavity. The anode is locked into position by the locking bolts either side of the central section. The complete anode assembly is held in place by four $\frac{1}{2}$" stainless steel bolts through the aluminium base plate into the bottom plate of the laser cavity.

Cathode mounting

The cathode comprises three components, viz, brass top, brass base and stainless steel mounting plate, as illustrated in fig. (2.4). The stainless mounting plate is supported at one end by two micrometer adjustors (VG type LMD25) and at the other end by a spring−loaded pivot arrangement, as shown in fig. (2.5). This permits fine adjustment of the electrodes during operation. Gross adjustment of the electrode spacing requires the cathode to be removed from the cavity and the pivot spacer changed. With this arrangement the cathode is electrically grounded to the laser cavity.

Cavity Flow shaping

This is held within the cavity by the side plates and by the epoxy castings in the case of the anode. These were constructed from 5mm high density poly−ethylene (HPDE) with the exception of the flow surface for which 3 mm PTFE sheet was used. Each assembly was fastened by M3 nylon screws. The flow−shaping is designed with removable end sections to allow access to the cathode support bolts during installation.

(2.1.2) Preionization

Trigger Wires

The stainless steel cathode base plate extends 30 mm beyond the width of the electrodes in order to support the trigger wire assemblies. As illustrated in fig's (2.4) and (2.6), a transversely mounted trigger wire arrangement was selected, this being chosen because of the difficulties associated with supporting the longitudinally mounted wires through the cathode as proposed by Chatwin [2.3]. In addition, it was found that the discharge was filamentary across the width of the electrode due to the trigger wires, thus, mounting the trigger wires transversely meant that the discharge non−uniformity would not affect resonator mode development. The trigger−wires comprise five assemblies, which are mounted on top of PTFE support pillars and electrically connected by brass clamps. The trigger−wire height relative to the cathode is adjusted by brass shims at the bottom of the PTFE support pillars.

(2.1.3) Electrical Connections.

Fig. (2.7) shows the electrical connections to the anode and cathode. The anode is connected to a high voltage busbar situated beneath the laser cavity by four high

voltage vacuum leadthroughs (VG type EFT10). Connection between the anode and the vacuum leadthroughs is achieved by PTFE insulated copper rods. On assembly the connecting rods are screwed into the anode, following which the vacuum leadthroughs are screwed into the tapped connecting rod until the flanges mate. The vacuum leadthrough is then turned to align the bolt holes on the vacuum flange. Power to the laser cavity is supplied by a high voltage coaxial cable (type URm−74), this being connected to the anode busbar by a glanded connector, as shown in fig. (2.8). With this arrangement the outer conductor of the coaxial cable is connected to a $^1/_{16}$" copper sheet which serves the dual function of electrically connecting the cathode − since this is grounded to the cavity structure − and supporting the HDPE anode safety enclosure. A service plate is provided as the side of the safety enclosure for access to the anode bus connection.

The trigger wire coupling capacitors are mounted in the bottom of the anode safety enclosure. Four 20 kV working, 0.02μF capacitors (Hivolt type TPM) are used and can be connected in any arrangement to provide variations in the coupling capacitance. The trigger wires are electrically connected to a EFT10 vacuum leadthrough at each end of the cavity and the coupling capacitors connected to these leadthroughs by URm−77 coaxial cables.

The laser cavity structure is grounded directly to the main laboratory supply panel by a 1" x $\frac{1}{4}$" brass conductor, which is connected by copper braid to one of the anode safety enclosure mounting bolts. This is the only direct earth in the power system.

(2.1.4) Electrode Assembly.

The anode and cathode are assembled on a roller table prior to installation in the cavity, as shown in plate (2). The cathode assembly is held above the anode assembly by aluminium supports at either end. This is accomplished outside the laboratory with the use of a gantry crane and the complete assembly wheeled into the lab on the roller table. When assembled inside the cavity, the cathode is supported by two micrometer adjustors and a spring loaded pivot arrangement, as shown in fig. (2.3) and fig. (2.5). Since the cathode is not attached to the aluminium baseplate, temporary assembly blocks are used to support the cathode during installation, as shown in fig. (2.9). The complete electrode assembly, including gas flowshaping, slides into the cavity whereupon the electrodes are secured in position.

The first operation is to secure the aluminium cathode baseplate by the four bolts into the top of the cavity. The cathode is then located with the spring−loaded support pins and the micrometer adjusters bolted to the stainless base plate; this

end section of the flow shaping to be removed. Once the cathode is secured, the aluminium supports are removed together with the aluminium mounting blocks, and the cathode and mounting plate bolted firmly in position. The anode assembly is then free to move and can be aligned with the electrical leadthroughs on the underside of the cavity.

(2.2) GAS CIRCULATOR DESIGN.

One of the main elements of work during the first half of the project was the design and construction of the high volumetric flow-rate circulator. This is required to remove gas discharge products from the laser cavity in the inter-pulse period. A high thermal capacity gas to water heat exchanger circuit is also incorporated in the circulator to maintain the working gas at as low a temperature as possible. The complete circulator is engineered to vacuum standard and systems incorporated for gas conditioning, control and instrumentation. Before considering the salient features of the design, details are given of the method used to calculate the gas mixture thermodynamic transport properties which were required for the design studies and simulations.

(2.2.1) Computation of Gas Mixture Properties.

The design of the laser cooling systems and gas conditioning systems requires accurate data for the thermodynamic transport properties for the range of laser gas mixtures. This is obtained by combining the thermodynamic data for each gas species in the mixture. The gas mixtures of interest have generally three primary constituents, ie. CO_2, N_2 and He. Fortunately, accurate thermodynamic data for these gases exist, thus, the problem is simply finding a suitable means of predicting bulk mixture properties from this data. The thermodynamic properties required include: Viscosity (μ), thermal conductivity (K), Specific heat (Cp), gas constant (R), Prandtl number (Pr), Specific heat (Cv) and ratio of specific heats (γ). Suitable means of calculating these properties will now be considered.

Specific Heats and Gas Constant.

Properties such as Cp, Cv and R can be obtained from a simple thermodynamic analysis by considering the enthalpy associated with each component mole fraction y_i. It can easily be shown that the mean mixture specific heat is given by [2.4]

$$Cp_m = \sum_{i=1}^{n} y_i \, Cp_i \qquad (2.1)$$

where Cp_i are the individual mixture specific heats. Similarly

$$R_m = \frac{1}{\sum \left(\frac{y_i}{R_i} \right)} \qquad (2.2)$$

Since C_p and R and C_v are related, the mixture specific heat Cv_m can easily be calculated from basic thermodynamics.

The properties of the individual components CO_2, N_2 and He are included in appendix A1. Fig. (2.10) shows a graph of the mixture specific heat v's helium concentration, with equal mole fraction of CO_2 and N_2. Clearly, as the specific heat of helium (Cp = 5.20 kJ/kgK) is much greater than that of N_2 and CO_2, the mixture Cp varies considerably with helium mole fraction. This is important in the selection of mixture compositions, since this determines the thermal capacity of the gas.

Mixture Viscosity

To calculate the viscosity of the low pressure multi-component gas mixture an extension of the rigorous kinetic theory of Chapman and Enskog [2.5] was employed. For an n-component mixture, this kinetic theory result may be approximated as

$$\mu_m = \frac{\sum_{i=1}^{n} \mu_i}{\left[1 + \sum_{j \neq i=1}^{n} \varphi_{ij} \left(\frac{y_i}{y_j} \right) \right]} \qquad (2.3)$$

where the coefficient φ_{ij} is calculated from

$$\varphi_{ij} = \frac{\left[1 + \left(\frac{\mu_i}{\mu_j} \right)^{\frac{1}{2}} \left(\frac{M_j}{M_i} \right)^{\frac{1}{4}} \right]^2}{\sqrt{8} \left[1 + (M_i/M_j)^{\frac{1}{2}} \right]} \qquad (2.4)$$

and

$$\varphi_{ji} = \left(\frac{\mu_j}{\mu_i} \right) \left(\frac{M_i}{M_j} \right) \varphi_{ij} \qquad (2.5)$$

where M_i, M_j are the individual component molecular weights. For the case of a three-component gas mixture, equation (2.3) becomes

$$\mu_m = \frac{\mu_1}{\left[\ 1 + \varphi_{12}\ (\frac{y_2}{y_1}) + \varphi_{13}(\frac{y_3}{y_1})\ \right]} + \frac{\mu_2}{\left[\ 1 + \varphi_{21}\ (\frac{y_1}{y_2}) + \varphi_{23}(\frac{y_3}{y_1})\ \right]} + \frac{\mu_3}{\left[\ 1 + \varphi_{31}\ (\frac{y_1}{y_3}) + \varphi_{32}(\frac{y_2}{y_3})\ \right]} \qquad (2.6)$$

Fig. (2.11) shows the calculated mixture viscosities for the range of mixtures 1:1:0 → 1:1:8. As the viscosities of the three gas components are very nearly equal, the mixture weighted viscosity shows only a small change with composition. Due to the temperature dependences of the constituents a linear increase is observed with temperature.

Mixture Thermal conductivity

To allow for both the translational and vibrational contributions the thermal conductivity for all pure components, K_i, is split into two parts, K_i^* and K_i^{**}, where

$$k_i^* = \begin{cases} K_i/\ [1 + 0.25\ (Cv_i/R_i - 1)] & \text{non-linear molecules } (CO_2) \\ K_i/\ [1 + 0.35\ (Cv_i/R_i - 1)] & \text{linear molecules } (N_2) \\ K_i & \text{monatomic molecules (He)} \end{cases}$$

and K_i^{**} is defined by

$$K_i^{**} = K_i - K_i^* \qquad (2.7)$$

This is termed the Wasseljewa expansion [2.5]. The mixture weighted thermal conductivity is calculated from

$$K_m = \frac{\sum_{i=1}^{n} K_i^*}{\left[\ 1 + \sum_{\substack{j=1 \\ j\neq i}}^{n} (\frac{M_{ij}}{M_i})^{\frac{1}{8}}\ \varphi_{ij}\ (\frac{y_j}{y_i})\ \right]} + \frac{\sum_{i=1}^{n} K_i^{**}}{\left[\ 1 + \sum_{\substack{j=1 \\ j\neq i}}^{n} \varphi_{ij}\ (\frac{y_j}{y_i})\ \right]} \qquad (2.8)$$

where M_{ij} is given by the expression

$$M_{ij} = \frac{(M_i + M_j)}{2} \qquad (2.9)$$

Fig. (2.12) shows the computed mixture thermal conductivities as a function of helium mole fraction and gas temperature. It can be seen that the mixture thermal conductivity K_m increases significantly with helium mole fraction.

The methods of calculating bulk mixture properties as detailed above have been confirmed experimentally by many workers for binary and multi−component mixtures [2.5]. For the low pressure gas mixtures of interest here, since all molecular species are non−polar, it is estimated that the predicted mixture properties are accurate to within ± 5%. No effort was made to confirm these results experimentally.

(2.2.2) Blower Selection.

In addition to supplying the required gas flow for continuous pulse mode operation of the discharge, the blower must be capable of operating under vacuum conditions. Thus, it is a prime requirement that the blower be leak tight to a high standard in order to limit atmospheric contamination of the laser gas mixture. Drive shaft seals must be designed to meet these requirements and additional seals provided between the gearbox and internal casing to prevent oil ingress into the gas system. The blower casing must also be designed to withstand the stresses induced at full vacuum during system pumpdown.

Chatwin [2.3] has investigated the suitability of commercially available gas compressors for high gas flow−rate CO_2 laser applications and has identified optimal compressor designs for this application. It was however concluded that development of a such compressor would be economically unviable and attention should be focussed on existing commercially available compressors. The performance characteristics of both centrifugal compressors and Roots blowers were studied with a view to matching these to the gas flow requirements of low pressure−loss circulator. At the gas flow−rates required for 5 kW mean power operation (25000 m^3/hr based on approximately 4 pulses per gas change) an Elliot 50P centrifugal compressor was identified as meeting the performance characteristics. Due to budget constraints during the present work it was not possible to purchase this machine and an alternative less expensive solution had to be found.

Roots blowers were identified as being the only economically viable solution and two STARVAC 7500 blowers were purchased. With the two blowers running in parallel the volumetric flow delivered is approximately 15000 m^3/hr. This is much lower than the

performance of the Elliot compressor, however, this was a necessary compromise given the limited development budget.

The main advantage of the roots blowers is that they are generally employed for vacuum roughing and backing pump applications and are therefore designed to vacuum specifications. Another advantage is a small variation of gas flow-rate with circuit pressure loss at low pressure ratios, hence, the device does not have to be accurately matched to the circuit flow/ΔP characteristics [2.3]. Fig. (2.13) shows a sectional drawing of the Starvac pump. It can be seen that the drive shaft is vacuum sealed by a viton lip seal (7) and that the gearboxes are sealed internally by two piston ring labyrinth seals (10). The oil used for the gearbox and drip-feed lubricator is Mobil DTE extra heavy, which has a vapour pressure of 1.3×10^{-2} torr at 100 °C.

(2.2.3) Ducting Design.

The ducting connecting the Roots blowers to the laser cavity was designed to give as uniform as possible velocity profile along the electrode length, although sacrifices had to be made in order to limit the circulator ducting to an acceptable size. As the prelimenary design studies undertaken by Chatwin [2.3] indicated that circuit pressure drop was not excessively high and would not reduce the gas flow significantly, the ducts were not designed with full aerodynamic transitions. Fig. (2.14) shows the main components of the circulator; a 3D computer model is also shown in Fig. (2.15).

The gas circulator comprises the two Roots blowers arranged in parallel with heat exchangers at inlet and outlet. The gas exiting from the second exchanger is fed through 250 mm diameter circular pipes to the inlet diffuser, which transforms the velocity profile to a uniform flow across the cavity gas inlet window. The diffuser is constructed of $\frac{1}{2}$" stainless steel, with internal aluminium flow guidance to distribute the flowing gas, as shown in (2.16). The aluminium flow guidance comprises a diffuser section and inlet nozzle; both sections can be removed by unbolting the end flange. After passing through the laser cavity the gas enters the outlet diffuser which incorporates similar internal flow guidance to minimise circuit pressure losses.

Mechanical flexibility for alignment during assembly is provided by stainless steel bellows, positioned either side of the Roots blowers and on the interconnecting pipes. These also cater for thermal expansion and bestow a measure of vibrational isolation between the blowers and the laser cavity. All circular flanges except the blower suction and discharge flanges are sealed by crushable metal rings. The main diffuser flanges and cavity fittings, e.g. lead-throughs and micrometer adjusters, all employ ultra high vacuum (UHV) flanges.

The laser cavity and the inlet/outlet diffusers are supported on a structure constructed of 100 x 100 mm rolled hollow section. The height of the cavity assembly can be adjusted by the 1" support screws; these lock firmly into position on the underside of the ducts and prevent any transverse movement. The Roots blowers are bolted into the concrete floor with "raw bolts." The height and position of the heat exchangers is adjustable to facilitate assembly. On assembly all components were arranged to give optimum cavity height and blower clearance, the stainless steel bends were then welded on the diffuser end flanges in situ. All flanges except on the bellows coupling the bends are bolted with M10 stainless steel fasteners. Due to a slight misalignment on the bends, high tensile steel bolts were used to provide sufficent force to crimp the sealing rings; it was found that the M10 stainless bolts sheared before the flanges sealed properly.

(2.2.4) Design of Laser Cooling System.

It is necessary to maintain the lasing gas at as low a temperature as possible since any increase in gas temperature results in population of the lower laser level, with a subsequent loss of efficiency. Due to the high design power levels and low conversion efficiency, the circulator must be designed to dissipate the substantial heat input in the discharge. In addition, it is also necessary to remove the heat input into the gas by the blowers. As shown in Fig (2.15), in designing the gas circulator provision for heat exchangers was included both before and after the Roots blowers. The design of the gas cooling system was constrained by the limited water supply available in the laboratory and, as as short term measure, a closed cycle reservoir circuit was built to supply a total cooling water flow of 4 l/s to the heat exchangers, as shown in Fig (2.17). The resevoir tank did not include any cooling circuit, thus, the tank was sized to give sufficient heat capacity for continuous operation at full power for a period of 30 minutes.

One of the main criterion in designing the cooling system was the need to ensure full vacuum integrity. Initially a heat exchanger design was proposed which could be manufactured in house, however, it was not possible to guarantee vacuum integrity of the many soldered components. It was therefore decided to purchase cooling coils similar to those used by Control Lasers Ltd, which were manufactured by S&P Coil Products, Leicester. Fig. (2.18) illustrates the type of coil used. This was modified as shown to give four counter–current crossflow tube passes, with eight tubes in each pass. In order to enhance gas side heat transfer the tube assembly is finned with 1/32" copper sheets.

Having identified a suitable exchanger coil, a design study was undertaken to estimate

the number of coils required in each exchanger. Details of the design caluclations are included for reference in appendix A2. Only a brief summary of the design procedure and important conclusions will be given here.

Design Specification

As the design calculations are involved and depend critically on the thermodynamic transport properties of the laser gas mixture, the design study was initially restricted to one gas mixture. A 1:1:8 mixture was chosen as this was identified by Khahra [2.1] to be the most suitable. In addition to the residual heat remaining in the gas from the discharge, the heat exchangers must also dissipate the blower power. The following design specification was used:

	Minimun total laser efficency	$\eta = 6\%$
	Mean output power	$P_o = 5$ kW
$\Rightarrow$	Residual cavity heat load	$Q = 80$ kW

With the inclusion of 18.5 kW maximum blower power, the total system heat load is

$$\underline{Qtot = 117 \text{ kW}}$$

Since the gas flow will be split evenly between the two circuits the design is considered with respect to half the above heat load. The following design specification was used.

Gas flowrate	$V = 7500$ m^3/hr
Gas pressure	$P = 200$ torr
Maximum cavity inlet temp	$T2 = 300$ K
Mean gas temperature	$Tmean = 325$ K
Water flow to each coil	$m_w = 0.5$ kg/s

Fig. (2.19) Shows a schematic of the cooling circuit and details the nomenclature used in the calculations. Since the blower power input results in a gradual temperature rise around the loop, which can only be calculated by a detailed knowledge of pressure losses, it was simply assumed that half of the blower power resulted in a temperature rise across the blower. To err on the conservative side, no allowance was made for conduction through the walls of the ducting.

Heat Transfer Coefficients.

The tubeside coefficient was calculated from the well known formula [2.6] for turbulent flow

$$Nu_{d,m} = 0.023\ (Re_{d,m})^{0.8}\ Pr_m^{0.33} \qquad (2.10)$$

At the design flow of 0.5 kg/s this predicts a tubeside coefficient h_i = 1.77 kW/m^{2}K. This is rather low and is the result of the low water Renolds number, Re = 5866.

The gas side heat transfer coefficient was evaluated for both the tube and fin surfaces by the methods detailed in reference [2.7]. For the staggered tube arrangement

$$Nu = 0.273\ Re^{0.635}\ Pr^{0.34} \qquad (2.11)$$

Where Re is calculated at the minimum cross flow area. This gives a coefficient for the tubes h_{ot} = 0.265 kW/m^{2}K. The coefficient for the fins was evaluated from

$$Nuf = 0.134\ Re^{0.681}\ Pr^{0.33}\ \left(\frac{y_f}{h_f}\right)^{0.2}\ \left(\frac{y_f}{\delta_f}\right)^{0.1134} \qquad (2.12)$$

giving h_{of} = 0.160 kW/m^{2}K. With a fin effectiveness φ = 21.56, the resultant gas side heat transfer coefficient, based on the primary surface area of the tubes is

$$\underline{h_o = 3.546\ kW/m^2K}$$

It can be concluded that with the restrictions on water flow, heat transfer is limited on the water side. Including a fouling resistance and tube conduction terms, the overall heat transfer coefficient was calculated as

$$\underline{U = 1.13\ kW/m^2K}$$

Coil Performance

Due to the complexity of the exchanger coils, the NTU method of heat transfer analysis was used, in favour of the log-mean-temperature-difference method, which relies on graphs of correction factors [2.8]. Since both fluids are "unmixed" the effectiveness of each pass is given by [2.9]

$$\epsilon_p = 1 - \exp\left[\frac{\exp(-N\ n\ C) - 1}{C\ n}\right] \qquad (2.13)$$

where

$$N = \frac{U\ A}{(m\ Cp)_{min}} \qquad \text{No. of transfer units}$$

$$n = N^{-0.22}$$

$$C = \frac{(mCp)_{min}}{(mCp)_{max}} \qquad \text{Capacity ratio}$$

For the specified gas and water conditions, the gas is the minimum head capacity fluid, giving a capacity ratio C = 0.443. From equation (2.15), the effectiveness per pass is ϵ_p = 0.1218. With four cross–flow passes in each coil, the overall coil effectiveness is calculated from [2.7]

$$\epsilon_c = \frac{\left[\frac{1 - \epsilon_p C}{1 - \epsilon_p}\right]^4 - 1}{\left[\frac{1 - \epsilon_p C}{1 - \epsilon_p}\right]^4 - C} = \underline{0.386} \qquad (2.14)$$

Number of Coils Required

Since the effectiveness of each coil is defined as

$$\epsilon_c = \frac{\text{Temperature change of minimum fluid}}{\text{Maximum possible temperature change}}$$

The gas temperature at the outlet of each coil to can be expressed in terms of the inlet gas temperature, T_i, and water inlet temperature, t_i, by

$$T_o = T_i - \epsilon_c\ (T_i - t_i) \qquad (2.15)$$

For the design specification used, based on an initial inlet temperature of 300 K, it was found that with two coils in each exchanger, that the temperature of the gas after passing once round the loop was 301 K. This was very close to the initial assumed value and indicates that this is close to the equilibruim gas temperature. Thus, it can be concluded that two coils in each exchanger provides satisfactory cooling for the specified mixture and flow conditions.

In order to investigate fully the off–design performance of the cooling system, a detailed transient system model was developed. Details of the derivation of the model equation are included in appendix A3.

Cooling System Modelling

The equations governing the transient thermodynamic behaviour of the cooling system were obtained by applying the first law to the system depicted in Fig. (2.19). This yielded.

$$Q_L + Q_b = Q_{EX} + M_g C_p \frac{dT_{mean}}{dt} \quad (2.16)$$

$$Q_{EX} = Q_{EX1} + Q_{EX2} \quad (2.17)$$

$$Q_{EX1} = m_g C_p (T_1 - T_2) = wC_{pw} (t_{2A} - t_1) \quad (2.18)$$

$$Q_{EX2} = m_g C_p (T_3 - T_4) = wC_{pw} (t_{2B} - t_1) \quad (2.19)$$

Where the above notation is defined in appandix A3. T and t are respectively the gas and water temperatures at the position indicated by the subscript. In deriving the solution it was assumed that to a good approximatation the mean gas temperature is given by

$$T_{mean} = \tfrac{1}{2} (T_1 + T_4) \quad (2.20)$$

It was also assumed that the effectiveness of both exchangers is constant. With two coils in each exchanger unit, the exchanger effectiveness ϵ can be shown to be equal to

$$\epsilon = \epsilon_c (2 - \epsilon_c) \quad (2.21)$$

Using the NTU relations

$$\epsilon = \frac{T_1 - T_2}{T_1 - t_1} = \frac{T_3 - T_4}{T_3 - t_1} \quad (2.22)$$

and eliminating variables, yields the following set of goverining equations.

$$\frac{dt_1}{dt} = \frac{2}{M_g C_p(2 - 2\epsilon + \epsilon^2)} \left[Q_L - m_g C_p(T_1 - T_4) - \frac{\epsilon(2 - \epsilon)}{2} M_g C_p \frac{dt_1}{dt}\right] \quad (2.23)$$

$$\frac{dt_1}{dt} = \frac{m_w C \epsilon}{M_w} \left[(T_1 - t_1) + (T_3 - t_1)\right] \quad (2.24)$$

$$T_3 = T_2 + \frac{Q_b}{m_g C_p} \quad (2.25)$$

$$T_2 = T_1 - \epsilon(T_1 - t_1) \qquad (2.26)$$

$$T_4 = T_3 - \epsilon(T_3 - t_1) \qquad (2.27)$$

These equations are arranged in a form which can be implemented directly for solution with the Advanced Continuous Simulation Language (ACSL). Appendix A3 includes a print-out of the ACSL code.

Fig. (2.20) shows the transient response of the gas temperature for a 1:1:4 mixture, with a gas flowrate of 7500 m^3/hr (each blower) and a cavity heat load and blower power of 80 kW and 18.5 kW respectively. It can be seen that due to the low thermal capacity of the gas that equilibruim is reached in approximately 10 seconds. For a 1:1:8 mixture at the design conditions, the computed equilibruim temperatures at the cavity inlet and outlet are respectively 28.3 °C and 81.8 °C. At these conditions 21.8 kW was removed in the first exchanger and 20.14 kW in the second exchanger.

The off-design performance was examined by varying the gas flowrate, mixture composition and cavity heat load. Fig's (2.21) and (2.22) show the equilibrium temperatures as a function of the cavity heat load for 1:1:4 and 1:1:8 mixtures. These results were computed at a constant blower power of 8 kW, assuming half of this appears as a temperature increase across the blowers. Fig's (2.23) and (2.24) show the equilibrium temperatures at both the full blower gas flow-rate and at 50% of the full flowrate. The following data was calculated at these settings

		3750	7500 m^3/hr	
Mass flowrate of gas	m_g	0.1069	0.213	kg/s
Capacity ratio	C	0.221	0.442	
Gas side heat transfer coeff.	h_o	2.211	3.537	kW/m^2K
Number of transfer units	N	0.229	0.136	
Coil effectiveness	ϵ_c	0.567	0.384	
Exchanger effectiveness	ϵ	0.812	0.621	

It is clear from these results that although increasing the gas flow-rate increases the gas side heat transfer coefficient, since the coil effectiveness, as given by equations (2.15) and (2.16), depends on the values of the capacity ratio and number of transfer units, the net result of increasing gas flow is a drop in exchanger effectiveness. As shown in fig. (2.24), the cavity outlet temperature is much higher at the lower flow-rate due to the reduced thermal capacity of the gas.

In conclusion, the cooling system was found to give excellent performance throughout the range of mixture compositions and cavity power levels and no design modifications were required. Plate (4) shows the internal components of the heat exchangers. The coils are held in a stainless steel vacuum chamber, which is sealed by 'o' rings on the top plate and on the copper header tubes.

(2.2.5) Gas System.

Fig. (2.25) illustrates the main components of gas systems, including system pumpdown, gas initialisation and cavity pressure control. This system was designed with vacuum isolating valves (Edwards type PVEK) at the inlet and outlet pipes to the gas circulator, a configuration which allowed all other gas components to be rated for atmospheric pressure operation. Pumpdown is provided by a rotary piston pump with a constant gas flowrate of 50 m^3/hr in the pressure range 0.1 – 760 torr. With a total circulator volume of 2.4 m^3, system pumpdown ($P < 1$ mbar) is achieved in approximately 20 minutes. All valves and pumps are controlled remotely from the circulator controller, which has provision for automatic gas refresh and cavity pressure control. This is interlocked with the power supply control module to trip the pulser in the event of the pressure exceeding a preset limit.

System Initialisation

The three primary constituent gases are supplied to the solenoid valves V_1–V_3 from regulated "K" cylinders. These are operated one at a time to fill the system in the correct partial pressures for the desired mixture. The flow into the vacuum chamber is controlled by the needle value NV_1. The system is initialized with the vacuum isolating valve S_2 open and valve S_3 closed. The complete initialisation process can be controlled automatically, with the partial pressures being set by BCD counters on the front panel of the control unit.

System Refresh

During continuous operation of the discharge the gas mixture becomes contaminated with dissociation products and O_2 from atmospheric leakage. To counteract the deletereous effects of the contaminants on discharge stability a fresh purge of gas is supplied to the laser. The refresh flow is controlled by the metering valves, with the flows being read on the variable area flowmeters. The system is capable of a controlled refresh flow from 0.01–0.1% of the total circulator volumetric gas flow. To prevent cavity pressure build up gas is pumped out of the system by the vacuum pump. During refresh the cavity pressure is controlled by a single PID control loop

comprising a pressure transducer and servo-driven control valve. A manually activated bypass valve is provided across the control valve for system pumpdown.

(2.2.6) Gas Recirculator Instrumentation.

The gas circulator was instrumented to provide the required data for performance analysis during operation. Fig. (2.26) indicates the position of the $\frac{1}{4}$" BSP tapping points. When deciding on suitable instrumentation, particular attention was paid to noise immunity in view of the excessive interference generated by the laser pulser.

Two-wire platinum resistance thermometers (PRT) were chosen for temperature measurement because of high noise immunity. The stainless steel sheathed probes were inserted at all the tapping points, with the leads being connected to a 12 way selector switch and digital panel meter. Four wire PRT's were also used to monitor the cooling water temperatures at the inlet and outlet from each heat exchanger. To permit a full thermodynamic performance analysis. These measurements were complemented by measurements of the water flows to each exchanger, for which turbine meters were used.

Strain guage pressure transducers (National semiconductor LX06015A) were selected for gas pressure measurements. Since these had a very low sensitivity it was decided to house the transducers remotely in a screened enclosure and feed the pressure to the transducers via static tubes. A schematic of the transducer assembly is shown in fig. (2.27). Due to the high cost of the transducers, pressure measurements were only made at the cavity inlet and outlet and and at the suction and discharge of both blowers. An additional pressure tapping in the cavity was connected to an Edwards EMV251 guage to give an accurate measurement of the cavity pressure. The output from the guage was also fed to a signal conditioning circuit for the control of gas refresh and initialisation.

(2.3) OPTICAL SYSTEM DESIGN.

The design of an optical resonator for the high PRF CO_2 laser has been investigated by Khahra [2.1], Spall [2.10] and Chatwin [2.3]. The majority of this work has been computational in nature, with the exception of the experimental results reported by Khahra. It is intended here to give a brief review of the important results obtained in the earlier studies, before considering the design chosen for the present development. Following this, some details of the beam delivery system will be given in section (2.3.2).

(2.3.1) Optical Resonator Design.

The first problem associated with the design of the optical resonator is matching the beammode volume to the geometry of the discharge. In this context Spall [2.10] proposed an unstable resonator configuration, since by careful design it is possible to obtain very high resonator coupling efficiencies. Fig's (2.28) and (2.29) show the unstable resonator configurations considered by Spall. Of these, the positive-branch confocal was chosen since the negative branch configuration has the disadvantage of an intra-cavity focal spot, which gives rise to undesirable local effects at high powers. It can be seen from fig. (2.28) that the radiation is coupled out of the cavity around the output mirror, an arrangement which makes the support of this mirror practically impossible, without in some way affecting the output beam. This problem is overcome by using a "scraper" mirror to extract the power from the cavity, as shown in fig. (2.30). This has the additional advantage of allowing the beam to be steered independently of the resonator axis.

The resonator design of fig. (2.30) is however not without problems. Firstly, the design and alignmenmt of the scraper mirror is extremely difficult. Secondly, the output beam takes the form of an annular ring of considerable diameter. This necessitates an equally large output window which must be capable of taking a full vacuum pressure differential and as such would be a very expensive item. In addition, the near-field pattern of this resonator is esssntially a uniformly illuminated annulus, giving a far-field pattern for the focussed beam with a strong central lobe, surrounded by annular rings of decreasing intensity. As the width of the annulus is increased, i.e. by increasing the output coupling, the amount of power in the surrounding rings at the focal spot is decreased. Therefore, a high focal spot intensity requires a high resonator output coupling.

Chatwin [2.3] has examined through simulations of the laser kinetics the influence of resonator design parameters on the temporal characteristics of the output pulse. As shown in fig. (2.31) the output pulse takes the form of a high intensity spike followed by a relatively constant plateau. As the spike has a detrimental effect on the materials processing, due to emitted plasma from the workpiece, the influence of resonator design parameters on spike height was examined. Fig. (2.32) shows the variation of spike height with the output coupling and cavity length. The main conclusion to be drawn from these results is that for a given mixture composition, the gain-switched spike can be suppressed by increasing the cavity length or decreasing the output coupling. Thus, returning to Spall's proposed design, fig. (2.30), this can only be achieved by reducing the resonator output coupling, as the resonator length is fixed by the size of the vacuum chamber. This makes the design of the scraper mirror

practically impossible and results in an output beam dominated by mirror edge effects. The requirements imposed by spike suppression are also in conflict with focal spot parameters. The unstable resonator was therefore dismissed on these grounds.

Stable Z resonator

In view of the difficulties associated with control of the spike with an unstable resonator, a stable resonator design was adopted. In order to increase the resonator coupling efficiency a Z configuration was chosen, as illustrated in fig. (2.33). With this arrangement the beam passes through the discharge three times in each direction. The increased resonator length also reduced spike height significantly. The beam is coupled out of the resonator via a 50 mm diameter, AR-coated zinc-selenide window. Three optics were purchased with reflectivities of 75%, 80% and 85%, in order to investigate the effect on spike height. The 20 meter radius of curvature and plain Z mirrors are gold coated copper. An intra-cavity water cooled aperture is included to restrict operation to lower order modes.

Mechanical design

The optical resonator is enclosed entirely within the stainless steel cavity chamber. Plate (5) shows the view looking in from the position of the output window. Fig. (2.34) shows a sectional drawing of the output window. This is supported in an optical mount with differential micrometers for adjustment. The output window is cooled both by an air jet on the face and by water around the edge. The rear mirror is also held in an adjustable optical mount with differential micrometers. The two Z mirrors are aligned during assembly with the aid of brass shims. All mirrors are water cooled.

(2.3.2) Beam Delivery.

The output beam is directed within a 2" aluminium pipe into a polycarbonate safety enclosure, which houses the for-optics assembly and work handling, as shown in fig. (2.35). The fore-optics includes a water cooled cone calorimeter/beam dump and a servo-driven focussing lens assembly. The beam is focussed onto the workpiece by a 100 mm focal length salt lens, as shown in fig. (2.36). This is gas cooled on the face and edge cooled through a water cooled copper heat sink. A gas nozzle is included for the co-axial assist gas jet. The fore-optics box includes provision for a HeNe laser which is used to align the optical resonator.

REFERENCES FOR CHAPTER (2)

[2.1] Khahra J.H., "Optimisation of the output characteristics of a pulsed carbon−dioxide laser for processing of materials." Ph.D. Thesis Univ. Birmingham, Dec 1976.

[2.2] Baranov V. Y., Malyuta D. D., Mezhevov V. S. "Utilization efficiency of gas flow pulse−periodic CO_2 lasers." Sov. J. Quantum electron 8(10), 1978.

[2.3] Chatwin C.R., "Thermodynamics of a pulsed carbon−dioxide laser for machining metals." Ph.D. Thesis Univ. Birmingham. U.K. 1979.

[2.4] Rogers G.F.C., Mayhew Y.R. "Engineering thermodynamics, work and heat transfer." Longman.

[2.5] Reid R.C., Sherwood T.K. "The properties of gases and liquids − their estimation and correlation." McGraw − Hill 1966.

[2.6] Burmeister L.C. "Convective heat transfer." Wiley.

[2.7] "Convective heat transfer during crossflow of fluids over plain tube banks." Engineering Science Data Unit.

[2.8] Butterworth D. "Introduction to heat transfer" Wiley.

[2.9] Wong H. "Handbook of essential formulae and data on heat transfer." Longman.

[2.10] Spall R. "Pulsed power supply for an unstable resonator." Ph.D thesis, Department of Mech. Eng., Univ. of Birmingham, 1979.

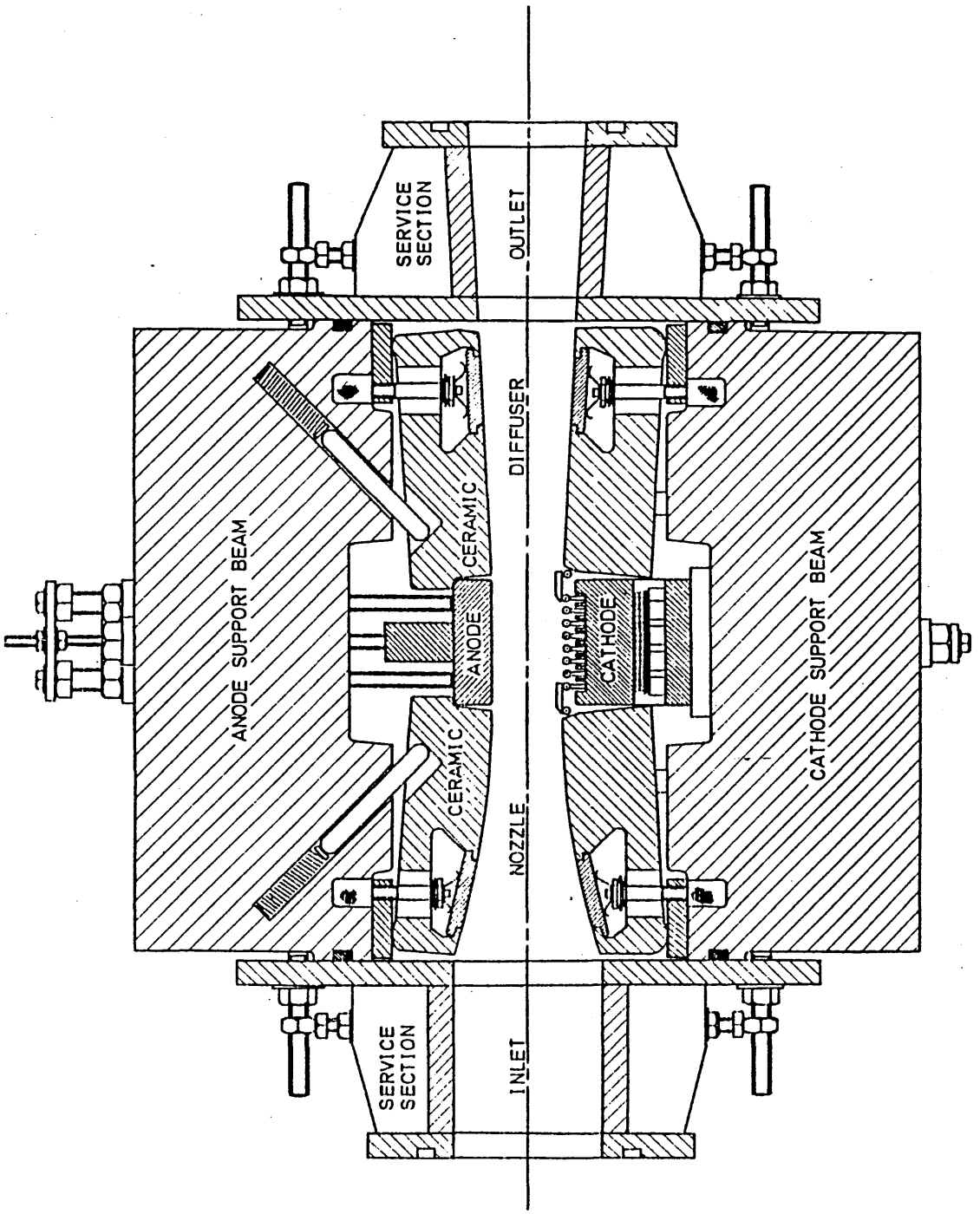

FIGURE 2.1 CAVITY DESIGN PROPOSED BY CHATWIN

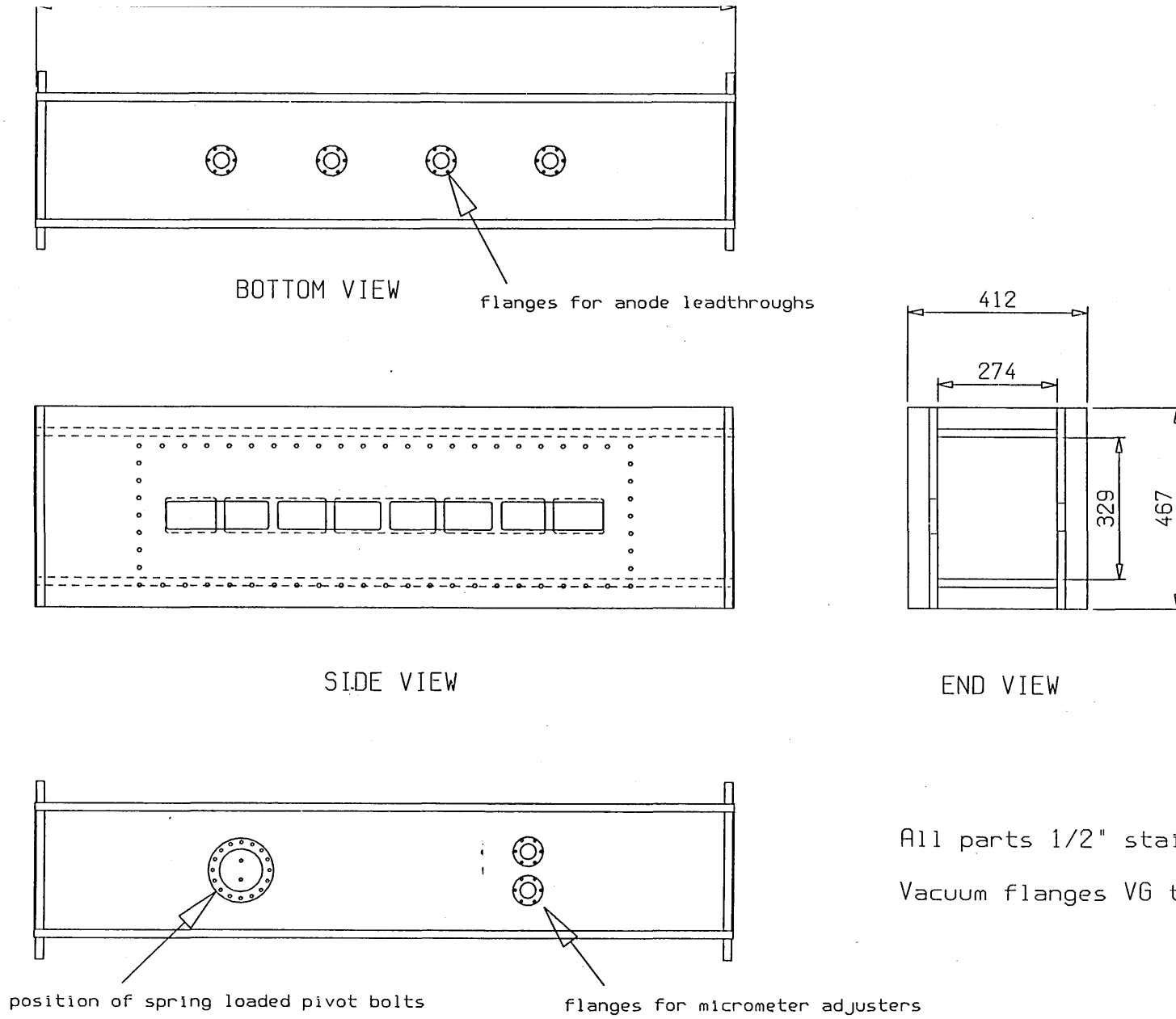

FIGURE 2.2 STAINLESS STEEL LASER CAVITY CHAMBER

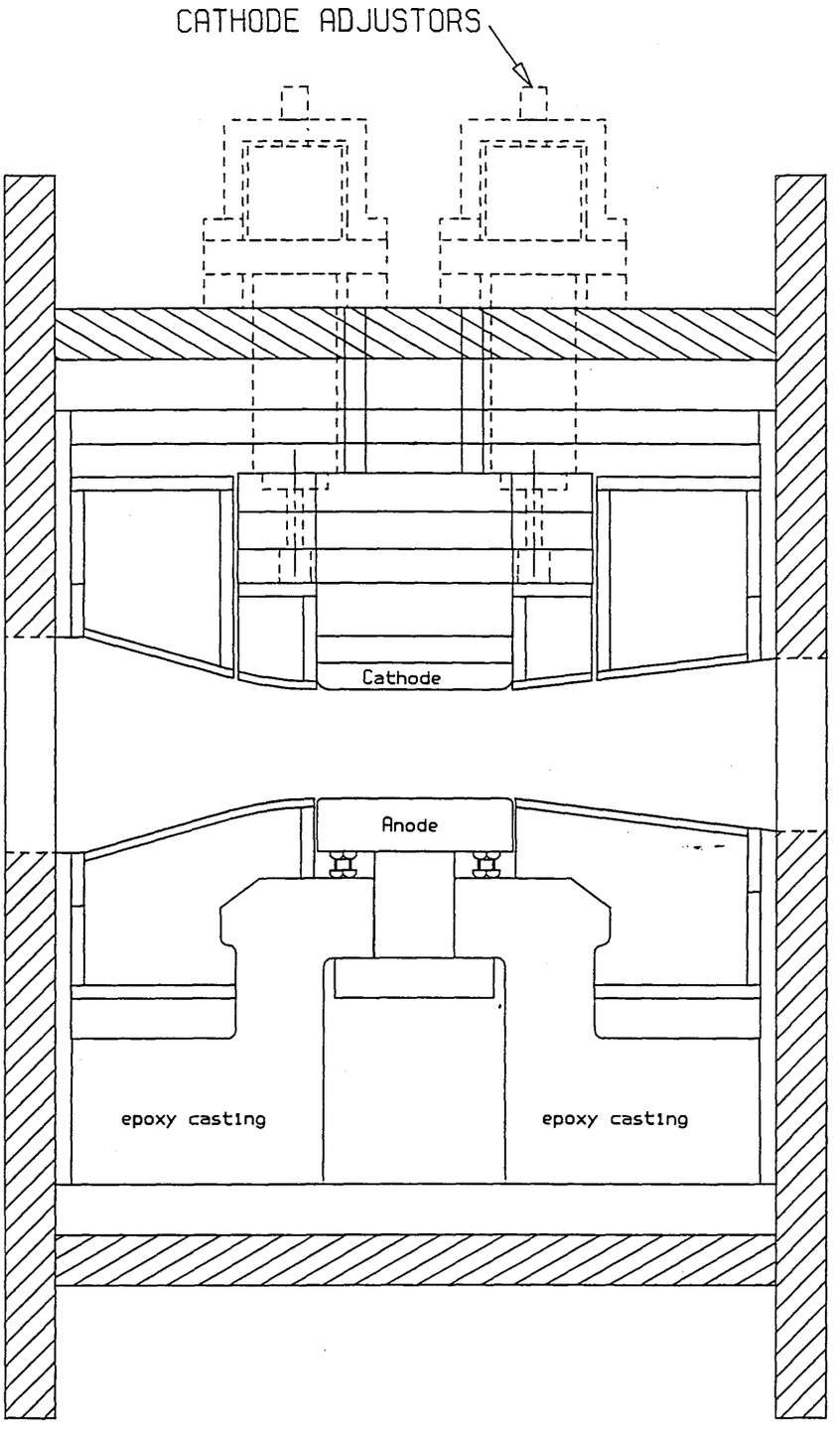

FIGURE 2.3 LASER CAVITY ASSEMBLY

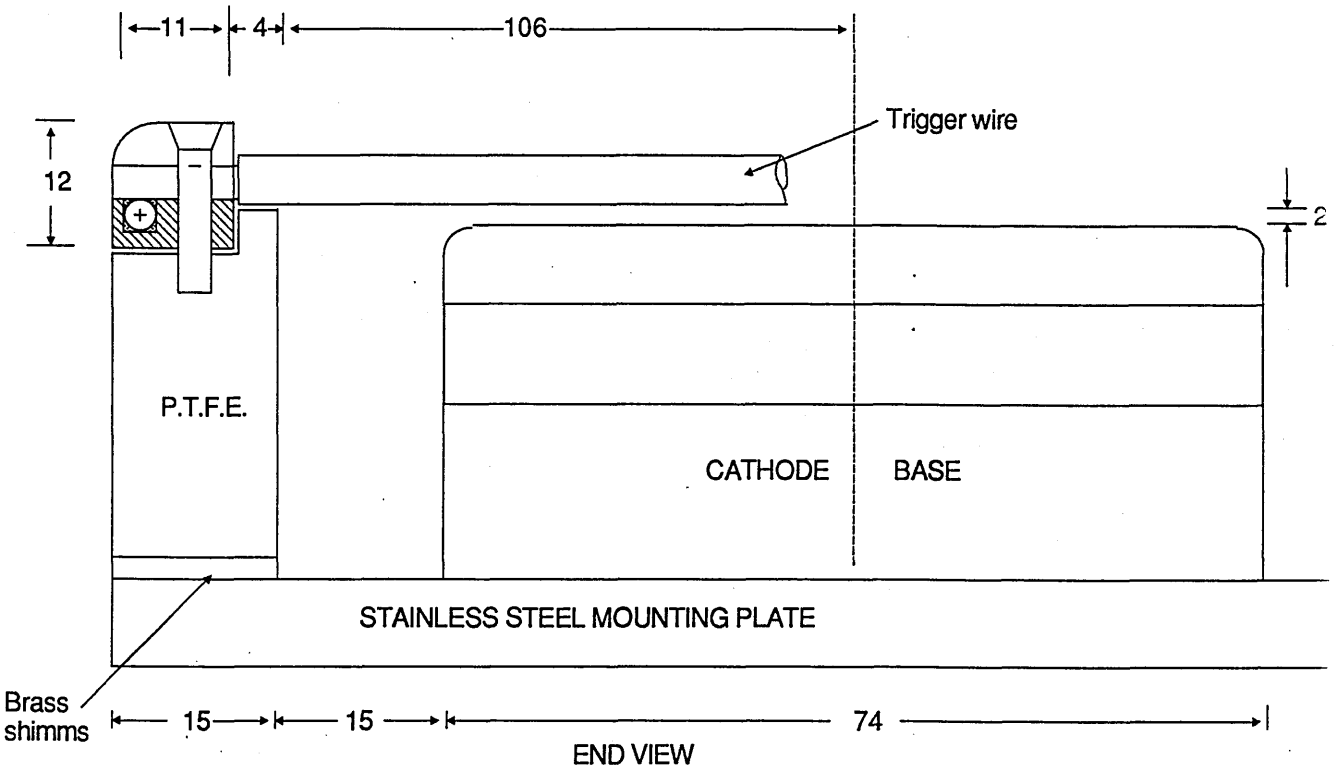

FIGURE 2.4 SCHEMATIC OF CATHODE

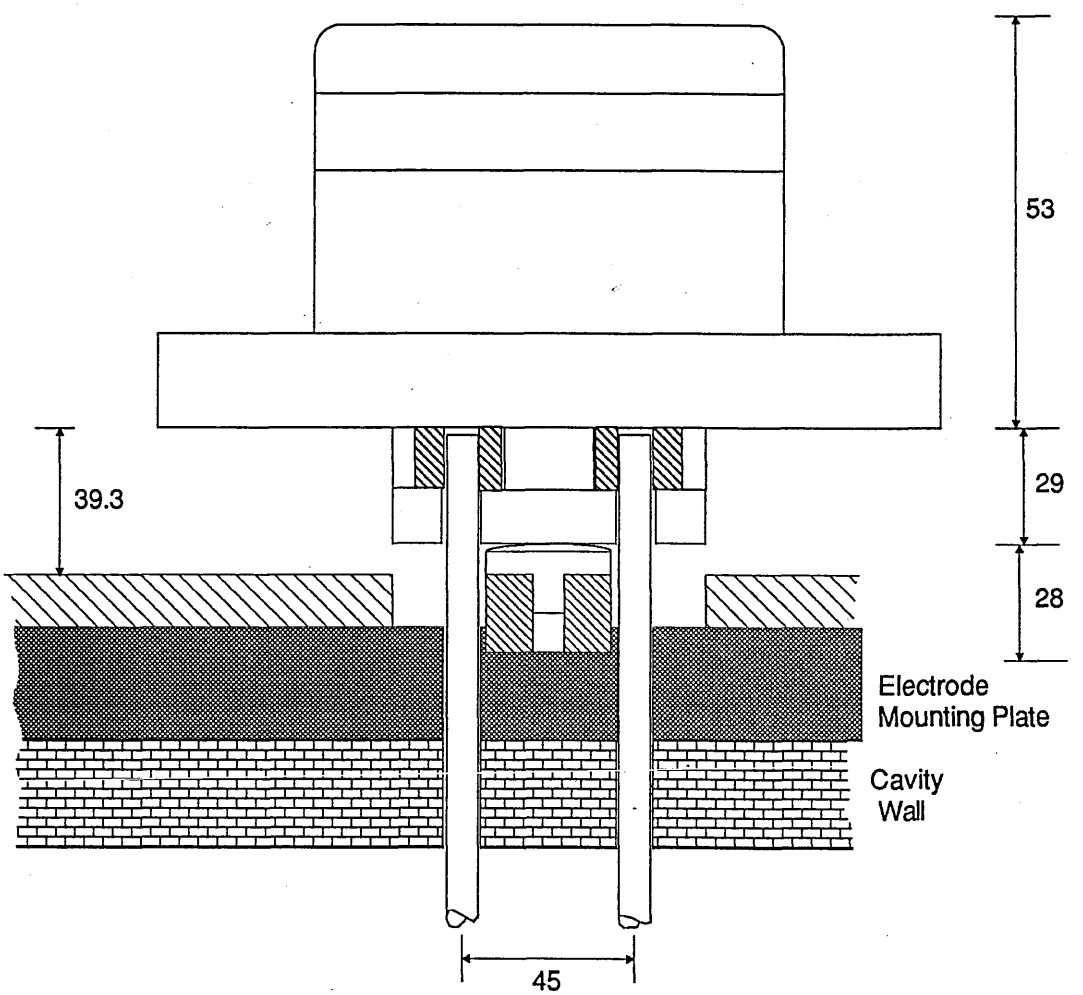

FIGURE 2.5 CATHODE PIVOT SUPPORT

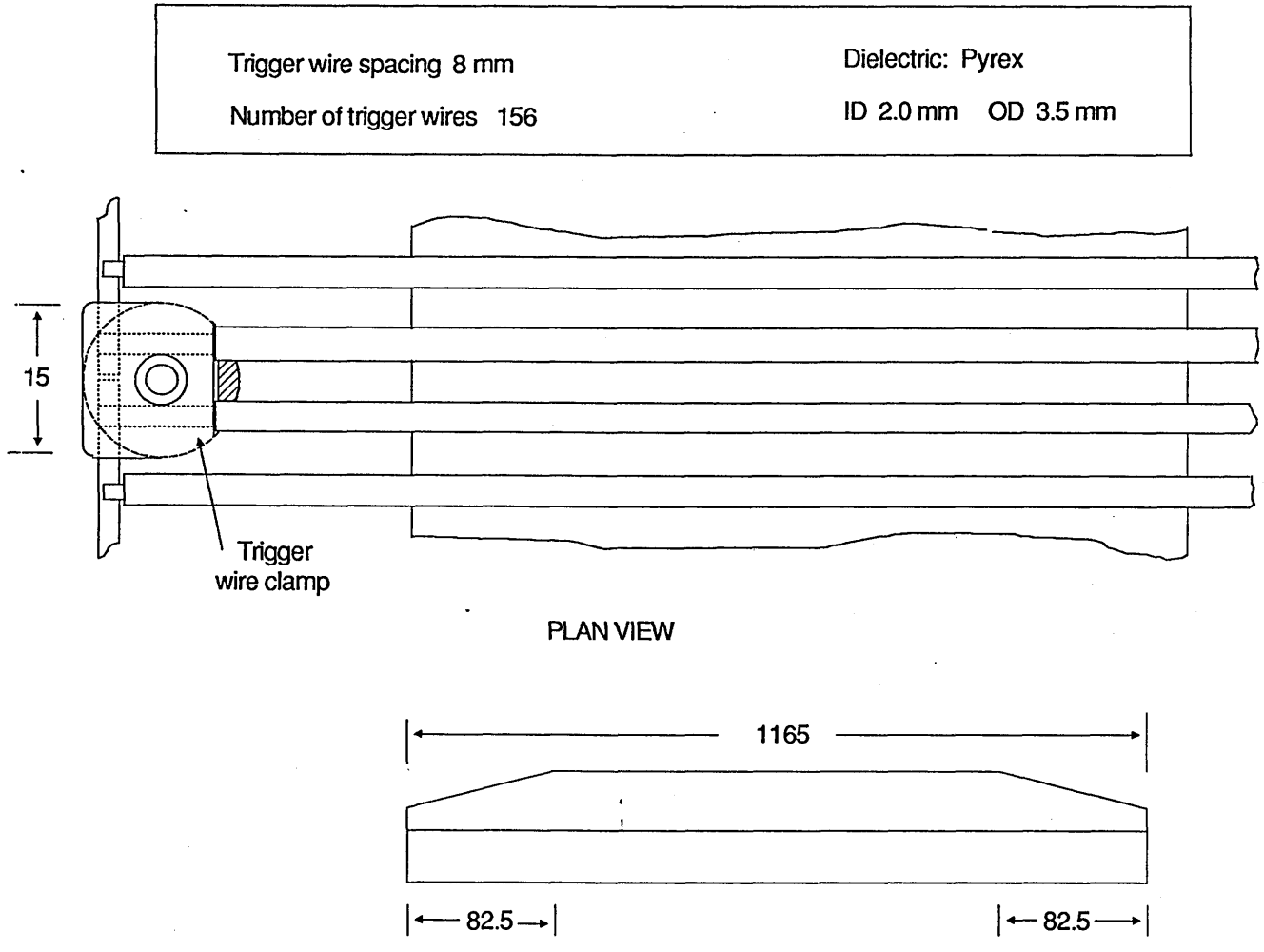

FIGURE 2.6 SCHEMATIC OF TRIGGER WIRE ASSEMBLY

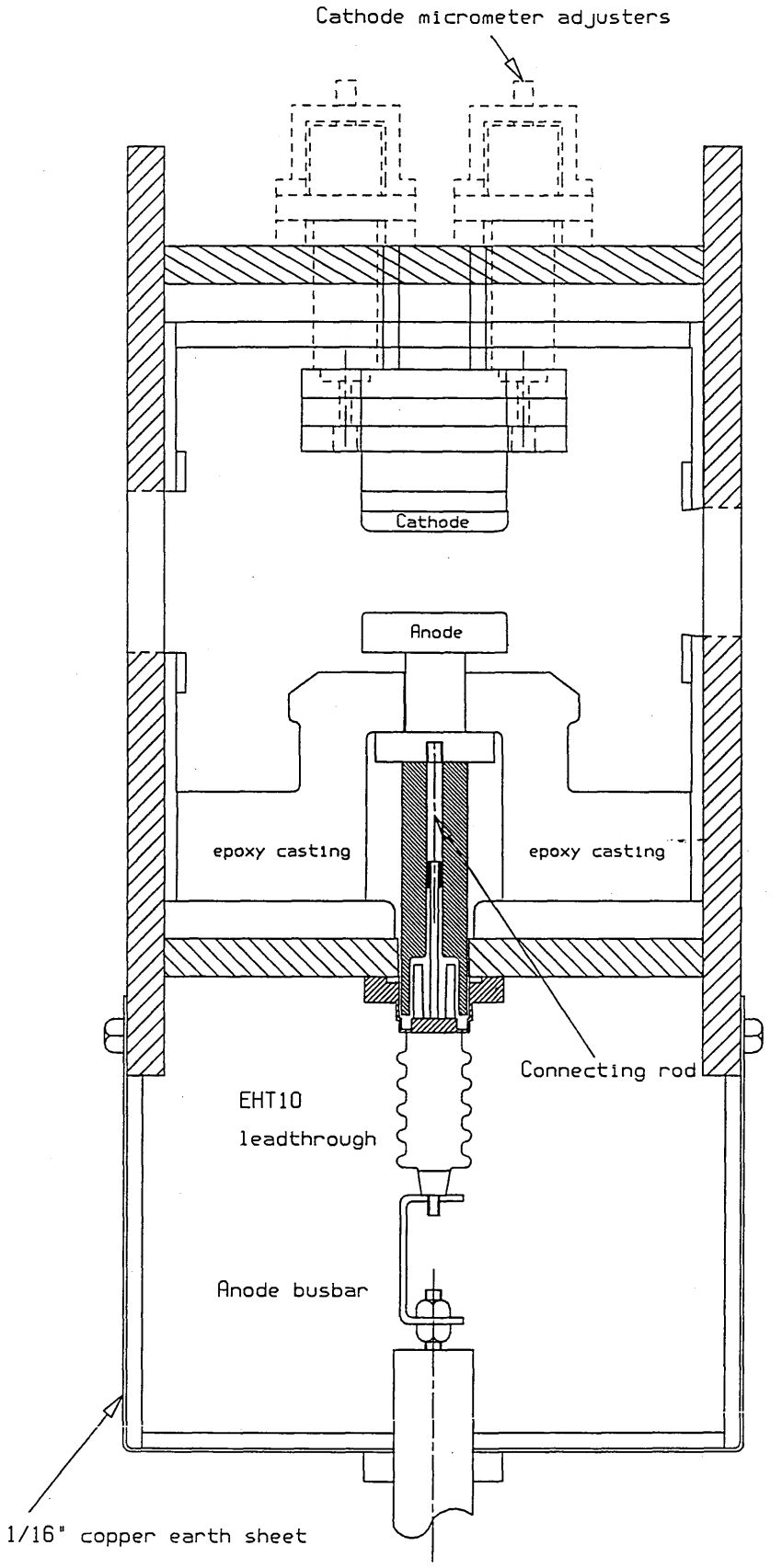

FIGURE 2.7 SCHEMATIC OF ELECTRICAL CONNECTIONS

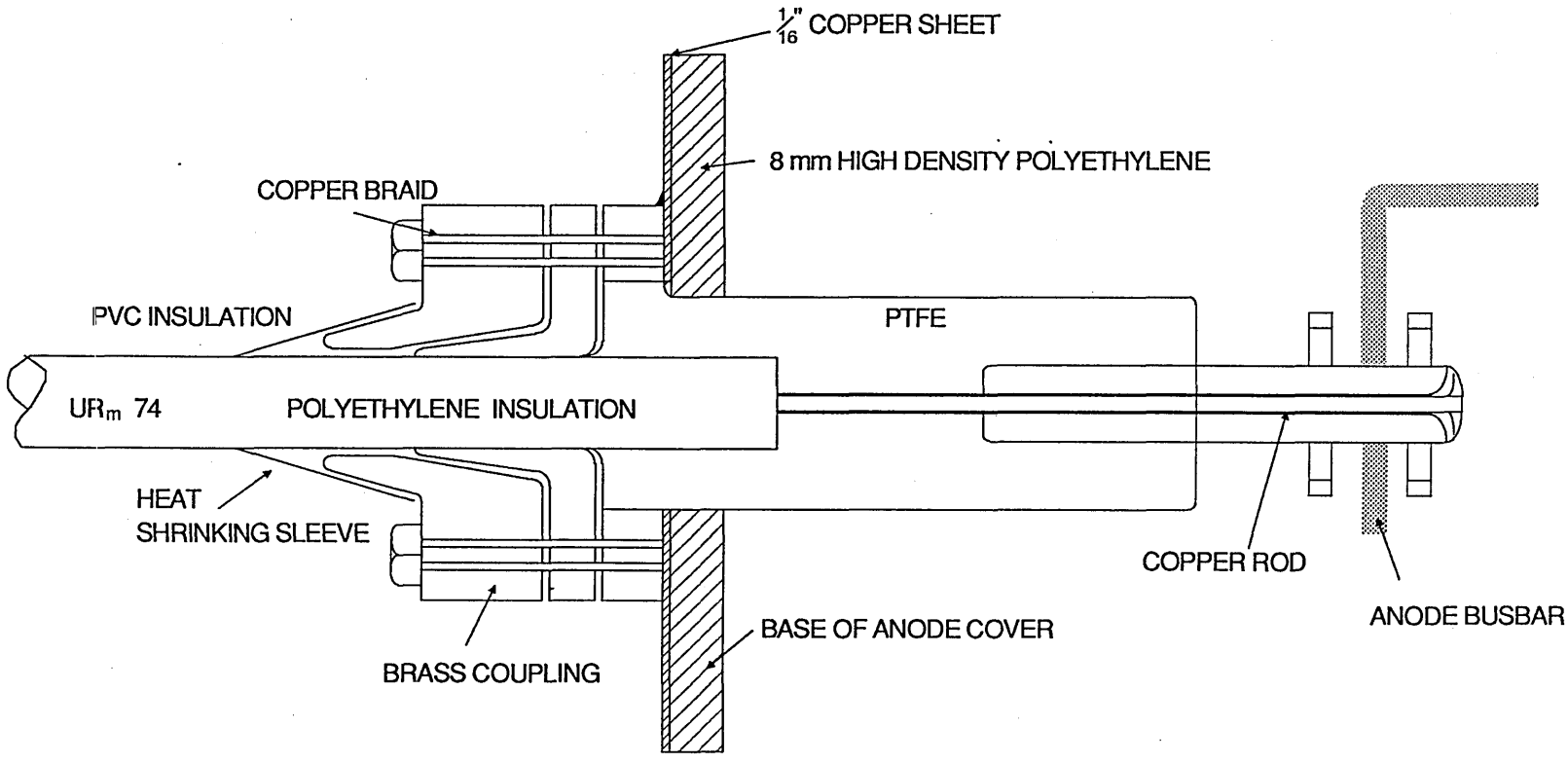

FIGURE 2.8 HIGH VOLTAGE CONNECTOR

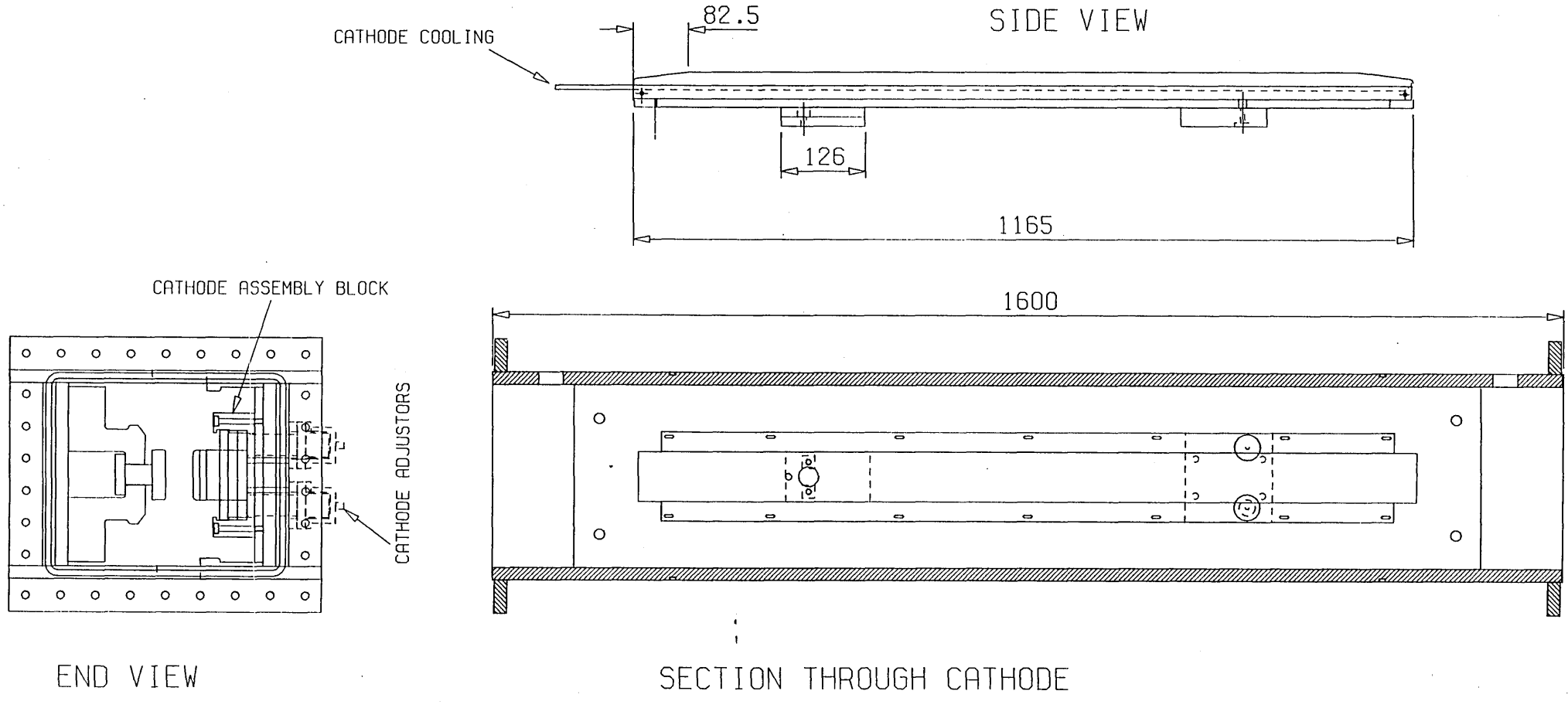

FIGURE 2.9 POSITION OF CATHODE MOUNTINGS

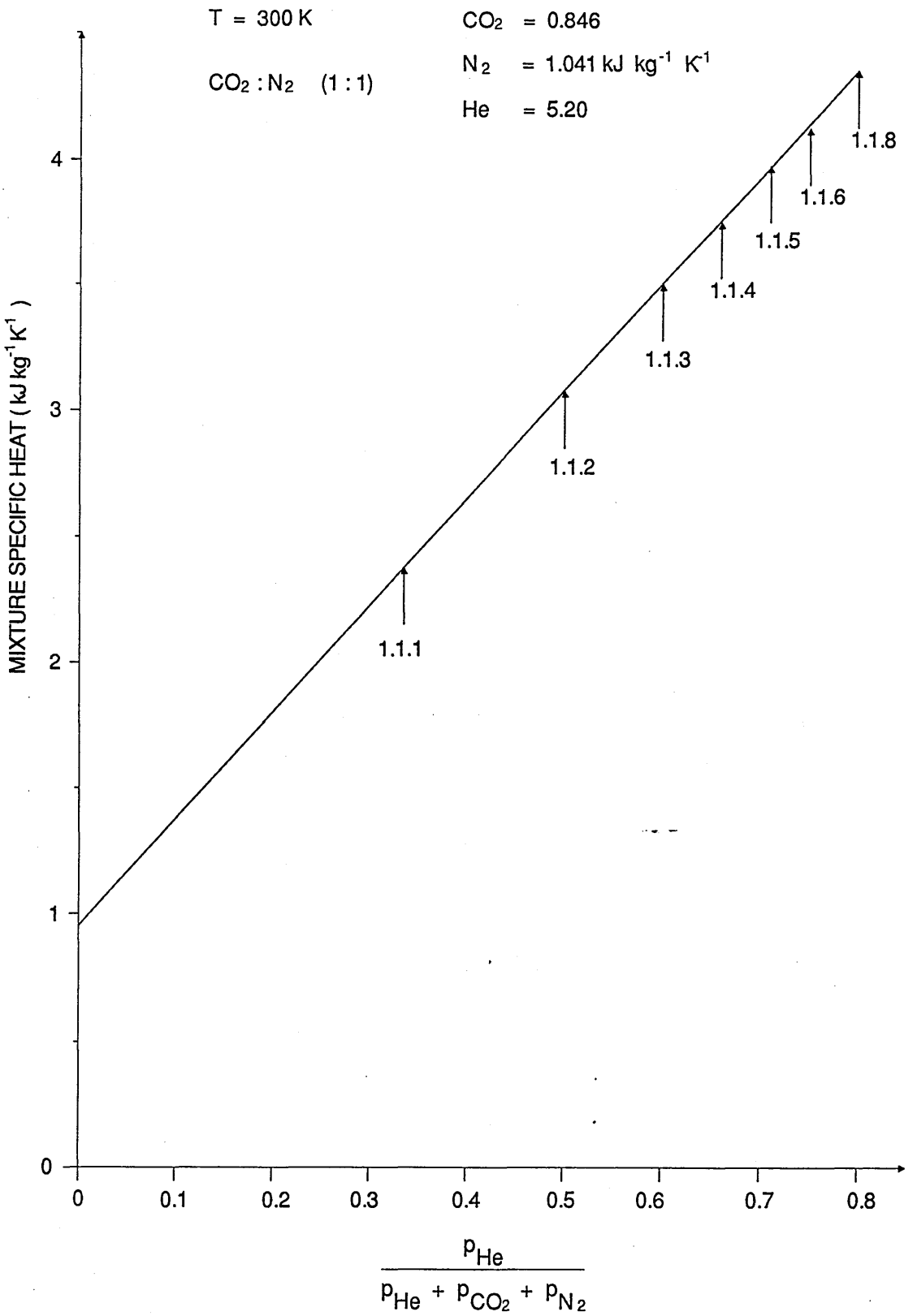

FIGURE 2.10 MIXTURE SPECIFIC HEAT vs HELIUM CONTENT

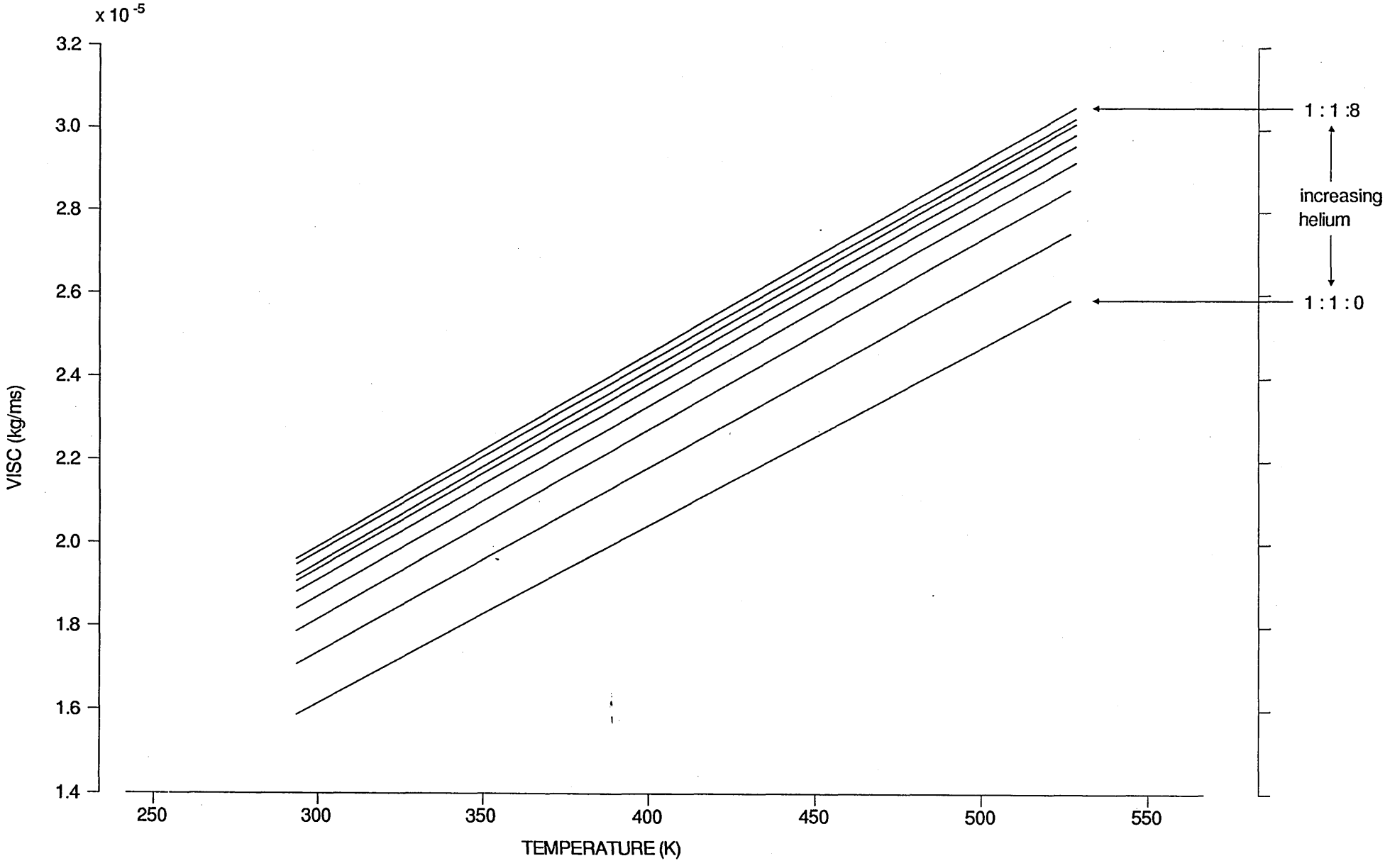

FIGURE 2.11 GRAPH OF MIXTURE VISCOSITY

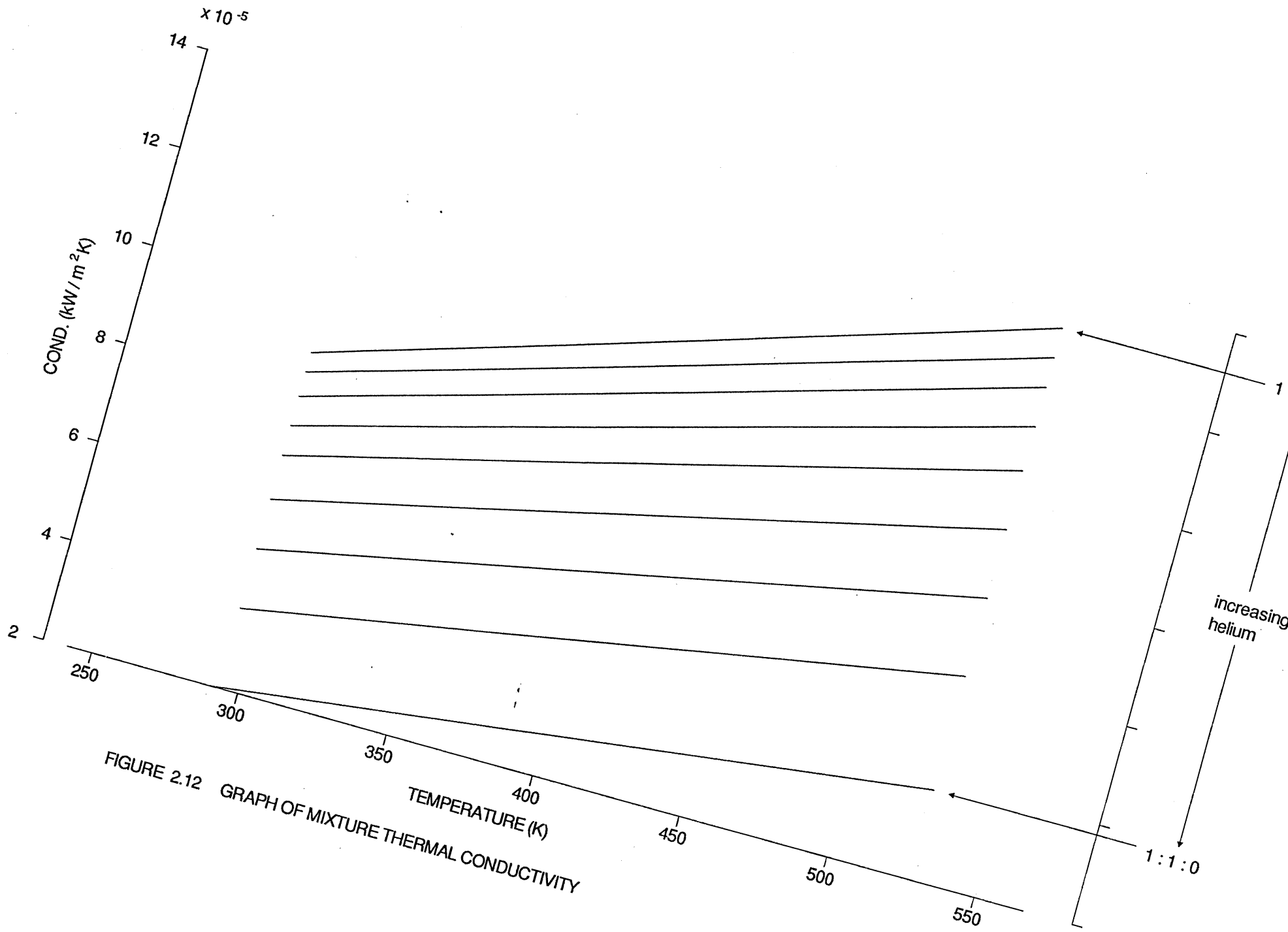

FIGURE 2.12 GRAPH OF MIXTURE THERMAL CONDUCTIVITY

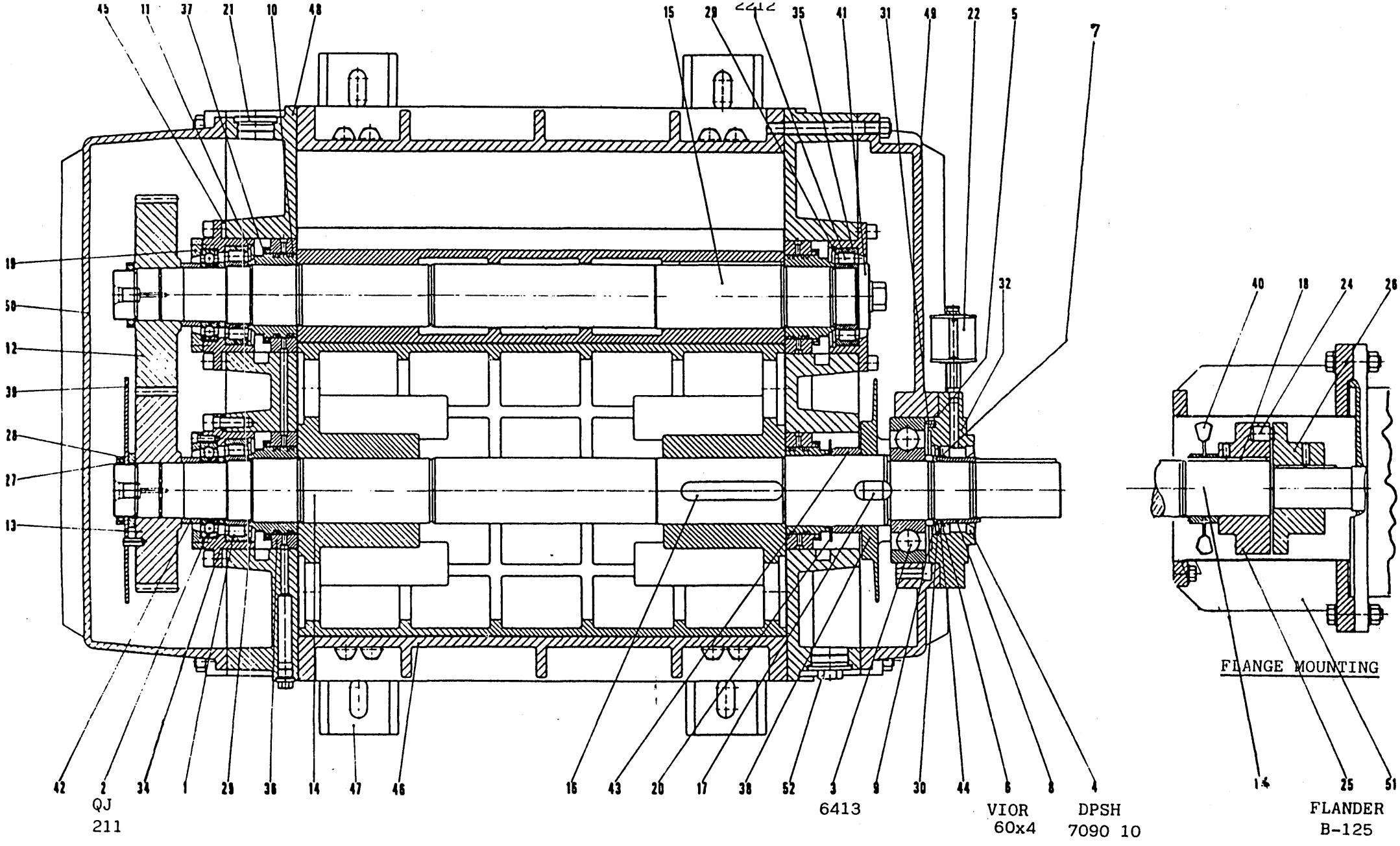

FIGURE 2.13 SECTIONAL DRAWING OF STARVAC 7500 BOOSTER PUMP

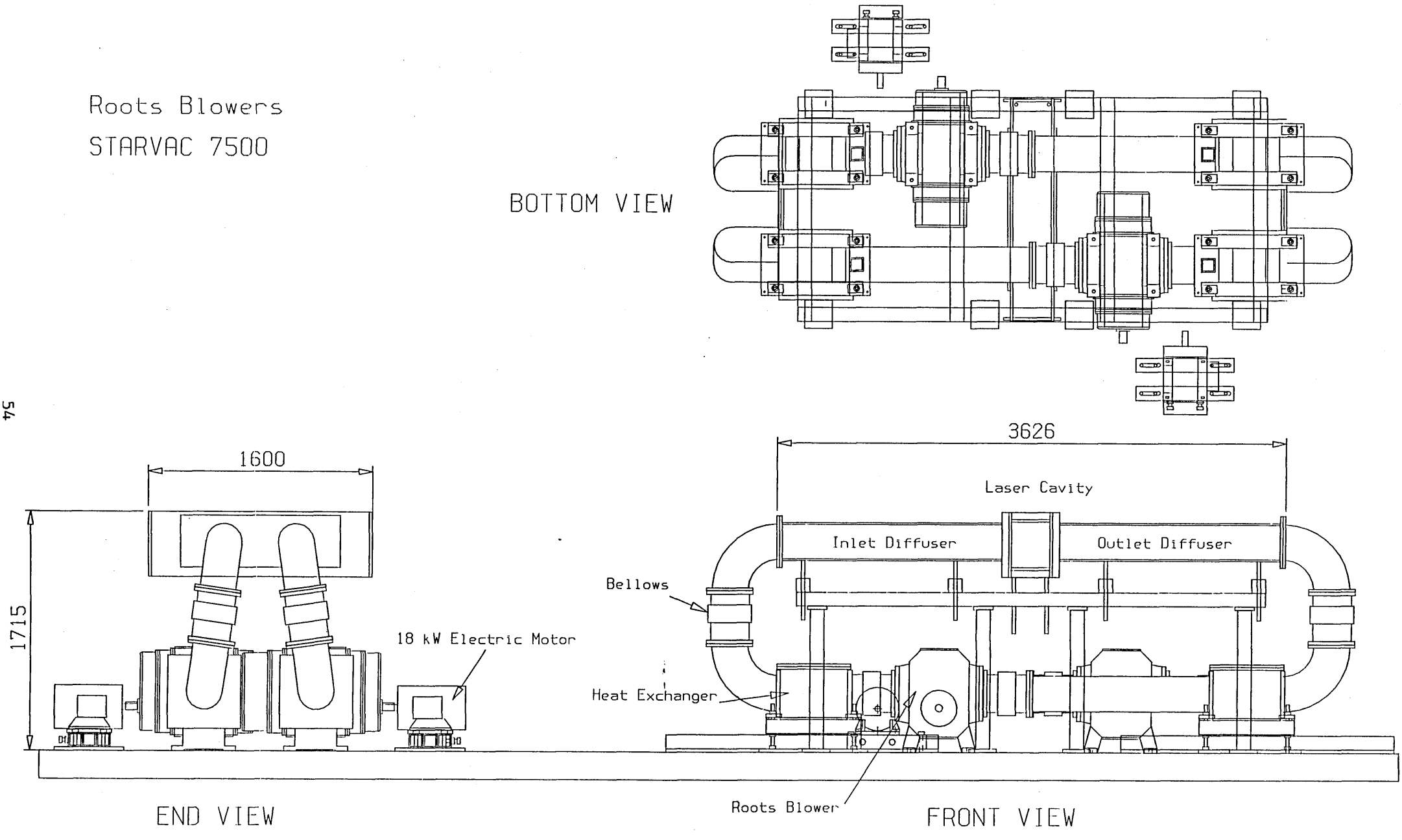

FIGURE 2.14 GAS RECIRCULATOR CONSTRUCTION

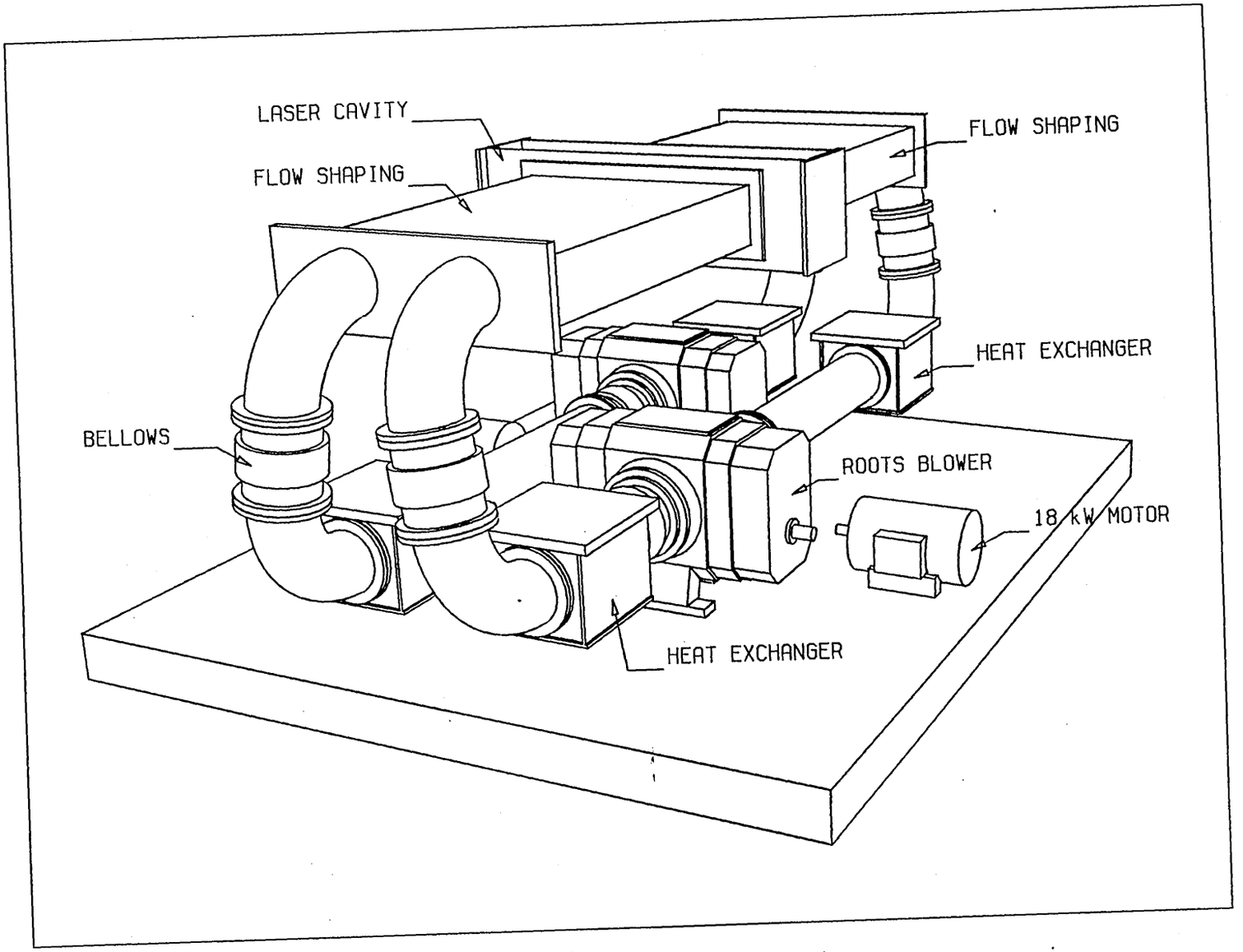

FIGURE 2.15 3D MODEL OF GAS RECIRCULATOR

Diffuser: all parts 1/4" aluminium plate

Duct: all parts 1/2" stainless

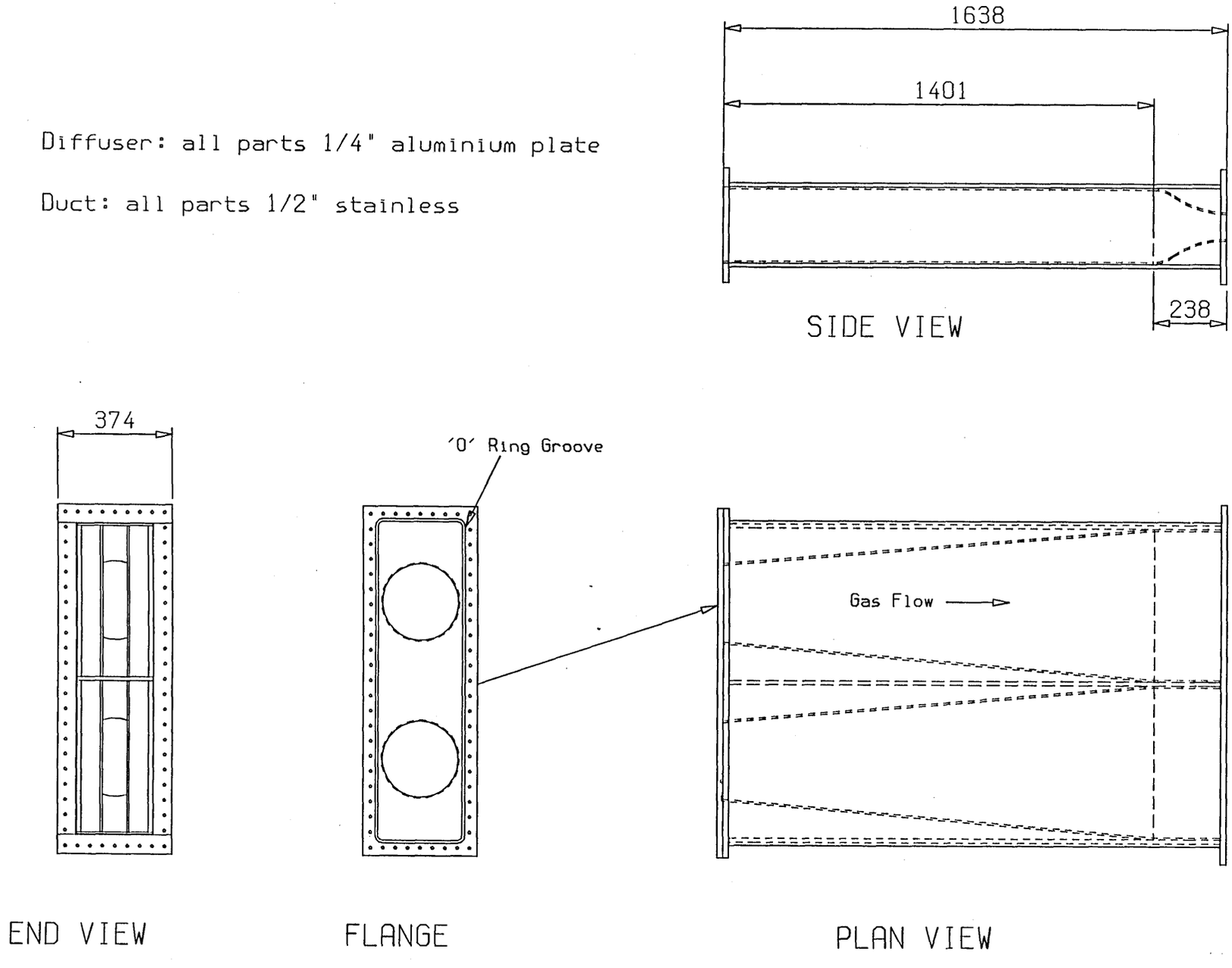

FIGURE 2.16 INLET DIFFUSER - INTERNAL FLOW GUIDANCE

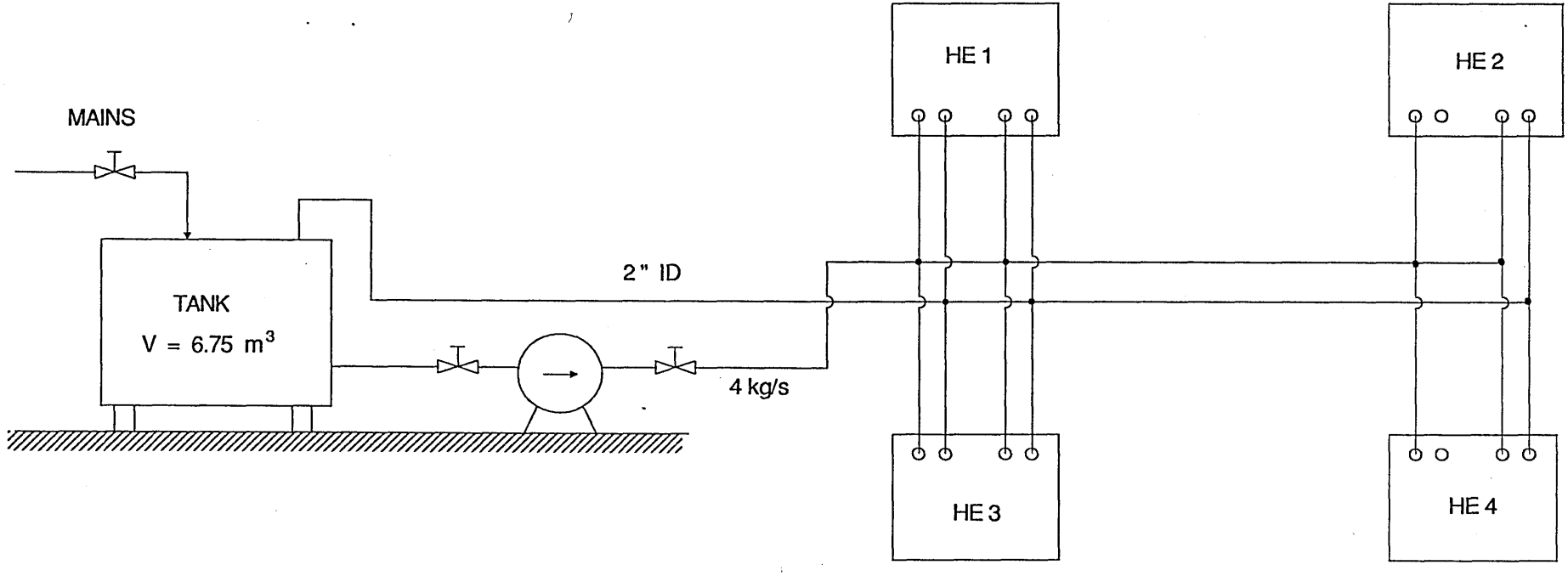

FIGURE 2.17 COOLING WATER SYSTEM

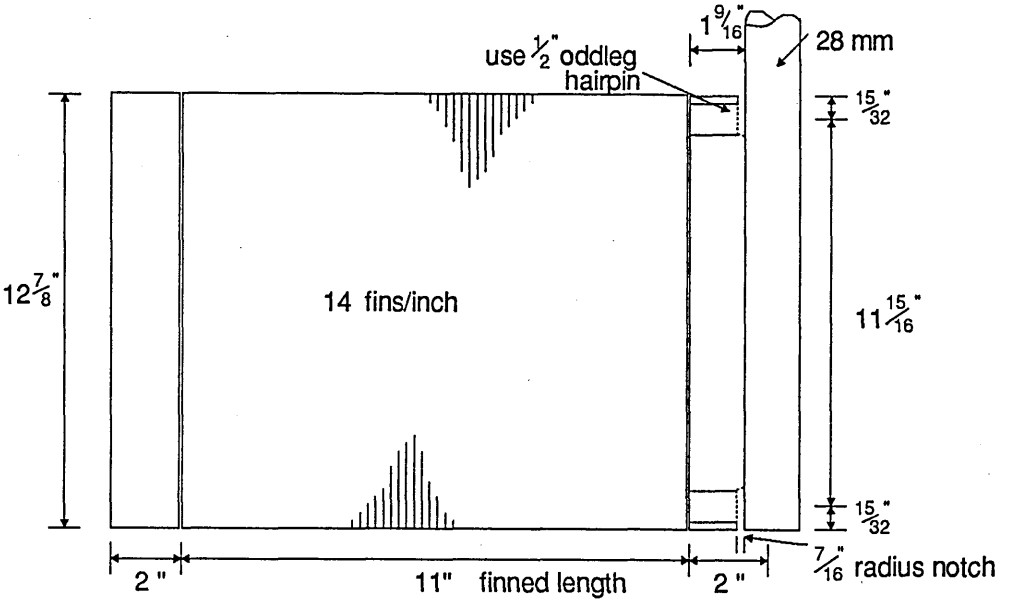

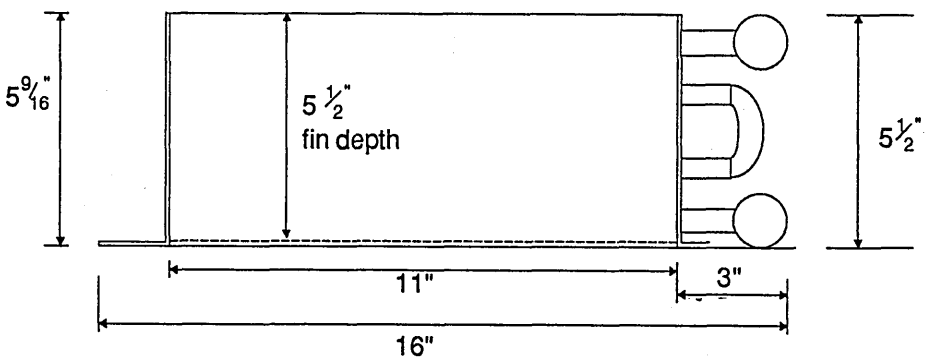

TUBES -
⅝" OD X .018" Wall Copper

FINS -
.006" Copper

CASE -
16G Copper

CONNECTIONS -
22 mm OD Copper BS2871

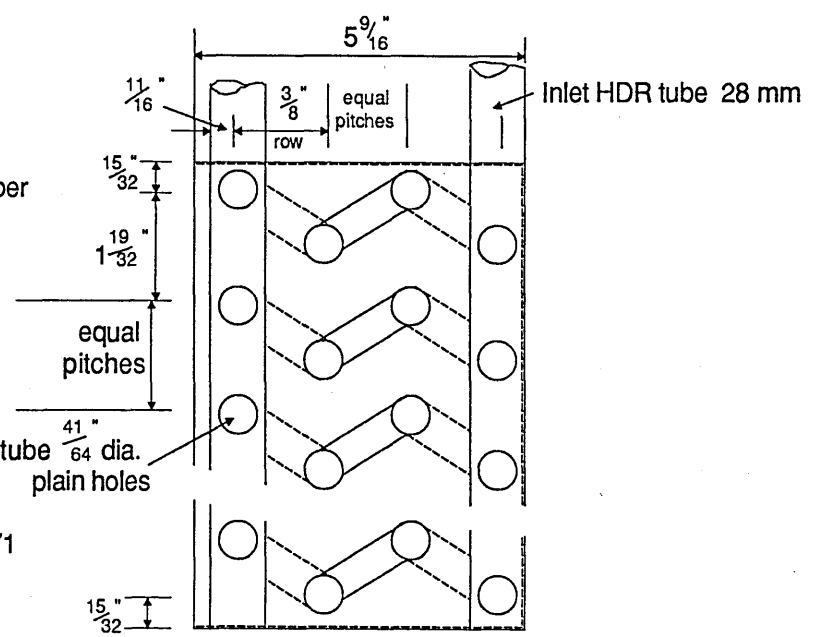

FIGURE 2.18 HEAT EXCHANGER COIL

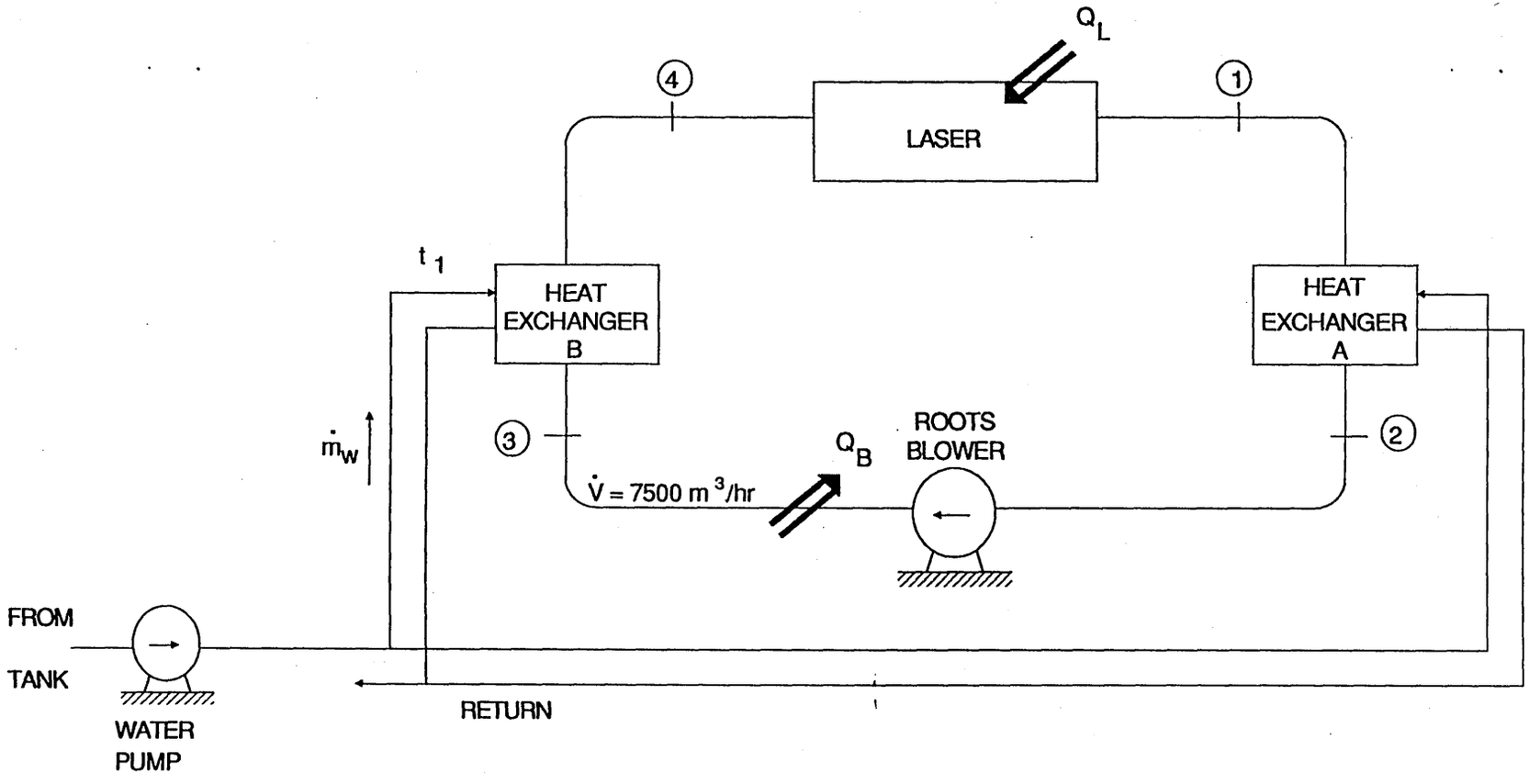

FIGURE 2.19 SCHEMATIC OF GAS RECIRCULATOR COOLING SYSTEM

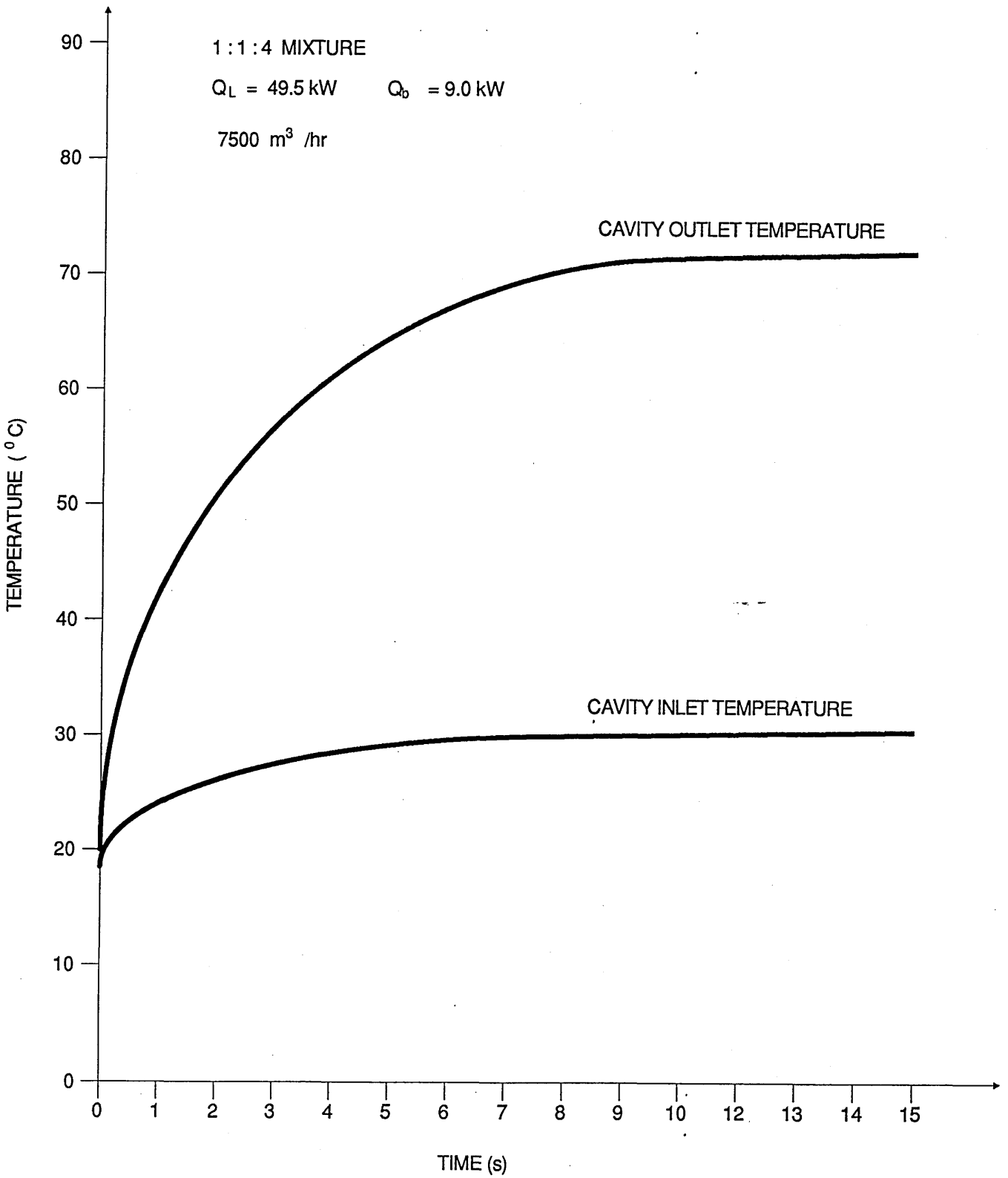

FIGURE 2.20 TRANSIENT RESPONSE OF SYSTEM TEMPERATURE

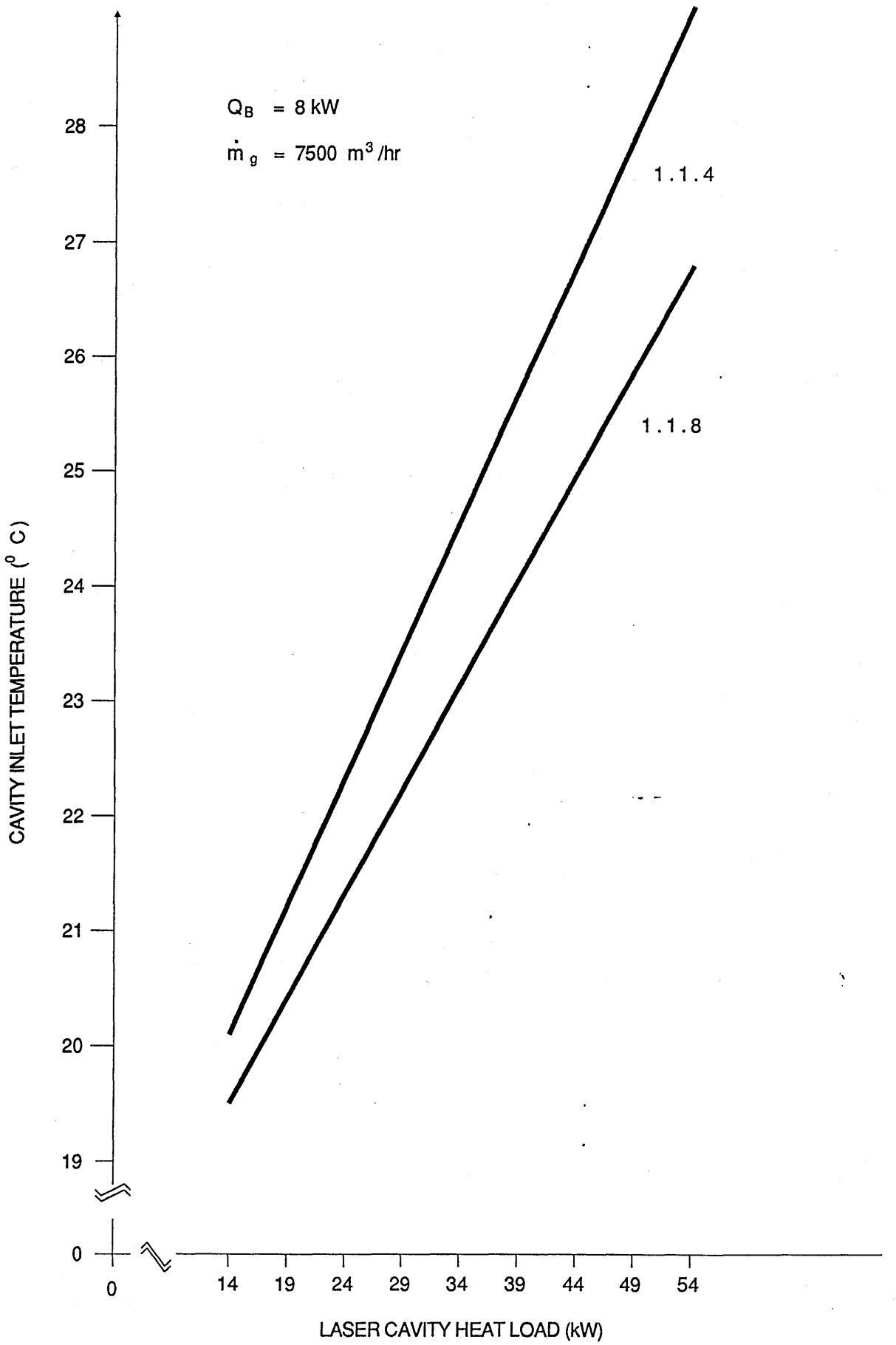

FIGURE 2.21 CAVITY INLET TEMPERTURE vs CAVITY HEAT LOAD

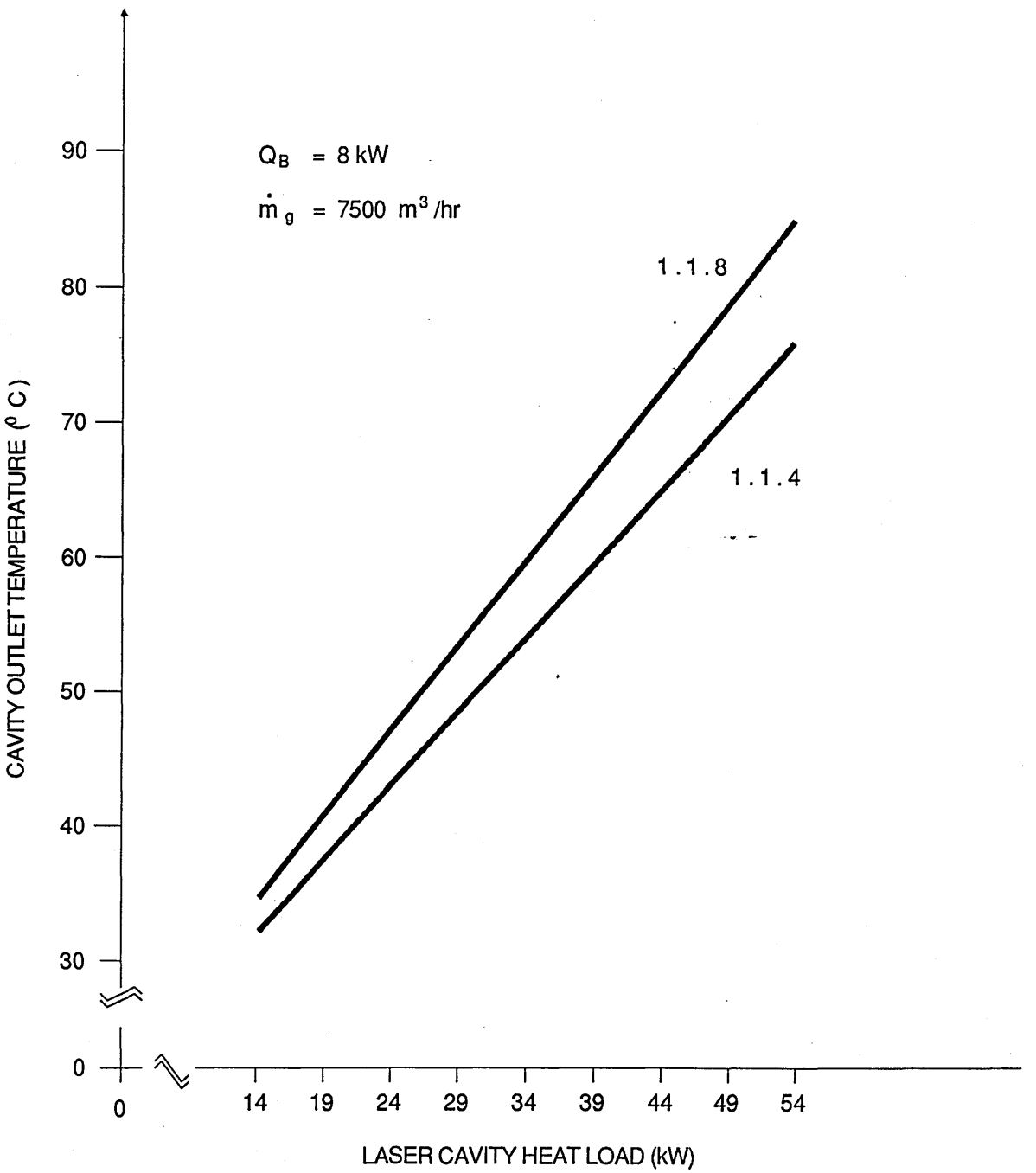

FIGURE 2.22 CAVITY OUTLET TEMPERATURE vs CAVITY HEAT LOAD

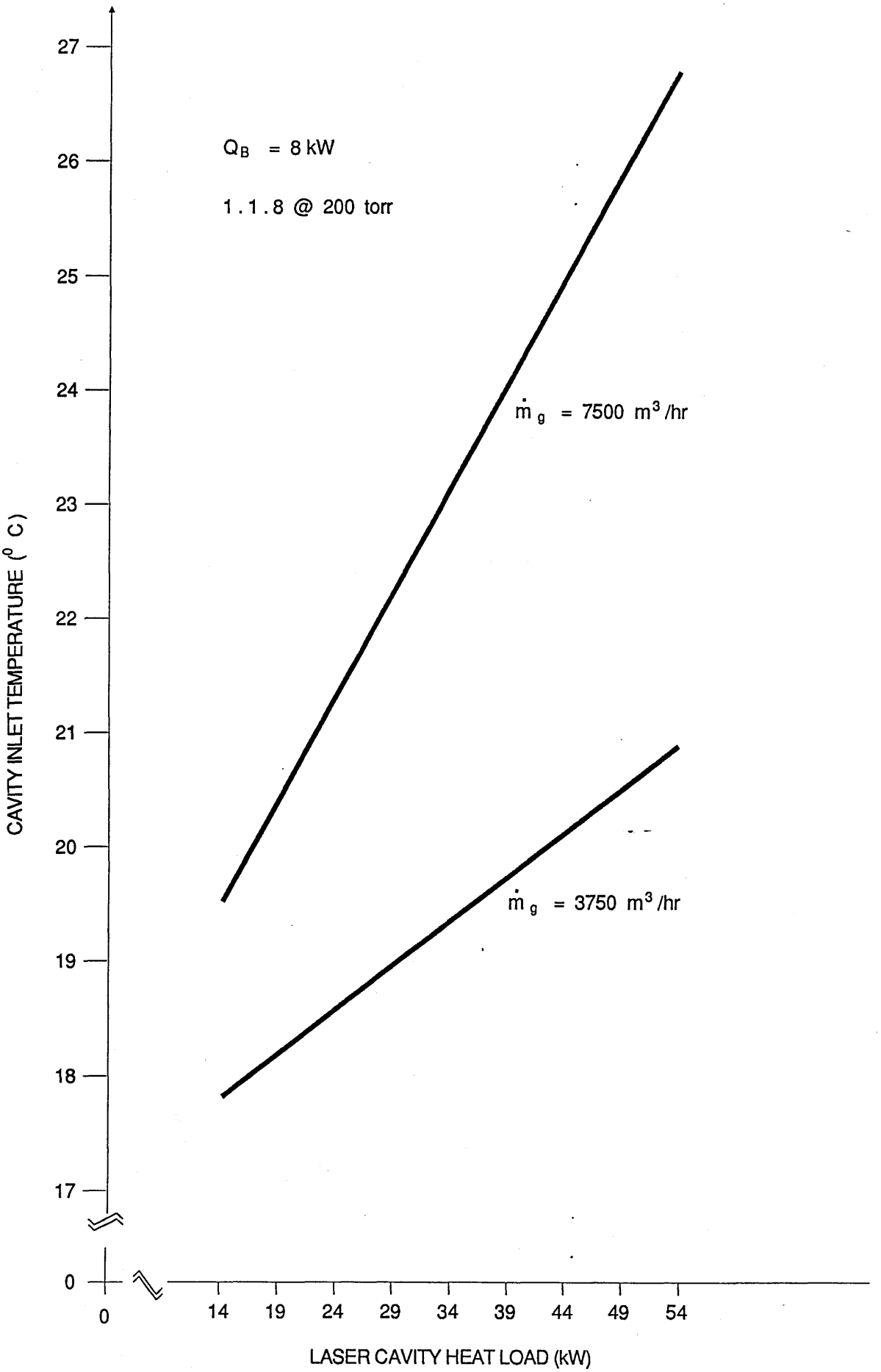

FIGURE 2.23 CAVITY INLET TEMPERATURE vs GAS FLOW

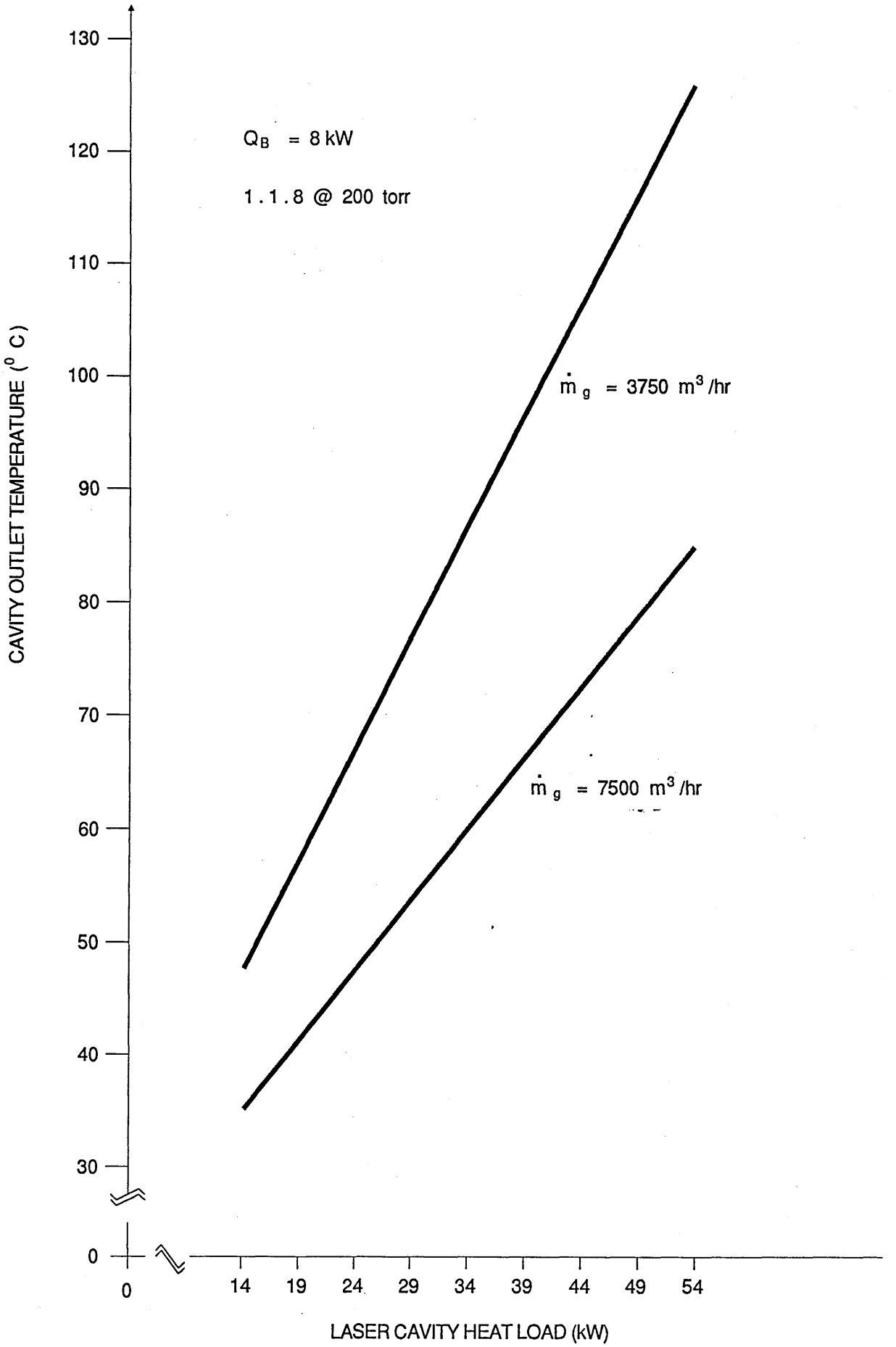

FIGURE 2.24 CAVITY OUTLET TEMPERATURE vs GAS FLOW

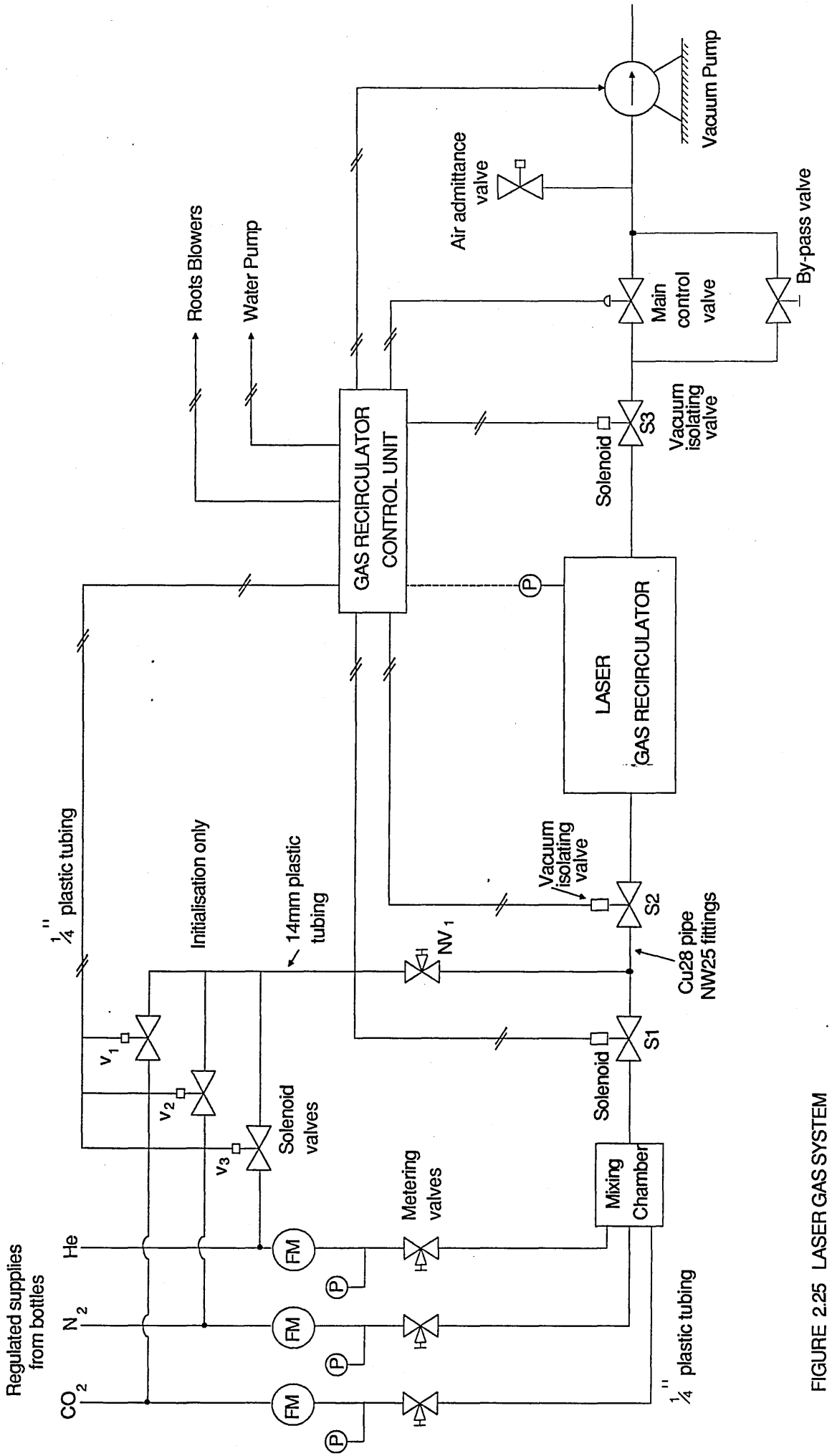

FIGURE 2.25 LASER GAS SYSTEM

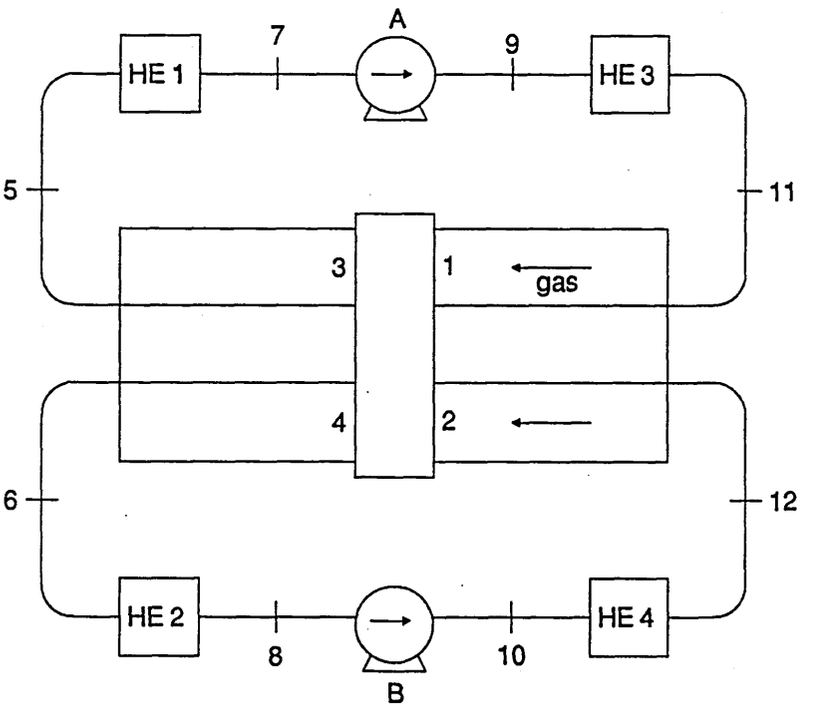

GAS CIRCUIT

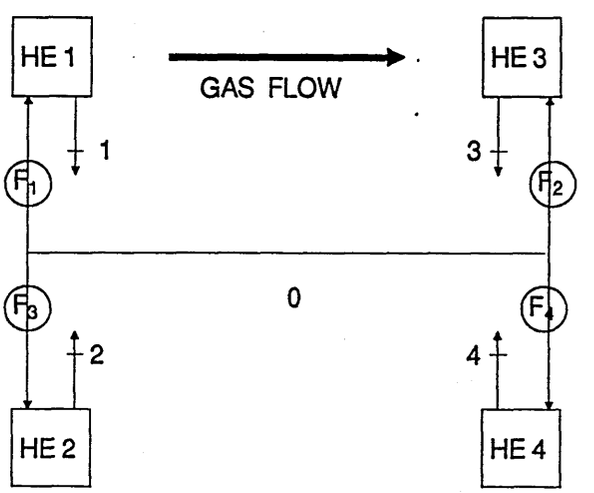

WATER CIRCUIT

FIGURE 2.26 SCHEMATIC OF INSTRUMENTATION POINTS

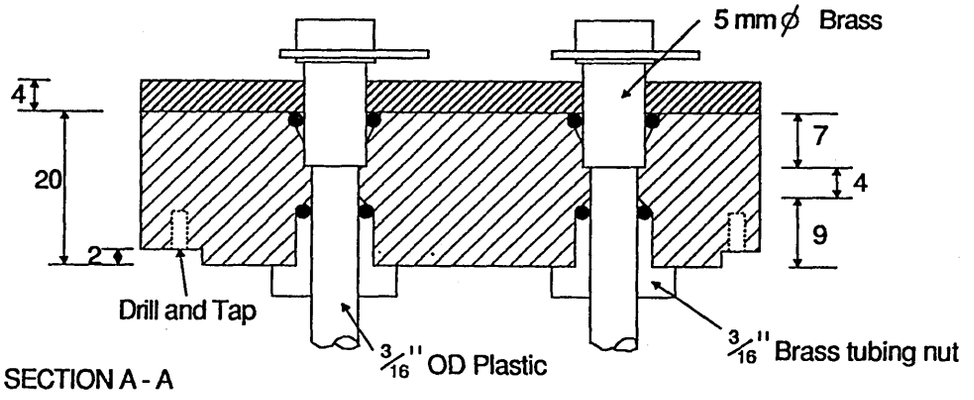

SECTION A - A

NB All 'O' rings 3/16" ID

Section diameter d = 2.62 mm

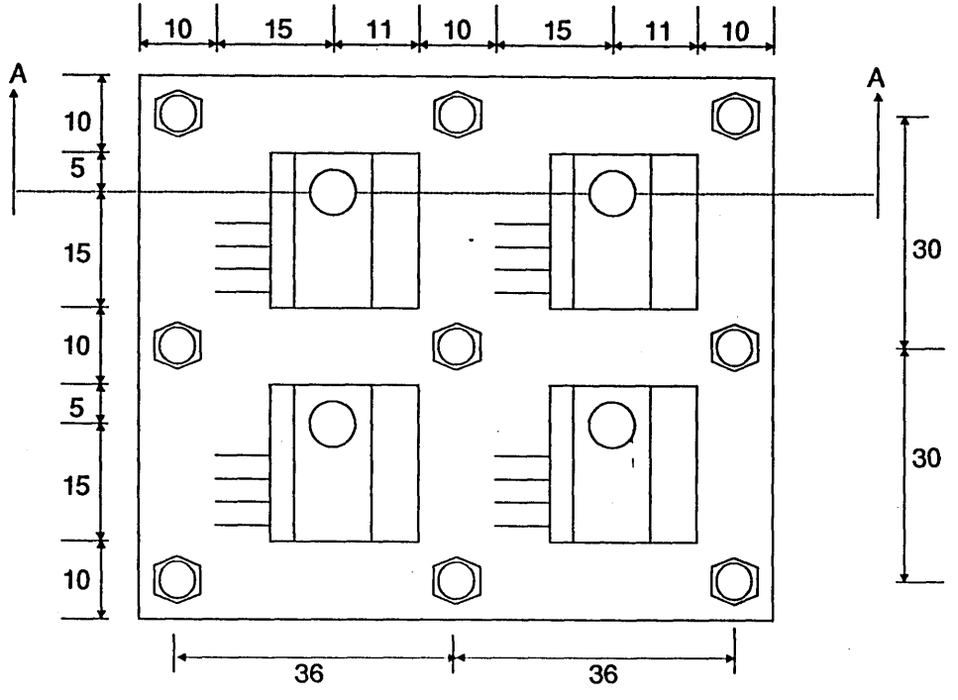

Transducer

National Semiconductor

LX06015A

FIGURE 2.27 PRESSURE TRANSDUCER ASSEMBLY

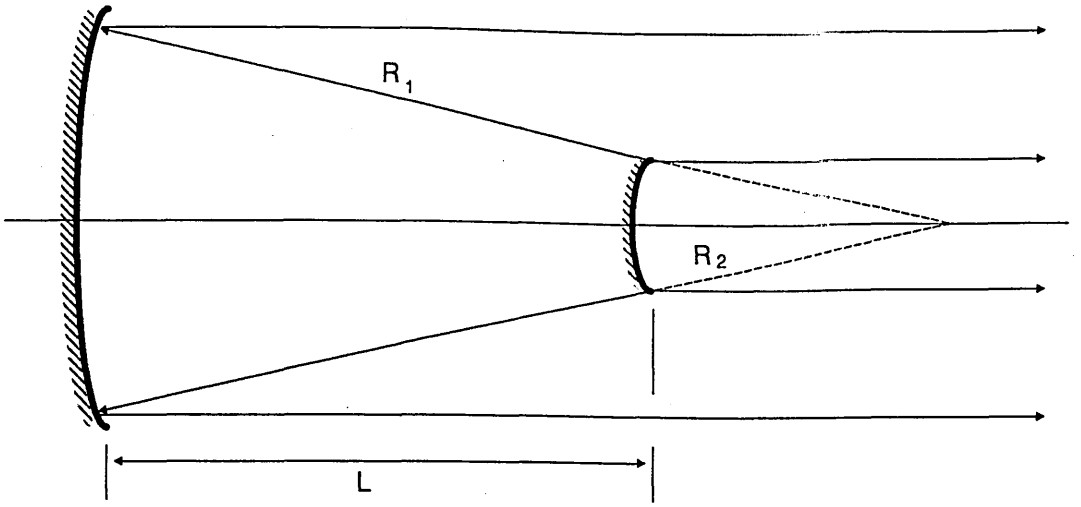

FIGURE 2.28 POSITIVE BRANCH CONFOCAL RESONATOR

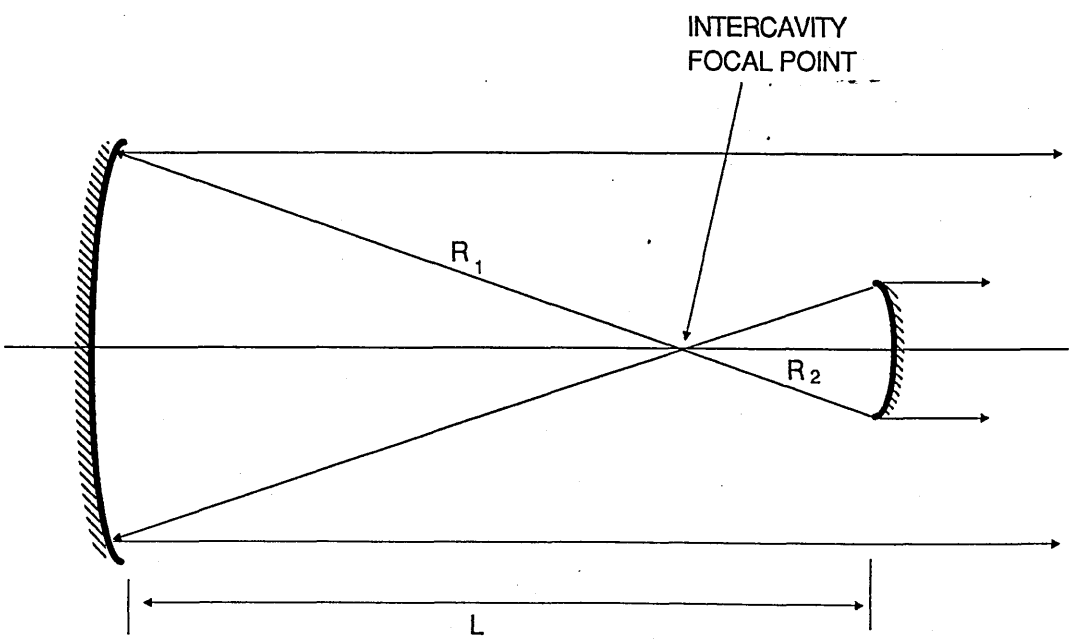

FIGURE 2.29 NEGATIVE BRANCH CONFOCAL RESONATOR

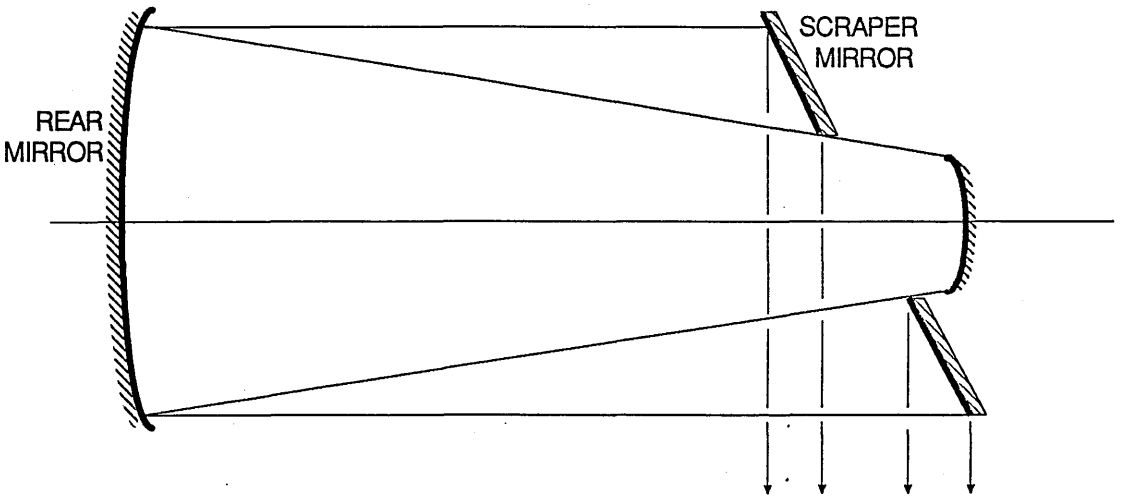

FIGURE 2.30 INTRACAVITY SCRAPER MIRROR

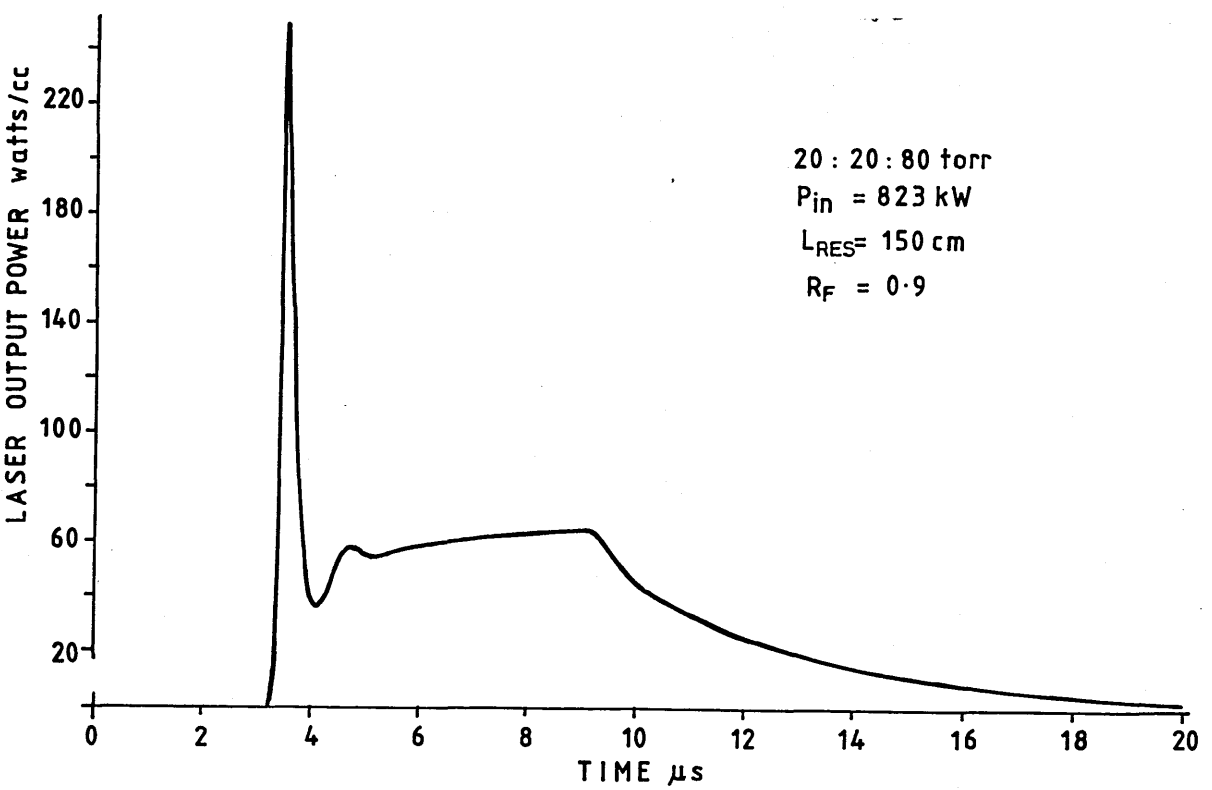

FIGURE 2.31 TEMPORAL CHARACTERISTICS OF OUTPUT PULSE

- Gas Mixture = 1:3:2
- Spike Power referred to Maximum Input Power = 230 Watt/cm^3
- Input Energy = 0.002J/cm^3
- Back Mirror Reflectivity = 0.99
- Injection Intensity I_i = 10^{-10} W/cm^2 ————
- Injection Intensity I_i = 1.0 W/cm^2 —— – ——

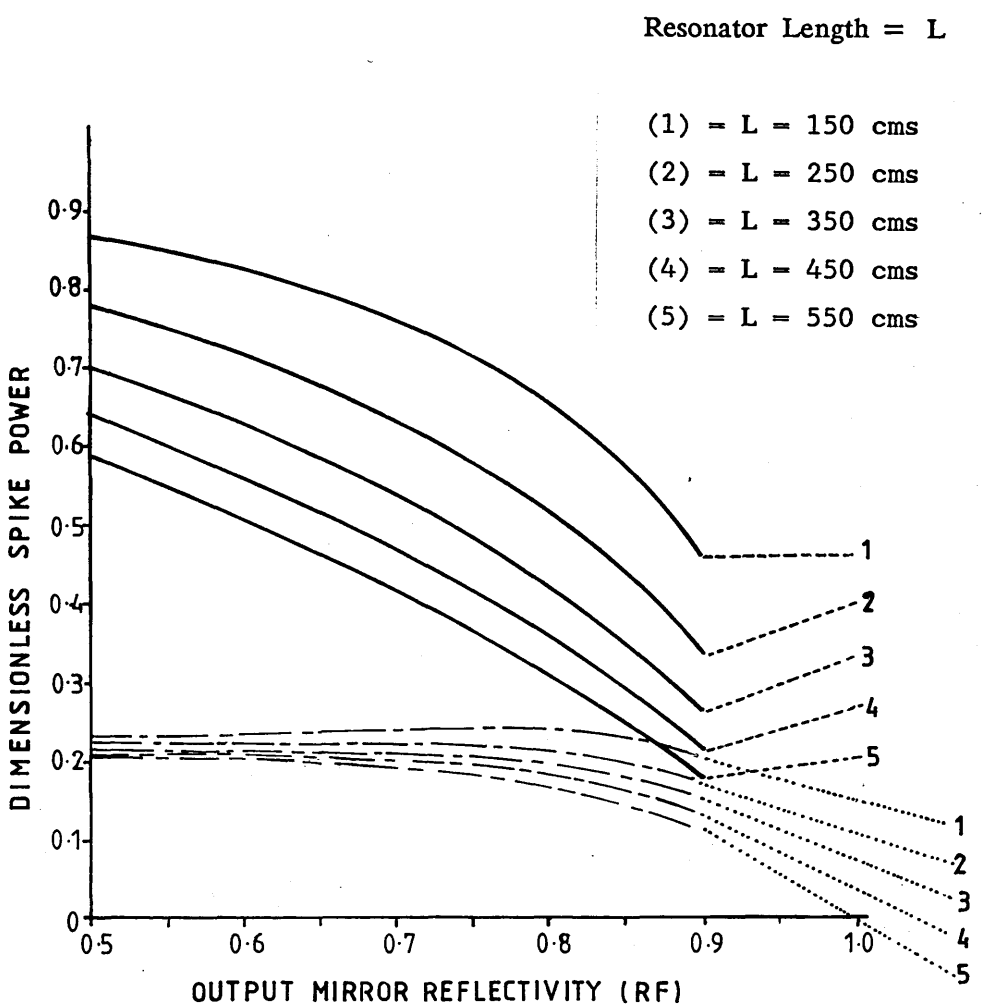

FIGURE 2.32 SPIKE POWER vs OUTPUT MIRROR REFLECTIVITY

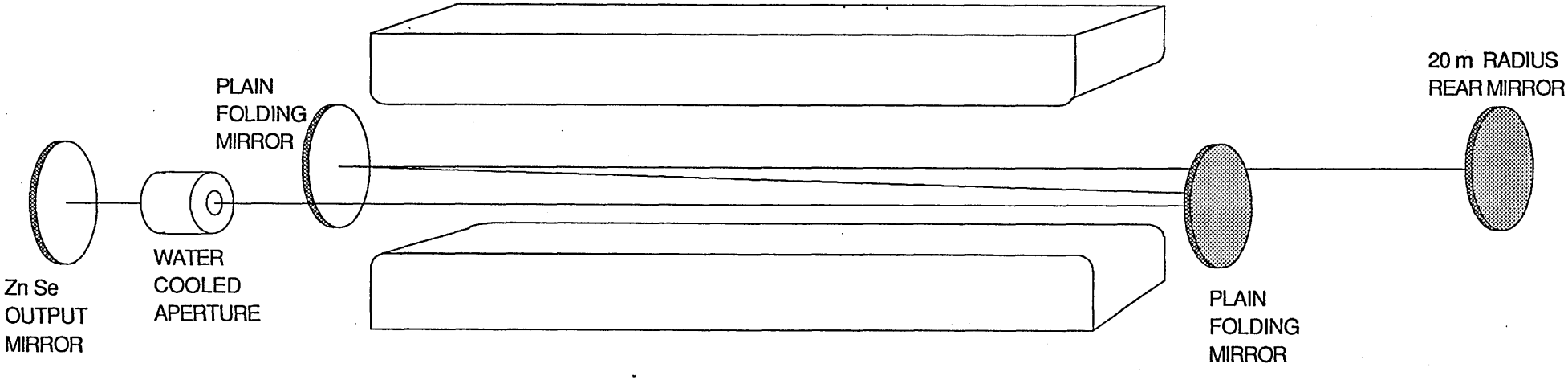

FIGURE 2.33 SCHEMATIC OF STABLE Z RESONATOR

OUTPUT WINDOW: ZINC-SELENIDE

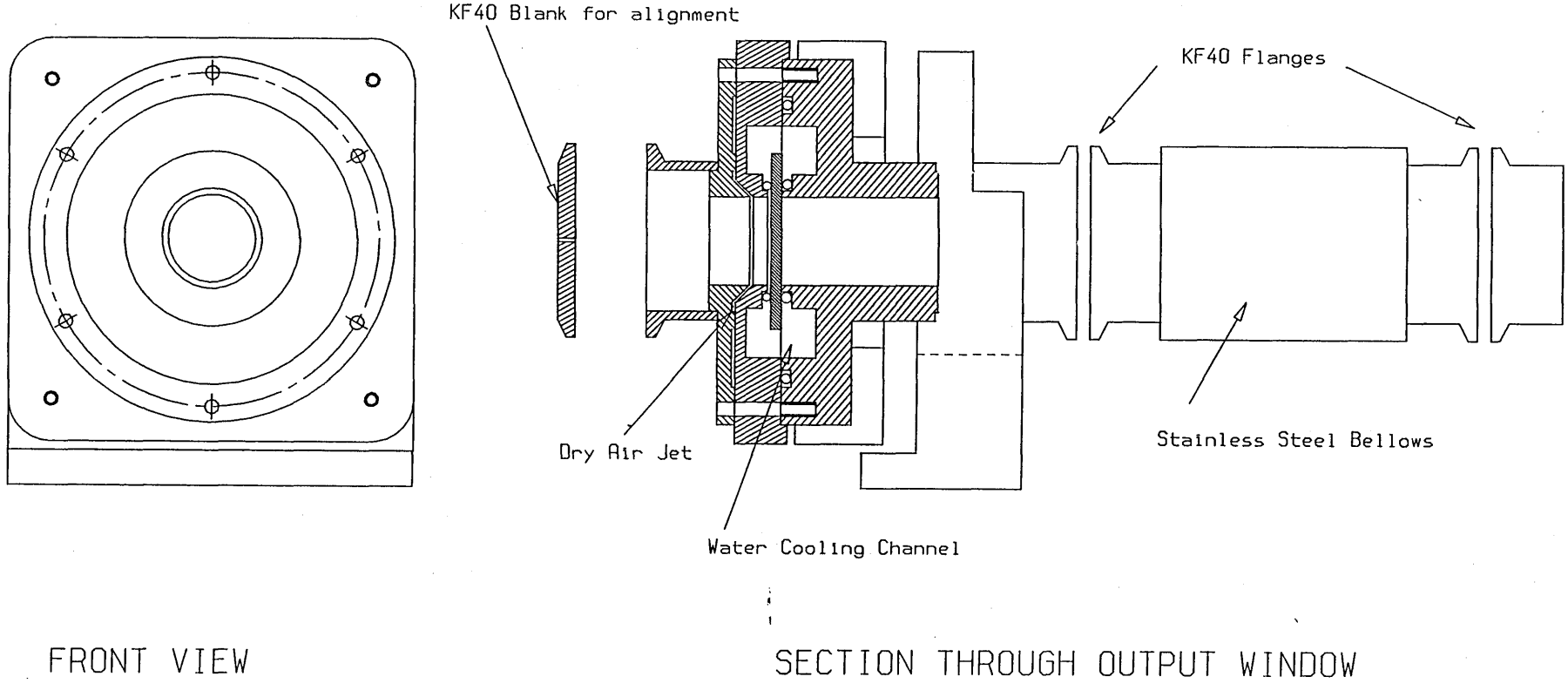

FIGURE 2.34 SECTIONAL DRAWING OF OUTPUT WINDOW

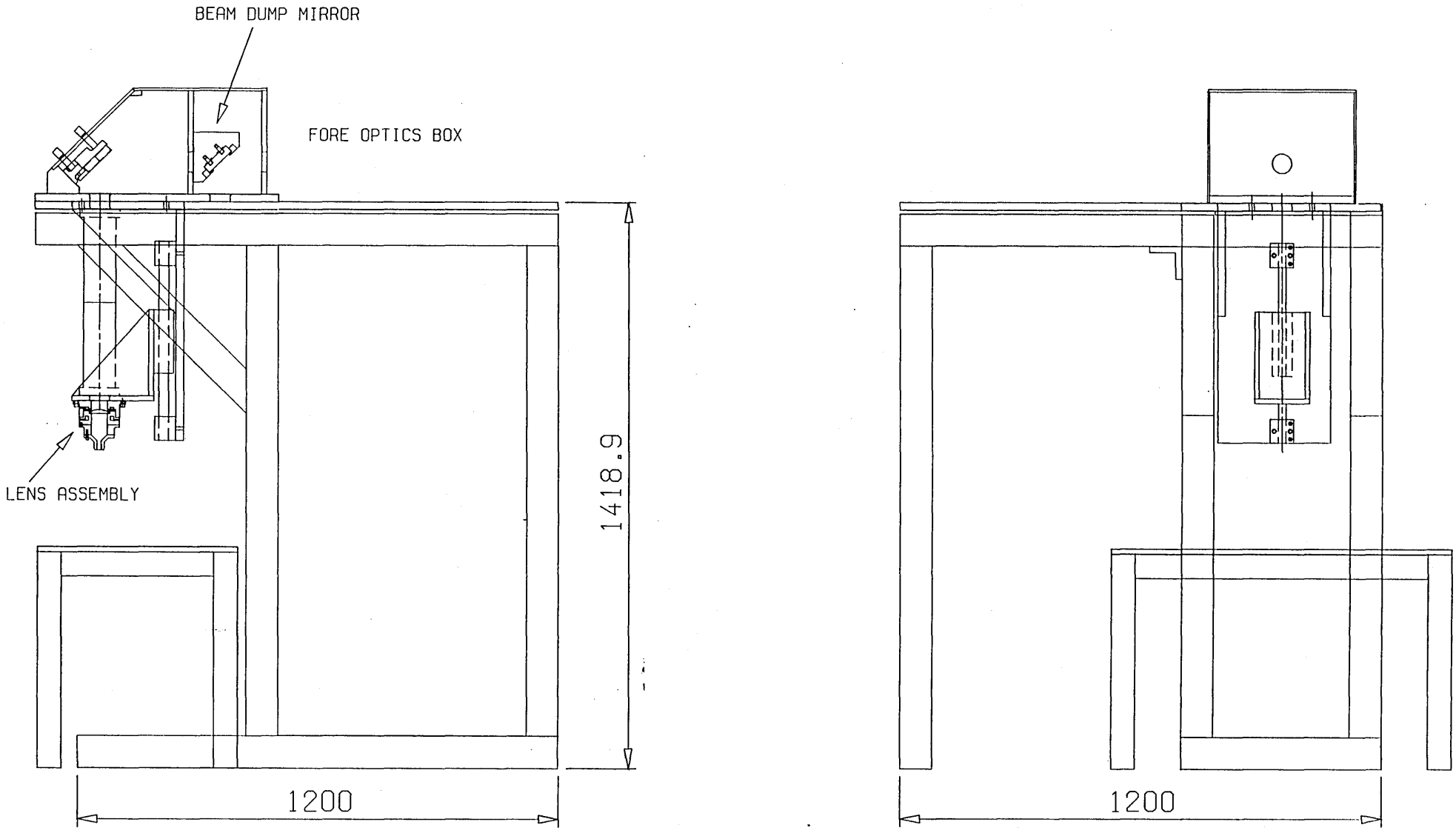

FIGURE 2.35 FORE-OPTICS ASSEMBLY

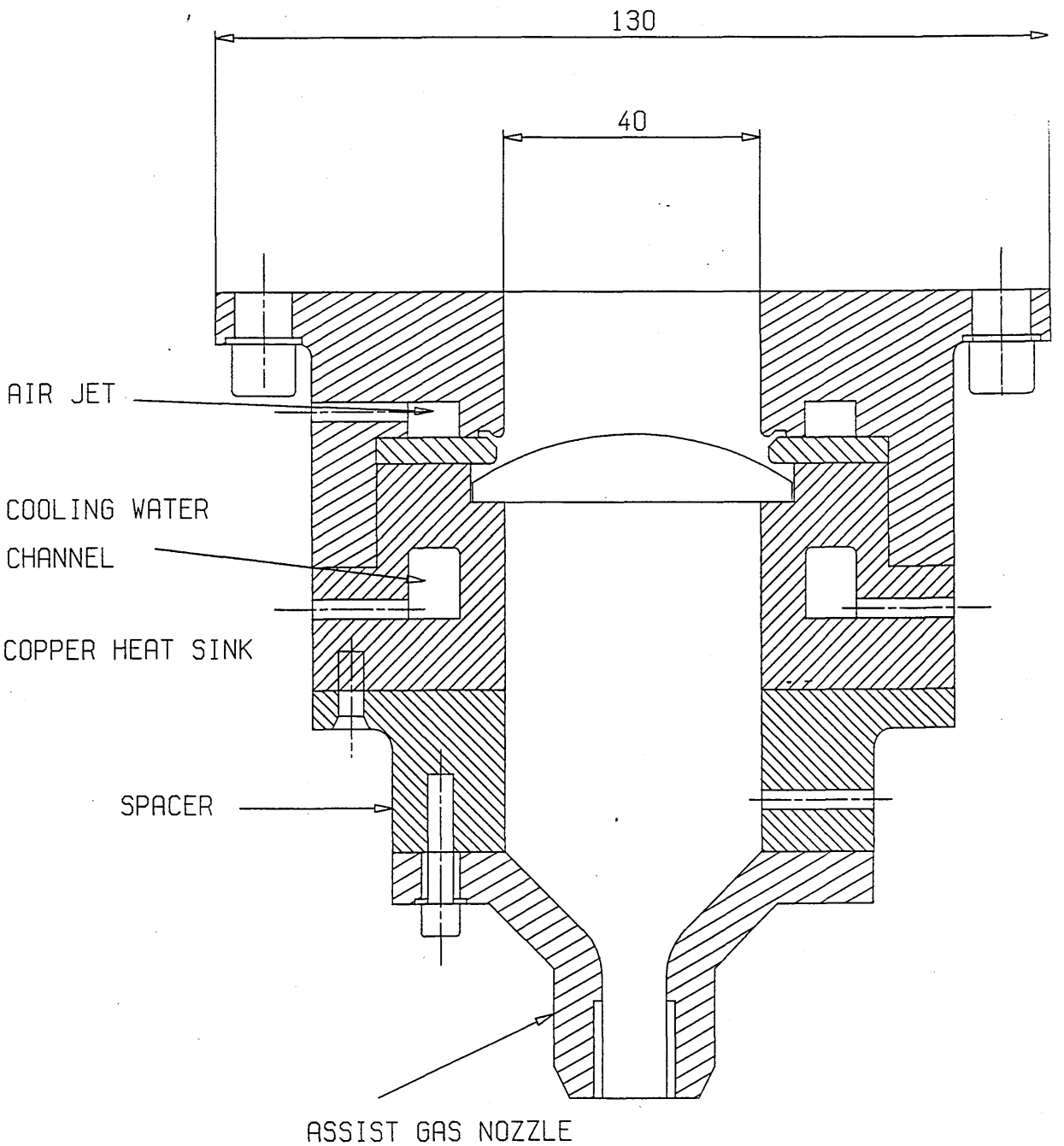

FIGURE 2.36 FOCUSSING LENS ASSEMBLY

(3.0) POWER SUPPLY DEVELOPMENT.

The pulser developed by Spall [3.1] was found to be capable of running in a burst mode at pulse repetition frequencies up to 10 kHz and was subsequently used to drive the prototype laser head used in Khahra's [3.2] experimental work. The main problem Spall experienced with the pulser was spurious triggering of the thyratrons, causing two switches to conduct simultaneously (fire−through). This problem was caused by cross coupling between the thyratron trigger/control circuits and the main pulser circuit.

In the prototype the thyratron trigger signals were generated at ground level with an amplitude of 10 volts and a duration of one microsecond. These signals were superimposed on the mains supply to the thyratron heater/isolation transformers, as shown in fig. (3.1). The trigger pulses were filtered from the low frequency mains supply on the high voltage side of the heater/isolation transformer and amplified in a resonant circuit before being applied to the control grid. The amplitude of the unloaded grid drive signal was approximately 300 volts, with a rise time of 1 μs.

The technique of coupling the trigger pulses through the heater transformer was quite ingenuous and had the advantage that few components were required on the high voltage side. The overall thyratron trigger circuit was therefore very compact. The design does have several limitations however, the most important being susceptibility to "pick–up." As the trigger circuits are essentially coupled to the main thyratron circuit via the stray capacitance of the heater and pulse transformers, cross coupling is possible between each thyratron. It was found that this coupling was sufficient to re−trigger the charging thyratron when the main discharge switch fired. Great care had to be taken in the layout of the pulser components and particular attention had to be paid to the elimination of ground loops. In addition, supression chokes had to be included on the control cables to minimise the interference effects.

Spall found that spurious trigger signals were being generated by the control unit. It was evident that the 5 volt logic circuits used were not able to function in such a noisy environment. A move to 15 volt logic circuits did improve the performance and allowed the DC supply voltage to be raised to 5 kV before random spurious signals caused the pulser to fire−through. Several additional components had to be added before the pulser could be brought up to full voltage safely. This included the addition of many decoupling components to the control cards and the incorporation of filters in the power supply lines of the control unit. In an attempt to improve the thyratron control characteristics, the control bias was increased from −50 to −70 volts. This represented the maximum possible with this circuit arrangement as the

limited trigger pulse amplitude precluded any further increase. However, even with this improvement, both the bias and the trigger pulse amplitude were well below the optimum values recommended by the manufacturers [3.3].

The main proirity in this research phase was therefore the re−design of the pulser trigger and control circuits. Since the problems were due to poor isolation between the main pulser circuit and the thyratron control circuits, it was decided to use fibre optic coupling techniques for the new trigger circuits.

Spall's work also highlighted the need for a robust DC supply, capable of surviving the fault transient generated during pulser fire−throughs. A high powered mercury arc rectifier was installed in the present facility because of its ability to tolerate the full short circuit current during overload conditions. Advantage was taken of the control features of the mercury arc rectifier to improve overload protection and power supply control.

In addition to the above modifications, the present development phase called for a controllable system which could be easily interfaced to CNC control equipment. The control circuits were therefore designed with the necessary flexibility for future expansion and integration into a laser manufacturing system.

(3.1) THE LINE TYPE PULSER.

In its basic form the line type pulser [3.4] comprises an energy storage network, a high voltage charging supply and two high voltage switches, as shown in fig (3.2). With the network initially discharged, switch S1 is closed and the network charged to a voltage $V_{no,}$ at which point S1 is re−opened. The stored energy is then transferred to the load by closing the discharge switch S2. At the end of the discharge pulse, S2 is opened and the network re−charged via switch S1 as before. This sequence is repeated at the desired frequency by controlling the firing sequence of the two high voltage switches.

For the present application the pulser must be capable of delivering approximately rectangular voltage pulses with a duration in the range 5 − 10 μs and pulse repetition frequencies up to 10 kHz. These pulses must be generated at the correct power and impedance level for excitation of the laser cavity. In the line type pulser the energy storage element also performs the task of pulse shaping and is therefore commonly referred to as the pulse forming network (PFN). The design of the PFN is based on the characteristics of long transmission lines, which by virtue of their distributed stray capacitance and inductance, discharge in series of steps. The exact

characteristics depends on the impedance of the line and the impedance of the load or, more precisely, the impedance mismatch between the line and the load. The line type pulser derives its name from its analogous behaviour to the discharge characteristics of a transmission line.

In order to simulate transmission line discharge characteristics the energy storage device essentially replaces a distributed system with a lumped network. By drawing this analogy with a transmission line it is possible to use transmission line theory to analyse the behaviour of the PFN and obtain some useful design guides. Before going on to discuss the design and operation of the line type pulser it is worthwhile at this stage to consider some of the characteristics of transmission lines, as this will give a valuable insight into the nature of the pulse generation process.

(3.1.1) Analogy With The Lossles Transmission Line.

A transmission line has in addition to distributed stray capacitance and inductance some dissipative elements which can usually be neglected in a wave analysis of the line without significantly affecting the predictions. The transmission line can therefore be idealised by the circuit of fig (3.3), which has a distributed capacitance and inductance per unit length equal to C and L respectively. It can be shown that the voltage and current at any point on the line can be expressed as [3.5]:

$$\frac{\partial^2 i}{\partial t^2} = \frac{1}{LC}\frac{\partial^2 i}{\partial x^2} \qquad (3.1)$$

$$\frac{\partial^2 v}{\partial t^2} = \frac{1}{LC}\frac{\partial^2 v}{\partial x^2} \qquad (3.2)$$

Equations (3.1) and (3.2) are forms of the familiar wave equation and physically represent an electromagnetic wave travelling with a speed $1/\sqrt{(LC)}$. It can also be shown that the current and voltage on the line are related by:

$$V = I\sqrt{\left(\frac{L}{C}\right)} \qquad (3.3)$$

where the quantity $\sqrt{(L/C)}$ is the characteristic impedance of the line and is normallly denoted Z_o. The speed at which the wave travels along the line can be shown to depend only on the medium surrounding the line and is equal to the speed at which an electromagnetic wave would propogate in the surrounding medium [3.5]. Thus, the speed of propogation represents physically the maximum rate at which energy can be stored in the magnetic and electric fields surrounding the line.

The question is: how can this be used to generate a rectangular voltage pulse? Consider the circuit of fig (3.4), which comprises a DC power source, two switches, a transmission line and a load. If the discharge switch S2 is open, the capacitance of the line can be charged to a voltage V_{no} by closing the charging switch S1, which is then opened and the discharge switch closed. At the instant the discharge switch is closed the load sees a voltage V_{no} and draws a current I_1. As the current is drawn from the line the voltage at the load end of the line drops from the initial value V_{no} to a lower value V_1 due to the impedance of the line. From current continuity:

$$I_1 = \frac{V_{no} - V_1}{Z_o} = \frac{V_1}{R}$$

Thus

$$V_1 = \frac{V_{no}\, R}{(R+Z_o)} \qquad (3.4)$$

This is as expected since the circuit is essentially equivalent to a voltage source V_{no} divided between two impedances R and Z_o. It is of interest now to reconsider this in terms of waves travelling along the line. At the instant the discharge switch is closed a wave, V_r, is reflected back along the line to the charging end. The magnitude of this wave can be found since:

$$V_1 = V_{no} + V_r$$

and using equation (3.4) we have:

$$V_r = \frac{-\, Z_o\, V_o}{(R + Z_o)} \qquad (3.5)$$

This wave travels along the line to the charging end where it is reflected. The magnitude of the return wave can be found from consideration of an incident wave of magnitude V_i hitting the boundary between two impedances Z_1 and Z_2, as shown in fig (3.5). The magnitude of the reflected wave can be found from current continuity at the boundary.

$$I = \frac{(V_i - V_r)}{Z_1} = \frac{(V_i + V_r)}{Z_2}$$

$$V_r = V_i \frac{(Z_2 - Z_1)}{(Z_2 + Z_1)} \qquad (3.6)$$

Since the charging switch is open circuit ($Z_2 = \infty$) the wave hitting the charging end will be reflected in phase without attenuation. This wave then travels back along

towards the load end and reaches there at a time $\tau = 2\delta$, where δ is the one way transmission time for the line. Therefore, at time τ after switch S2 is closed, the voltage across the load will change to:

$$V_2 = V_1 - V_r - V_r \frac{(Z_o - R)}{(Z_o + R)} \qquad (3.7)$$

The third term in the above equation accounts for the initial wave being reflected from the load a second time. Substituting (3.4) and (3.5) into (3.7) gives

$$V_2 = V_{no} R \frac{(R - Z_o)}{(R + Z_o)^2} \qquad (3.8)$$

This process of wave analysys can be continued and it is apparent that the load voltage will change each time the initial reflected wave returns to the load end of the line. The discharge will therefore take the form of a series of steps of duration τ, representing the time it takes the wave to travel to the charging end and back. Since, for the present application we are considering generating only one pulse, it is of interest to consider how the discharge characteristics vary with R and Z_o.

When the load is matched to the line ($R = Z_o$) all of the energy stored in the line is transferred to the load in a single pulse and there is no residual voltage on the line at time τ, fig (3.6a). If the line has a positive mismatch ($R > Z_o$), a positive residual voltage will be present on the line at the end of the first pulse and the discharge takes the form of gradually reducing positive voltage steps, as shown in fig (3.6b). If a negative mismatch is present ($R < Z_o$), a negative residual voltage will be present on the line at the end of the pulse and each successive pulse will see a smaller residual of opposite sign to the previous pulse.

When a mismatch is present all the energy stored in the line will not be transferred to the load in a single pulse. If only one pulse is required this would entail dumping the residual energy, therefore, in order to obtain maximum transfer efficiency, all that needs to be done is to match the line to the load. This seems sensible in principle, however operation of the pulser dictates the need for a small negative residual voltage on the line at the end of the pulse, to reverse bias the switching devices and allow them time to recover (section 3.1.4). Fortunately, power transfer efficiency is not too sensitive to the degree of mismatch required for control purposes and typically a load impedance variation of 30% from the matched condition will result in only a 3% loss in energy transfer efficiency.

It has been shown that the discharge of energy stored in the capacitance of a transmission line can produce a single rectangular voltage pulse if the line impedance is matched to the load impedance. For short pulses ($\tau < 250$ μs) this can be achieved with a suitable length of high voltage cable. For a 10 μs pulse approximately 760 metres of cable would be required [3.4]. It is obvious that a high voltage line of this length would be impractical hence some form of simulating network is required. This is known as the Pulse Forming Network (PFN).

(3.1.2) The Pulse Forming Network.

The design of a network that produces a rectangular output pulse is a mathematical problem in network synthesis. As might be anticipated no network having a finite number of elements can exactly simulate the characteristics of a transmission line, which in reality has distributed, rather than lumped, parameters. The logical way to design such a network would be to work backwards from the required pulse shape to determine the impedance function necessary to produce it. This procedure proves too difficult and it is simpler to analyse the pulse in terms of its frequency components. It is assumed that a network designed to produce a steady state alternating waveform with the same characteristics as the required pulse will produce a pulse shape reasonably close to the desired form. This assumption has proved surprisingly valid in practice.

Based on the above method Guillemin [3.6] outlines design techniques for a PFN which will produce pulses with a parabolic rise and fall and shows that this can be achieved with the parallel admittance type network, shown in fig (3.7a). These are of limited value as the capacitors generally have a wide range of values, making manufacture difficult and expensive. However, it is possible to derive three further useful canonical forms of the admittance network, as shown in figs (3.7b), (3.7c) and (3.7d). The most important pulse forming network obtained from combining the canonical network forms is the type D network, which has the advantage of equal capacitance in each mesh. The problem associated with the type D network is the appearance of negative inductance values in the shunt legs, which are produced as a result of making all the capacitors of equal value. Fortunately, negative inductances are physically realizable as mutual inductance elements. Type D networks with the negative shunt inductance replaced with mutual inductance between the coils are referred to as type E networks. Fig (3.8) shows the equivalent type E network for the network of fig (3.7d). With reference to the values of inductance, it is obvious that the centre sections have almost equal self and mutual inductance and it has been found in practice that the inductors of a type E network can be made equal without affecting the pulse shape appreciably.

One way of reducing a type E network to this latter physical form consists of winding a continuous inductance on a former, with a total inductance $L_n = \tau Z_n/2$. The total network capacitance $C_n = \tau/2Z_n$, is divided equally between the sections and each capacitor is connected to a tap on the inductor. The taps are located to obtain equal inductance for all sections except the ends, which should have 20 to 30 percent more self inductance. The ratio of length to diameter of the coil is chosen to give a mutual inductance which is 15% of the self inductance of each centre section.

Type E networks are the most commonly used for high voltage pulse generators because of the ease with which the network can be designed and constructed. The parameters required for the design are the pulse shape and the network impedance, from which it is possible to derive the total network capacitance, C_n, and the network inductance, L_n, from equations (3.9) and (3.10).

$$C_n = \frac{\tau}{2Z_n} \qquad (3.9)$$

$$L_n = \frac{\tau Z_n}{2} \qquad (3.10)$$

The number of meshes required depends on the degree of accuracy required from the pulse. Clearly, as the number of meshes is increased the output from the network will tend closer to the specified rectangular output pulse shape. A useful design guide can be obtained as most of the energy in the pulse is associated with the frequency band between zero and several times $1/\tau$. A very conservative estimate of the upper frequency limit might be taken as $10/\tau$ and equating this to the cut−off frequency of the low pass filter sections

$$f_c = \frac{1}{\pi\sqrt{(LC)}}$$

$$\sqrt{(LC)} = \frac{\tau}{10\pi} \qquad (3.11)$$

The quantity $\sqrt{(LC)}$ represents the delay time per section. Thus an N section network structure should produce a pulse of duration:

$$\tau = 2N\sqrt{(LC)} \qquad (3.12)$$

Substituting (3.12) into (3.11) yields an upper limit on the number of meshes required of N=16. For pulses of 10 μs duration, experience has shown that networks with this number of elements give excellent results. Moreover, as the pulse width τ is reduced the number of sections can also be reduced without significantly altering the accuracy of the output pulse. Typically 2–5 meshes are required for pulses in the range 0.5−2.5 μs. This feature permits a single type E network to be used to generate

pulses from the maximum pulse width down to a 10% pulse width simply by disconnecting the appropriate number of meshes.

Spall used the above technique to design a 100 Ω, 14 section PFN, with a maximum pulse duration of 10 μs and a rise time of approximately 1 μs. This was designed on the basis of Khahra's [3.2] experimental data on the characteristics of the gas discharge load and the observation that the discharge impedance is typically 100 Ω. This was somewhat erroneous since the impedance of the discharge is essentially governed by the external circuit impedance. The correct design procedure involves a knowledge of the allowable discharge energy density in order to determine a suitable value for the network impedance Z_n. This will be considered in section (4.3).

(3.1.3) Charging Techniques For Line Type Pulsers.

The charging cycle of a line type pulse modulator is a controlled transfer of energy from the source supply to the PFN. Although the charging circuit has little effect on the output characteristics of the pulser, the design of the circuit and the choice of components are of vital importance to the overall operation and efficiency. There are three important considerations in the design of the charging system, viz: (i) The same amount of energy must be stored in the network for each pulse. (ii) The charging element must isolate the power supply from the load during the pulse and for a short time immediately after the pulse, to allow time for the thyratron switch to recover. (iii) Since the pulser being considered is a high power device it is essential that the charging circuit be designed for high efficiency.

The charge cycle can be controlled by either an inductive or resistive element in the charging circuit, however efficiency precludes the use of resistive charging techniques for all but the lowest power devices as the efficiency can never be greater than 50%. The use of inductive charging elements makes it possible to design charging circuits with very high efficiency and improves the isolation between the source supply and the load. The charging supply can either be of the DC or AC type; invariably DC types are used for high frequency pulsers. The design of the charging circuit involves the selection of a suitable charging inductor. In addition to this, some practical constraints dictate the need for additional components in the charging circuit in order to improve voltage hold-off characteristics and performance. Before going on to discuss some practical charging circuits, it is worthwhile at this stage to consider the basic theory of inductive charging.

The transfer of energy from a DC power supply to a PFN can be analysed by the circuit model of fig (3.10). It is assumed that an ideal switch connects a supply of

constant voltage to the charging inductor L_c. Since the PFN inductance can usually be neglected in comparison to the charging inductance, the PFN can be modelled as a capacitor equal in capacitance to the total capacitance of the network, C_n. If the network is initially charged to a voltage $V_n(0)$, then upon closing the charging switch, the PFN voltage and current can be found from:

$$V_n(t) = V_s + [\ V_n(0) - V_s\ ]\ \mathrm{Cos}(\omega t) \qquad (3.13)$$

$$I(t) = \frac{[\ V_s - V_n(0)\ ]\ \sin(\omega t)}{\sqrt{(L_c/C_n)}} \qquad (3.14)$$

where $\omega=1/\sqrt{(L_cC_n)}$ is the resonant frequency of the circuit. Equations (3.13) and (3.14) are shown graphically in fig (3.11). It can be seen that the network charges up to a maximum voltage in a time equal to half the period of resonance of the circuit, at which point the current reverses and the network begins to discharge. A charging diode is normally included in series with the charging choke to prevent current reversal at this point and maintain the network at the peak voltage. Thus, with a charging diode included the network would reach a final voltage $V_n = 2V_s - V_n(0)$. Clearly any residual voltage present on the network before the charging cycle begins will alter the final network voltage. If the network is fully discharged before the charging cycle, the inductive charging circuit will simply act as a voltage doubler. The time at which the PFN reaches the maximum voltage is given by $\tau_c=\pi\sqrt{(L_cC_n)}$, from which it is possible to obtain the value of the charging inductance L_c required for a given charging time τ_c.

The circuit of fig (3.10) contains several assumptions and in practice circuit losses will result in a slightly lower network voltage than predicted by equation (3.13). At the mean powers required for the present application, it is quite difficult to provide a constant DC supply voltage from the charging supply, which usually requires some smoothing capacitance across the output terminals to minimize droop. The actual value of smoothing capacitance can in some instances be prohibitively high and can cause problems in circuit protection in the event of a pulser fault. Care is required in the design of the DC supply if problems of output pulse variation are to be avoided. Several practical charging circuits have evolved which meet the demanding requirements of high powered pulsers, which are basically variations of the standard inductive charging circuit. Some common examples will now be considered.

In the majority of pulser applications a circuit such as that shown in fig (3.12a) operates in a satisfactory manner [3.7]. However, because the charging diode D

conducts at the instant it becomes forward biased, it follows that in some cases the time available for the switching thyratron to recover may be insufficient for reliable operation. For hydrogen thyratron modulators with duty cycles in excess of 0.001 it is usually necessary to delay the re-charging of the PFN [3.8].

By replacing D in the circuit of fig (3.12a) with a triggered diode it is possible to delay the charging cycle until recovery of the switching thyratron is complete. This technique is referred to as "command charging" and a suitable circuit utilising a hydrogen thyratron is shown in fig (3.12b). In practice this circuit does not always work because of the effects of grid-anode stray capacitance in the charging switch [3.4]. This allows the cathode of the charging thyratron to be pulled down relative to the grid level at the instant the switching thyratron is triggered. This can result in re-triggering of the charging switch and subsequent fire-through in the pulser. Fortunately, a simple but satisfactory solution to the problem exists, as illustrated in fig (3.12b). Here a small capacitor is connected in parallel with the charging thyratron. This has the effect of coupling the anode and cathode together and consequently sandwiches the grid between them. The parallel connection of L_2 and R_2 act to delay the potential across the tube during the transient. This arrangement works well in practice, especially in devices with a small grid-anode stray capacitance.

A simple but obvious variant of the above circuit is to interchange the position of the triggered diode and the charging inductor, as illustrated in fig. (3.12). L_c then acts to isolate the charging switch from the transient caused by the switching thyratron and in most cases makes the capacitor C unnecessary. However, the disadvantage of this circuit is that ringing in the charging inductor following cessation of the charging current results in the cathode of the charging switch being driven positive relative to the anode. In severely underdamped circuits this transient may approach three times the anode voltage and consequently damage the charging switch. This system, though simple and effective, is therefore only suitable for relatively low voltage applications.

Spall's prototype pulser incorporated a charging circuit similar to the circuit of fig (3.12c), this being chosen for the reasons outlined above. When the new trigger circuits were installed it was found that insufficient protection had been included to prevent a pre-trigger on the charging switch when the discharge switch fired. Some aspects of the above circuits were incorporated in an attempt to solve this problem, however, it was not possible to solve the problem by these methods. A more detailed discussion on the problems encountered and the modifications incorporated in the charging circuit is given in section (3.6).

(3.1.4) Design of a Line Type Pulser for Gas Laser Pumping.

The discussion so far has dealt with the specific components necessary for a line type pulser: these include a pulse forming network, some form of inductive charging circuit and two high voltage switches. This section will consider how a line type pulser can be configured for gas laser pumping and examine some of the constraints imposed on circuit design.

From Khahra's [3.2] experimental work on the gas discharge it was concluded that the discharge voltage is independent of the discharge current and depends only on the gas mixture composition (see section 4.3). It is therefore possible to match the PFN to the gas discharge load simply by ensuring that the network is charged to the twice the discharge voltage. Since the discharge current is controlled by the impedance of the PFN, specification of this impedance requires a knowledge of the maximum allowable power density in the gas discharge. From the limited amount of data available on the discharge, Spall [3.1] designed a 100 Ω, 10 μs PFN, and produced the following specification for the pulser.

Network impedance	$Z_n = 100\ \Omega$
Pulse duration	$\tau = 5\text{-}10\ \mu s$
Pulse rise time	$t_r = 1\ \mu s$
PFN charge voltage	$V_{no} = 10\text{-}20$ kV
Peak pulse power	$P_{max} = 1$ MW
Maximum pulse repetition frequency	$prf = 10$ kHz
Mean output power	$P_{mean} = 100$ kW

For a pulse duration of 10 μs at a PRF of 10 kHz, the duty cycle δ=0.1, thus, a command charging system is required [3.8]. The peak power levels, together with the very high PRF, impose considerable constraints on the selection of switches for the pulser. In addition, the low impedance of the discharge dictates the use of switches with an extremely low impedance if a high overall transfer efficiency is to be attained. Hydrogen thyratrons are particularly suited to this application and typical tube voltage drops at these current levels are less than 30 volts. The problem associated with their use for the present application are the constraints imposed on tube recovery time at such a high operating frequency and duty cycle. A CX1528 thyratron was identified as meeting the specifications for both the charging and switching positions in the pulser circuit. Based on the above specifications it was possible to arrive at a basic conceptual design for the laser pulser. This will now be considered and some important implications deduced regarding the configuration of the pulser circuit.

The most common circuit for a line type pulser is illustrated in fig (3.13a). This configuration has the advantage that the cathode of the discharge thyratron is grounded thus considerably simplifying the design of the thyratron trigger and heater circuits. This circuit can also be easily designed to reverse bias the discharge tube at the end of the pulse, ensuring rapid switch−off and recovery. However, the circuit does have the disadvantages that a negative voltage pulse is produced at the output terminals and the PFN must be charged through the load. This circuit is therefore of advantage only in situations where a matching pulse transformer is available to correct the phase inversion and allow the slower charging current to pass through the primary windings with minimum power loss. It would not be possible to use this circuit configuration for the present application, since the gas discharge load would be in series with the PFN during the charging cycle. Because of the low stray capacitance of the gap, most of the charge voltage would appear across the cavity, leaving the PFN virtually uncharged.

Given the advantages of grounded cathode operation for the main switch, it would seem feasible to re−configure the circuit as shown in fig (3.13b). The problem this time is again due to the nature of the load. The discharge gap essentially isolates the switching thyratron from the PFN voltage and makes triggering practically impossible. Thus, it is apparent that if the laser is to be coupled directly to the pulser, then this will require floating the discharge switch at the full PFN voltage, as shown in fig (3.13c).

The pulser circuit of fig (3.13c) operates satisfactorily when the PFN is properly matched to the gas discharge load. However, should the load vary from the matched conditions, the subsequent residual energy remaining on the network after the pulse must be dumped before the next charging cycle can begin. In the event of this energy not being removed several possible faults can occur in the pulser. If the load goes short circuit as is common when arcing occurs in the laser, the network will swing negative at the end of the pulse. The charging cycle will then build on this resulting in a substantially higher charging voltage on the PFN. If allowed to continue for a series of pulses, this will result in the network reaching a dangerous voltage level and the possibility of breakdown in the network or other pulser components. Additionally, if the discharge impedance were larger than the matched condition, the positive residual on the network at the end of the discharge pulse could result in the PFN switch latching on. If the charging cycle was initiated before all the the residual energy was dissipated, this would cause the pulser to fire−through.

The problems associated with mismatching can be overcome by the addition of a tailbiter switch and inverse diode assembly into the pulser circuit, fig. (3.14). When

the network swings negative at the end of the discharge pulse (negative mismatch), the residual energy is dissipated in the overswing resistor R. The tailbiter switch is only necessary for operation when the load impedance is greater than the network impedance and is triggered at the end of the pulse from the network. Consequently, any positive residual voltage on the network is immediately inverted and the energy dissipated in the overswing resistor as before.

The circuit of fig (3.14) is essentially the same as the basic line type pulse modulator developed by Spall and was shown to be capable of running in burst mode at the full PRF of 10 kHz. In order to achieve the specified performance from the pulser, it was found necessary to make some additions to the pulser circuit. The modifications required were incorporated to improve the switching and recovery characteristics of the CX1528 thyratrons and offer protection in the event of a fault. With the experience gained on the early prototype circuit, it was decided to re-design some of the circuits and overcome the limitations of the prototype. The developmental work carried out in this phase of the research program will be considered in the remainder of this chapter.

(3.2) THYRATRON TRIGGER CIRCUITS.

Each of the three CX1528 thyratrons in the line type pulser must be triggered in the correct sequence by application of a high voltage trigger pulse to the control grid. The main problem associated with achieving this in practice is the need to apply the trigger pulse to the charging and discharge switches while they are "floating" at the full PFN voltage. Spall's [3.1] trigger circuit, as shown in fig (3.1), used the thyratron heater/isolation transformer to provide the necessary voltage isolation between the trigger pulse generator and the thyratron grid circuit. Although this circuit worked up to the full PRF of 10 kHz, many problems were experienced with spurious firing of the thyratrons, causing a fire-through in the pulser. The problem was identified as pick-up in the trigger pulse generator circuit and was due to capacitive coupling through the thyratron heater transformer. Filter components were incorporated in the control lines to alleviate these problems but had the disadvantage that this attenuated the trigger signal pulses. It was therefore decided to use fibre optic coupling techniques for the new trigger circuits in order to overcome the interference problems.

Spall's trigger circuit produced an "unloaded" output pulse of approximately 300 volts, with a rise time of 1 μs; this being offset against a control bias level of -70 volts. The low bias voltage of these early circuits gave rise to thyratron control problems [3.3], whilst the low trigger pulse amplitude resulted in a relatively long anode delay time. In view of these limitations, it was decided to re-design the thyratron trigger

circuits with a higher control bias and improved output pulse characteristics. However, this increased the power required for the trigger circuits, which although small in comparison to the pulser power, must be supplied through an isolating transformer rated at the full operating voltage of the pulser. Such transformers are expensive and rather bulky for 20 kV working voltage.

Fortunately, it was found that there was sufficient spare capacity on the thyratron heater/isolation transformers used by Spall to supply the trigger circuit power. The new trigger circuit was therefore designed for a 6.3 V rms supply, this being obtained directly from the secondary of the thyratron heater/isolation transformer. Although the tailbiter switch is grounded, it was decided to incorporate the same floating trigger circuit arrangement as the other switches because of the improvements offered in screening.

(3.2.1) Trigger Circuit Specification.

The CX1528 thyratron has two grids which can be driven in a variety of ways, depending on the circuit duty and the performance required [3.3]. For the present application the main constraint on the thyratron is the limited recovery time.

Grid 2 control and trigger:

Control bias: To maintain the tube in the non-conducting state a negative control bias must be applied to grid 2 relative to the cathode. EEV [3.3] recommend a loaded grid bias voltage in the range -50 to -200 volts. Although minimum recovery time can be obtained with the highest possible bias, this necessitates the use of an equally high trigger pulse amplitude. A bias voltage level of -160 volts was chosen for the new trigger circuit as this optimised both recovery time and grid power.

Trigger pulse amplitude: The trigger pulse amplitude must be substantially greater than the bias level if minimum anode delay time is required. It was decided that a peak amplitude of 1000 volts would be more than adequate as improvements in anode delay time reduction are marginal above this level.

Trigger pulse duration: The trigger pulse must be of sufficient duration to allow time for the grid-anode space to break down. The minimum specified duration is 1 μs. As pulses of a longer duration provided no advantage for this particular application, the design was based on a 1 μs pulse width.

Rate of rise of trigger pulse: With the exception of the trigger pulse amplitude, the main parameter affecting anode delay time is the control grid dV/dt. Minimum recommended value is 4 kV/μs. As a value greater than this is difficult to attain with the relatively slow slew rate of power MOSFETS, this was chosen as the design value.

Grid drive impedance: The impedance in the grid circuit determines the grid drive current. Since this also limits the bias current during the recovery period, this has a significant effect on tube recovery time. The design value is therefore a compromise between recovery time and grid power. A design value of 100 Ω was selected as satisfying both requirements.

Grid 1 control and trigger:

For the fastest and most precise triggering, grid 1 should be DC primed with a current of approximately 100 mA. As this has the adverse effect of increasing the recovery time and makes the tube more prone to spurious firing, it was decided not to incorporate this on the laser pulser. The increase in anode delay time without DC priming was felt to be an acceptable trade off for the improvement in recovery time. Instead, it was decided to RC couple grid 1 and grid 2, so that a single output pulse triggered both grids. To summarise, the trigger circuit design was based on the following specification:

Loaded grid 1 bias voltage	V_{bias} = -160 V
Trigger pulse amplitude	V_t = 1000 V
Trigger pulse duration	τ_p = 1 μs
Trigger pulse dV/dt	dV_p/dt = 4 kV/μs
Grid 1 impedance	R_1 = 100 Ω
Grid 2 trigger pulse	RC couple to grid 1

(3.2.2) Design of CX1528 Trigger Circuit With a Mosfet Output Stage.

The new trigger circuits were designed with a high power MOSFET output stage, as shown in fig. (3.15). In order to match the characteristics of the available devices with the circuit specification, it was necessary to use a step-up pulse transformer in the output stage. This offered the additional advantages of improved grid recovery and isolated the MOSFET from the thyratron grid circuit. A detailed design for this circuit can be found in appendix B1. The important conclusions drawn from this study will now be discussed.

Power mosfet selection

From a survey of power MOSFET devices a Philips type BUZ45B was selected [3.9]. This device provided the necessary peak power and mean power ratings with a maximum voltage rating of V_{ds}(max)=500 volts. Although devices were available with higher voltage ratings their peak power limitations made them unsuitable for this application. In order to prevent the transient voltage on the FET rising above the maximum rating, it was necessary to reduce the operating voltage to 340 V. The power for the output stage was supplied from a +340 V supply card, as shown fig. (3.19). For a 1000 V output pulse, the transformer has a step-up ratio of 1:2.9, giving a grid current pulse of approximately 8 amps. This results in a total FET peak current of 25 amps and a mean drain current of 250 mA at 10 kHz prf. This compares with an FET rating of I_{ds}(max)=30 A and I_{ds}(mean)=350 mA.

Pulse transformer

Fig. (3.16) shows the equivalent circuit for the output stage. The secondary load Z_2 referred to the primary represents the combined effects of the grid drive impedance R_1 and the CX1528 grid-cathode drop. From this it is apparent that the FET must conduct the pulse transformer magnetizing current in addition to the main pulse current. The rise time of the output pulse is controlled both by the FET turn-on time and the pulse transformers leakage inductance. The pulse transformer design was based on a peak magnetizing current of 1 amp at the end of the 1 μs FET gate pulse. A pair of ferrite U cores was selected which satisfied the peak flux requirements. The air gap was chosen to give an optimum winding configuration with minimal leakage inductance, in order to minimize the pulse rise-time. The transformer has double primary and secondary windings, wound on ABS formers with a PTFE secondary screen bobbin, as shown in fig. (3.17). The complete transformer assembly is encapsulated in silicon rubber and the primary/secondary isolation tested up to 5 kV.

Bias supply

The bias supply of -160 volts was connected to the thyratron grid via the secondary of the pulse transformer. This configuration was adopted because the inductance of the pulse transformer produces a large inverse voltage on the control grid during the thyratron recovery period [3.3], which significantly reduces the recovery time. A pulse capacitor C_1 was connected directly from the pulse transformer output to the screen on the trigger unit to conduct the trigger pulse current. The bias supply circuit is shown in fig. (3.19).

Reciever circuit

This circuit, fig. (3.18), amplifies the signal from the fibre optic receiver to a level sufficient to trigger the BUZ45B. The light pulse at the recieving end of the fibre-optic is detected by the photo-diode and amplified by the LM353N dual op-amp. This signal then triggers a 555 timer connected as a 1 μs monostable pulse generator whose output is used to trigger the BUZ45B. As the signal generated by the photo-diode is quite small, the amplifier necessarily has a high gain and the circuit is therefore particularly susceptible to pick-up. The Schmitt trigger was added to improve the noise immunity of the circuit. In addition, the circuit card was fabricated with an earth screen on both sides and the amplifier card enclosed in a screened box. High quality CMOS integrated circuit components were chosen because of their excellent noise immunity.

Circuit layout and wiring

The complete circuit diagram for the MOSFET trigger unit is shown in fig (3.19). The circuit is housed in a screened enclosure and mounted on ceramic pillars to provide the necessary isolation from ground. The power to the unit is supplied from the secondary of the thyratron heater transformer T1 at 6.3 V rms. This is stepped up to 240 V rms in transformer T2, which feeds the +340 V supply card directly. All the circuit components are mounted on an earth sheet within the enclosure, which is "grounded" to the CX1528 cathode via one of the supply leads from the heater transformer. To avoid ground loops the grounded power lead was used as the return for the trigger pulse current. The control pulse from the trigger signal generator was coupled to the reciever circuit with a high quality polymer fibre optic cable.

(3.2.3) MOSFET Circuit Performance.

The trigger circuit was first tested into a dummy load of 150 Ω connected directly across the secondary of the pulse transformer. The power to the unit was supplied from 240 V mains, with the voltage on the FET controlled by a variac. transformer, as shown in fig. (3.20). This allowed the output voltage to be gradually increased up to the full 340 V level.

When the unit was first switched on it was found that the BUZ45B and several of the IC's in the reciever circuit had blown. The problem was traced to a bad earth on the reciever circuit, which caused the full mains voltage to be applied to the gate of the FET. Several more FET's were blown as a result of bad earths and it was decided to re-wire the unit with single point earthing. In addition to this, fuses were

incorporated in the AC supplies to the +340 V card and the bias supply card, to prevent the full 340 V being applied to the amplifier board when the FET blew. Some problems were also experienced with self triggering of the FET. This was traced to pick−up from the pulse transformer and was rectified simply by screening the FET from the pulse transformer. With the above modifications the trigger circuit was tested up to the full output voltage and pulse repetition frequency. No further problems were experienced with the circuit on the dummy load.

The output pulse from the trigger unit at the full FET voltage of 340 V and a gate pulse of 1 μs is shown in fig. (3.21). The characteristics of the trigger pulse can be summarised as follows:

Peak pulse amplitude	V_p = 864 V
Rise time (10-90%)	t_r = 0.75 μs
Rise time (0-100%)	t_r = 1.25 μs
Rate of rise	dV/dt= 2 kV/μs
Pulse duration	τ = 2.0 μs

It is clear from the above data that the trigger circuit falls short of the design specification in respect of the trigger pulse amplitude and rise−time. The lower peak amplitude is due to losses in both the pulse transformer and the FET. The rate of rise of voltage is limited both by the transformer leakage inductance and the FET turn on time. The turn on/turn off characteristics of the FET are illustrated in fig. (3.22). On a purely resistive load the BUZ45B has a turn on delay time t_d= 50 ns and a rise time t_r= 100ns. It is clear that the pulse duration is longer than the 1 μs design value because of the relatively slow turn off time of the FET.

It was concluded that any further improvement in output characteristics would involve considerable develoment and, although the performance was below specification, the characracteristics of the output pulse represented a major improvement over Spall's circuit. No modifications were therefore made to the trigger circuit at this stage in an attempt to improve the output characteristics.

Before commissioning the laser pulser in full, the performance of the three thyratrons and trigger circuits were evaluated in a high voltage test circuit, as shown in fig. (3.23). This comprised a high voltage supply, a 250 Ω, 10 μs PFN and a variable impedance load. The power to the trigger circuit was supplied from the secondary of the thyratron heater transformer. The power was switched on and after a five minute thyratron warm−up period, the PFN was charged to 5 kV and a trigger pulse applied. The thyratron fired on the first attempt but failed on subsequent attempts.

On inspection it was found that the FET had blown as a result of a high voltage from the 340 V supply card. This was due to the output from the thyratron heater transformer being 7.3 V instead of 6.3 V rms. Although this voltage was above the maximum heater voltage specified by EEV, it was decided not to reduce the voltage on the secondary of T1, as these transformers had been used by Spall, it was assumed that this voltage was correct. In order to bring the voltage inside the trigger unit back to the correct level of 240 V rms, the step−up transformer T2 was modified by adding two turns to the primary winding. With this modification the trigger units were succsessfully tested up to a full PFN voltage of 20 kV. It was found that the trigger unit worked equally well with a pure resistive load and a matched gas discharge load in the test circuit. The only problem encountered was the occasional failure of the FET. This occurred only a few times and as no fault in the circuit could be found, the failure was put down to bad handling of the rather sensitive FET. It was found that great care had to be taken in handling the the FET as it was easily damaged by "static" during installation.

It was not possible to assess such factors as recovery time and anode delay time on the test circuit because of the floating switch arrangement. The test circuit was also limited in that only single shot tests could be carried out. After each thyratron and trigger unit had been tested they were connected into the laser pulser circuit for final evaluation. A full account of the commissioning procedure is given in section (3.6). The major conclusions from the commissioning work, in relation to the design and performance of the trigger circuit, can be summarised as follows.

The MOSFET trigger circuit operated satisfactorily on the PFN charging switch up to the full DC supply voltage of 10 kV. During the first phase of pulser commissioning the laser cavity was replaced with a water cooled, 50 Ω, resistive load. The PFN was charged up to a voltage of 11 kV and the DC supply isolated before the discharge switch was fired. It was found that the FET failed when the switch fired. It was concluded that the failure was the result of the thyratron grid spike. This was not experienced on the test circuit or on the charging switch because of the much lower anode di/dt. All attempts to measure the magnitude of the thyratron grid spike failed because of the difficulties experienced triggering the Tektronix 648 oscilloscope.

Several modifications were made to the trigger circuit for the discharge switch to protect the FET from the thyratron grid spike, which was believed to be coupled to the FET via the stray capacitance between the windings of the pulse transformer PT1. The modifications, as illustrated in fig. (3.24), included: (i) Connecting a series of fast recovery avalanche diodes directly from the control grid to the cathode. (ii) Connecting a varistor across the souce and drain of the FET. (iii) Connecting a low

pass filter in the thyratron grid line.

Only a marginal improvement in reliability was achieved with the above methods of protection. In view of these difficulties and since no solution to the problem of protecting the MOSFET could be found, it was decided to examine the suitability of other power devices for the CX1528 trigger circuit.

(3.2.4) Design of Trigger Circuits With a Thyratron Output Stage.

Commissioning of the pulser circuit highlighted the problems associated with the thyratron grid–spike and the reliability of the power mosfet in the trigger circuits. After considerable perseverance it was finally decided to replace the FET with a more robust device. A small glass envelope thyratron was selected, because of its fast switching characteristics and reliability. The problem with using a thyratron was the added complexity of the thyratron support circuitry, which includes both a cathode heater supply and trigger circuit. In addition, the thyratron circuit has to be operated at a high voltage and the circuit designed to ensure recovery of the tube at the end of the pulse. A detailed design for the thyratron based trigger circuit can be found in appendix B2. Some of the important features of the design will be presented here before going on to discuss trigger circuit performance.

An inverter circuit was proposed for the CX1528 trigger circuit output stage, as shown in fig. (3.25). This was chosen principally because it allows the cathode of the trigger tube to be grounded and therefore considerably simplified the design of the associated trigger circuit. It is also possible with careful design of the inverting pulse transformer to satisfy the recovery requirements for the trigger thyratron. The inverter circuit is equivalent to a parallel RLC circuit, fig. (3.26), where L is the pulse transformer shunt inductance and R is the secondary load impedance referred to the primary coil. As the pulse transformer is the major cost item in the circuit, it was decided to examine the possibility of using the step–up transformer built for the MOSFET trigger circuit, as a step–down transformer in the inverter circuit. From appendix B2, the step down ratio is r = 0.345, giving a load referred to the primary R=900 Ω. The pulse transformer primary inductance will now be 2.9 mH.

With the above values of R and L it is clear that the pulse duration will be controlled by the RC time constant. Thus, for a trigger pulse with a 1 μs time constant, the value of capacitor C1 will be approximately 0.001 μF. It can be shown that the circuit damping factor is given by [3.10]

$$\xi = \frac{1}{2R}\sqrt{\left(\frac{L}{C}\right)} \qquad (3.15)$$

With R = 900 Ω and C = 0.001 μF, the circuit will be critically damped if

$$L > 4\ R^2\ C = 3.2\ \text{mH}.$$

It is clear, therefore, that using the original pulse transformer will give rise to a circuit which is slightly underdamped ($\xi = 0.946$). This is exactly what is required since this will produce a current reversal through the trigger thyratron and cause the tube to switch off. It was decided to operate the trigger thyratron at an anode voltage of 3.5 kV in order to produce an output pulse with an amplitude in excess of 1 kV.

Thyratron selection

For an operating voltage of 3.5 kV, the peak trigger thyratron current is 3.8 A, with a mean current of 35 mA at 10 kHz PRF. A small glass envelope thyratron, EEV type FX2530 was selected for this circuit duty, as this tube satisfied the operating conditions and had the required recovery characteristics.

Charging circuit.

Capacitor C_1 must be charged to the full voltage of 3.5 kV during each cycle. In order to give the FX2530 the maximum possible recovery time, a DC resonant charge circuit was chosen, with a charge time $\tau_c = 95\ \mu s$. With this charge period the charging choke has an inductance of 0.9 H. This was constructed of two coils of 1124 turns in series on a pair of gapped ferrite U cores. The 1.75 kV, DC supply was designed for a maximum of 5% ripple voltage.

FX2530 trigger circuit.

The FX2530 trigger thyratron is a triode tube which must be triggered by a high voltage pulse on the control grid. In addition, the cathode heater requires a current of 4 A at 6.3 V rms. The following specification was selected from the manufacturers data:

Unloaded grid drive pulse amplitude	$V_p = 340$ V
Pulse duration	$\tau = 2.0\ \mu s$
Pulse rise time	$t_r = 1.0\ \mu s$
Grid drive impedance	$R = 470\ \Omega$

Fig. (3.27) illustrates the basic components of the FX2530 trigger circuit. The trigger pulse amplitude was selected as 340 V, since this can be obtained directly from

rectified 240 V supply. This circuit is identical to the MOSFET trigger circuit for the CX1528 tube but is of much lower output power. The pulse transformer PT2 has a turns ratio of 1:1 and was designed around a ferrite pot-core assembly (Mullard type FX2243). This design gives a peak FET current of 770 mA and a mean curent of approximately 10 mA at 10 kHz PRF. An IRF740 MOSFET was selected for this duty. The circuit also includes protection to limit the peak inverse voltage on the FET: this includes a "freewheel" diode across the primary of the pulse transformer and a fast avalanche diode connected directly across the drain source of the IRF740.

Circuit protection

In view of the relatively high voltage in the inverter circuit, it is necessary to incorporate some means of protecting the circuit components in the event of a fault. The two most likely problems are: thyratron latch-on and overvolting due to load short circuits. The first of these problems is overcome by tripping the supply to the HT transformer when the current through the thyratron exceeds the normal operating value. This was achieved by a current trip positioned on the FX2530 cathode line, as shown in fig. (3.28). To prevent excessive voltage developing across the thyratron during load faults, an inverse diode and resistor are connected directly across the FX2530 trigger thyratron.

Circuit description.

Fig. (3.29) illustrates the main components of the CX1528 trigger circuit. This utilises most of the components from the prototype MOSFET circuit with the exception of the BUZ45B. The output from the amplifier card is now used to trigger the IRF740 in the FX2530 trigger circuit. The power to the unit is supplied as before from the CX1528 isolating transformer at a voltage of 6.3 V rms and stepped up to 240 V rms in transformer T2. The HT transformer T3 and 340 volt FX2530 trigger supply card are both connected directly to the 240 V output of transformer T2. The 100 V rms supply for the CX1528 bias card is obtained from transformer T5. The complete circuit assembly is mounted on an earth sheet and screened in a metal enclosure, as shown on plate (6). As in the MOSFET trigger circuit, the supply lead which is common with the CX1528 cathode is used as the trigger pulse current return.

(3.2.5) Thyratron Circuit Performance.

During the initial tests it was found that the amplitude of the FX2530 trigger pulse from PT2 was much lower than the design value. As a result it was necessary to rewind the pot core transformer PT2 with the turns ratio 20:45. This was necessary in

order to increase the flux in the core and ensure good magnetic coupling between the primary and secondary. This modification resulted in a peak FX2530 trigger pulse of 320 V, but increased the peak FET current to 1.2A.

To allow the output voltage to be increased in stages during commissioning, the HT transformer T3 was supplied from a variac, with all other transformers and circuits supplied directly from mains. A dummy load of 150 Ω was connected across the secondary of the pulse transformer. With a voltage of 1 kV on the inverter charging circuit (measured across C_2) a single trigger pulse was applied to the unit. The peak output voltage recorded at this setting was 672 V. The trigger pulses were then applied continuously at a PRF of 100 Hz and the supply to the HT transformer slowly increased up to the full 240 V rating. At this setting the inverter charging voltage was measured as 1.8 kV, with a corresponding peak output pulse voltage of 1.25 kV. The PRF was then increased until the unit failed at approximately 4 kHz.

On inspection it was found that one of the diodes in the inverse diode circuit had blown and further tests indicated that this was the result of a high FX2530 voltage. A peak voltage during the charge cycle of 4.1 kV was recorded. As this exceeded the combined ratings of the three series diodes in the inverse diode circuit it was decided to reduce the DC charging voltage to 1.4 kV and, in addition, add an extra diode in the inverse diode circuit. It was found that the IRF740 failed on several occasions and this was found to be due to the peak voltage being exceeded during turn-off. In view of these failures the IRF740 operating voltage was reduced to 300 V.

Fig (3.30) shows a single recording of the FX2530 voltage and pulse transformer output voltage on the commissioning circuit, with a DC charging voltage of 1.42 kV. Due to the regulation of the HT transformer, the output voltage dropped from the initial value of 1.42 kV down to 1.17 kV at 10 kHz PRF. However, it was observed that the plateau of the output pulse remained at approximately 1000 V throughout this range of operating frequency. With the variac set to give a DC charge voltage of 1.42 kV (approximately 200 V rms), the trigger circuit was tested successfully up to the full operating frequency of 10 kHz with no further problems.

The original circuit was modifed to bring the DC charging voltage down to 1.42 kV and the IRF 740 operating voltage down to 300 V. Since both circuits required an AC supply of approximately 200 V rms, transformer T5 was replaced with a 200 VA unit, with a secondary winding of 200 V to supply both the 300 V supply card and the HT transformer T3. Transformer T5 was also wound for the 100 V rms supply for the bias supply card and an isolated 6.3 V rms supply for the FX2530 heater. The CX1528 trigger circuit, complete with all modifications is shown in fig. (3.31).

The performance of the trigger circuit was then examined in the same test circuit as the MOSFET trigger circuit, fig. (3.23). The output lead from the trigger circuit was connected to grid 2 of the CX1528 thyratron via a 100 Ω resistor. The unit was initailly tested with no voltage on the PFN. A recording of the output trigger pulse, measured between the 100 Ω grid resistor and the thyratron cathode, is shown in fig. (3.32). It can be seen that this pulse exhibits a slightly larger ringing amplitude than the pulse recorded on a purely resistive load, this being due to the effects of the CX1528 grid–cathode break–down. Also shown is a recording of the grid/cathode voltage, which clearly illustrates the voltage collapse as the grid/cathode space breaks down. The characteristics of this breakdown gives a good indication of the condition of the tube. For a CX1528 tube operating at the correct reservoir current, the grid/cathode voltage should collapse to approximately 30 V. The trigger circuit was tested with no anode voltage on the CX1528, up to the full operating frequency of 10 kHz. No problems were experienced with the trigger circuit and it was found possible to switch the trigger pulses on at any frequency.

Following the the above test, the PFN in the test circuit was charged to 10 kV and the thyratron fired on single shot. As in the case of the MOSFET trigger circuit, the switching performance was examined with both a resistive load and gas discharge load in the test modulator. No failures occurred and the trigger circuit was tested successfully on single shot with a maximum voltage of 20 kV on the PFN.

The three completed trigger units were then installed in the laser pulser for final evaluation. Details of the commissioning work on the pulser will be considered in section (3.6). It was not found necessary to make any major modifications to the trigger circuits as the laser pulser was successfully completed with these trigger units. Operational experience with the pulser has shown the trigger circuits to be very robust, with practically no failures occurring, even during a fire–through in the pulser.

(3.3) PULSER DC CHARGING CIRCUIT.

The high voltage pulse forming network (PFN) must be charged to the correct voltage prior to each discharge pulse. Methods of achieving this have been considered briefly in section (3.1.3), where it was concluded that the most suitable technique is that of resonant charging from a DC supply. With reference to the specifications for the pulser, as given in section (3.1.4), it is clear that the DC supply must have an output voltage in the range 5–10 kV and be capable of delivering a mean power of approximately 100 kW. In addition, since any fluctuation in the DC supply voltage will give rise to a fluctuation in the output voltage from the pulser, it is essential

that the DC supply be designed with minimum ripple voltage.

The DC supply used by Spall comprised a 133.5 kVA transformer and a solid state, three phase bridge rectifier. The output voltage from the rectifier was smoothed with a 0.25 μF high voltage capacitor. During Spall's development work on the pulser, many fire-throughs occurred and the subsequent fault current resulted in damage to the solid state rectifier stack. It was found that even the fastest acting fuses did not protect the rectifier diodes under these overload conditions. This problem was exacerbated by the need to bypass the fuses during switch on as the transformer inrush currents exceeded the fuse ratings.

It was therefore decided to install a high power mercury arc rectifier (MAR) system in the present facility, since this would be capable of running under the full pulser short circuit conditions. In view of the problems experienced on Spall's prototype, it was also decided to re-design the DC supply overload protection circuitry and to integrate this with the pulser control/overload circuits. A more detailed account of this work can be found in section (3.4), however, some aspects of the overload circuits, relating in particular to the control of the DC supply, will be discussed in this chapter.

(3.3.1) General Description.

The high PRF line type pulser is resonantly charged from a high voltage DC supply, which due to the limited space available is situated outside the laboratory and enclosed within a safety screen. The main components of this system are a high voltage step-up transformer and a high power mercury arc rectifier, fig. (3.33). The supply is rated at 133.5 kVA and is capable of supplying the pulser continuously at the full operating frequency of 10 kHz. The 133.5 kVA three phase transformer is connected to the main supply panel via 200 amp HRC fuselinks, contactor and moulded case circuit breaker (MCCB). The transformer is delta-star configuration with a rated output line voltage of 10 kV. This can be tapped down to 50% of the rated line voltage in ten equal steps by setting the taps on the side of the transformer.

Fig. (3.33) also shows a schematic of the DC supply control circuitry, which is housed in the main supply panel and in the cabinet within the safety enclosure. This circuitry provides the control for the main contactor and the grid and excitation supplies for the MAR. In addition to these functions, this circuitry integrates the overload protection circuitry of the DC supply and the pulser. Power for the control circuits is obtained from the auxiliary power switch situated on the main supply panel.

(3.3.2) Mercury Arc Rectifier.

The switch from the solid state rectifier bridge to the MAR was brought about by the need for the power supply to tolerate short circuit faults. The MAR system installed has a rating of 600 kW at a line voltage of 10 kV and is therefore capable of supplying the full transformer short circuit current (see section 3.4). In addition to this, the MAR set has several operational features which are beneficial to the control and safety of the power supply, including:

(i) Variable control of the DC output voltage.
(ii) Rapid arc suppression in the event of a fault condition or emergency.
(iii) A means of isolating the pulser from the DC supply without switching off the mains feed to the high voltage transformer.

Connection to the HV transformer

The MAR comprises six AR64 excitron tubes connected in a three phase bridge configuration, as shown in fig. (3.34). The tubes are numbered from left to right 1,3,5 on the top rack and 2,4,6 on the bottom rack. The negative busbar is situated above the top rack with the positive busbar situated behind the surge arrestors. The MAR is connected directly to the three phase output terminals of the step up transformer. The transformer is delta–star configuration with a vector reference Yd11, such that the secondary phase voltage leads the respective primary voltage by 30 degrees. The neutral point of the star is connected to the terminal on the side of the transformer. This is not required for the normal running of the power supply, however, it is necessary to use this to phase the MAR grid signals correctly with the transformer output.

AR64 Excitron tube

High voltage AR64 excitron tubes are single anode, pool cathode, mercury arc rectifiers, requiring continuous DC excitation [3.11]. The main features of this tube are shown in fig. (3.35). When an AC voltage is applied to the tube, the point at which conduction begins can be controlled by the control grid voltage. When the grid is maintained sufficiently negative with respect to the cathode, the electrons emitted from the cathode are maintained within the grid cathode space and the tube will not conduct during the positive half cycle. Only when the grid is raised to approximately cathode potential during the positive half cycle can conduction begin. Once conduction is initiated the grid looses control and this is only regained when the current reverses or commutates to another tube.

Excitation supplies

The excitation is initiated by the dipper, which is mounted above the mercury pool and balanced so that the graphite ignition electrode rests in the pool. When the excitation supply is switched on a short circuit current passes through the windings of the gapped reactor to the dipper. This reactor is positioned next to the tube such that the stray flux produced attracts the armature of the dipper, lifting the ignition electrode out of the mercury pool. As this lifts out of the pool an arc is initiated and the current falls to the normal excitation value. The normal excitation current produces sufficient stray flux in the reactor to hold the dipper above the pool and maintain the arc. A 38V DC supply is used for the ignition and excitation, which is obtained from the secondary of the excitation transformer 502T, fig. (3.36). A spark gap 502SG is fitted between the dipper and the cathode so that, should the excitation fail, the energy stored in the choke will be absorbed by the resistor 502R2. Under normal running conditions the excitation current can vary between 1.4 and 3.1 amps, depending on the main anode current. This can be measured off load by connecting an ammeter in the dipper supply line: this should give a reading of 4.1 amps.

MAR Grid supplies

The MAR employs a phase control system for controlling the firing points of the six excitron tubes. In this method a negative bias of -70V DC and an AC signal of 148 V rms are simultaneously applied to the control grid. Each excitron can fire only during the positive half cycle of the anode waveform if the grid is driven to approximately cathode potential during that period. By adjusting the phasing of the grid AC signal relative to the excitron anode supply, it is possible to control the point where conduction begins. Fig. (3.37) illustrates how the MAR input line voltage varies with time and lags the respective phase voltage by 30 degrees. The output voltage from the three phase bridge circuit is the envelope of the line voltage waveforms. For each cycle of the mains there are six oscillations on the output waveform.

The firing sequence of the excitron tubes is illustrated in fig (3.38). It is clear that each tube conducts for $2\pi/3$ radians and commutation occurs at the intersection of the line voltage waveforms. Also, both tubes on the same phase line fire in anti-phase to each other, e.g. period from tube 4 commencing conduction to tube 3 commencing conduction is π radians.

As discussed previously, the excitron will conduct when the grid is brought to cathode potential and this is controlled by altering the phasing of the grid signal relative to

the excitron anode supply. This is achieved by means of a variable phase shifting transformer, which feeds both the grid and excitation transformers via a zig-zag transformer 500T, as shown in fig. (3.34). The zig-zag transformer was necessary for the MAR's previous duty where two sets were coupled together in parallel for six phase rectification, with the grid and excitation supplies for both sets being supplied from the one phase shifting transformer. The zig-zag transformers corrected the grid signal phasing between the sets to the required 30 degrees difference. For the present application it was decided not to remove the zig-zag transformer since all the necessary connections were made to the grid and excitation transformers, 508T and 502T. All that was required was to make the necessary allowance for the 10 degree lag produced by the zig-zag by compensating in the phase shifting transformer i.e. advance by 10 degreees from correct setting.

The control grid phasing is set by advancing the control grid signal with respect to the HV phase voltage, such that the grid fires before the normal commutating point. The grid fires when the AC signal exceeds the bias voltage (-70V dc) such that the grid is at cathode potential. This occurs 28 degrees after the zero point of the grid AC signal. With reference to fig (3.37) it is clear that commutation occurs 30 degrees after the zero point of the anode phase voltage (eg red phase) and for normal running it is recommended that the grid should fire 20 degrees in advance of this point. With reference to fig (3.39), it is clear that for this condition to be satisfied, angle α should be 10 degrees.

As the two tubes on each phase fire in anti-phase to each other, the grid control signals must also be in anti-phase. This is shown by the solid and broken lines in fig. (3.39). Examination of the tube firing sequence, fig. (3.40), reveals that tube 4 fires 30 degrees after the red phase voltage passes through zero. Therefore, the control signal for this tube is represented by the solid line of fig. (3.39). This is also true for tubes 2 and 6 if the reference phase voltage is taken as the one feeding the tube. Thus, it is possible to check the grid signal phasing by monitoring the grid signals on any of the tubes in the bottom rack using the feed line as the reference phase voltage together with main transformer neutral. If the top tubes are to be checked, it should be noted that the control signal will be antiphase, as shown by the dashed line, fig. (3.40b).

The phasing is set by the phase shifting transformer and this can be set prior to commissioning by advancing the secondary phase voltage 60 degrees ahead of the primary phase voltage. This is essentially the free running condition. This method of phasing the control signals is used when setting up the system. Once this has been achieved it is possible to fine tune the output DC waveform by adjusting the position

of the phase shifting transformer rotor when the DC supply is on load. This can be done by the phase shifter remote control unit, which plugs directly into the control bus on the main supply panel (see appendix B3). If desired, it is possible to offset the phasing so that a reduced output voltage is produced. Generally, this should be avoided, since it tends to reduce the life of the excitron tubes.

(3.3.3) DC Supply Control Circuits.

The DC supply is controlled locally from the main supply panel outside the laboratory, with a visual indication of the status being given on the instrument panel. All control actions are performed by two control circuits. One circuit is housed in the main supply panel, which controls the mains feed to the high voltage transformer. The other circuit, the MAR control circuit, is housed in the relay cabinet within the safety enclosure: this controls the MAR grid and excitation supplies. Full details of these circuits can be found in appendix B3, together with a description of circuit operation. Both the DC supply control circuits are interlocked to provide a controlled shut-down in the event of a fault or overload. These trip circuits are fully interlocked with the pulser overload protection circuitry; this task being implemented by the power supply control module inside the laboratory. A full account of the overload/trip circuits is given in section (3.4).

The control circuits are designed in order that the correct start-up sequence is performed. All trip circuits must be set prior to switch-on. When the main contactor is energised, the DC output voltage from the rectifier can be set by the phase shifting transformer. The excitron grid drive can be operated remotely on the main control module within the laboratory to isolate the pulser from the charging supply during minor operational changes to the gas recirculator.

(3.3.4) DC Supply Commissioning.

Proir to commissioning, all excitron tubes were removed from the rack and the anodes heated for approximately thirty minutes to vaporize any mercury deposited on the anodes. This is generally not required, however, since the tubes had not been used for a considerable period of time, this was carried out as a precautionary measure. After completing and checking the wiring installation, the first step in the commissioning programme involved phasing the excitron grid signals to the transformer output.

In the initial wiring installation, the excitation transformer 502T was supplied directly from the auxiliary power lines, with the grid transformer 508T supplied from the

phase shifter. This was adopted because it was felt that the phase shifting transformer available was not capable of supplying both the grid and excitation power requirements. With the auxiliary power on, the excitation supply was energised and the excitation currents checked on all the excitrons. With the grid supplies disconnected at the excitron socket, the grid drive was energised and the phasing of the grid waveforms examined. It was found that the output from the phase shifter had a high third harmonic content, indicating saturation of the transformer core [3.12]. The problem was found to be due to the connections between the grid and excitation transformers (see fig 3.36) and the phasing between the output from the phase shifter and the supply to the excitation transformer. This problem was overcome by supplying both the grid and excitation transformers from a single phase shifter, as shown in fig. (3.36). The phase shifter was advanced to the correct setting i.e. secondary voltage 50 degrees in advance of the primary supply.

Low voltage test

Before preceeding to a full voltage test, the rectifier was examined at a reduced voltage. In the test circuit, as shown in fig. (3.41), the primary supply to the main transformer was fed through a three phase auto-transformer to reduce the output voltage from the high voltage transformer. The tap setting was set to 50% rated output voltage. The high voltage output from the MAR was dumped into an air cooled load, comprising thirty 1 kW electric fire elements. The following test data was obtained:

Primary phase voltage	V_{1p} = 85.7 V rms
Primary line current	I_{1l} = 10.0 A rms
Secondary phase voltage	V_{2p} = 1030 V rms
Mean DC current	I_{dc} = 1.3 A

Using the known resistance of the load (R=1800 Ω, measured at room temperature) it is possible to determine the theoretical performance of the rectifier and compare this with the test data. From the above data, the mean DC voltage is:

$$V_{dc} = I_{dc} \times R$$

$$V_{dc} = 1.3 \times 1803 = \underline{2344\ V}$$

This compares well with the recorded voltage waveform and confirms the current measurement. The theoretical performance of the rectifier can be obtained following the methods outlined in reference [3.13]. For a three phase bridge rectifier.

Mean DC voltage

$$V_{dc} = 1.351 \times V_{21}$$

$$= 1.351 \times \sqrt{3} \times 1030 \qquad V_{dc} = \underline{2408\ V}$$

Mean DC current

$$I_{dc} = \frac{V_{dc}}{R} = \frac{2408}{1800} \qquad I_{dc} = \underline{1.338\ A}$$

Transformer VA rating

$$VA = 1.05 \times V_{dc} \times I_{dc}$$

$$= 1.05 \times 2408 \times 1.338 \qquad VA = \underline{3.383\ kW}$$

Secondary line current

$$I_{21} = 1.414 \times I_{dc}$$

$$= 1.414 \times 1.338 \qquad I_{21} = \underline{1.89\ A}$$

Primary line current

$$I_{11} = \frac{I_{21} \times V_{2p}}{V_{11}}$$

$$= \frac{1.89 \times 1030}{\sqrt{3} \times 85.7} \qquad I_{11} = \underline{13.1\ A}$$

It can be seen that the theoretical predictions are slightly higher than the actual values recorded, however, this is to be expected as the above equations do not account for losses in the transformer and rectifier.

High voltage test (5 kV line voltage).

On completion of the low voltage test, the variac was removed and the primary of the transformer reconnected to the main supply panel. The transformer tapping was set to 50 % rated output voltage. The output of the MAR was connected to the same dummy load as used in the low voltage test. Thus, the test circuit and instrumentation used was identical to the low voltage test circuit, fig. (3.41), with the transformer being connected directly to the main supply panel. A high voltage probe was connected to the positive busbar on the MAR to measure the DC output voltage. The following test data was recorded, with the output waveform from the rectifier being shown in fig. (3.42).

Primary line current	I_{11}	= 32.1 A
Secondary phase voltage	V_{2p}	= 3000 V

Mean DC voltage	V_{dc}	= 5950 V
Mean DC current	I_{dc}	= 3.3 A

As above, the following theoretical values can be calculated, based on the measured secondary phase voltage and load resistance [3.13]:

V_{dc}	=	7020 V
I_{dc}	=	3.894 A
VA	=	28.7 kVA
I_{21}	=	5.506 A
I_{11}	=	39.8 A

Comparing the above values with the test data, it is clear that neglecting losses in the transformer and rectifier gives rise to a considerable error in the predictions. This is mainly the result of a voltage drop in the transformer due to the leakage reactance and not due to voltage loss in the excitron tubes. It can be shown that the transformer reactance also produces a commutation loss. This voltage drop can be estimated from [3.14]:

$$\Delta V = \frac{3 \times I_{DC}}{\Pi} \qquad (3.18)$$

Where X is the transformer leakage reactance/phase. From appendix B4:

$$\underline{X = 80.1\ \Omega}$$

giving:

$$\Delta V = \frac{3 \times 80.1 \times 3.894}{\Pi}$$

$$\Delta V = \underline{298\ V}$$

Thus, taking into account the effect of the transformer leakage reactance, the predicted DC voltage is:

$$V_{dc} = \underline{6722\ V}$$

This modification to the calculations brings the theoretical predictions much closer to the actual test data, although there still remains a significant discrepancy, particularly in the calculated DC output voltage. Nevertheless, the results are in reasonable agreement and from the test data we have a conversion efficiency:

$$\eta = \frac{5950 \times 3.3}{\sqrt{3} \times 415 \times 3.3} \quad \Rightarrow \quad \underline{\eta = 85.0\ \%}$$

This compares well with the theoretical maximum efficiency for the three phase bridge rectifier (with no commutation losses and no diode losses) of 95.5 %. It would have been of advantage to test the DC supply up to the full power ratings, however, the limitations on the dummy load power capacity did not permit this. The final assessment of system performance was left until the laser pulser was completed.

(3.4) OVERLOAD PROTECTION CIRCUITRY.

The pulser and DC charging supply were designed on the basis of normal running conditions and component ratings selected accordingly. However, it is possible that during normal operation of the power supply several overload and fault conditions can arise, resulting in substantially higher than normal power levels in the system. Such faults must be detected and brought under control before any of the power supply components are damaged. In view of the high voltage levels on the system, care must be taken in the design of the protective circuitry to ensure that the switching transients induced by the overload trips do not create further problems in component protection. As the overload circuits themselves are subject to possible failure suitable back−up protection must be provided. Although each fault condition can initially be considered in isolation, it is also necessary to consider the interaction of the trip systems, if proper discrimination is to be assured.

The first step in the design of the overload protection circuitry was the specification of all possible faults and the calculation of prospective fault currents. Suitable fault detection and trip systems were then designed to bring the system under control in a timescale sufficient to ensure protection of the system components. The design of the protective circuits therefore required *a priori* knowledge of equipment fault capabilities, this data being determined from the appropriate electrical standard. However, several of the system components were not covered by standards and it was therefore necessary to make an educated judgement in this instance. As both faults on the pulser and charging supply give rise to a fault current in the high voltage transformer, it has been possible to isolate several different faults with a single common trip circuit on the main three phase supply lines. Thus, the main overload protection for the system comes from the circuit breaker on the supply panel, with backup protection being provided by the HRC fuselinks. It was found that this trip system was satisfactory for the majority of faults on both the charging supply and pulser, however, additional fault detection circuitry was incorporated to reduce the fault clearance times to an acceptable level for all possible faults.

(3.4.1) Excitron Backfire.

An excitron backfire is the condition whereby one or more of the excitrons in the mercury arc rectifier (MAR) looses its rectifying properties and conducts in the reverse direction. This is a common fault on high powered MAR's and is normally caused by deposits of mercury on the anode of the excitron tubes. This fault is equivalent to a short circuit across two of the lines on the secondary of the HV transformer. It is also possible that two excitrons can backfire almost simultaneously, resulting in a full three phase short circuit on the secondary of the HV transformer. The latter case is the worst possible fault condition, it is also the simplest to analyse as the magnitude of the three phase currents are the same i.e. currents are symmetric. This is illustrated in fig. (3.43). It is clear that fault current is limited by the impedance of the transformer windings or, more specifically, the leakage impedance. The calculation of the prospective fault current therefore requires a knowledge of the transformer impedance, which is obtained from short circuit test data. Details of this can be found in appendix B4 for 50% and 100% transformer tap settings.

Following the normal methods for fault studies, it is common practice to include only the reactive impedance in the calculation of prospective fault current. Strictly speaking the reactance required for the calculation is the sub−transient reactance [3.15], however, since this data is difficult to obtain, the steady state transformer reactance was used. As given in appendix B4, the phase reactance for each transformer tap settings is:

50% rated output	$X_2 = 42.61\ \Omega$
100% rated output	$X_2 = 27.13\ \Omega$

From fig. (3.43) the secondary fault current is given by

$$I_f = \frac{V_1}{X_2} \qquad (3.20)$$

Referring this to the transformer MVA base and voltage base, it can be shown [3.16] that the fault current is given on a per unit basis by

$$I_{fb} = \frac{1}{X_b} \quad \text{(per unit)} \qquad (3.21)$$

Where X_b is the base impedance value. Thus a transformer with 4% impedance will have a three phase short circuit fault current 25 times the normal full load current of

the transformer. From appendix B4, X_b = 0.0382 pu (per unit) at 100 % rated output, giving a primary fault current of I_{fb} = 26.18 p.u. The HV transformer rated primary current is 193.5 amps, thus, the three phase fault current is 5.07 kA.

The case of a single excitron backfire is much more difficult to analyse due to the unsymmetrical nature of the fault i.e. if the fault occurs between the blue and yellow phase lines, fig. (3.44), the red phase current will be zero. The solution to this problem involves resolving the asymmetric current into a set of three symmetric components [3.16], termed positive, negative and zero sequence groups. This method is referred to as the method of "symmetrical components." Before this method can be used it is necessary to determine values for the three sequence impedances, which depend on the transformer winding and earthing configuration. It can be shown that the positive and negative sequence impedance are both equal to the transformers' leakage impedance. With a floating star point on the secondary side of the transformer, no zero sequence currents can flow and the zero sequence impedance is threrefore infinite. Using this method, it can be shown [3.16] that the secondary fault current is given by

$$I_F = \frac{j\sqrt{3}\, V_1}{Z_1 + Z_2} \qquad (3.22)$$

Where $Z_1 = Z_2$ are the positive and negative sequence impedances. The above fault current will be equal to the line current in two of the phases with no current flowing in the third phase. This can be related to a primary fault current, however, due to the asymmetry in the fault current, the three current ratios across the transformer bank are different, with the greatest primary line current being given by

$$I_{11} = \frac{2\, V_{21} \times I_{21}}{\sqrt{3} \times V_{11}} \qquad (3.23)$$

This is 15% higher than the primary line current for a balanced three phase fault of the same magnitude. The prospective secondary and primary fault currents have been calculated for both a single and double excitron backfire, at the 50% and 100% tap settings on the HV transformer. Table (3.2) and (3.3) detail the results. It is clear that a single excitron backfire gives rise to the same maximum prospective fault current on the primary as the three phase fault.

Such high fault currents passing through the transformer can cause both mechanical and thermal damage and it is therefore necessary to restrict the duration of the overcurrent fault. The transformers' through fault capabilities were determined

following the guidelines set out in ANSI/IEEE C57.12−1980 and a damage curve drawn, as shown in fig. (3.45). In order to protect the transformer it is necessary to trip the three phase supply in a time shorter than the damage protection time. For this purpose both a moulded case circuit breaker and high rupture capacity (HRC) fuselinks are incorporated in the mains feed to the transformer (see fig 3.33).

TABLE (3.2) Prospective fault currents (amps rms) 50% rated output

Fault type	secondary line current	primary line current
line to line short	58.67	806
three phase	67.75	806

TABLE (3.3) Prospective fault currents (amps rms) 100% rated output

Fault type	secondary line current	primary line current
line to line short	184.3	5067
three phase	212.8	5067

The HRC fuselinks are included as backup protection for the complete overload circuits and as such are not normally called upon to operate. The main criterion in selecting the fuselinks was their ability to withstand the transformer magnetising inrush current. As no data was available on the inrush transient for this transformer, the inrush was estimated from the designers' rule: inrush equivalent equals 12 times full load current for 100 milliseconds [3.17]. Fuselinks were then selected with a pre−arcing time which lay to the right of this, as shown in fig. (3.45). It can be seen that for prospective fault currents below 2400 amps that these fuselinks do not protect the transformer. The fuselinks will, however, protect the cable from the supply panel to the transformer as the minimum fusing current is less than 1.5 times the cable current carrying capacity [3.18].

In order to overcome the limited protection offered by the fuselinks at low currents, a circuit breaker was selected with a characteristic which lay to the left of the transformer damage curve, fig. (3.45). This device has both thermal and mechanical

trips and in addition has a trip coil, which requires a 24 V DC supply to activate the circuit breaker. It can be seen that although this provides protection throughout the range of fault current, the breaker characteristic cuts the transformer inrush characteristic. As a result, it has been found in practice that the circuit breaker occasionally trips when the transformer is connected on line. This is quite acceptable and simply requires the circuit breaker to be reset. Also shown on the protection diagram of fig. (3.45) are the prospective fault currents for excitron backfire. It is clear that with the transformer on a 50% tap setting that the low fault current gives rise to a rather long tripping time. In view of this problem it was decided to detect the overcurrent fault directly with current transformers mounted on the feeds to the rectifier, and produce a signal to trip out the hold on supply to the circuit breaker. With this trip system it has been possible to reduce the tripping time to less than one cycle of the mains. Details of this overload circuitry are given in section (3.4.3)

The combined protection characteristic of the circuit breaker and the HRC fuselinks, together with the MAR overload trip system, ensure protection of all the components in the charging supply in the event of an excitron backfire. In most instances the circuit breaker will be activated by the MAR overload unit, which in addition, will trip the grid and excitation supplies for the MAR. It will be apparent from the following discussions that the protective circuitry on the charging supply provides backup protection for the pulser in the event of a fire through.

(3.4.2) Mercury Arc Rectifier Overload Unit.

It has been shown that in the event of either an excitron backfire or pulser fire through that the prospective fault current can be relatively small when the transformer taps are set for 50% rated output. With reference to fig. (3.45), it is clear that such faults may persist in the system for times approaching a minute before the circuit breaker thermal trip is activated. Although the charging supply components would not be damaged by fault currents of this magnitude, if the overcurrent is due to some fault on the pulser circuit, then the pulser components could be damaged as a result of the long tripping time. Since the charging supply protection provides backup protection for the pulser overload circuit, it is necessary to assist the circuit breaker during less severe overload conditions. The protection system therefore incorporates the necessary detection circuits, which pick up any abnormal current level and energise the circuit breaker trip coil. A further improvement in protection is also realised by tripping the grid and excitation supplies to the MAR at the same time as the circuit breaker is tripped.

The fault detection circuit comprises three 32:0.16 current transformers (CT)

positioned on the high voltage supply lines to the MAR (see fig. 3.33). These are mounted on acetal supporting collars to isolate them from the high line voltage. The secondary terminals of the CT's are connected to the MAR overload unit, which is housed in the relay cabinet within the safety enclosure. In the event of the output from any of the CT's exceeding the trip setting in the overload unit, the grid trip relays in the MAR auxiliary control circuit are activated (see appendix B4).

A circuit diagram for the MAR overload unit is shown in fig. (3.46). The output voltage from the CT's, which is determined by the line current and the load resistors R_1 etc, is rectified and fed to the non−inverting terminal of a voltage comparator. When the comparator voltage, which is thus proportional to the transformer secondary line current, exceeds the trip voltage set by P_1, the output from the comparator changes state. If this occurs in any of the three comparators IC1−IC3, transistor TR1 will fire the thyristor. This energises the three grid trip relays BA, BB, BC simultaneously and suppresses the rectifier grid and excitation supplies. The hold on supply for the circuit breaker is fed through a normally closed auxiliary contact of relay BC, so that the main circuit breaker trips when the grid trip relays are energised.

The MAR overload circuit is designed for the fastest possible operating time, thus, the grid trip relays are energised on fault to take advantage of the faster turn on characteristics of the grid trip relays, as opposed to their much slower release time. Fail safe protection is provided by transistor TR2 and relay RLA1. The hold−on supply for the contactor is fed through a normally open contact on RLA1, which must therefore be energised before the circuit breaker can be set: this requires the overload unit power on and the 150 volt grid trip supply to be active.

The threshold voltage on the comparators can be varied in the range 3.0 to 7.0 volts by adjusting pot P_1. With a CT burden of 100 Ω (R_1,R_2,R_3), the corresponding trip current settings are 7−25 Amps rms. Experience with the system has shown that a trip current setting of less than 20 amps will detect the fault current resulting from a pulser fire−through on 50% transformer tap setting, and will therefore provide satisfactory backup protection for the pulser overload circuit.

(3.4.3) Pulser Fire−through.

As the pulser is working close to the recovery limits on the CX1528 thyratrons, it is highly likely that two thyratrons may conduct simultaneously. Two possible faults could occur, viz: the discharge switch fires before the charging switch recovers or the charging switch fires before the tailbiter recovers. Both cases represent a short circuit

across the ouput of the charging supply and will result in a high fault current passing through the conducting thyratrons, as illustrated in fig. (3.47). It can be seen that the fault current will be supplied from the charging supply smoothing capacitor and the mains via the high voltage transformer. A resistance R is included in the circuit which represents the combined transient short circuit resistance of the pulser. The inductance L_c is the inductance of the charging choke.

Consider now what happens during the initial part of the fault transient. To simplify the calculation at this stage, it is assumed that no current is drawn from the rectifier and that the complete fault current is supplied from the smoothing capacitor C_s. Assuming C_s is charged to a voltage V_o prior to the fire-through, then the following equation can be written for the smoothing capacitor voltage.

$$V_c = V_o - \frac{1}{C_s} \int I_f \, dt \qquad (3.24)$$

Where I_f is the fault current, which is given by the solution of

$$\frac{d^2 I_f}{dt^2} + \frac{R}{L_c} \frac{dI_f}{dt} + \frac{I_f}{L_c C_s} = 0 \qquad (3.25)$$

Writing

$$\alpha = \frac{R}{2L_c} \qquad \text{and} \qquad \omega = \sqrt{\left[\frac{1}{L_c C_s} - \left(\frac{R}{4L_c}\right)^2 \right]}$$

The solution to equation (3.25) for two distinct and imaginary roots is given by

$$I_f = \exp(-\alpha t) \left[A \sin(\omega t) + B \cos(\omega t) \right] \qquad (3.26)$$

With the initial boundary conditions $I_F = 0$ and $V_c = V_o$ @ $t = 0$, the fault current and smoothing capacitor voltage are given by

$$I_F = \frac{V_o}{L_c \omega} \exp(-\alpha t) . \sin(\omega t) \qquad (3.27)$$

$$V_c = V_o \exp(-\alpha t) \left[\cos(\omega t) + \frac{\alpha}{w} \sin(\omega t) \right] \qquad (3.28)$$

For the laser pulser circuit the following values can be given for the short circuit model.

R =	4.0 Ω	
L_c =	5.0 mH	charging inductance
Cs =	0.25 μF	smoothing capacitance

With these values in the above parameters, it is found that the damped natural frequency ω = 28284 rad/s. With an initial charging voltage V_o= 10 kV, the peak fault current passing through the thyratrons is 69.2 amps. As illustrated in fig. (3.48), it can be seen that at the instant the fault current falls to zero, the smoothing capacitor will be almost fully reverse charged. At this point in time the model is inadequate to describe the subsequent fault transient as the thyratrons will normally prevent this current reversal. Depending on the magnitude of the following voltage transient, several possible things can happen [3.19].

Assuming the switches withstand the suddenly applied reverse voltage, then the power supply will re−charge the smoothing capacitor, which is likely to overshoot the normal working voltage. This results in the PFN voltage being exceeded during subsequent charging cycles, whereupon the tailbiter or discharge switch are likely to prefire and cause a second fault cycle. If this sequence of events is repeated too often it can result in failure of the smoothing capacitor, which is not designed for full voltage reversal. Failure of the PFN can occur due to overvolting and the life of the switches will be shortened especially if the ratings are exceeded.

Alternatively, should the switches fail to hold off the reverse voltage, the resulting arc will cause a large current to flow back through the switches and the capacitor voltage will resonate back positive. Reverse arcs will rapidly cause damage to the switch and result in the loss of ability to hold off its rated voltage.

From equation (3.27) it can be shown that the peak fault current is given approximately by

$$I_f\ (max) \approx V_o \sqrt{(\frac{C_s}{L_c})} \qquad (3.29)$$

This can be ralated to the normal peak charging current

$$I_c\ (max) = V_o \sqrt{(\frac{C_n}{L_c})} \qquad (3.30)$$

Thus, the ratio of peak fault current to peak charging current is simply the square root of the ratio of smoothing capacitance to PFN capacitance. The constraints imposed on the allowed ripple on the output pulse from the pulser limits the amount by which this can be reduced. If a large smoothing capacitor is required for output pulse stability, then there exists the possiblity that the high fault current will saturate the charging choke. This will result in a rapid increase in the fault current with only stray inductance limiting the ringing frequency. It is for this reason that iron is still used in place of ferrite for the cores of high power charging chokes, because the much higher working flux density (1.8 Tesla as opposed to 0.3 Tesla for ferrite) gives a much higher margin of safety on fault current protection.

For the present values for C_n and L_c, the peak charging current, at 10 kV supply voltage, is 32 amps. Thus, the ratio of fault current to peak charging current is 2.24. In designing the charging choke the peak flux was limited to 50% of the maximum working value. Thus, if a fire-through was to occur when the charging supply was at full voltage of 10 kV, this would almost certainly result in saturation of the charging choke and an excesively large fault current. Since the combined reverse voltage ratings of two CX1528 thyratrons (i.e. 80 kV) prevents the current reversal, the fire-through will terminate at this point. However, as the pulser is likely to fire-through on the next charging cycle, the fault current will continually increase as the smoothing capacitor voltage is pumped up by the charging supply at the end of the fault cycle.

It was found that when a fire-through did occur, albeit due to an control error which resulted in the thyratrons being triggered in the wrong sequence, the follow through current from the charging supply caused the thyratrons to latch on. This is in contrast to the above scenario and is evidence that the effects of the charging supply follow through current must be considered in the transient fault analysis. This problem is difficult to resolve, however, some general conclusions regarding the effects of the charging supply can be drawn from the fault described.

The fire-through occured when the transformer was set to 50% output, giving a line voltage of 5 kV. An estimate of the follow through current can be made by neglecting the charging choke reactance and considering the fire-through as a line to line fault on the transformer, with a fault impedance Z_f equal to the resistance in the pulser circuit. Using the method of symmetrical components, it can be shown that the prospective secondary fault current is [3.16].

$$I_f = \frac{\sqrt{3}\, V_1}{(Z_1+Z_2+Z_f)} \qquad (3.31)$$

With $Z_1 = Z_2 = 42.61\ \Omega$ (appendix B4) and $Z_f = 4.0\ \Omega$, the secondary fault current is

approximately 56 amps. Thus, the maximum peak current will be less than the corresponding mean direct current from the rectifier, which is in this case 39.6 amps. Since the actual current will be less than this value, it is clear that in this instance the choke did not saturate, as the current is below the maximum design value.

It can therefore be concluded that in the event of a fire−through ocurring on the pulser, it is likely that the thyratrons will latch on due to the follow through current from the charging supply. Normal operation of the laser requires a mean charging voltage in the range 6.7 kV to 10 kV, corresponding to a transformer line voltage in the range 5 kV to 7.4 kV. Thus, from equation (3.27), the maximum prospective secondary fault current would be 95.6 amps, with a corresponding mean pulser fault current of approximately 70 amps. This is below the maximum design value for the charging choke and it can therefore be concluded that throughout the full operating voltage of the pulser, it is not likely that the charging choke will saturate. The components therefore which are most susceptible to damage during a fire−through are the two conducting thyartrons.

Following consultations with EEV, it was felt that in view of the limited data available on the total pulse capabilities of the CX1528 tube, a very conservative figure should be taken to avoid possible damage. A value of 5.0 Coulombs was taken as the maximum single pulse capability. With a maximum possible mean fault current of 70 Amps, this requires the fault to be cleared in 70 milliseconds or less. A target fault clearing time of 40 milliseconds was chosen i.e. two cycles of the mains.

When the prospective secondary fault current is referred to the transformer primary it can be shown that for the charging voltages required, the prospective primary fault current lies in the range 770−1945 amps. With reference to fig. (3.45) the respective clearing times are 20 seconds−300 milliseconds; the faults being cleared by the circuit breaker. These are considerably longer than necessary clearing times for protection of the thyratrons and some additional means of detecting and isolating the fault was therefore required. In order to achieve the desired protection, a fault detector was positioned on the grounded supply lead between the smoothing capacitor and the pulser earth sheet. In the event of the mean pulser current rising above a preset level, the circuit breaker is activated and the grid and excitation supplies to the MAR are suppressed.

The fault detector consisted of a current shunt resistance, a high speed relay and a high power avalanche diode, connected as shown in fig. (3.49). The current shunt was constructed from a length of "brightray" resistance strip which was folded to minimise the size and inductance of the shunt. The shunt resistance was measured as 0.43 Ω,

giving a trip current of 11.7 Amps. As the fault current is considerably higher than the trip setting, an avalanche diode with a reverse breakdown voltage of 10.0 volts is connected in parallel with the shunt to protect the relay. With this arrangement it was found that the circuit breaker was activated within 15 milliseconds of the fault current exceeding the trip setting and including the circuit breaker response time, the total clearing time was less than the desired 40 milliseconds.

In addition to the above system it was found that the protective circuitry incorporated for charging supply protection (section 3.4.4) also cleared a fault of this magnitude within approximately 60 milliseconds. This system therefore provides backup protection in the event of the pulser trip circuit failing.

(3.4.4) Pulser Overload Current Monitor.

During normal running of the pulser several less severe overload conditions can arise which do not require the mains supply to be cleared. Such a condition developes when the laser discharge impedance changes significantly from the impedance of the PFN. As discussed in section (3.1.4), any impedance mismatch between the PFN and the load results in a residual voltage on the PFN at the end of the discharge pulse and subsequently this is dissipated in the inverse diode assembly. It is common for arcing to occur in the discharge when the gas pressure is at the maximum value and consequently the impedance of the discharge drops to a very low value. In this instance most of the energy supplied to the PFN will be dissipated in the inverse diode resistor stack, which is not rated for the full power of the pulser. This overload condition must therefore be detected and suitable action taken. As the overload is caused by a problem outwith the control of the power supply, all that is required is that the thyratron trigger signals be suppressed and an indication given of the fault. In addition to this action, it is also possible to take advantage of the MAR grid drive and isolate the charging supply from the pulser by opening the phase shifter contactor.

A circuit diagram for the protective circuitry that detects this overload condition is shown in fig. (3.50). In the event of the discharge impedance dropping to a low level, the current passing through the inverse diode assembly increases. This is monitored by a current transformer CT1, the output of which is fed to an integrating circuit comprising R_1, R_2 and C_1. The values of these components are chosen so that under normal operating conditions the peak voltage on on C_1 is 2.5 volts at the maximum operating frequency of 10 kHz and an impedance mismatch of five percent; this being required for reverse biasing the discharge switch at the end of the pulse. The threshold level on the comparator IC1 is set at a voltage of 3.2 volts by pot P_1.

In the event of the discharge impedance mismatch increasing above 20%, the voltage on C1 exceeds the trip setting and the output from the comparator changes state, resetting the output from the flip-flop (IC4) high. This turns off transistor TR1 and opens the relay RLA1, which is interlocked with the hold on supply for the phase shifter contactor (see drawing ES-MAR-1 appendix B4) thus tripping the MAR grid drive. The output from the flip-flop is also coupled through a fibre-optic to the thyratron driver circuit in the control module. When the output from the flip-flop goes high, the thyratron trigger pulses are suppressed (see section 3.5).

(3.4.5) Overload Circuit Interlocks and Safety.

In addition to component protection requirements, particular attention was also paid to both the controllability of the system and the safety requirements of the installation. All wiring therefore adheres to the IEEE wiring regulations and where possible components are earthed. An emergency stop ring is provided in the lab which is interlocked with the main circuit breaker, to isolate the mains feed to the transformer in an emergency. All high voltage areas are safety interlocked to the circuit breaker to trip the mains supply in the event of someone entering the area. Nevertheless, the system contains many capacitive components which can remain charged even when the mains is isolated. Caution must therefore be exercised when working with the system and components grounded with the earthing stick before physical contact is made.

All safety and fault detection circuits feed back to the circuit breaker on the main supply panel. A schematic for this circuit is shown in fig. (3.51). This circuit is designed so that all protection circuits must be active before the circuit breaker and main contactor can be set. As the circuit breaker requires a 24 volt supply to activate it, the circuit is designed so that in the event of this supply failing, the main contactor will open. Phase failure protection is also provided to prevent current imbalance should one of the HRC fuselinks blow.

(3.5) POWER SUPPLY CONTROL.

The discussion thus far has considered the design and operating characteristics of the charging circuit and pulser: the final task remaining is the integration of all power supply circuits into a working and controllable system. The circuits which implement the control actions were designed to meet the requirements for control of materials processing and provide the interface for future expansion of the laser manufacturing system. Particular attention was also paid to the necessary safety requirements of the electrical installation, in order to provide a controlled shut-down in the event of an emergency. In addition, it was necessary to interlock the thyartron control signals with

the interlocks on the laser beam delivery system as required by the laser safety regulations.

The heart of the control system is the power supply control module, fig. (3.52), which generates the control signals for the three pulser thyratrons and controls all system safety and overload circuits. The control module comprises three printed circuit boards, viz: thyratron sequence card, PRF control card and the safety/overload card. All circuits in the control module are designed around the series 4000 CMOS range of integrated circuits. These were chosen because of their excellent noise immunity i.e. with 15 volts supply, the noise immunity threshold is 6.75 V, which makes these devices five times less sensitive to magnetically coupled noise than similar TTL devices.

(3.5.1) Thyratron Sequence Card.

The trigger units for the three pulser thyratrons are controlled by fibre-optic links from the main control module. For 10 kHz running, the PFN charging cycle lasts approximately 50 μs and following a 10 μs recovery period for the charging thyratron, the discharge thyratron is fired. The tailbiter is triggered at the end of the 10 μs discharge pulse to dump the residual energy in the PFN. This sequence is controlled by the thyratron sequence card, fig. (3.53), which comprises four dual multivibrators (HEF4528). Table (3.5) details the logic function for this device.

TABLE (3.5) Logic table for HEF4528 monostable-multivibrator

pin 5/11	pin 4/12	pin 3/13	pin 6/10	pin 7/9
H → L	L	H	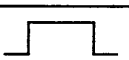	
H	L → H	H	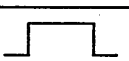	
X	X	L	L	H

The clock pulse from the PRF control card is applied to pin 4 of IC1. The output from pin 6 goes high on the positive edge of the clock pulse and remains high for the period set by R_5 and C_2 i.e. $\tau = R_5C_2$. The output from pin 10 also goes high on the positive edge of the clock pulse, switching on the T1 for 2 μs: this energises the LED, D_3, and triggers the charging thyratron. The output from pin 10 of IC4 is connected to pin 4 of IC2, causing pin 6 to go high on the positive edge of the clock pulse for the time set by R_7, R_9 and C_4. Pin 6 of IC4 goes high on the negative edge of the output pulse from pin 6 of IC2 and remains high for a time set by R_{12} and C_7. On the negative edge of the output pulse from pin 6 of IC4 transistor T2 is fired for 2 μs to trigger the discharge switch. This occurs 60 μs after

the positive edge of the clock pulse. The tailbiter switch is fired 10 μs after the discharge switch as set by R_8, R_{10} and C_5 on IC2.

(3.5.2) PRF Control Card.

The clock pulse for the thyratron sequence card is generated by the PRF control card, fig. (3.54). This allows the pulser to be controlled in single shot, burst mode and continuous mode at any pulse repetition frequency up to 10 kHz. Clock pulses with a 50% duty cycle are generated by the 4047 multivibrator working in the astable mode, with the frequency being set by C_1, R_3 and pot P_1. To allow the full 10 kHz frequency range, an external switch is provided to change from the 100–1000 Hz range to the 1–10 kHz range. The 4047 is triggered by a high on pin 5, this being obtained from the output of the 4013 D type flip–flop. The output from the flip–flop is set by the start and reset push buttons on the control panel and also by the BCD controlled burst mode counter.

When operating in the continuous mode, with switch SW1 set to position A, the pulses are switched on by the start button on the control panel and stopped by the reset button. In the burst mode, the trigger signal for the 4047 will go high when the start button is switched and will remain high for the period set by the BCD counter circuit. The clock input for the counter is derived from the rectified mains supply, after squaring the signal with a 4093 Schmitt trigger. This circuit allows bursts to be generated in the range 10 milliseconds to 10 seconds.

In order to suppress the thyartron trigger signals in the event of a fault on the pulser or safety condition, the output from the PRF ganerator card is interlocked with the overload/safety card. The clock pulse from the 4047 is gated by the 4073 AND gate, which requires a high from the overload circuit card to enable the pulse output to the thyratron sequence card. All interlock conditions on the safety/overload card must therefore be active before any control pulse can be sent to the thyratron sequence card. A single trigger pulse can also be applied to the sequence card, this being generated by the 555 monostable and gated by the 4073 AND gate.

(3.5.3) Overload Protection Card.

The control module is directly interlocked with the main circuit breaker and the MAR rectifier overload unit to shut down the power supply in the event of a fault arising on the pulser or an emergency stop being activated. The control module also monitors the current passing through the inverse diode stack on the pulser circuit and dissables the thyratron trigger signals if the current exceeds a preset limit. These functions are

exercised by the safety/overload card, fig. (3.54).

The current passing through the inverse diode stack is monitored by a current transformer CT1, the output from which is fed to input terminals A-A on the overload card. The output voltage from the current transformer is set by resistor R_1 and fed to the integrater circuit comprising R_2, C_1 and R_3. When the output voltage from the integrator exceeds the threshold voltage on the comparator, as set by R_6, the comparator changes state and sets the output on the pulse enable line low, disabling the thyratron trigger pulses. The threshold on the comparator IC2 is set to trip the thyratron trigger signals when load impedance falls below 50% of the PFN impedance. This ensures that the power ratings of the resistors in the diode stack are not exceeded and that the thyratron trigger signals are suppressed in the event of an arc developing in the laser cavity.

The emergency stop ring is monitored, such that in the event of an emergency stop button being activated, the thyartron trigger signals are disabled and the relay RLA1 switched off. This is interlocked with the main circuit breaker trip coil and the grid trip relays on the MAR. Thus, in the event of an emergency, the circuit breaker is activated and the grid trip relays energised to suppress the MAR excitron grid signals (see section 3.4).

In addition to the above protection, the thyratron heater currents are monitored by the shunt resistors R_{49}, R_{50}, R_{51} and optically coupled to the comparator IC8. This circuit prevents the thyratron trigger pulses being applied before the minimum heating time has expired. This time is set for 5 minutes by the DIL switch.

(3.6) PULSER COMMISSIONING.

Following completion of the experimental work on the single shot test circuit, as described in section (3.2.3), the thyratrons and mosfet trigger circuits were installed in the pulser circuit. Although the DC charging supply was fully commissioned by this stage in the research programme, it was decided to use a small high voltage power supply for the initial commissioning work on the pulser, in order to limit the fault power levels in the event of a fire-through. As the pulser components had not been used for a considerable length of time, all components were tested for voltage rating and the values of inductance and capacitance measured prior to installation in the pulser circuit. The pulser circuit was commissioned in stages in order to develop some confidence with the operating characteristics before a full cycle and high frequency test were undertaken.

(3.6.1) PFN Charging Circuit Test.

All components on the PFN discharge circuit were disconnected and a TEK P6015 high voltage probe connected to the PFN; in addition to measuring the PFN voltage, this allowed the charge to leak away with a time constant of approximately 5 seconds. The main supply cable from the rectifier set was disconnected and the high voltage commissioning supply connected to the DC input socket on the pulser, as shown in fig. (3.56). As the commissioning supply had a charging resistance of 5 MΩ, the leakage resistor connected across the smoothing capacitor was disconnected to prevent division of the supply voltage. The charging current was measured with a pearson wide band current transformer mounted on the PFN ground lead. With the charging voltage set to 6.74 kV a single trigger pulse was applied to the charging thyratron. A recording of the PFN voltage and charging current waveforms obtained are shown in fig. (3.57).

It is clear that the charging cycle takes approximately 48 μs and that network reaches a final voltage of approximately 11 kV. It is worthwhile to compare these figures with the theoretical values, based on the measured circuit values for the charging inductance and PFN capacitance. Expressions for the charging current and PFN voltage were derived in section (3.1.3) assuming a constant supply voltage. Thus, for the above supply voltage of 6.74 kV, a charging inductance of 5 mH and a PFN capacitance of 0.05 μF, the following comparison can be made:

TABLE (3.4) Charging circuit performance: supply voltage 6.74 kV

Circuit parameter	Experimental	Theoretical
Peak charging current	17.15 A	21.3 A
Final PFN voltage	10.93 kV	12.8 kV
Charging period	48.0 μs	49.7 μs

It can be seen that there is a considerable error between the predicted and measured values of both peak charging current and final network voltage. This is larger than expected given the uncertainties in the experimental measurements. The discrepancy is mostly the result of the assumption that the supply voltage remains constant during the charging cycle, however, due to the relatively low smoothing capacitance there will be an appreciable droop on the supply voltage during the cycle. A more accurate prediction of charging circuit performance must therefore take into account the finite

capacitance of the charging supply. Neglecting the current supplied by the transformer during the charging cycle, it can be shown that for resonant transfer from the smothing capacitor, C_s, to the PFN capacitance, C_n, that the final network voltage is given by:

$$V_o = \frac{2\ V_{dc}\ C_s}{(C_s + C_n)} \qquad (3.32)$$

and the peak charging current is given by:

$$I_c(max) = V_{dc} \surd\left(\frac{C_{eff}}{L_c}\right) \qquad (3.33)$$

Where C_{eff} is the effective capacitance in the charging circuit. As the smoothing capacitor is essentially in series with the PFN capacitance, the effective capacitance is given by

$$C_{eff} = \frac{C_s\ C_n}{(C_s + C_n)} \qquad (3.34)$$

With the measured values for C_s and C_n, the effective capacitance C_{eff}=0.042 μF. From equation (3.32) the final network voltage V_o = 1.67 V_{dc}, which compares with the figure of $2V_{dc}$ for resonant charging from a fixed voltage source. Thus, using equations (3.32) and (3.33) the predicted final network voltage and peak charging current are 11.25 kV and 19.5 amps respectively. This is in closer agreement with the measured values given in table (3.4).

A second high voltage probe was connected to the cathode of the charging thyratron to obtain further information on the recovery characteristics. The recorded voltage waveform together with the associated charging current are shown in fig. (3.58), from which it can be seen that the supply voltage waveform exhibits a droop as expected. Following cessation of the charging current at the point of current reversal, the cathode voltage rings up to a peak voltage of 15.7 kV, giving a reverse bias across the charging thyratron of −9 kV. This is due to the stray capacitance in the charging circuit, which is charged to a voltage of approximately 5.5 kV at the instant the thyratron switches off, while the PFN is at a voltage of approximately 10.7 kV. The resonant circuit formed by the stray capacitance, the charging inductance and the PFN capacitance rings with a period of 20 μs until the losses in the circuit damp out the oscillations.

The charging circuit was tested several times on the commissioning supply, with the

DC supply voltage gradually increased to the full 10 kV rating. On several occasions the MOSFET in the trigger circuit was found to have blown. No fault could be found in the trigger circuit and as it was not possible to obtain a measurement of the MOSFET voltage during the charging cycle, due to the floating cathode arrangement, it was not possible to determine the cause of the failures. However, as this was experienced only a few times it was felt that the charging circuit was performing satisfactorily for a full cycle test to be carried out and no effort was made at this stage to improve the reliability of the MOSFET trigger circuit.

(3.6.2) PFN Discharge Circuit Test.

The performance of the PFN discharge circuit was examined on single shot control with the output from the discharge switch being fed into a 50 Ω water cooled dummy load. The connection from the charging choke was removed and the PFN resistively charged from the high voltage commissioning supply. Recordings of the discharge voltage and current for a PFN voltage of 11.0 kV are shown in fig. (3.59). It can be seen that the load voltage falls to a level of 3.6 kV, which is in agreement with an impedance mismatch of 50% (V_l = 1/3 V_{no}).

As with the charging circuit tests it was found that the MOSFET in the trigger unit failed on several occasions. Although the PFN was charged to the same voltage prior to each test, the failures were experienced in only approximately ten percent of the pulses. It was concluded that the failures were the result of the thyratron grid spike being coupled to the MOSFET via the stray capacitance of the pulse transformer. As the amplitude of the thratron grid spike varies considerably from pulse to pulse, this explained the apparent random failure pattern. Various methods of protecting the MOSFET were incorporated into the trigger circuit (see section 3.2.5), however, only a marginal improvement in reliability was achieved. In spite of these difficulties it was decided to proceed to a full cycle test.

(3.6.3) Full Cycle Test.

The pulser circuit was fully assembled, with the exception of the tailbiter, and the output from the discharge thyratron connected to the 50 Ω dummy load. The DC supply input was connected to the high voltage commissioning supply and the smoothing capacitor charged to 5 kV. The relative firing times of the thyratrons were set on the firing card to give 200 μs delay between the trigger pulses for the charging and discharge thyratrons. When a control pulse was applied, the pulser fired through and it was found that the MOSFET in the discharge thyratron trigger unit had blown. The MOSFET was replaced and the test repeated: again the pulser

fired-through and the MOSFET failed. Attempts to determine the cause of the fire-through were hindered by the continual failure of the MOSFET trigger circuits. In view of the problems being experienced it was felt that major modification to the trigger units were necessary in order to improve reliability.

The MOSFET trigger circuits were replaced with a high voltage inverter circuit, with a small glass envelope thyratron as the switching element (section 3.2.4). As before these circuits were tested on both the PFN charging and discharging circuits: all tests were completed with no failures of the trigger units being experienced. The pulser was then re-assembled as before for a full cycle test. As with the MOSFET circuit it was found that the pulser fired-through on the first attempt, however, the new trigger circuits were not damaged by the fault transient. After repeating the test several times, it was found that the charging thyratron was being triggered at the instant the PFN discharge transient reached the charging end of the PFN (ie 5 μs after discharge switch fires). It was concluded therefore, that the fire-through was not being caused by a spurious trigger signal from the charging thyratron trigger unit, as this would have been experienced at the instant the discharge switch fired.

(3.6.4) Fire-through Protection.

It was found that the charging thyratron was being triggered back into conduction by the PFN discharge transient. As shown in fig. (3.59), when the discharge switch fires the voltage at the load end of the PFN falls to a level determined by the impedance match between the PFN and the load. The voltage wave produced travels along the PFN to the charging end, whereupon, it is reflected in phase and travels back to the load end. The net effect is that the voltage at the charging end of the PFN drops to $(V_l - V_{no})$, where V_l is the load voltage, fig. (3.60); this occurs one transit time after the discharge switch fires. For a 50% mismatch and with the PFN charged to 11.0 kV, the amplitude of the voltage transient is -14.7 kV. The time taken for the voltage to fall is equal to the resonant period of one LC mesh, which is approximately 1 μs, giving a transient dV/dt of -14.7 kV/μs.

The cathode of the charging thyratron is subject to this voltage transient, although the amplitude is reduced slightly by the effects of the charging choke and the stray capacitance of the PFN connecting cable. Because of the close control grid/anode spacing, the CX1528 thyratron has a grid-anode stray capacitance of approximately 35-40 pF. This is much larger than the grid cathode stray capacitance and as a result causes coupling between the grid and anode circuits. When the thyratron is subject to a fast transient, the voltage divides across the stray capacitance and since $C_{ga} >> C_{gc}$, most of the voltage appears across the grid-cathode gap. In this particular instance,

the amplitude of the voltage transient is sufficient to pull the cathode down, while, due to the effects of the grid–anode stray capacitance, the grid is maintained at approximately anode potential. As this is essentially the same as driving the grid positive with respect to the cathode, the thyratron can be triggered into conduction if the transient voltage exceeds the bias level on the control grid.

The solution to the problems associated with the high grid–anode stray capacitance is therefore to ensure that the grid and cathode are sufficiently coupled to prevent the grid being driven to cathode potential. Alternatively, it is possible to reduce the amplitude of the voltage transient by including an LC filter in the line between the charging switch and the PFN. Several different filters were designed for this purpose, however, no marked improvement in performance was observed. The fire–through problem was solved by a modification of the firing arrangement on the charging thyratron, which allowed the grid to be coupled directly to the cathode.

In both the MOSFET trigger circuit and the FX2530 based trigger circuit, the thyratron is triggered by driving the control grid sufficiently positive with respect to the cathode to overcome the grid–cathode bias voltage of –150 volts. Fig. (3.61) illustrates the output stage of both trigger circuit designs, from which it can be seen that the grid is coupled to the cathode via R_1, C_1 and the secondary winding of the pulse transformer. When the cathode is subjected to the fast voltage transient from the PFN discharging, the cathode is momentarily driven below bias level and the thyratron fires. The problem arises because the combined impedance of R_1 and the inductance of the pulse transformer allows the cathode to be pulled down with respect to the control grid for a time sufficient for the tube to fire, even though the grid and cathode are coupled by the bias capacitor C_1. In an attempt to couple the grid and cathode more closely, several values of coupling capacitor were connected directly between the grid socket and cathode. It was found that for a coupling capacitor of 470 pF that the amplitude of the trigger pulse was reduced by approximately 150 volts and no improvement in protection was observed. It was not possible to increase the size of the coupling capacitor sufficiently to overcome the grid–anode coupling, before loading of the trigger circuit became critical.

The problems associated with grid–anode coupling were overcome by making use of the fact that the thyratron can be triggered by driving the cathode negative with respect to the control grid, since this is essentially the same as driving the control grid positive with respect to the cathode. A circuit for achieving this is shown in fig. (5.62). In this circuit configuration, the grid and cathode are coupled by the capacitor C_1, which is chosen to be much larger than the grid–anode stray capacitance. The tube is triggered by a negative pulse on the secondary of the pulse transformer, with

the trigger pulse current passing through R_1, C_2 and the secondary of the pulse transformer. The cathode of the thyratron is connected to the virtual ground by a diode D_1, which conducts the main anode current pulse, but does not conduct during the trigger pulse. The output from the thyratron is now taken from the virtual ground on the trigger circuit. When the PFN discharge wave hits the charging thyratron, since $C_2 >> C_{ga}$, most of the voltage appears across the grid–anode gap. With this arrangement the grid is more closely coupled to the output than the cathode and as a result will be driven more negative than the cathode during the PFN discharge transient. The grid is therefore driven more negative with respect to the cathode and the tube remains in the non–conducting state.

The main dissadvantage with this mode of operation is the need for the trigger pulse diode D_1. This must be able to transmit the full anode current when the thyratron fires and hold off the trigger pulse voltage. Because the diode requires a finite time to commence conduction, during which time it will experience the full anode voltage, this may damage the diode. If the switching speed of the diode is too slow it is possible that the anode current will not reach a critical level during the trigger pulse and the thyratron will therefore fail to fire. In order to overcome these problems it was necessary to subject the diode to a small forward biasing current. This was obtained directly from the thyratron heater supply, as shown in fig. (3.63). A bias current of approximately 3 milliamps was found to give satisfactory protection to the diode under all operating conditions.

Only the trigger circuit for the charging thyratron was modified as described above, since only this tube is subject to such a fast, high voltage transient. The trigger circuits of both the tailbiter and discharge thyratrons remained as before. It was found that this modification prevented the charging switch from firing when subject to the PFN discharge transient and, with the pulser connected to the high voltage commissioning supply, the full cycle test was completed without further problems being experienced. The commissioning supply was then disconnected and the pulser fed from the main DC charging supply. The pulser was successfully tested in a burst mode up to the full operating frequency of 10 kHz with no further work being required.

REFERENCES FOR CHAPTER (3)

[3.1] Spall R. "Pulsed power supply for an unstable resonator." Ph.D thesis, Department of Mech. Eng., Univ. Of Birmingham, 1979.

[3.2] Khahra J.H., "Optimization of the output characteristics of a pulsed carbon–dioxide laser for processing of materials." Ph.D. Thesis Univ. Birmingham, Dec 1976.

[3.3] "Hydrogen Thyratrons." English Electric Valves, Product data.

[3.4] Glasoe and Lebacqz "Pulse Generators." Radiation Laboratory Series. McGraw – Hill.

[3.5] Chipman R. A. "Transmission lines." Schaum Outline Series.

[3.6] Guillemin E.A. "A historical account of the development of a design procedure for pulse forming networks." Radiation Laboratory, report no.43 october 1944.

[3.7] Hooper E.H. "An evaluation of charging techniques for line type pulsers." 12th Power Modulator Symposium, 1982.

[3.8] Scoles G.J. "Triggered charging techniques for pulse generator circuits." 12th Power Modulator Symposium. 1982.

[3.9] "Power MOS transistors." Mullard technical handbook. Book 1, part 1f, 1984.

[3.10] Durney C.H., Harris L.D., Alley C.L. "Electric circuits – theory and engineering applications." Holt Saunders.

[3.11] "The use of English Electric glass excitron rectifiers." English Electric publication E6/RDD/PDA 22/5/58.

[3.12] Say M.G. "Alternating current machines." Pitman.

[3.13] Jackson S.P. "Selection and application of metallic rectifiers." McGraw – Hill.

[3.14] Starr A. T. "Electronics." Pitman

[3.15] Weedy. R.G. "Electric power systems." John Wiley.

[3.16] Blackburn J.L. "Protective relaying." Marcel Dekker.

[3.17] Blume R.G. "Transformer Engineering." 2nd edition. John Wiley.

[3.18] Wright A., Newbery P.G. "Electric fuses." IEE Power Engineering Series.

[3.19] Kettle L.J., Newton B.P. "Fault protection in high power modulators." Sevententh Power Modulator Symposium. 1986.

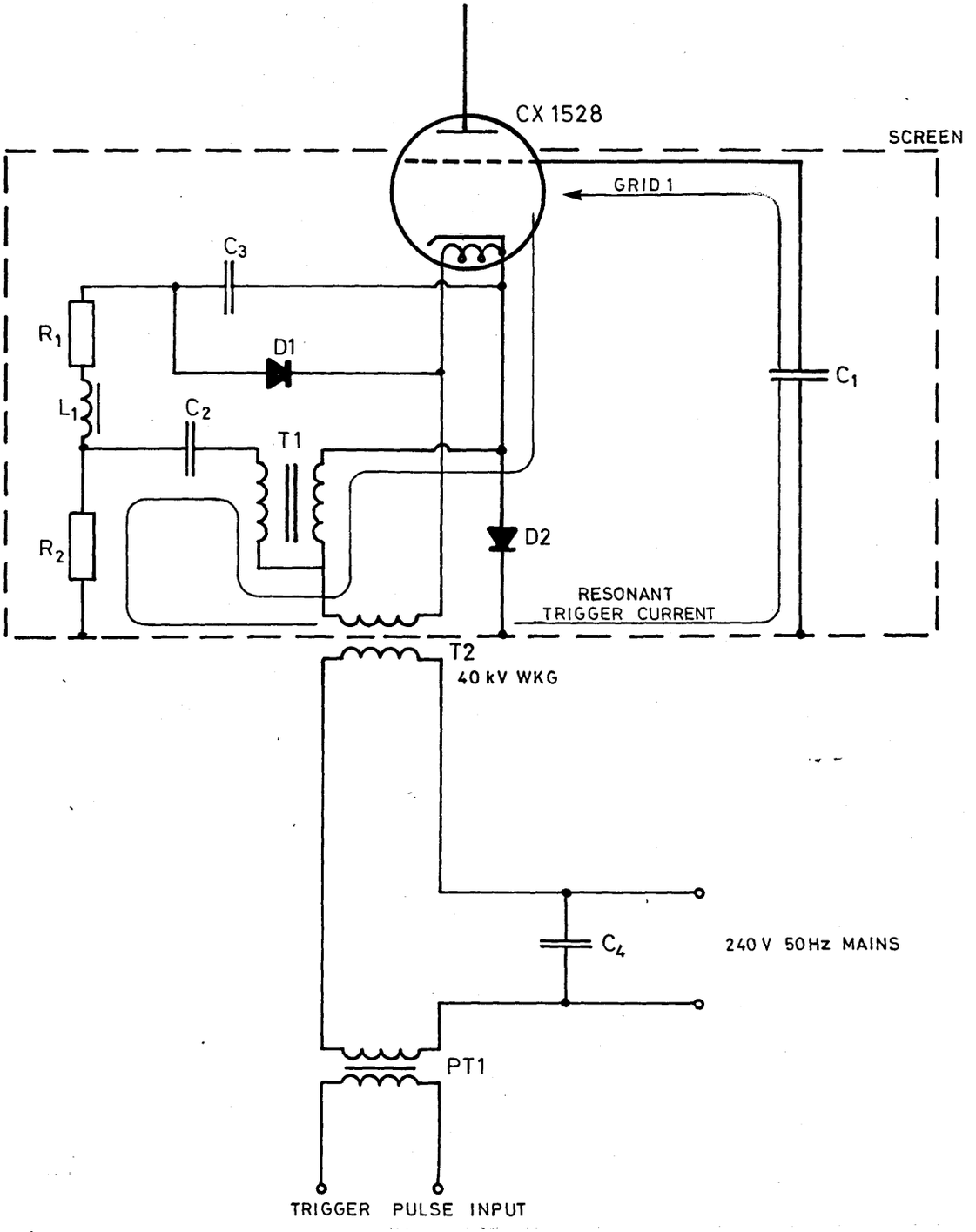

FIGURE 3.1 SPALL'S PROTOTYPE THYRATRON TRIGGER CIRCUIT

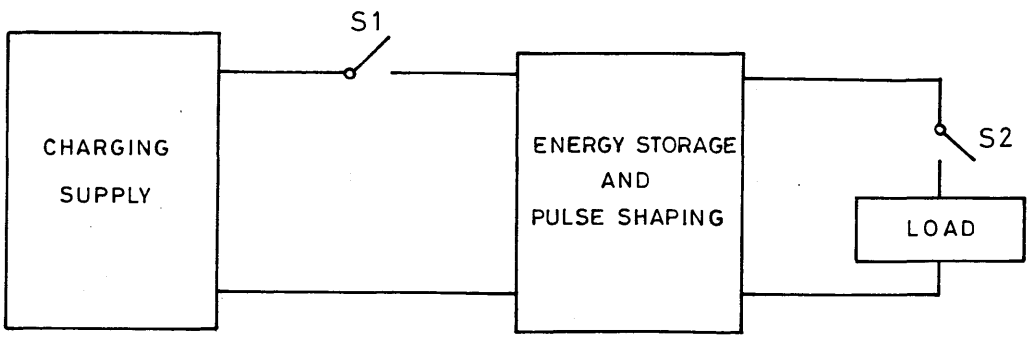

FIGURE 3.2 BASIC COMPONENTS OF A LINE TYPE PULSER

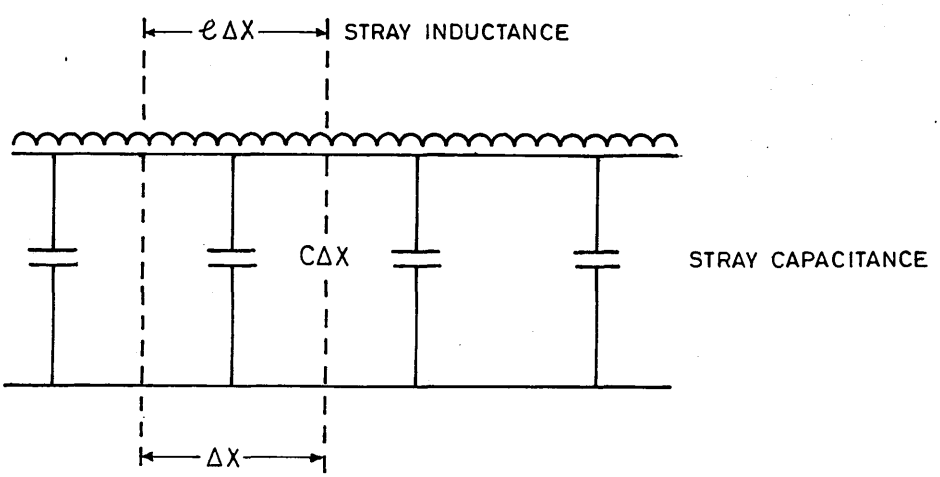

FIGURE 3.3 EQUIVALENT CIRCUIT FOR LOSSLESS TRANSMISSION LINE

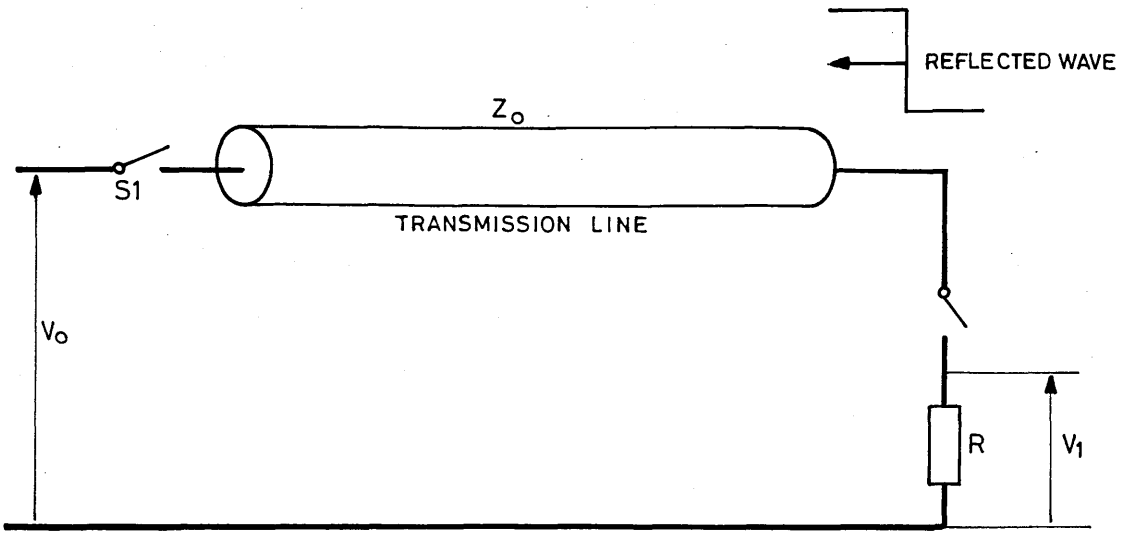

FIGURE 3.4 DISCHARGE CIRCUIT FOR LOSSLESS TRANSMISSION LINE

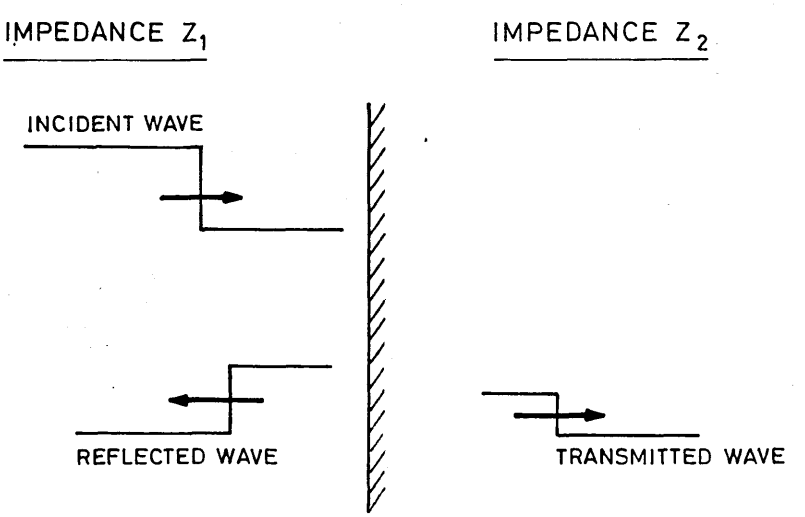

FIGURE 3.5 TRANSMISSION OF A WAVE AT THE BOUNDARY OF TWO IMPEDANCES

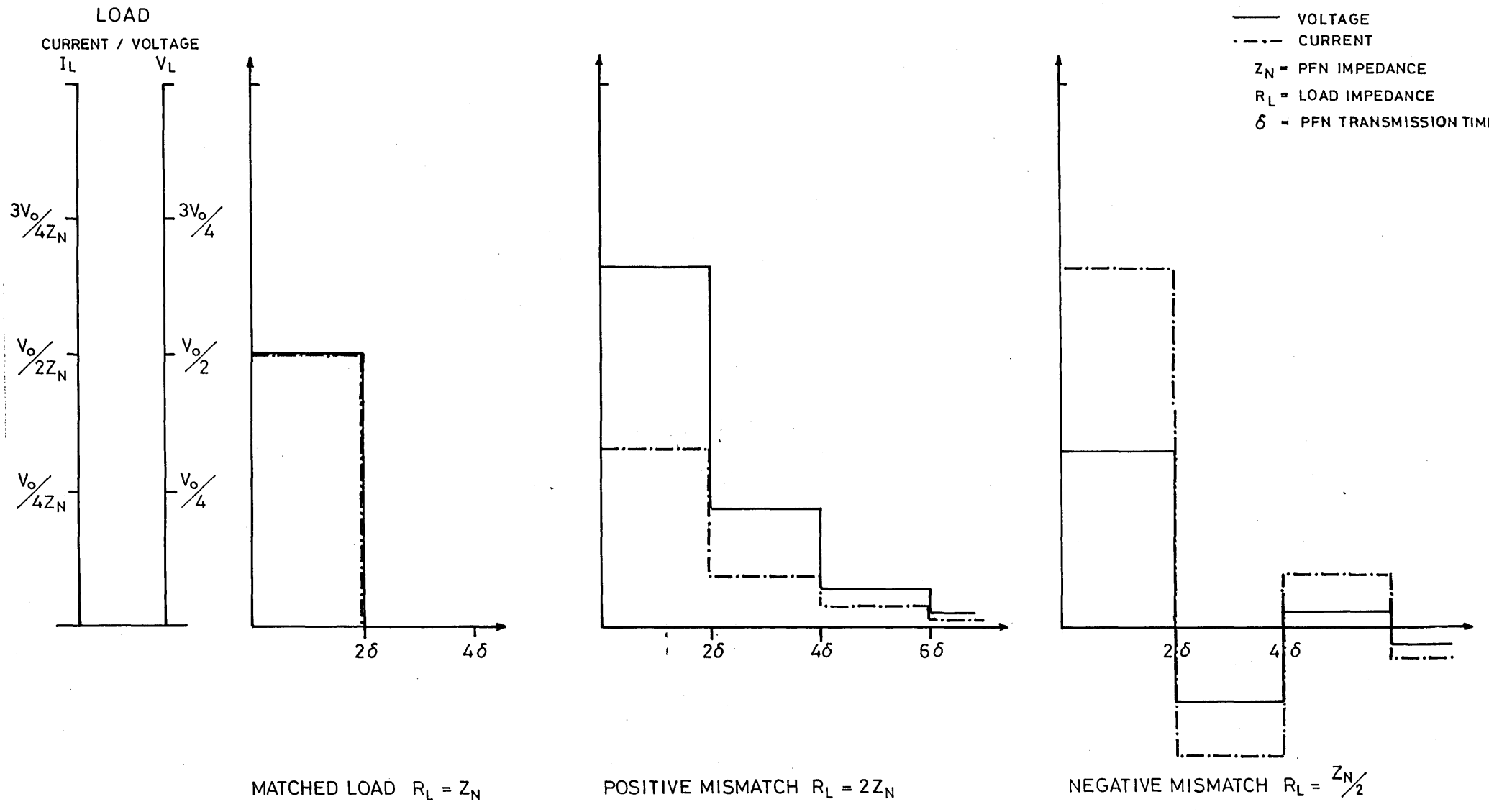

FIGURE 3.6 DISCHARGE CHARACTERISTICS OF A LOSSLESS TRANSMISSION LINE

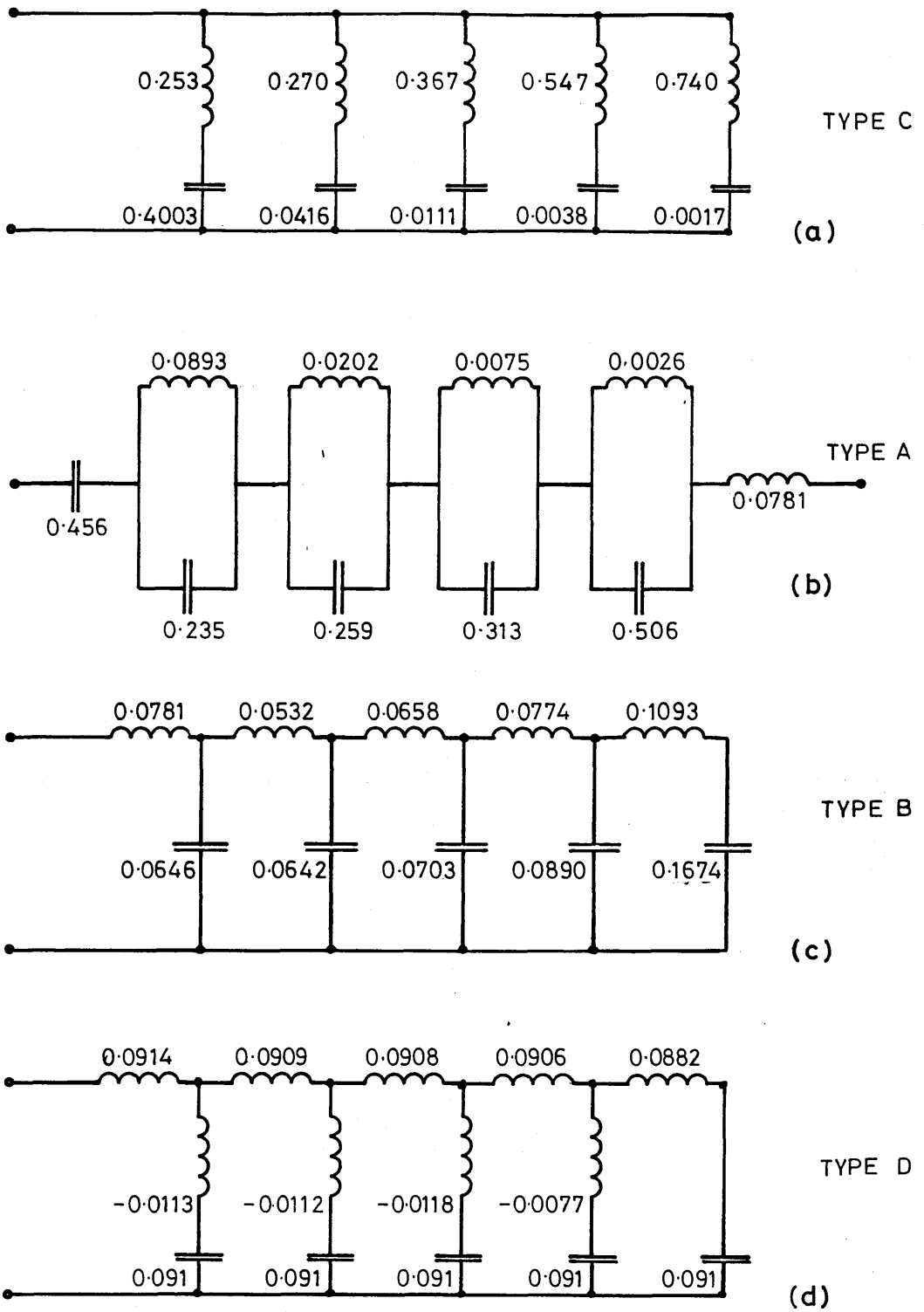

Equivalent forms of a five section Guilleman network. Multiply value of L by $Zn\tau$ and C by τ/Zn, with τ in units of microseconds, to get L in μH and C in μF.

FIGURE 3.7 EQUIVALENT FIVE SECTION PULSE FORMING NETWORKS

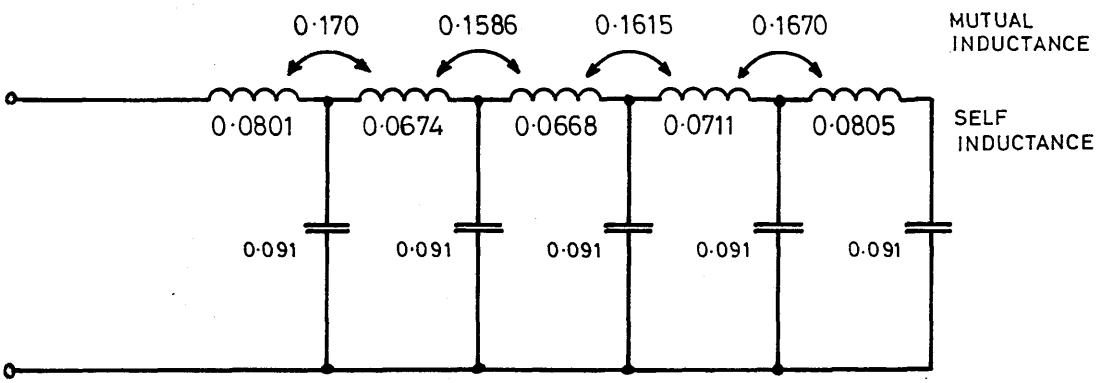

FIGURE 3.8 TYPE E PULSE FORMING NETWORK

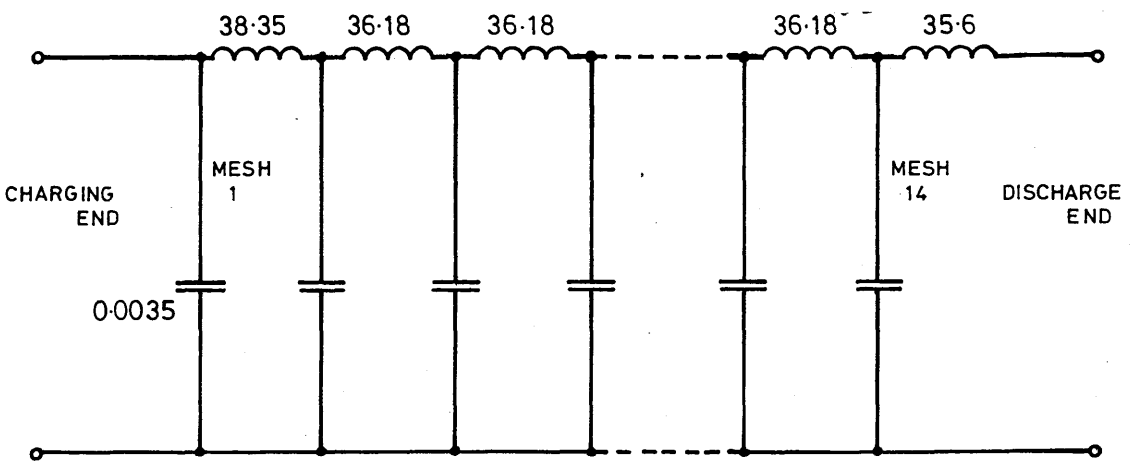

$\tau = 10\mu s$ $\quad Zn = 100\Omega$

$C_N = 0{\cdot}05\mu F$ $\quad Ln = 512\,\mu H$

FIGURE 3.9 SPALL'S 14 SECTION 100 Ω PULSE FORMING NETWORK

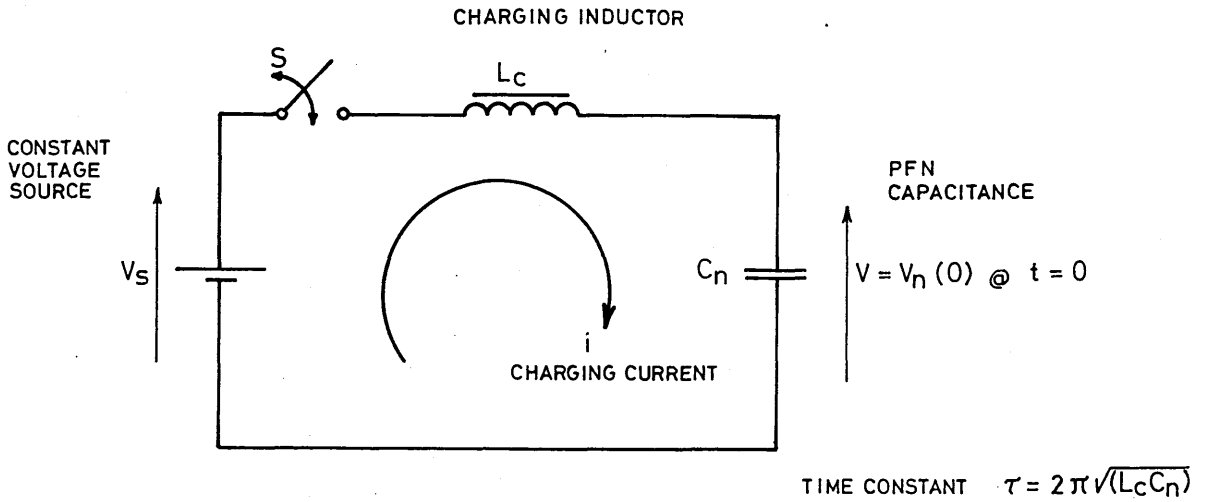

FIGURE 3.10 CIRCUIT MODEL OF IDEAL CHARGING CIRCUIT

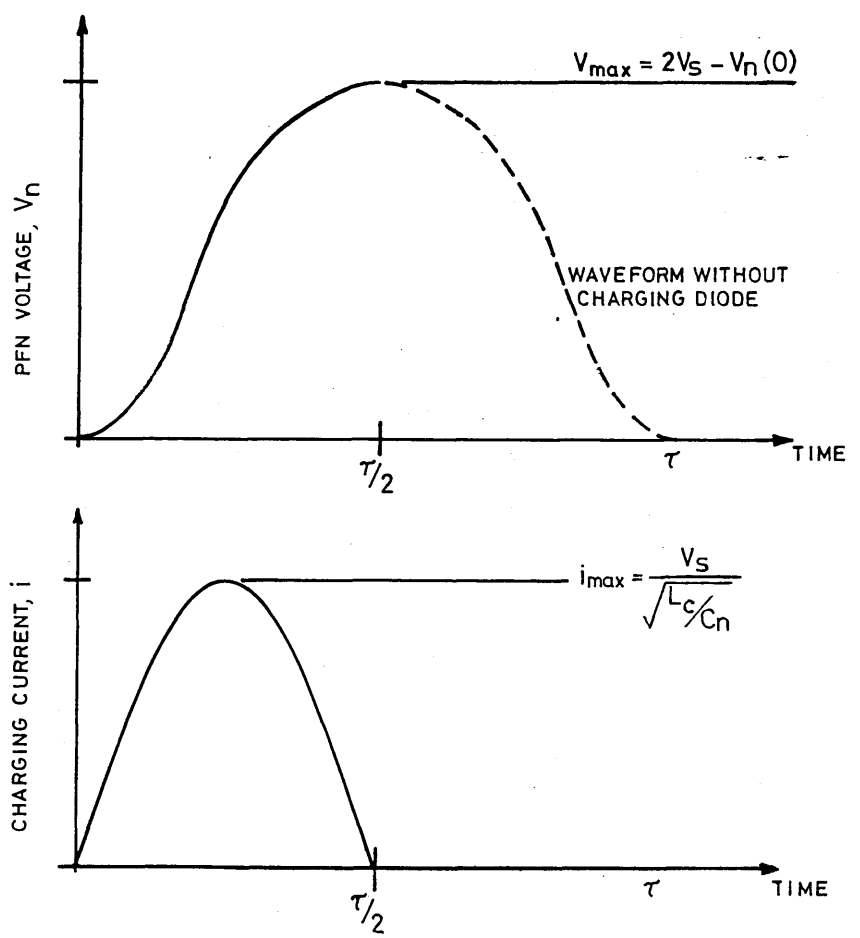

FIGURE 3.11 CHARGING CIRCUIT AND VOLTAGE WAVEFORMS

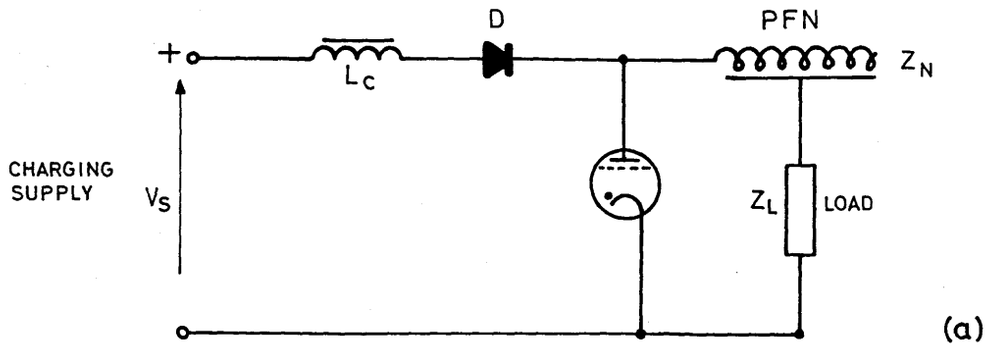

BASIC INDUCTANCE CHARGING CIRCUIT

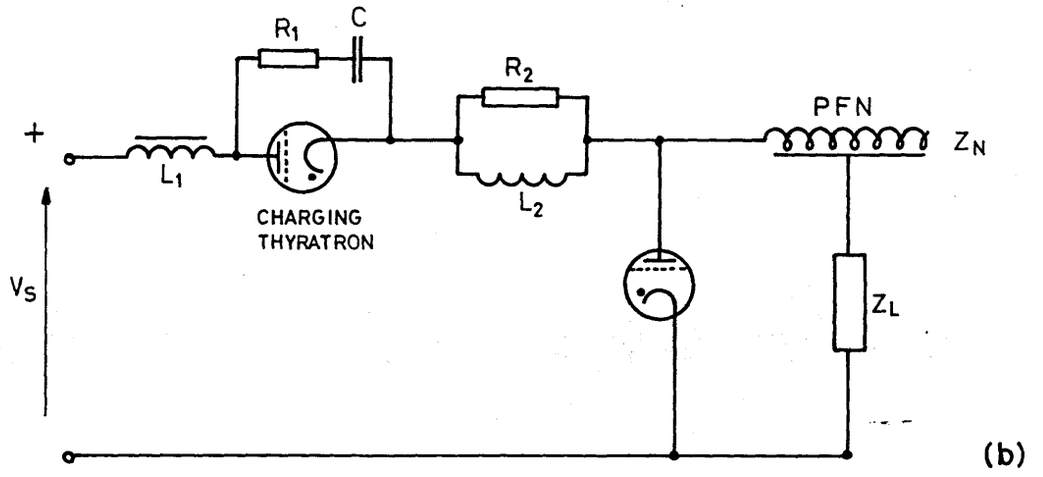

CHARGING CIRCUIT WITH TRIGGERED CHARGING DIODE

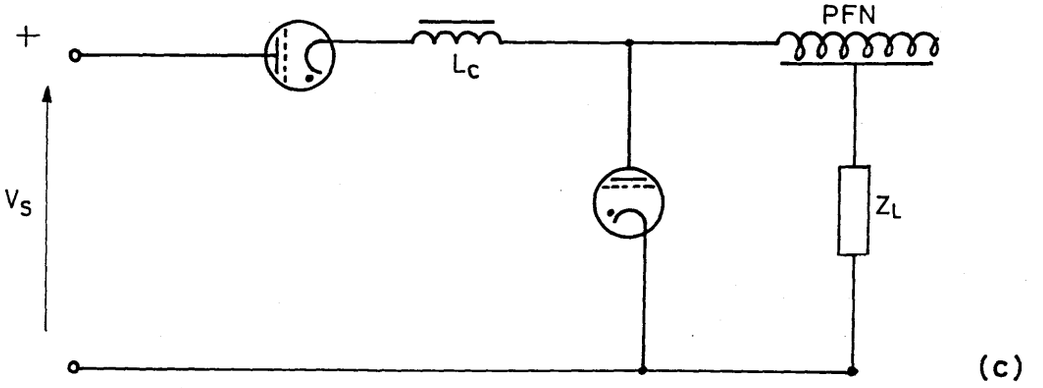

SIMPLE CHARGING CIRCUIT FOR LOW VOLTAGE PULSER

FIGURE 3.12 CHARGING CIRCUIT FOR A LINE TYPE PULSER

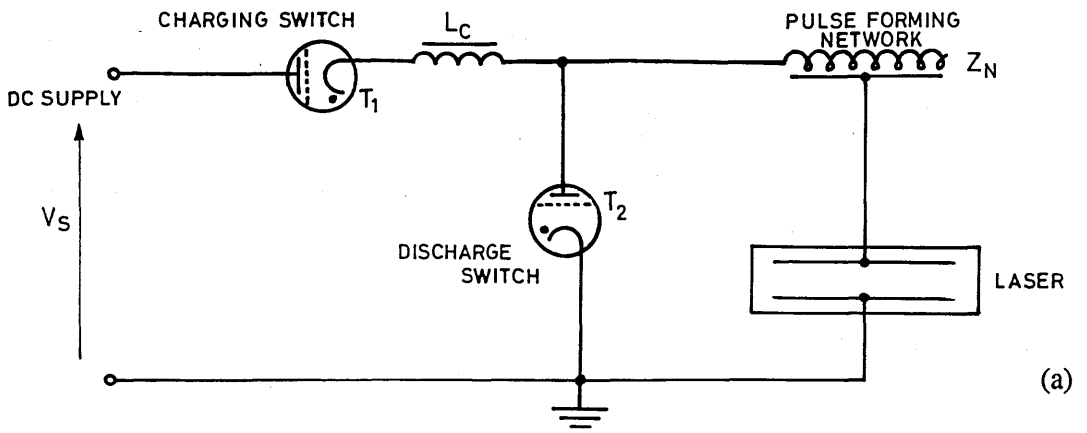

COMMON LINE TYPE PULSER CONFIGURATION

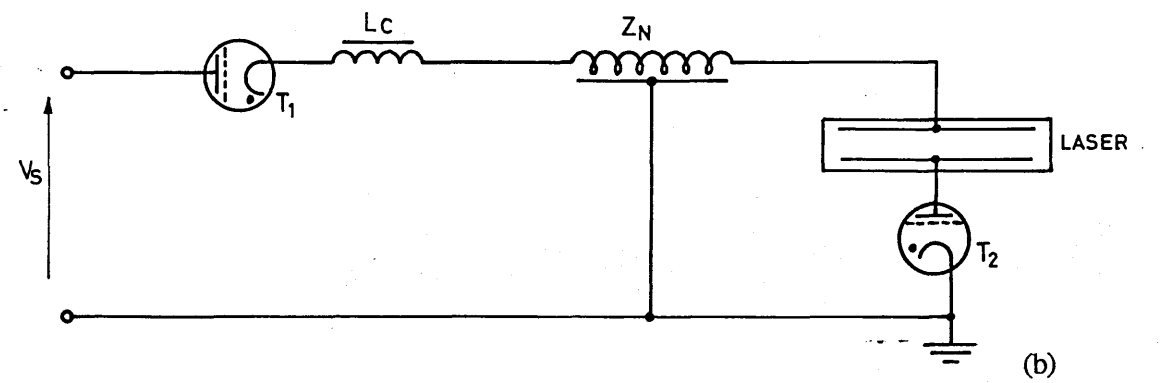

ALTERNATIVE PULSER CONFIGURATION WITH GROUNDED THYRATRON

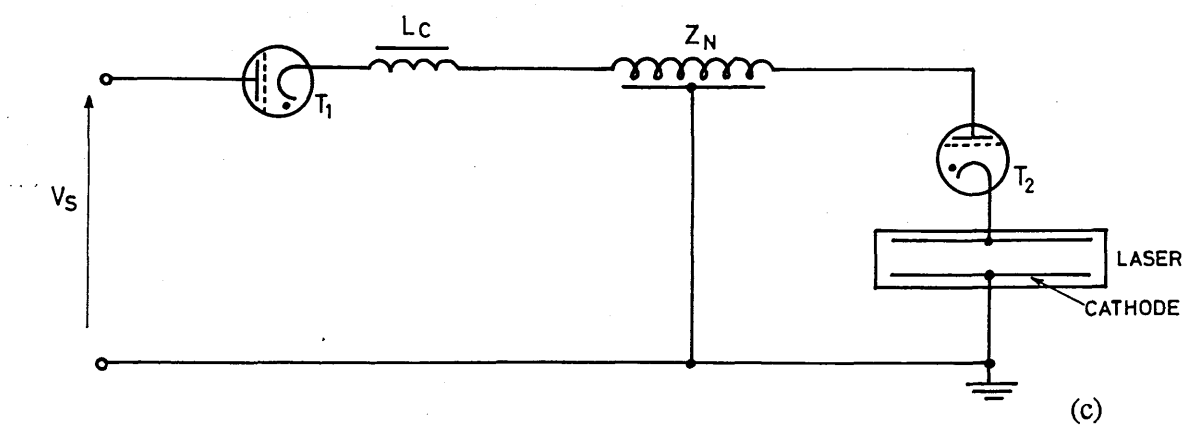

PULSER WITH GROUNDED LASER CATHODE

FIGURE 3.13 LINE TYPE PULSER CONFIGURATIONS FOR GAS LASER PUMPING

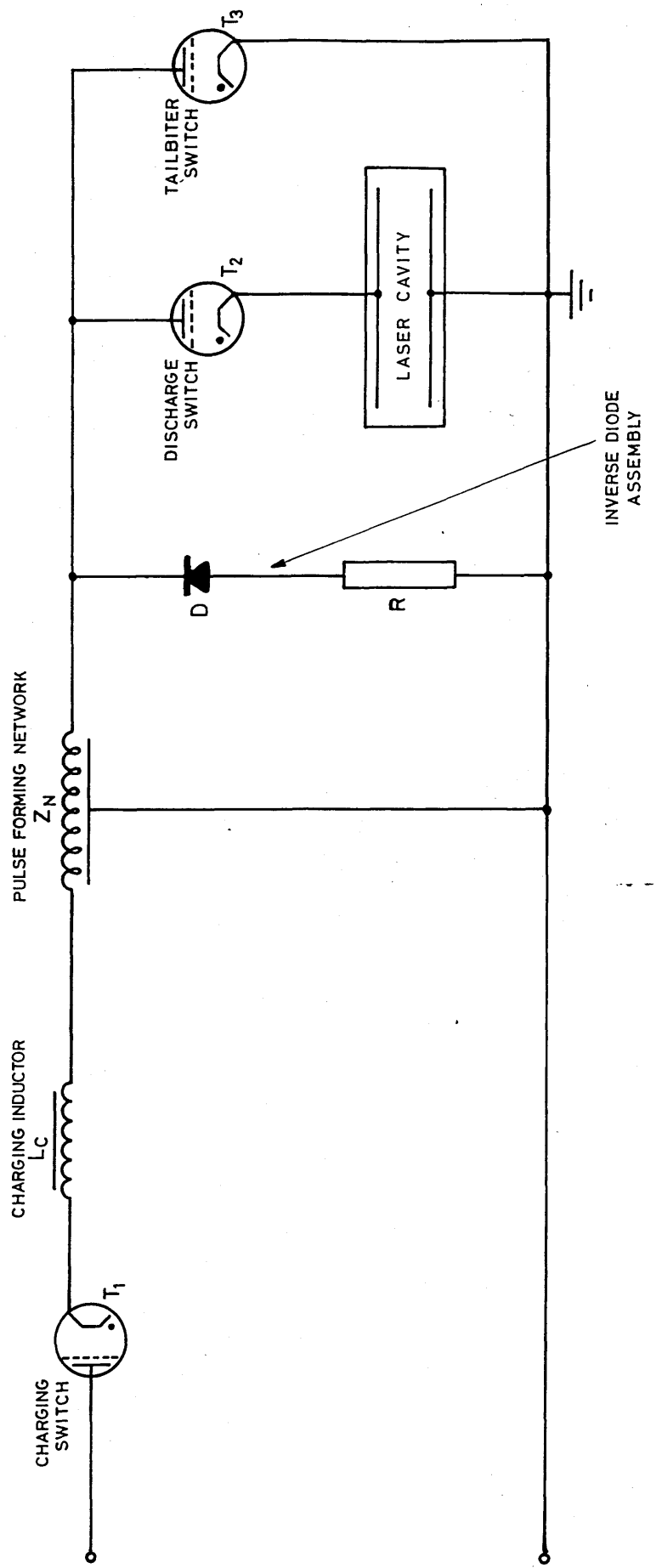

FIGURE 3.14 LINE TYPE PULSER WITH OVERSWING DIODE STACK

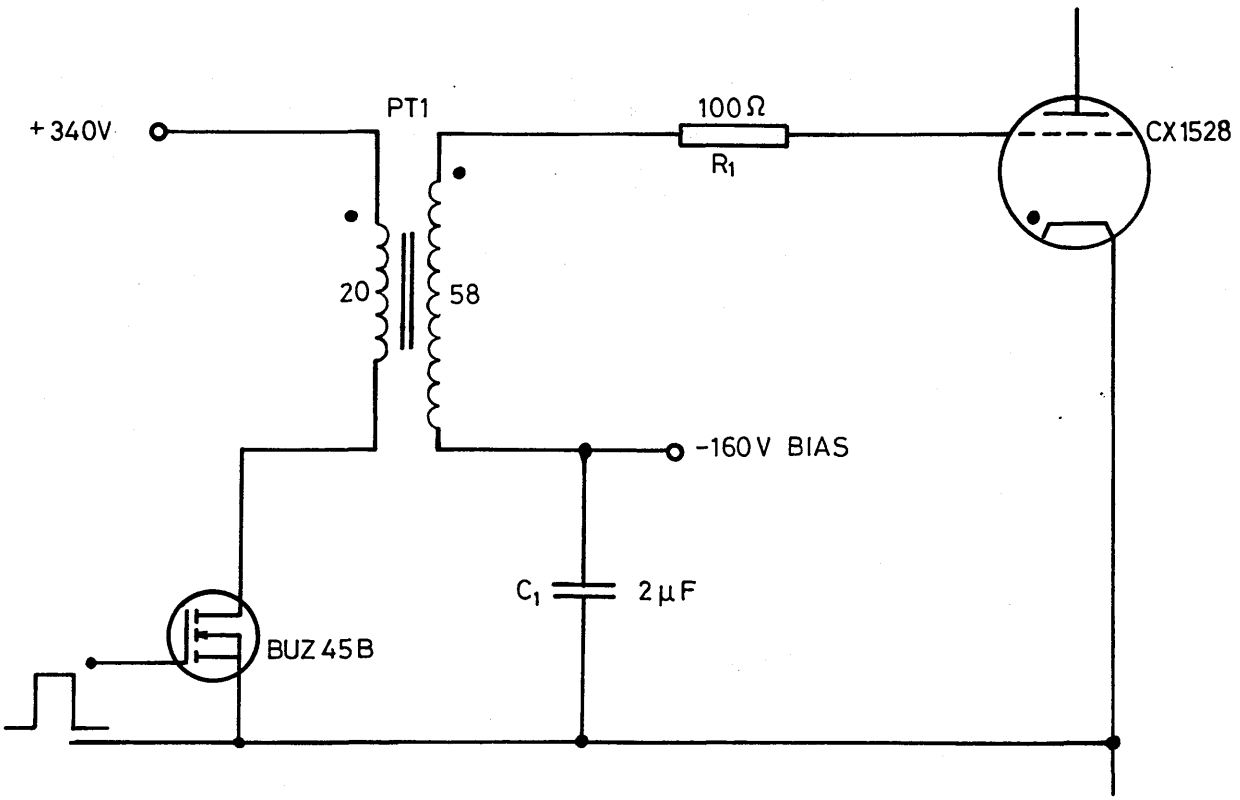

FIGURE 3.15 OUTPUT STAGE OF MOSFET TRIGGER CIRCUIT

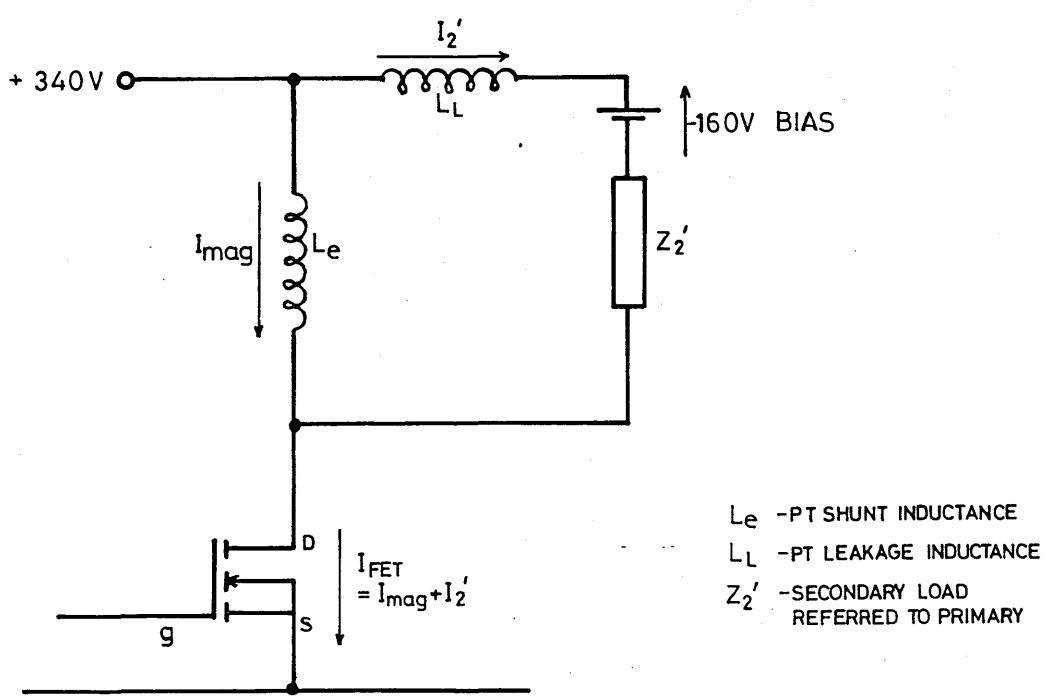

FIGURE 3.16 EQUIVALENT CIRCUIT FOR MOSFET OUTPUT STAGE

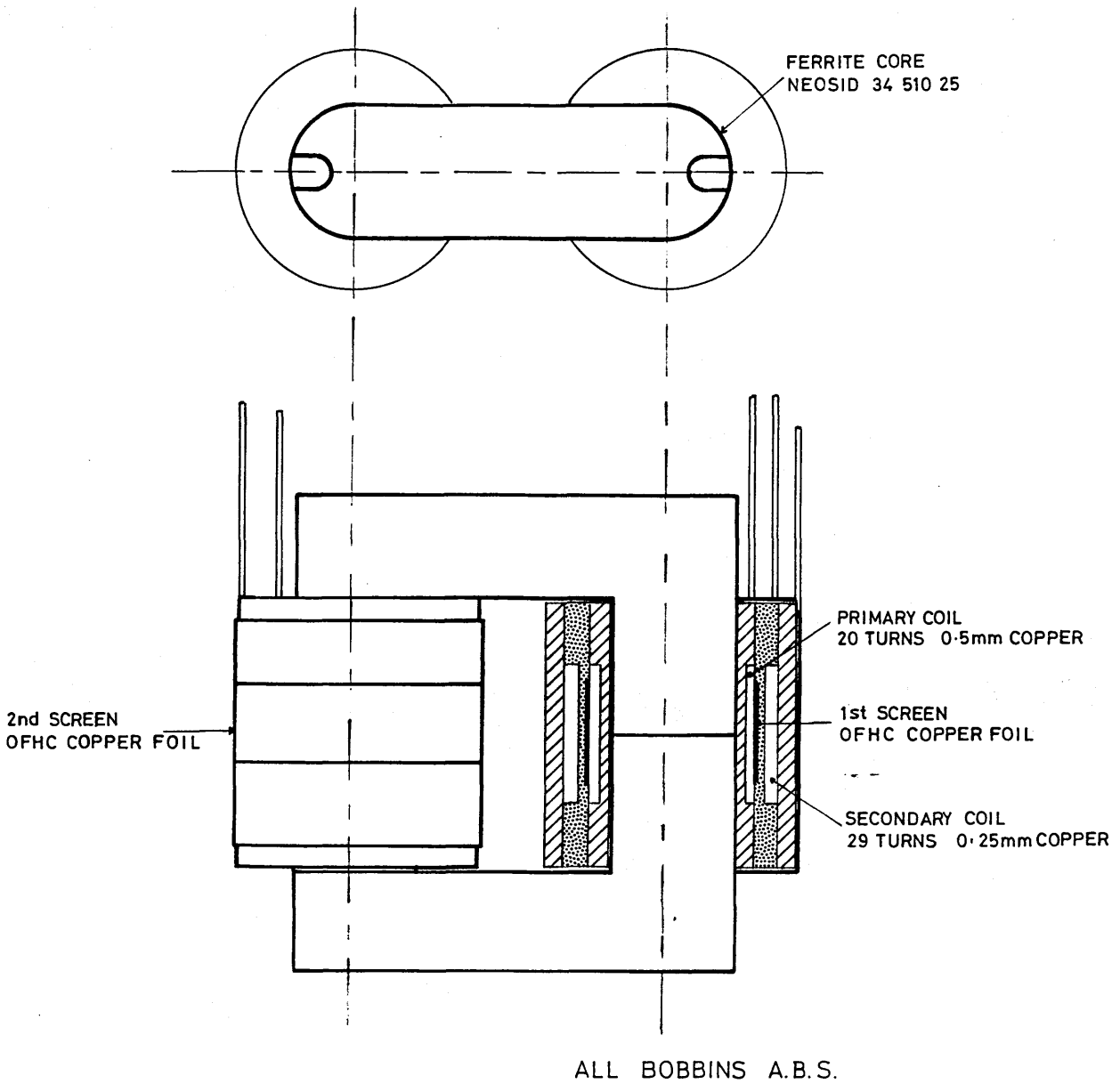

FIGURE 3.17 SCHEMATIC OF PULSE TRANSFORMER

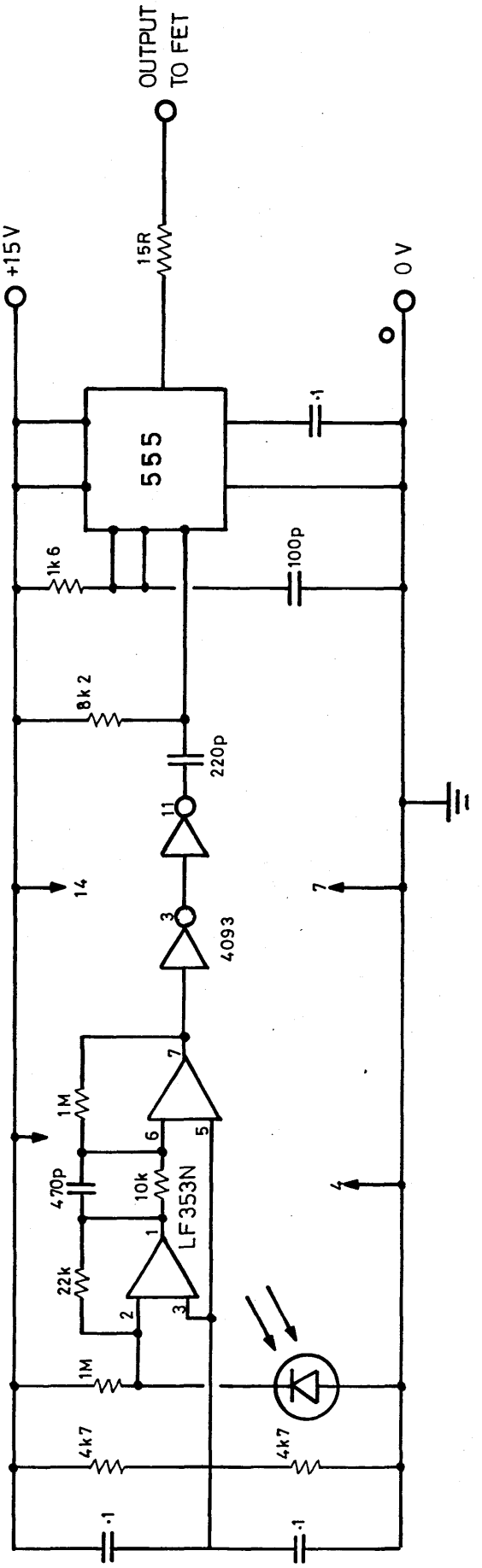

FIGURE 3.18 RECEIVER CIRCUIT

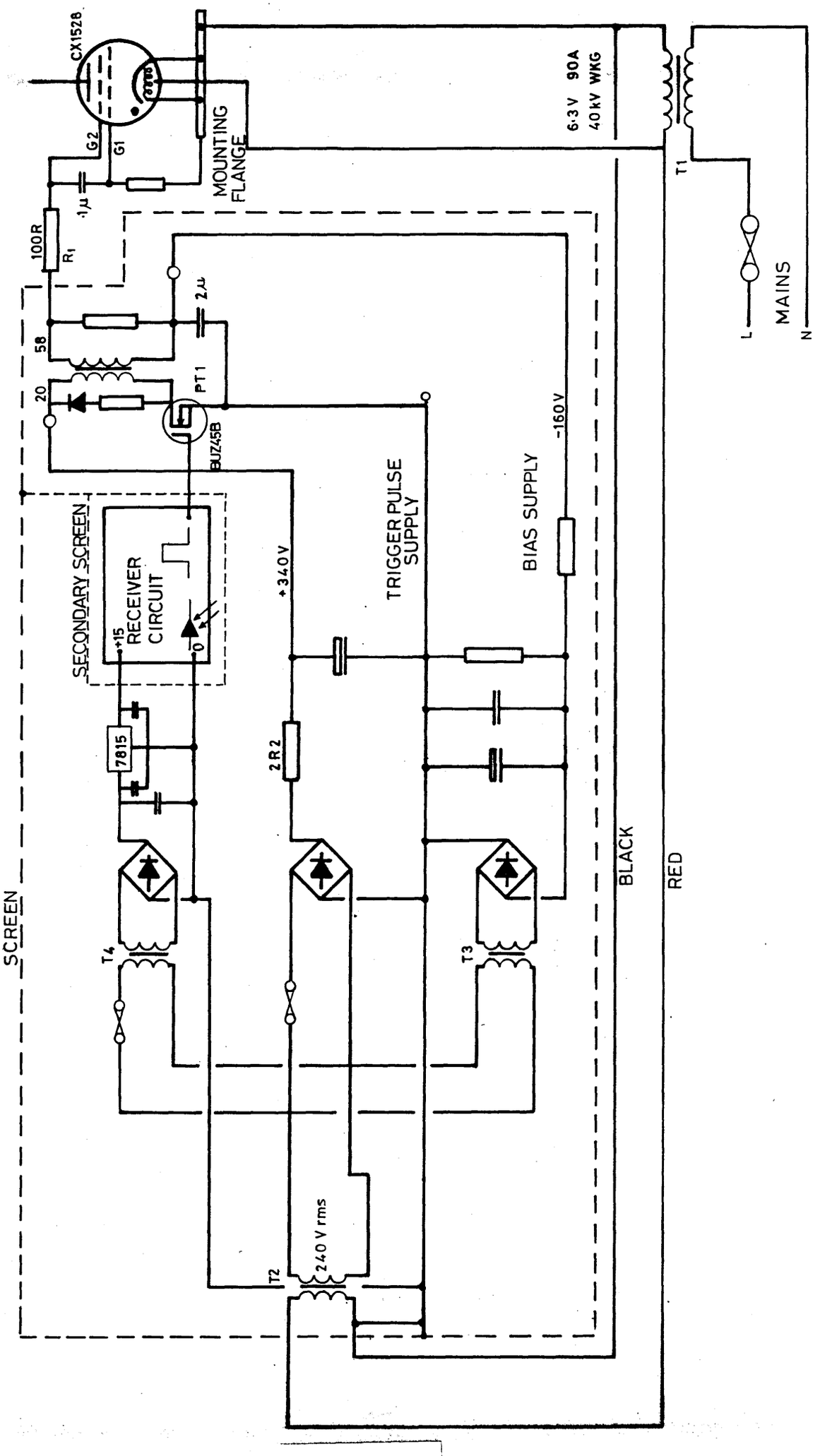

FIGURE 3.19 CX1528 MOSFET TRIGGER CIRCUIT

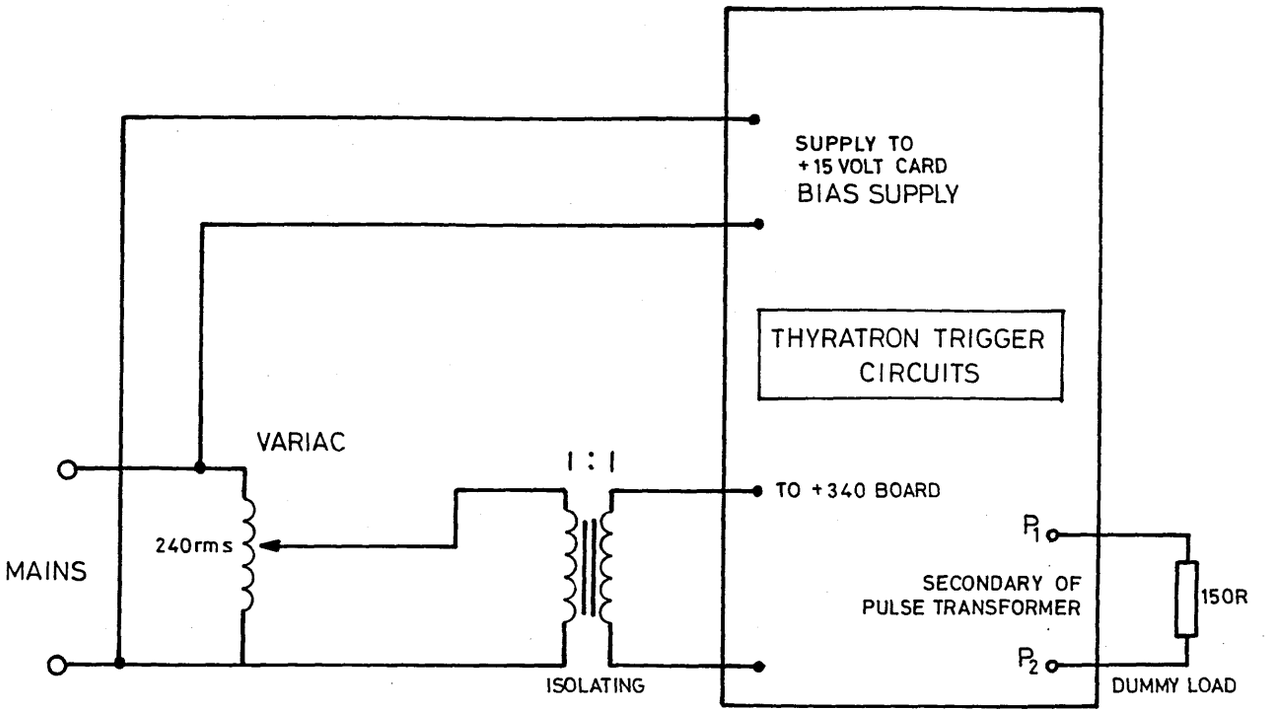

FIGURE 3.20 TRIGGER CIRCUIT COMMISSIONING SUPPLY

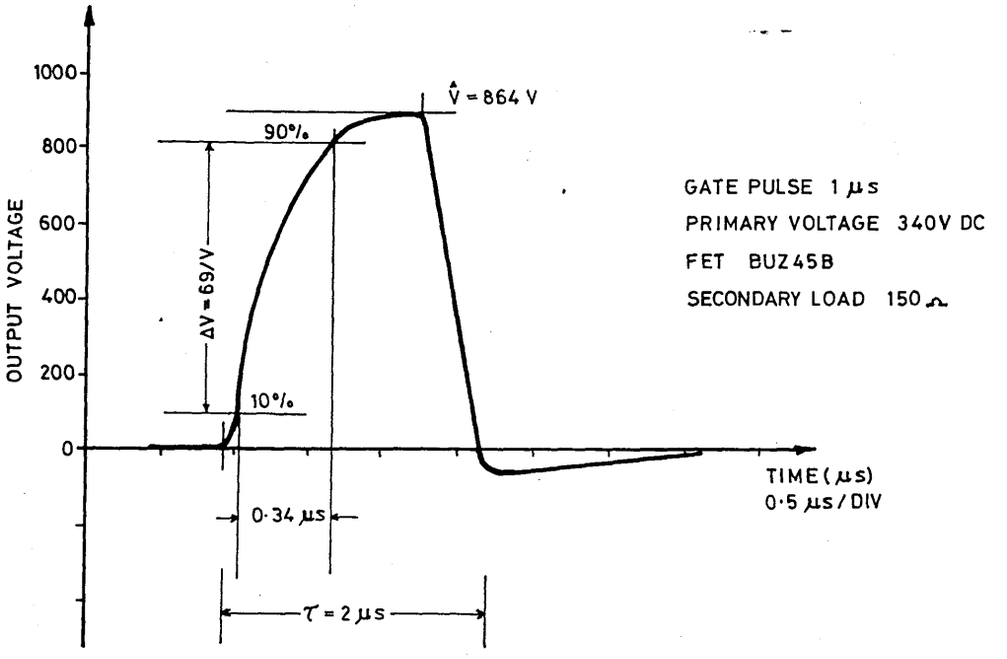

FIGURE 3.21 MOSFET CIRCUIT OUTPUT PULSE

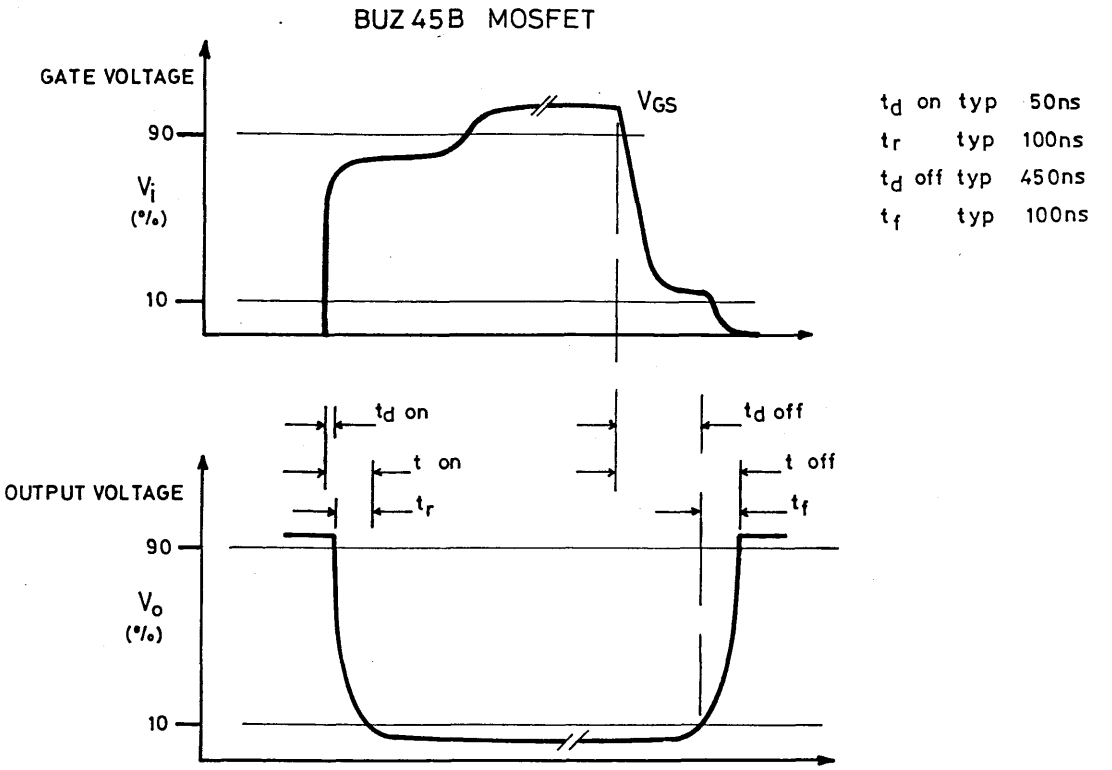

FIGURE 3.22 MOSFET SWITCHING CHARACTERISTICS

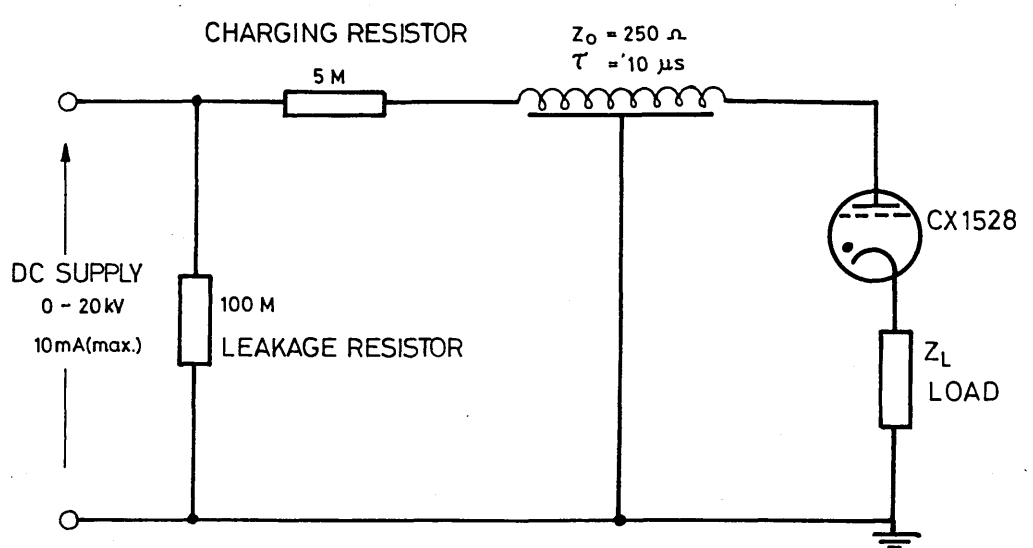

FIGURE 3.23 THYRATRON TEST CIRCUIT

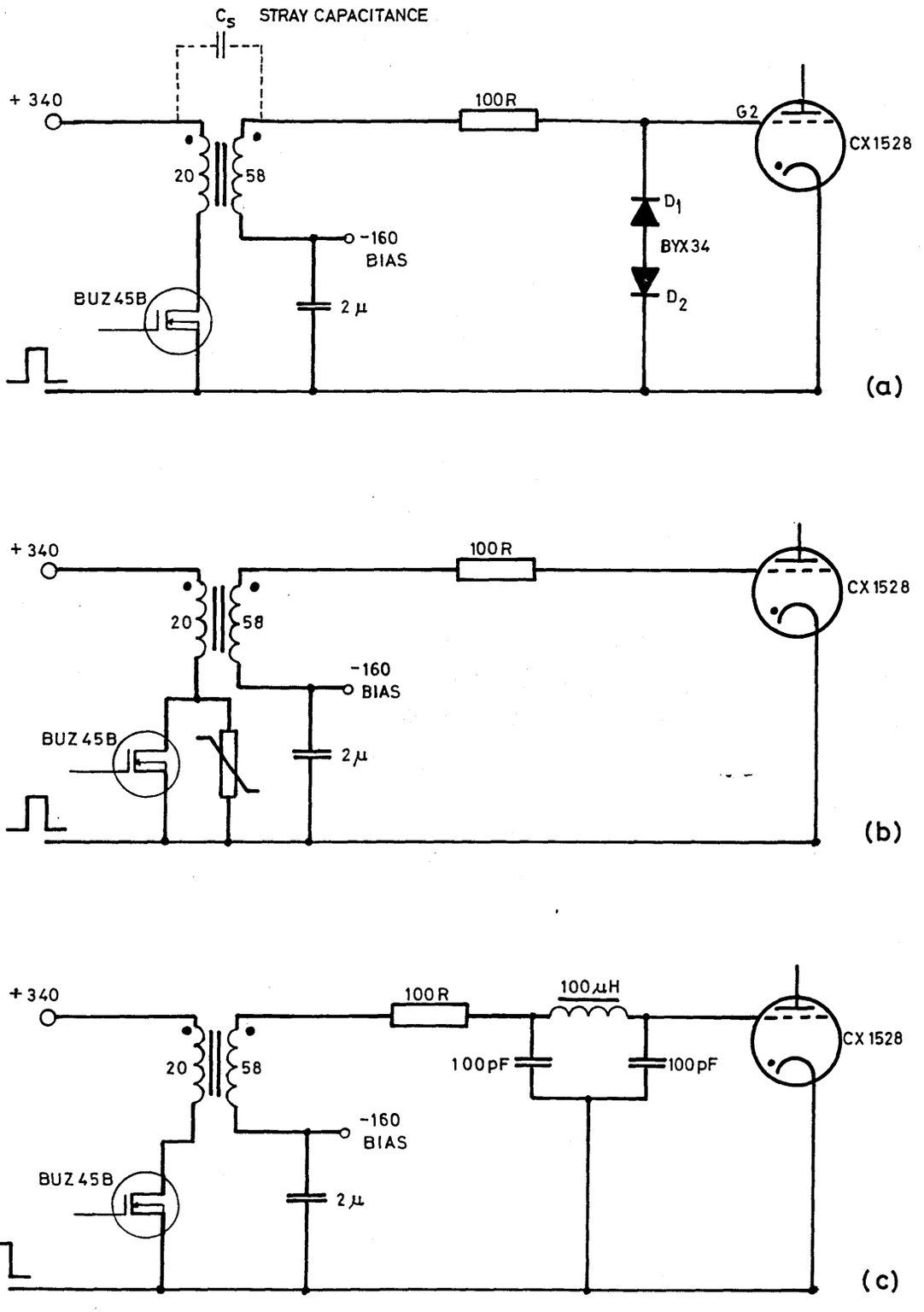

FIGURE 3.24 MOSFET PROTECTION FROM GRID SPIKE

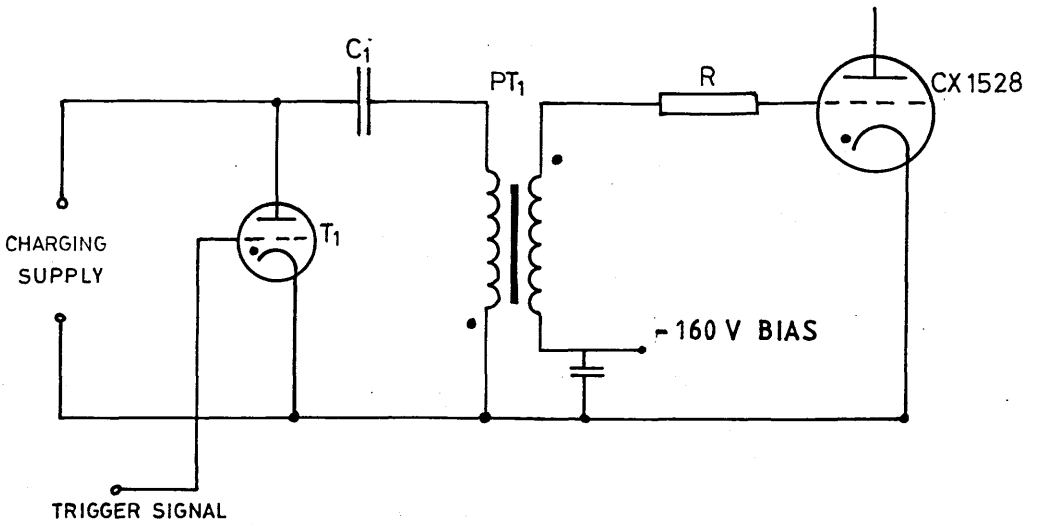

FIGURE 3.25 INVERTER TYPE TRIGGER CIRCUIT

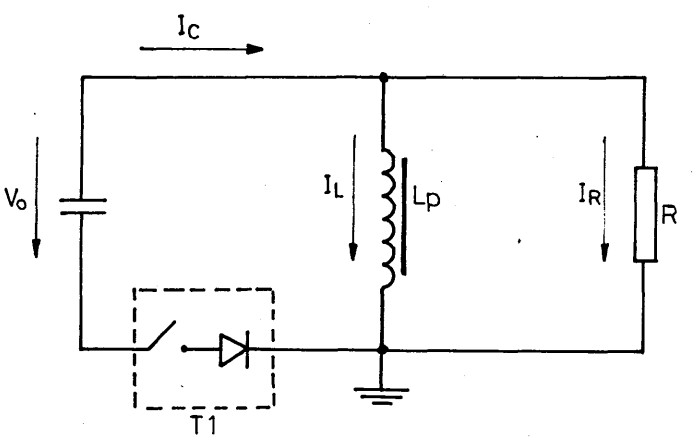

FIGURE 3.26 EQUIVALENT CIRCUIT FOR INVERTER

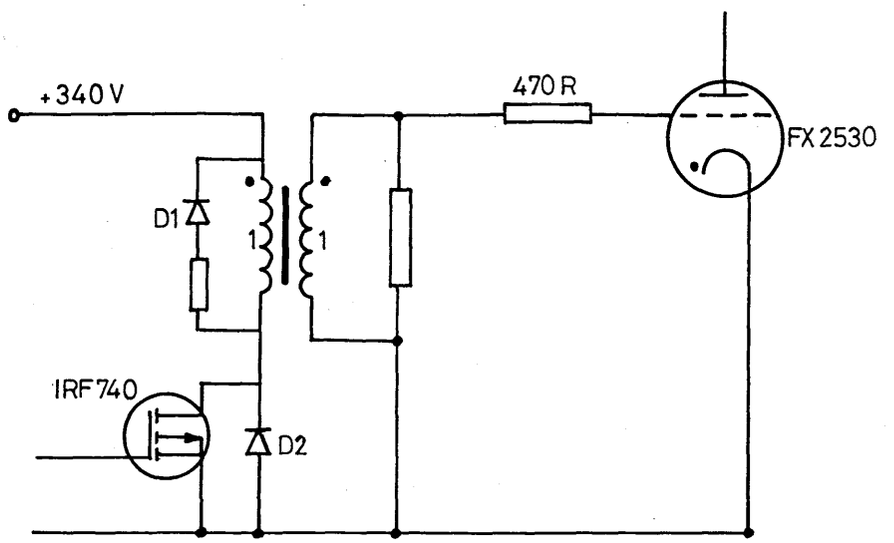

FIGURE 3.27 FX2530 TRIGGER CIRCUIT

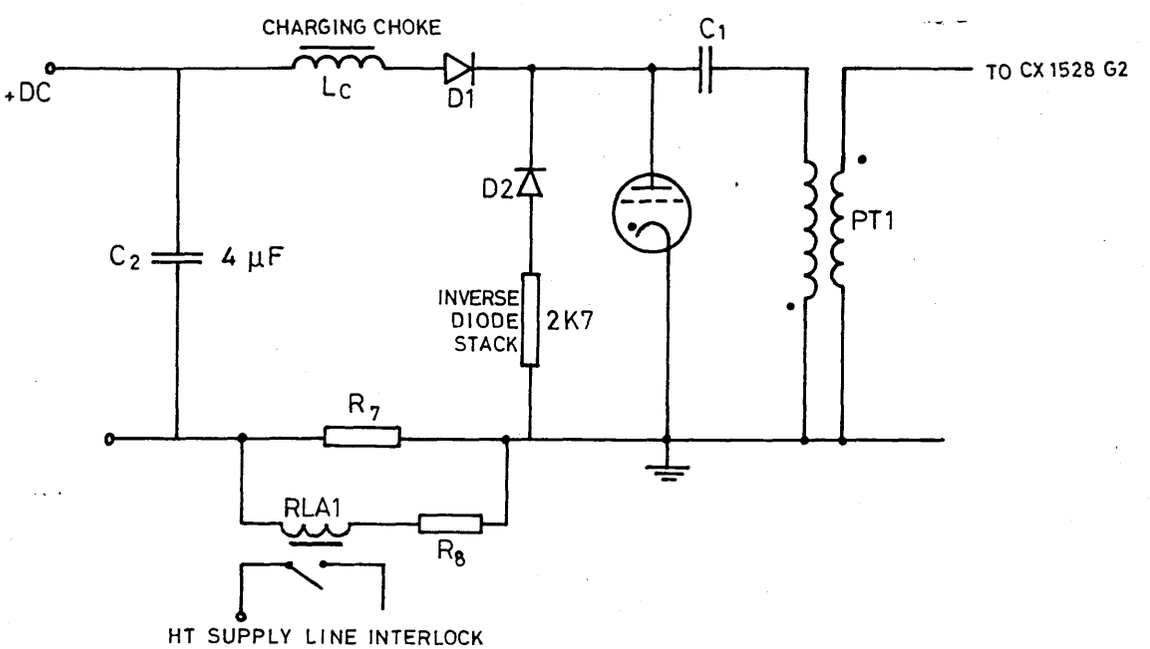

FIGURE 3.28 TRIGGER CIRCUIT PROTECTION

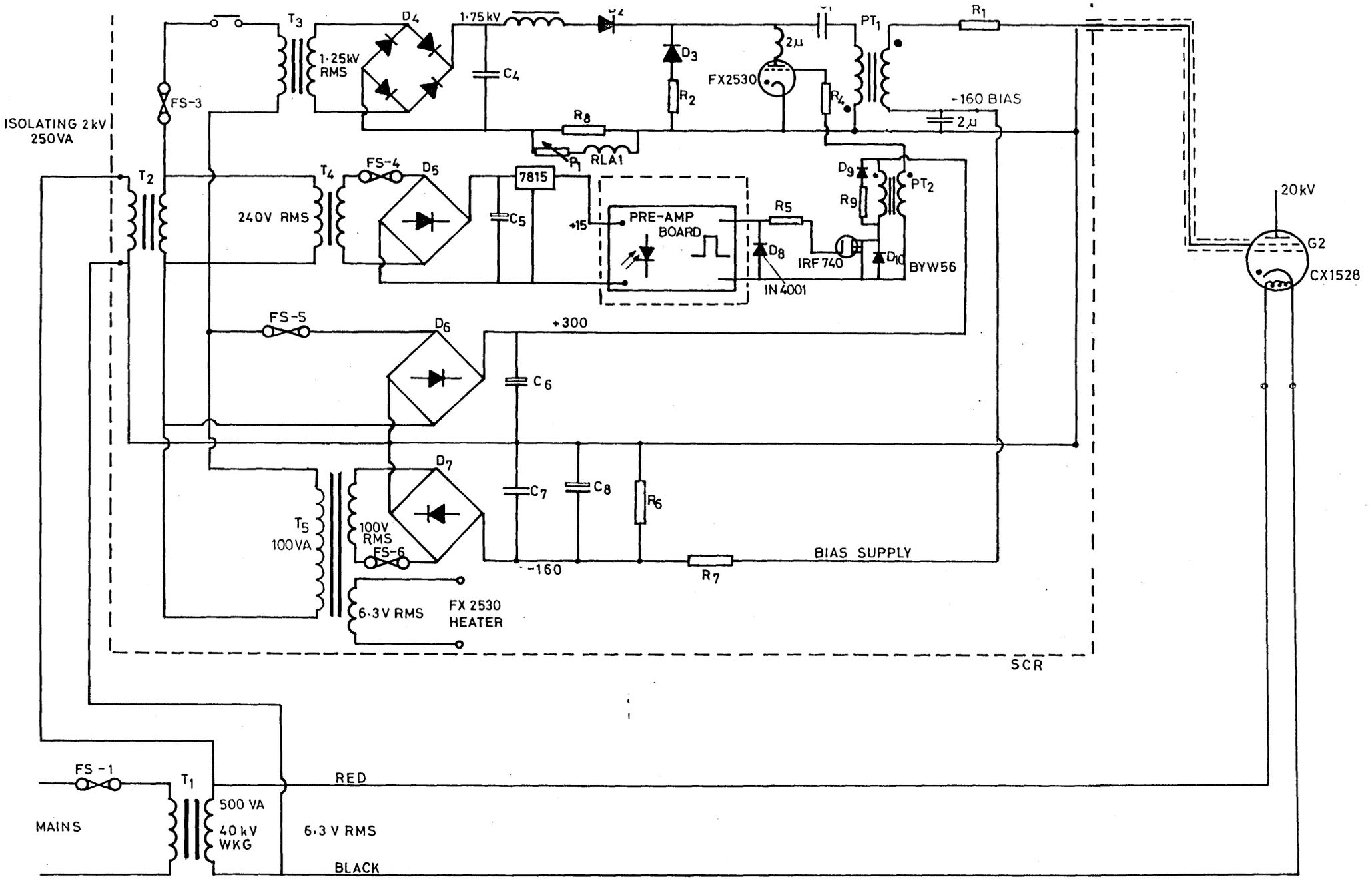

FIGURE 3.29 CX1528 TRIGGER CIRCUIT

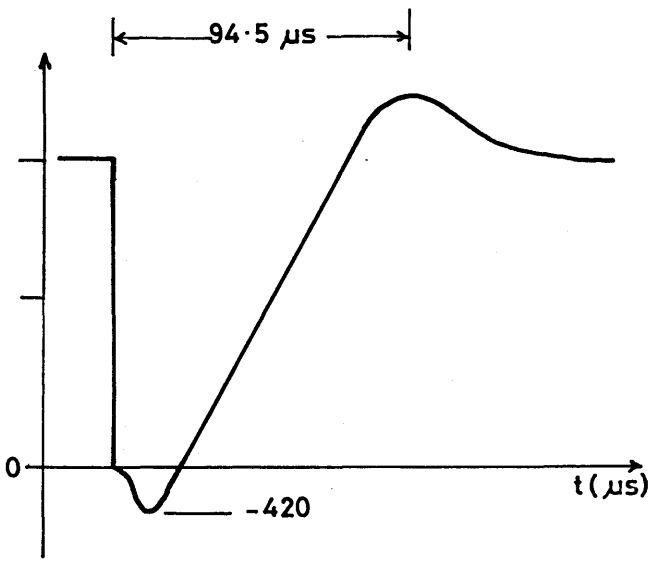

(a) FX 2530 ANODE VOLTAGE

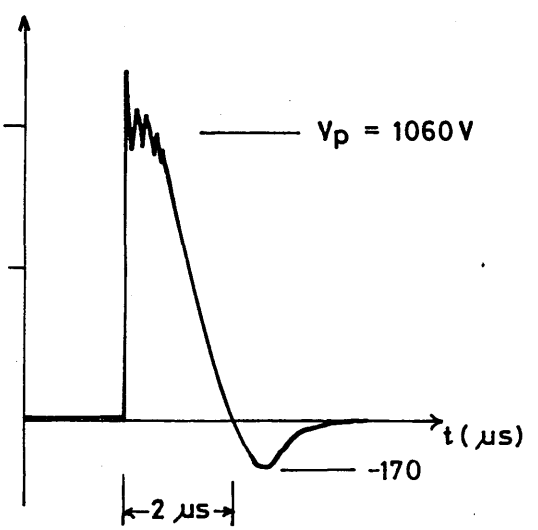

DATA:
PRF = 1 kHz
V_{DC} = 1·36 kV
R_L = 150 Ω

(b) PULSE TRANSFORMER PT2 SECONDARY STAGE

FIGURE 3.30 TRIGGER CIRCUIT OUTPUT CHARACTERISTICS: DUMMY LOAD

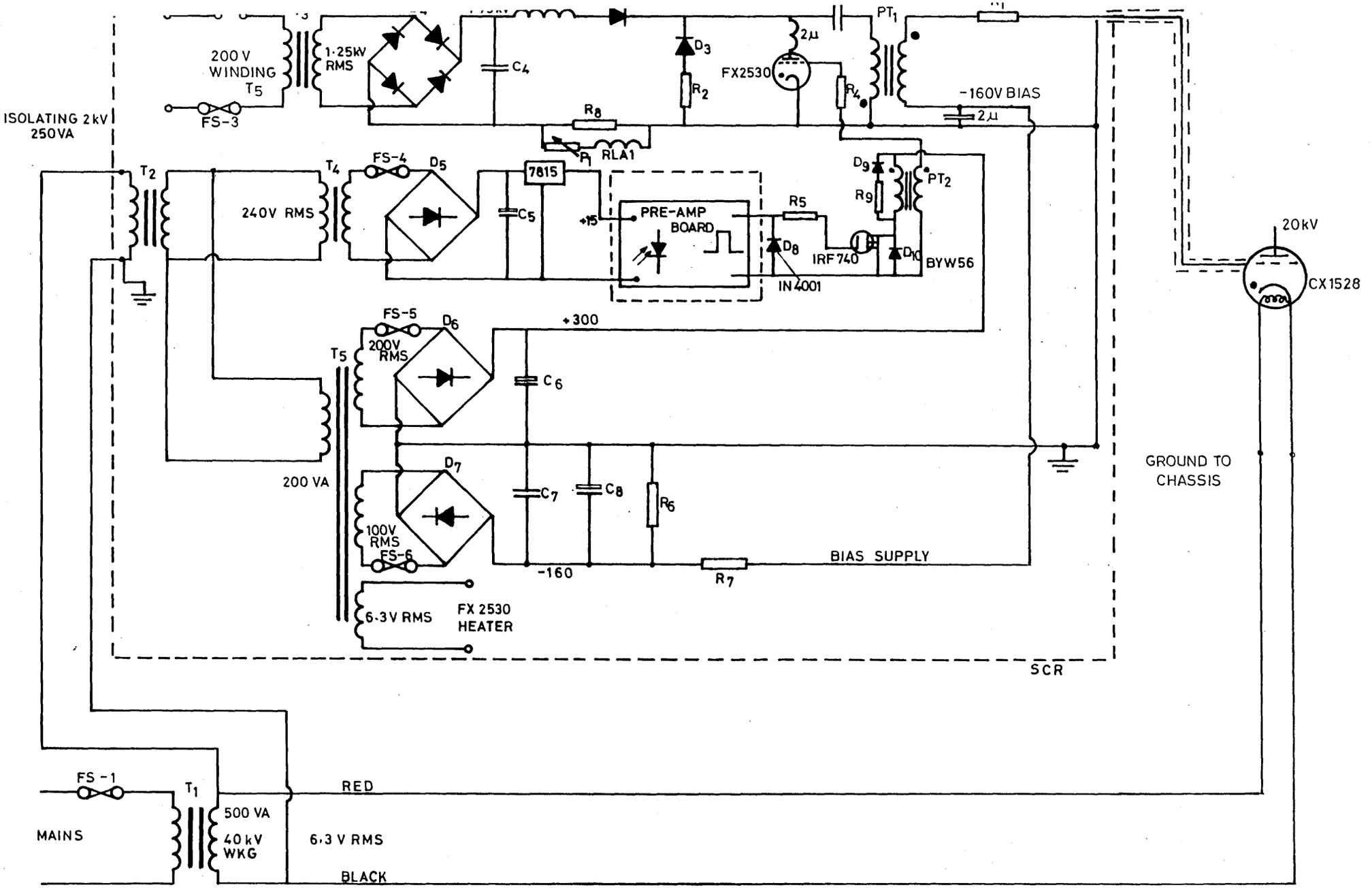

FIGURE 3.31 MODIFIED CX1528 TRIGGER CIRCUIT

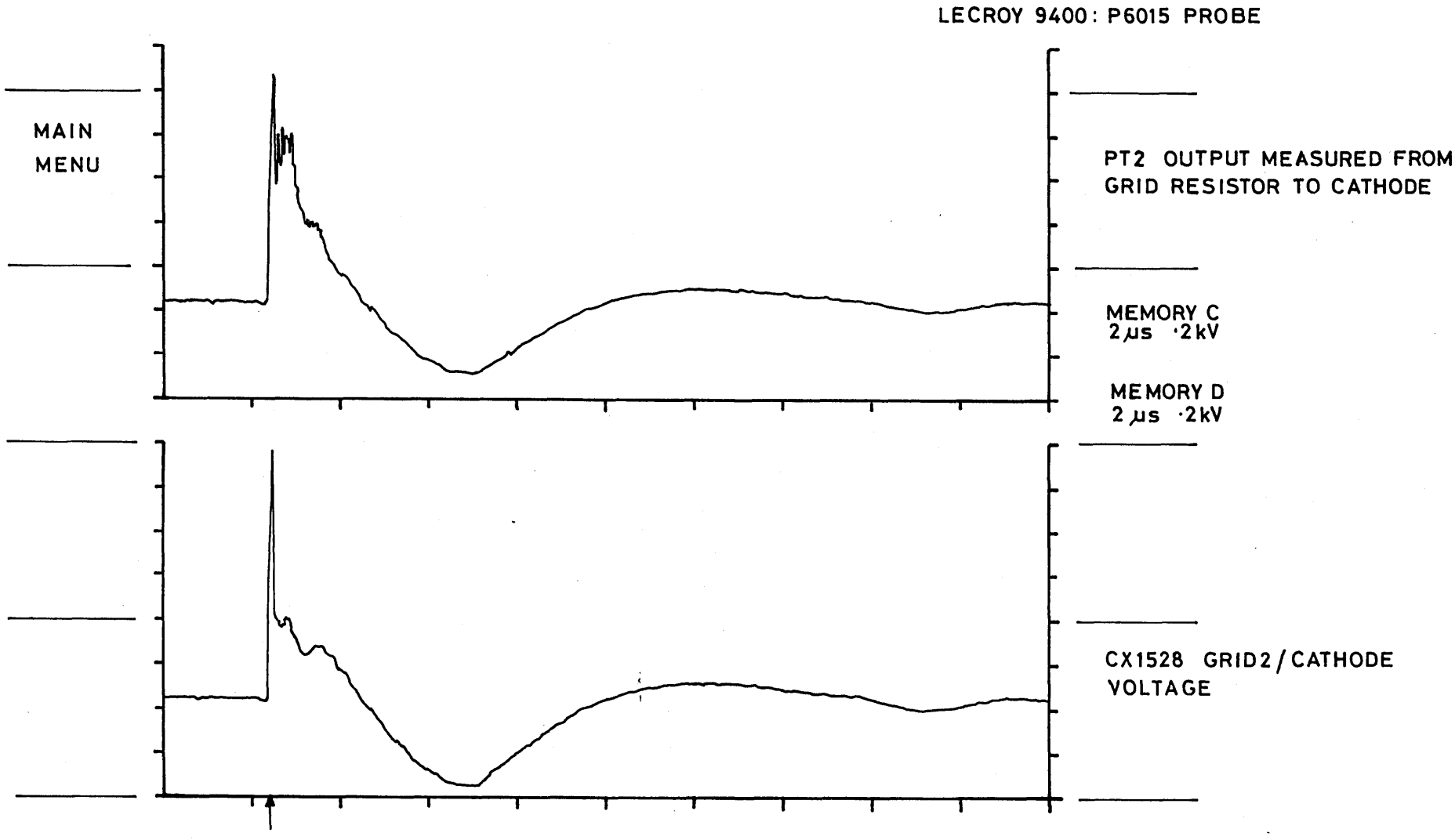

FIGURE 3.32 TRIGGER CIRCUIT OUTPUT CHARACTERISTICS: THYRATRON LOAD

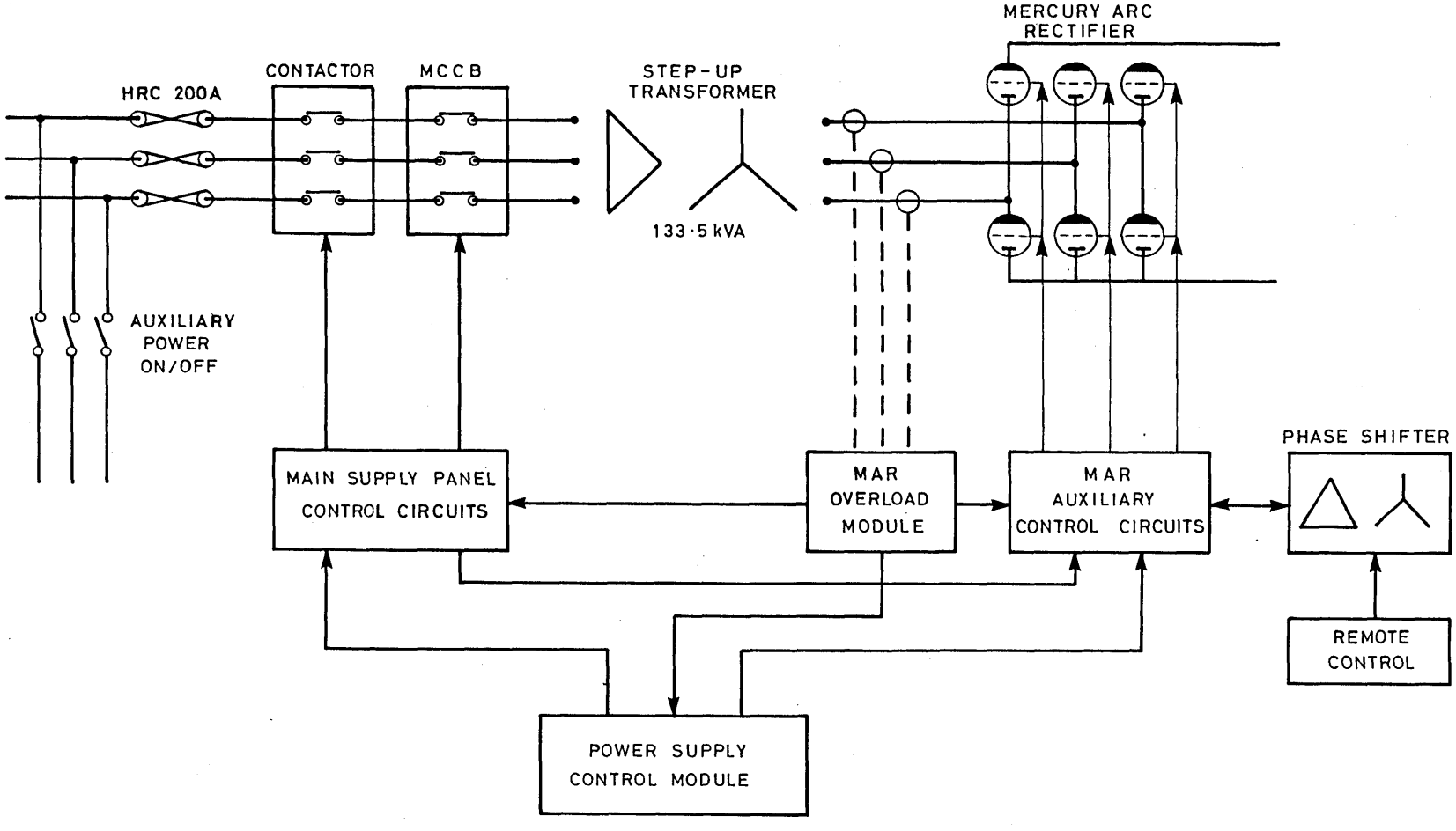

FIGURE 3.33 SCHEMATIC OF DC CHARGING SUPPLY

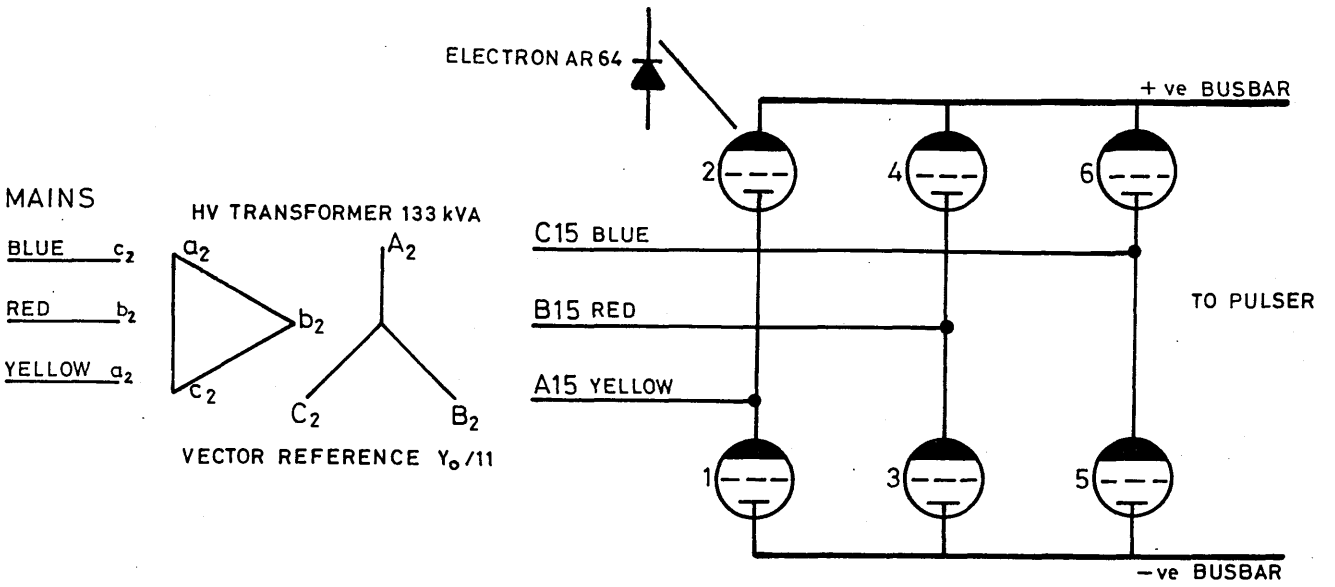

FIGURE 3.34 MERCURY ARC RECTIFIER

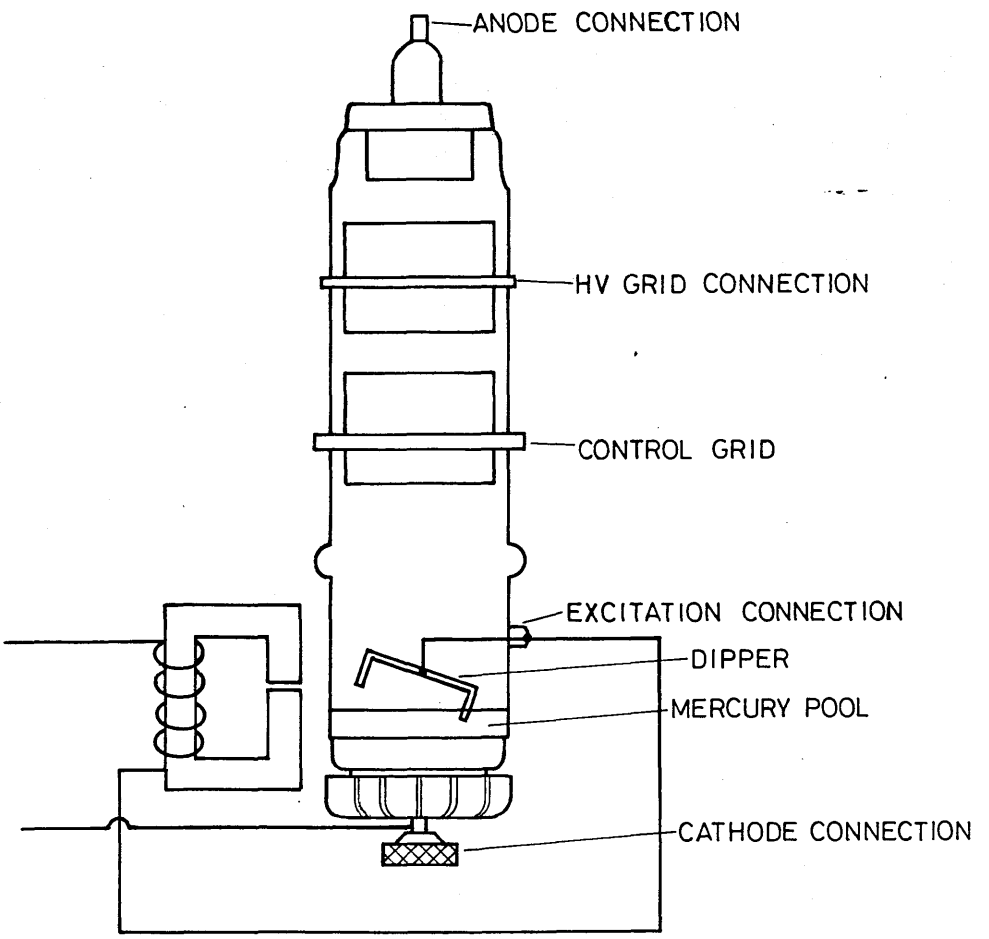

FIGURE 3.35 AR64 EXCITRON TUBE

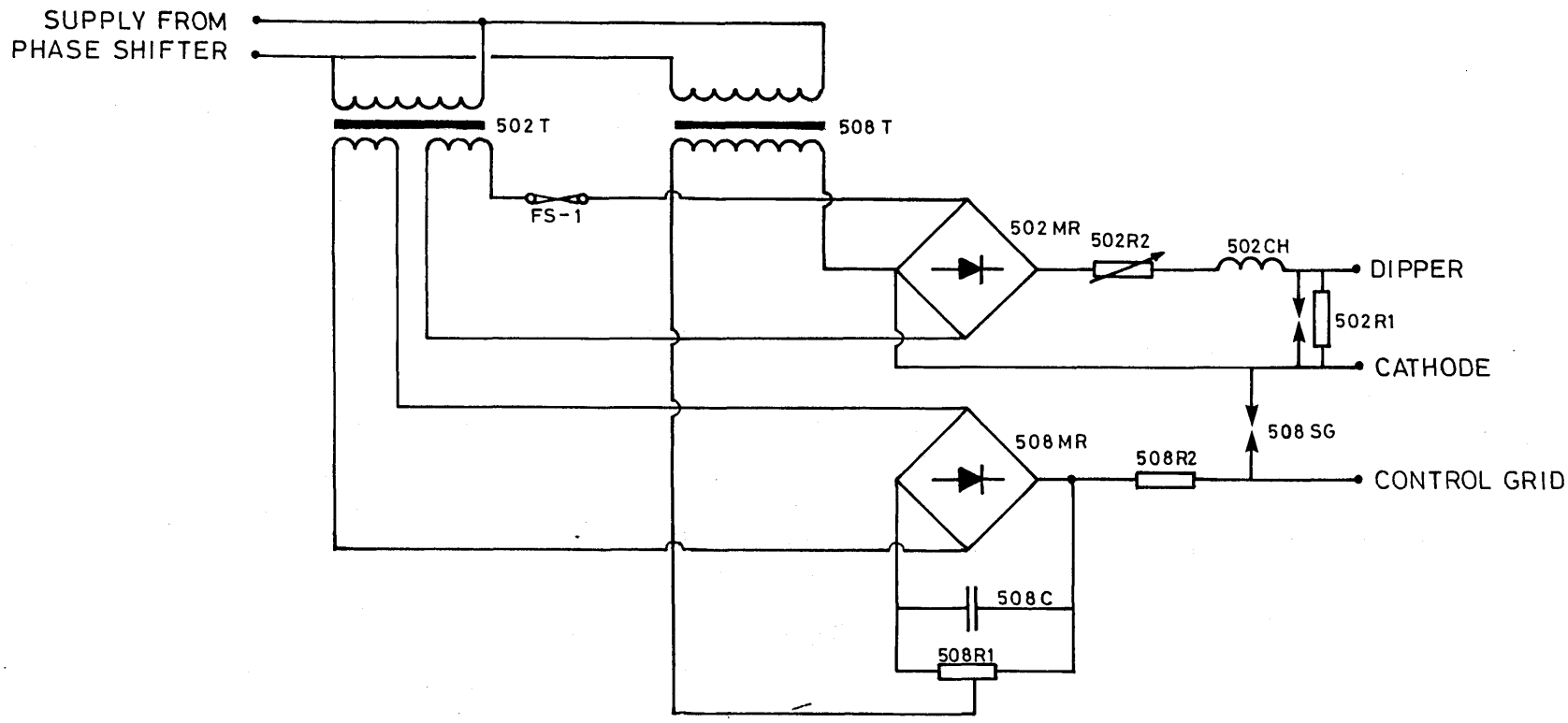

FIGURE 3.36 AR64 GRID AND EXCITATION SUPPLY CIRCUIT

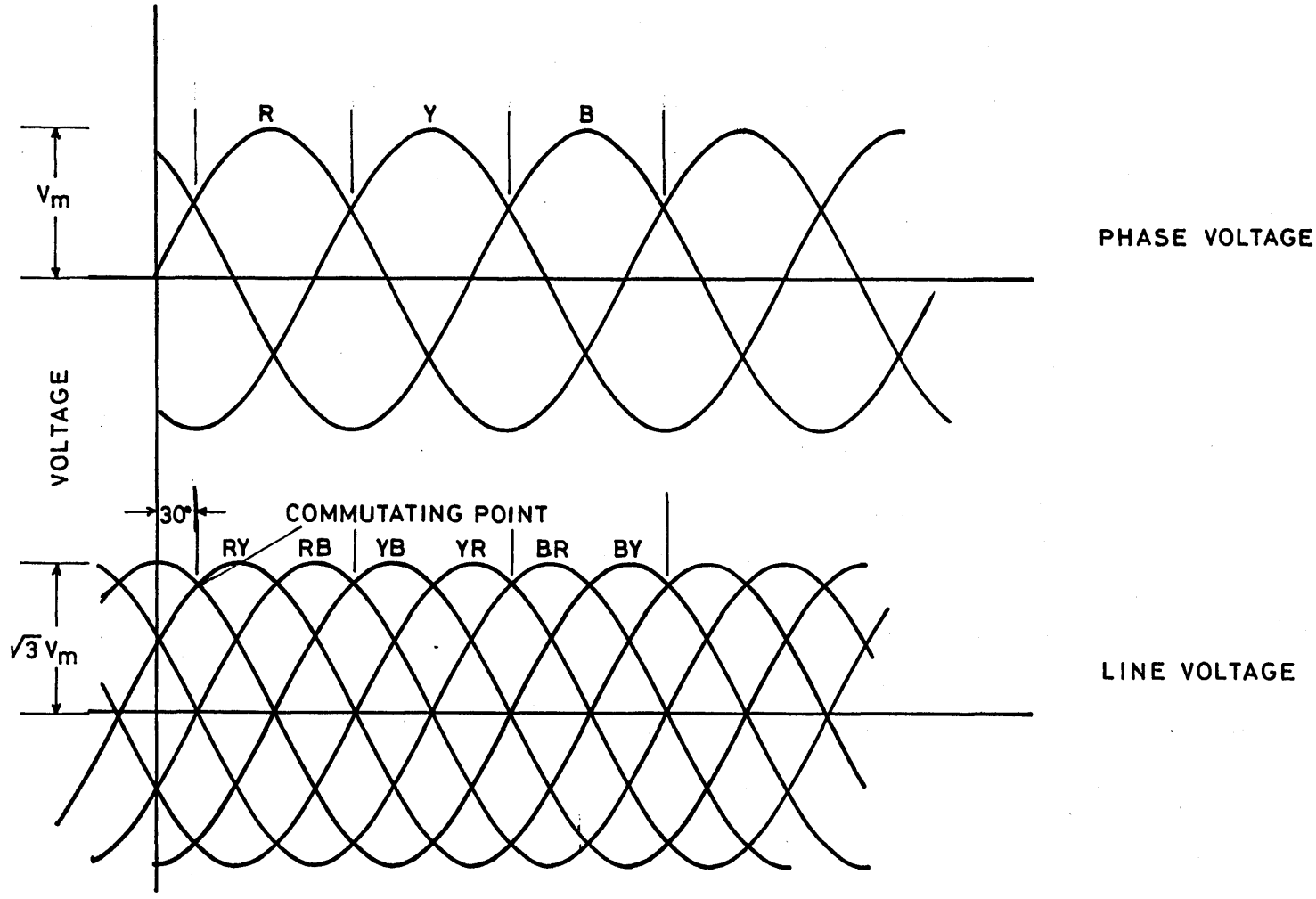

FIGURE 3.37 MAR LINE VOLTAGE WAVEFORM

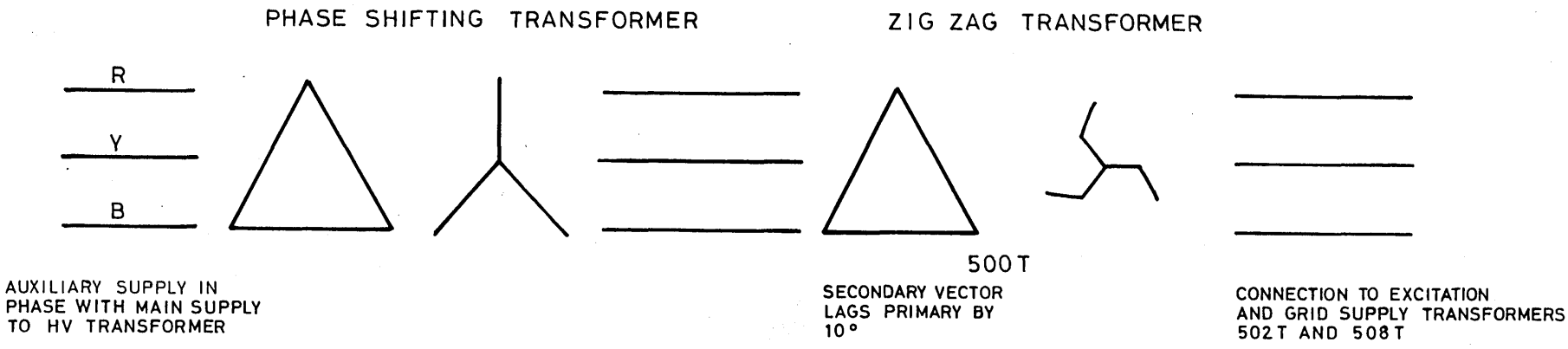

FIGURE 3.38 EXCITRON PHASE CONTROL CIRCUIT

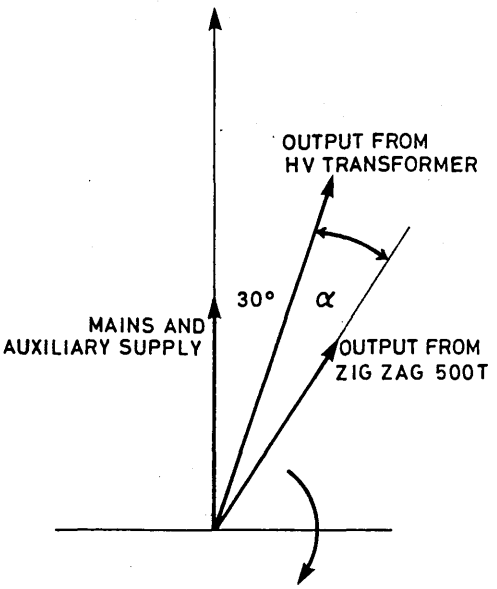

a) Phasor diagram

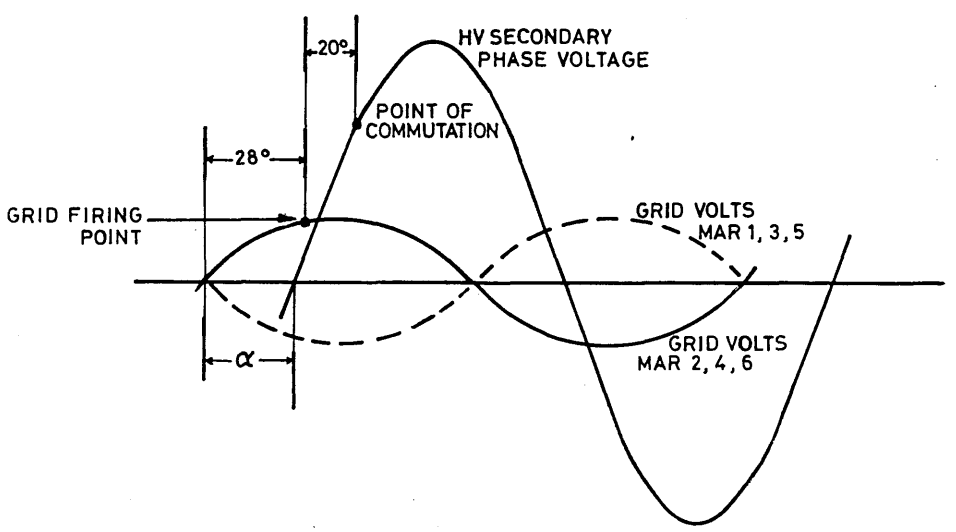

b) Grid waveform

FIGURE 3.39 CONTROL GRID PHASING

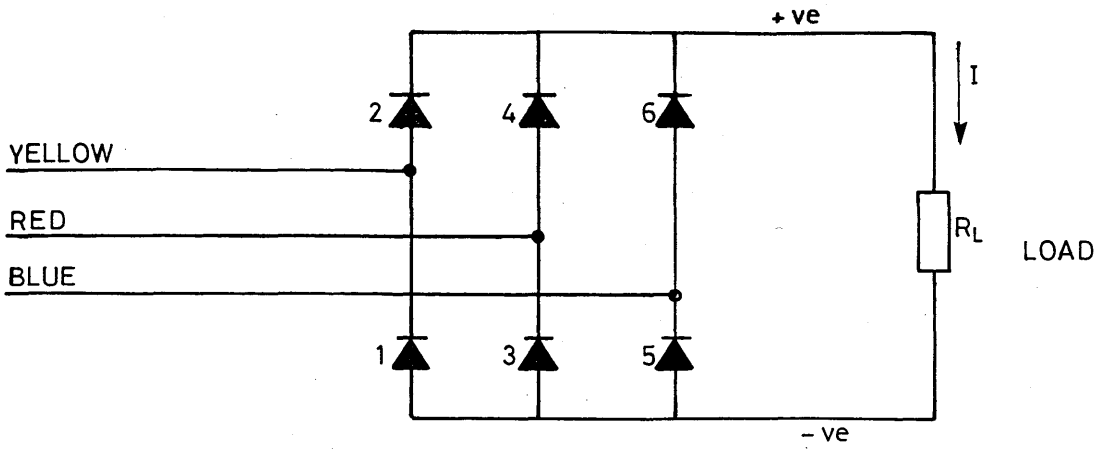

(a) MAR System schematic

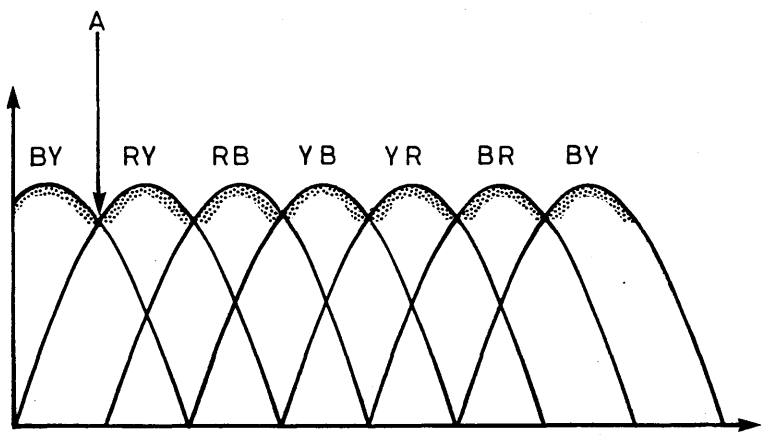

(b) DC Output

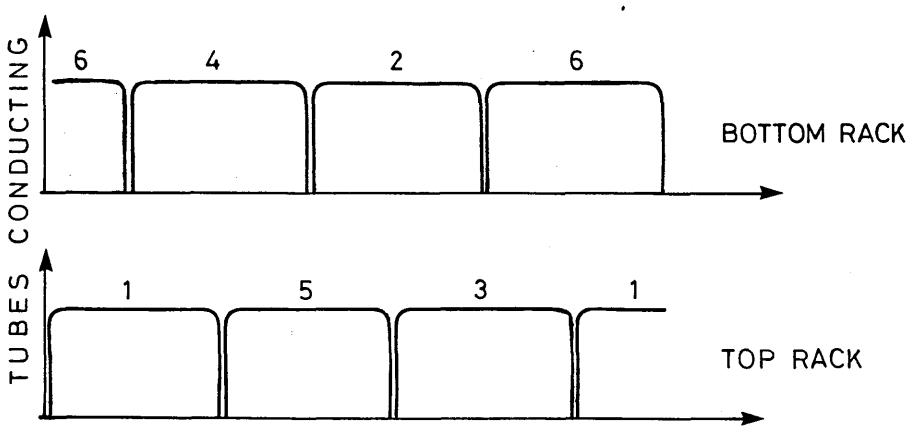

(c) EXCITRON Firing Sequence

FIGURE 3.40 EXCITRON FIRING SEQUENCE

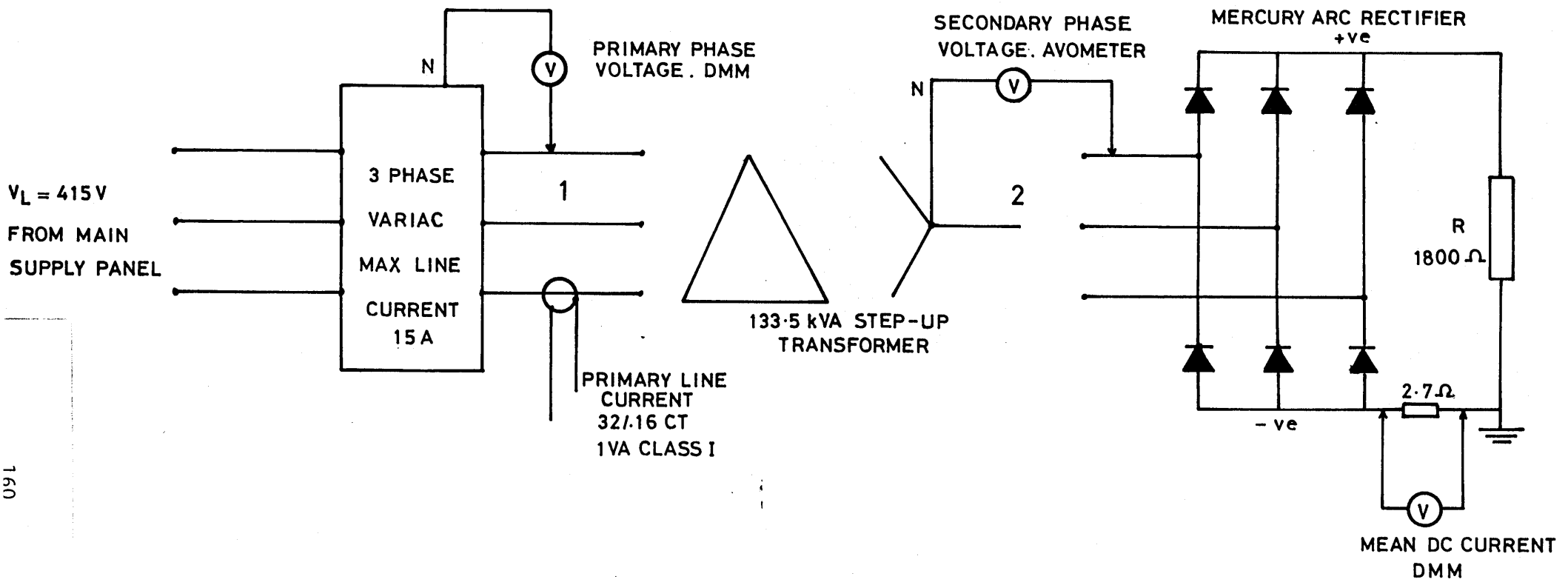

FIGURE 3.41 LOW VOLTAGE TEST CIRCUIT

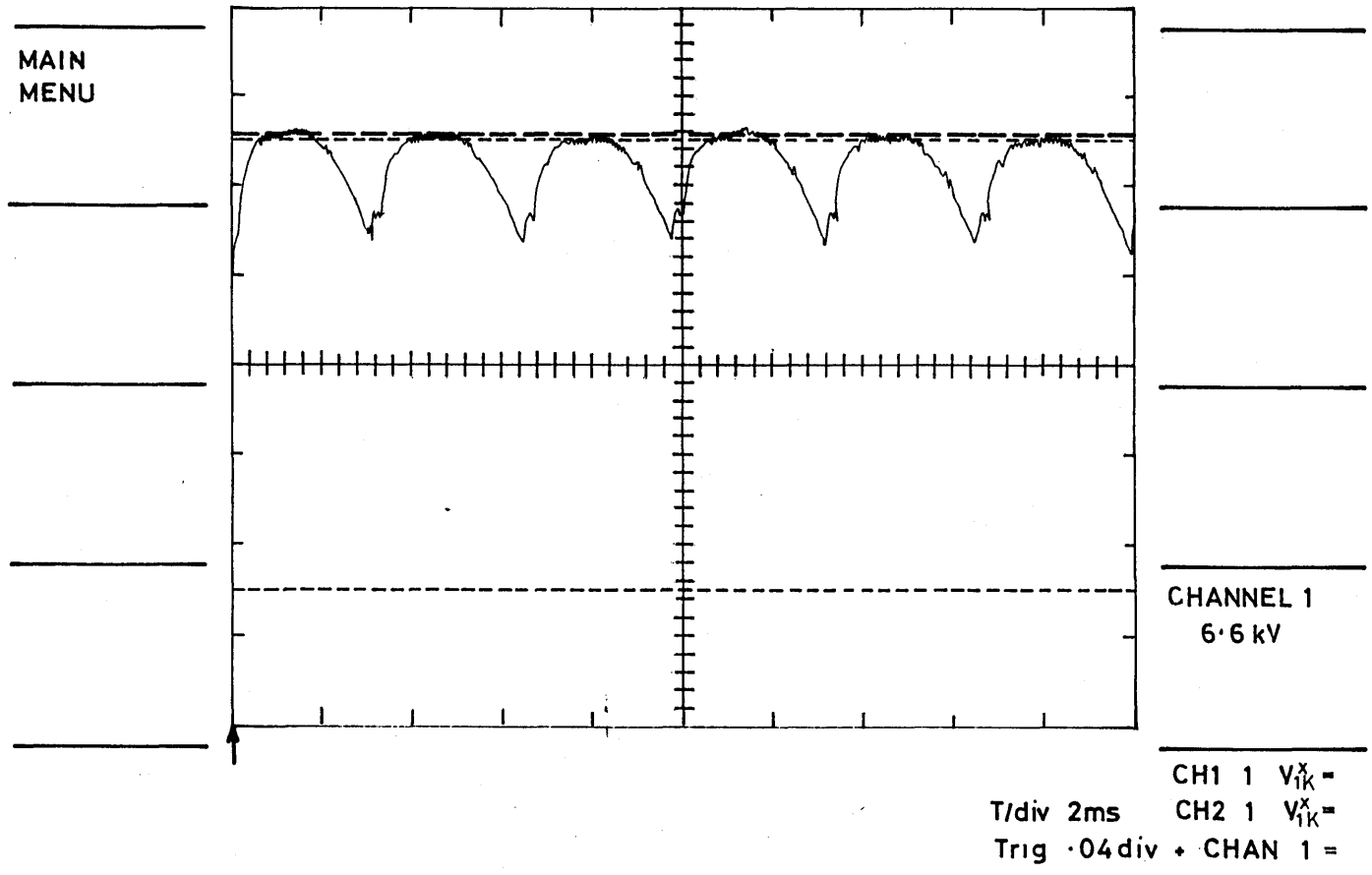

FIGURE 3.42 RECTIFIER OUTPUT AT 50% RATED LINE VOLTAGE

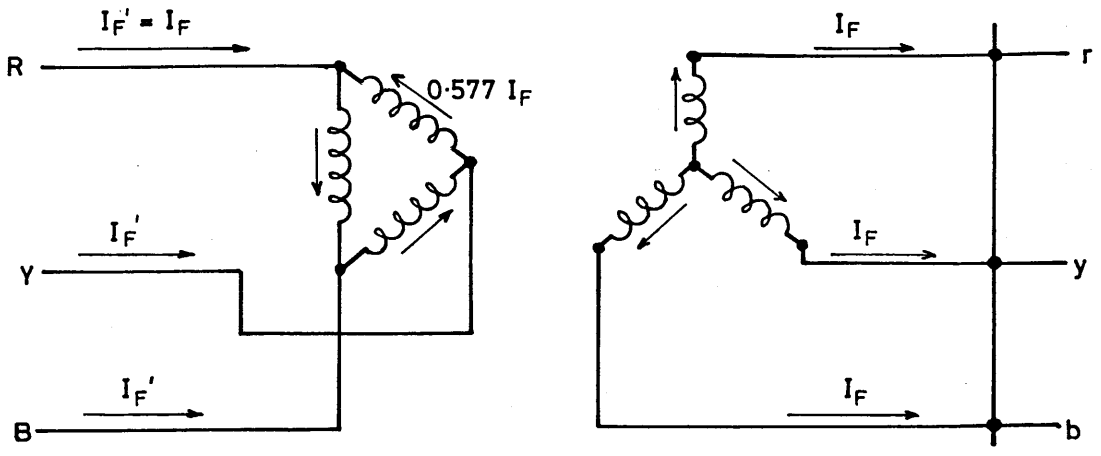

Normalised for unity turns ratio

FIGURE 3.43 THREE PHASE FAULT ON RECTIFIER

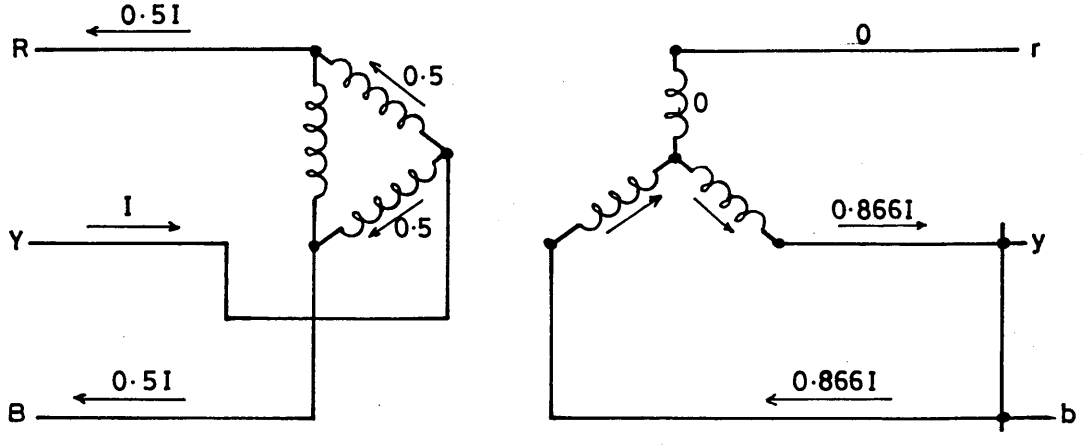

Normalised for unity turns ratio

FIGURE 3.44 LINE TO LINE SHORT CIRCUIT

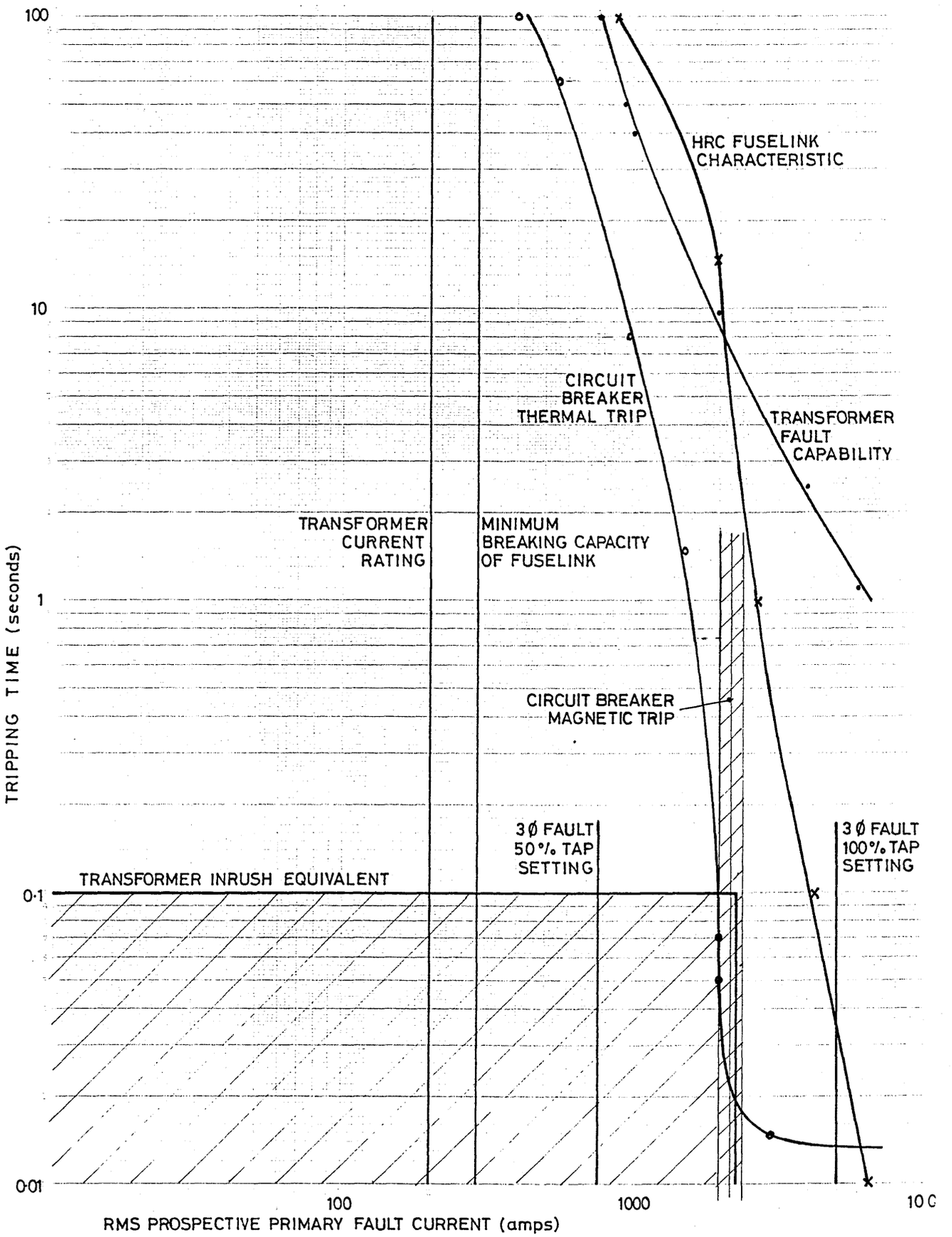

FIGURE 3.45 DC SUPPLY OVERLOAD PROTECTION DIAGRAM

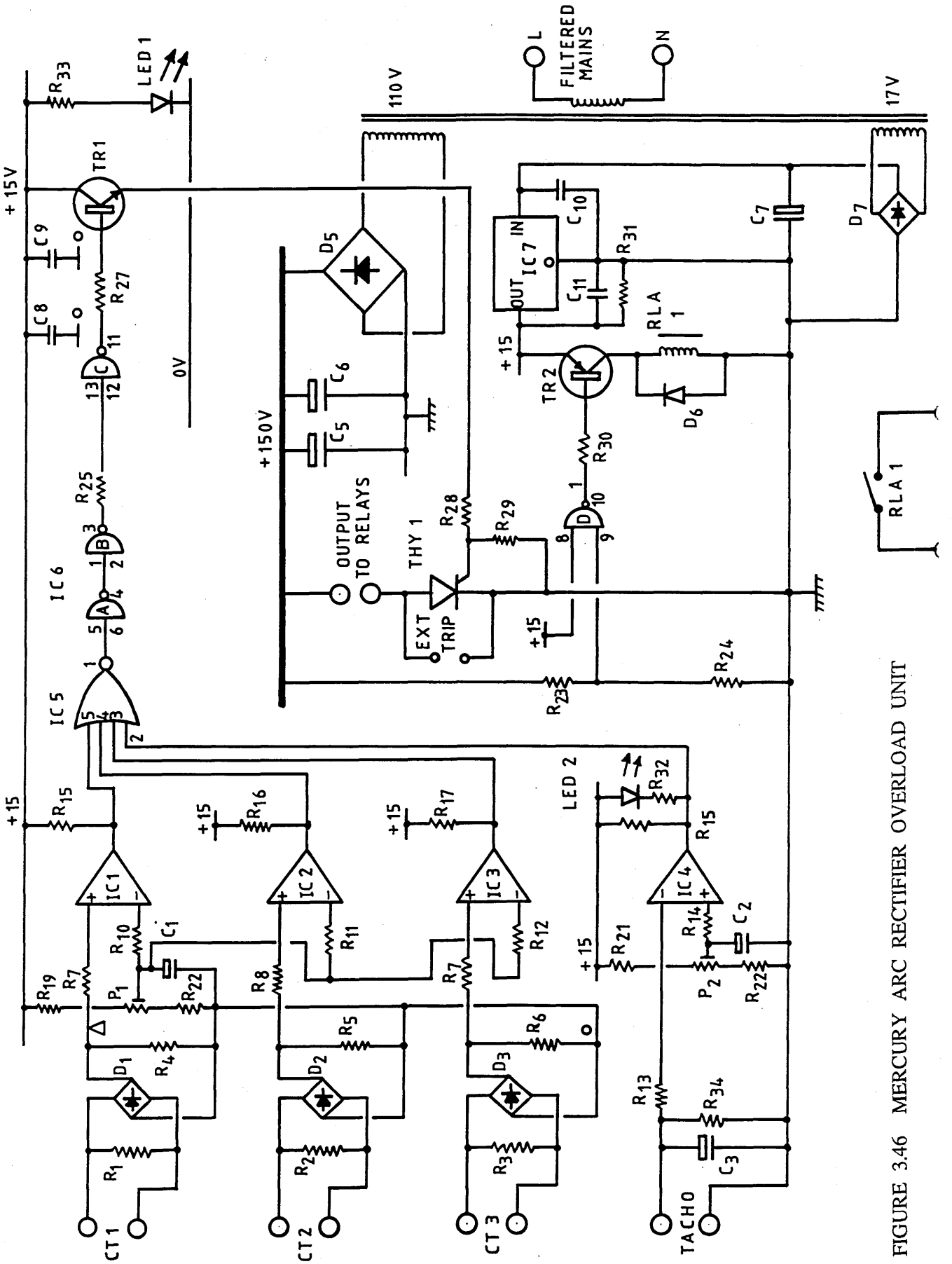

FIGURE 3.46 MERCURY ARC RECTIFIER OVERLOAD UNIT

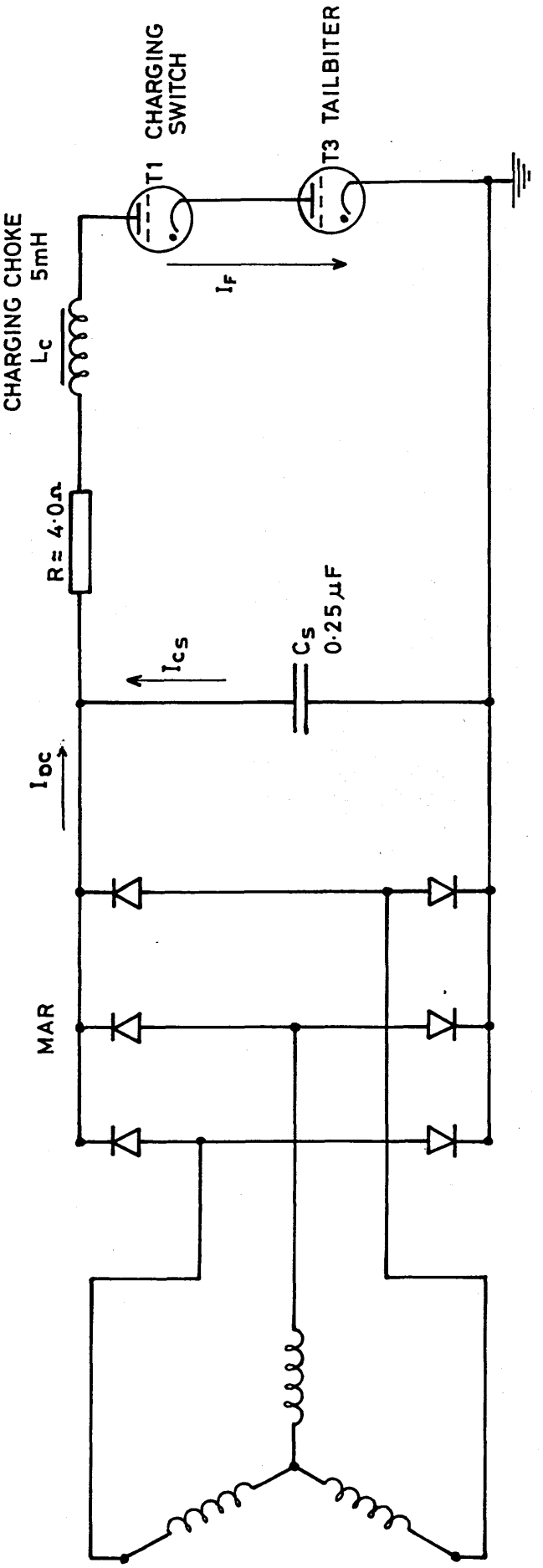

FIGURE 3.47 EQUIVALENT CIRCUIT FOR PULSER FIRE THROUGH

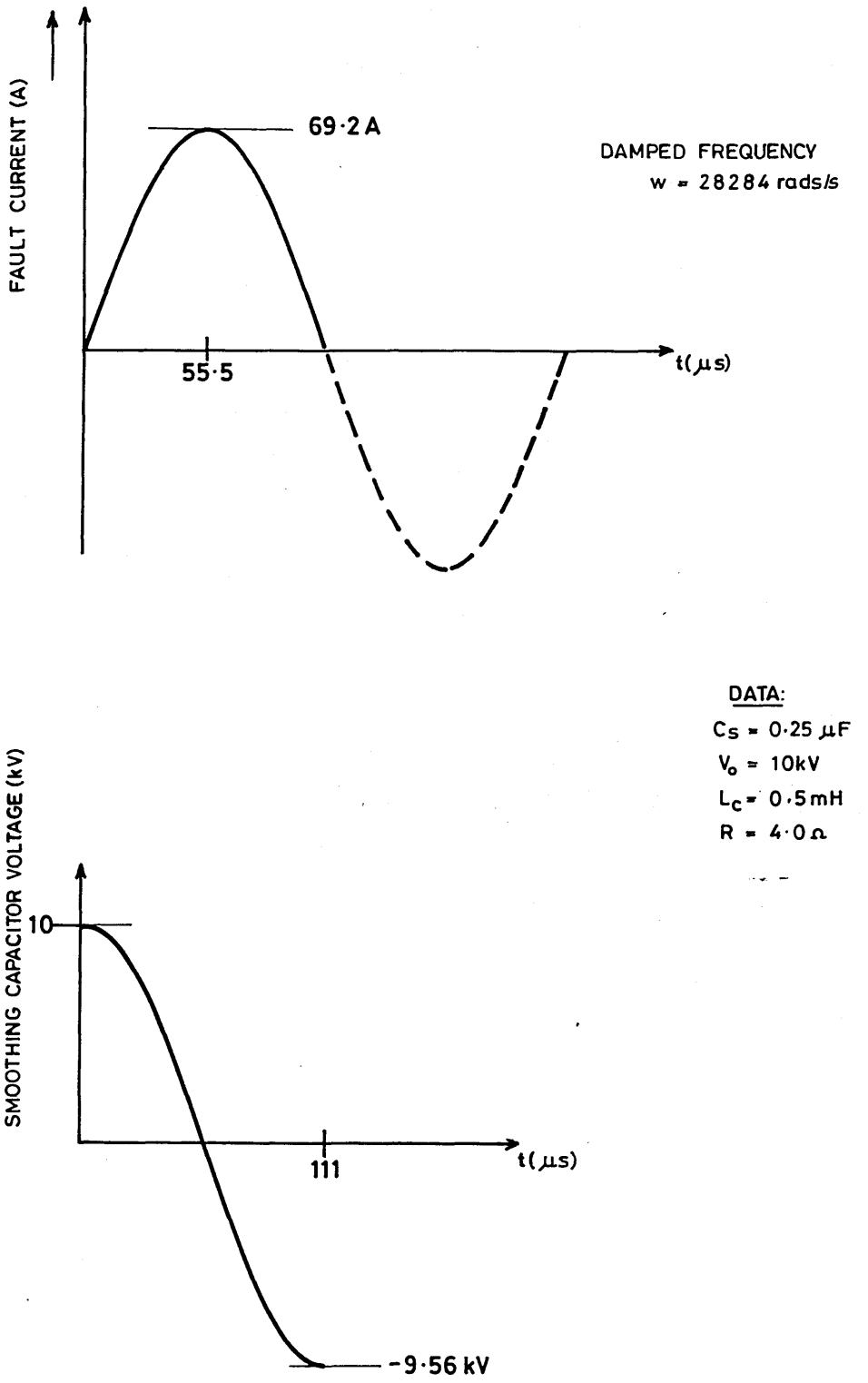

FIGURE 3.48 FAULT TRANSIENT FOR A PULSER FIRE THROUGH

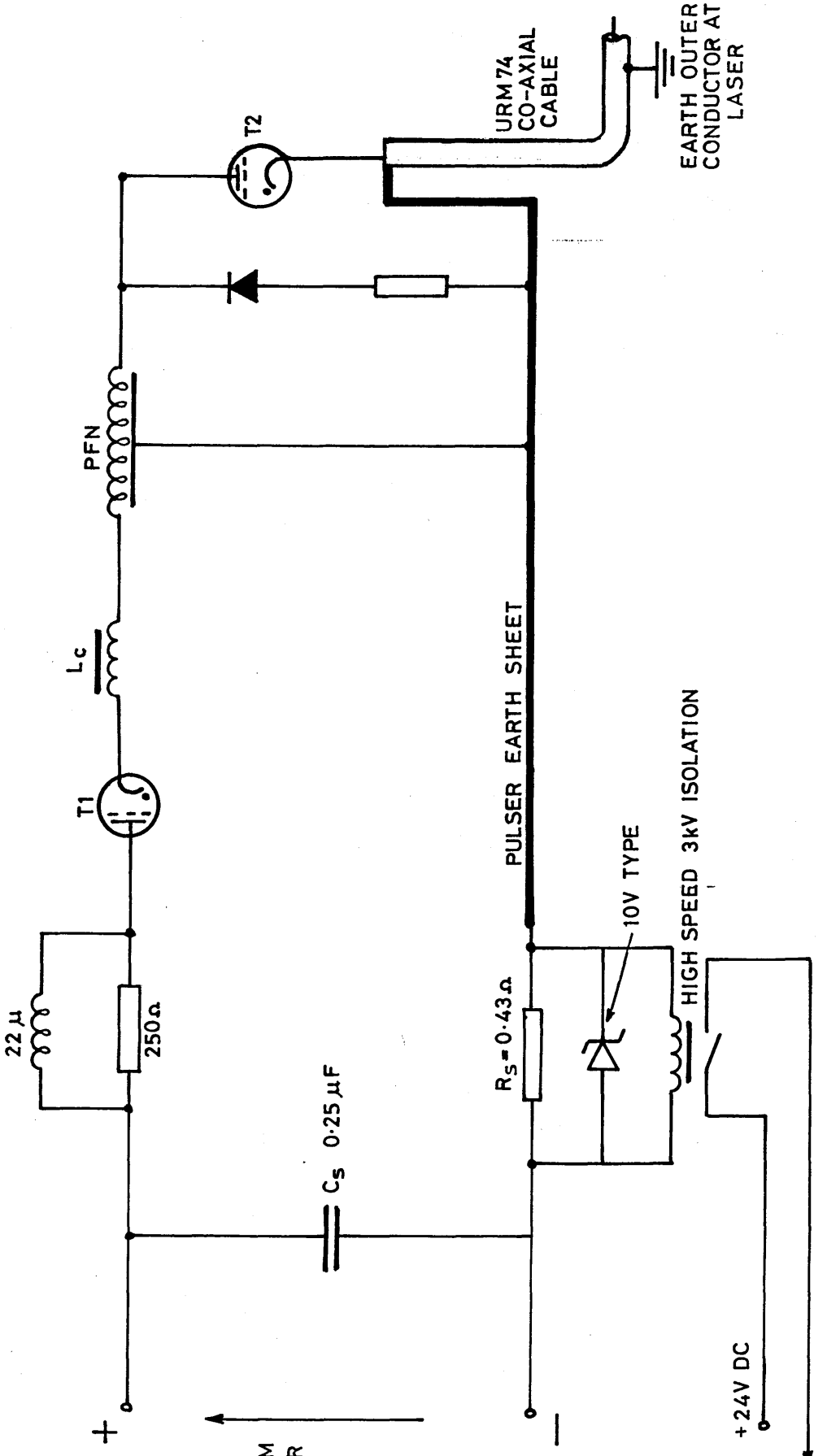

FIGURE 3.49 PULSER OVERLOAD MONITOR

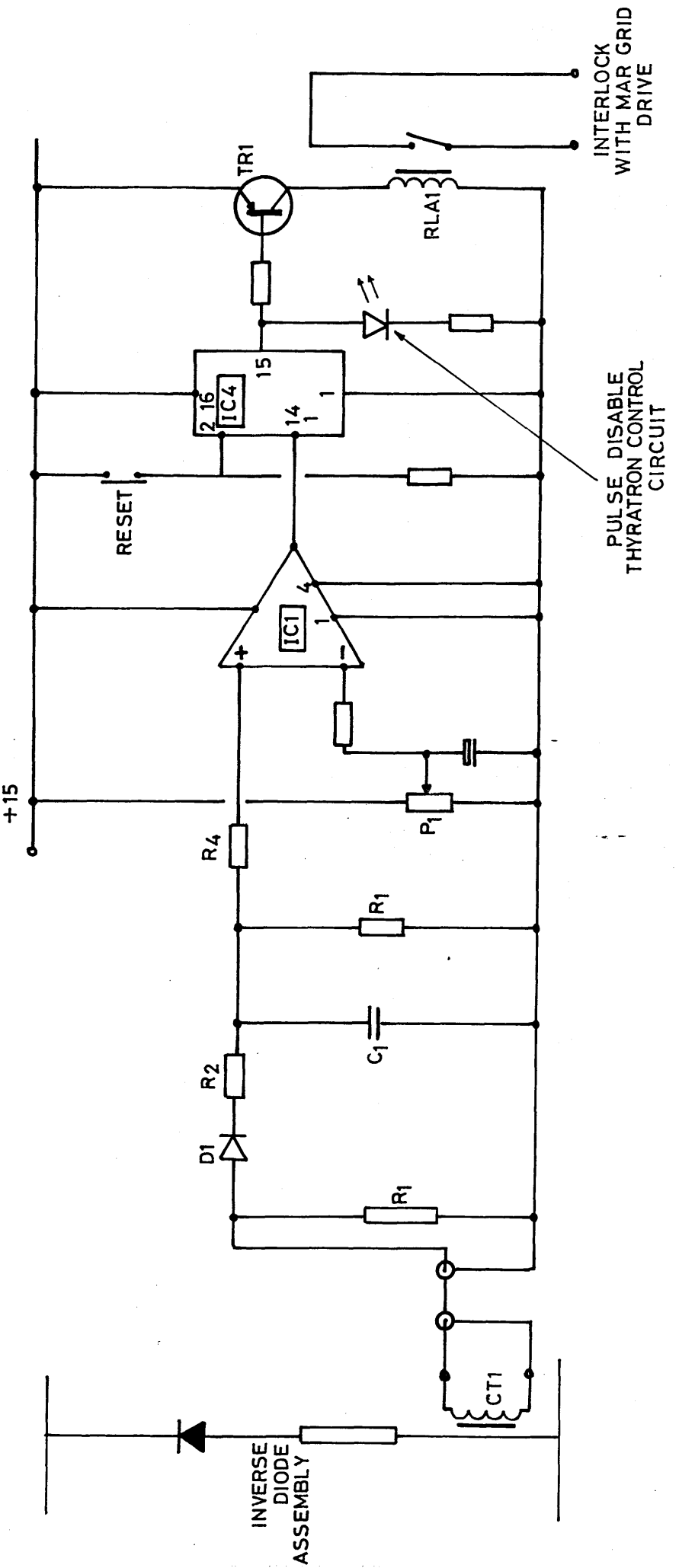

FIGURE 3.50 PULSER OVERSWING CURRENT MONITOR

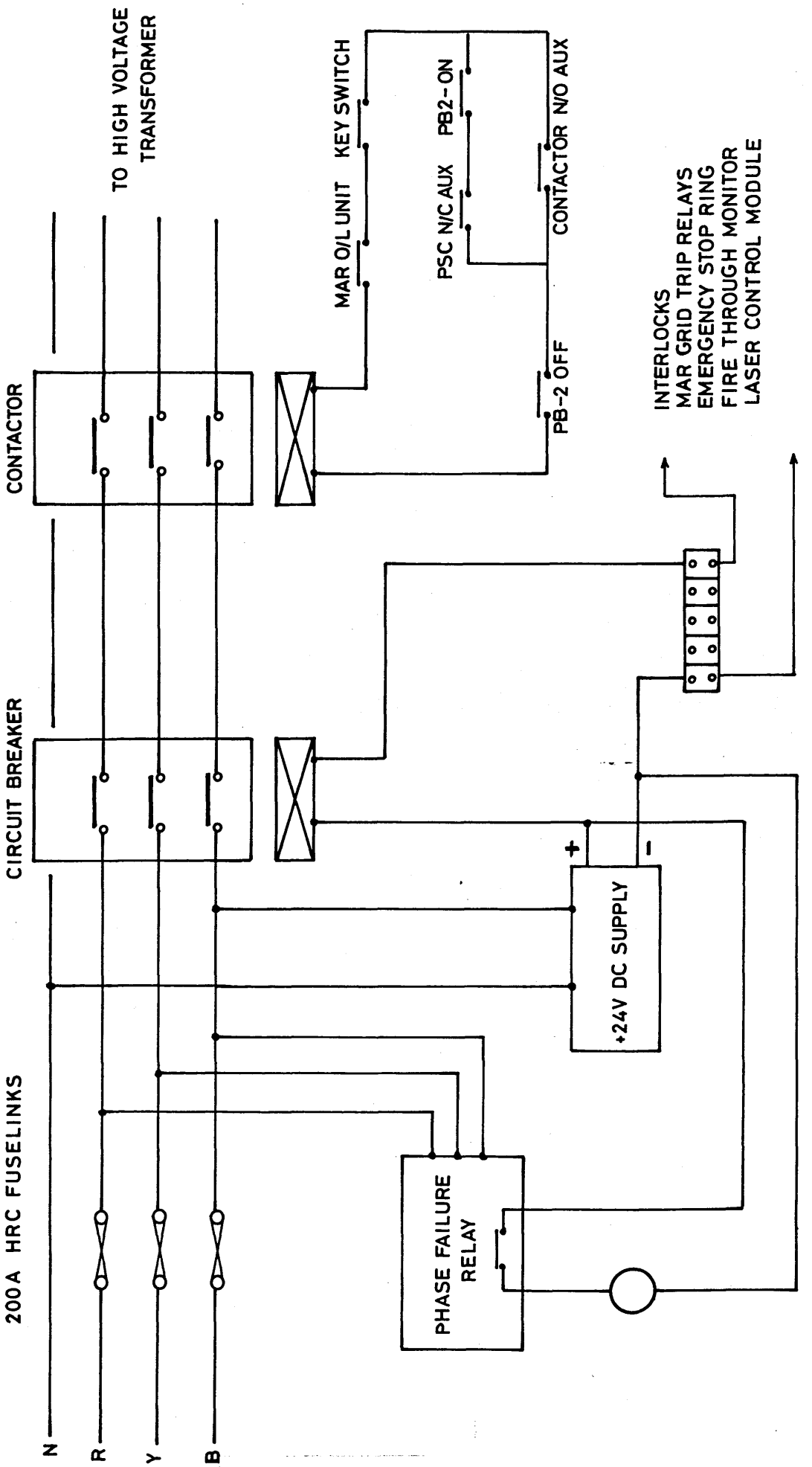

FIGURE 3.51 MAIN SUPPLY PANEL INTERLOCKS

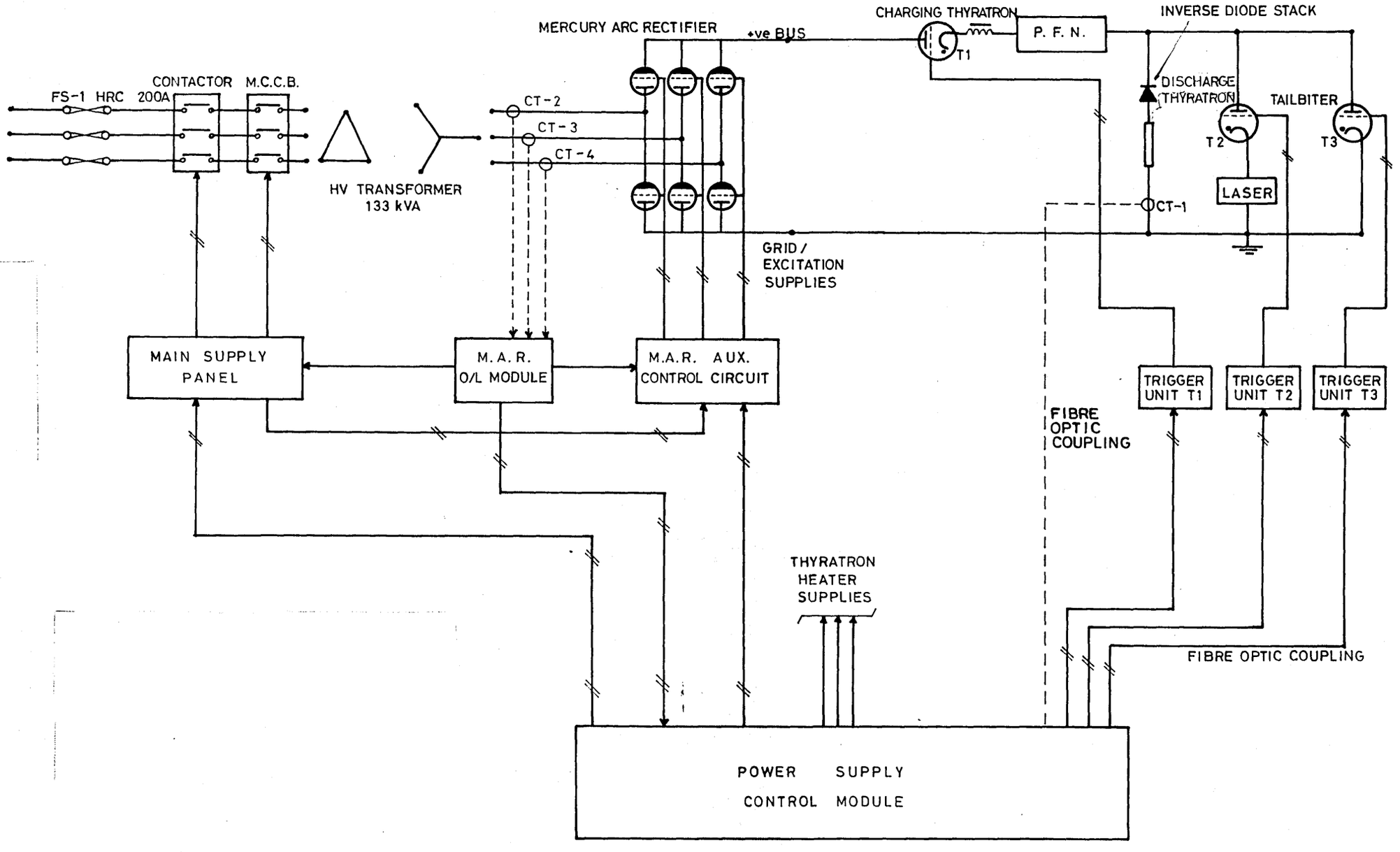

FIGURE 3.52 SCHEMATIC OF POWER SUPPLY CONTROL SYSTEM

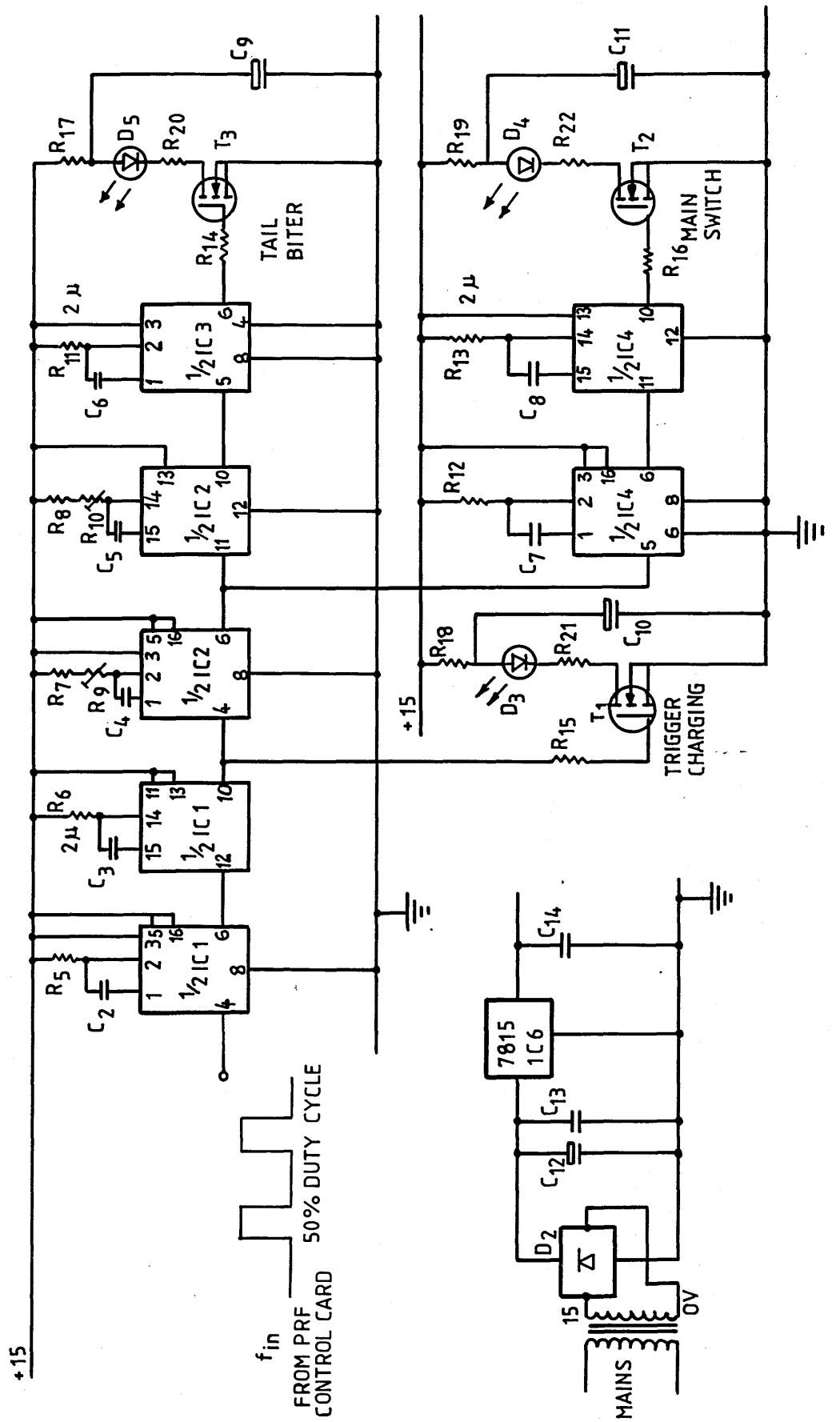

FIGURE 3.53 THYRATRON SEQUENCE CARD

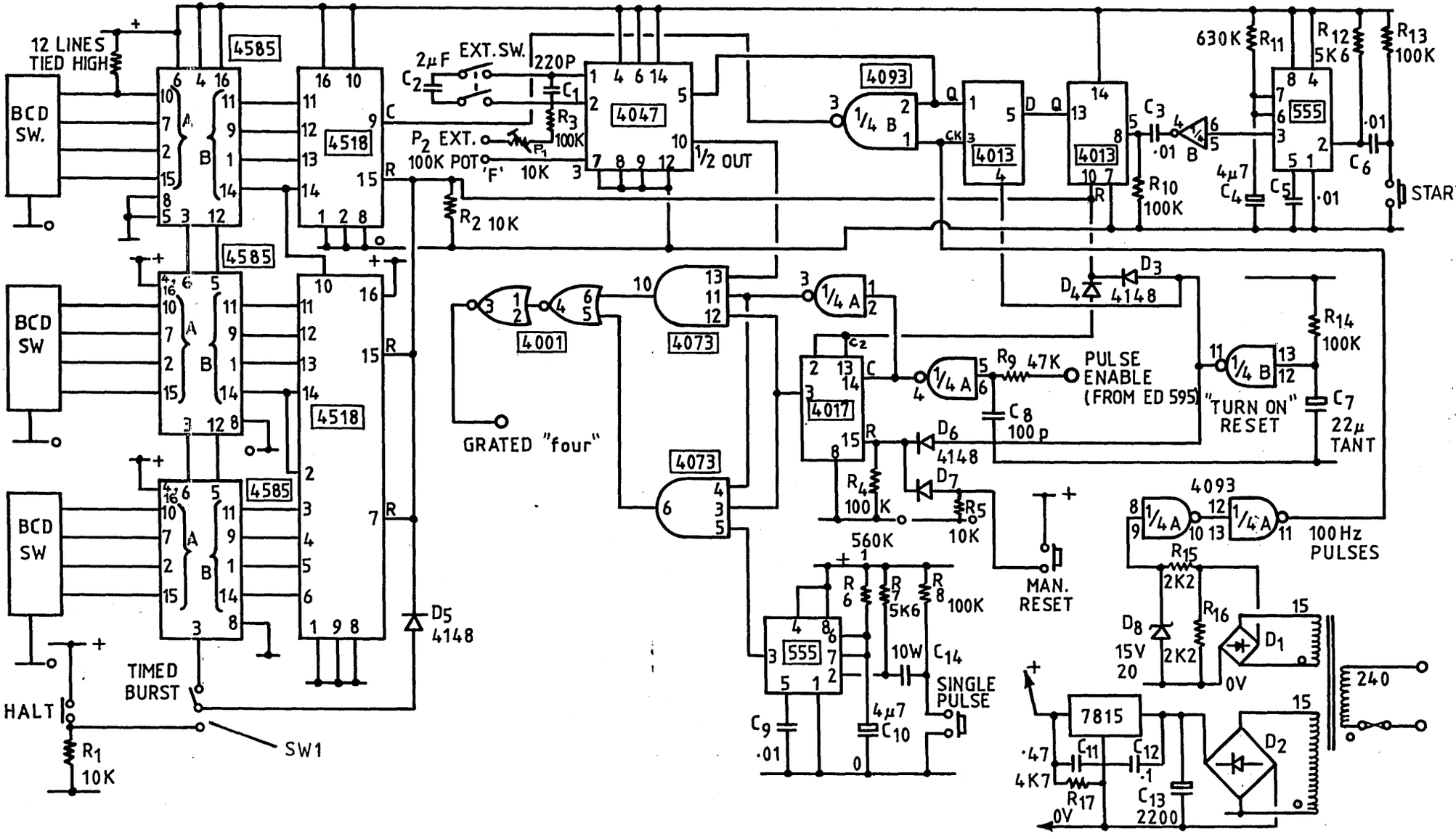

FIGURE 3.54 PRF CONTROL CARD

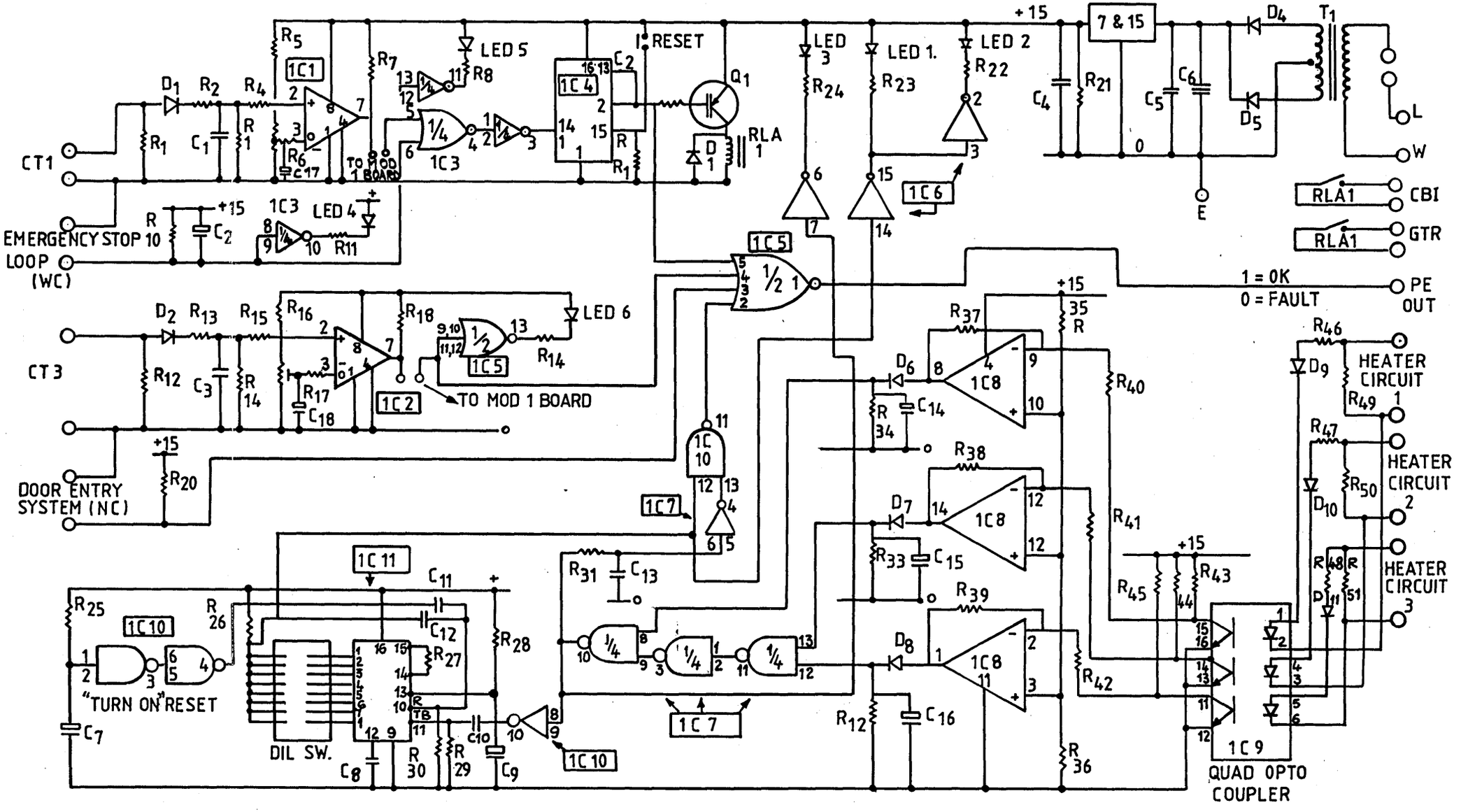

FIGURE 3.55 SAFETY/OVERLOAD CARD

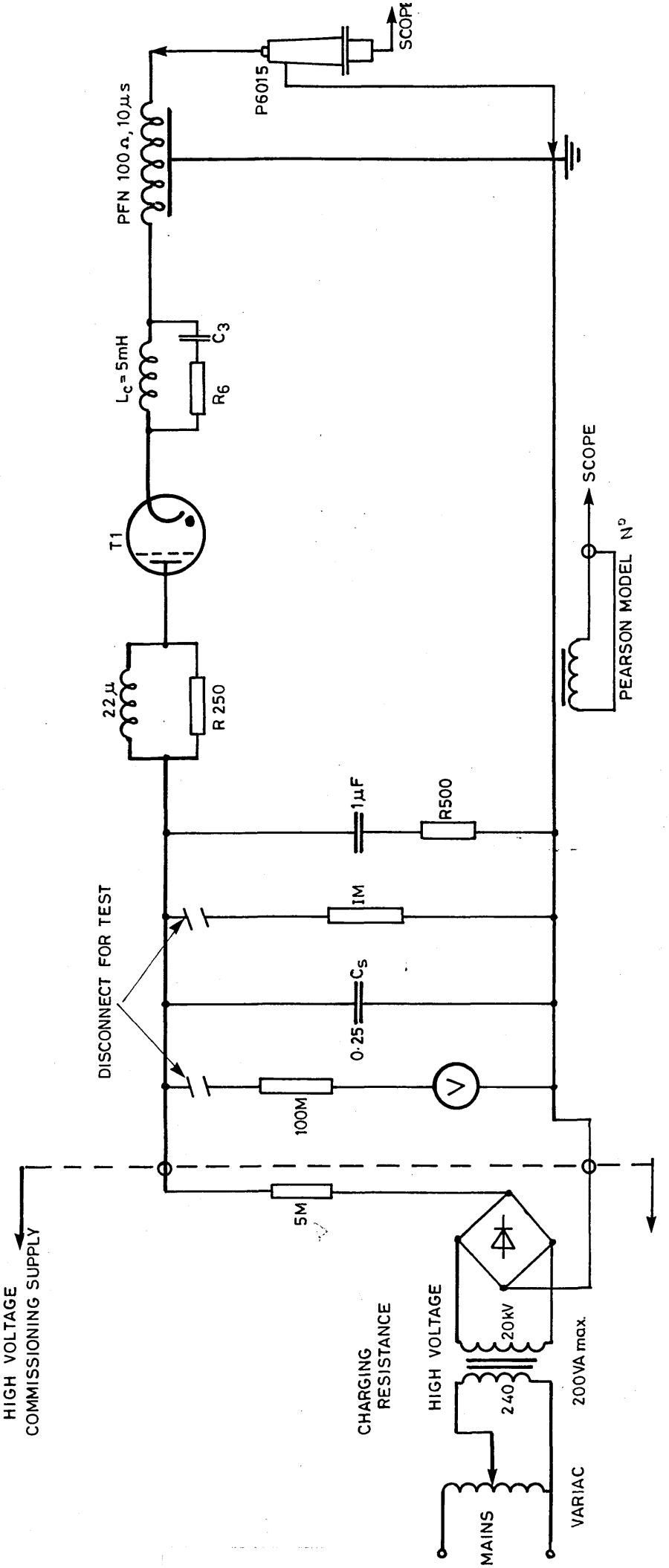

FIGURE 3.56 PFN CHARGING CIRCUIT TEST

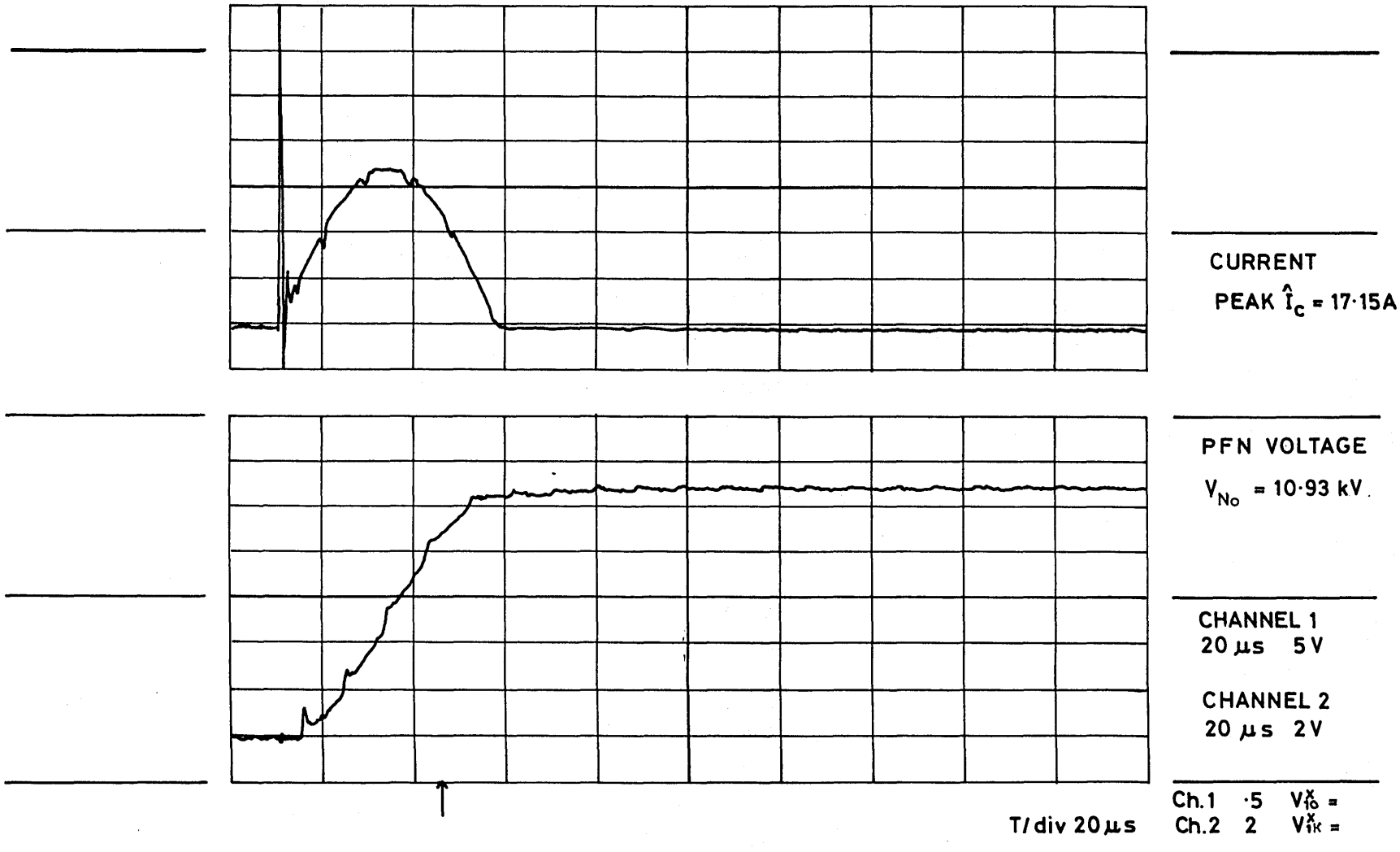

FIGURE 3.57 PFN CHARGING CYCLE WAVEFORMS

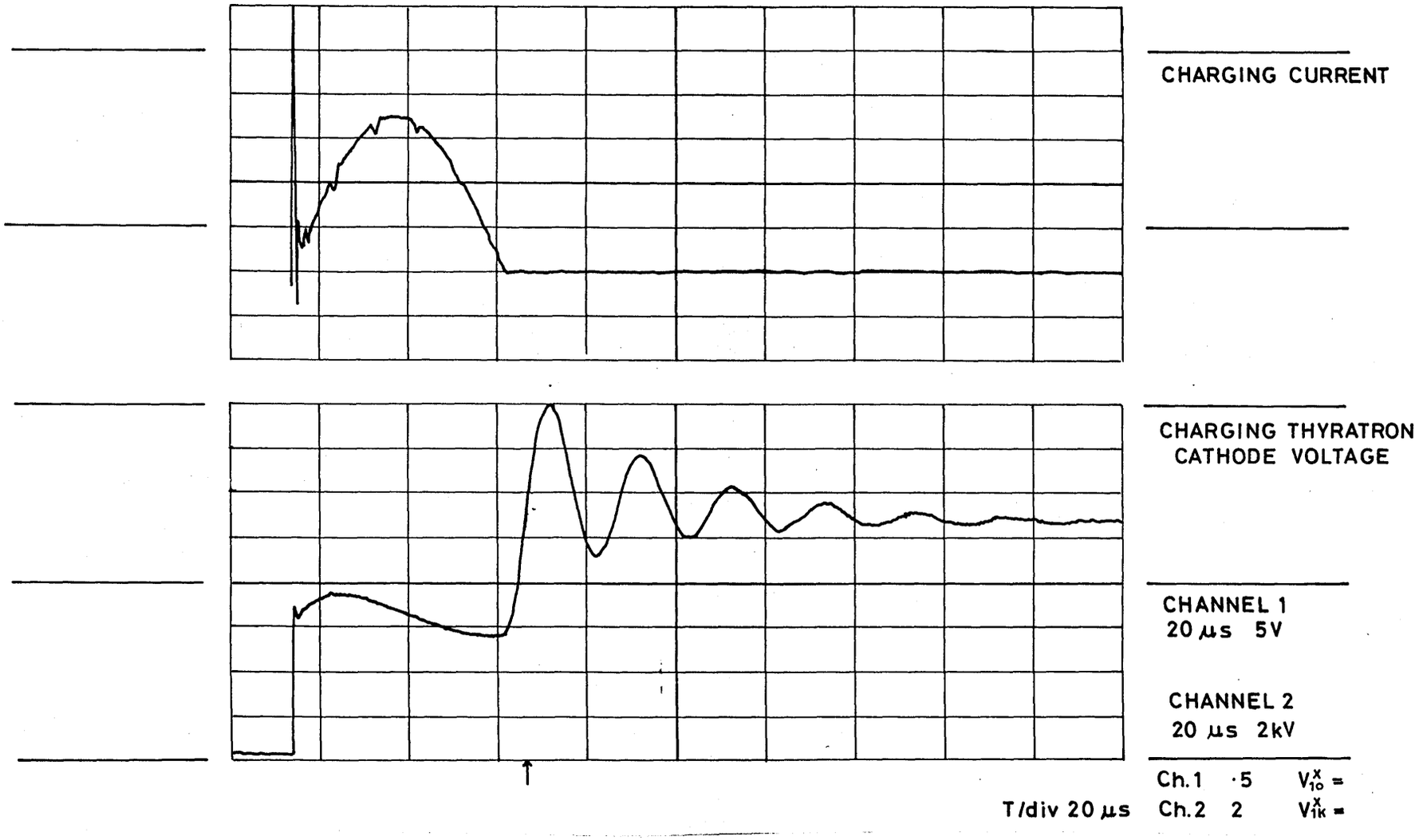

FIGURE 3.58 CHARGING THYRATRON CATHODE VOLTAGE

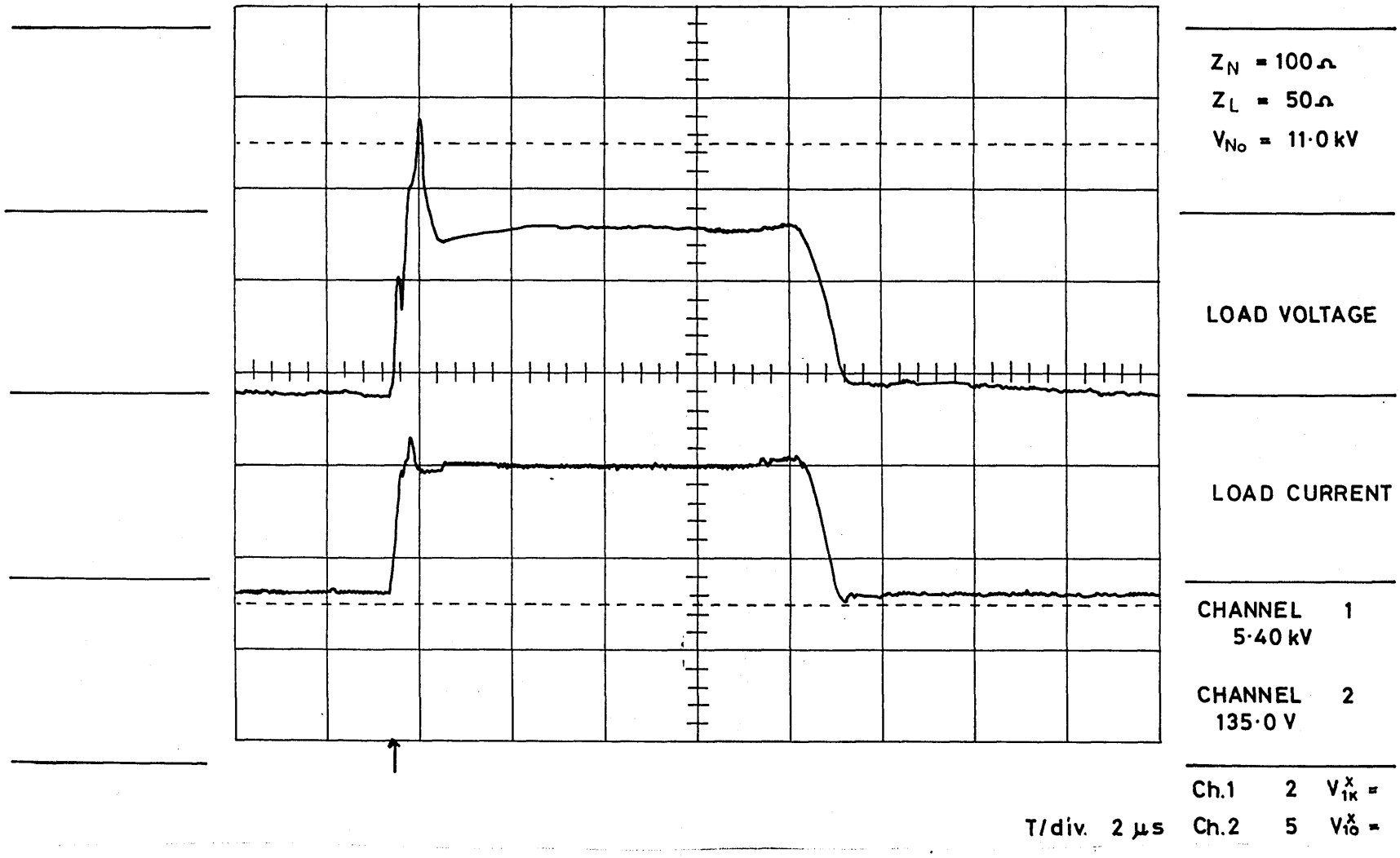

FIGURE 3.59 PFN DISCHARGE WAVEFORMS

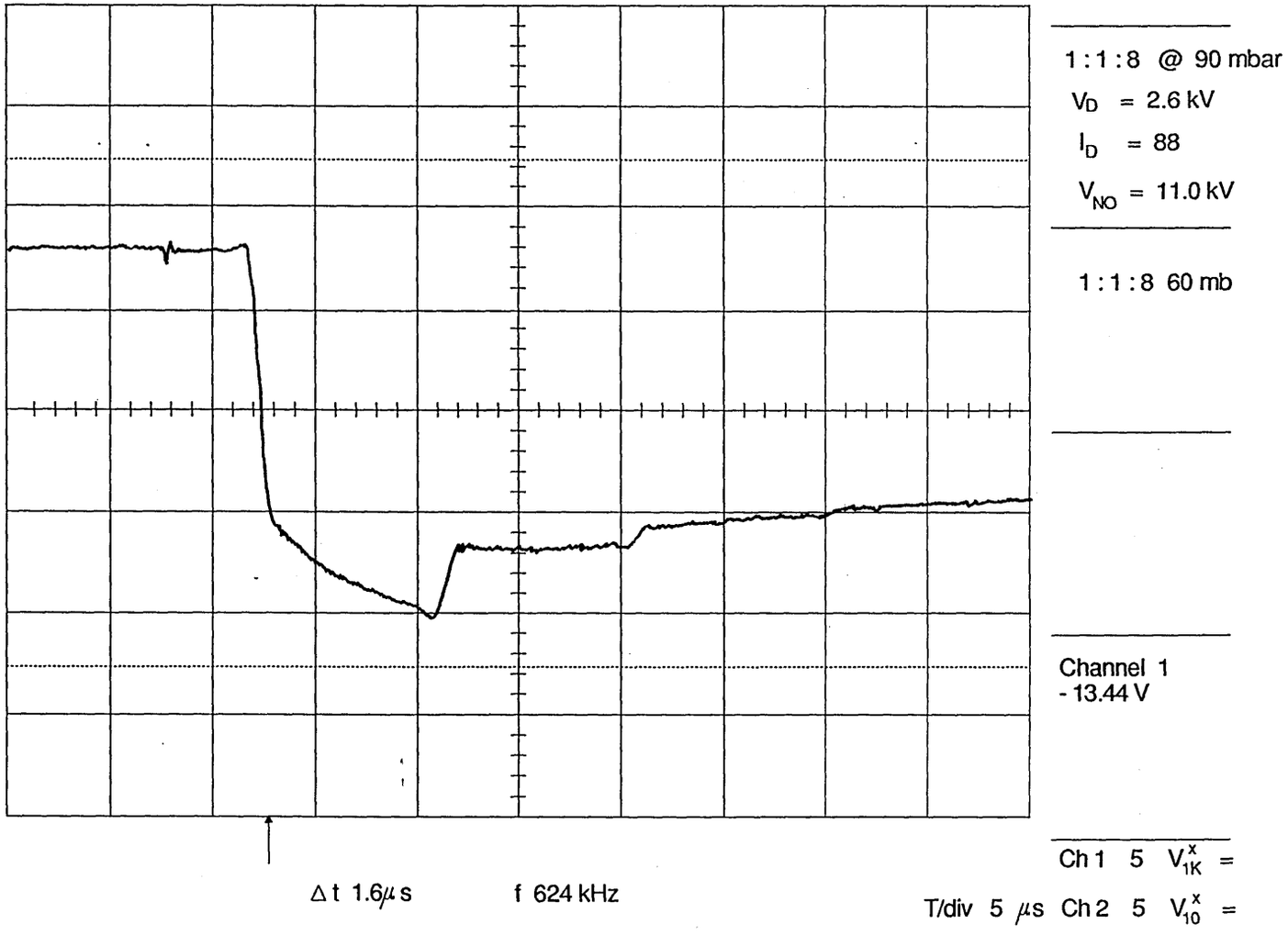

FIGURE 3.60 CHARGING THYRATRON CATHODE VOLTAGE DURING PFN DISCHARGE

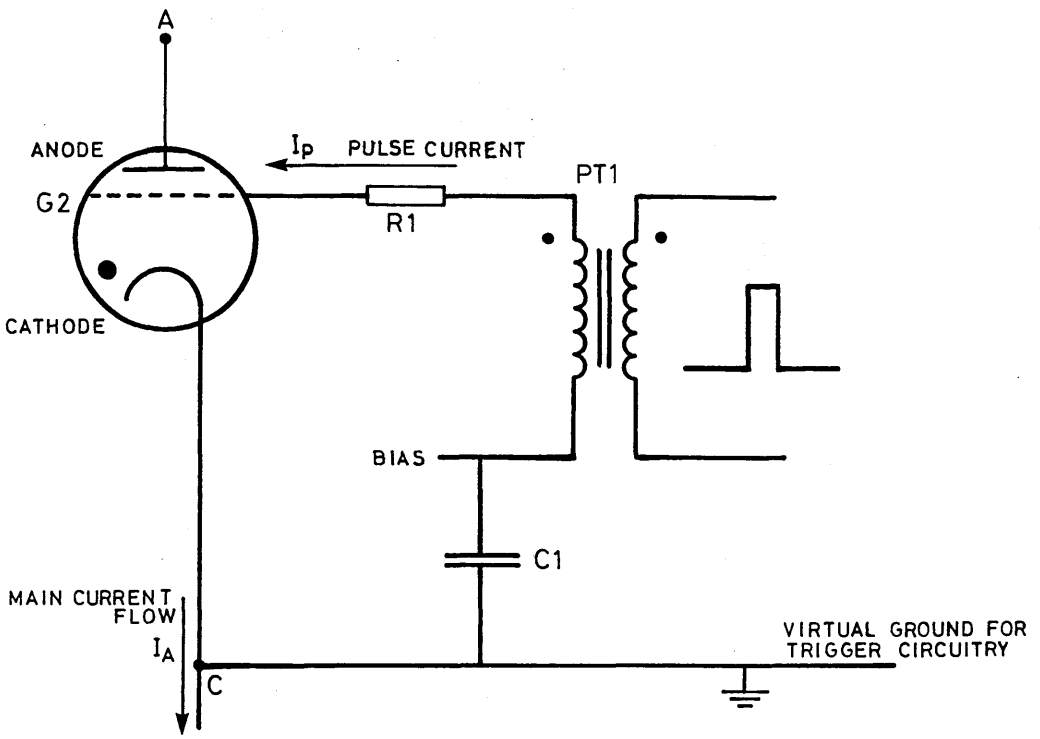

FIGURE 3.61 GROUNDED CATHODE TRIGGER CIRCUIT

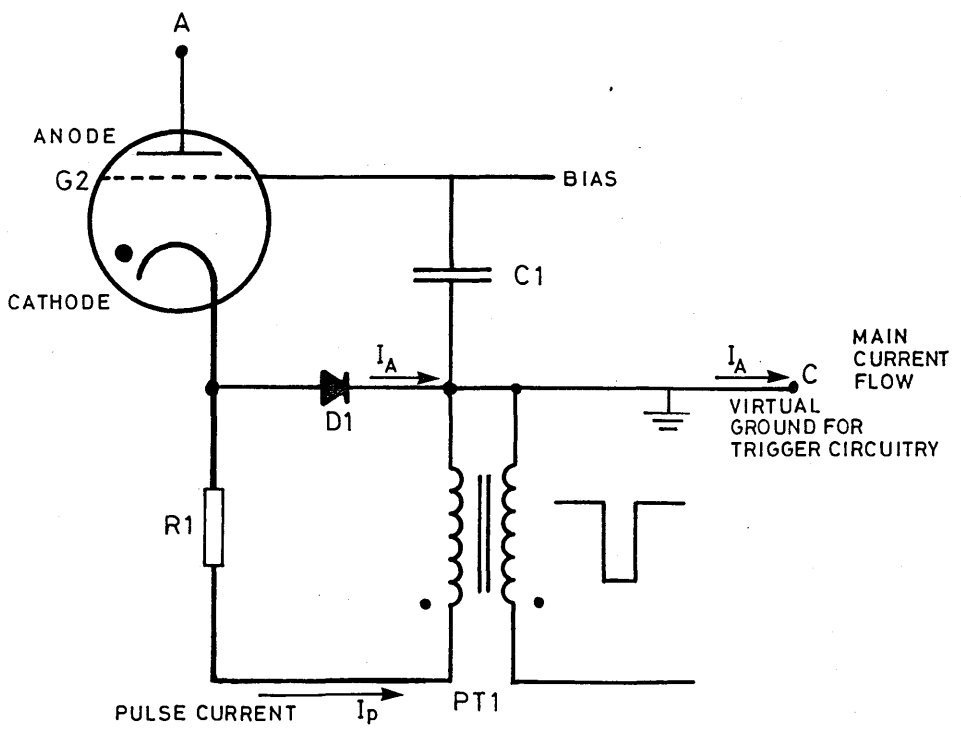

FIGURE 3.62 VIRTUAL GROUND TRIGGER CIRCUIT

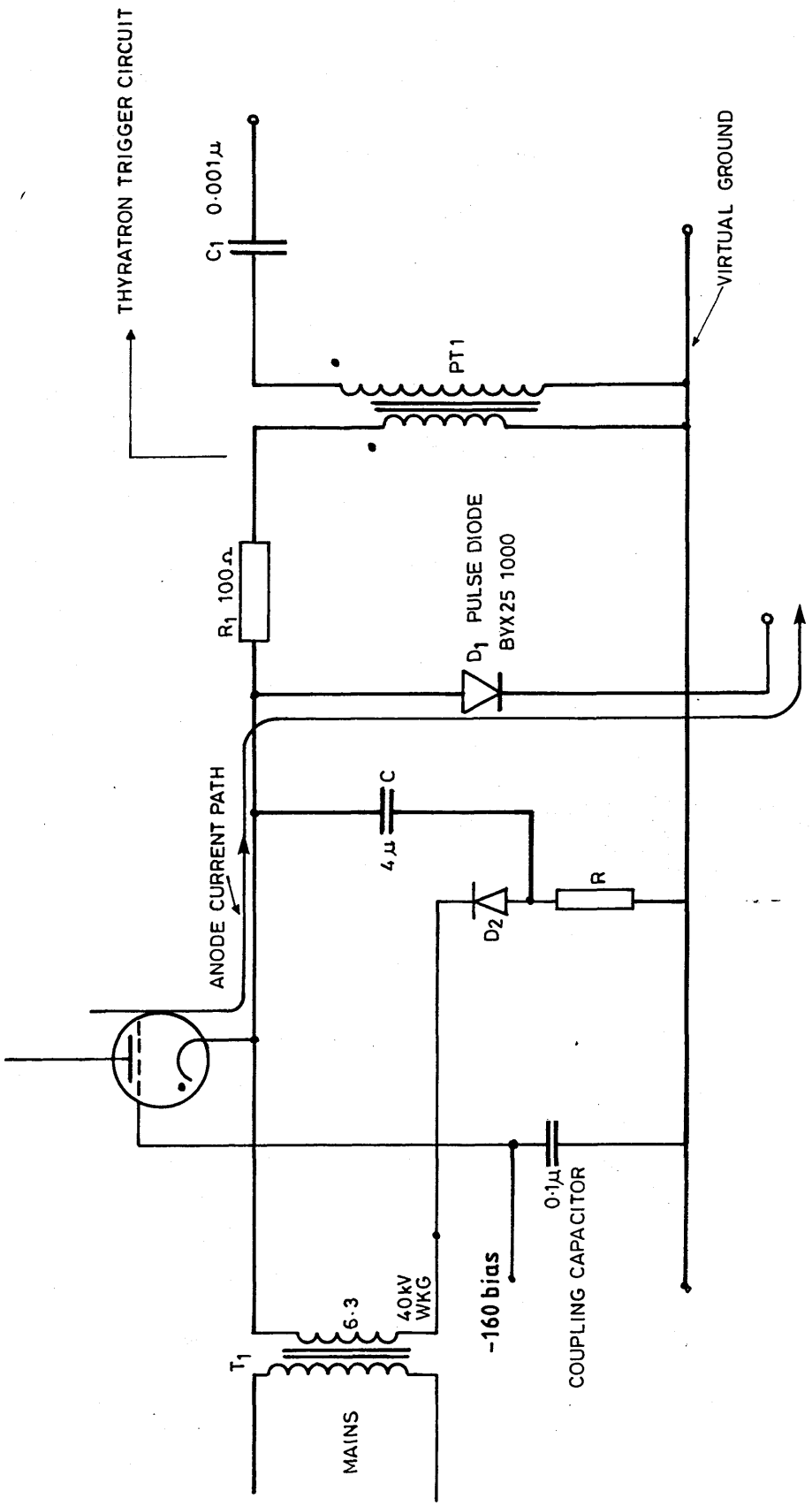

FIGURE 3.63 PULSE DIODE BIAS CIRCUIT

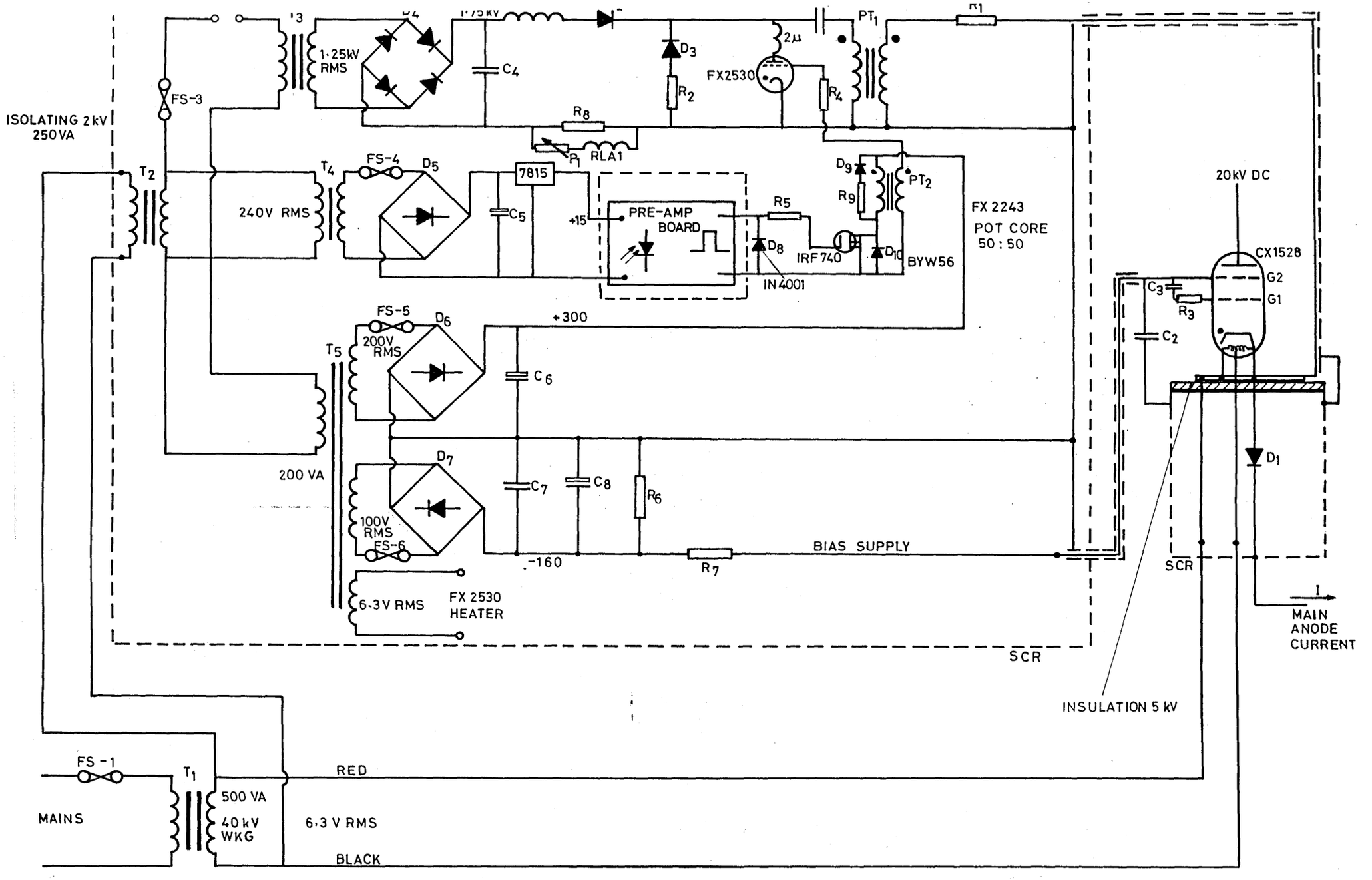

FIGURE 3.64 MODIFIED CHARGING THYRATRON TRIGGER CIRCUIT

(4.0) THE GAS DISCHARGE SYSTEM.

(4.1) THE GLOW DISCHARGE AND LASER PUMPING.

Efficient laser pumping requires the excitation of large volumes of gas at high pressure. The simplest technique for achieving this is to ensure that the electrical discharge is both self-sustaining and diffuse. Such characteristics are typical of the glow discharge regime, so called because the discharge is generally very luminous. However, the fundamental limitation of the self-sustained glow discharge is its inherent instability, which results in the discharge changing from a diffuse glow to a constricted arc. This latter discharge regime is unsuitable for laser pumping as the discharge current is constricted into a series of intense conducting filaments, with minimal excitation of the active laser volume. The major effort of this phase of the research was to identify the mechanisms which lead to the glow-to-arc transition and to examine methods of preventing the development of this instability.

The glow discharge is just one type of discharge which is self-sustaining and therefore requires no external source of ionization to maintain current conduction in the gas. The principal mechanisms which provide the supply of conduction electrons from the cathode include electron emission by positive-ion bombardment and photo-emission. The glow discharge is characterised by a very diffuse spreading of the conduction current across the electrode surfaces, and as such can be employed to electrically excite large volumes of gas. Moreover, it has been found that self-sustained glow discharges provide near optimum excitation of many molecular gas laser systems, e.g. CO_2, CO and excimer. This rather fortunate property stems from the fact that the active gas constituents have large cross sections for vibrational excitation by electron impact, resulting in a large percentage of the discharge energy being coupled into the vibrational modes. Some of the energy gained by the electrons from the applied field also goes into both translational and electronic excitation of the gas. Thus, the electrical characteristics of the gas, which are determined by the ionization and attachment coefficients, control the Electron Energy Distribution Function (EEDF) and play an important role in governing the vibrational excitation efficiency. Although energy coupled into electronic excitation of the gas ends up as translational energy (i.e. heat) and can therefore be considered as a loss, some ionization is required for the discharge to be self-sustaining. This is in contrast to E-beam pumped discharges, where an external source of ionization maintains the conduction current and the EEDF can be optimised by altering the applied field independently of the ionization source. The disadvantage of E-beam pumping is the inherent complexity of the system and the need for fragile foil windows in the cavity; in most applications the relative simplicity of the self-sustained glow discharge more than outweighs the increased

efficiency obtained with E-beam pumping.

The gas discharge conditions in pulsed mode operation are vastly different from the CW mode. In the pulsed mode, high specific energy loadings can be achieved simply by ensuring that the pulse duration is shorter than the arc formation time. However, it is a necessary requirement that the gas in the inter-electrode region be cleared in the inter-pulse period to prevent arcs developing. For high PRF operation this necessitates rapid removal of the gas from the electrode region. A transverse discharge arrangement, as shown in fig (4.1), was selected for the high PRF CO_2 laser as this allowed the maximum possible gas clearing rate from the inter-electrode region, with minimal pressure drop. The other principle advantage bestowed by the transverse discharge arrangement is a relatively low breakdown voltage, which was advantageous for the design of the pulser circuit.

(4.2) ELECTRICAL CHARACTERISTICS OF PULSED LASER DISCHARGES.

It is apparent from the above discussion that the electrical characteristics of the laser gas are critical to the overall efficiency of the laser. In this section it is intended to review some of the important properties of glow discharges, including: breakdown, glow discharge formation and discharge stability. This brief resume will facilitate analysis and discussion of the experimental results.

(4.2.1) Transverse Discharge Breakdown Voltage.

There are two types of electrical breakdown which can convert an initially non-conducting high pressure gas between two parallel electrodes into a highly conducting plasma upon the application of a high voltage pulse: one is the classical Townsend breakdown and the other is the plasma streamer breakdown [4.1]. Even though the basic processes for both breakdown mechanisms is electron multiplication through impact ionization, the conditions for the occurence and applicable ranges of applied field to gas density ratio (E/N) are quite different, so it is important to make a distinction between the two.

Townsend Breakdown Mechanism.

The well known Townsend or Paschen breakdown mechanism is characterised by a large number of successive electron avalanches that originate from secondary electron generation. The space-charge field caused by differentail motion between the electrons and positive ions is assumed to be so weak as to be completely negligible. Continuous exponentiation of the electron current within the discharge gap is assumed to be

maintained by a positive feedback of the Townsend avalanche process, through secondary electron emission at the cathode surface.

Consider the case of two uniform field electrodes seperated by a distance d, with a steady applied field E, as shown in fig (4.2). Assuming that electrons are emitted from the cathode, say by photo-emission, these will drift towards the anode under the applied field. If the applied field is sufficiently high, some of the electrons may gain sufficient energy to cause impact ionization of the neutral molecules. The probability of ionization is high when the electron energy is slightly higher than the ionization potential of the neutral molecule i.e. $U_e - eV_i \approx 0.1-1eV$. The ionization rate depends both on the electron energy distribution function (EEDF) and on the cross section for electron impact ionization.

Hasan [4.2] has obtained the EEDF for typical CO_2 laser discharges from a numerical solution of the Boltzmann transport equation. For a given mixture, as shown in fig (4.3), the EEDF is a function of the reduced field (E/N), where N is the neutral particle density. The critical dependence of the distribution function on (E/N) results from the fact that the energy gained by an electron from the field is directly proportional to (E/N). As the ionization potentials of the primary molecular species in the discharge are CO_2 (13.8eV), N_2 (15.6eV) and He (24.5eV), it is clear that only electrons in the high energy tail of the distribution are responsible for ionization. The mean ionization rate for the gas mixture is obtained by integrating the energy dependant rate constant for ionization over the EEDF and averaging over the molecular species composition. The computer code BOLTZ [4.3] has been modified to evaluate α from the following integration [4.4].

$$\frac{\alpha}{N} = \frac{8\pi e^2}{W m^2} \sum \int Q_j \, u \, f(u).du \qquad (4.1)$$

where the summation is made over all inelastic cross sections, Q_j, producing electrons. The value of α given by equation (4.1) is the number of ionization collisions per unit path length in the direction of the applied field. This is generally referred to as the Townsend first ionization coefficient [4.1].

In addition to ionization, electrons can be lost by the processes of attachment and recombination. It is found that for the mixtures of interest here, the principal electron loss mechanism is dissociative attachment [4.5]. The mean attachment coefficient is obtained in the same way as the ionization coefficient, by integrating over the EEDF. Fig. (4.4) shows the ionization and attachment coefficients as a function of the reduced field (E/N) for typical CO_2 laser gas mixtures.

Returning to fig. (4.2), in travelling a distance dx in the field direction, the electron current increases by the amount

$$dn = n\ (\alpha - \eta)dx \tag{4.2}$$

where n is the number of electrons entering the element dx. Integrating from x= 0 to x= d and assuming that n_o electrons leave the cathode per second, gives the number of electrons reaching the anode:

$$n = n_o\ \exp\ ((\alpha-\eta)d) \tag{4.3}$$

Thus, each electron emitted from the cathode results in an electron avalanche. In order for such a discharge to be self sustaining, in traversing the gap each avalanche must cause another electron to be emitted from the cathode. The processes which are responsible for such "secondary" electron emission include photo−emission and postive ion bombardment [4.1]. Defining the Townsend secondary ionization coefficient γ as the number of electrons released from the cathode per incident positive ion and letting

n = number of electrons reaching the anode per unit time
n_o = number of photo-electrons emitted from the cathode
n_+ = number of electrons emitted from the cathode by positive ion bombardment

Thus,

$$n = (n_o + n_+)\ \exp\ ((\alpha-\eta)d)$$

$$n_+ = \gamma\ (n - (n_o + n_+))$$

eliminating n_+ gives

$$n = \frac{n_o\ \exp\ [(\alpha-\eta)d]}{1 - \gamma\ [\exp\ [(\alpha-\eta)d]-1]} \tag{4.4}$$

Since the anode current is directly proportional to the electron current, we have

$$I = \frac{I_o\ \exp\ ((\alpha-\eta)d)}{1 - \gamma\ (\exp\ ((\alpha-\eta)d))} \tag{4.5}$$

As the applied voltage is increased, the ionization rate correspondingly increases, resulting in an increase in the electron current at the cathode. At a critical value of the applied field, the denominator of equation (4.5) approaches zero, causing a rapid increase in the anode current. The condition satisfied by

$$\gamma\ (\exp\ ((\alpha-\eta)d)\ -\ 1)\ =\ 1 \qquad (4.6)$$

defines the onset of sparking and is referred to as the Townsend breakdown criterion. Once this is established the discharge will be self−sustaining and can continue in the absence of the photo current I_o. An alternative expression for the breakdown criterion is obtained by rewriting equation (4.6) in the form

$$(\alpha-\eta)d = \ln\left(\frac{1}{\gamma} + 1\right) = K \qquad (4.7)$$

Since γ is typically of very small value ($\approx$ 0.1) K is approximately constant and is for a Townsend discharge of the order of 2 to 3. From the data for attachment and ionization coefficient, fig (4.4), it is possible to deduce the critical reduced field (E/N) at which Townsend breakdown will occur. For a 1:1:4 mixture with a 4 cm electrode gap it is found that the breakdown field is approximately 1.9×10^3 V/cm, corresponding to an applied voltage of 7.6 kV.

The above analysis, although containing many of the important breakdown mechanisms, is applicable only when the voltage is increased slowly up to the breakdown level. Under pulse excitation the breakdown voltage is generally higher than the "static" breakdown voltage. It is an additional requirement that the duration of the applied voltage pulse must be greater than the breakdown delay time of the gap: this is the sum of the statistical time lag and the formative time lag. The statistical lag is the time taken for an initiatory electron to appear in the gap due to cosmic rays, uv etc. The formative time lag is the time taken for the discharge current to grow to some critical level and is dependant on the secondary processes responsible for cathode electron emission.

If positive−ion bombardment at the cathode surface is the main source of secondary electrons, the minimum time required for positive feedback to become effective would be some fraction of the positive−ion transit time. Thus, a relatively long formative time lag ($\approx 10^{-6}$ sec) is observed in a Townsend breakdown.

Streamer breakdown mechanism.

In many applications, and in particular high pressure laser discharges, experimentally measured time lags have been found to be much shorter than the timescales predicted by the Townsend mechanism, e.g. formative time lags as short as 10^{-9} seconds are not uncommon in high pressure preionized TEA lasers [4.6]. Moreover, under certain

conditions it is found that complete gap breakdown can result from a single primary electron avalanche. Both these effects are attributed to the effect of space−charge enhanced fields at the head of the primary avalanche; this being neglected in the Townsend theory. Fig (4.5) shows diagramatically the electric field around the avalanche as it progresses across the gap and the resultant modification to the original field E_o. The large space charge fields that develop are due to the relatively low mobility of the positive ions as compared to that of the electrons. On the timescale of interest in a typical pulsed laser discharge, the electrons are free to move towards the anode while the positive ions are essentailly frozen in space. At some critical point where the space charge field at the head of the electron avalanche becomes comparable to the applied electric field, streamer development begins. At this point secondary avalanches are initiated by photoionization in front of and behind the primary avalanche, fig (4.6). Both anode and cathode directed streamers develop which move at a greater velocity than that of the primary avalanche.

The cathode directed streamer is primarily the result of the positive space charge left behind the avalanche head, as shown in fig (4.6). In the surrounding gas, photo−electrons are produced which initiate secondary avalanches directed along strong field lines towards the stem of the primary avalanche. As the negatively charged avalanche head propagates towards the anode and exponentiates, it also leaves behind a positively charged tail which continues to lengthen and intensify at an accelerating pace until the anode and cathode are eventually connected by the self propogating plasma streamer. Thus according to this theory, breakdown will occur whenever a single primary electron avalanche is allowed to develop to the critical point of streamer initiation anywhere within the electrode gap.

Consider an electron avalanche propagating towards the anode as shown in fig (4.5). The lateral extent (perpendicular to the field direction) of an individual avalanche is usually assumed to be due to diffusion, although electrostatic repulsion may be comparable in some cases [4.6]. For free electron diffusion it can easily be shown that the radius of the avalanche head is given by

$$r^2 = Z\,\lambda_e \qquad (4.8)$$

where Z is the distance from the cathode that the avalanche has travelled and λ_e is the electron mean free path. The space charge field due to the electrons in the avalanche is approximated by assuming that the avalanche head is spherical and contains n_e electrons.

$$E_r = \frac{e\,n_e}{4\,\pi\,\varepsilon_o}\,r2 \qquad (4.9)$$

Where e is the electron charge, ε_o is the permittivity of free space and the number of electrons in the avalanche head is given by the Townsend equation

$$n_e = \exp(\alpha Z) \qquad (4.10)$$

Equating the space charge field at the surface of the avalanche head to the applied field E_o gives the critical track length Z_{crit} which an avalanche must propagate in the field direction to initiate streamer breakdown.

$$\alpha Z_{crit} = \ln\left(\frac{4 \pi \varepsilon_o E_o \lambda_e}{e}\right) + \ln Z_{crit} \qquad (4.11)$$

Equating Z_{crit} to the gap spacing d gives Raether's breakdown criterion [4.1]. The first term on the right hand side of equation (4.11) is fairly insensitive to the gas parameters and is approximately 20 in mks units for typical breakdown conditions. For example, for a 1:1:4 mixture at a total pressure of 156 mbar, with an applied field of 1.5×10^5 V/m and assuming $\lambda_e = 2.5 \times 10^{-5}$ cm, gives the streamer breakdown condition

$$\alpha d = 21.68 + \ln d \qquad (4.12)$$

where d is measured in centimeters. Thus for a gap of 4 cm, streamer breakdown will occur if $\alpha d > 23.1$. This compares with a total avalanche gain of approximately 2.4 for Townsend breakdown in the same gas mixture. The avalanche gain corresponding to Townsend breakdown is therefore a factor of 6 smaller than that required for streamer breakdown. Consequently, the applied field strength required for Townsend breakdown is generally much weaker than required for streamer breakdown.

The type of breakdown which occurs in any particular case is important, at least as far as laser pumping is concerned, since the discharge must develop into a uniform volumetric glow for optimum laser excitation. The streamer mechanism tends to favour arc formation, therefore in conditions where Raether's criterion is satisfied, stringent requirements are imposed on gas conditioning prior to application of the voltage pulse, if stable glow discharge development is to occur. The initiation of the discharge in the arc mode is avoided by preionizing the inter-electrode volume. Common preionization techniques employed in laser systems include: UV, corona discharges, spark arrays, X-ray and E-beam. When pulse excitation is employed some form of gas preionization is required, irrespective of the breakdown mechanism, since the statistical time lags would preclude breakdown under the short pulse durations typical of high pressure gas lasers.

(4.2.2) Quasi−Steady Discharge Characteristics.

Provided care is taken in the initiation of the discharge, a weakly ionized and uniform glow discharge will develop throughout the inter−electrode volume. In the case of pulsed discharges, the discharge current will increase through the process of electron impact ionization until it becomes limited by the output impedance of the driving circuit. For the gas conditions and the levels of pulse excitation of interest in the present work, the discharge is found to operate at a quasi−static voltage and current level, characteristic of low pressure glow discharges [4.7]. In the case of pulse excitation the allowable input energy density for glow discharge stability is several orders of magnitude higher than that permitted in continuous discharges. However, for high repetition rate systems, the same requirements are imposed on gas flow conditioning as in the continuous case, and the allowable mean, continuous power inputs are of the same order in both cases. Fig. (4.7) illustrates the important characteristics of gas discharges, including the initial pre−breakdown, glow and arc regimes. These reults are obtained by supplying the current to the discharge via a variable resistor R.

As shown in fig (4.7), the operating point must lie somewhere on the load line, given by [4.8]:

$$I = \frac{V_o - V_d}{R} \qquad (4.13)$$

Where V_o is the supply voltage, V_d is the discharge voltage and R is the series resistance. The operating point is determined by the intersection of the load line and the discharge characteristic. Point A represents a sub−breakdown Townsend discharge with external ionization. As the series resistance is gradually reduced, point S is reached where the discharge becomes self−sustaining, the voltage at this point being given by the Townsend breakdown criterion. Breakdown and establishment of a "normal" glow discharge at S is accompanied by a drop in the discharge voltage. As the resistance is dropped still further, the "abnormal" glow regime is entered; so called because this regime has a positive V−I characteristic. At some point C on the abnormal glow, the discharge voltage collapses to a very low level as the glow discharge breaks down into intense arcs.

Clearly, the load line defined by R_2 allows several possible operating points. The question as to which of the operating points is actually realized in practice can be answered by considering the stability of each point. It can be shown that a necessary condition for discharge stability is given mathematically by:

$$\frac{dV_d}{dI} + R > 0 \qquad (4.14)$$

where dV_d/dI is the slope of the discharge V−I characteristic at the point of intersection with the load line. From fig (4.7) it can be deduced that points B and D are stable, while point C is unstable. Whether point B ar D is attained in practice, depends critically on the method used to initiate the discharge, the specific energy loading and applied voltage pulse characteristics. If the inter−electrode volume is properly preionized and the temporal characteristics of the applied voltage pulse are correct, stable glow discharges can be obtained at high specific energy densities. However, the increased power densities typical of pulsed CO_2 laser discharges essentially drive the discharge into an abnormal glow, beyond the "static" characteristic, i.e. to the right of point C. Operating points in this regime are thus inherently unstable and consequently tend to move towards the arc regime. The fundamental limitation in pulse excitation of gas lasers is therefore the allowable energy input per pulse which will not produce arcing in the discharge: for any gas mixture composition this determines both the maximum pulse power and the pulse duration.

It is found from measurements on static glow discharges that space charge effects play an important role in the maintenance of the glow discharge current, with the discharge comprising several regions of different luminosity [4.8]. These regions are characteristic of the accumulated space charge; it is therefore found that the electric field varies along the discharge length. Fig. (4.8) shows a plot of the longitudinal variation of electric field, voltage and current density for a typical low pressure laser discharge. Although there are many different regions − the structure actually observed depends critically on the type of gas, total pressure and discharge current − as far as laser excitation is concerned, the discharge can be broadly split into two main regions, namely: the positive column and the cathode fall. In the positive column the voltage varies linearly along the length, giving rise to a constant field and excitation rates. The positive column is almost electrically neutral, with equal numbers of positive and negative charges and is charactersitic of a weakly ionised plasma (fractional ionization N/n_e of approximately 10^{-6} is typical). In the pulsed discharges of interest in the present work, the positive column occupies almost the entire discharge length and it is therefore possible to take a constant value of applied field E when calculating vibrational excitation rates. The cathode fall region is small in comparison to the positive column and is characterised by a steep voltage gradient. This region is necessary for maintenance of the discharge, as positive ions are accelerated by the enhanced field to an energy favourable for emission of an electron upon impact with the cathode. For typical CO_2 laser discharges, the cathode fall is usually of the order of 300 V and can generally be neglected in calculations of the vibrational excitation

rates [4.10].

(4.2.3) Stability of Self-Sustained Pulsed Glow Discharges.

Extension of homogeneous avalanche/self-sustained discharges to large volumes and long pulse lengths clearly involves two consecutive steps. The first and more crucial step is initiating and sustaining the electron avalanche process until the desired transient state of the plasma is uniformly reached throughout the discharge volume. The second step is simply a matter of maintaining the plasma spatial homogeneity and temporal stability over the desired length of time. Once spatial homogeneity is reached the plasma must not be allowed to develop any spacial instability mode which could break up or collapse the homogeneous current dsitribution into concentrated arc channels over the timescale of interest. This phenomenon - called glow to arc transition - is generally associated with some relatively slow process, such as growth of thermal instability modes within the plasma or the development of hot spots on the electrode surfaces [4.6]. Filamentary or arclike discharges may also result from the avalanche initiation process if insufficient care has not been taken to ensure homogeneous avalanche formation. Obviously, such inhomogeneities should be considered as being caused by improper formation processes and should not be confused with the glow-to-arc transition phenomenon.

Current understanding of the mechanisms leading to glow-to-arc transition is on a firm physical basis, however, due to the complexity and highly non-linear nature of the problem, accurate predictions of such parameters as arc formation time are possible in only the simplest of cases. Haas [4.11] has identified the major plasma-kinetic instability modes relevant to CO_2 lasers. This work has been furthered by Nighan [4.12] and Jacob [4.13] *et al*, who have established three principal modes of instability in CO_2 laser discharges, namely: a thermal mode, an ionization mode and an acoustic mode. The principal mechanisms driving each of these instabilities is a perturbation in neutral particle density (decrease), which leads to a local increase in electron density. In discharges containing only atomic species, perturbations in neutral particle and electron properties couple directly. A large local increase in electron density therefore causes additional heating of the gas by way of elastic collisions, thereby providing the positive feedback mechanism required for the process to be unstable [4.12]. Such a sequence of events will result in the growth of any initial disturbance if thermal conduction cannot dissipate the local concentration of heat.

In mixtures containing molecular gases the situation is considerably more complicated, as in addition to the features outlined above, it is necessary to consider the effects of vibrational and rotational excitation. The sequence of events accompanying a constant

pressure small amplitude disturbance in gas temperature (or density) is illustrated in fig. (4.9). As for the atomic species, a local decrease in gas density leads to an almost instantaneous response in electron temperature. However, there are now two primary feedback mechanisms resulting in enhanced gas heating: vibrational relaxation and electron–molecule collisions. Thus, even in the simplest molecular gas discharge, the coupling between disturbances in neutral particle and electronic properties is substantially more complicated than in an atomic plasma.

It is found experimentally that there exists a specific energy input threshold above which a stable glow discharge cannot be maintained. This "single–shot" threshold depends on *inter–alia:* the preionization conditions, the electrode geometry, the pulse duration and temporal characteristics of the applied voltage pulse and the gas mixture composition. At levels of excitation below this threshold it is possible to sustain homogeneous glow discharges. However, it is an additional requirement of high repetition rate systems that the discharge products must be removed from the electrode region in the inter–pulse period, if stable operation in a continuous pulse mode is to be attained. If any plasma inhomogeneity is not convected out of the electrode region, this will grow in subsequent pulses until arcing occurs. This places rather stringent requirements on gas flow velocities for high repetition rate systems and in particular, for continuous operation at a PRF of 10 kHz the required flow velocity is "economically" unattainable.

(4.3) QUASI–STEADY OPERATING CHARACTERISTICS.

The pulsed discharge can be considered in two stages: an initial formative period which is short in comparison to the pulse length and a quasi–steady phase where the discharge is maintained at near optimum conditions for laser pumping. For efficient excitation of the upper CO_2 laser level, it is essential that the electron energy distribution peaks in the 1 – 3 eV range. Since the main parameter controlling the EEDF is the reduced field E/N, it is important to study how this parameter varies with gas mixture composition and discharge current.

(4.3.1) Measurement of Discharge Voltage and Current.

The output from the high voltage pulser is fed to the discharge electrodes via a URm74 co–axial cable, which is coupled to the high voltage connector on the anode safety cover (see fig. (2.7) chapter 2). For reasons of safety, it was decided to measure the anode voltage and current at the pulser end of this transmission cable. As the cable is short and has an impedance which is close to the PFN impedance, no significant error is incurred by measuring the voltage at this point. However, as the

high voltage bus under the laser feeds both the anode and the preionizing circuit, the current measured at this point is the sum of the anode and preionizing currents. Since the preionizing current lasts typically 0.5 μs, during the quasi-steady phase of the discharge the only current flowing is the anode current and therefore no error is introduced if the plateau value of current is used.

Fig (4.10) shows typical discharge V-I characteristics for a 1:1:4 gas mixture with a 100 Ω, 10 μs PFN. It is important to note that following a relatively short initial transient, the discharge voltage and current collapse to an almost steady level for the remainder of the pulse. It has been found that over a range of operating currents and pressures, the ratio of the quasi-steady applied field to neutral particle density E/N - calculated from the plateau voltage - is dependent only on the gas mixture composition and is independent of the discharge current, electrode spacing and total gas pressure. This is in agreement with the findings of Denes and Lowke *et al* [4.8].

The dependence of the quasi-steady discharge E/N on discharge current, total gas pressure and mixture composition has been investigated by Khahra [4.9] and more recently by Hasan [4.2]. Fig. (4.11) and fig. (4.12), taken from Hasan [4.2], show the dependence of E/N on gas pressure and discharge current. The experimental results of fig (4.11) were obtained with a constant current of 60 Amps, this being achieved by increasing the PFN voltage in accordance with the gas pressure. It is clear that for pressures above 80 torr E/N remains approximately constant, whilst below this pressure E/N shows a gradual increase as the total pressure is reduced. This effect is the result of the cathode fall voltage becoming a significant percentage of the positive column voltage: as the pressure is reduced the positive column voltage reduces linearly with the pressure, but the cathode fall voltage decreases at a slower rate. The net result is therefore an increase in E/N.

Fig (4.12) also shows that as the current is increased above 100 Amps, E/N gradually increases. This effect is attributed to the fact that the discharge is an abnormal glow. Any growth in anode current must therefore be attained by an increase in the cathode current density as the discharge occupies the full electrode surface area. Such an increase in current density can only be maintained by an increased cathode fall and this gives rise to a gradually increasing quasi-steady reduced field.

(4.3.2) Theoretical Prediction of Quasi-Steady Voltage.

The above experimental observations can be explained by a simple 1D model of the discharge. For an element of the positive column the electron number density increases in accordance with [4.8].

$$\frac{dn_e}{dt} = \alpha V_d n_e - \eta V_d n_e - \gamma n_e^2 \qquad (4.15)$$

Where α is the ionization coefficient, η is the attachment coefficient, γ is the recombination coefficient and V_d is the drift velocity. This equation is valid for the positive column of a glow discharge assuming electrical neutrality. This model also neglects the effect of the cathode fall, which is assumed to be negligible in comparison to the positive column voltage. When $\gamma n_e \ll \eta V_d$ equation (4.15) predicts that quasi-steady operation i.e. $dn_e/dt=0$ will occur when $\alpha = \eta$, which implies a fixed quasi-steady value of E/N. Thus, the quasi-steady value of E/N is given by the intersection of the characteristic curves for α and η, as shown in fig. (4.4). Table (4.1) lists the experimentally measured values of the quasi-steady E/N for the range of gas mixtures of interest here and compares these with the theoretical values obtained from the intersection of the ionization and attachment coefficients.

It can be seen that there is excellent agreement between the two sets of values, thus confirming the simple 1D model of the positive column. Moreover, since the coefficients for attachment and ionization are obtained from a numerical solution of the Boltzmann transport equation, the results also validate this theoretical model.

TABLE (4.1) Experimental and Theoretical Values of E/N.

Gas Mixture	Theoretical E/N $\times 10^{-16}$ Vcm^2	Experimental E/N $\times 10^{-16}$ Vcm^2
1 : 1 : 0	8.6269	8.7571
1 : 1 : 1	6.3216	6.3933
1 : 1 : 2	5.1362	5.2283
1 : 1 : 4	3.9048	3.9892
1 : 1 : 6	3.2509	3.2912
1 : 1 : 8	2.8423	2.8942
1 : 2 : 0	8.4119	8.5213
1 : 2 : 1	6.7464	6.8121
1 : 2 : 2	5.7279	5.8287
1 : 2 : 4	4.5307	4.6065
1 : 2 : 6	3.8389	3.9023
1 : 2 : 8	3.3681	3.5022
1 : 3 : 0	8.2972	8.3848
1 : 3 : 1	6.9925	7.0851
1 : 3 : 2	6.1096	6.2041
1 : 3 : 4	4.9815	5.0408
1 : 3 : 6	4.2835	4.3583
1 : 3 : 8	3.7891	3.9272

Also shown in fig (4.11) and fig. (4.12) is the variation of quasi-steady E/N with

mixture composition. This dependence is shown more clearly in fig (4.13) and (4.14). It can be seen that increasing the percentage of CO_2 increases the value of E/N, whilst increasing the percentage of helium decreases the operating E/N.

The above effects can be explained with the characteristic curves for attachment and ionization, fig. (4.4) and fig. (4.15). The addition of helium to the gas mixture increases the average electron energy, as helium has a small collision cross section and consequently both the ionization and attachment coefficients increase. As the operating point is simply given by the intersection of the α and η curves, the net result is a shift in the quasi-steady E/N to a lower value. With the addition of CO_2 to the discharge, the mean electron energy is reduced, due to the large collision cross sections for vibrational excitation, with a resultant drop in both the ionization and attachment coefficients and a consequent shift in E/N to a higher value.

(4.3.3) Matching The PFN To The Gas Discharge.

The quasi-steady operating charactersitics of the pulsed discharge has an important implication for the design of the pulser circuit. For optimum power transfer from the PFN to the gas discharge, the effective impedance of the discharge must be matched to the impedance of the PFN. It can be shown that the discharge current is given by (see section 2.1).

$$I_d = \frac{V_{no} - V_d}{Z_o} \qquad (4.16)$$

Where V_o is the PFN charge voltage, V_d is the quasi-steady operating voltage and Z_o is the PFN impedance. The impedance of the discharge is therefore:

$$Z_d = \frac{V_d}{V_{no} - V_d} \times Z_o \qquad (4.17)$$

Matching requires $Z_o=Z_d$, which is achieved simply by charging the PFN to twice the quasi-steady discharge voltage. It is clear that the discharge current is being controlled by the PFN impedance and in this sense the gas discharge cannot be considered to have a real impedance: it simply takes on the impedance of the driving circuit. Since the PFN impedance controls the current at the matched condition, Z_o is chosen on the basis of allowable energy input into the discharge.

(4.4) PREIONIZATION AND DISCHARGE FORMATION.

The potential to establish a uniform glow discharge depends critically upon the ability

to preionize the gas prior to application of the voltage pulse, with stringent requirements being imposed on both preionization electron density and spatial uniformity. An understanding of the development of the discharge during this initial phase is therefore crucial, as inhomogeneities developing in this phase quickly lead to filamentary discharges and a loss of CO_2 vibrational excitation. Experimental work was undertaken to establish the breakdown mechanisms operative and to investigate the efficacy of the double discharge technique for initiating volume-stabilized glow discharges. The work can broadly be split into two main areas: preionization and discharge formation. Although in reality preionization preceeds discharge formation, the breakdown mechanisms operative in the formative phase of the discharge determine the necessary preionization conditions and this will therefore be considered first.

(4.4.1) Discharge Formative Time Lags.

Fig. (4.16) shows the main components of the pulser and discharge system together with some approximate values of the dominant stray capacitances in the connecting leads etc. The trigger wires are coupled directly to the anode busbar by the coupling capacitor C_c; this comprises four 20 nF pulse capacitors which can be connected in any combination to give a capacitance in the range 5 nF - 80 nF. Experiments were performed to measure the discharge current and voltage and to establish the relationship between these parameters and the circuit variables in the initial phase of the discharge. During the first set of experiments the current and voltage were measured at the pulser end of the URm74 transmission cable, as shown by point A in fig. (4.16). This was chosen because of the limited space available within the anode safety enclosure to position the current transformer and high voltage probe. It was assumed that recordings made at this point were accurate measurements of the discharge voltage and current.

Fig. (4.17) shows a recording of the discharge voltage and current from which it can be seen that the initial transient lasts approximately 2 μs, at which point the voltage and current reach the quasi-steady values. From inspection of the voltage trace, since the peak voltage is of the order of 8 kV and the effective attachment coefficient for the corresponding field is approximately 3.01 cm^{-1}, it is clear that the total avalanche gain ($\alpha d \approx 12$) is much less than that required for streamer breakdown and that the discharge operates in the classical Townsend regime. However, since formative delay times of the order of an electron transit time are generally observed with Townsend discharges, the current waveform is inconsistent with this regime as the discharge current starts simultaneously with the rising voltage pulse. This discrepancy is due to the position of the current transformer: the current actually measured is the sum of the main discharge current and the trigger-wire current. To check the results a

measurement was made of the trigger-wire current, this being measured on the trigger-wire connecting lead. As shown in fig. (4.18), the trigger-wire current is approximately 70 Amps with a duration of 700 ns.

The immediate conclusion to be drawn from the above results is that the trigger-wire circuit dominates the initial discharge of the PFN. Fig. (4.16) is therefore not a true representation of the discharge current during the formative phase of the discharge, as the trigger wire current is much higher than the discharge current. In order to obtain a true measurement of discharge current it was necessary to place the current transformer directly on one of the ceramic anode leadthroughs and to disconnect the other three leadthroughs. Fig. (4.19) shows a recording of the discharge voltage and current measured at this point (point B) with an expanded time scale of the same settings shown in fig. (4.20). From these measurements it is clear that the discharge current does not start to increase until the arrival of the primary electron avalanches at the anode, which is in agreement with the Townsend breakdown theory.

It is of interest to analyse the above experimental results in terms of a series of simultaneous avalanches propagating towards the anode, each being initiated from electrons produced by the trigger-wire discharge. For the moment the exact characteristics of the trigger-wire emission will not be considered, it will simply be assumed that the trigger-wires can be modelled as a constant current source I_o. Since the initial charge densities are small during the first transit from cathode to anode, space-charge fields can be neglected and free diffusion of electrons can be assumed. Thus, for a small element of time Δt, the avalanches will travel a distance Δx in the field direction given by

$$\Delta x = V_d \, \Delta t \qquad (4.18)$$

where V_d is the drift velocity for the applied field E/N, as measured from the recorded voltage. In traversing the gap the initial current will grow according to

$$\frac{\Delta I}{\Delta t} = (\alpha - \eta) \, V_d \, I \qquad (4.19)$$

Thus, the ratio of current reaching the anode to initial trigger-wire source current, I_o, can be expressed as

$$\frac{I_a}{I_o} = \Pi \exp \left[(\alpha - \eta) \, V_d \, \Delta t \right] \qquad (4.20)$$

Where the product is taken from x=0 to x=d, the electrode separation. The above expressions can be used to numerically evaluate the propagation of the ionizing wave from the recorded discharge voltage of fig. (4.20). Table (4.2) details the calculations

based on a time step of 80 ns. Values for V_d and ionization and attachment coefficients are obtained from reference [4.2].

TABLE (4.2) Ionizing Wave Propagation.

Δt (ns)	$E/N \times 10^{-16}$ Vcm^2	$V_d \Delta t$ cm	$\Sigma V_d \Delta t$ cm	$(\alpha-\eta)$ cm^{-1}	$e[(\alpha-\eta)\Delta x]$	$\Pi e[\ ]$
80	0.618	0.290	0.290	0	1	1
160	1.410	0.374	0.664	-0.008	0.997	0.997
240	2.120	0.448	1.112	-0.027	0.988	0.985
320	2.82	0.522	1.634	-0.290	0.859	0.846
400	3.80	0.628	2.262	-0.190	0.887	0.750
480	4.51	0.705	2.967	0.78	1.733	1.30
560	5.13	0.770	3.730	2.02	4.730	6.15
640	5.30	0.785	4.515	2.75	8.660	53.28

The first point to note from the above calculations is that due to the slow rate of rise of anode voltage, electron attachment is larger than ionization and the number density of electrons in the avalanche actually decreases up until $t \gtrsim 400$ ns. The above results are illustrated in fig. (4.21) and fig. (4.22) from which it can be seen that the ionizing wave reaches the anode at $t \approx 590$ ns, with a total avalanche gain of 13.5.

It can be seen from fig. (4.20) that the discharge current starts to grow 530 ns after the start of the voltage pulse. This is in good agreement with the predicted value above, however, the results are still difficult to interpret as it is virtually impossible to specify the point at which breakdown actually occurs. It is normal gas discharge practice to take the formative time lag as the time elapsed from the appearance of an initiatory electron in the gap to the commencement of the potential fall across the gap produced by the current increase [4.14]. It is not possible to use this definition with the above circuit arrangement as the rate of rise and collapse of the anode voltage is dominated by the trigger-wire circuit. In view of these problems it is best to calculate the formative time lag as the time for the discharge current to grow to a specific, and measurable, value. This can then be used as a reference for comparison of results.

It is of interest to consider the magnitude of the current pulled off from the trigger-wires, which can be estimated by comparing the theoretical predictions of Table (4.2) with the actual recorded current waveform. At time $t \simeq 590$ ns the measured current is approximately 26.67 Amps and using the predicted value for the

current gain of 13.5, it is possible to deduce that the effective trigger−wire current is of the order of 2.0 Amps. This is a good estimate provided that space−charge fields are negligible, this being true when the plasma Debye length is much longer than the characteristic dimensions of the discharge [4.15]. Calculating the Debye length λ_d from the following expression [4.15]

$$\lambda_d = \sqrt{\left[\frac{\epsilon_o K T}{n_e e^2} \right]} \qquad (4.21)$$

Where n_e is the electron density, T is plasma temperature and all other symbols have there usual meaning. The electron density can be estimated from

$$n_e = \frac{I}{V_d e A} \qquad (4.22)$$

where A is the discharge cross sectional area. From Table (4.2) at t = 590 ns the reduced field is 5.3×10^{-16} Vcm^2, giving a drift velocity of 0.968×10^7 cm/s. Taking T= 300 K, A = 475.2 cm^2 and I = 26.7 Amps, gives λ_d = 6.3 mm. Since this is smaller than the discharge dismensions the assumption of weak space−charge fields is incorrect. In order to obtain an accurate estimate of the discharge current growth it is necessary to include the effects of space−charge field at the head of the ionizing wave. Kline [4.16] has obtained solutions of the current continuity equations under conditions similar to the above and found that initially the current grows at a rate $\alpha V_d I$ as predicted by the Townsend theory. However, when the calculated electron density reaches a value such that the corresponding Debye length is comparable to the smallest dimension of the developing avalanche, phase 2 begins and the calculated current growth rate decreases due to space−charge effects. A numerical solution of the discharge current growth including the effects of space−charge and electrical circuit parameters is currently being developed to investigate more thoroughly the temporal and spatial growth of the plasma. This will be reported by Watson [4.17] in a future dissertation. By extrapolating the results of Kline [4.16] it is estimated that the reduction in current growth rate due to space−charge fields is negligible in this case as the plasma is weakly ionized, and to a good approximation the Townsend growth rate can be used.

In addition to the above experiment several modifications were made to the discharge circuit in an attempt to improve discharge stability; these included the addition of peaking capacitors across the electrodes and changing the value of the coupling capacitor C_c. It is of interest to consider some of these results in terms of discharge formation.

Fig. (4.23) shows the recorded voltage and current with a 10 nF peaking capacitor

connected directly across the anode/cathode and compares the results with the earlier results of fig. (4.20), which were obtained with no peaking capacitor. It can be seen that the voltage rise−time has been reduced considerably by the addition of the peaking capacitor C_p and the discharge current does not start to grow until approximately 1 μs after the start of the voltage pulse. As for the results of fig. (4.20), it is possible to analyse the results numerically. Table (4.3) details the calculations; the results are also illustrated in fig. (4.24) and fig. (4.25).

TABLE (4.3) Ionizing Wave Propagation With 10 nF Peaking Capacitor.

Δt (ns)	E/N $\times 10^{-16}$	$V_d \Delta t$ cm	$\Sigma V_d \Delta t$ cm	$(\alpha-\eta)$ cm^{-1}	$e[(\alpha-\eta)\Delta x]$	$\Pi e[\ ]$
80	0.265	0.250	0.250	———	1	1
160	0.530	0.280	0.530	———	1	1
240	0.796	0.308	0.838	———	1	1
320	1.320	0.364	1.200	-0.008	0.997	0.997
400	1.590	0.396	1.598	-0.013	0.994	0.991
480	1.950	0.432	2.030	-0.043	0.981	0.972
560	2.30	0.468	2.498	-0.100	0.954	0.927
640	2.65	0.506	3.001	-0.175	0.915	0.849
720	3.09	0.544	3.548	-0.310	0.844	0.716
800	3.32	0.576	4.124	-0.360	0.812	0.581

The above results show that with a 10 nF peaking capacitor the electron avalanche current reaching the anode is less than the current pulled off from the trigger−wires. From fig. (4.24), the ionizing wave reaches the anode 780 ns after the start of the voltage pulse, however, no current is detected until approximately 880 ns. This discrepancy is due to the fact that the avalanche current is actually diminished in crossing the gap; for the electron transit the total avalanche gain is approximately 0.60. As the oscilloscope setting was 50 A/div, it is not surprising that the small current associated with the arrival of the ionizing wave is not detected.

It is apparent that with these experimental conditions the discharge current growth is being dominated by the plasma exponentiation rate and not by the external circuit components. To a good approximation, the discharge current in the post−avalanche phase grows in accordance with equation (4.19) i.e.

$$\frac{dI}{dt} = (\alpha - \eta)\, V_d\, I$$

Thus,

$$I(t) = I_a(t_o) \exp\left[(\alpha - \eta)\, V_d\, (t - t_o)\right] \qquad (4.23)$$

Where t_o is the time of arrival of the avalanches at the anode after the start of the voltage pulse and $I_a(t_o)$ is the magnitude of the current reaching the anode at this time. Equation (4.23) predicts that for a given applied field the discharge current will grow exponentially with a time constant τ given by

$$\tau = [(\alpha - \eta)\, V_d]^{-1} \qquad (4.24)$$

This time constant varies considerably over the range of E/N for the experimental conditions of interest here. For the results of fig. (4.23), in the post-avalanche period the E/N varies from 3.3×10^{-16} to 4.5×10^{-16} cm^2, corresponding to a variation of τ from 1.3 μs to 80 ns. The sensitivity of plasma growth to the applied field in this range complicates the discharge modelling as accurate values for α and η as a function of E/N are required.

It is of interest to examine what effect C_p has on the magnitude of the current pulled off from the trigger-wires. From fig. (4.23), it takes approximately 1.17 μs for the current to grow to 10.0 Amps and by extending the calculations of Table (4.3) to this point in time, it can be shown that the total current gain is 1.415. The effective trigger-wire current is therefore $10/1.415 \simeq 7$ Amps. This compares with 2.0 Amps for the same conditions with no peaking capacitor. Fig (4.26) compares the trigger wire voltage and current waveforms for both cases; it can be seen that the effect of C_p has been to reduce the peak trigger-wire current and the rate of rise of trigger-wire voltage.

The above results may be explained by the fact that although the peak trigger-wire current is reduced by the addition of the peaking capacitor, the trigger-wire voltage is also reduced. It is therefore more likely that electrons will escape the trigger-wire field and avalanche towards the anode. It should, however, be pointed out that the above calculations are sensitive to the values used for α and η. In view of the marginal difference between the effective trigger-wire current with and without C_p, it is not possible to draw firm conclusions from the numerical predictions presented here, although with a more detailed model, including space-charge effects, a better quantitative description of the trigger-wire performance could be obtained.

(4.4.2) Preionization Requirements.

In view of the limited diffuse spreading ability of the secondary electrons and ions associated with each primary electron avalanche during an overvolted breakdown, homogeneous discharge formation requires an initial distribution of free electrons within the discharge volume at the onset of the breakdown process. Due to the limited penetrating power, intensity and efficiency of preionization sources it is generally desirable to keep the level of preionization required for homogeneous discharge formation as low as possible.

A. J. Palmer [4.18] proposed a simple physical model for estimating the preionization requirements for initiating a volume stabilized glow discharge. The basic requirement of the model was that the preionization electron density be large enough to cause appreciable spatial overlap of the primary electron avalanches and consequential smoothing of the space-charge field gradients at the stage when streamer formation would otherwise occur.

In streamer breakdown theory it is assumed that the time development of a single primary electron avalanche does not depend on the simultaneous presence of other primary electron avalanches. Accordingly there is no explicit dependence of the breakdown criterion, equation (4.11), on the initial number density of primary electrons. Implicit in the formulation of the breakdown criterion is that the space-charge can develop strong local gradients since it is this feature which causes the discharge to become filamentary. In the case where the space-charge field is due to just a single primary electron avalanche, strong field gradients clearly exist due to the limited diffuse spreading of the individual avalanche patches. As the number of simultaneous avalanches is increased beyond a certain level, one would expect the adjacent avalanche patches to overlap.

Palmer's model, as illustrated in fig. (4.27), consisted of calculating the radius of the avalanche head at the critical track length - defined as the point at which the field due to the avalanche space-charge is equal to the applied field - and equated this to the separation of the primary electron avalanches. For typical TEA CO_2 laser breakdown conditions this predicts an initial electron density of the order of 10^4 cm^{-3} is required.

The minimum preionization requirement predicted by Palmer's model is consistent with the experimental measurements of Levatter [4.6] and Kunhardt *et al* [4.19] and is generally true for high pressure CO_2 lasers when the streamer breakdown criterion is satisfied. With reference to the experimental results of section (4.4.1) it is clear that

for the results reported so far, the discharges operate in the Townsend regime and Palmer's minimum preionization density is not strictly applicable. From the streamer breakdown criterion, equation (4.11), streamer breakdown will occur when

$$\frac{(\alpha - \eta)}{N} = \frac{23.1}{N\,d} \qquad (4.25)$$

Where N is the neutral partcle density and d = 4 cm is the electrode separation. Using the perfect gas law N = P/KT gives

$$\frac{(\alpha - \eta)}{N} = \frac{23.909\times10^{-17}}{P\ (\text{mbar})} \qquad (4.26)$$

For a given mixture and gas pressure, P, it is possible to deduce, from tabulated values of α and η, the applied field necessary for streamer formation. The applied instantaneous voltage necessary for streamer breakdown can then be calculated. Results of this computation for 1:1:4 and 1:1:8 gas mixtures are shown in fig. (4.28). It can be seen that the critical voltage for streamer breakdown is lower for the 1:1:8 mixture due to the increased ionization rate resulting from the higher mean electron energy. Clearly, with any real pulser circuit there will be a finite voltage rise-time and the peak voltages required for streamer breakdown will be significantly higher than those of fig. (4.28). With the slow voltage rise-time and low peak voltage obtained from the pulser circuit, it can be concluded that all the mixtures of interest in this application will break down in the classical Townsend avalanche mode, with the possible exception of helium rich mixtures at low pressure.

With the trigger-wire system, the minimum electron density at the cathode due to the trigger-wire/cathode (auxiliary) discharge is of the order of $10^9 - 10^{10}$ cm^{-3}, which is much higher than Palmer's figure. However, the preionization is localised at the cathode and unlike UV and X-ray preionizers, does not extend throughout the full discharge volume. It has been found that the trigger-wire technique provides a satisfactory means of initiating the discharge at pressures below 200 mbar; at pressures above this the discharge is filamentary from the outset and no glow develops [4.9]. Since it is advantageous to extend the stable operational envelope to higher pressures, it is of interest to consider the principal mechanisms responsible for preionization in CO_2 laser gas mixtures, and to consider these in terms of the design and operation of the trigger-wires.

It has already been pointed out that the trigger-wires release a burst of electrons at the cathode, coincident with the rising anode voltage. In addition to this it may also be possible that UV emission from within the auxiliary discharge may preionize the

gas ahead of the primary electron avalanches. Mechanisms of UV generation and UV-photo-emission in CO_2 laser gas mixtures have been studied by Babcock [4.20], McKen [4.21] and Scott *et al* [4.22]. It is now generally accepted that UV radiation of wavelength ≃ 120 nm (10.5 eV) in the CO_2 spectral window is responsible for photo-ionization in CO_2 lasers. However, since the ionization potentials of all the main laser gas constituents are greater than 10.5 eV, it was concluded that single-photon ionization of impurities, with ionization potentials less than 10.5 eV, was the principal source of electrons. Low ionization potential impurities (LIP) present in the research grade helium, such as low molecular weight alkenes e.g. propene, have been found to be present up to a concentration of 0.5 ppm and these impurities have been identified as the major source of preionization.

The factors influencing UV emission have been investigated by Scott [4.22] for spark preionizers and by Marchetti [4.23] for corona preionizers. N_2 concentration in the spark or corona discharge has been found to be the major source of UV, although ionized electrode material in the spark plasma was found to contribute significantly to the UV emission. A linear dependence on N_2 content and a cubic dependence on peak current have been found for UV emission at a wavelength of 120 nm.

(4.4.3) Trigger-Wire Voltage and Current.

In the discussion of discharge formation and formative time lags it has been sufficient to assume that the trigger-wires act simply as a source of electrons for the main discharge. By analysing the discharge formation in terms of simultaneous electron avalanches, the magnitude of the effective trigger-wire current has been estimated to be approximately 3 to 7 amps, which is of the order of 5 - 10 % of the trigger-wire/cathode discharge current. No attempt has been made so far to explain the fundemantal processes operative in the trigger-wire/cathode discharge, it is therefore intended here to examine in detail the performance of the trigger-wire system, with a view to optimizing the controlling parameters.

The results reported in this section were all recorded with the 1000 x 74 mm^2 electrode and the following trigger-wire geometry:

Dielectric: Pyrex glass OD = 3.5 mm ID = 2.0 mm
Length of wires = 130 mm
No. of Wires = 104
Height above cathode = 0.53 mm
Wire spacing = 8 mm

Prior to any experimental work, the trigger−wire/cathode stray capacitance was measured with a capacitance bridge; for the above arrangement this was measured as 0.36 nF. The trigger wire height above the cathode was measured with feeler gauges, 0.53 mm being the average of several readings along the length of the electrode. For each experiment, measurements were taken of the trigger−wire and anode voltages, together with the trigger−wire current. Voltages were measured with TEK P6015 probes. The trigger−wire current was measured on the connecting lead with a Pearson wide−band current transformer. All waveforms, unless otherwise specified, were recorded at a PRF of 100 Hz.

Fig. (4.29) shows the recorded trigger−wire voltage and current for the above trigger−wire geometry, with a coupling capacitance of 10 nF. Fig. (4.30) shows the simultaneous recording of both anode and trigger−wire voltages. As shown in fig. (4.30), the trigger−wire voltage follows the anode voltage profile with the only difference being a small reduction in voltage. This agrees with the measurements of Khahra [4.9], however, Khahra was unable to obtain measurements of the trigger−wire current due to excessive interference and concluded wrongly that preionization electrons were available throughout the duration of the main voltage pulse. This is clearly not the case, as the trigger−wire current pulse is present only when the anode voltage is changing, and is typically 650 ns in duration.

Close inspection of the trigger−wire waveforms reveals some interesting points. Firstly, during continuous pulse operation, the trigger−wires aquire a negative residual voltage of approximately 1000 V. Secondly, the trigger−wire current is present only when the anode voltage is changing, a positive current when dV_a/dt is positive and a negative current when dV_a/dt is negative. Both these effects tend to suggest that the trigger−wires are capacitive in nature i.e. $I = C\ dV/dt$. From fig. (4.29), the current rises quickly and remains relatively constant at a value of approximately 70 amps for the duration of the voltage rise−time. With the voltage rise−time taken as 9.23 kV/μs, the effective trigger−wire capacitance is estimated to be 7.6 nF.

The above estimate of the trigger−wire capacitance is much larger than the measured stray capacitance of 0.36 nF. This apparent discrepancy led to the conclusion that upon breakdown of the trigger−wire gap, the electrons attach to the outer surface of the dielectric, although a small percentage escape the trigger−wire field and avalanche towards the anode. The effective capacitance is therefore not the measured stray capacitance − from the trigger−wires to ground − but the capacitance from the wires to the outer surface of the pyrex glass. The trigger−wires can therefore be modelled as a perfect cylindrical dielectric, with the effective capacitance per unit length given by

$$C = \frac{2 \pi \epsilon_o \epsilon_r}{\ln (D/d)} \qquad (4.27)$$

Where ϵ_o is the permittivity of free space, ϵ_r is the relative permittivity of pyrex glass and d, D are respectively the inner and outer diameters of the glass tubing. With $\epsilon_r = 5$, the capacitance per unit length is 0.5 nF/m, giving the effective capacitance of the complete assembly $C_e = 6.76$ nF. In view of the simplicity of this calculation, this is in good agreement with the value of 7.6 nF deduced from the experimental results.

The above result is important inasmuch as it allows the trigger−wire current to be predicted for a given rate of rise of anode voltage and, in addition, highlights methods of controlling the current i.e via ϵ_r and dV/dt. Still two problems remain to be resolved: firstly, at what point does the trigger−wire/cathode gap actually break down, and secondly, what parameters control the voltage rise−time.

To answer the first question several careful measurements were made of the trigger−wire voltage and current. As shown in fig. (4.31), it was observed that a small glitch was always present on the trigger−wire voltage trace at approximately 1000 − 1500 V from the steady voltage level; this appeared to be accompanied by a sudden increase in the trigger−wire current. During this initial period the trigger−wire current is of the order of 8 − 10 Amps, with a corresponding $dV/dt \simeq 1.9 \times 10^{10}$ V/s. This sugggests a capacitance in the range 0.42 − 0.52 nF, which is in close agreement with the measured trigger−wire/cathode stray capacitance. After this point the effective trigger−wire capacitance increases to 7.6 nF. It can be concluded therefore, that the sudden increase in trigger−wire current at a voltage in the range 1000 − 1500 V is the result of breakdown of the trigger−wire/cathode gap.

To answer the second question, namely, what parameters control the rate of rise of anode voltage, measurements were made with different values of coupling capacitance C_c in the circuit? Recordings of the anode and trigger−wire voltages with $C_c = 20$ nF and $C_c = 5$ nF are shown in fig. (4.32) and fig. (4.33) respectively, with a comparison of both anode waveforms being shown in fig. (4.34). It should be noted that the trigger−wire voltage trace is positioned for ease of comparison; the trigger−wires actually have a negative residual voltage as indicated by the data at the side of the figure. It is evident from these results that the trigger−wire and anode voltages are almost identical, with the only difference being a reduction in the amplitude of the trigger−wire voltage. It can be deduced from the waveforms that the voltage division ratio V_a/V_{tw} is constant after the point of trigger−wire/cathode breakdown: from fig's (4.32) and (4.33), the following data can be obtained.

$C_c = 20$ nF $\qquad V_a/V_{tw} \simeq 1.40$

$C_c = 5$ nF $\qquad V_a/V_{tw} \simeq 2.23$

Clearly, the coupling capacitance simply attenuates the anode voltage in the ratio

$$\frac{V_a}{V_{tw}} = \frac{C_c + Ce}{C_c} \qquad (4.28)$$

Where C_e is the effective trigger−wire capacitance. From the above data for the voltage division ratio, $C_c = 20$ nF $\Rightarrow C_e = 8.0$ nF and $C_c = 5$ nF $\Rightarrow C_e = 6.2$ nF. These values are in good agreement with the value of 7.6 nF calculated from the voltage rise−time and trigger−wire current.

Thus, during the breakdown period of the anode/cathode gap, i.e before the arrival of the anode current, the pulser circuit "sees" a load comprising the coupling capacitance C_c in series with the effective trigger−wire capacitance C_e. As all other capacitances and currents are negligible during this period, the trigger−wire capacitance C_e controls the rate of rise of anode voltage, as this is fixed by the trigger−wire geometry. It is of interest therefore to examine what effect C_c has on the trigger−wire current. As shown in fig. (4.35) and fig. (4.36), decreasing C_c from 20 nF to 5 nF reduces the width of the trigger−wire current pulse − measured from the leading edge to the zero crossing − from 800 ns to 580 ns. It is also observed that both the rate of rise of trigger−wire voltage and amplitude of the trigger−wire current do not vary significantly over this range C_c. Clearly, the point of current reversal on the trigger−wire current trace is coincident with the collapse of the anode voltage waveform; this has already been shown to be due to growth of the main discharge current, as shown in fig. (4.23).

In view of the dependence of trigger−wire pulse duration on the growth of current in the main gap, it is not possible to explain the effects of C_c via a simple circuit model. However, during the pre−breakdown period (main gap), the rise time of the anode voltage can be estimated from the circuit model of fig. (4.16) and an approximate value obtained for the trigger−wire current. It can be shown from analysis of this circuit that the coupling capacitance has a marginal influence on the magnitude of the trigger−wire current. Although increasing C_c increases the fraction of the anode voltage appearing across the trigger−wires, this has the additional effect of reducing the rise−time. Over this range of C_c these effects tend to cancel each other out, giving rise to a constant dV/dt and hence trigger−wire current.

The results presented so far in this section provide a good description of how the

trigger−wires behave, in terms of operating currents and voltages, and some simple design rules can be derived through which it is possible to optimize the critical trigger−wire parameters. No attempt has been made thus far to describe the process operative in the breakdown of the trigger−wire/cathode gap, although it has been found that the breakdown voltage is in the range 1000 − 1500 V. From this measurement it can be concluded that the maximum field strength − including the effects of electrode geometry − is of the order of 10^5 − 10^6 V/m.

In view of the very short statistical time lag observed in the trigger−wire/cathode discharge, some mechanism, other than background radiation sources, must be responsible for the production of initiatory electrons. It would appear that the most likely candidate is field emission from the cathode. However, the applied field necessary for field emission is of the order of 10^7 − 10^8 V/cm [4.1], which is two orders higher than the maximum field in this case. Nevertheless, as pointed out by Morgan [4.24], the field may be enhanced locally due to sub−microscopic irregularities and the applied field required for field emission could be considerably lower than the accepted values quoted above.

Upon the release of electrons from the cathode, the current grows rapidly under the applied field. For the breakdown voltage of approximately 1500 V the corresponding reduced field is of the order of 10^{-15} V cm^2. With reference to the tabulated values for α and η (see reference 4.2), it is clear that this field is below the level required for streamer formation and the discharge is in the classical Townsend regime. It is therefore highly unlikely that the trigger−wire/cathode discharge will produce much UV, particularly in the 120 nm waveband, and it can be concluded that practically no volumetric preionization of the main anode/cathode gap occurs.

The above arguments are valid for both single−shot and high frequency pulsed conditions. However, it should be noted that measurements of the trigger−wire voltage and current on single−shot produced erratic waveforms. Indeed, with some pulses the trigger−wire/cathode gap did not break down at all. This is in contrast to operation in the continuous pulse mode where the voltages and current traces were very stable, even at 100 Hz PRF. Although no recordings are available for presentation here, it was observed that both current and voltage waveforms became more stable at higher PRF's. This could be due simply to changes in the operating voltages of the pulser circuit, as is common with all capacitive circuits where resonant charging is employed and charge leakage is significant. However, it is believed that some other mechanism is responsible for stabilizing the trigger−wire breakdown waveforms. It may be possible that residual preionization from the previous pulse is significant. This could be confirmed by spectroscopic studies of the gas during the inter−pulse period.

The results presented in this section are important as they quantify the performance of the trigger−wires. Before any final conclusions can be drawn on the performance of the trigger−wires a final assessment must be made of improvements gained in discharge stability. This will be considered in section (4.5).

(4.4.4) Design and Development of an Independent Preionizer.

It was decided to examine the benefits of delaying the main anode voltage pulse with respect to the preionizing pulse. To obtain the desired control over the preionizing pulse, both in terms of peak current and firing time relative to the main voltage pulse, a new "preionizer" circuit was designed to supply the trigger−wires independently of the main pulser.

Circuit Design.

In designing the preionizer circuit the first problem was to establish a reasonable specification for the output pulse voltage and rise−time. It was decided not to vary the peak current significantly from the values obtained with direct capacitive coupling. The following specification was felt to be attainable with current thyratron technology, without recourse to pulse compression circuits.

Effective load capacitance	C_e	= 7 - 11 nF
Peak trigger-wire voltage	V	= 3.0 kV
Current pulse duration	τ	= 500 ns
Rate of rise of voltage	dV/dt	= 6.0 kV/μs

With the above specification, the maximum trigger−wire current is 66 Amps. A lower peak voltage was chosen simply to reduce the power rating of the circuit; in any case, the peak voltage need only be above the trigger−wire/cathode breakdown voltage (approximately 1500 V) since the current is controlled by dV/dt.

Fig. (4.37) illustrates the design of the preionizer circuit, which utilizes a hydrogen thyratron to transfer charge from an intermediate storage capacitor C_1 to the effective trigger−wire capacitance C_e. The transfer of charge is controlled by the inductance L_1, thus, the equivalent circuit of the output stage is a series CLC circuit, fig. (4.38). The following expressions can be given for the capacitor voltages during the transient [4.25].

$$Vc_2 = [\, Vc_1(0) - Vc_2(0) \,] \quad \frac{C_1}{C_1 + C_2} \quad [\, 1 - \cos \omega t \,] \qquad (4.29)$$

$$Vc_1 = Vc_1(0) \left[1 - \frac{C_2}{C_1 + C_2} (\cos \omega t - 1) \right] \qquad (4.30)$$

Where C_2 is the equivalent series capacitance of C_e and C_c and $Vc_1(0)$ and $Vc_2(0)$ are respectively the initial voltages on capacitors C_1 and C_2. The resonant frequency ω is given by

$$\omega = \frac{1}{\sqrt{(L_1 C)}} \qquad (4.31)$$

where C is the equivalent capacitance of C_1 in series with C_2

$$C = \frac{C_1 C_2}{C_1 + C_2} \qquad (4.32)$$

Since the thyratron will prevent current reversal, C_2 will reach a peak voltage at time $t = \tau$, where τ is the width of the half sinusoid, given by:

$$\tau = \pi \sqrt{(L_1 C)} \qquad (4.33)$$

The capacitor voltages at the end of the cycle, for the special case of $Vc_2(0) = 0$ can then be expressed as

$$Vc_2 (t=\tau) = \frac{2 Vc_1(0) C_1}{C_1 + C_2} \qquad (4.34)$$

$$Vc_1 (t=\tau) = Vc_1(0) \frac{C_1 - C_2}{C_1 + C_2} \qquad (4.35)$$

In addition, the circuit current can be calculated from

$$I (t) = \frac{Vc_1(0)}{\sqrt{(L_1/C)}} \sin \omega t \qquad (4.36)$$

Full details of the design of the preionizer circuit can be found in appendix C1. It is sufficient to note here that the main problem associated with the development of the circuit is to ensure recovery of the thyratron S1. Although this will switch off at the point of current reversal, as C_1 is resonantly charged from a DC supply, it is possible that the thyratron may become forward biased before it has had sufficient time to recover. The transient characteristics of the preionizer circuit, as described by equations (4.34), (4.35) and (4.36) are illustrated in fig. (4.39). It can be seen that in order to increase the time available for recovery, capacitor C_1 is made smaller than C_2, giving a negative residual on C_1 at the point of current reversal. This also slightly increases the peak voltage on C_1 at the end of the DC resonant charge cycle

[4.26].

It should also be noted that the output from the pulser circuit is capacitively coupled to the trigger−wires via the capacitor C_c. This arrangement was selected in order to prevent any possibility of the thyratron latching on. For the maximum design load of C_e = 11 nF and a coupling capacitance C_c = 0.1 μF, a value of C_1 = 8 nF was chosen to give sufficient overswing on C_1. For these values and a peak output voltage across the trigger−wires of 3.0 kV, C_1 must be resonantly charged to 3.73 kV. For a pulse duration of 0.5 μs, the required inductance is L_1 = 5.7 μH, giving a peak thyratron current of 104 Amps.

A glass envelope thyratron (EEV type CX1191) was selected for the preionizer circuit, as this combined excellent recovery characteristics with a peak current rating of 400 Amps and a peak inverse voltage rating of 16 kV. The CX1191 thyratron is triggered by a pulse on grid 2 from the CX1191 trigger circuit, as shown in fig. (4.40). This is almost identical to the circuit used for the FX2530 thyratrons in the main pulser trigger units (see section 3.2). The main switching element in the circuit is an IRF 740 MOSFET, the output of which is coupled to the grid via the pulse transformer PT1. The circuit employs a control bias of −100 V and has a forward drive impedance R_1 = 100 Ω. Fig. (4.41) shows the recorded output pulse voltage from the trigger circuit with an FET voltage of 326 V and grid 2 connected to ground with a shorting link. The peak trigger voltage is 309 V, with a duration of approximately 1 μs and a rate of rise of voltage dV/dt ≈ 0.73 kV/μs. This is just below the manufacturers quoted figure of 1 kV/μs, however, this was found to be acceptable and no modifications were made to the circuit to improve this.

Timing between the main pulser circuit and the preionizer circuit was achieved by adding an extra fibre−optic emitter on the thyratron firing card (see section 3.5.1). This modification allowed the preionizer to be fired up to 10 μs in advance of the main discharge thyratron. The reciever/amplifier circuit used in the main pulser trigger units was also used in the preionizer to drive the IRF 740.

The DC resonant charge circuit for C_1 was designed for a maximum PRF of 10 kHz. A 90 μs charge cycle was chosen, giving a required charging inductance L_c = 0.1 H and a peak charging current of 0.53 Amps. This was manufactured, as illustrated in fig. (4.42), from two FX3860 ferrite U cores, with 565 turns split between the two bobbins. A series string of 8 BYW−56 avalanche diodes was used for the charging diode D_1.

Fig. (4.43) shows the schematic of the complete preionizer circuit. Auxiliary power is

supplied at 240 V rms to the isolating trasformer T1, which feeds the CX1191 floating deck assembly. Power to the circuit is supplied by a 15 A single phase variac, which feeds the step−up transformer T3. The rectified and smoothed output from T3 supplies the output stage of the preionizer circuit.

Circuit Commissioning and Testing.

Before testing the preionizer circuit into the trigger−wires, the circuit was tested into a dummy load comprising 4 x 3000 pF capacitors in parallel. A 500 Ω ceramic tube resistor was connected across the load, to discharge the capacitors with a time constant of approximately 5 μs, as shown in fig. (4.44). The output voltage and current were measured with a TEK P6015 probe and Pearson current transformer. Fig. (4.45) shows the recorded voltage and current traces for a DC supply voltage of 1 kV, (measured across the 16 μF smoothing capacitor).

The capacitance of the dummy load was checked first by measuring the discharge time constant RC ≈ 5.75 μs. Combining this with the value of 500 Ω for the discharge resistor gives C_2 = 11.5 nF. This is the total series capacitance of C_c and C_d. From the recorded current pulse width τ it is possible to check the value of the inductance L_1:−

$$L_1 = \left(\frac{\tau}{\pi}\right)^2 \frac{1}{C} \qquad (4.37)$$

Where

$$C = \frac{C_1 C_2}{C_1 + C_2} = 4.72 \text{ nF}$$

Thus

$$\underline{L_1 = 7.3\ \mu H}$$

This is slightly higher than the design value of 5.7 μH, however, the value of L_1 is not critical as this needs to be changed to accommodate variations in the load capacitance, whilst maintaining a constant pulse length. As a final check, the peak thyratron current can be found from equation (4.36). Using the measured value for $Vc_1(0)$ = 1866 V and the above values for L_1 and C, gives I = 47.4 Amps. This is in good agreement with the recorded peak value of 49.5 Amps.

Following the circuit checks described above, the DC voltage was gradually increased up to 2 kV, at which point the output voltage was measured as 1680 V. Increasing the DC voltage further caused the thyratron to latch on. This was found to be due to two problems, as illustrated by the waveforms of fig. (4.46). These show that the actual charging time is 41 μs, instead of the design value of 90 μs. This was found to be due to the incorrect setting of the charging inductor air gap. It can also be

seen that capacitor C_1 does not fully discharge and a small positive voltage still remains at the point of current reversal. This, combined with the fast charge, time caused the thyratron to latch on. These results are not in agreement with equation (4.34) which predicts a negative residual voltage on C_1, since $C_1 < C_2 \approx 11.5$ nF. In addition, the measured peak output voltage at 2 kV i.e. 1687 V is below the theoretical value of 2184 V, based on $C_1 = 5$ nF, $C_2 = 11.5$ nF and the measured value of $Vc_1(0) = 3600$ V. This discrepancy can be attributed to switching losses in the thyratron and leakage in the discharge resistor.

In view of the above and in order to prevent the thyratron latching on, C_1 was reduced to 5 nF. The charging inductance was also increased to 164 mH to give the same 90 μs charging period; this was achieved simply by reducing the size of the core air gap to 1.53 mm.

Fig. (4.47) and fig. (4.48) show the effect of reducing C_1 from 8 nF to 5 nF. It can be seen that with $C_1 = 5$ nF and $V_{dc} = 1$ kV, the voltage overshoots to -250 V at the point of current reversal. Reducing C_1 also decreases the peak output voltage, since this is proportional to the ratio $C_1/(C_1 + C_2)$. With this value of C_1, the circuit was successfully tested up to a DC voltage of 2.75 kV, giving a peak voltage output of 2367 V.

Following the commissioning tests, the dummy load was removed and the output from C_c connected directly to the trigger−wires. The first tests into the trigger−wires were conducted without the main anode/cathode discharge. It was found that with a DC voltage of 1 kV the thyratron latched on when the unit was triggered; this was due to the low output voltage being insufficient to cause breakdown of the trigger−wire/cathode gap. In this case the load capacitance was just the measured stray capacitance $C_s = 0.36$ nF, and since this was much smaller than C_1, the thyratron was still forward biased at the point of current reversal. To overcome this problem a pre−load of 12 nF was connected in parallel with the trigger−wires, as illustrated in fig. (4.49). Fig. (4.50) shows the recorded trigger−wire voltage and current for this arrangement. The measured rate of rise of voltage ≈ 2.14 kV/μs together with a trigger wire current of the order of 850 mA, gives the effective trigger−wire capacitance $C_e \approx 0.39$ nF, which is in agreement with the measured stray capacitance. Clearly, at this voltage level the trigger−wire cathode gap is not breaking down.

It was observed that the trigger−wire current showed a sudden increase when the measured peak output voltage reached approximately 1480 V. Recorded waveforms with a DC supply voltage of 2.5 kV are shown in fig. (4.51). It can be seen that

once this voltage is reached, the current rapidly increases to a peak of 8.0 Amps. This was attributed to breakdown of the trigger−wire/cathode gap. Once breakdown is initiated, the charge stored in the pre−load capacitor C_d is quickly shared with the effective trigger−wire capacitance C_e; with reference to the results of section (4.4.3), this is approximately 7.6 nF.

In addition to the rapid increase in trigger−wire current, once breakdown is established, the trigger−wires obtain a negative residual voltage of −500 V, as shown in fig. (4.51). This was also observed with direct capacitive coupling. This can be explained by the circuit models of fig. (4.52), which attempt to show the sequence of events occuring during the pulse. After the thyratron is fired the voltage on C_d rises and since $C_c \gg C_s$, most of this voltage also appears across the trigger−wire/cathode gap. When the critical voltage is reached across C_s, the trigger−wire/cathode gap breaks down and the effective trigger−wire capacitance increases to $C_e \approx 7.6$ nF as a discharge is established between the trigger−wires and cathode. At this point in time the total load capacitance on the pulser circuit is approximately 20 nF. This state continues until the voltage ΔV across C_s falls below the critical level for maintenance of the discharge. The discharge subsequently terminates, however, this leaves a residual electron charge on the surface of the dielectric, giving rise to a negative residual voltage on the trigger−wires. At the instant the discharge terminates, the negative residual voltage will also appear across the dummy load capacitance C_d. This leaks away through the leakage resistor R_l, giving zero voltage on the load capacitance at the start of the next pulse. However, due to the residual charge −Q stored on the trigger−wires, the applied voltage on susequent pulses must rise to a level sufficient to overcome this charge, before the trigger−wire/cathode gap will break down.

The residual voltage appears mostly across the glass−to−cathode stray capacitance C_{gc}, since this is much smaller than the wire−to−glass capacitance C_e. As C_s (measured stray capacitance) is simply the series combination of C_{gc} and C_e, it is possible to calculate a value for C_{gc}. With $C_e = 7.6$ nF and $C_s = 0.36$ nF, this gives $C_{gc} = 0.38$ nF. Since the residual voltage is measured across C_s, it is possible to calculate the magnitude of the residual charge $Q = 0.36\text{x}10^{-9} \times 500 \triangleq 0.2\ \mu C$.

It is clear that because of the need for the dummy load capacitance, the output voltage will be lower than the design value, as the combined load capacitance is now 20 nF. With $V_{dc} = 2.5$ kV and $Vc_1(0) = 4.38$ kV, the peak output voltage should be:

$$V_o = \frac{2 \times C_1}{(C_1 + C_2)} \times Vc_1(0) = 1752 \text{ V}$$

This compares with a measured peak value of 1350 V relative to ground and a residual voltage of −500 V, as shown in fig. (4.51). This discrepancy is due to both circuit losses and the effect of the residual charge.

Although the above tests demonstrated the problems in driving a high current into the trigger−wires, with the resultant current being much smaller than the design specification, it was nevertheless possible to demonstrate breakdown of the trigger−wire/cathode gap. This was achieved at PRF's up to 10 kHz with a maximum trigger−wire current of approximately 10 Amps. When the preionizer was running a glow discharge could be seen between the trigger−wires and cathode, indicating that the gap was breaking down uniformly along the electrode.

The preionizer was finally tested with the main pulser also running. The preionizer firing time was synchronized with the main discharge thyratron by monitoring the trigger pulse at the grid of the discharge thyratron and the trigger−wire current, as shown in fig. (4.53). As the collapse of the thyratron trigger pulse is coincident with the rise of the anode voltage, this point was synchronized with the breakdown of the trigger−wire cathode gap. With a DC voltage of 2.5 kV on the preionizer, a uniform glow discharge was established between the anode and cathode when running at PRF's up to 1 kHz. It was found that due to the low output voltage from the preionizer, the discharge failed to fire on single−shot mode. It was also observed that the trigger−wire current and voltage were slightly different from the values recorded without the main discharge. A higher peak current was measured (15.5 Amps as compared to 8.0 Amps) as well as a higher peak voltage (1723 V as compared to 1350 V). The residual voltage was also reduced from −500 V to −420 V.

Clearly, the preionizer circuit performance falls short of the design specification, both in terms of peak output voltage and peak trigger−wire current. This is due to the problems associated with driving the trigger−wires. In order to obtain the same current and voltage levels, as generated by direct capacitive coupling, some improvements are required to the circuit. A pulse transformer output stage with a saturating inductor would provide the optimum solution. However, the circuit described above, with the provision of a dummy load capacitance, has been shown to be capable of initiating a uniform glow discharge in the main electrode gap. This circuit was used to examine the effects of delayed firing of the main voltage pulse. The results of this work are reported in section (4.5). With an improved preionizer circuit design it would be possible in future work to investigate the effects of varying the peak trigger−wire current.

(4.5) DISCHARGE STABILITY.

The maximum attainable laser power depends critically upon the ability to generate a homogeneous and stable glow discharge in the laser cavity. With the high specific energy loadings typical of pulsed CO_2 lasers, the glow discharge is inherently unstable and if insufficient care is taken in sustaining the discharge over the excitation pulse length, the discharge will very rapidly deteriorate into highly conducting arcs, with subsequent loss of CO_2 vibrational excitation (00^01). In some cases the discharge will simply become striated with intense conducting filaments, with a visible glow still present throughout the discharge volume. At very high specific energy loadings the glow may be suppressed completely with a single arc carrying the discharge current. If adequate preionization conditions are not established prior to application of the excitation pulse, a homogeneous glow discharge may not develop. This phenomenon should be distinguished from the glow-to-arc transition, which occurs after a given time even when the discharge is established uniformly. It is possible to avoid the glow-to-arc transition by keeping the pulse length short in comparison to the arc formation time [4.27]; a technique which is used extensively in TEA CO_2 lasers. However, it is not possible to take advantage of this in the present application as matarials processing requirements dictate both the discharge power loading and excitation pulse duration. It is therefore of interest to examine the stability of the discharge at the desired excitation level and pulse length and to examine the critical dependence of the glow-to-arc transition on the design of the discharge cavity.

(4.5.1) Gas Discharge System Development.

The design of the gas discharge system, as detailed in section (2.3) was based on the experimental results of Khahra [4.9] and on work conducted in a prototype discharge chamber. The electrode system developed, as shown in fig. (4.55), utilized transversely mounted trigger-wires, these being chosen principally because of mechanical design considerations and additionally because the straitions produced in the discharge by the trigger-wires were transverse to the direction of beam propagation and as such would not affect resonator mode development. The trigger-wires were split into six sections for ease of manufacture and were electrically connected by brass trigger-wire clamps. This arrangement allowed the trigger-wire/cathode spacing to be set to the desired level and permitted the electrodes to be aligned independently of the trigger-wires.

The first series of discharge experiments was conducted in the laser cavity before completion of the gas recirculator; the cavity being vacuum sealed on the end flanges and gas windows by perspex covers. With static gas conditions in the cavity, the discharge could only be fired in single shot or with a short burst of pulses. The

initial tests on the discharge also facilitated final commissioning of the pulser circuit. For these tests the pulser was fed from the main DC power supply. To build confidence with the system, a 1:1:8 mixture at a total pressure of 30 mbar was used as this had proven to be stable in the previous tests in the discharge chamber. With a PFN voltage V_{no} = 11.3 kV (50% tap setting on main transformer) and the full 10 μs PFN, it was found that the discharge was stable on single shot, however, due to the low gas pressure, the energy input into the discharge was very small $E_d \approx$ 0.97 J. At a PRF of 100 Hz and a burst period T_b = 100 ms, arcing was always observed in the centre of the electrodes. However, it was found that the arcing occured at the end of the pulse train and up to seven pulses could be input into the gas at this PRF and energy loading, without arcing.

Following the above tests the gas recirculator was commissioned and all further tests were conducted with flowing gas. Cavity flow-shaping was not installed at this stage as it was intended to manufacture this from machinable-ceramic once the electrode geometry was finalized. It should therefore be noted that the flow velocity profiles would have been highly non-uniform and care should be taken when comparing the figures given here against results with full cavity flow-shaping. The blowers were installed initially at the lowest speed setting of 935 rpm.

In order to increase the power into the discharge a 1:1:4 mixture at a total pressure of 84 mbar was examined, with the gas recirculator running and the full 10 μs PFN charged to 11.3 kV. The discharge voltage and current - measured on the plateau of the pulse - for these settings were respectively 4.02 kV and 72.3 A, corresponding to an input energy E_d = 2.90 J. With a burst length of 100 ms the discharge was found to be stable up to a PRF of 600 Hz; at PRF's above this level arcs were observed on the downstream side of the electrodes, beteween the side of the cathode (join between base and top plates) and the brass trigger-wire clamps, as illustrated in fig. (5.56). A piece of 3/8" perspex was clamped to the side of the cathode in an attempt to prevent these arcs, as shown in fig. (4.57). No improvement in discharge stability was found, as the arc simply travelled around the perspex to the trigger-wire clamp as before.

Some tests were conducted with the perspex insulators in place, with a 1:1:8 mixture at a total pressure of 60 mbar. With a burst length of 1 second it was possible to take the PRF up to 600 Hz before arcs appeared between the trigger-wire clamps and the cathode; at this PRF the main discharge was still homogeneous. As the PRF was increased to approximately 1.8 kHz, the cathode/trigger-wire arc appeared to detach from the brass clamp and transfer to the anode, producing a highly curved arc on the downstream side of the electrodes, as illustrated in fig. (4.58). Even at this

frequency a homogeneous discharge was still present between the anode and cathode. As the PRF was increased further to approximately 2 kHz, the external arc became very intense and the anode/cathode glow was extinguished. On some occasions the arc detached to the cathode and transferred to the edge of the cavity gas outlet window.

As the above problems were initiated by the trigger−wire/cathode arc, it was decided to replace the brass clamps by PTFE clamps, as shown in fig. (4.59). It was hoped that by completely insulating the trigger−wire joints and minimising the field generated by the trigger wire supports that the arcs would be suppressed. With this arrangement it was necessary to solder the trigger wire sections together for electrical continuity. With these modifications only occasional arcs were observed from one of the supports and with a burst length of 10 ms, it was possible to take the PRF up to 5 kHz without arcing. It was, however, observed that the discharge luminosity decreased with increasing PRF. Inspection of the anode voltage and current waveforms revealed that the discharge voltage collapsed after approximately 2 μs, to a few tens of volts, whilst the current increased to the full PFN short circuit level. In addition, the collapse of the voltage waveform was not experienced on single shot, only on high frequency burst mode.

It was found that the short circuit waveforms were due to breakdown inside the anode vacuum leadthroughs, as illustrated by fig. (4.60). This problem was cured by insulating the copper lead within the ceramic shield, as shown in fig (4.61). With all four anode lead−throughs modified in this way, the above test with the 1:1:8 mixture was repeated. This time the PRF could only be increased to 1600 Hz (10 ms burst length) before arcs appeared in the main discharge. The arcs appeared first at the knee of the electrodes on the downstream side. It was found that the arcs could be moved to the knee at the other side of the electrode by adjusting the electrode alignment (approximately 1 mm measured at the end). In transferring the arc to the other end, at an intermediate point in the alignment, the arcs were observed to oscillate between the two ends of the electrodes. Clearly, conditions at the knee were more favourable for arc development. It was felt that this was due to the combined effects of non−uniform electric field and poor gas flow over the end sections of the electrodes; this being due to the absence of cavity flow−shaping and the fact that the electrodes were longer than the gas inlet window.

To overcome the above problems several modifications were made to the electrodes; these included reducing the length to the same as the gas window (i.e. 1000 mm) and increasing the edge radius of curvature to 3/8", as shown in fig. (4.57). In addition, as faint discharges could be seen between the bottom plate of the anode, tracking across the surface of the epoxy supports to the cathode, the brass plate on the

bottom of the anode was replaced with a piece of high density polyethylene.

The stability results reported thus far have been for very low pressure helium rich mixtures, where the conditions are unsuitable for laser operation, as the specific energy input is below the level required for gain in the laser cavity [4.9]. However, the above tests served to highlight several critical aspects of the design of the gas discharge system and with the above electrode modifications, it was possible to extend the operation to much a higher pressures. Moreover, the modifications permitted the discharge to be run continuously, allowing a more thorough analysis of discharge stability to be undertaken.

(4.5.2) Single Shot Discharge Stability Limits.

During the initial electrode development tests it was found that for the low pressure mixtures examined, the discharge was always stable on single shot. Clearly at such low energy inputs, the growth time for the glow-to-arc transition is longer than the 10 μs pulse duration. In order to obtain the desired output pulse characteristics from the laser, it was necessary to extend the stable operational envelope to much higher gas pressures. It is therefore of interest to consider what the stable single-shot discharge energy loading is, as this sets an upper limit on the attainable laser pulse energy. Khahra [4.9] found that up to 9 J could be deposited in the helium free gas mixture, with a pulse length of 10 μs and a maximum pressure in the range 100 - 120 torr. The concentration of CO_2 in the gas mixture was found to be critical, with stable discharges only being obtained in mixtures with CO_2 partial pressure below 35 torr. Due to overall scale of the present development, it was not possible to conduct a comprehensive series of tests on the stability of the full range of gas mixtures. Although such a study would have provided valuable information, it was decided to concentrate on the mixtures identified by Khahra to be the most suitable, and to confirm the experimental results previously obtained.

Table (4.4) summarizes the results reported by Khahra, which were obtained by gradually increasing the PFN voltage until arcing occurred; a small gas purge was used to counteract the effects of atmospheric leakage and dissociation. To duplicate Khahra's experimental conditions tests were conducted without the blowers running; no gas purge was used as the volume of the system ($\approx$ 2.4 m^3) was much larger than Khahra's prototype. As the instrumentation was calibrated in milli-bars, the nearest equivalent gas mixture was used. In order to obtain the desired control over the PFN voltage, the pulser was fed from the high voltage commissioning supply, fig. (3.56). The results obtained are summarized in table (4.5).

Table (4.4) Khahra's single-shot discharge stability limits.

Mixture Torr	E/P $Vcm^{-1}torr^{-1}$	V_d kV	V_{no} kV	I_d Amps	E Joules
20:20:80	11.0	5.41	17.1	117	6.32
20:40:40	18.0	7.34	19.0	116	8.56
30:30:0	29.2	7.13	20.0	129	9.0

Table (4.5) Single-shot discharge stability limits.

Mixture milli-bar	E/P $Vcm^{-1}torr^{-1}$	V_d kV	V_{no} kV	I_d Amps	E Joules
26:26:104	11.3	4.8	19.7	150.5	7.56
27:54:54	16.1	6.6	19.0	126.5	7.34
40:40:0	26.8	6.4	19.0	132.5	7.18

From inspection of the above results it would appear that no improvement in discharge stability has been achieved. However, the results reported in Table (4.5) were obtained with highly accurate voltage and current probes, and in addition, the quoted energy input was obtained directly form the LeCroy 9400 digital storage oscilloscope, as given by the recorded V−I traces, fig's (4.63), (4.64) and (4.65). It is likely therefore that the dicrepancies are due to the limitations of Khahra's instrumentation and to the fact that integration of the discharge energy was done by hand from photographs of the V−I traces. In particular, it is apparent that Khahra's voltage measurements are much higher than the values obtained in the present investigation; this alone could account for the higher values of input energy.

As the 1:1:4 mixture gave the highest allowable energy input, it was decided to examine the stability of this mixture at even higher pressures. When the total pressure was increased to 204 mbar, it was not possible to increase the discharge energy input above the value quoted in Table (4.5) before arcing occured. Typical discharge voltage and current waveforms for this mixture are shown in fig. (4.66); the voltage can be seen to collapse after approximately 5 μs as the glow discharge collapses into an arc.
In conclusion, the figures given for discharge energy in Table (4.5) represent the maximum attainable with the present electrode/preionization system. Although these energy inputs are sufficient to meet the laser pulse characteristics required for machining, the values obtained are much lower than reported by Kline *et al* [4.28] for a similar device. For instance, Kline found that up to approximately 100 J/litre

could be input into a 10 litre discharge volume at a total pressure of 800 torr, with a pulse length of 12.4 μs. This system comprised a 10x10x100 cm^3 discharge volume, initiated by 480 spark preionizers positioned behind a flat mesh cathode. Extrapolating this result to the present discharge volume of 3 litres implies a maximum allowable energy input of the order of 300 J at the same operating pressure. Since the only difference between the system under investigation here and the system reported by Kline, is the preionization source, it can be concluded that the maximum allowable input energy reflects the fundamental limitations of the trigger–wire, double–discharge system.

(4.5.3) Continuous Pulse Mode Stability.

Final discharge stability tests involved an assessment of the parameters controlling the allowable continuous power into the discharge. The first test was performed to determine the maximum continuous operating PRF as a function of gas pressure, whilst holding the gas flowrate constant. Unfortunately, it was not possible to hold the pulse energy constant during this test as the discharge voltage increases with increasing gas pressure. Although this could be done by reducing the PFN voltage in accordance with increasing gas pressure, the desired control over the PFN voltage was not available on continuous running. The results reported therefore reflect a variation in both pressure and discharge energy. The experimental settings of the first test were as follows:

Blower speed 2453 rpm (no cavity flow–shaping)
PFN pulse length τ = 10 μs PFN voltage V_{no} = 11.0 kV

With the above settings the gas pressure was increased to the desired level and the pulser switched on at a PRF of 100 Hz. The PRF was then gradually increased until arcs appeared in the discharge; this point was taken as the maximum PRF, f_{max}. Although the PRF could be increased above f_{max} to the point of complete glow–to–arc transition, it has been found that the increase in power obtained does not significantly increase laser output power due to optical inhomogeneities in the gain meduim (see section 5.1). Table (4.6) summarizes the results obtained for a 1:1:8 gas mixture.

It was observed that arcs began to develop first in the centre of the electrodes on the downstream edge; these became more intense as the PRF was increased, spreading upstream into the discharge. The PRF at which arcing occured was significantly reduced by the presence of any irregularities on the electrodes or trigger–wires. For instance, a crack in the trigger–wire glass limited the maximum PRF to a few

hundred Hertz. The results for 130 mbar and 140 mbar reflect the sensitivity of the discharge to electrode surface irregularities as these results were obtained with a small pit on the anode due to intense arcing in the earlier tests; the maximum attainable PRF is therefore lower than expected.

Table (4.6) Continuous discharge stability limits.

Pressure mbar	V_d V	I_d Amps	E Joules	f_{max} Hz	P Watts
60	1710	96.5	1.78	1111	2061
70	1930	91.8	1.92	1101	2174
80	2180	89.0	2.06	1065	2215
90	2530	83.5	2.21	1000	2160
100	2750	84.0	2.43	876	2128
110	3000	78.6	2.50	842	2181
120	3230	75.0	2.57	752	1933
130	3510	72.4	2.76	627	1731
140	3767	77.8	2.84	600	1704

NB. 1:1:8 gas mixture, no intra-cavity flow-shaping

It is apparent from the results of Table (4.6) that the maximum PRF decreases with increasing gas pressure and pulse energy. More surprising, however, is that the maximum discharge power remains approximately constant over this range of operating conditions. It is not clear from these results why this should be so? It is interesting also that higher PRF's can be attained in burst mode e.g. for a 1:1:8 mixture at a total pressure of 60 mbar and a burst length of 50 ms, it is possible to take the PRF up to 2 kHz before arcs appear. It is possible to conclude, since the glow-to-arc growth time is longer than the 10 μs pulse length at these pulse energies, that the occurene of arcs at a given PRF somehow reflects the accumulated growth of the instability over a sequence of pulses. This can only occur when the gas residence time is greater then the excitation period $1/f_{max}$. At a blower speed of 2453 rpm, the mean gas flow velocity is approximately 41 m/s, giving a gas residence time $t_{gc} \approx 1.8$ ms; this is greater than the excitation period for all conditions in Table (4.6).

It was found that the gas flowrate was the major parameter controlling the allowable discharge power. For the above tests the blowers were run at the maximum speed in order to identify the absolute maximum discharge power ratings and, due to system development constraints, it was not possible to conduct a thorough investigation of the

critical dependance of discharge power on gas flowrate. However, the results given in table (4.6) can be compared with results obtained with the cavity flow-shaping in place, as detailed in Table (4.7). It can be seen that a significant increase in discharge power was obtained by the improvements in gas velocity profile.

These results demonstrate the importance of gas flow in maintaining a glow discharge under conditions of continuous pulse excitation. It is clear that at these levels of excitation it is possible to run with a cavity gas residence time greater than the excitation period i.e. more than one pulse can be input into each block of gas passing through the cavity. It is useful to qauntify this in terms of a "clearing ratio" CR, defined as

Table (4.7) Continuous discharge stability limits.

Pressure mbar	V_d V	I_d Amps	E Joules	f_{max} Hz	P Watts
60	1850	100	2.07	1213	2511
70	2070	94.5	2.105	1267	2667
80	2310	82.5	2.07	1200	2484
90	2600	88.0	2.48	1044	2589
100	2820	79.5	2.43	977	2374
110	3120	74.0	2.45	897	2198
120	3320	77.0	2.70	865	2335
130	3510	71.5	2.73	850	2321
140	3670	67.5	2.81	739	2077

NB. 1:1:8 gas mixture with intra-cavity flow-shaping.

$$CR \equiv \frac{\text{minimum time between arc-free pulses}}{\text{cavity gas residence time}}$$

$$CR = \frac{\upsilon}{f_{max}\, W} \qquad (4.38)$$

Where υ is the mean gas velocity, f_{max} is the maximum PRF and W is the electrode width. It is possible to calculate the clearing ratios for the above results, however, CR would in this case be dependent upon both pressure and discharge energy. To elucidate the true relationship between clearing ratio and input energy, a second test was conducted; this time the mixture total pressure was held constant and the input energy varied by changing the PFN voltage. Table (4.8) details the results for a 1:1:8

mixture at a total pressure of 100 mbar. These results are for the same gas flow conditions as Table (4.7) i.e. blower speed 2453 rpm.

Table (4.8) Continuous dicharge stability limits.

V_{no} kV	V_d kV	I_d Amps	E Joules	f_{max} Hz	P Watts	CR
10.96	2.70	83.4	2.32	980	2268	0.560
13.15	3.06	99.0	2.98	808	2399	0.685
15.79	2.62	128.0	3.77	600	2262	0.923

1:1:8 gas mixture 100 mbar. Blower speed 2453 rpm.

It can be seen that the clearing ratio increases with increasing input energy, with a minimum value CR = 0.56 being obtained at the lowest input energy. These results are not in agreement with the results of Dzakowic [4.29] who found a minimum clearing ratio of CR = $\sqrt{3}$. Fig. (4.67) shows the results reported by Dzakowic for a 55 cm^{-3} discharge volume with a 1:1:8 mixture at 400 torr and gas flow velocity of 41.5 m/s. Three distinct regions can be identified. At low specific energy densities the clearing ratio is dominated by boundary layer diffusion; a value of CR = $\sqrt{3}$ is found for laminar boundary layers. At high energy inputs the single-pulse glow stability limit is reached and the clearing ratio tends to infinity. In the region between these two extremes it is found that the clearing ratio is dominated by the expansion of the discharge products in the upstream direction, as illustrated by fig. (4.68). It is therefore a necessary requirement to clear the discharge products expanded into the upstream region, as well as those within the discharge volume, before the following pulse is applied.

Fig. (4.68) also illustrates the spatial and temporal position of the pressure waves accompanying the expansion of the gas. For the case where the current pulse lasts only a few microseconds, the glow discharge time is negligible when compared with the gas displacement time. The inter-electrode gas undergoes constant pressure heating during the discharge pulse. A shock wave forms and separates from the contact surface (boundary between heated and unheated gas); this moves away from the heated region with a speed greater than sonic. The contact surface also moves out into the surrounding region, but with a speed which is slightly less than sonic. The contact surface stops its outward movement when the outward expansion waves, moving at sonic velocity in the discharge products, overtakes the contact surface (for clarity in the figure only the leading edge of the expansion wave is shown). The contact surface is displaced a distance X into the surrounding gas at this point in time. The characteristics of the expansion process as described have been confirmed

experimentally by Baranov *et al* [4.30] using both Schlieren and interferometric flow visualization techniques.

If the gas velocity is much smaller than the sonic velocity, the gas expansion time will be a negligibly small fraction of the gas clearing time τ_{clear}. This can be expressed as:

$$\tau_{clear} = \frac{X}{v/\beta} + \frac{W}{v} \qquad (4.39)$$

The equilibrium position of the discharge products can be found from an analysis of the pressure wave propagation, employing the common techniques used in shock tube theory [4.31]. However, detailed calculations are required for the expansion waves and it is simpler to obtain the equilibrium solution from simple thermodynamic theory. Assuming that the gas undergoes constant pressure heating during the pulse and isentropic expansion after the pulse, then the resultant clearing ratio, based on equation (4.38), can be shown to be equal to

$$CR = 1 + \frac{1}{2}\beta\,[\,(1+\epsilon)^{1/\gamma} - 1] \qquad (4.40)$$

where

$$\epsilon = \frac{(1-\eta)E_i}{Vol\ \rho\ C_V\ T}$$

is the normalized energy density, β is the ratio of approach to inter-electrode flow areas, γ is the ratio of specific heats, ρ and T are respectively the density and temperature of the unheated gas, η is the electrical to optical energy conversion efficiency and $(1-\eta)$ is the fraction of the electrical input energy that ends up as heat. For the results of Table (4.7) ϵ is of the order 0.01 to 0.02. It is therefore possible to conclude that the expansion of the heated gas is negligible in this case. It is possible to show – from basic shock wave theory – that the shock generated at the levels of excitation reported here is indeed very weak ($P/P_o \approx 1.02$).

In comparing the results obtained with the experimental results of Baranov and Dzakowic, it is not clear what the dominant process controlling the clearing ratio is. As gas expansion is negligible it could be concluded that boundary layer diffusion is the dominant process. However, the results obtained are not in agreement with those of Baranov. The discrepancy may be due to the difference in experimental conditions, as the results reported by Baranov are for a pulse duration of 1 μs and, in addition, are at a higher specific energy density (40 mJ/cc as compared with 1 mJ/cc).

Final tests were conducted with the 1:1:8 mixture to maximise the single pulse energy

and continuous discharge power. It was found possible to run at a total pressure of 160 mbar with an input energy of 5.42 Joules and a maximum PRF of 420 Hz (10 μs PFN, 75% tap setting). Further increases in energy could not be realized by either increasing pressure or PFN voltage, without complete collapse of the glow. Attention was then focussed on other mixtures.

The stabilty of a 1:1:4 mixture at a total pressure of 156 mbar was examined under continuous pulse excitation. It was found that with the main transformer tap setting at 70% (corresponding to an input energy of 4.96 Joules.) and a PRF of 100 Hz, only occasional arcing was observed in the discharge. When the transformer tap setting was changed to 80%, intense arcs were observed at the knee on the electrodes, even at the minimum PRF of 100 Hz. At this setting a recording was taken of the discharge voltage and current, as shown in fig. (4.69); it can be seen that arcing occurs after approximately 7.4 μs. At this level of excitation it was not possible to increase the PRF above 200 Hz before the glow discharge collapsed completely. In an attempt to increase the mean discharge power, the excitation pulse duration was reduced to 7 μs by removing four meshes from the PFN. With the transformer tap setting at 80%, corresponding to an input energy of 4.73 Joules, as shown in fig. (4.70), the maximum PRF attained without flow-shaping was 383 Hz. When the test was repeated with the cavity flow-shaping in, the maximum PRF attained was 300 Hz. This was inconsistent with previous tests at 60% and 70% tap settings, which had shown improvements in maximum PRF with the flow-shaping in position.

It was observed that during a series of experiments on a single fill of gas that the discharge quality deteriorated with time. This was found to be true even when the discharge was not run for approximately fifteen minutes. As the last result for a 1:1:4 mixture was obtained at the end of a series of tests, the results were checked with a fresh fill of gas. It was found that for the same conditions the maximum PRF was now 470 Hz; this compares with the previous value of 300 Hz. It was concluded that the deterioration in discharge quality was the result of atmospheric leakage into the system. During the tests the leak rate was typically 1 mbar/hr, from which it is possible to calculate an O_2 contamination of approximately 340 ppm due to leakage over the fifteen minute period. This level of oxygen contamination is consistent with arcing in TEA laser systems, as reported by Yamabe *et al* [4.32]. The principal cause of arcing in TEA CO_2 lasers is found to be loss of preionization electrons by three-body attachment to O_2 molecules [4.33]. However, it has been shown that the discharge conditions under investigation here does not have such stringent preionization density requirements as those of TEA lasers, since the discharge breakdown is in the classical Townsend regime. It is therefore unlikely that the principal cause of arcing is the same in this case. Nighand and Wiegand [4.34] have shown that O^- ions play an

important role in the instability of CO_2 laser discharges. They found that when attachment is a strong function of electron temperature an attachment-induced ionization instability could occur. It is shown that a necessary condition for this to be satisfied is that the negative ion density become comparable to the electron density, and in this respect, clustering reactions involving the initial species of negative ion (O^-) and its parent molecule have been shown to play an important role. Given the calculated O_2 concentration in the laser gas, due to leakage alone, it is possible that the observed arcing is due to this ionization instability. Some important aspects of this instability phenomenon plus other relevant instability theory will be considered in section (4.5.4).

In conclusion, it has been found possible to run the discharge in a continuous pulse-mode with a 1:1:4 mixture at a total pressure of 156 mbar. The maximum attainable single-shot energy limit was 7.56 Joules. In conditions of continuous pulse excitation the maximum continuous discharge power was 2890 Watts, corresponding to a 7 μs pulse, a pulse energy E = 2.89 Joules and a PRF of 1 kHz. It was found that a 1:1:4 mixture at 160 mbar, with the full 10 μs pulse duration and an energy input of 6.06 Joules, gave the highest continuous laser output power; however, the maximum PRF attainable was limited to 400 Hz. Thus, although it is possible to obtain higher continuous discharge powers, this is usually achieved at a low pulse energy/high PRF and the increased power is not manifest as an increase in the laser output power because of reduced laser excitation efficiency.

(4.5.4) Theory of Discharge Instability Mechanisms.

In section (4.5.3) it has been sufficient to examine the effects of varying gas discharge parameters on the stability of the discharge, with no reference being made to the fundamantal processes operative in the glow-to-arc transition (GAT). It is intended in this section to consider some mechanisms responsible for the GAT, and thereby elucidate the principal source of the instability. As the GAT phenomenon is the manifestation of growth of an instability mode within the weakly ionized discharge plasma, it can be analysed by the techniques commonly employed in hydrodynamic stability [4.36].

Because of the highly non-linear nature of the plasma, several sources of instability exist, and a rather extensive description of the plasma is required in order to determine the dominant physical processes. However, as displayed in Table (4.9) - reported by Haas [4.11] - the characteristic times associated with the processes of importance are spread over a very large range (10^{-10} to 10^{-2} sec), permitting significant simplifications of the problem. This is indicative of the fact that for a very

TABLE 4.9 Characteristic times. Typical discharge conditions (diatomic molecule-atom mixture, $p \sim 10\text{-}100$ torr, $T \sim 300\text{-}600$ °K, $T_e \sim 0.5\text{-}2.0$ eV, $T_v \sim 1000\text{-}5000$ °K. $n_e/n \sim 10^{-8}\text{-}10^{-6}$, $l \sim 1$ cm; for a plane wave with wave number k the characteristic length $l = k^{-1}$).

	Process	Characteristic time	Range of values(sec)
I	Space-charge relaxation	$\tau_C = \epsilon_0/\sigma \sim \nu_m/\omega^2_{pe}$	$10^{-10} - 10^{-9}$
II	Collisional energy transfer		
i	electron heating	$\tau_e = (3/2)n_e\kappa T_e/(J_e^2/\sigma_e) = 3/2\nu_u^{-1}$	$10^{-9} - 10^{-8}$
ii	translation-rotation heating	$\tau_T = nC_pT/(J_e^2/\sigma_e) \sim (n/n_e)(C_p/K)(T/T_e)\nu_u^{-1}$	$10^{-3} - 10^{-2}$
iii	vibration heating	$\tau_v = n_m C_v^v(T_v)T_v/(J_e^2/\sigma_e) \sim (n_m/n_e)[C_v^v(T_v)/\kappa](T_v/T_e)\nu_u^{-1}$	$10^{-3} - 10^{-2}$
iv	vibrational relaxation	$\tau_{VT} = [n_a k_{10}(1-e^{-\epsilon/\kappa T})]^{-1}$	$10^{-4} - 10^{-2}$
III	Plasma kinetic processes		
i	direct ionization	$\tau_i = [nk_i]^{-1}$	$10^{-6} - 10^{-5}$
ii	electronic state ionization	$\tau_i^* = [n^*k_i^*]^{-1}$	$10^{-6} - 10^{-4}$
iii	attachment (dissociative)	$\tau_a = [nk_a]^{-1}$	$10^{-6} - 10^{-5}$
iv	detachment (direct neutral & associative)	$\tau_d = [nk_d]^{-1}$	$10^{-6} - 10^{-4}$
v	electronic excitation	$\tau_* = [nk*]^{-1}$	$10^{-6} - 10^{-4}$
vi	electronic quenching	$\tau_q = [n*k_q]^{-1}$	$10^{-6} - 10^{-5}$
vii	electron-ion dissociative recombination	$\tau_r^{(e)} = [n_p k_r^{(e)}]^{-1}$	$10^{-6} - 10^{-5}$
viii	ion-ion recombination	$\tau_r^{(i)} = [n_p k_r^{(i)}]^{-1}$	$10^{-6} - 10^{-5}$
IV	Transport and other processes		
i	sound propagation	$\tau_{S_T} = l/a$	$10^{-5} - 10^{-4}$
ii	translation-rotation energy conduction	$\tau_T = (nC_v l^2/\lambda_T^T)$	$10^{-3} - 10^{-2}$
ii	viscous dissipation	$\tau_\mu = \rho l^2/\mu$	$10^{-3} - 10^{-2}$
iv	vibrational energy conduction	$\tau_v = n_m C_v^v(T_v) l^2/l_v^v$	$10^{-2} - 10^{-1}$
v	electron thermal conduction	$\tau_{Te} = (3/2)n_e\kappa l^2/\lambda_e$	$10^{-7} - 10^{-6}$
vi	ambipolar diffusion	$\tau_{amb} = l^2/[(1-\sigma_e/\sigma)D_e]$	$10^{-5} - 10^{-4}$
vii	negative-ion diffusion	$\tau_{neg} = l^2/[(\sigma_n/\sigma)(n_e/n_n)D_e]$	$10^{-5} - 10^{-4}$

wide range of physical conditions the various instability modes are effectively decoupled. It can be seen that the characteristic time for electron energy relaxation is very short relative to the time required for ionization and attachment. Thus, the temporal response of electron energy density to a local disturbance is effectively instantaneous as compared to the time required for changes in charged-particle density: the electron properties can therefore be considered as quasi-steady. In addition, during evolution of the modes associated with the charged particle and electronically excited species production processes, the neutral gas properties are effectively frozen.

The criterion for the growth of the various instability modes relevant to the conditions occuring in convectively cooled CO_2 lasers have been detailed extensively by Haas [4.11]. Such plasmas are characterized by a value of fractional ionization below 10^{-6}, a mean electron energy of approximately 1 eV, and an effective vibrational temperature of the order of 5000 K. The calculations indicate that small amplitude fluctuations present within the discharge (e.g. neutral gas density, electron density) excite several different wave modes. These are listed below, together with the characteristic growth times.

space charge relaxation mode	10^{-10} - 10^{-8} sec
electron thermal mode	10^{-8} - 10^{-7} sec
ionization mode	10^{-6} - 10^{-5} sec
electronically-excited-species production mode	10^{-6} - 10^{-4} sec
sound mode	10^{-5} - 10^{-4} sec
vibrational energy relaxation mode	10^{-4} - 10^{-3} sec
heavy particle thermal mode	10^{-4} - 10^{-3} sec
vorticity mode.	10^{-3} - 10^{-2} sec

It is of interest to consider which of the above modes dominates the growth of instabilities for the discharge regime of interest here. For similar discharge conditions Nighand and Wiegand have reported that the ionization instability criterion can be satisfied when negative ion densities are comparable to the electron densities [4.34]. They have also reported that arcing can be initiated in CO_2 lasers by either a growth in translational or vibrational temperature [4.12]. This thermal instability has also been reported by Jacob and Mani [4.13]. The basic features of both of these modes of instability will therefore be considered and conclusions drawn regarding the experimental stability results of section (4.5.3).

Coupled Ionization and Negative−Ion Modes.

It is found that in the absence of negative ions that the ionization mode is always stable and decays on a time scale comparable to the ionization and electron positive−ion recombination times. However, if collisional attachment is important and substantial numbers of negative ions are present relative to the electron density, the essential features of the ionization mode are modified and an additional wave mode associated with the negative ions appears. Specifically, it has been found that when electron and negative ion densities are comparable and the electron attachment rate increases strongly with electron temperature, an ionization instability can occur.

For the positive column of the discharge plasma the electron conservation equation may be expressed in the form [4.34].

$$\frac{\partial n_e}{\partial t} = n_e\, n\, K_i - n_e\, n_p\, K_r^e - n_e\, n\, K_a + n_n\, n\, K_d \quad (4.41)$$

Where n_e, n, n_n and n_p are the respective number density of electrons, neutrals, negative−ions and positive ions. K_i and K_a are the mixture weighted electron rate coefficients for direct ionization and attachment, K_r^e is the positive−ion − electron recombination coefficient and K_d is the negative−ion electron detachment coefficient. In determining the instability criterion, the critical dependence of these rate coefficients on electron temperature T_e is required. Fig's (4.71) and (4.72) show the data for K_i and K_a as reported by Nighand *et al* [4.34]. It should be noted that for all the molecular species present in CO_2 laser discharge plasmas, except H_2O, the dissociative attachment reactions all lead to the production of the same negative ion O^-. Coefficients for the detachment of the electron from O^- by way of the associative attachment reaction

$$MN + O^- \rightarrow MNO + e$$

are well known for a number of effective detaching species, e.g. CO. When detachment is unimportant, positive−ion − negative−ion recombination balances attachment. Thus, the steady state form of equation (4.40) indicates that in this limit

$$K_i = K_a + \left(\frac{n_p}{n}\right) K_r^e \quad (4.42)$$

However, for almost any reasonable fractional ionization $K_a \gg (n_p/n)K_r^e$, thus self−sustained discharge operation requires that ionization balance the entire loss of electrons through attachment, i.e. $K_i \approx K_a$. This occurs for an electron temperature

in the range 1 − 2 eV as shown in fig. (4.73). This has been confirmed experimentally for the conditions of interest here by Khahra [4.9] and more recently by Hasan [4.2].

The relative magnitudes of the electron temperature dependences of the ionization and attachment coefficients have a fundamental influence on discharge stability. Therefore, it is convenient to define a parameter reflecting the electron dependence of the rate coefficient independent of its magnitude. The fractional, or logarithmic, derivative with respect to electron temperature is useful for this purpose i.e.

$$\hat{K} \equiv \frac{T_e}{K}\frac{\partial K}{\partial T_e} = \frac{\partial \ln K}{\partial \ln T_e} \qquad (4.43)$$

For the species corresponding to the data of fig's (4.71) and (4.72), the values of $\hat{K}_i$ are in the range 10 − 30, while the values of $\hat{K}_a$ range from approximately zero to 20. Haas [4.11] has shown that the quasi−steady relationship coupling the perturbation amplitudes T_{ek} and n_{ek} is expressed by the relation:

$$\frac{T_{ek}}{T_e} = \left(\frac{-2\cos^2\Phi}{1+\hat{\nu}_u-\hat{\nu}_m\cos 2\Phi}\right)\frac{n_{ek}}{n_e}$$

$$\frac{T_{ek}}{T_e} = \left(\frac{-2\cos^2\Phi}{\hat{\nu}'_u}\right)\frac{n_{ek}}{n_e} \qquad (4.44)$$

where $\hat{\nu}_m$ is electron momentum transfer collision frequency, Φ is the angle between the direction of the applied field and the direction of the wave propagation vector, as illustrated in fig. (4.74), and $\hat{\nu}'_u$ is defined as

$$\hat{\nu}'_u \equiv 1 + \hat{\nu}_u - \hat{\nu}_m \cos 2\Phi$$

The *caret* notation refers to the logarithmic derivative taken with respect to electron temperature. Equation (4.44) reveals two important properties of the response of the plasma to a local disturbance. Firstly, the disturbance in electron temperature and electron density are strongly coupled only along the direction of the steady applied field and current. Secondly, as numerical analysis of the gas mixtures and electron temperatures typical of CO_2 laser discharges show that the magnitude of $\hat{\nu}'_u$ is usually in the range 1 − 5 (i.e. a positive quantity), equation (4.44) indicates that the perturbations in T_{ek} and n_{ek} are usually 180^0 out of phase. Therefore, it can be concluded that in the majority of cases a positive local increase in electron density is *initially* accompanied by a decrease in electron temperature. This happens because of

the quasi-steady nature of the electron energy response and the typical relationship between the electron temperature dependences of the electron exchange and momentum transfer frequencies.

If temporal amplification of an initial disturbance in electron density occurs, an instability in the production and loss process will result. The possible occurence of this ***ionization instability*** in CO_2 laser plasmas can readily be assessed by examining the first order perturbation of the electron continuity equation (4.42). It can be shown that a positive feedback mechanism coupling disturbances in electron energy and particle conservation does not exist in recombination dominated plasmas [4.34]. Instability of the ionization mode is found to depend on the presence of negative-ions, with the instability criterion being given by

$$\left(\frac{-2\,\cos^2\Phi}{\hat{\nu}_u'} \right) \left(1 - \frac{K_a \hat{K}_a}{K_i \hat{K}_i} \right) n K_i \hat{K}_i$$

$$- \left(\frac{n_e}{n_p} n_p K_r^e + \frac{n_n}{n_e} n K_d + \frac{n_n}{n_p} n_p K_r^i + \frac{n_e}{n_n} n K_a \right) > 0 \qquad (4.45)$$

When only direct impact ionization and recombination processes are important the ionization instabiltiy criterion (4.45) reduces to

$$n K_i \left(\frac{-2\,\cos^2\Phi}{\hat{\nu}_u'} \hat{K}_i - 1 \right) > 0 \qquad (4.46)$$

Since $\hat{K}_i > 0$, reflecting the strong increase in electron production rate with increasing electron temperature and since $\hat{\nu}_u' > 0$, equation (4.46) can never be satisfied and the ionization mode is stable under these conditions. Thus, the difference between equations (4.45) and (4.46) reflect the important influence of negative-ion processes such as attachment and detachment, on the stabilty of the electron production and loss.

It can be concluded that it is a necessary condition for the ionization satability to occur - in the presence of negative-ions - that the quantity

$$\frac{K_a \hat{K}_a}{K_i \hat{K}_i} > 1$$

Practically this requires that the attachment coefficient be an increasing function of the electron temperature and be of a magnitude comparable to the ionization coefficient. When this quantity exceeds unity, the loss of electrons resulting from attachment dominates over electron production from ionization during a positive

fluctuation in electron temperature. This reinforces the relationship between the initial perturbations in T_e and n_e as defined by equation (4.43). This positive feedback mechanism at the collisional level leads to the attachment–induced ionization instability when the effect of electron temperature disturbances is sufficient to overcome the damping influence of recombination and attachment.

Coupled Thermal and Vibrational–Relaxation Modes.

The thermal and vibrational modes detailed by Haas [4.11] have been further investigated by Nighand and Weigand [4.12] and also by Jacob and Mani [4.13]. These modes have been shown to be consistent with arcing in CW CO_2 laser discharges.

In molecular gases it is necessary to consider the effects of vibrational and rotational excitation as well as translational excitation. For the gas mixtures and levels of excitation typical of CO_2 lasers it is possible to simplify the description of the plasma considerably, whilst still providing a description adequate for prediction of instability criteria. It is assumed that the CO_2 asymmetric stretch and N_2 vibrational modes constitute a single vibrational mode at a temperature T_v, and that these modes remain coupled during a disturbance. In addition, it is assumed that the CO_2 symmetric stretch mode and bending mode, and all rotational levels of the CO_2 and N_2 are in equilibrium at a translational temperature T.

The sequence of events accompanying a constant pressure small–amplitude disturbance in gas temperature (or density) is illustrated in fig. (4.9). As for any atomic species a local decrease in gas density leads to an effectively instantaneous response in electron temperature. The resultant increase in electron density strongly affects vibrational excitation of the molecules. There are two primary positive feedback mechanisms resulting in enhanced gas heating, namely, vibrational relaxation and electron molecule collisions. When the response of the electron properties can be considered quasi–steady, the coupled temporal response of disturbances in T_v and T result in a quadratic expression for the disturbance growth rate ν_g, which can be expressed in the form [4.12]

$$\nu_g = -\frac{1}{2} b \mp \frac{1}{2} \sqrt{(b^2 - 4 c)} \qquad (4.47)$$

where

$$b \simeq (nC_pT)^{-1} \left[\frac{KT}{l^2} + \underbrace{\frac{nC_pT}{\tau_{vt}}}_{(3)} + \underbrace{JEF_v (2 + \tau_{vt}) + JEF_t \frac{\delta n_e/n_e}{\delta n/n}}_{(2)} \right] \qquad (4.48)$$

$$c \simeq \frac{(nC_pT)^{-1}}{\tau_{vt}} \left[\underbrace{\frac{KT}{l^2}}_{(1)} + JE \left(\frac{\delta n_e/n_e}{\delta n/n} \right) \right] \qquad (4.49)$$

The numbered terms in equations (4.48) and (4.49) correspond to the processes indicated in fig. (4.9). C_p, n, and K are respectively the specific heat, the neutral particle density and the thermal conductivity. F_v and F_t are the fractional power transferred to vibration and translation, and l is the scale size of the local disturbance. J is the current density, E the electric field, and τ_{vt} is the V−T relaxation time. the parameter τ_{vt} is defined as

$$\overset{\wedge}{\tau}_{vt} \equiv \frac{\partial \ln T_{vt}}{\partial T} \qquad (4.50)$$

which reflects the sensitivity of the rate coefficient for V−T relaxation to changes in temperature. With JE set equal to zero, it is easily shown that the two roots of equation (4.46) are

$$\nu_g = \left(\frac{-KT}{l^2} \right) \frac{1}{nC_pT} \qquad \text{and} \qquad \nu_g = -(\tau_{vt})^{-1}$$

These are respectively the damping rate of local concentrations in heat by thermal conduction and the damping rate for disturbance in vibrational energy due to V−T relaxation. The two intabilty modes are therefore referred to as the *thermal* and *vibrational* modes, corresponding to disturbances in T and T_v respectively.

For either mode of instability to occur ($\nu_g > 0$) b must be negative (thermal instability) or b and c must be of opposite sign (vibrational instability). Thus, in general the thermal and vibrational instabilities can occur individually or simultaneously. Since the thermal conduction term KT/l^2 is always positive, this mechanism has a stabilizing influence as expected.

It is found that the fractional electron density disturbance exhibits a pronounced spatial variation due to the non−isotropic nature of the perturbation in electron temperature. Since the electron density increases with a local decrease in gas density, the term $(\delta n_e/n_e)/(\delta n/n)^{-1}$ is always negative. From the results reported by Nigand and Wiegand this parameter is very strongly peaked in the direction perpendicular to the current and field, as shown in fig. (4.75). Therefore ν_g will first become positive in this direction, a condition favouring filamentation of the plasma. It can also be seen from fig. (4.75) that the presence of negative ions substantially alters steady state

plasma properties, with the result that the electron energy disturbance in attachment dominated plasmas is significantly larger than in recombination dominated plasmas. As the term $(\delta n_e/n_e)(\delta n/n)^{-1}$ is the multiplier of the unperturbed power, JE, it is clear that the presence of negative ions has a significant adverse effect on the modes of instability under consideration.

The nature of the V−T relaxation process can lead to the thermal instability ($b<0$) when the V−T relaxation time is a strongly decreasing function of the gas temperature, in which case the quantity $(2 + \tau_{vt})$ may become negative. This reflects the fact that when electrical power transfer to vibration is large, local heating of the gas due to a surge in V−T relaxation may be sufficient to overcome the stabilizing influence of thermal conduction.

Nigand and Weigand have shown that for conditions typical of CW CO_2 laser discharges the vibrational instability always occurs, with a corresponding growth time of the order of 10^{-3} sec. This is consistent with the experimental observation that the gas residence times in CW devices must be kept to below 10^{-3} sec. The growth time for this instability is seen to reduce considerably with both increasing gas pressure and power density. Perhaps of greater significance is the possibility of a transition from a vibrational instability to the thermal instability driven by vibrational relaxation. In addition, the computed growth times are significantly less when dissociative attachment is assumed to be the major electron loss process.

SUMMARY.

From the stabilty criteria derived by Haas it is found that for the plasma conditions typical of high power electrically excited molecular lasers, the possible modes of instability include the attachment−induced ionization mode and the coupled vibrational−thermal mode. The instability of these modes depend critically on the electron temperature dependences of the rate coefficients for all the charged particle production and loss processes, particularly those involving ionization, attachment and detachment. In addition, the vibrational instability depends on the gas temperature dependence of the V−T relaxation rate coefficient and the magnitude of the gas thermal conductivity.

Although the instability analysis describes certain physical characteristics of the local behaviour of molecular gas discharge plasmas, the possibility exists that the presence of boundaries and plasma flow gradients introduce effects of equal or greater significance as regards stability. In addition, it is known that the instabilities manifest themselves as filamentation and constriction of the plasma current density. Precisely

how the instabilities discussed here lead to constriction, particularly the ionization instability mode which is unstable only along the direction of the applied field, is still not yet fully understood.

In general, these modes are stabilized by transport processes. However, it should be noted that an external source of ionization will exert a stabilizing influence only on the ionization instability. The stability of the vibrational−thermal mode is shown to be critically dependent on the gas temperature dependence of the V−T relaxation rate coefficient and is shown to be relatively insensitive to the details of the charged and electronic species kinetics. Consequently, the stability of this mode has been found to be insensitive to the application of an external source of ionization. This instability mechanism therefore constitutes a general limitation to high power laser discharge stability.

From the experimental single−shot stability results of section (4.5.2), it is possible to conclude that the attachment−induced ionization instability is the most likely mechanism leading to the onset of arcing, since only this mode can grow within the micro−second time scale observed for arc development. This mechanism could also be responsible for the accumulated growth of the instability over a series of pulses − including a quenching period between pulses − as observed experimentally. In order for the instabilities to grow to the stage where arcing occurs local plasma inhomeogeneities must remain in the electrode region for a duration longer than the inter−pulse period. At higher input powers the minimum time between arc free discharges can be twice the average gas residence time in the cavity, as calculated from the measured gas flow−rate. It can be concluded, since it has already been shown that gas expansion of the discharge products is negligible at the power densities reported here, that clearing of the gas from the electrode region is dominated by boundary layer flow and diffusion.

In conclusion, the relevant instability modes within the discharge plasma have been identified. It has been found that both modes are adversely affected by the presence of negative ions, which is in agreement with the experimental deterioration in discharge quality due to atmospheric leakage. However, modelling work is required in order to estimate the growth rate of the ionization instability as a function of oxygen contamination. Experimental work could also be undertaken on the effects of detaching species, e.g. CO, as these could exert a stabilizing influence and ulimately lead to a higher discharge power level.

(4.6) CONCLUSIONS AND RECOMMENDATIONS.

The experimental work undertaken on the characteristics of the gas discharge has attempted to improve the understanding of the factors critical to laser performance, such as discharge formation and discharge stability. It has been found that the double-discharge electrode system is limited both in terms of allowable single-shot energy and continuous power. With the available gas flowrate it has only been possible to extend stable operation to a maximum continuous PRF of 1 kHz and a continuous discharge power of approaching 3 kW. These values fall considerably short of the design specification.

From a comparison of the single-shot stability limits with those reported by Kline [4.28], it is clear that since the only difference in the two electrode systems is the preionization source, it can be concluded that the poor performance obtained reflects the design of the trigger-wire system. It has been found that any local inhomogeneities in the discharge will be amplified by the ionization instability until the point of arcing. Inspection of the anode after several hours continuous running reveals a characteristic striped pattern, corresponding to the position of the trigger wires, which is indicative of a non-uniform discharge current density. This inhomogeneous conduction current may be responsible for the observed limitations in discharge stability.

It has also been shown that for high repetition rate systems the discharge products must be removed from the electrode region in the inter-pulse period, in order to prevent accumulated growth of the plasma inhomogeneities. From the measurements of arcing times under burst mode conditions, it can be concluded that the discharge products remain within the electrode region for durations longer than the inter-pulse period. Such times are incompatible with the convective clearing time calculated from the average gas velocity. It is possible that the low clearing rate is due to the adverse effects of the trigger-wires on boundary layer flow and diffusion.

In addition to the assessment of the discharge stability limitations, results have been reported on other important characteristics of the gas discharge system. It has been shown that the discharge breakdown phase operates in the classical Townsend regime, in contrast to the streamer breakdown process typical of high pressure TEA CO_2 lasers. The formative period of the discharge has been analysed in terms of multiple electron avalanches and the effective trigger wire emission current calculated. The breakdown of the trigger-wire/cathode gap has also been investigated and an independent high frequency preionizer circuit built to examine the effects of delayed preionization. Such studies have provided valuable information for the future design of

laser perionization sources.

The trigger−wire system has been found to be unsuitable fro the high PRF CO_2 laser due to the adverse effects on discharge current uniformity and gas clearing efficiency. Future extension of the pulse power levels and continuous mean powers therefore requires major development of the electrode system.

(4.6.1) Proposal for Extension to Higher PRF's.

The insatbility mechanisms which lead to the constriction of the discharge current are inherent properties of the discharge plasma. It is therefore extremely difficult to impose a stabilizing influence on the discharge, without at the same time reducing laser efficiency. Since it is clear that any inhomogeneities in the plasma will eventually lead to arcing, efforts are best directed at homogenization of the plasma. The electrode system should therefore be designed for uniformity in current density and applied field. In addition, the gas flow conditioning must ensure that the velocity profile is as uniform as possible.

Perhaps the most significant finding of this investigation is that at the very low power densities required here, the arc development time is longer than the 10 μs pulse duration. This combined with the quenching of local inhomogeneities in the inter−pulse period allows the PRF to be increased significantly above the accepted minimum clearing ration CR = $\sqrt{3}$ [4.29]. As the single pulse energy is increased the clearing ratio correspondingly increases. Thus, as long as the pulse energy is much less than the single−shot discharge stability limit, it is possible to achieve a clearing ratio significantly less than unity. For instance, with the spark preionized system employed by Kline [4.28] the power density could be increased by two orders of magnitude for the same pulse duration. It would be interesting to find out what the maximum attainable PRF is with this system at low power densities.

The problem associated with extending the system developed by Kline to higher PRF's would be the development of the spark array source for 10 kHz operation; this may present practical difficulties in ensuring adequate lifetime due to electrode erosion. Alternatively, the discharge could be initiated by a Corona preionization source [4.23], which would be capable of much longer lifetimes. This would require the development of a very high dv/dt spiker circuit to generate the required UV flux characteristics, i.e. 120 nm wavelength. A proposed electrode system based on a corona preionizer is illustrated in fig. (4.76). It can be seen that the dielectric trigger electrodes are positioned behind a screen mesh cathode; an arrangement which has minimal effect on gas flow.

One other possible solution to the problems experienced with discharge stability would be to resistively ballast one of the electrodes, to make the discharge inherently stable. From extrapolation of the results reported by Baranov [4.30] and Ivanchenko [4.35], it is possible to deduce that a ballast resistance value of approximately 900 Ω would be sufficient. Fig. (4.77) shows a proposed design for a ballasted cathode, comprising approximately 500 resistively ballasted pins. With this arrangement some means must also be provided for initiating the discharge, however, as this should be less susceptible to arcing, a single corona source positioned on the downstream side of the electrodes may produce satisfactory performance. The electrode design shown should be adequate for short continuous runs, allowing the performance to be assessed before a major electrode/cavity development is undertaken.

In addition to the above proposals, it would also be worthwhile to examine the effects of gas flow turbulence on the stability of the discharge, as significant improvements have been reported in discharge stability by several workers including: Myshenkov and Mukhviladze [4.36] and Shwartz and Wasserstrom [4.37]. It is apparent that flow turbulence stabilizes the discharge via homogenization of the plasma and enhancement of thermal diffusivity. Methods of generating micro−turbulence have been reported by Hill [4.38].

REFERENCES FOR CHAPTER (4)

[4.1] Kuffel. E., Zaengl. W. S. "High Voltage Engineering Fundementals." Pergamon Press.

[4.2] Hasan M. A. "Thermodynamics of a transiently pumped CO_2 gas laser plasma." Ph.D. Thesis, Department of Mechanical Engineering, University of Glasgow. 1989.

[4.3] Smith. K., Thomson R. M. "Computer modelling of gas lasers." Plenum Press.

[4.4] Lowke J. J., Phelps A. V., Irwin B. W. "Predicted electron transport coefficients and operating characteristics of CO_2: N_2: He mixtures." J. App. Phys., Vol. 44, No. 10, 1973.

[4.5] Smith A. L. S "Gas laser discharges." Proceedings of the 23rd Scottish summer school in physics. 1982.

[4.6] Lavatter J. I., Shao Chi Lin. " Necessary conditions for the homogeneous formation of pulsed avalanche discharges at high gas pressures." J. App. Phys. 51(1), 1980.

[4.7] Denes L. J., Lowke J. J. " VI characteristics of pulsed CO_2 laser discharges." App. Phys. Lett., Vol. 23, No. 3, 1973.

[4.8] Cobine J .D. "Gaseous conductors – theory and engineering applications." Dover Publications.

[4.9] Khahra J.H., "Optimisation of the output characteristics of a pulsed carbon–dioxide laser for processing of materials." Ph.D. Thesis Univ. Birmingham, Dec 1976.

[4.10] Judd C. P., Wada J. Y. "Investigation of a UV preionized discharge and CO_2 laser." IEEE J. of Q.E., QE – 10 No.1, 1974.

[4.11] Haas A. "Plasma stability of discharges in molecular gases." Phys. Rev. A8 1017 . 1973.

[4.12] Nighand W. L., Wiegand W. J. "Causes of arcing in CW CO_2 convection laser discharges." App. Phys. Lett., Vol. 25, No. 11 1974.

[4.13] Jacob J. H., Mani S. A. "Thermal instability in high power laser discharges." App. Phys. Lett., Vol. 26, No. 2, 1975.

[4.14] Dutton J. Haydon M. A. Llewellyn Jones F. "Formative time lags in electrical breakdown of gases." Brit. J. App. Phys. pp 170 −175, 1953.

[4.15] Bittencourt J. A. "Fundamentals of plasma physics." Pergamon Press.

[4.16] Kline L. E. "Calculations of discharge initiation in overvolted parallel−plane gaps." J. App. Phys., Vol. 45, No. 5, 1974.

[4.17] Watson I. A. " Development of a high prf CO_2 laser for materials processing applications." Ph.D thesis, Department of Mech. Eng. Univ. of Glasgow. To be published.

[4.18] Palmer A.J. "A physical model for the initiation of atmospheric−pressure glow discharges." App. Phys. Lett., Vol.25, No. 3, 1974.

[4.19] Kunhardt E. "Electrical breakdown of gases: the prebreakdown stage." IEEE Trans. − on Plasma Sci., Vol PS − 8, No. 3, 1980.

[4.20] Babcock. R. V., Liberman I., Partlow W. D. IEEE J. Q. E. QE − 12 29 1976.

[4.21] Mcken D. C., Sequin H. J., Tulip J. "Photoionization parameters in the carbon dioxide laser gases." IEEE J. Q. E. QE−12, 1976.

[4.22] Scott S. J., Smith A. L. S. "Ultraviolet photoionization in TEA CO_2 lasers." App. Phys. Lett., 41 783, 1982.

[4.23] Marchetti R., Penco E. "Optimization of corona discharge preionization sources for CO_2 lasers." J. App. Phys. 54(10), 1983.

[4.24] Morgen G. "Glow Discharges." London Meuthen.

[4.25] Durney C. H. Harris L. D. Charles L. A. "Electic circuits, theory and engineering applications." Holt−Saunders International Editions.

[4.26] Glasoe G.N. Labacqz J.V. "Pulse Generators." Radiation Laboratory Series. Wiley.

[4.27] DeMaria A. J. "Review of high power CO_2 lasers." Proc. IEEE, Vol. 61, No. 6, 1973.

[4.28] Kline L. E., Denes L. J., Perchersky M.J. "Arc suppression in CO_2 laser discharges." App. Phys. Lett., Vol 29, No. 9, 1976.

[4.29] Dzakowic G. S., Wutzke S. A. "High pulse rate glow discharge stabilization by gas flow." J. App. Phys., Vol. 44, no. 11, 1973.

[4.30] Baranov V. Y., Malyuta D. D., Mezhevov V. S. "Utilization efficiency of gas flow pulse−periodic CO_2 lasers." Sov. J. Quantum electron 8(10), 1978.

[4.31] Wright J. K. "Shock Tubes." London Meuthen.

[4.32] Yamabe C., Matsushita T., Sato S. Horii K. " Characteristics of a TEA CO_2 laser preionized by UV light." J. App. Phys. 51(3) 1980.

[4.33] Norris B., Smith A. L. S. "Attachment loss of photo−ionization electrons in TEA CO_2 lasers." J. Phys. D. App Phys., Vol 10, 1977.

[4.34] Nigand W. L., Weigand W. J. "Influence of negative−ion processes on steady state properties and striations in molecular gas discharges." Phys. Rev. A. Vol. 10, No. 3 1974.

[4.35] Ivanchenco A. I., Soloukhin R.I, Fidel'man G. I., Yakobi Y. A. "Stability of a flat electric discharge with convective cooling." Sov. Phys. Tech. Phys., Vol. 20, No. 11, 1975.

[4.36] Myshenkov V. I., Mukhviladze G. M. "Suppression of the ionization instability in a gas discharge by turbulent transport." Sov.J. Plasma Phys. 4(2) 1978.

[4.37] Shwartz J., Wasserstrom E. "The role of gas flow and turbulence in electric discharge lasers." Israel J. Tech. Vol 13 pp122−133, 1975.

[4.38] Hill A. E. " Uniform electrical excitation of large−volume high−pressure near−sonic CO_2:N_2:He flowstreams." App. Phys. Lett. Vol 18, No. 5, 1971.

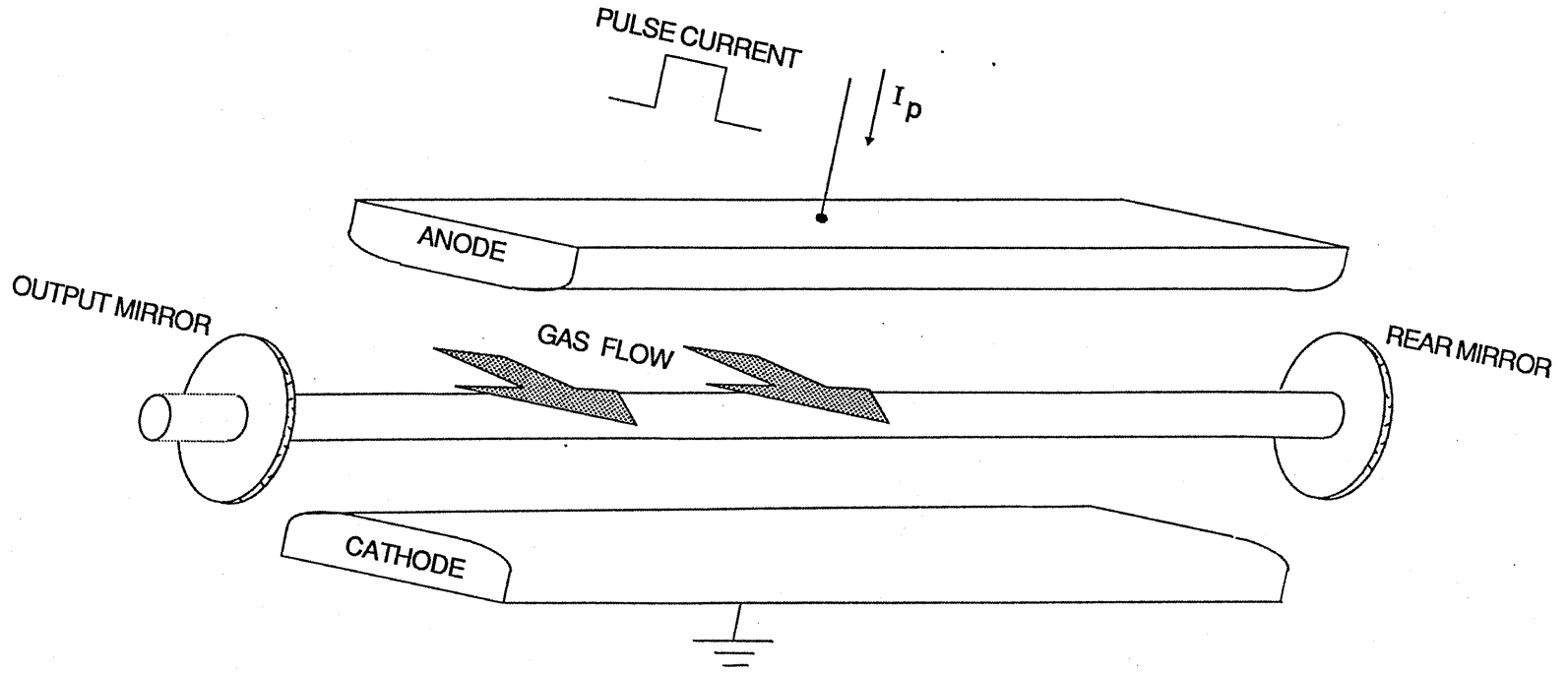

FIGURE 4.1 TRANSVERSE DISCHARGE SYSTEM

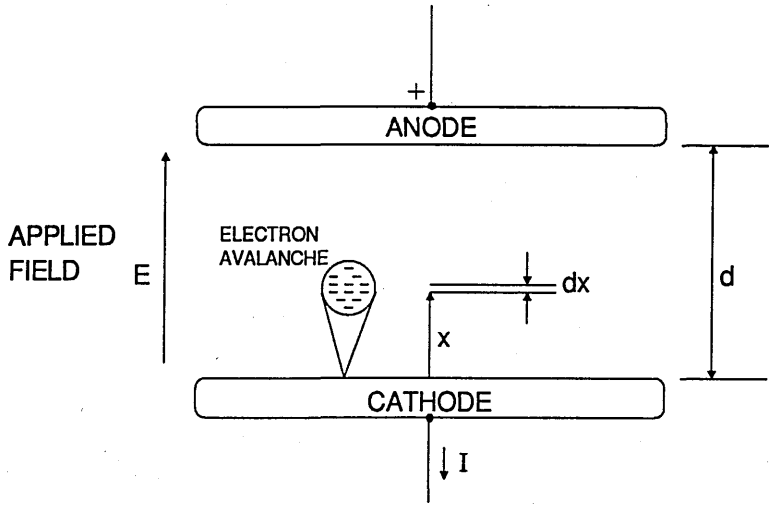

FIGURE 4.2 BREAK-DOWN IN A UNIFORM FIELD GAP

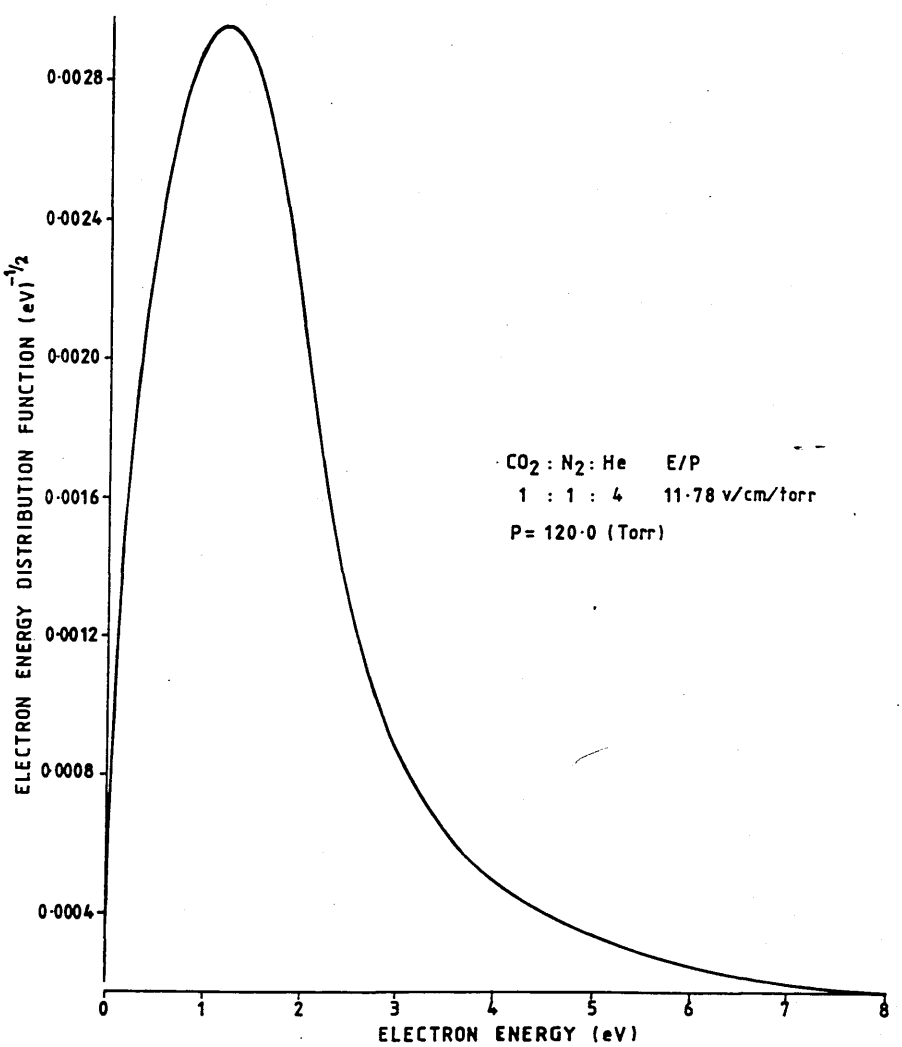

FIGURE 4.3 ELECTRON ENERGY DISTRIBUTION FUNCTION

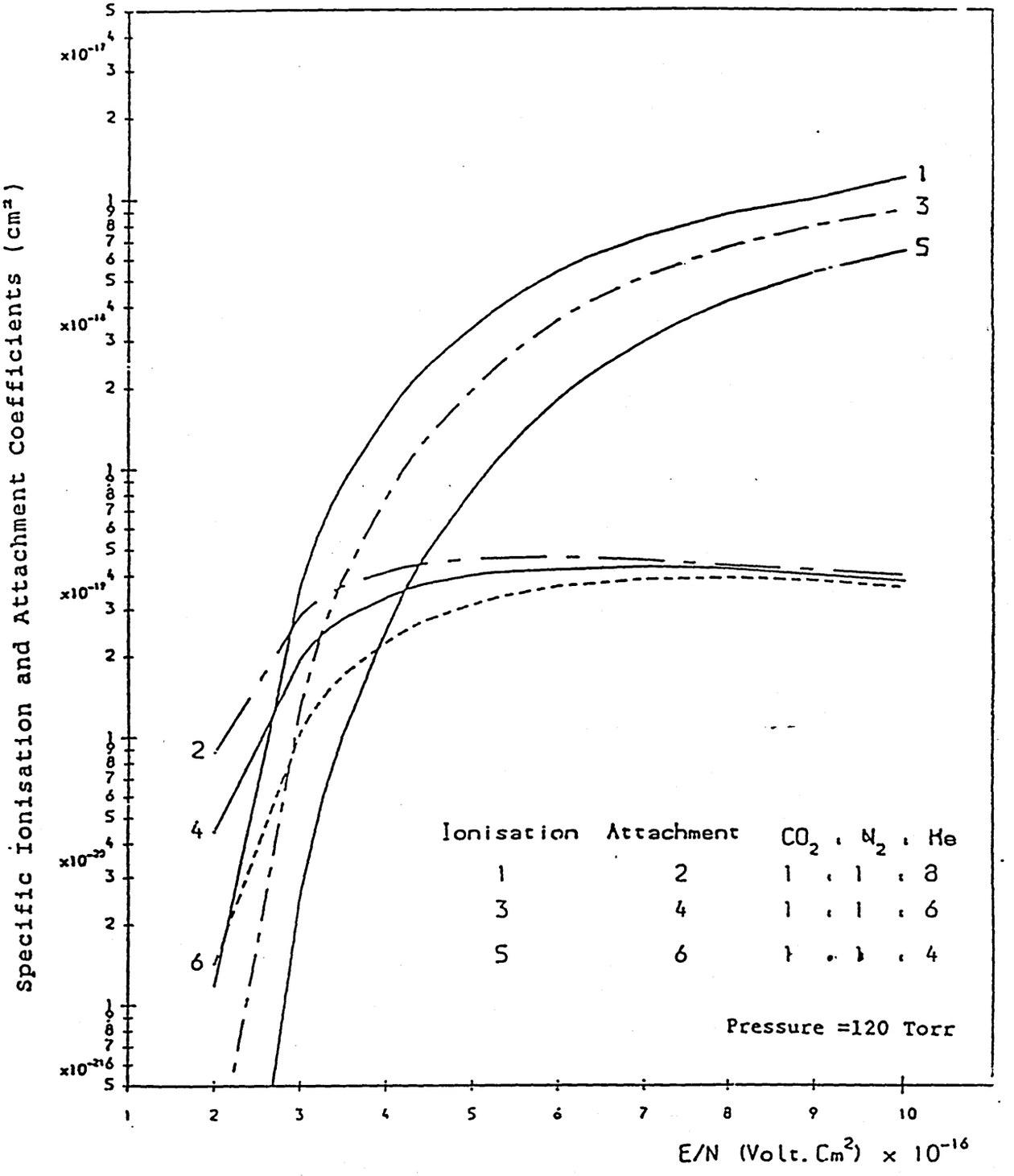

FIGURE 4.4 SPECIFIC IONIZATION AND ATTACHMENT COEFFICIENT VERSUS (E/N)

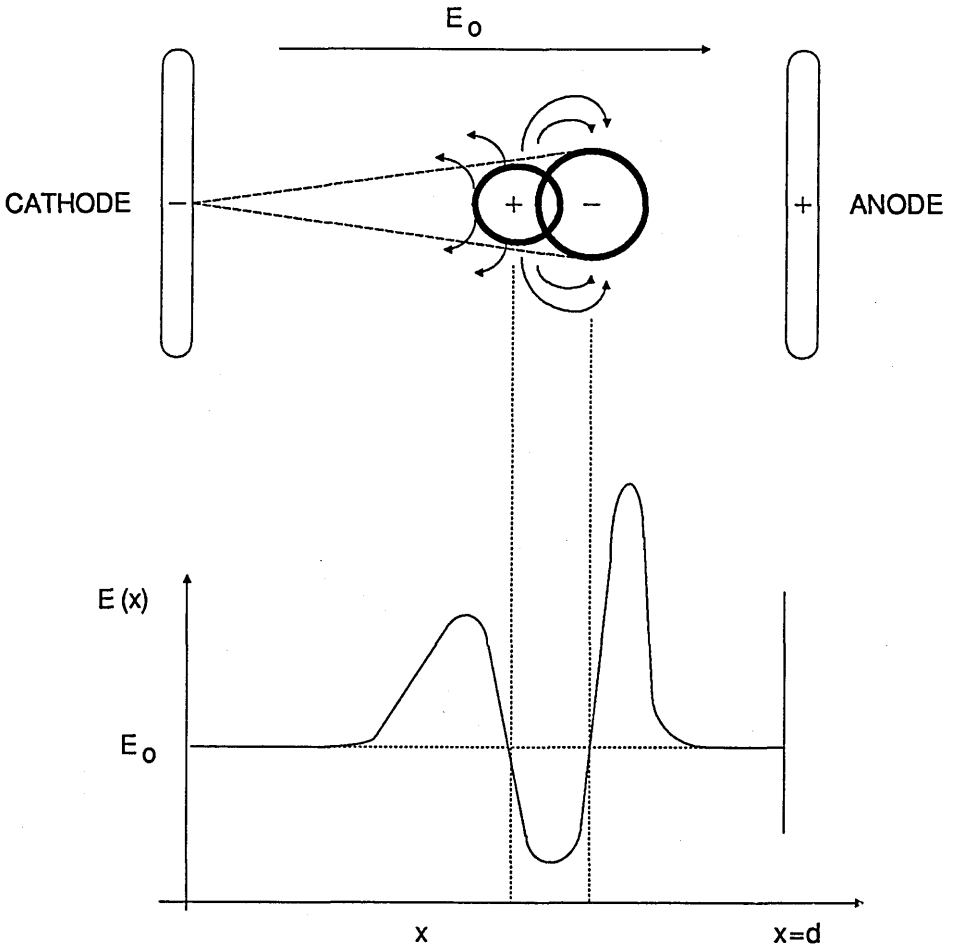

FIGURE 4.5 FIELD DISTORTION DUE TO SPACE CHARGE OF AN ELECTRON AVALANCHE

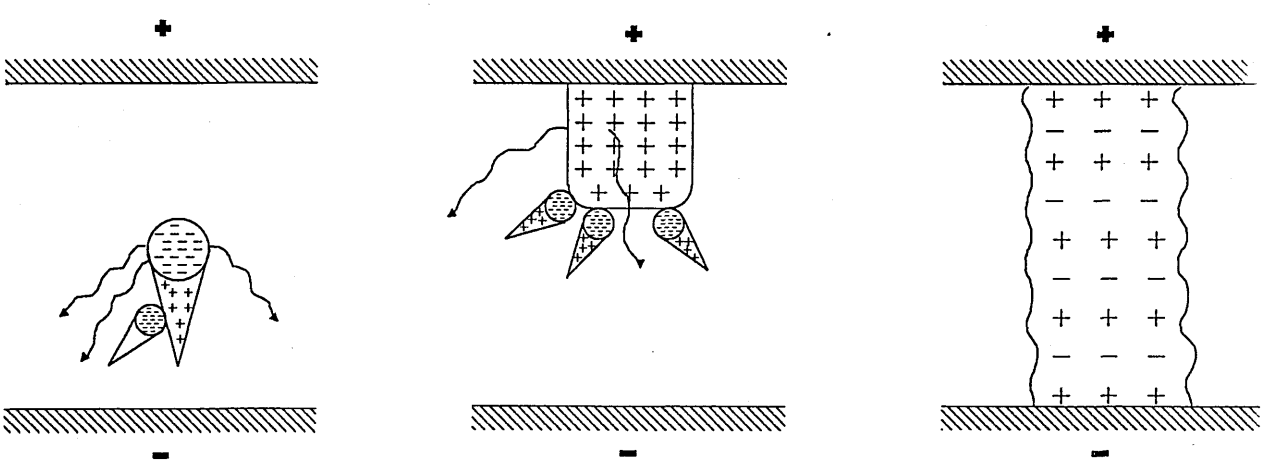

FIGURE 4.6 SCHEMATIC OF STREAMER DEVELOPMENT

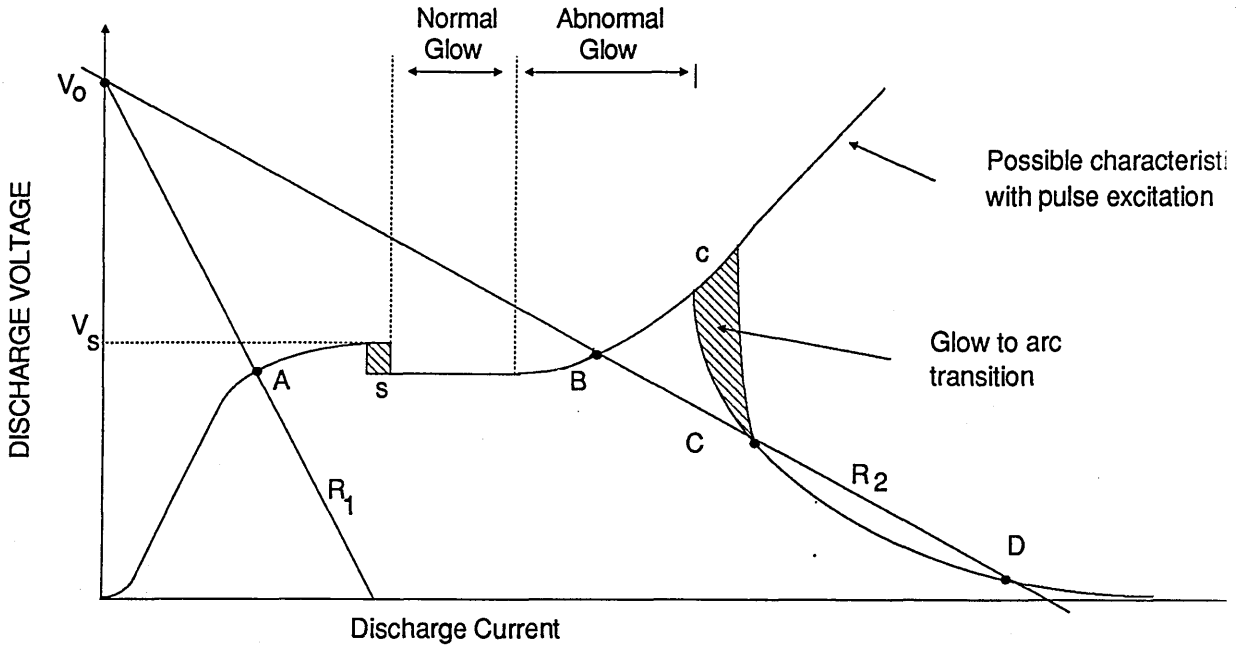

FIGURE 4.7 STATIC GAS DISCHARGE CHARACTERISTICS

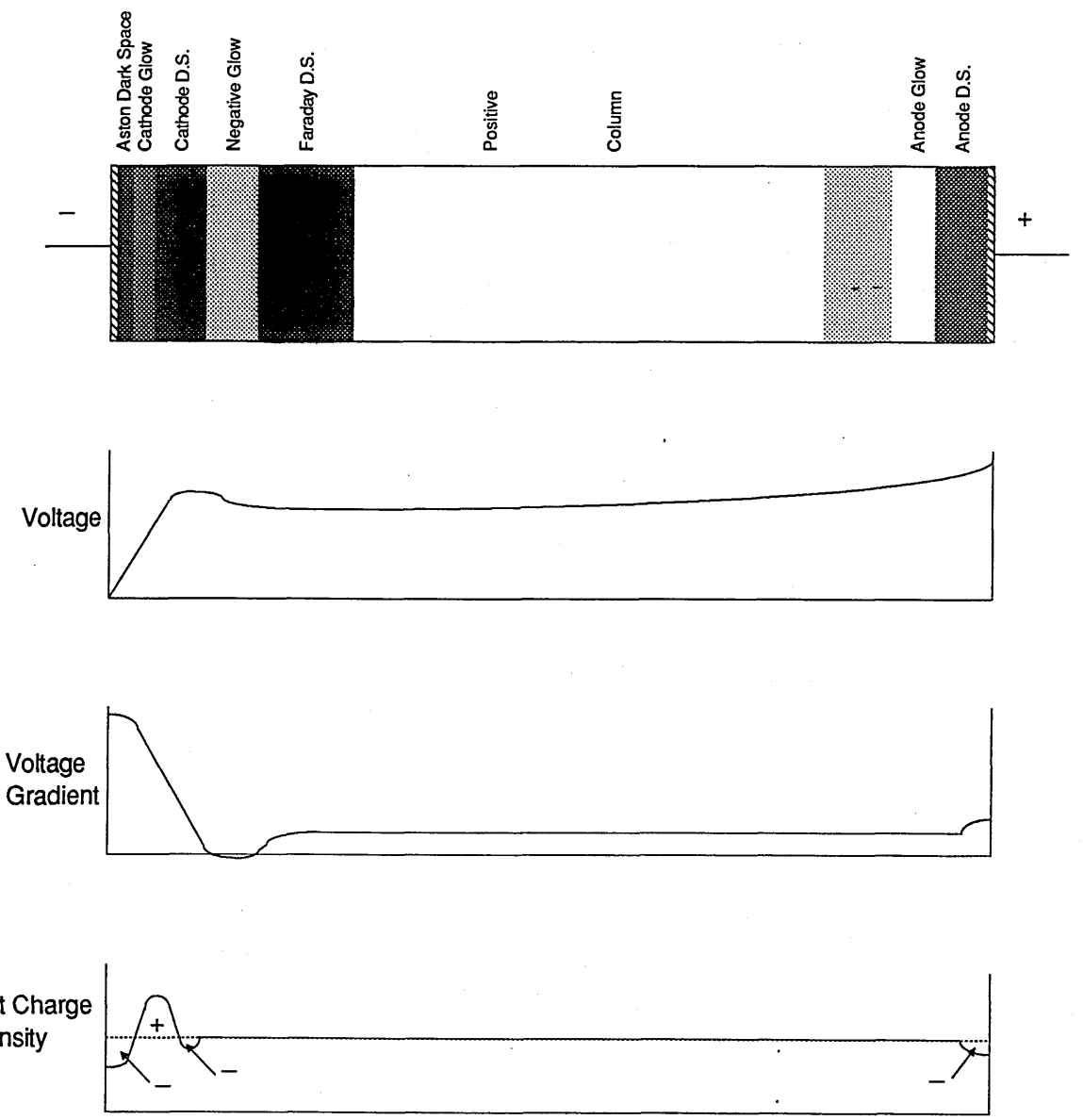

FIGURE 4.8 CHARACTERISTICS OF GLOW DISCHARGE

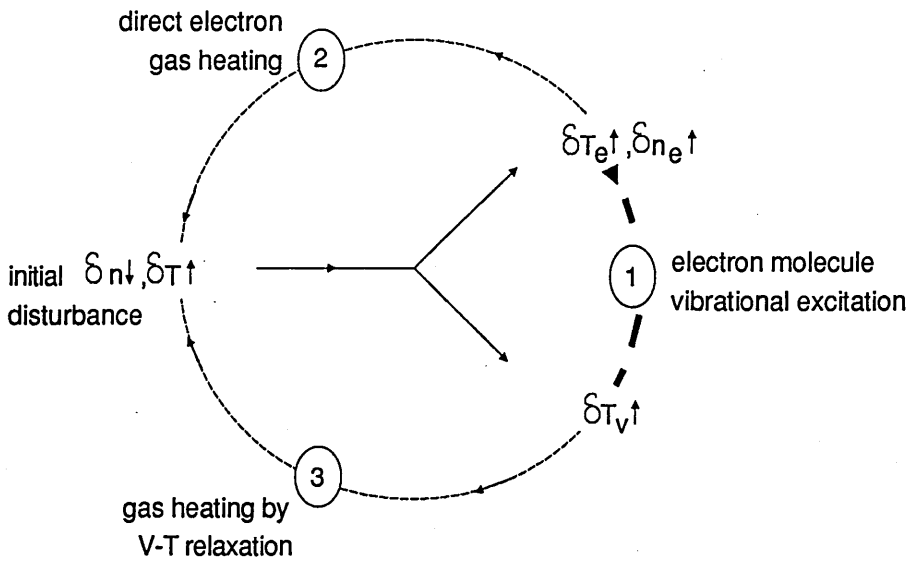

FIGURE 4.9 THERMAL INSTABILITY MECHANISM

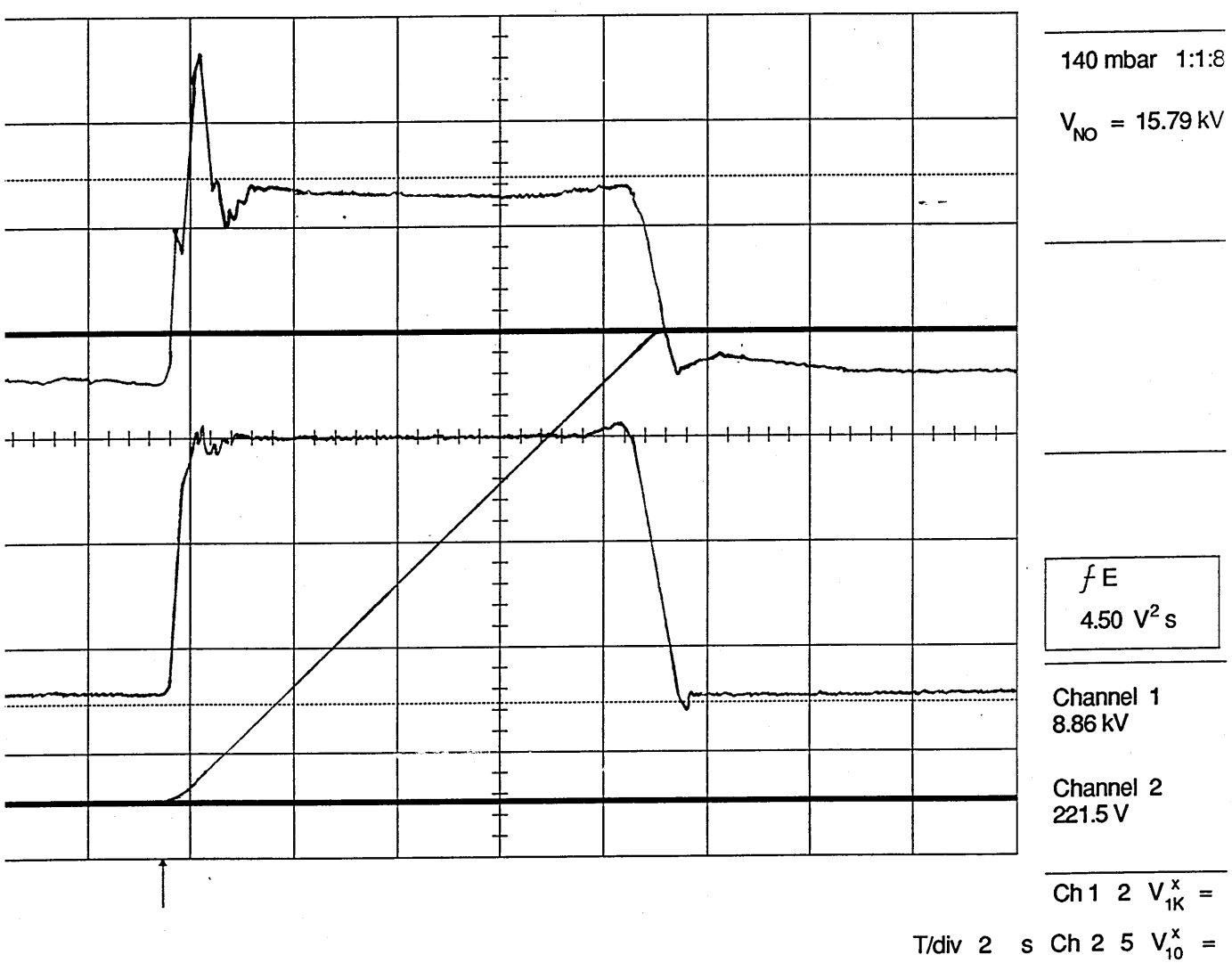

FIGURE 4.10 GLOW DISCHARGE V-I CHARACTERISTICS

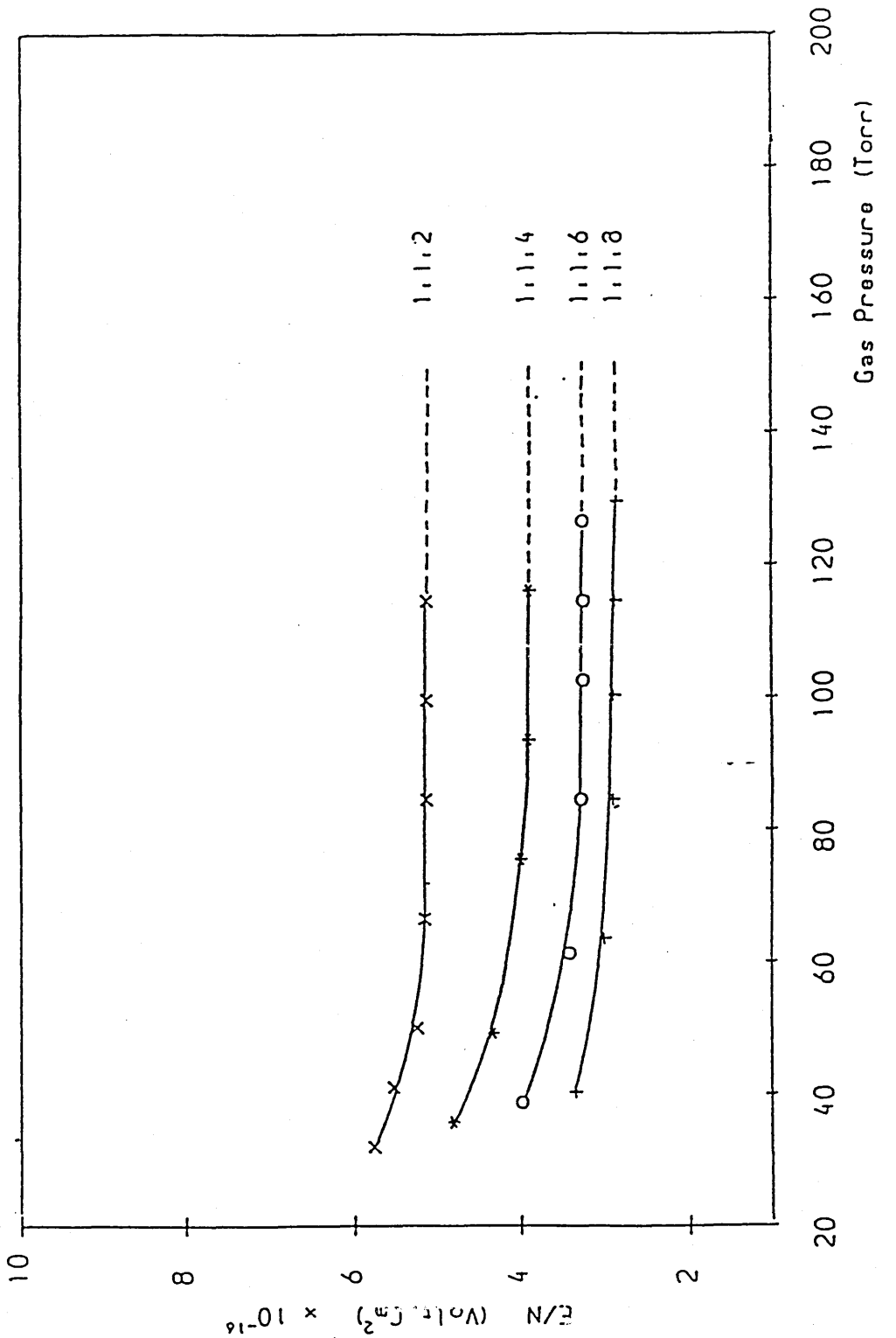

FIGURE 4.11 GRAPH OF (E/N) VERSUS GAS PRESSURE

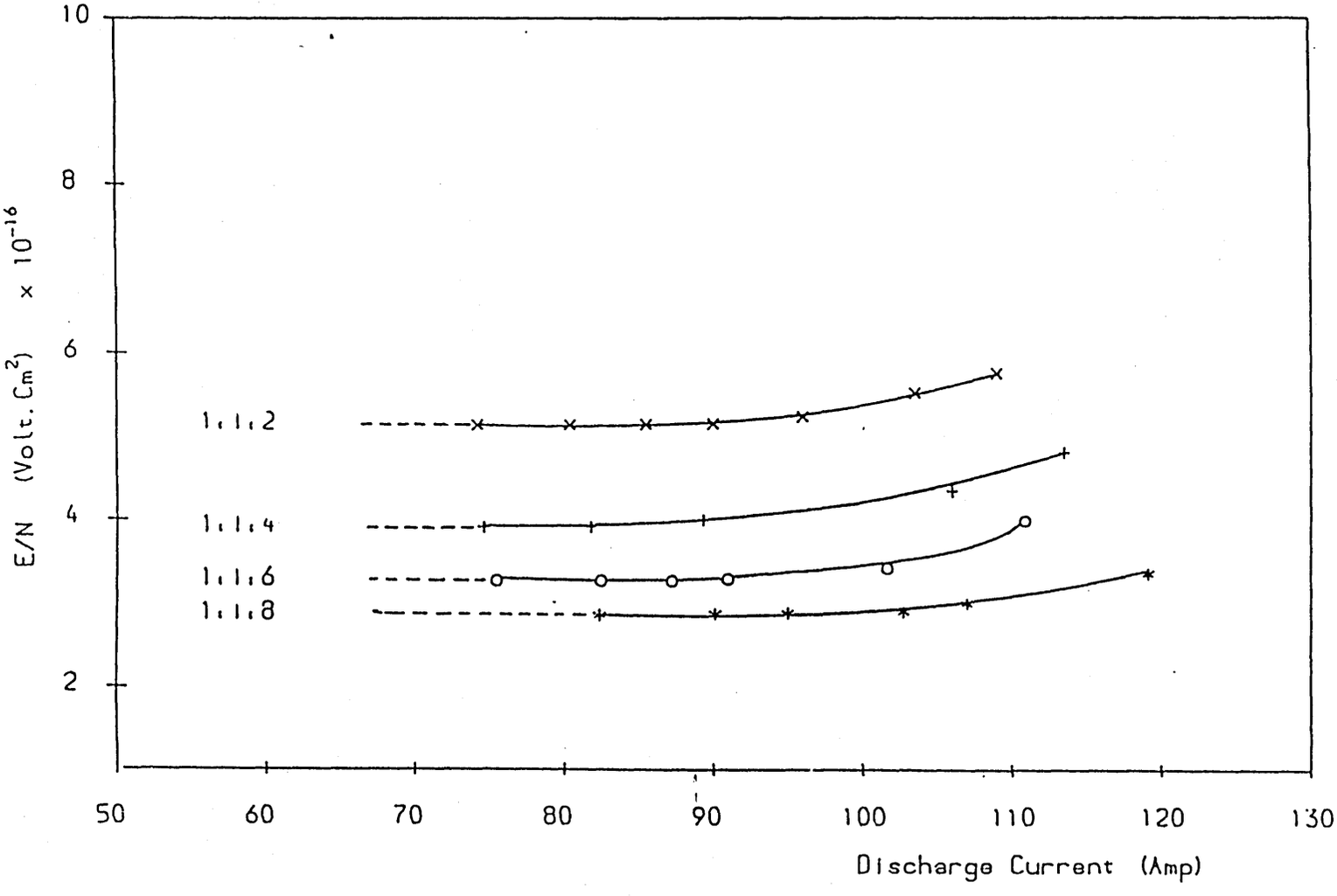

FIGURE 4.12 GRAPH OF (E/N) VERSUS DISCHARGE CURRENT

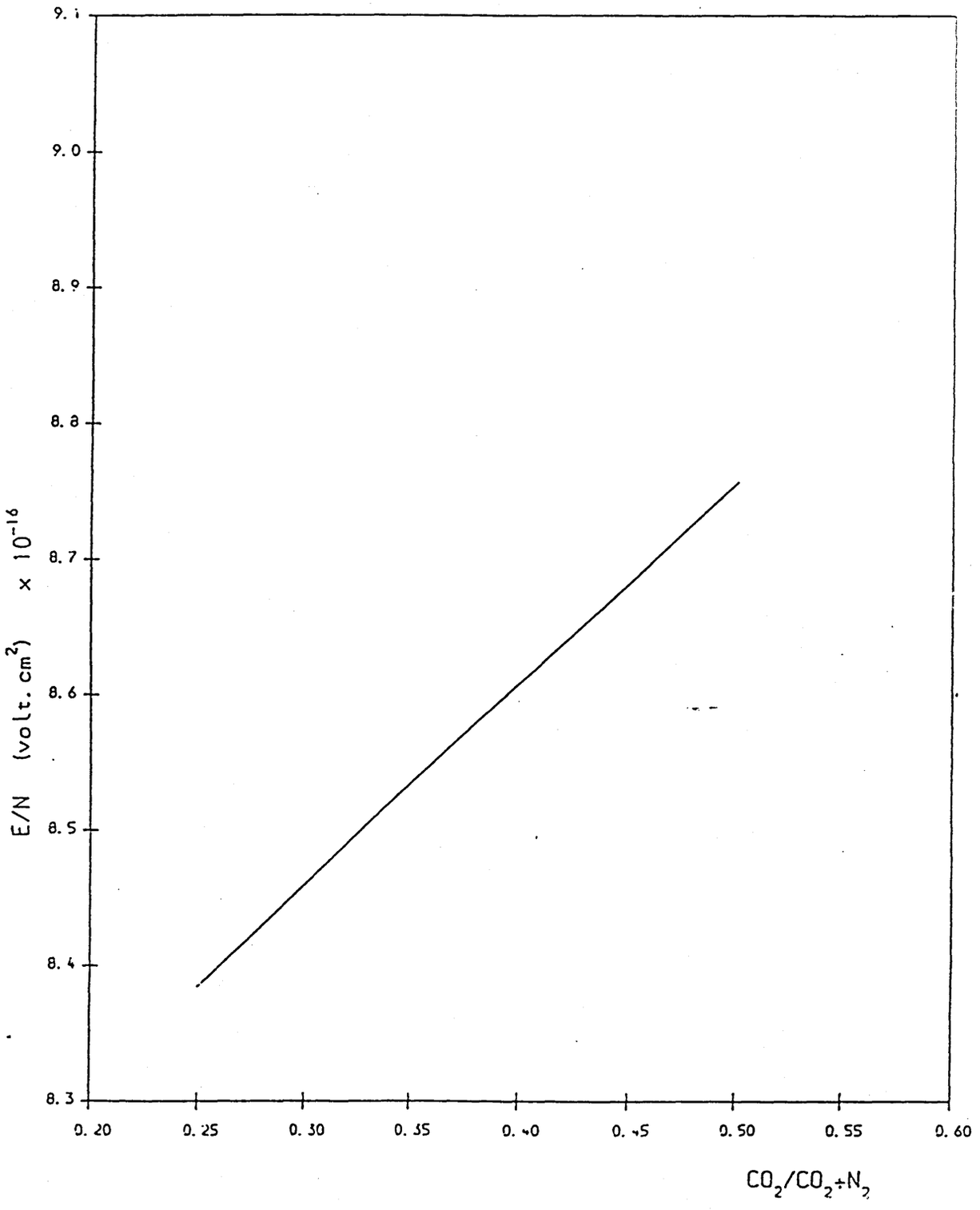

FIGURE 4.13 GRAPH OF (E/N) VERSUS CO_2 CONTENT

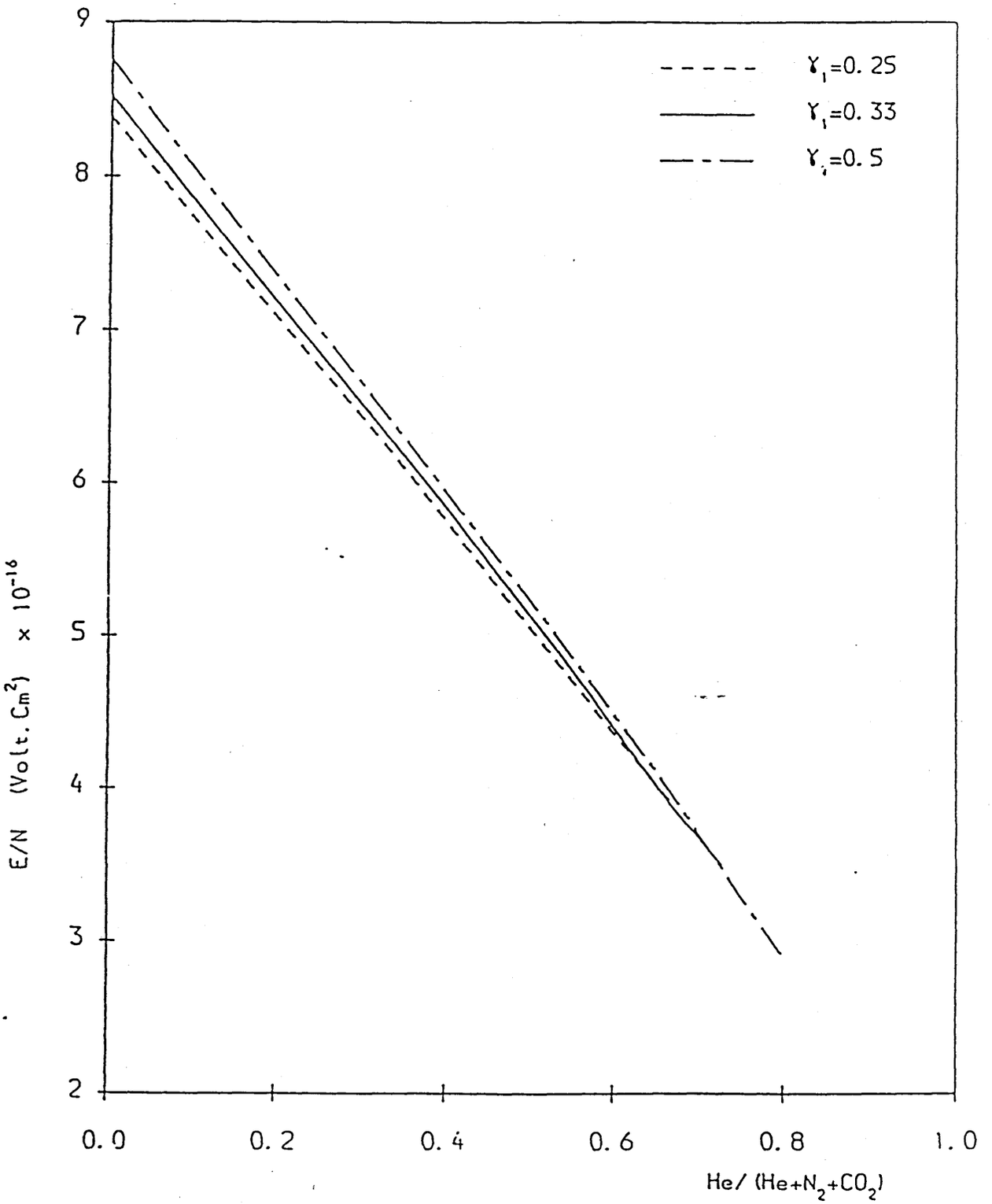

FIGURE 4.14 GRAPH OF (E/N) VERSUS He CONTENT

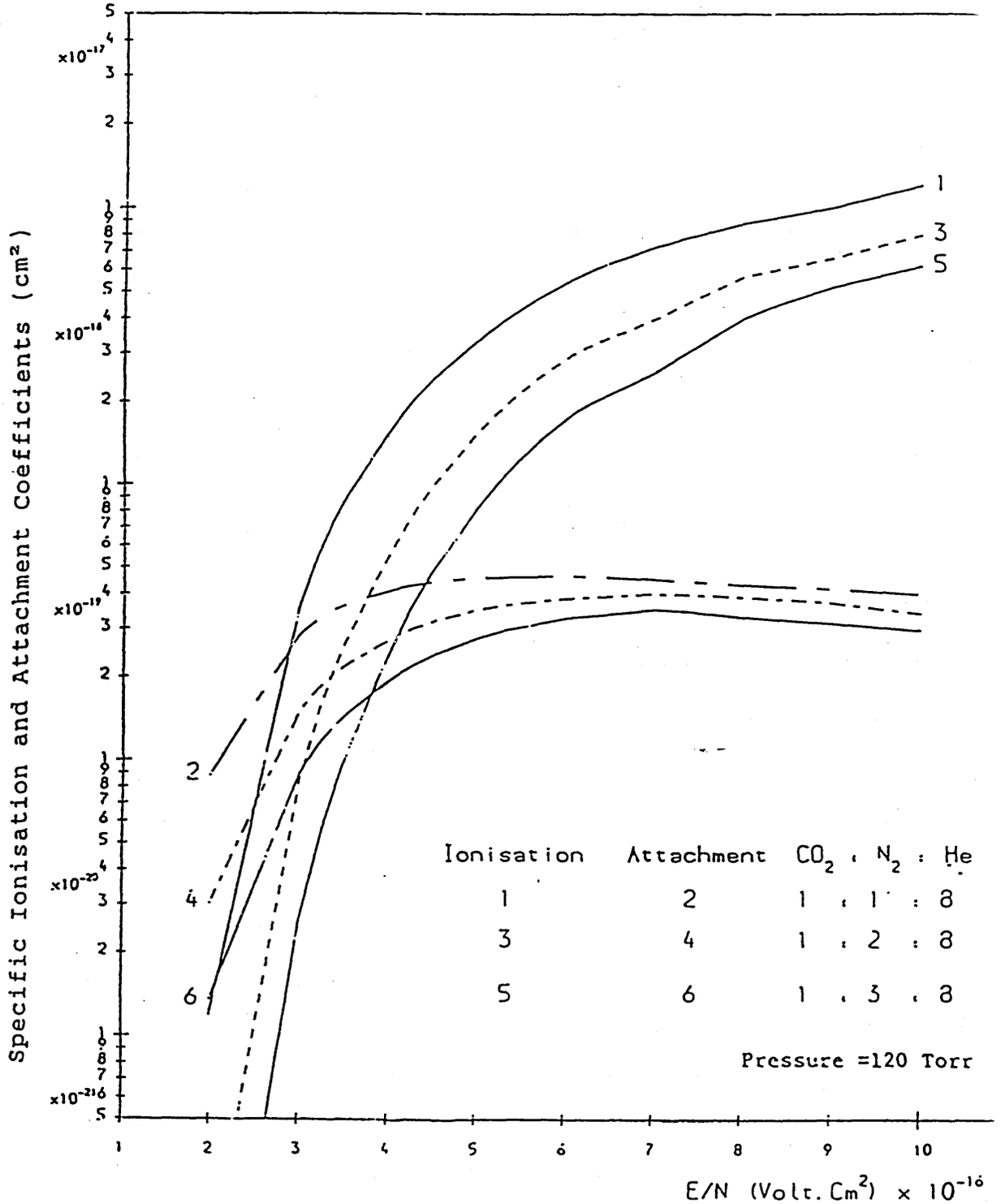

FIGURE 4.15 SPECIFIC IONIZATION AND ATTACHMENT COEFFICIENT VERSUS (E/N)

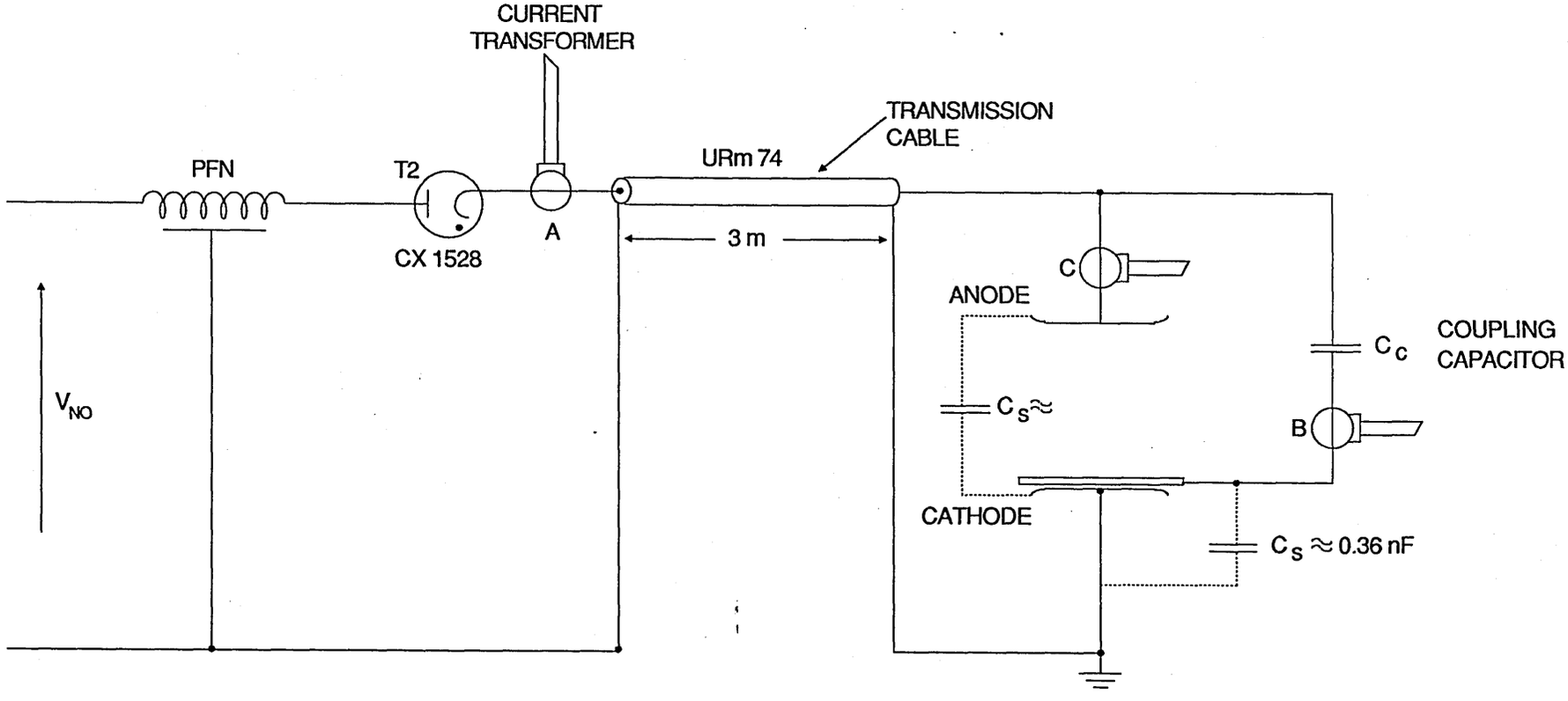

FIGURE 4.16 SCHEMATIC OF GAS DISCHARGE CIRCUIT

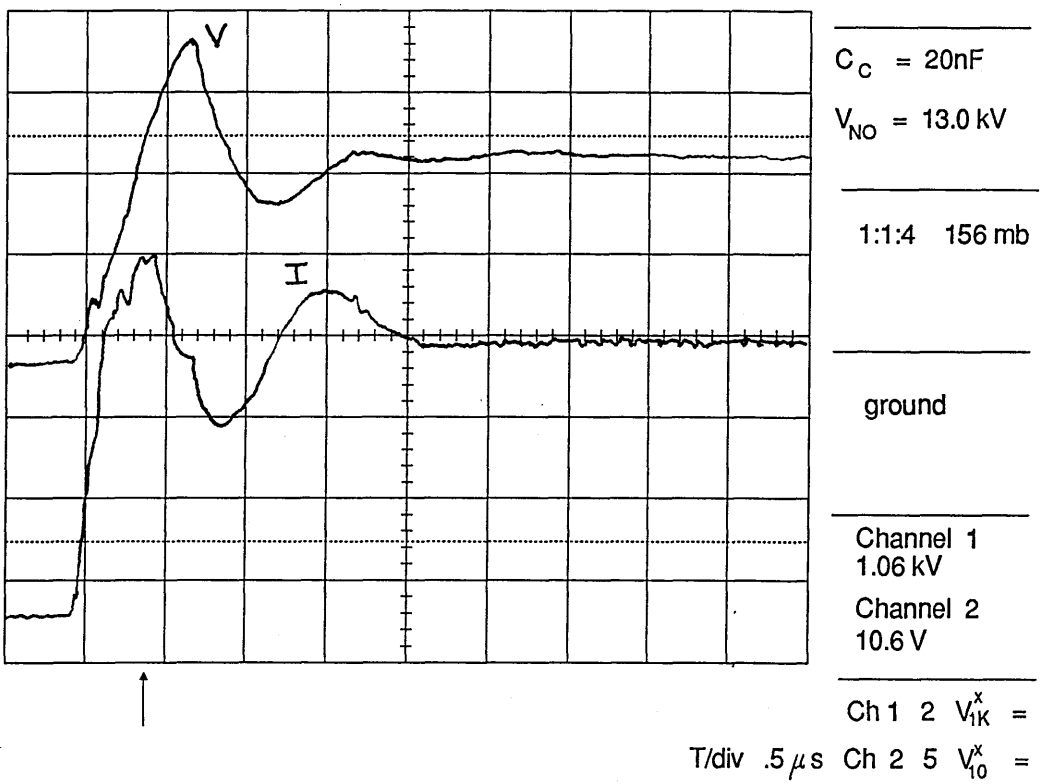

FIGURE 4.17 DISCHARGE VOLTAGE AND CURRENT

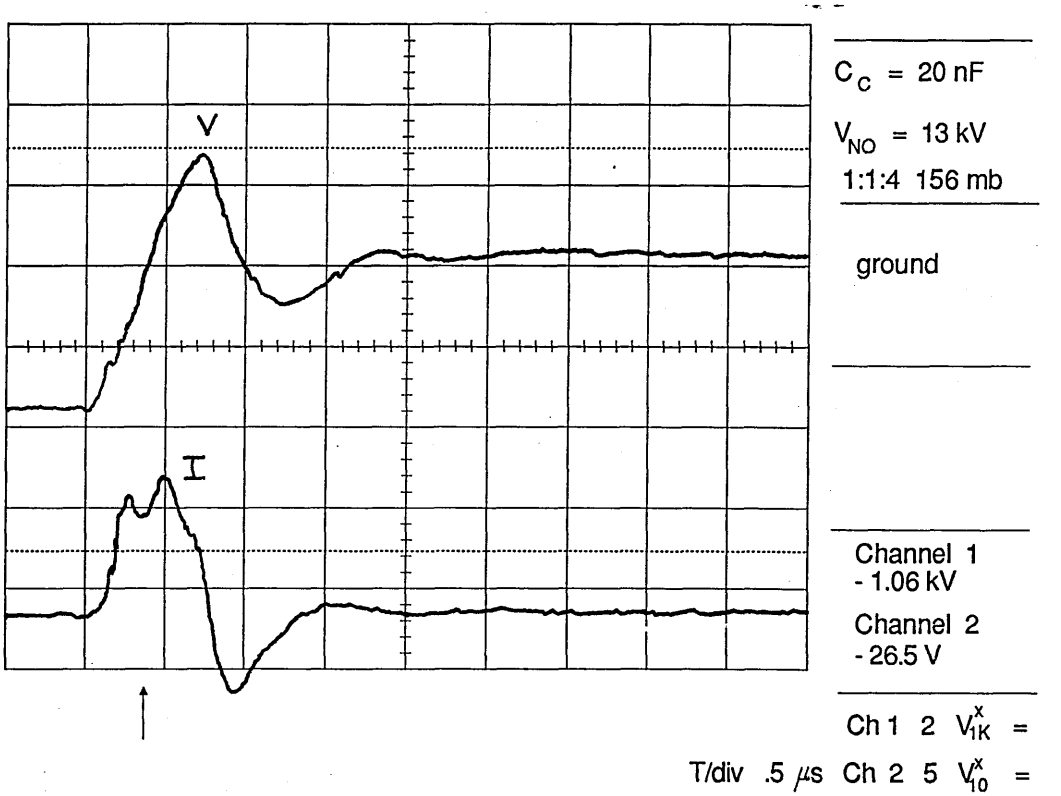

FIGURE 4.18 TRIGGER WIRE VOLTAGE AND CURRENT

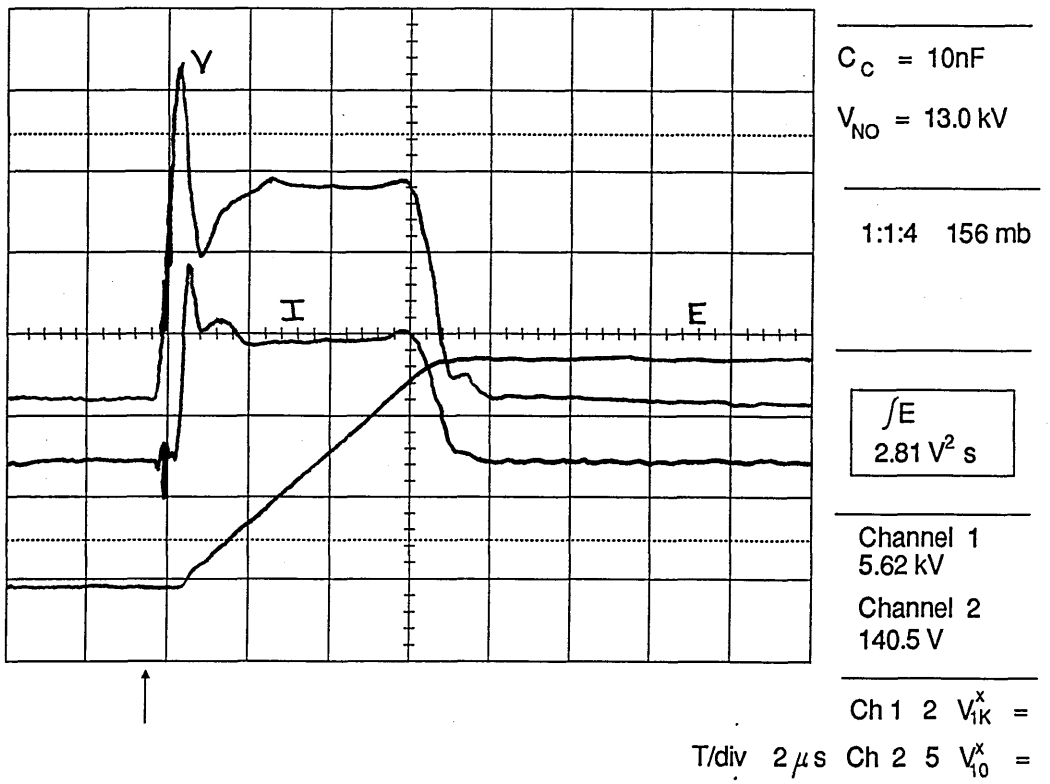

FIGURE 4.19 TRUE DISCHARGE VOLTAGE AND CURRENT

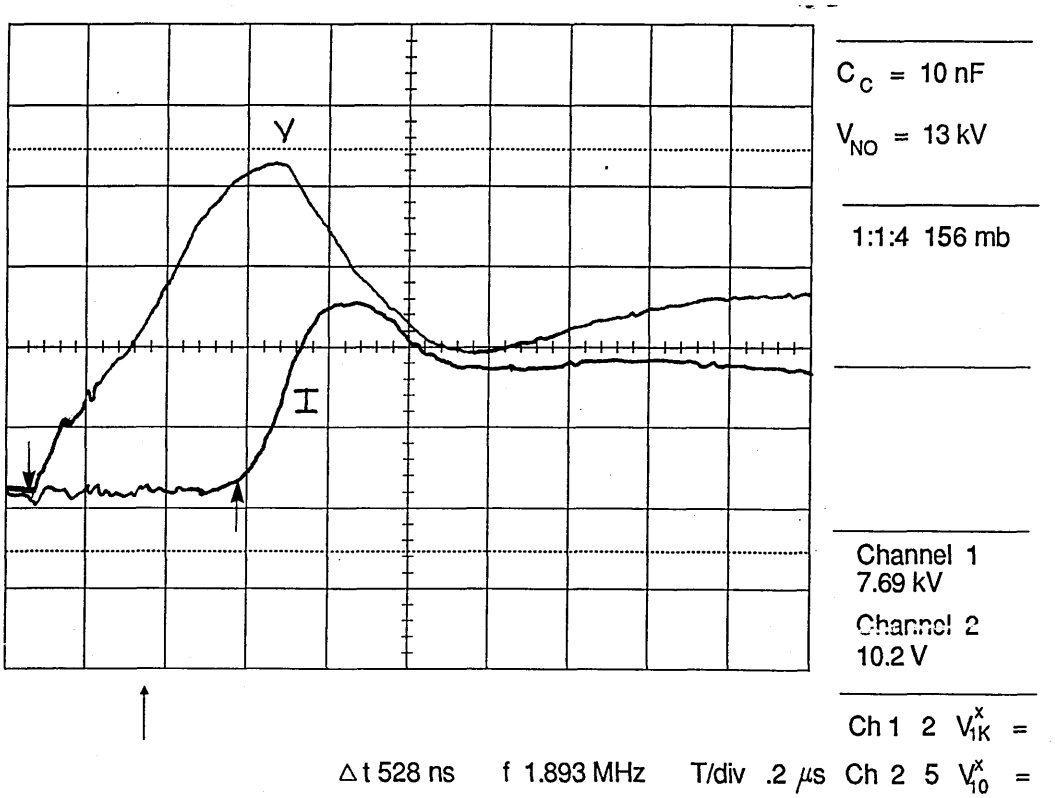

FIGURE 4.20 TRUE DISCHARGE VOLTAGE AND CURRENT - BREAKDOWN PHASE

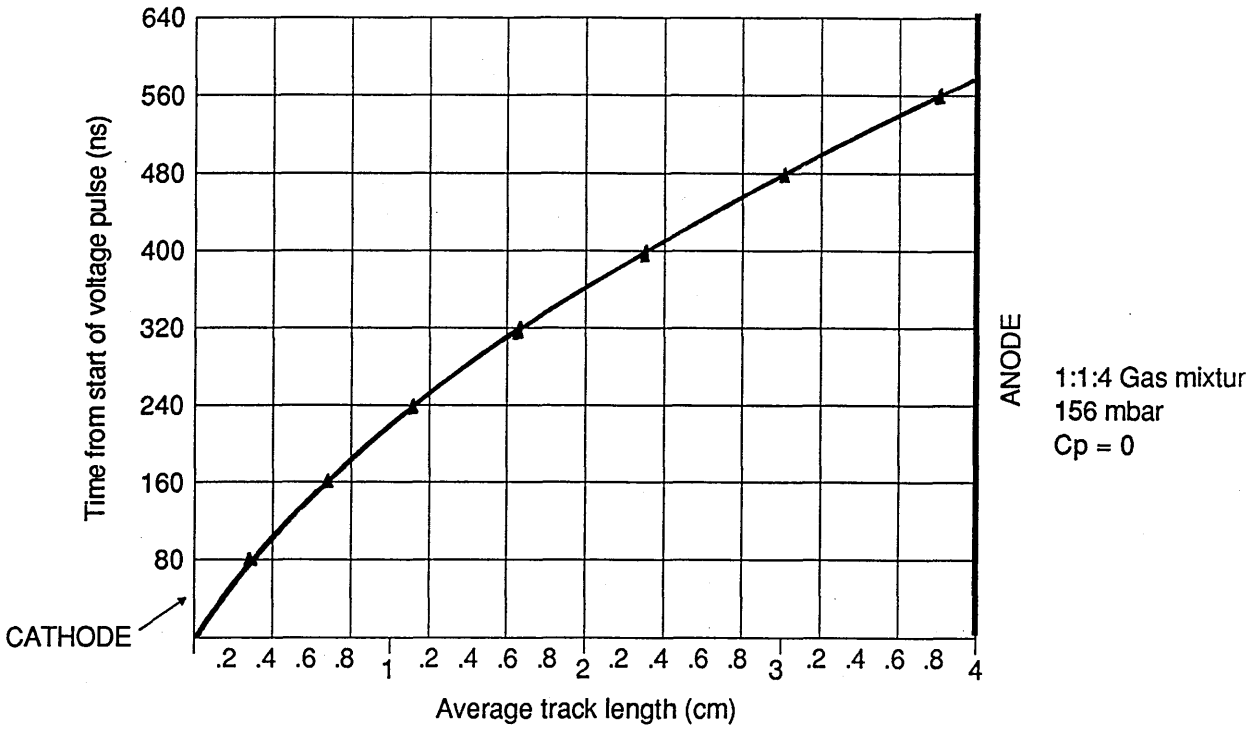

FIGURE 4.21 AVALANCHE TRACK LENGTH vs TIME

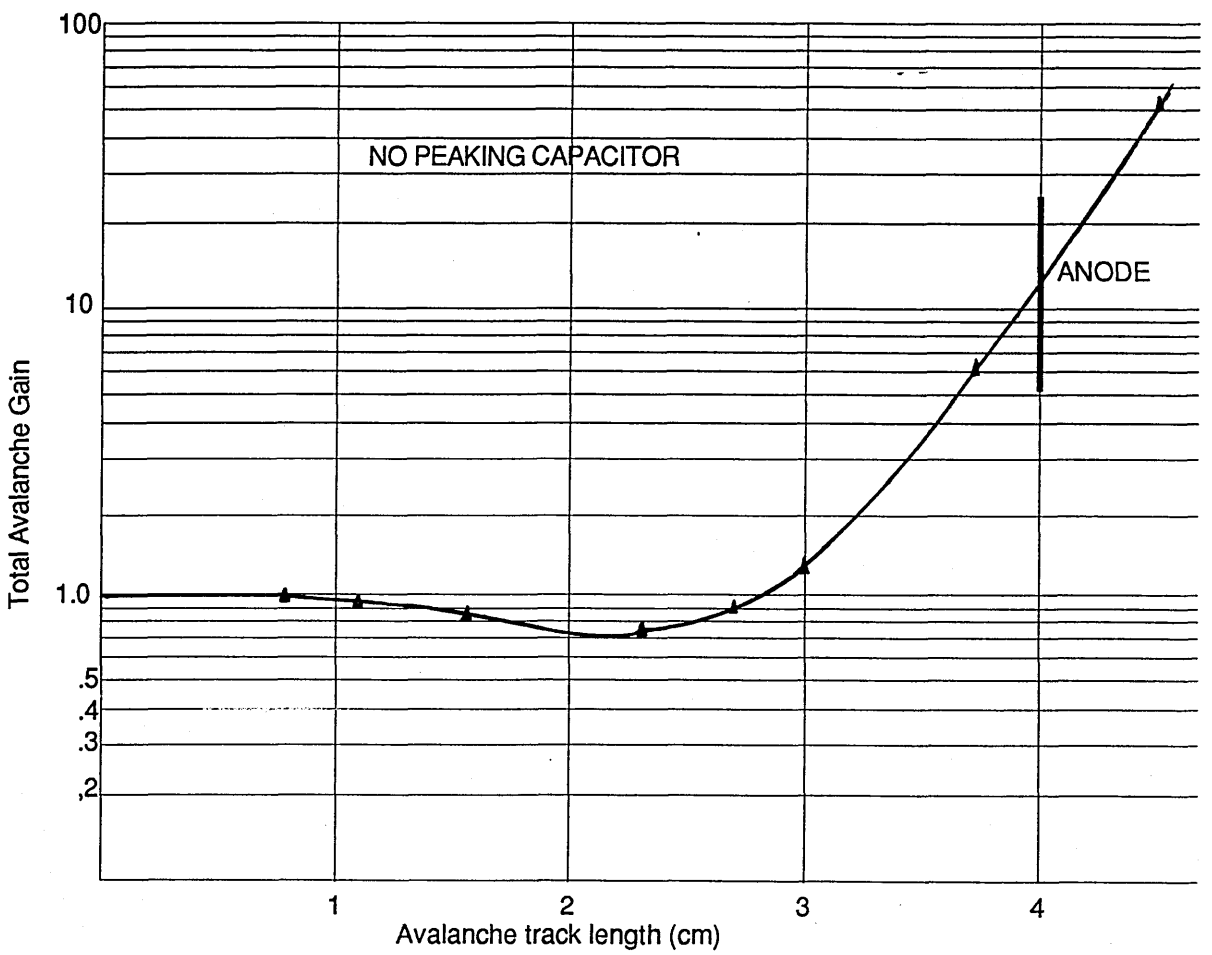

FIGURE 4.22 TOTAL AVALANCHE GAIN vs TRACK LENGTH

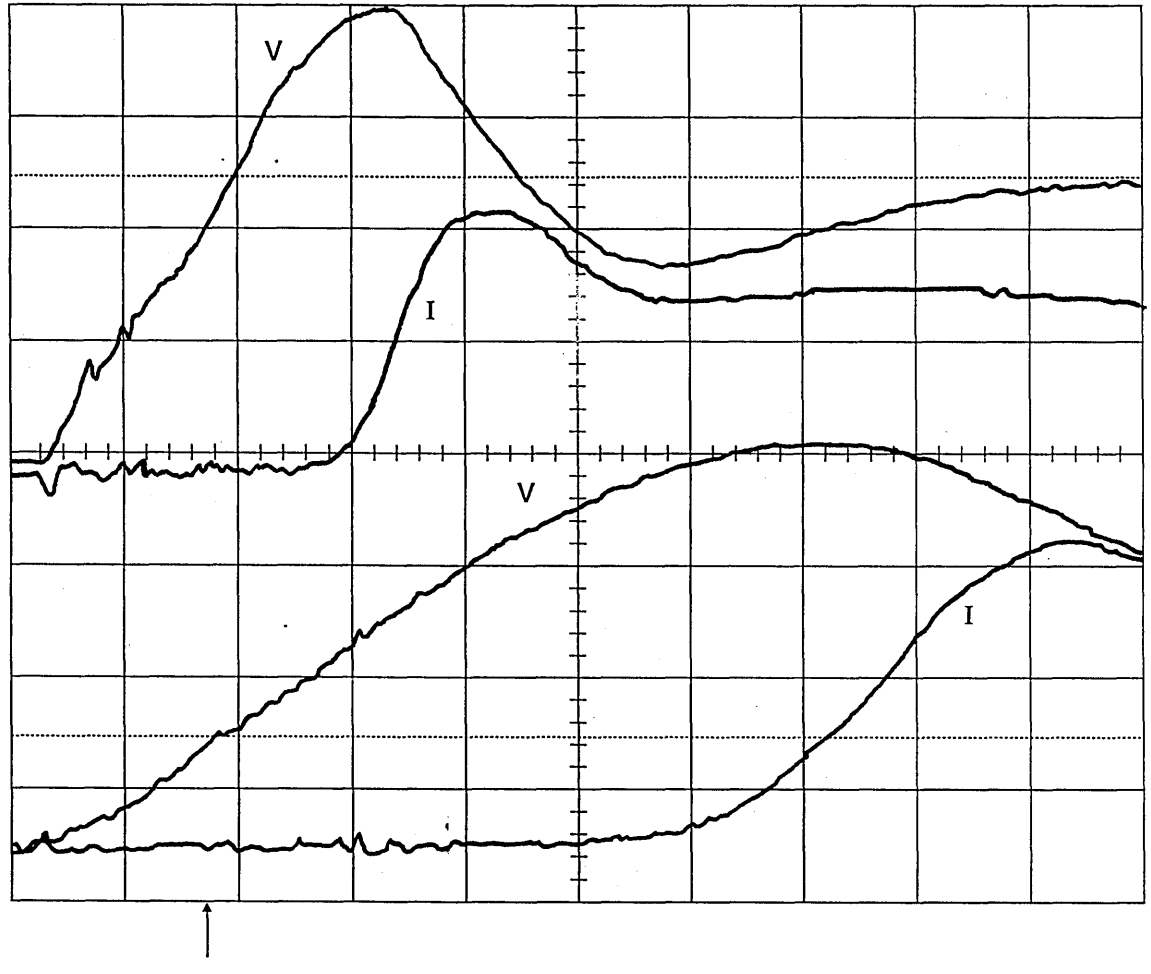

FIGURE 4.23 EFFECT OF PEAKING CAPACITOR ON BREAKDOWN TRANSIENT WAVEFORMS

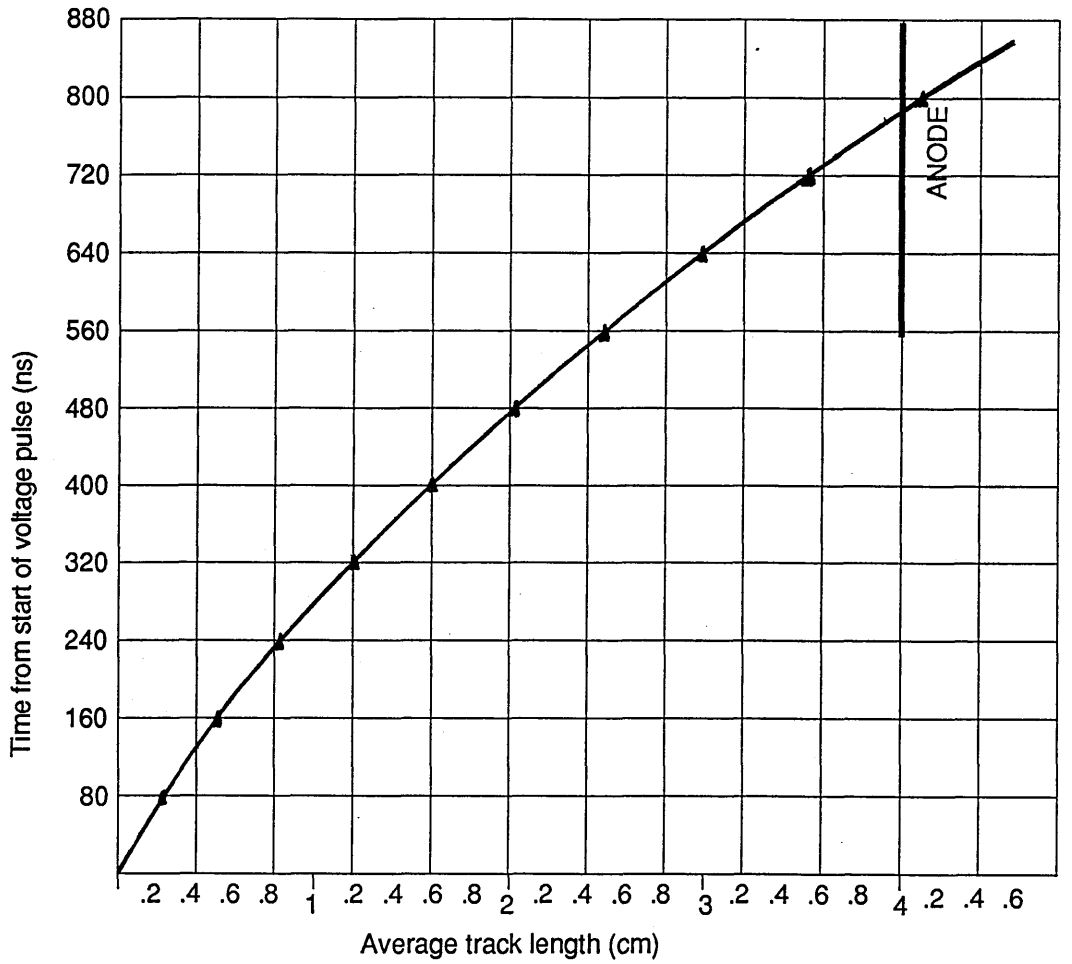

FIGURE 4.24 AVALANCHE TRACK LENGTH vs TIME WITH 10 nF PEAKING CAPACITOR

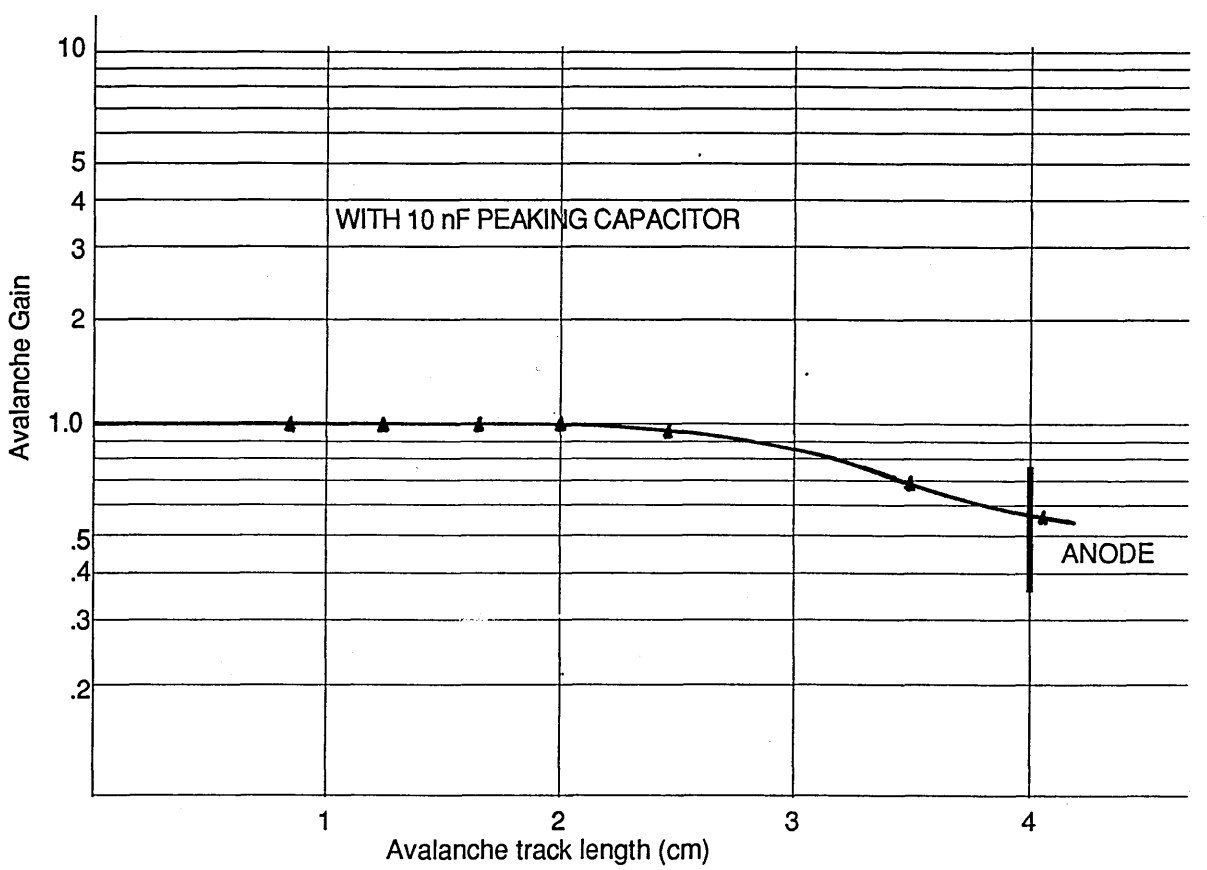

FIGURE 4.25 AVALANCHE GAIN vs TRACK LENGTH

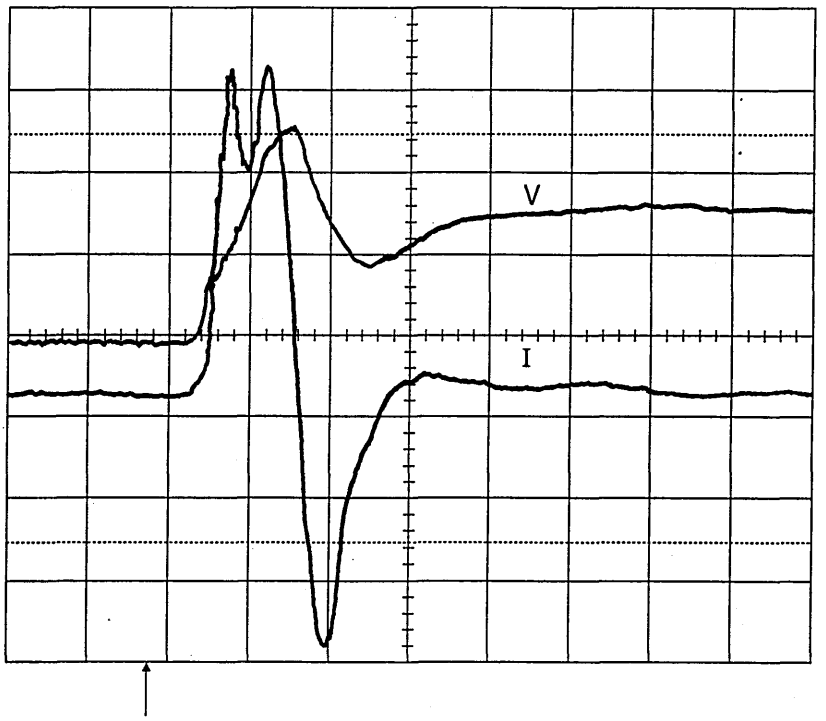

C_C = 10nF

V_{NO} = 13.0 kV

No peaking capacitor

1:1:4 156 mb

Channel 1
.5 μs 2 kV

Channel 2
.5 μs 20 V

Ch 1 2 V_{1K}^{x} =

T/div .5 μs Ch 2 2 V_{10}^{x} =

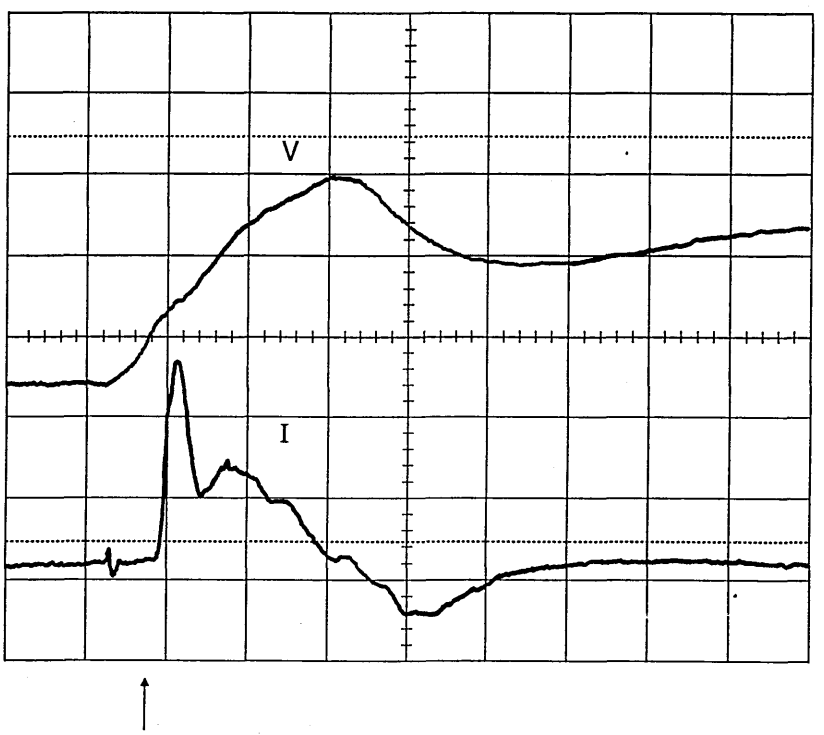

C_C = 10 nF

C_p = 10 nF

grooved electrode

Trig wire height
1.91 mm

ground

Channel 1
- 1.20 kV

Channel 2
- 12.0 V

Ch 1 2 V_{1K}^{x} =

T/div .5 μs Ch 2 2 V_{10}^{x} =

FIGURE 4.26 EFFECT of Cp on TRIGGER WIRE VOLTAGE / CURRENT

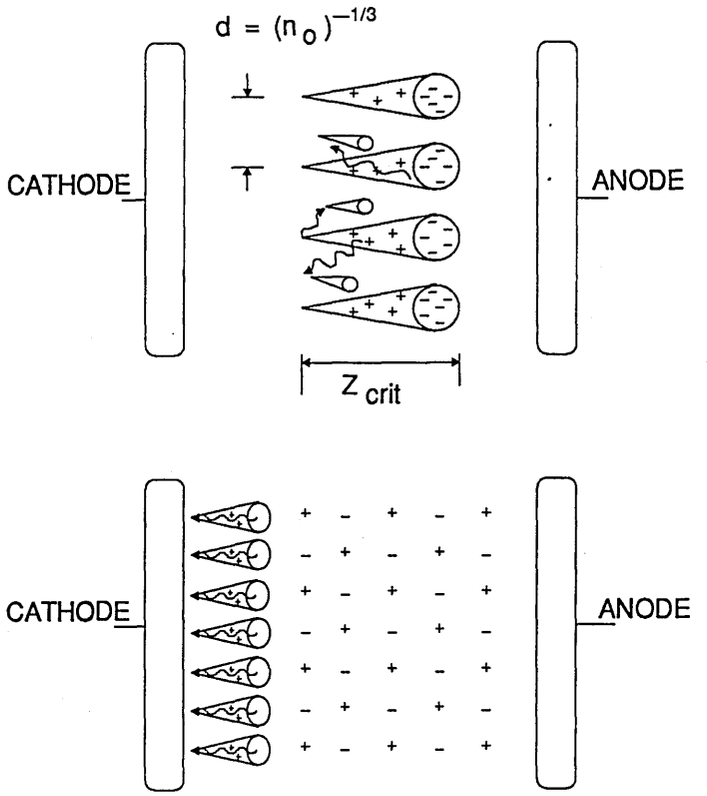

FIGURE 4.27 PALMER'S MODEL OF PREIONIZATION

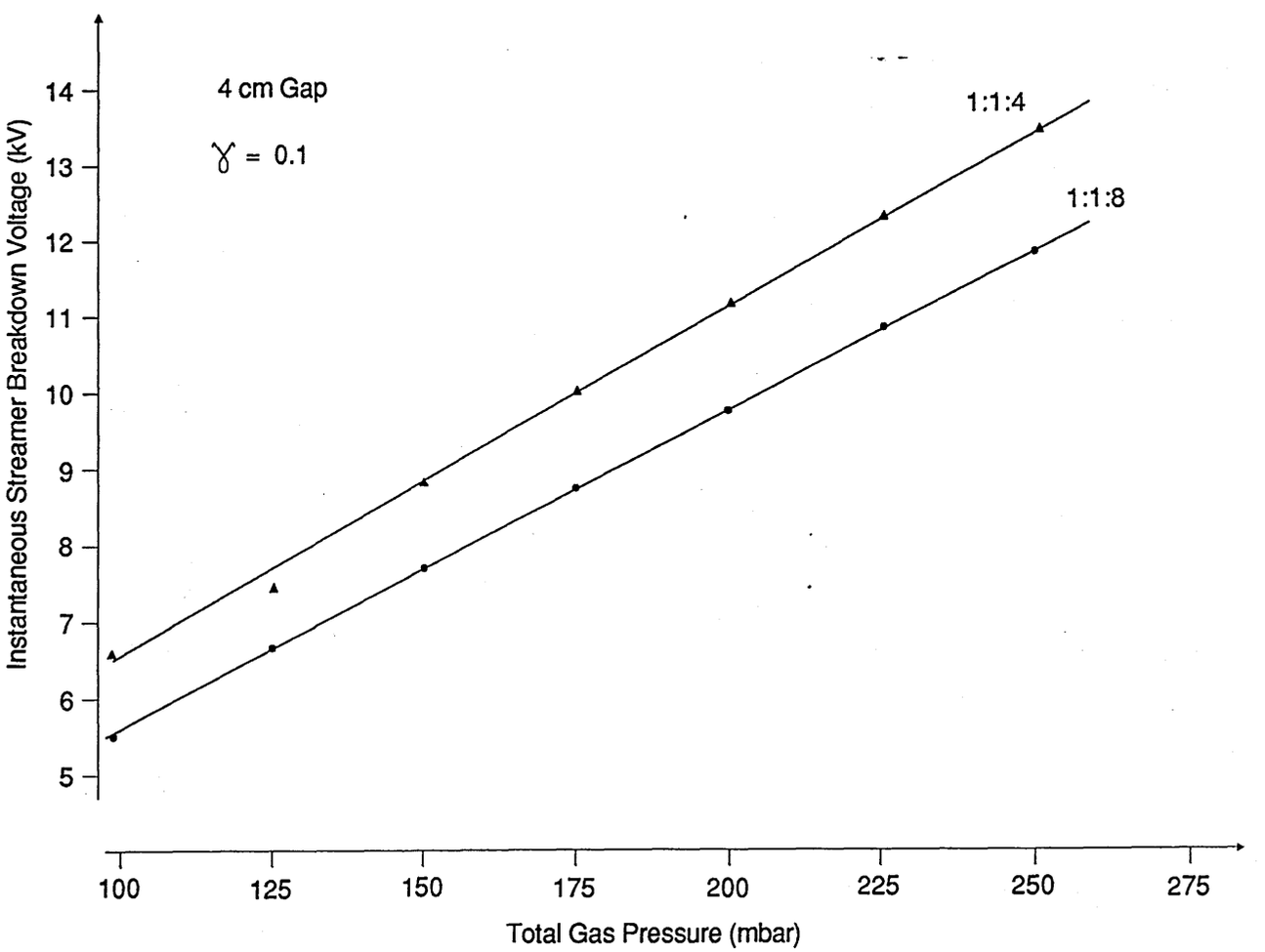

FIGURE 4.28 STREAMER BREAKDOWN VOLTAGE vs GAS PRESSURE

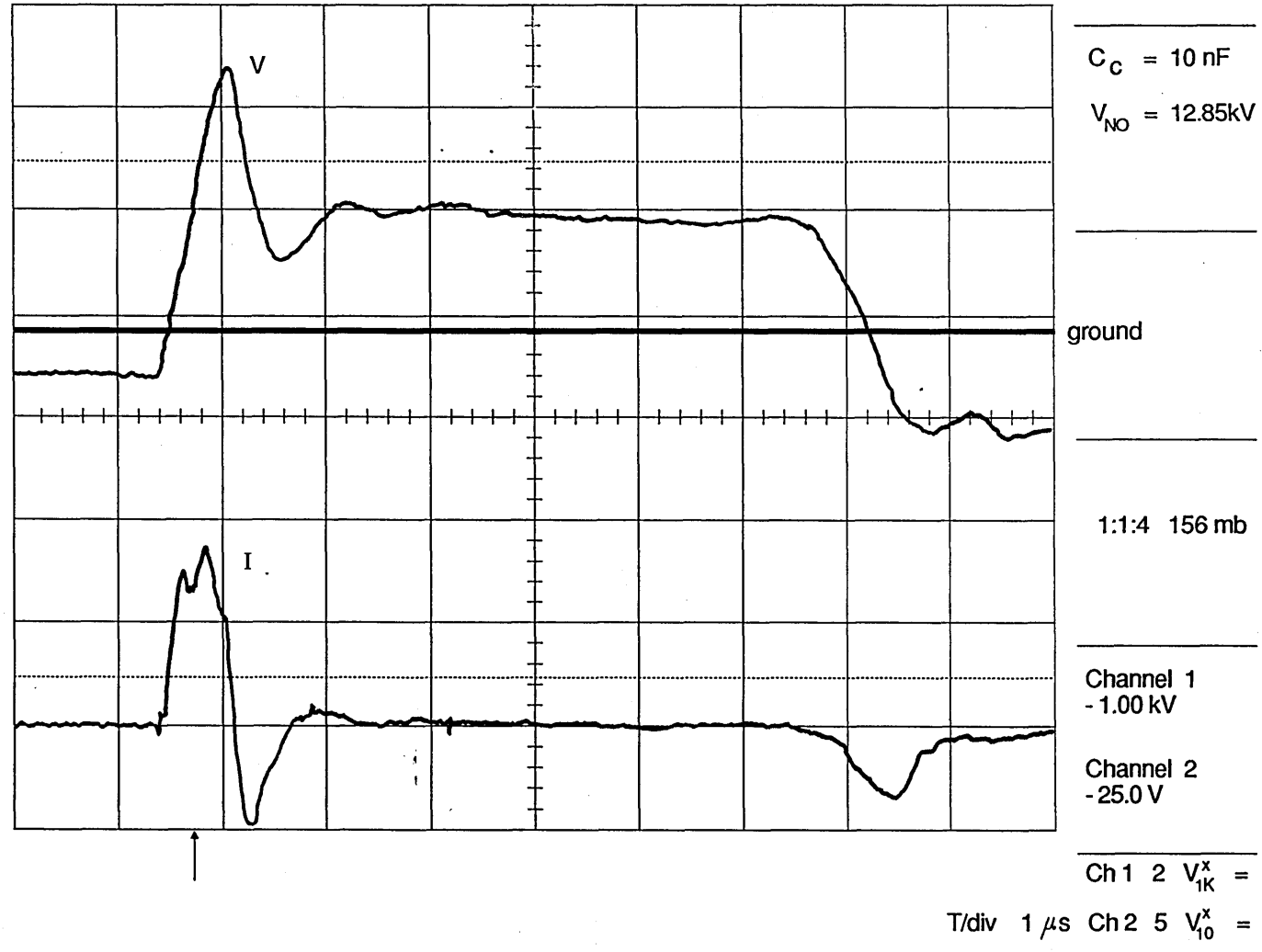

FIGURE 4.29 TRIGGER WIRE VOLTAGE AND CURRENT

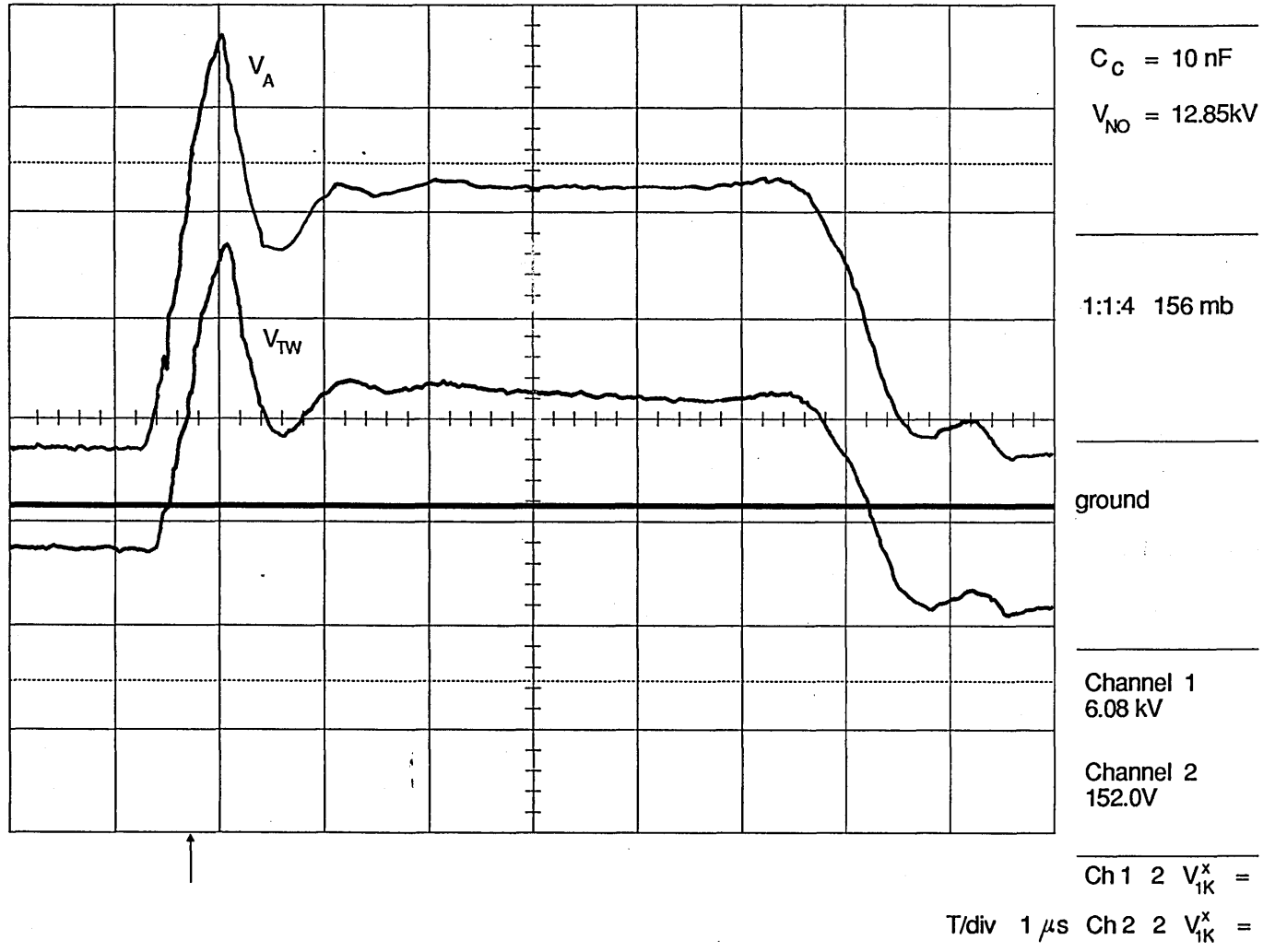

FIGURE 4.30 TRIGGER WIRE VOLTAGE AND ANODE VOLTAGE

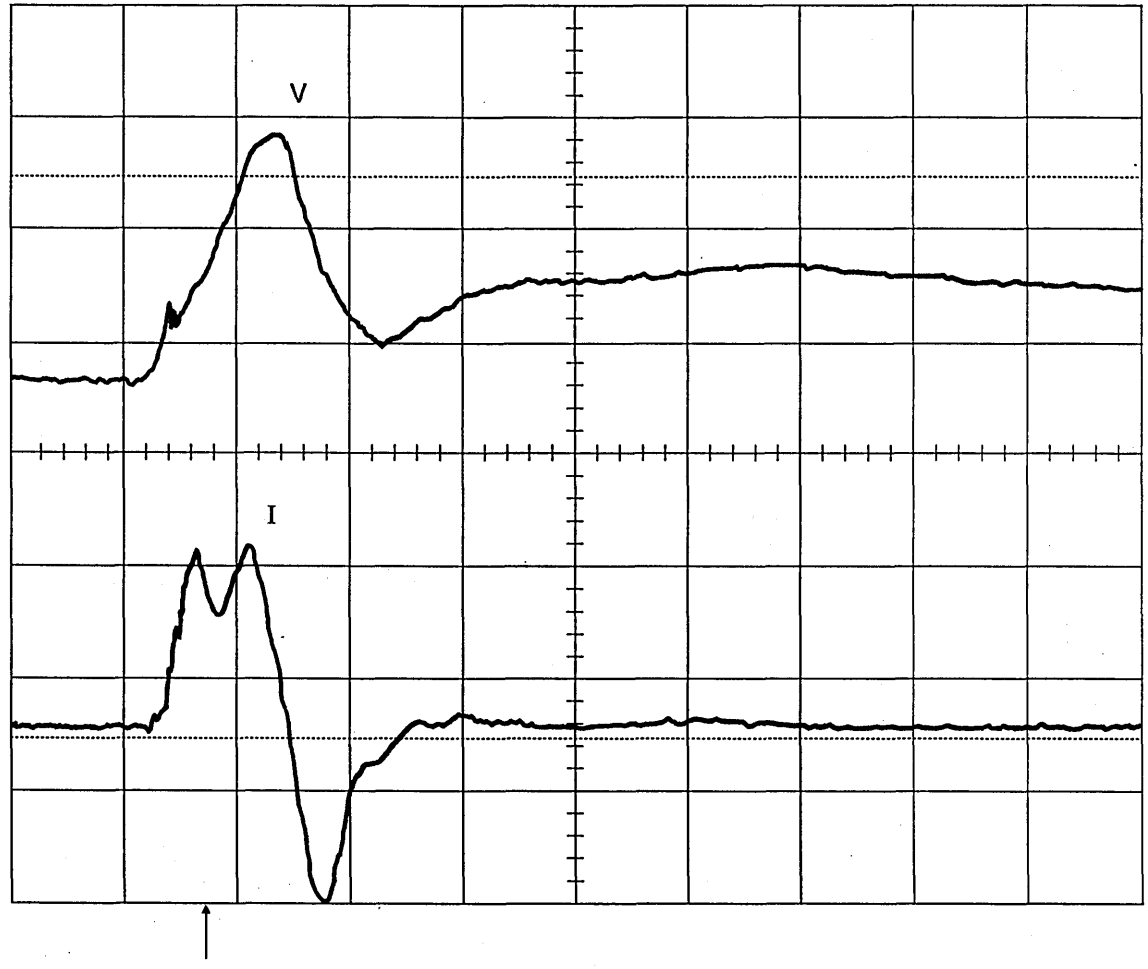

FIGURE 4.31 TRIGGER WIRE VOLTAGE AND CURRENT

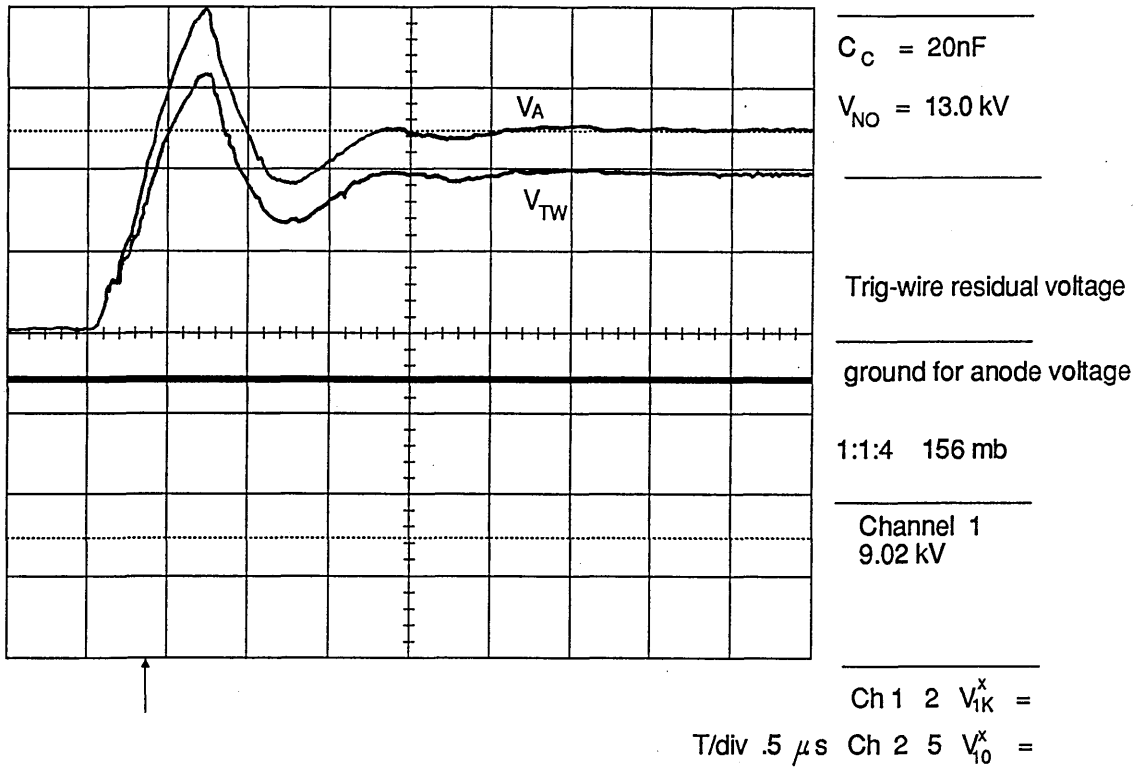

FIGURE 4.32 TRIGGER WIRE/ANODE VOLTAGE C_C = 20 nF

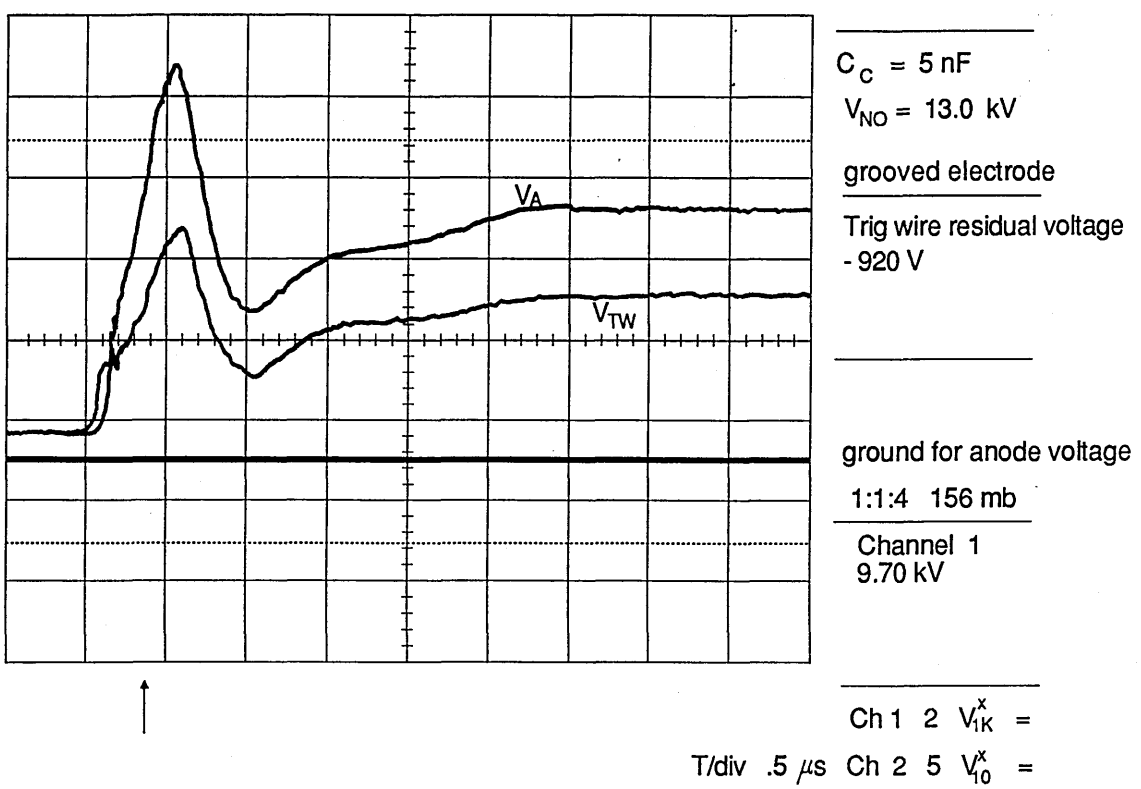

FIGURE 4.33 TRIGGER WIRE/ANODE VOLTAGE C_C = 5 nF

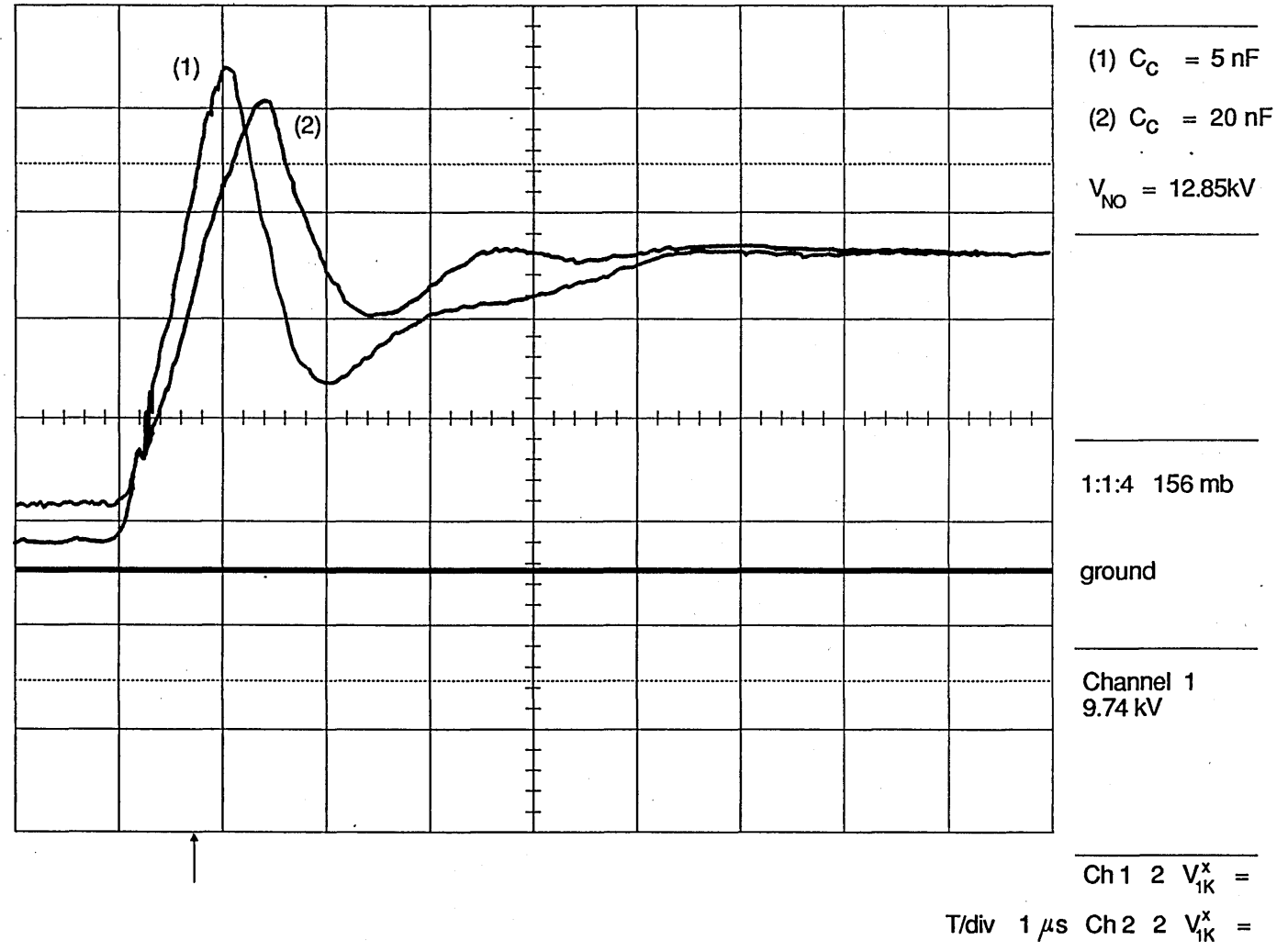

FIGURE 4.34 ANODE VOLTAGE WAVEFORMS vs C_C

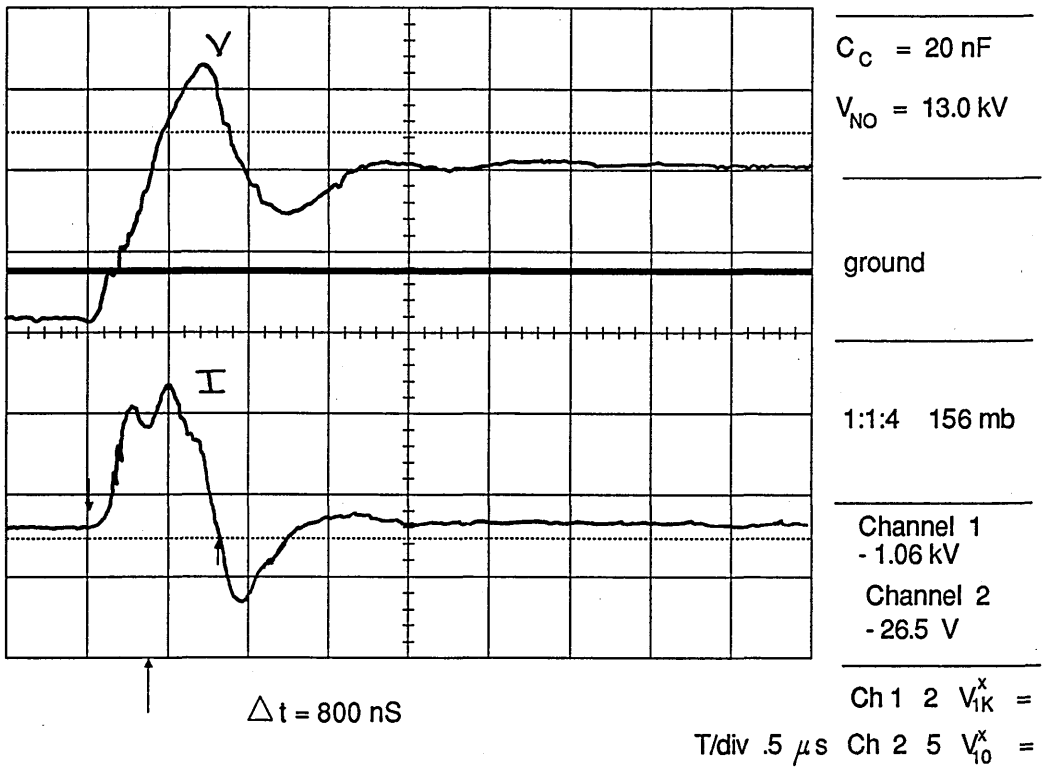

FIGURE 4.35 TRIGGER-WIRE VOLTAGE AND CURRENT C_C = 20 nF

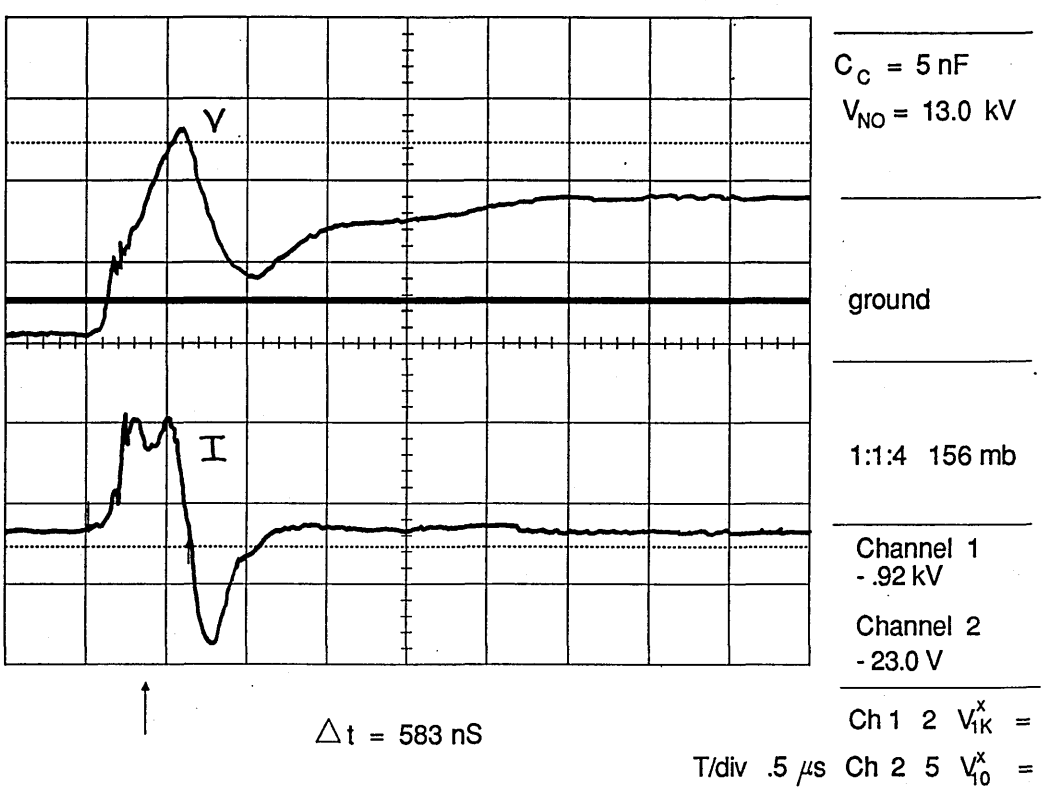

FIGURE 4.36 TRIGGER-WIRE VOLTAGE AND CURRENT C_C = 5 nF

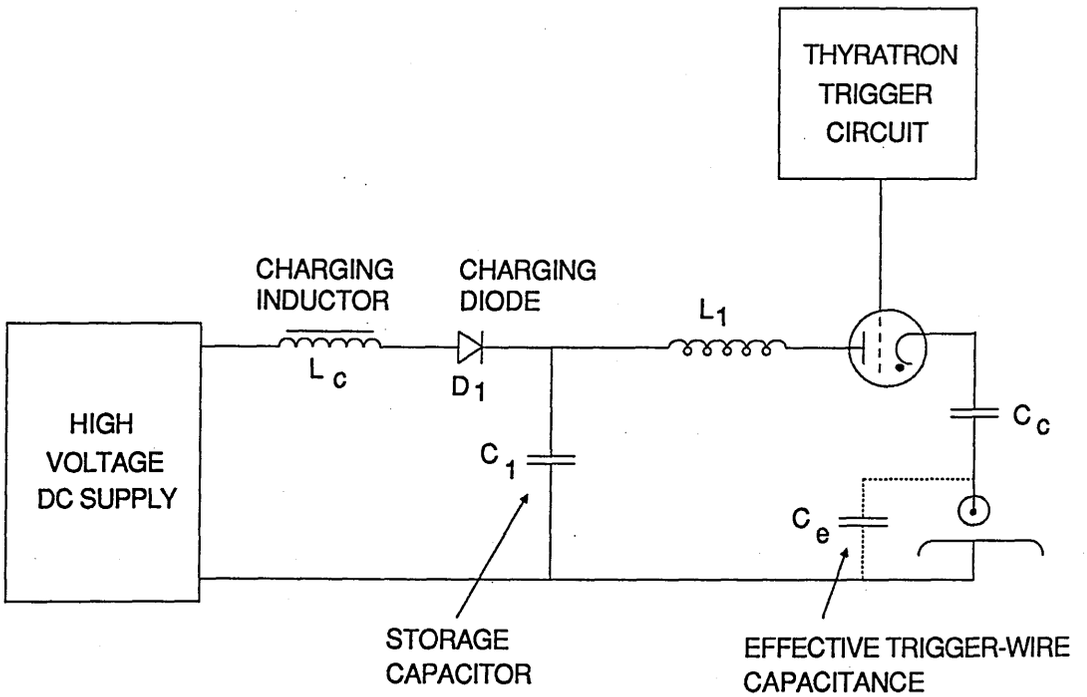

FIGURE 4.37 SCHEMATIC OF PREIONIZER CIRCUIT

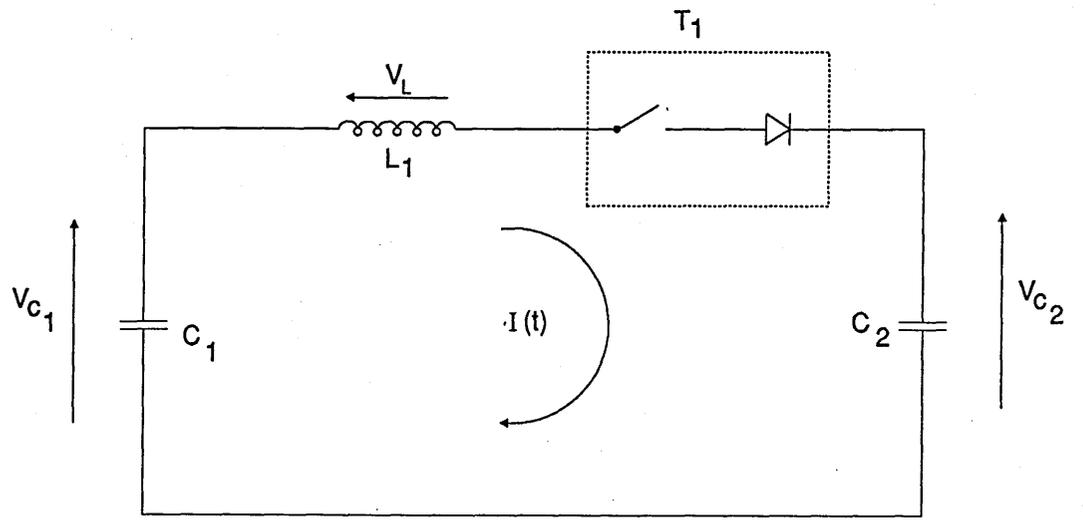

FIGURE 4.38 EQUIVALENT CIRCUIT OF OUTPUT STAGE

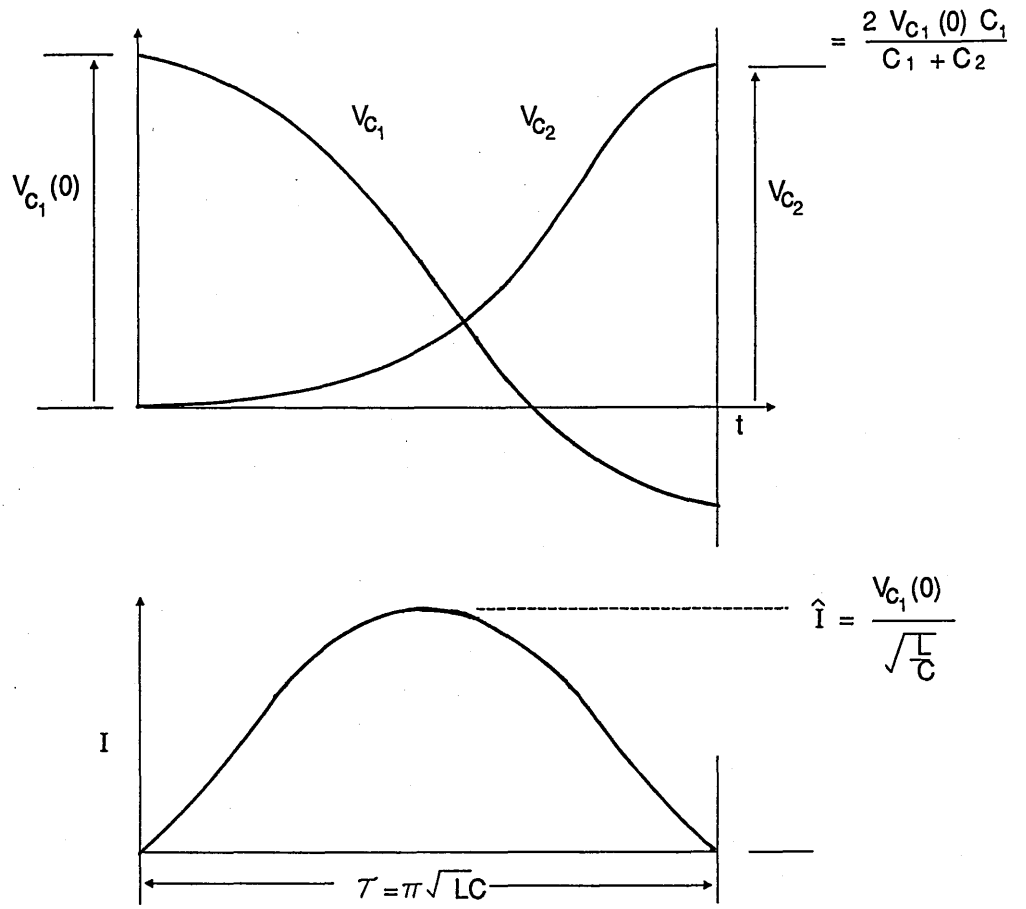

FIGURE 4.39 TRANSIENT RESPONSE OF CLC CIRCUIT

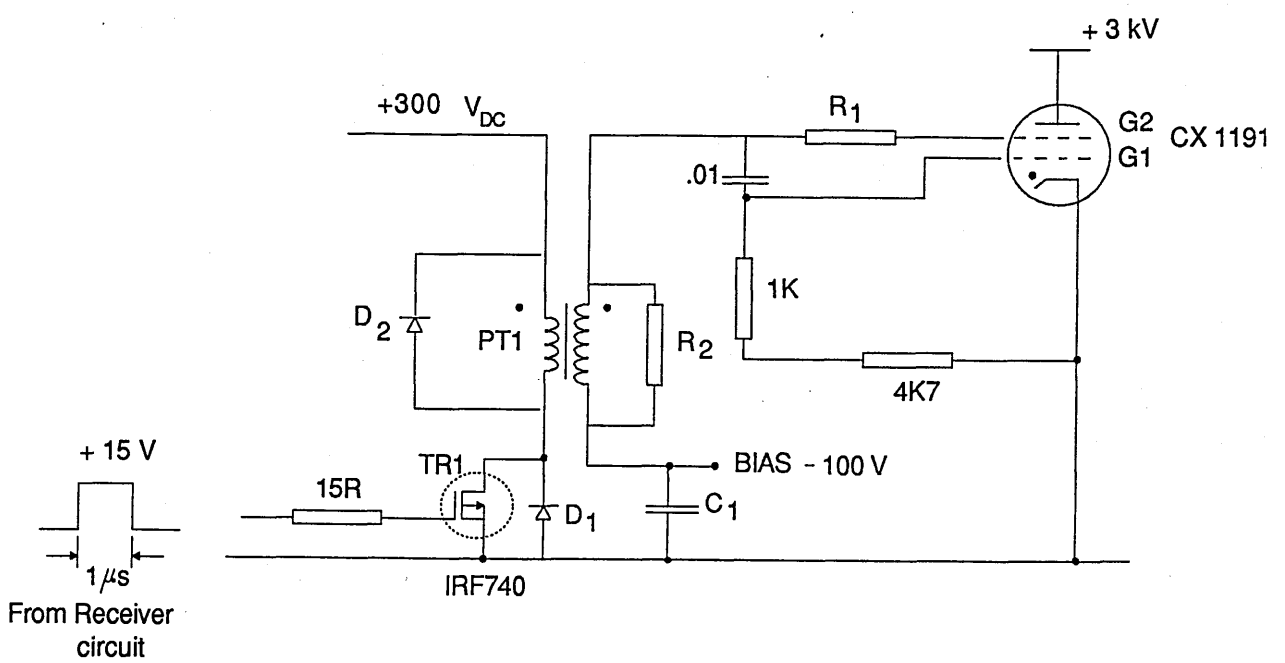

FIGURE 4.40 CX1191 TRIGGER CIRCUIT

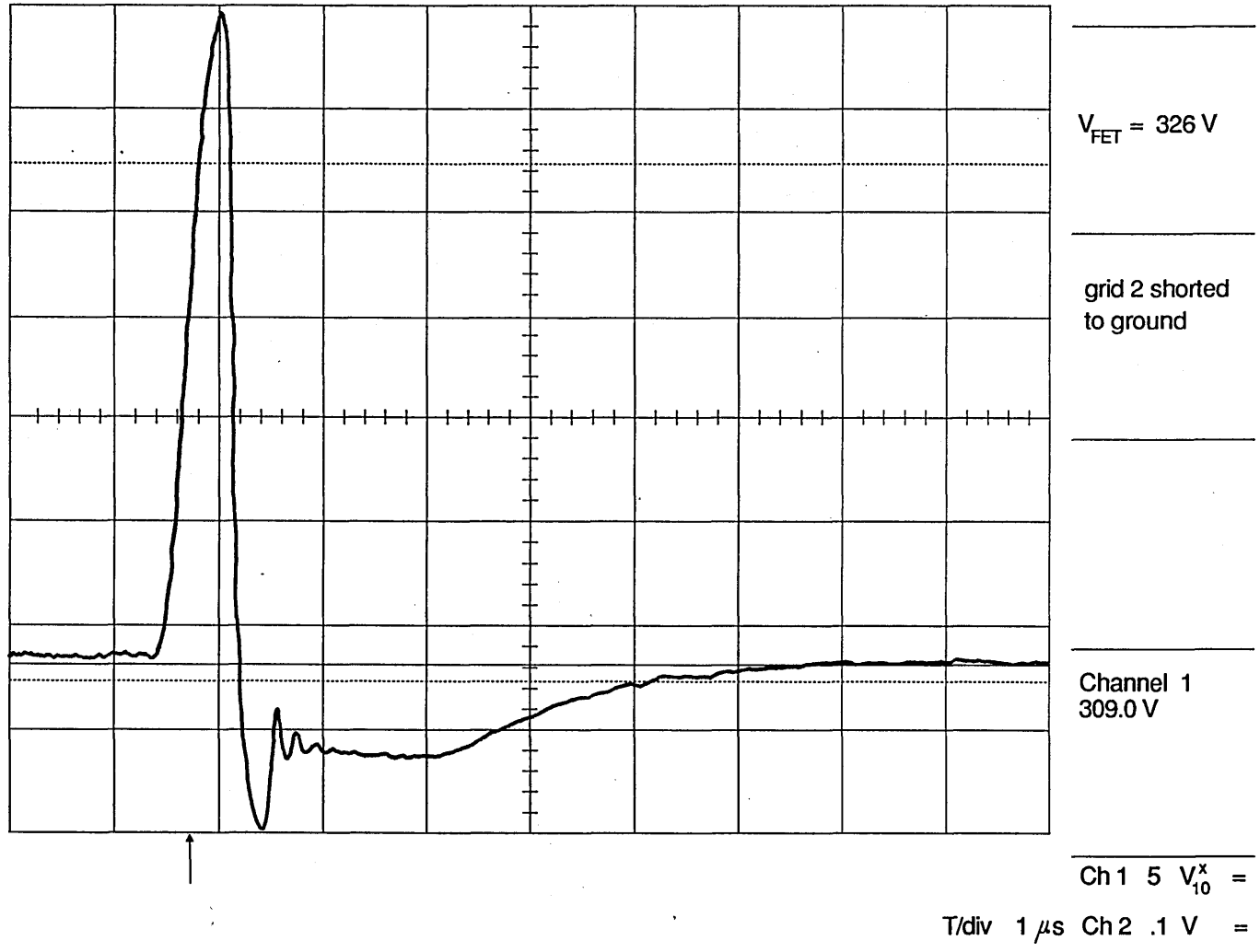

FIGURE 4.41 CX1191 TRIGGER PULSE

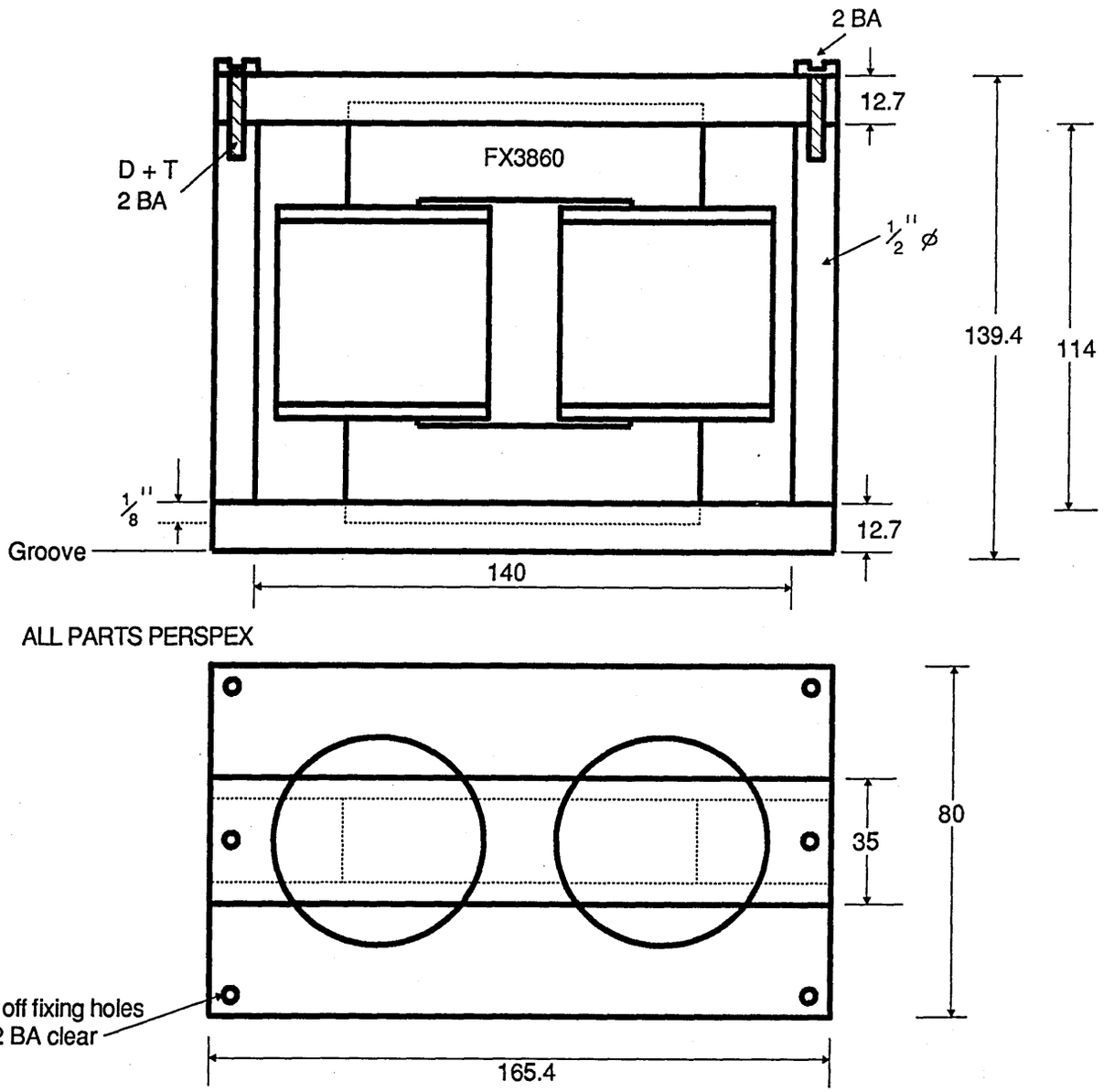

WIRE GAUGE 0.8 mm TOTAL No. TURNS 565

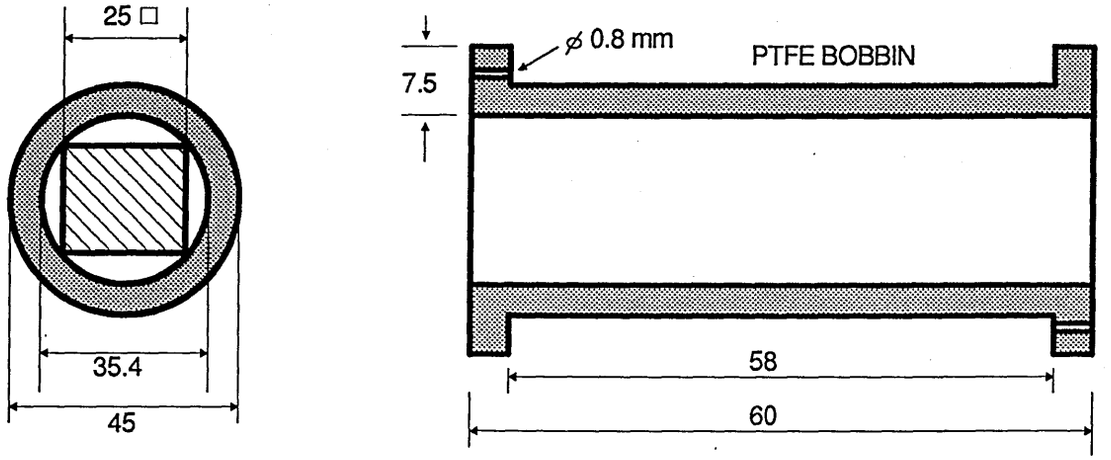

FIGURE 4.42 MECHANICAL DESIGN OF CHARGING INDUCTOR

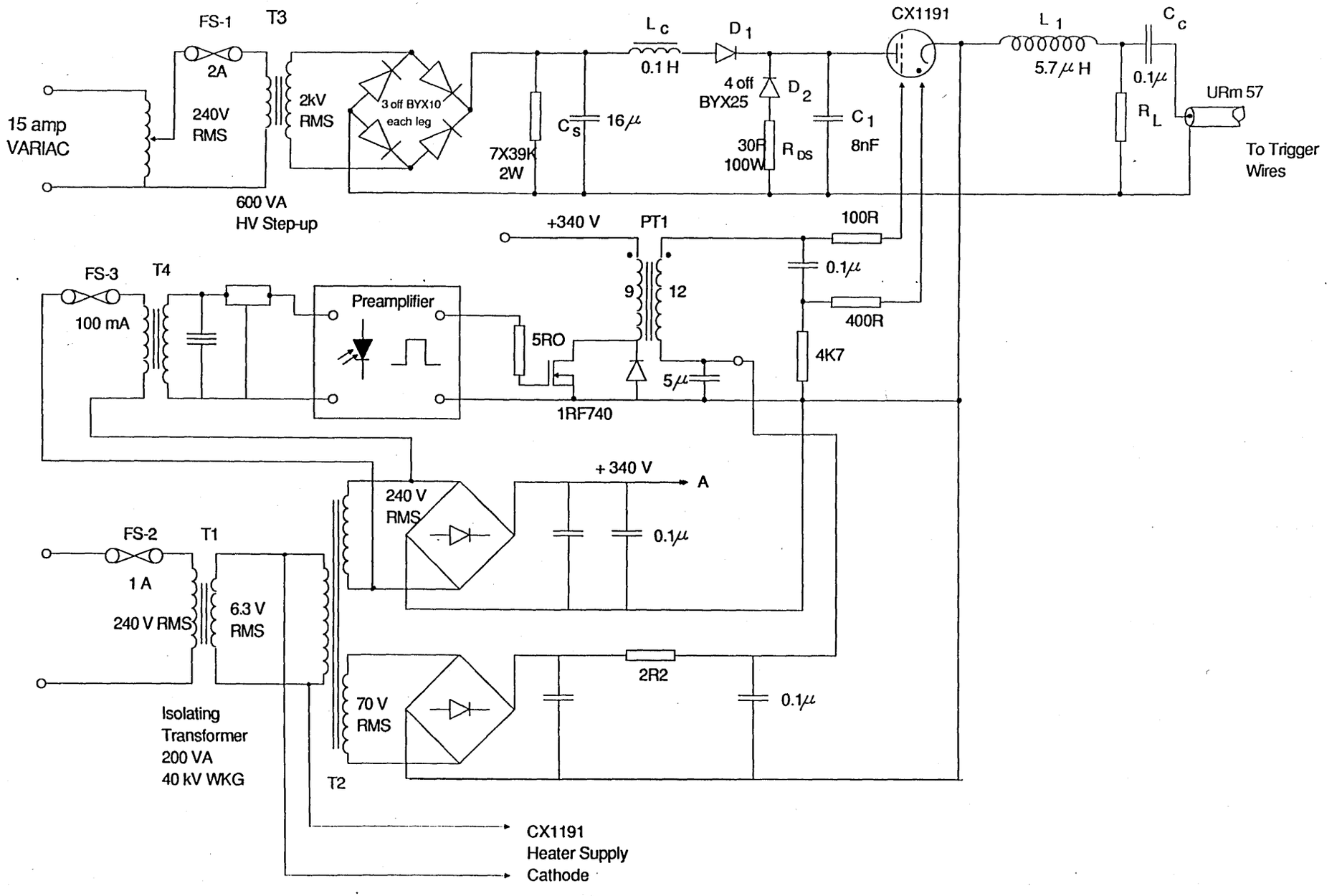

FIGURE 4.43 SCHEMATIC OF PREIONOZER CIRCUIT

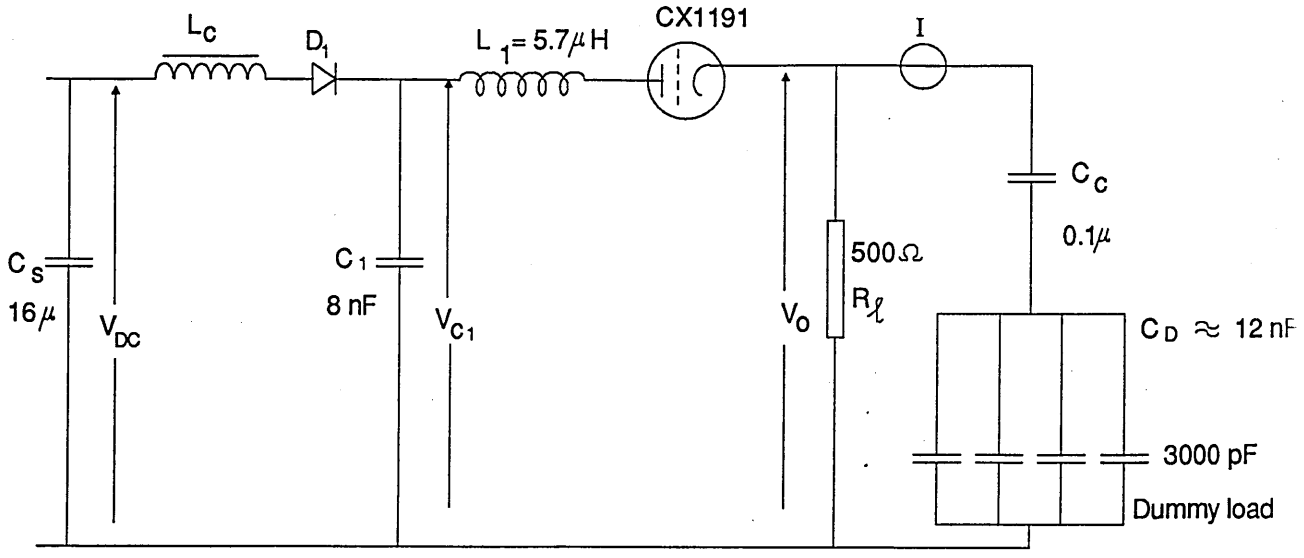

FIGURE 4.44 PREIONIZER COMMISSIONING CIRCUIT

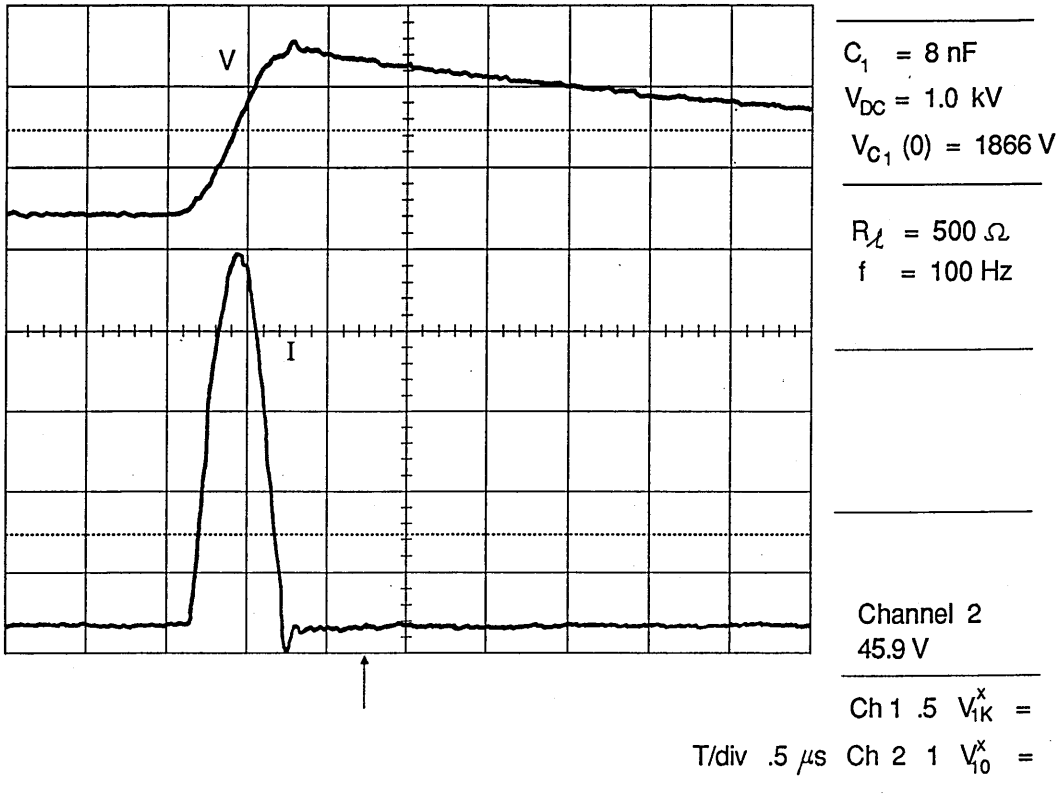

FIGURE 4.45 PREIONIZER OUTPUT ON COMMISSIONING CIRCUIT

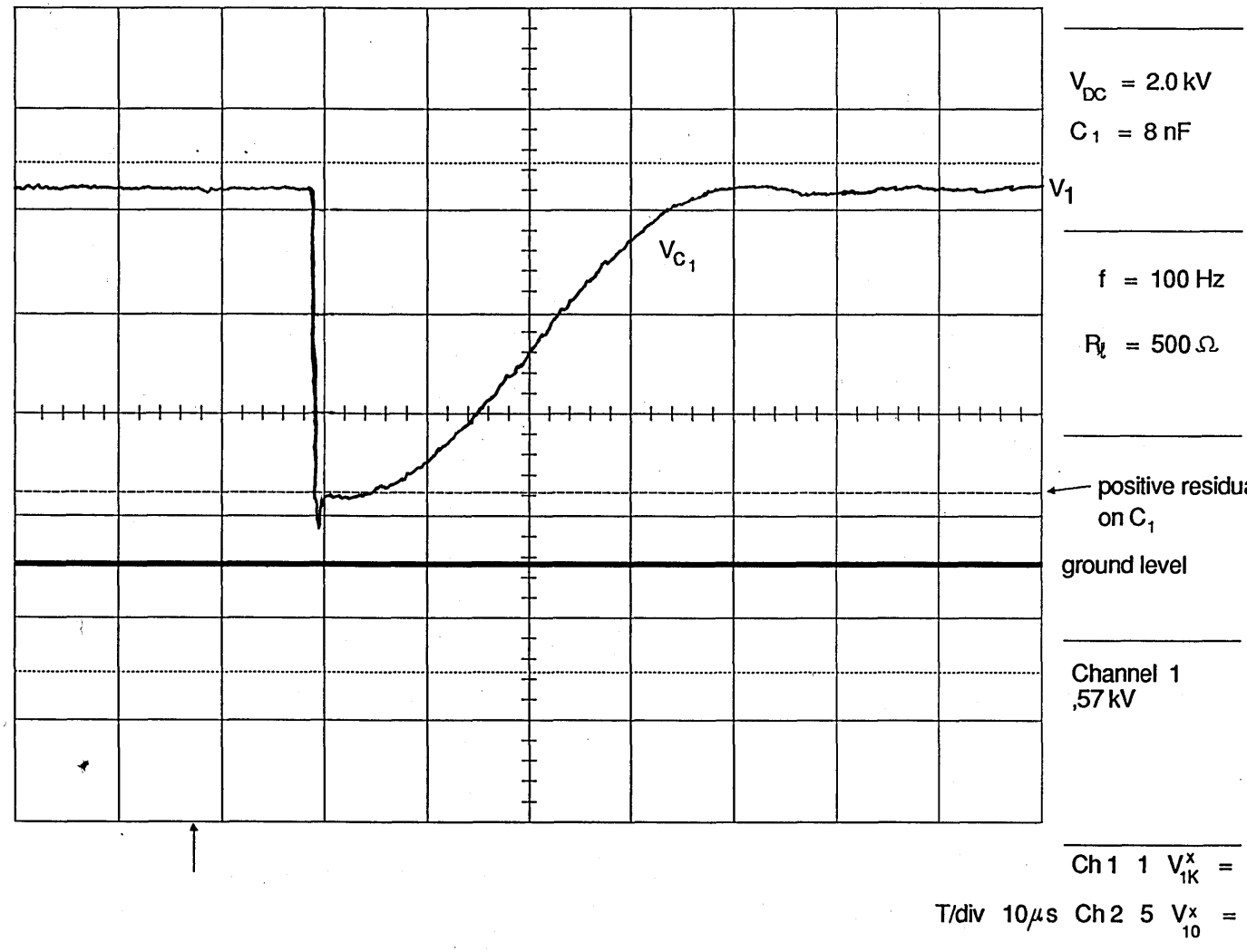

FIGURE 4.46 C_1 CHARGING CYCLE VOLTAGE

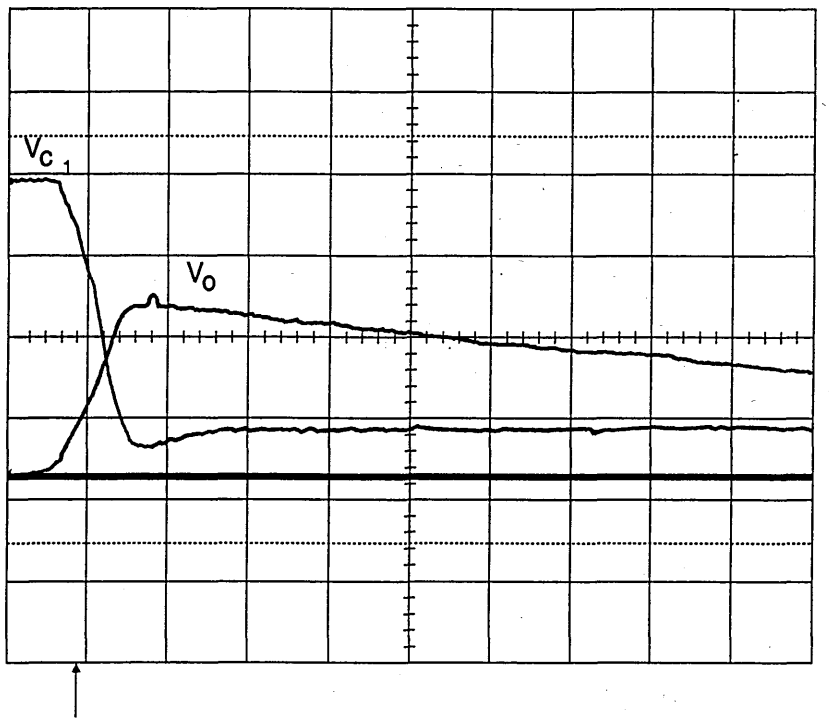

C_1 = 8 nF

V_{DC} = 1 kV

R_ℓ = 500 Ω

f = 100 Hz

ground

Channel 1
155 V

Channel 2
-155 V

Ch 1 .5 V_{1K}^{x} =

T/div .5 μs Ch 2 .5 V_{1K}^{x} =

FIGURE 4.47 C_1 VOLTAGE AND OUTPUT VOLTAGE : C_1 = 8 nF

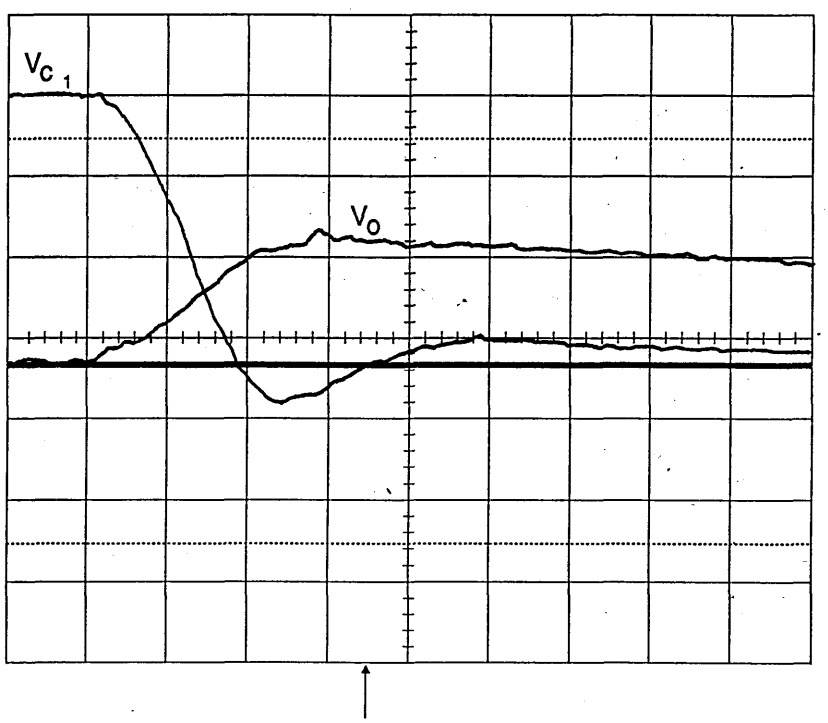

C_1 = 5 nF

V_{DC} = 1.0 kV

R_ℓ = 500 Ω

f = 100 Hz

ground

Channel 1
1670 V

Channel 2
1670 V

Ch 1 .5 V_{1K}^{x} =

T/div .5 μs Ch 2 .5 V_{1K}^{x} =

FIGURE 4.48 C_1 VOLTAGE AND OUTPUT VOLTAGE : C_1 = 5 nF

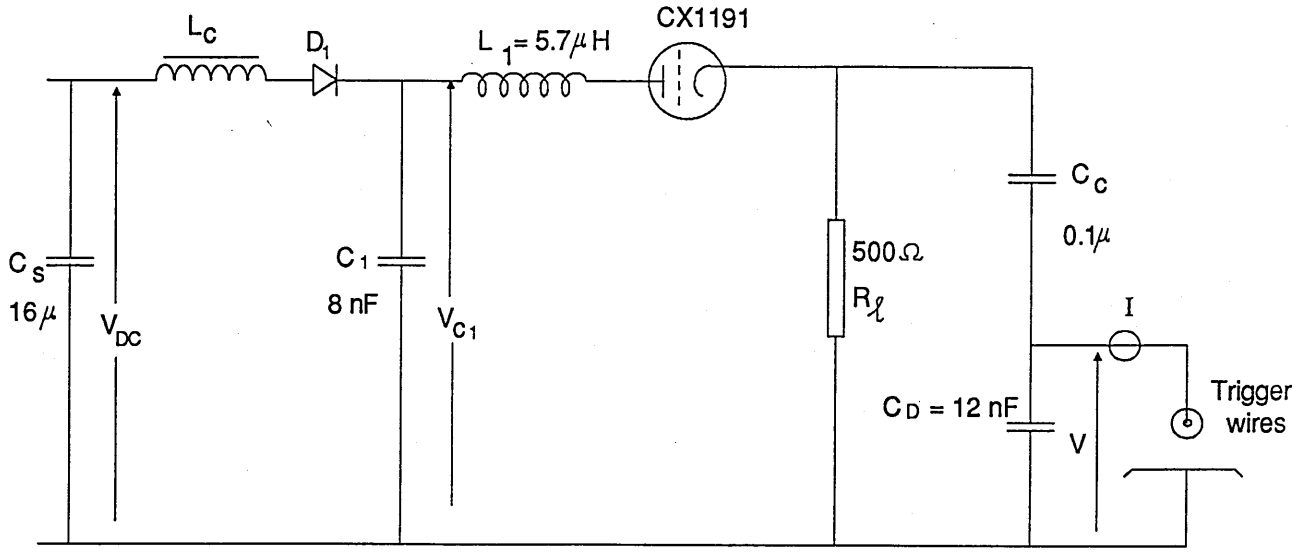

FIGURE 4.49 PREIONIZER OUTPUT CIRCUIT WITH PRELOAD

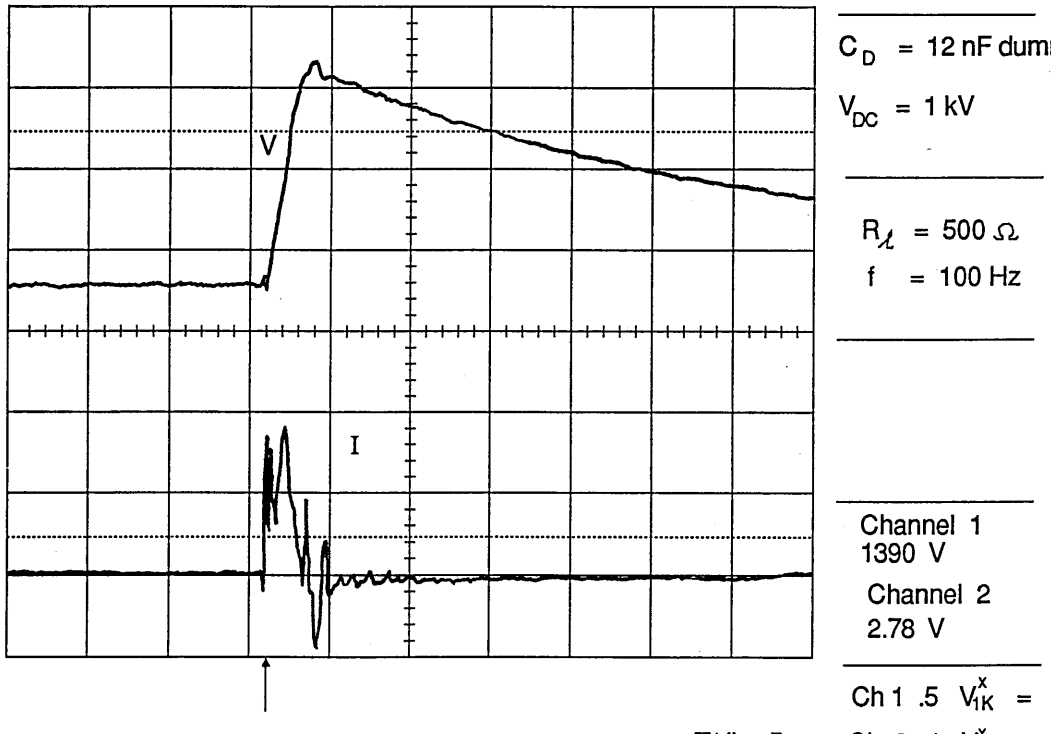

FIGURE 4.50 TRIGGER-WIRE VOLTAGE AND CURRENT

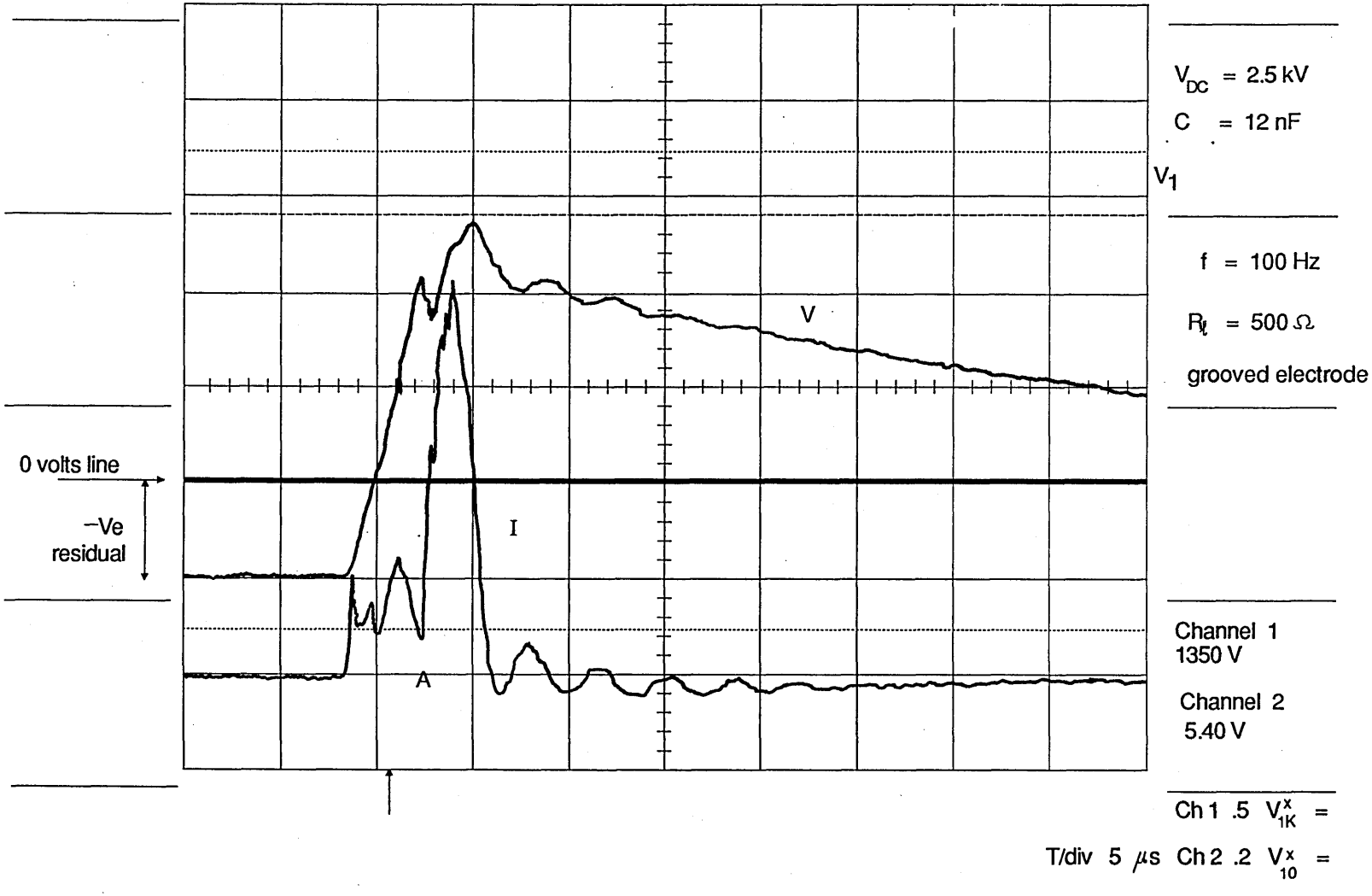

FIGURE 4.51 TRIGGER WIRE VOLTAGE AND CURRENT.

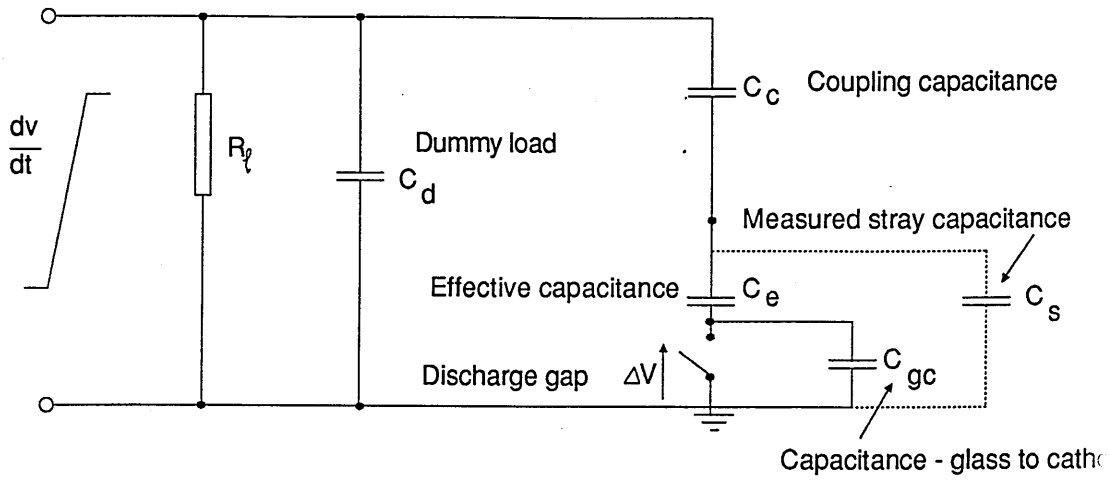

(a) Pre-breakdown phase

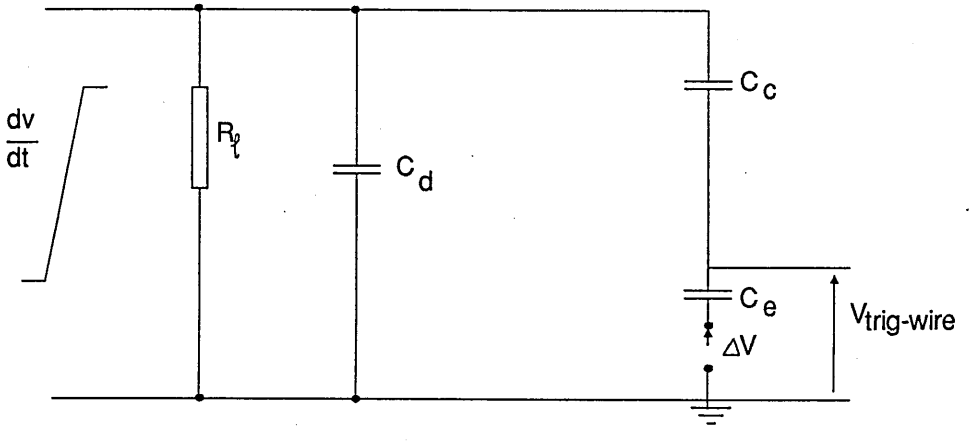

(b) Discharge phase

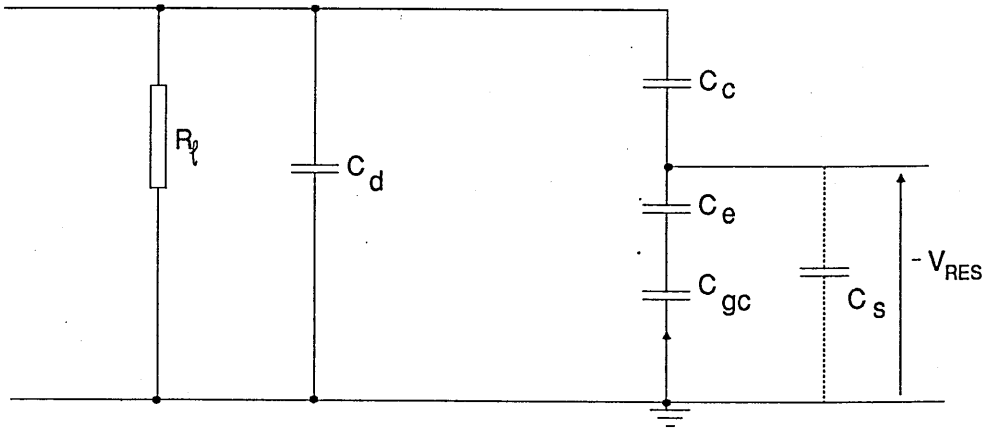

(c) Post-breakdown phase

FIGURE 4.52 CIRCUIT MODELS FOR TRIGGER WIRE BREAKDOWN

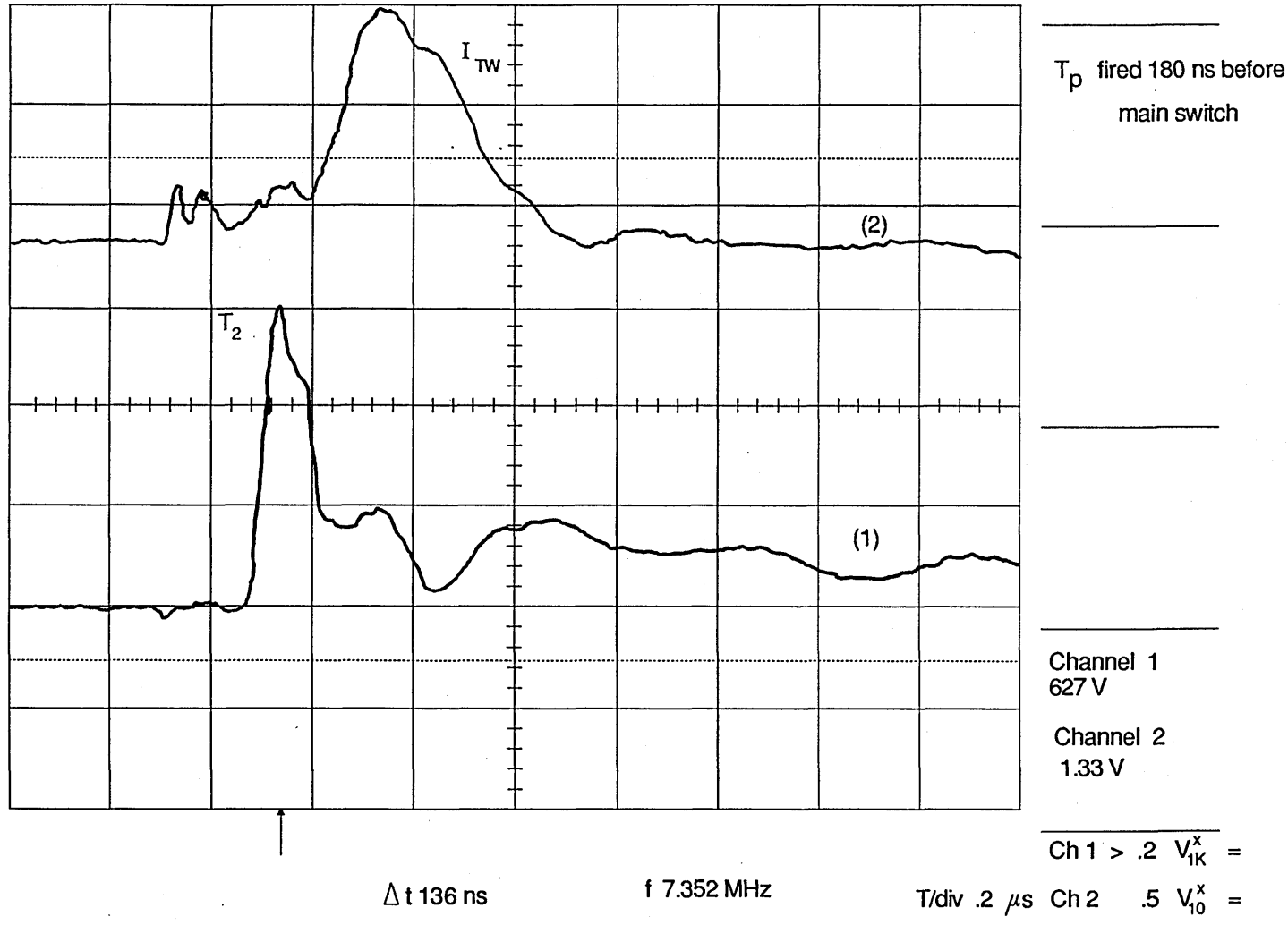

FIGURE 4.53 TRIGGER WIRE CURRENT / T_2 TRIGGER PULSE

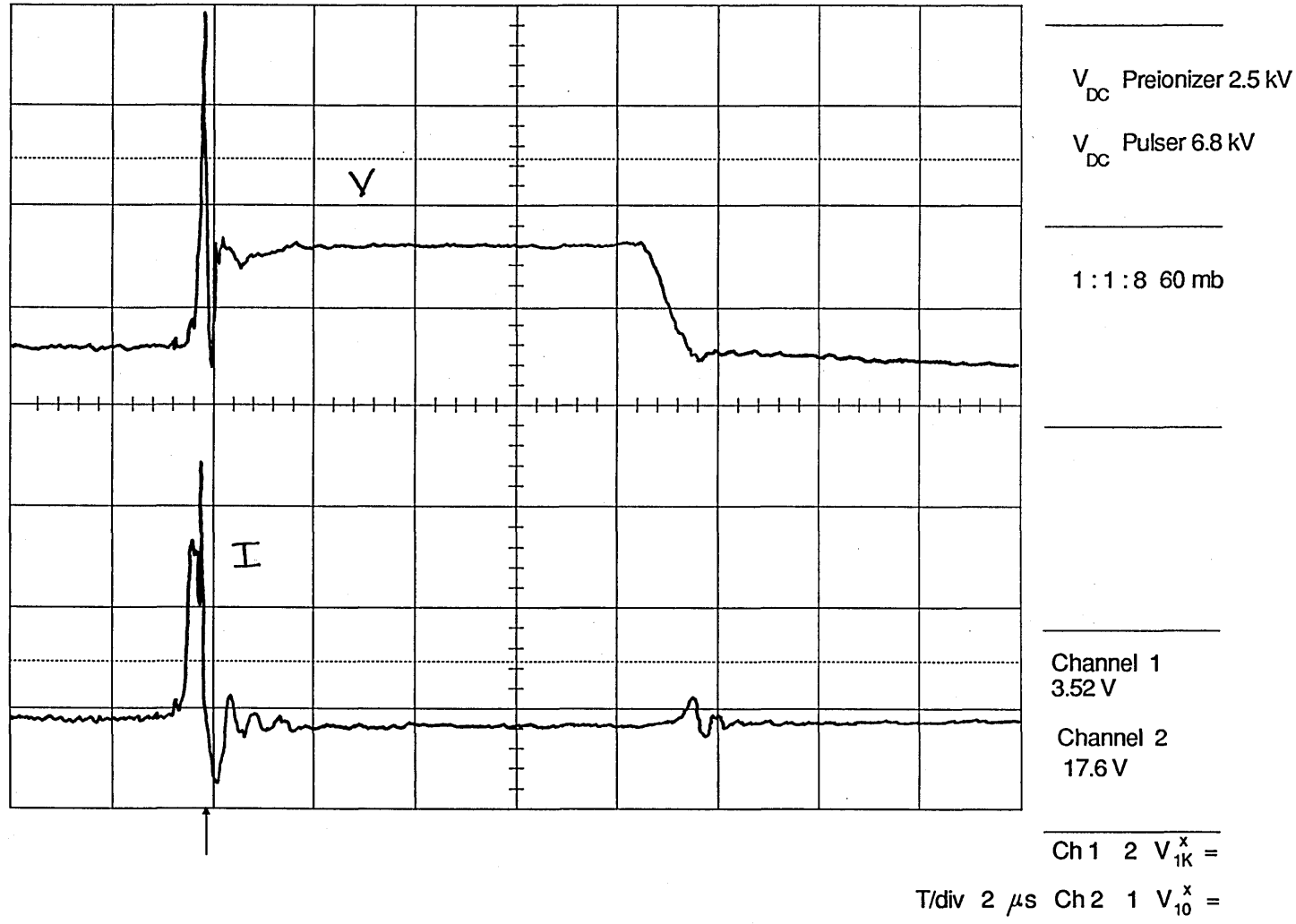

FIGURE 4.54 DISCHARGE VOLTAGE / TRIGGER WIRE CURRENT .

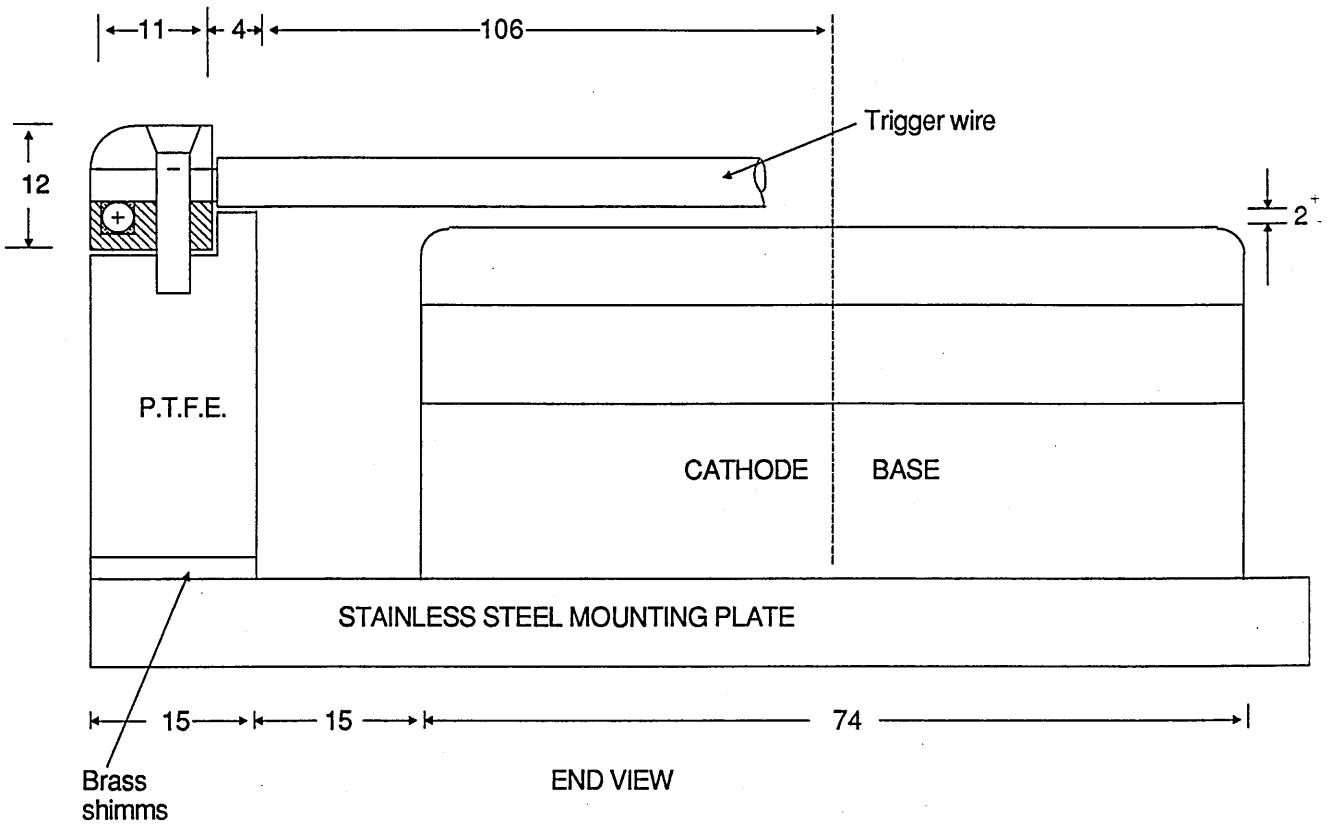

Trigger wire spacing 8 mm	Dielectric: Pyrex
Number of trigger wires 156	ID 2.0 mm OD 3.5 mm

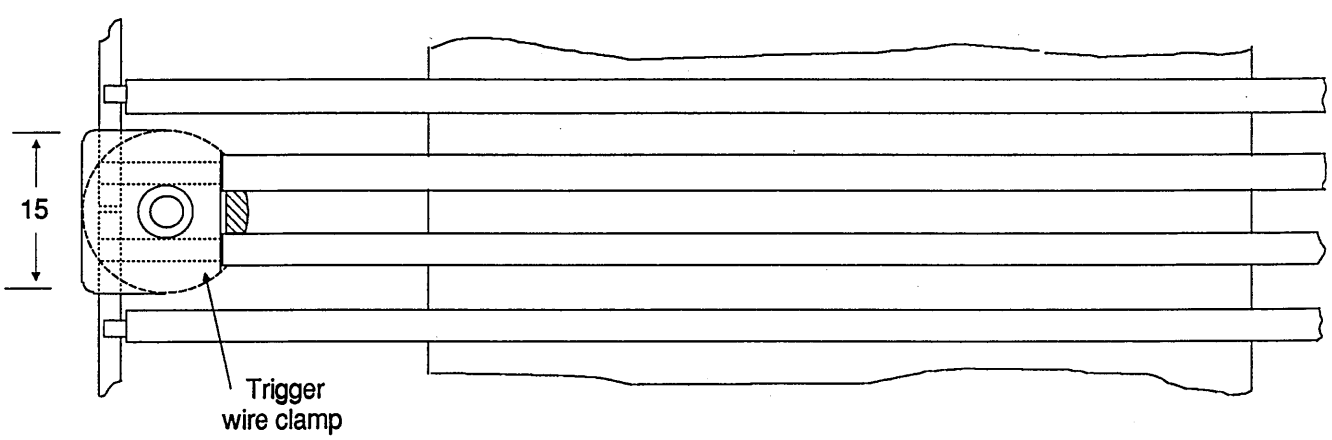

PLAN VIEW

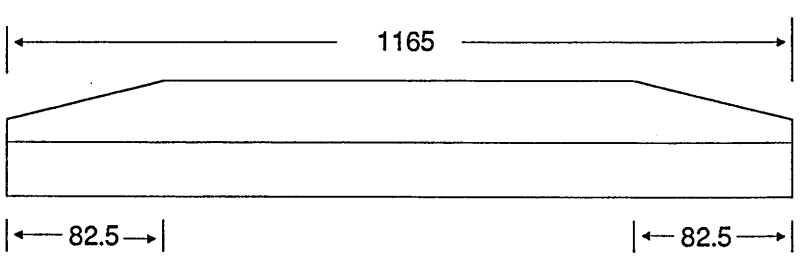

SIDE ELEVATION

FIGURE 4.55 DETAILS OF PROTOTYPE ELECTRODE ASSEMBLY

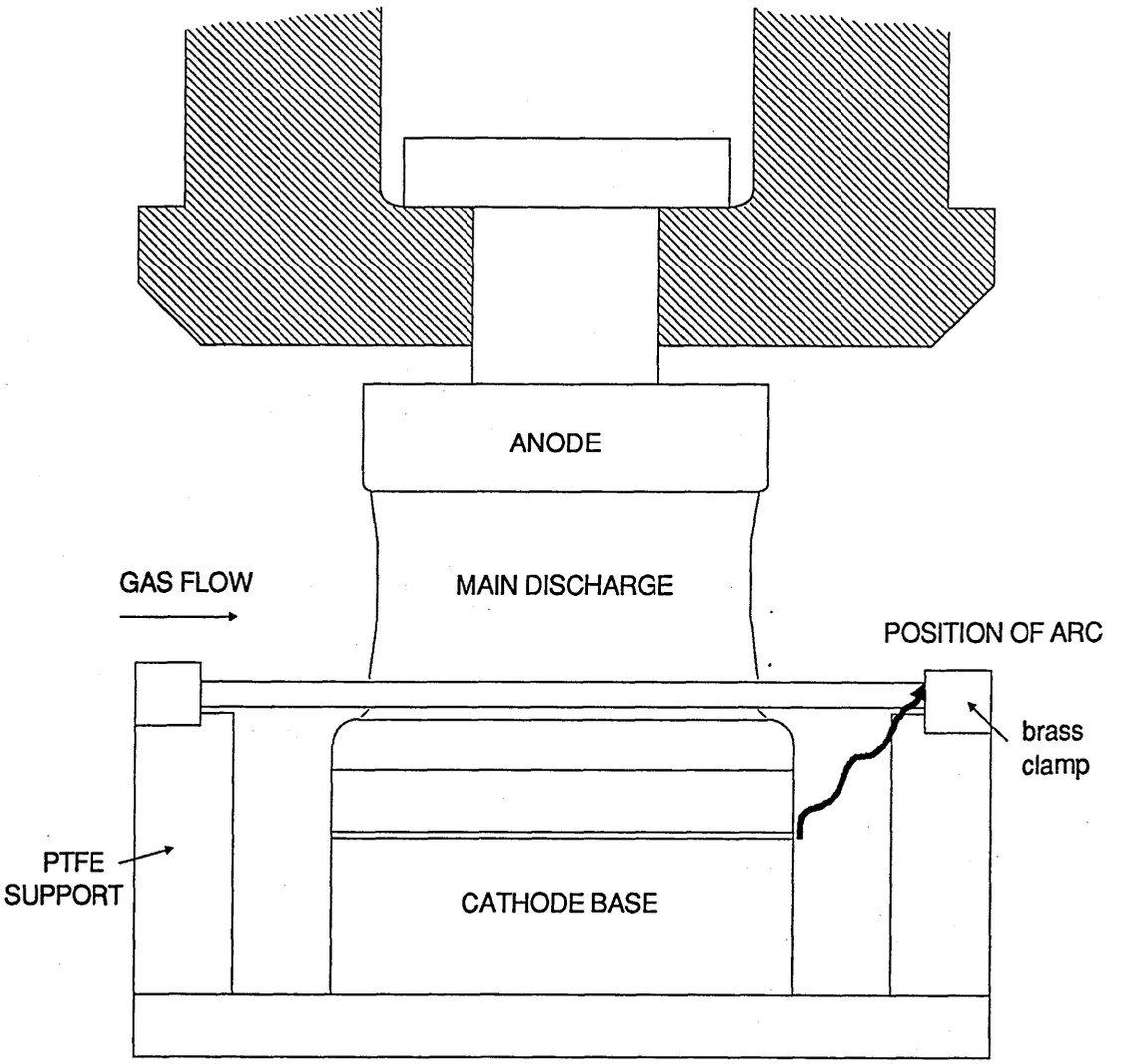

FIGURE 4.56 POSITION OF DISCHARGE ARC

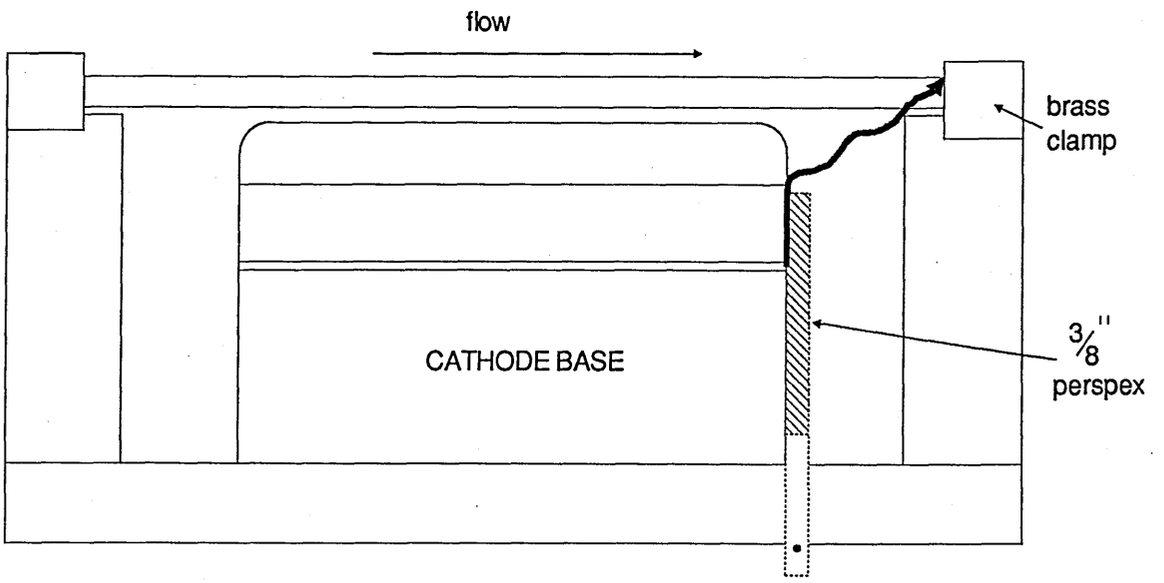

FIGURE 4.57 CATHODE ASSEMBLY WITH PERSPEX INSULATOR

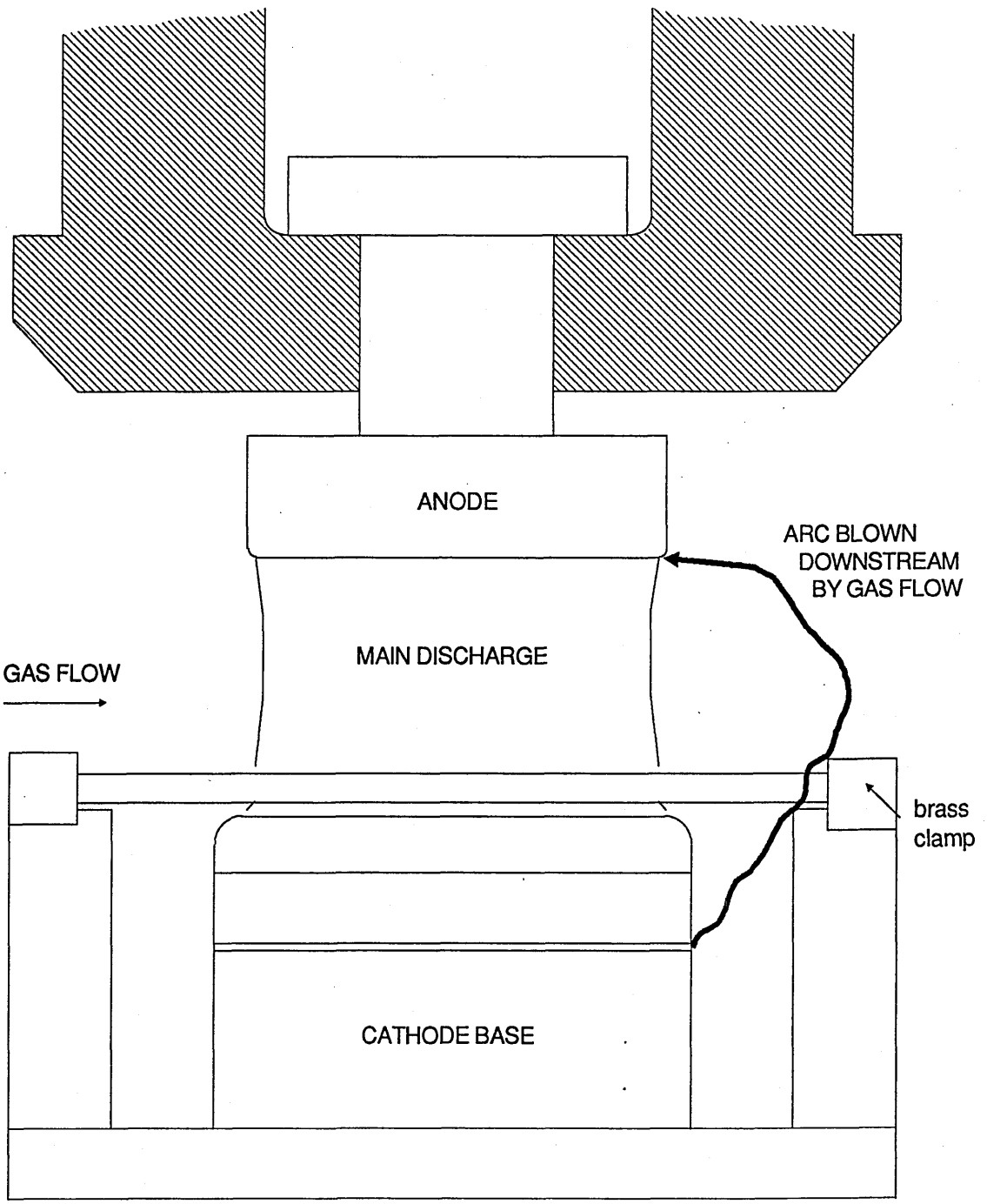

FIGURE 4.58 CURVED ARC ON DOWNSTREAM SIDE OF ELECTRODES

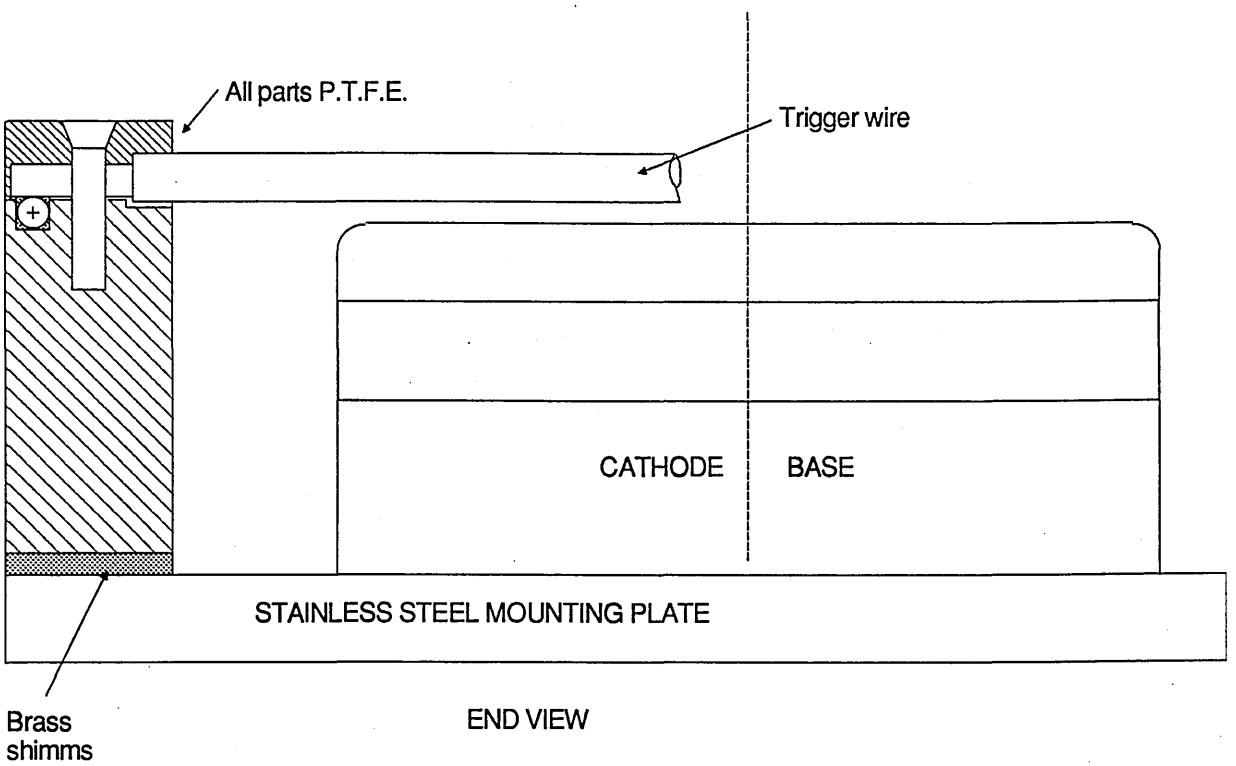

Trigger wire spacing 8 mm	Dielectric: Pyrex
Number of trigger wires 104	ID 2.0 mm OD 3.5 mm

FIGURE 4.59 MODIFIED TRIGGER WIRE CLAMPS

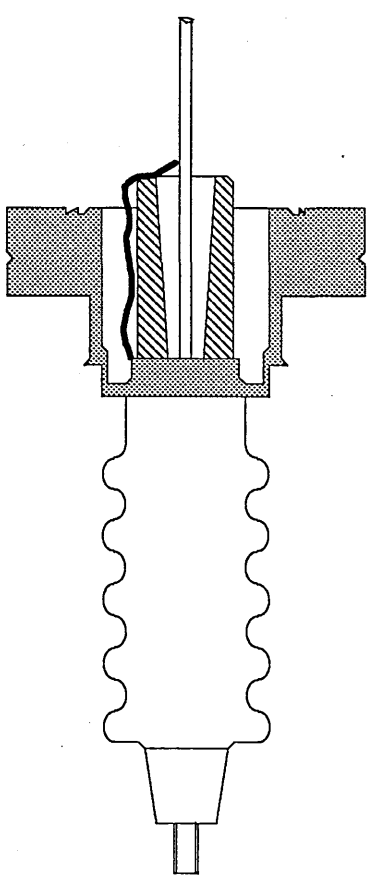

FIGURE 4.60 BREAKDOWN IN ANODE LEADTHROUGHS

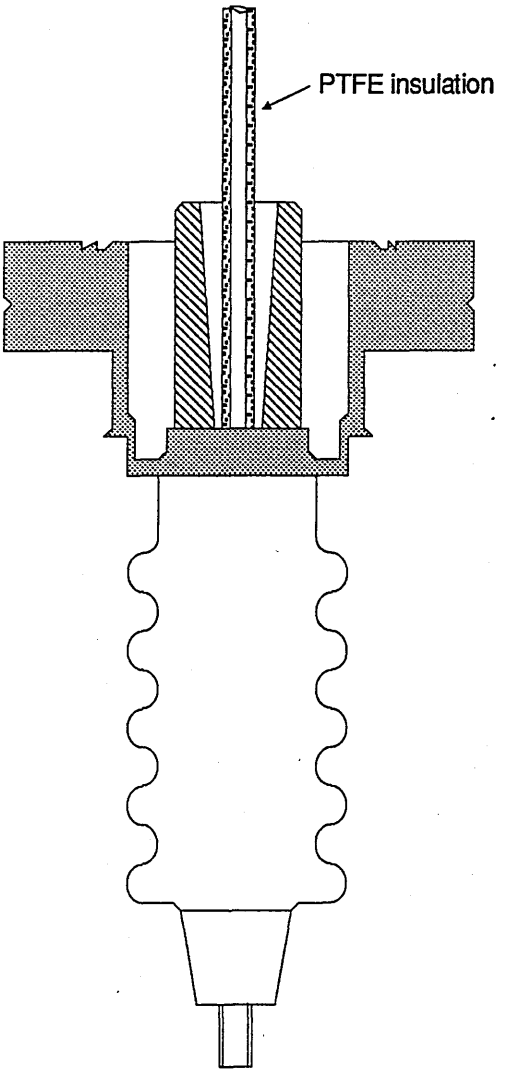

FIGURE 4.61 INSULATED ANODE LEADTHROUGH

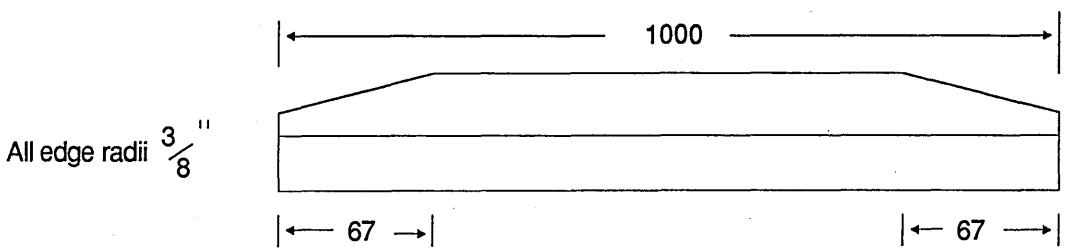

SIDE ELEVATION

FIGURE 4.62 MODIFIED ELECTRODE PROFILE

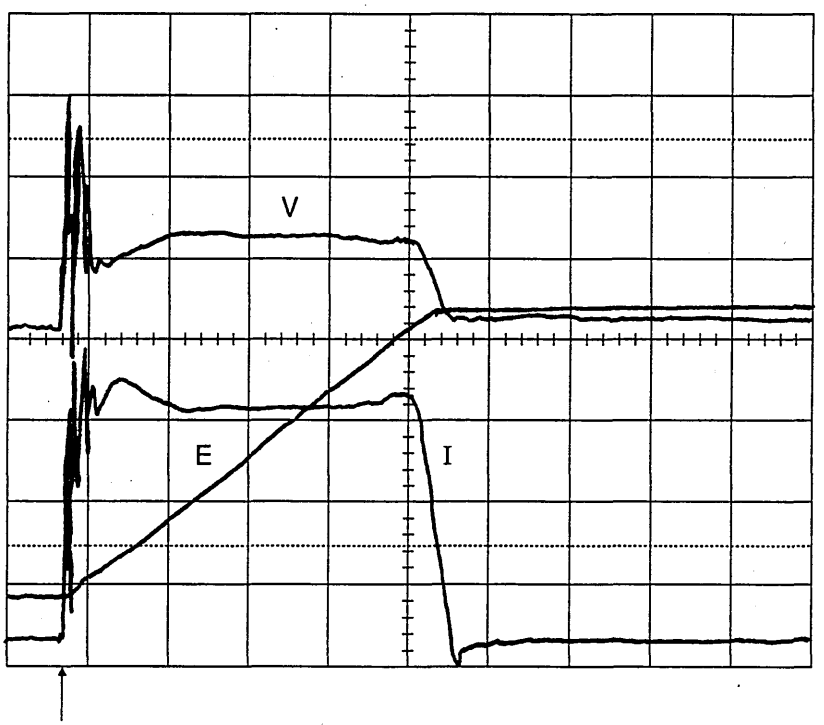

V_{NO} = 19.7 kV

1 : 1 : 4 156 mbar

$\int E$
6.96 V^2s

Channel 1
17.40 V
Channel 2
174.0 V

Ch 1 5 V_{1K}^{x} =

T/div 2 μs Ch 2 5 V_{10}^{x} =

FIGURE 4.63 DISCHARGE VOLTAGE AND CURRENT 1:1:4 156 mbar

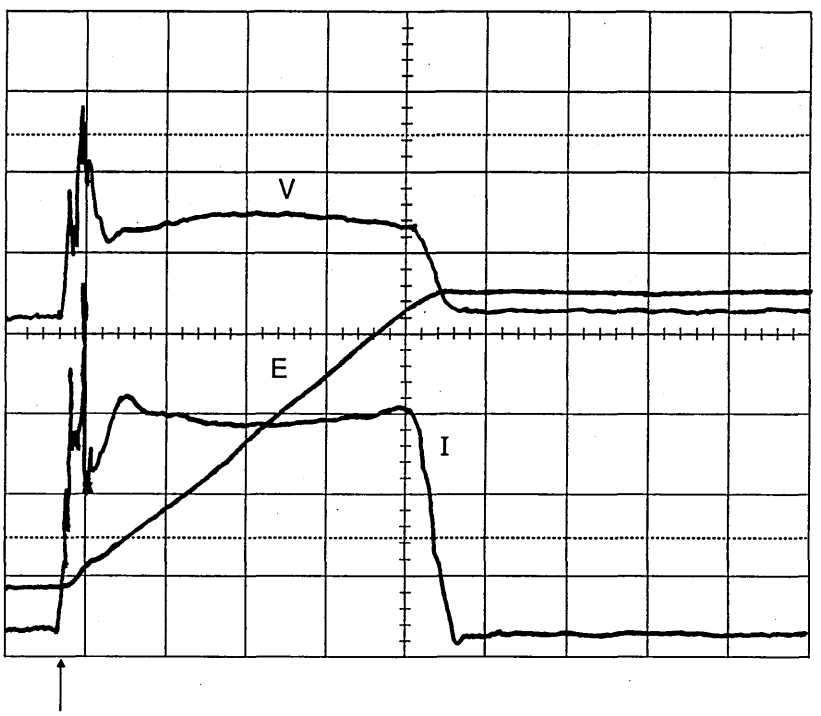

V_{NO} = 19.0 kV

27 : 54 : 54 mbar

$\int E$
7.34 V^2s

Channel 1
18.35 kV
Channel 2
183.5 V

Ch 1 5 V_{1K}^{x} =

T/div 2 μs Ch 2 5 V_{10}^{x} =

FIGURE 4.64 DISCHARGE VOLTAGE AND CURRENT 27:54:54 mbar

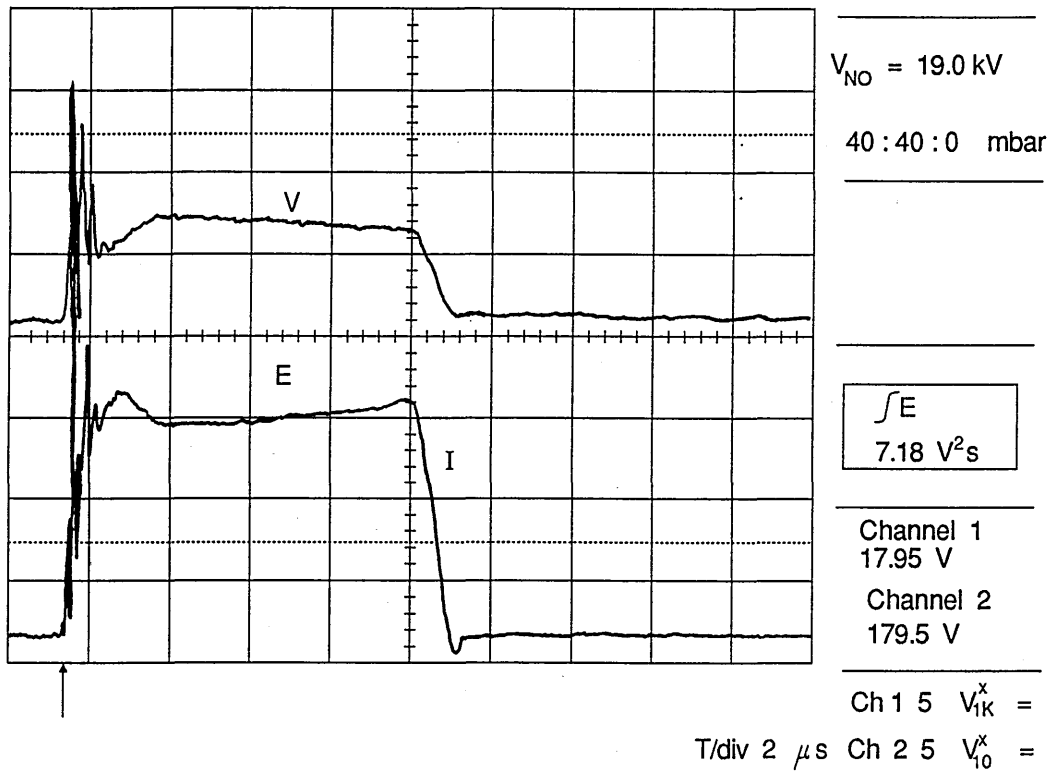

FIGURE 4.65 DISCHARGE VOLTAGE AND CURRENT 40:40:40 mbar

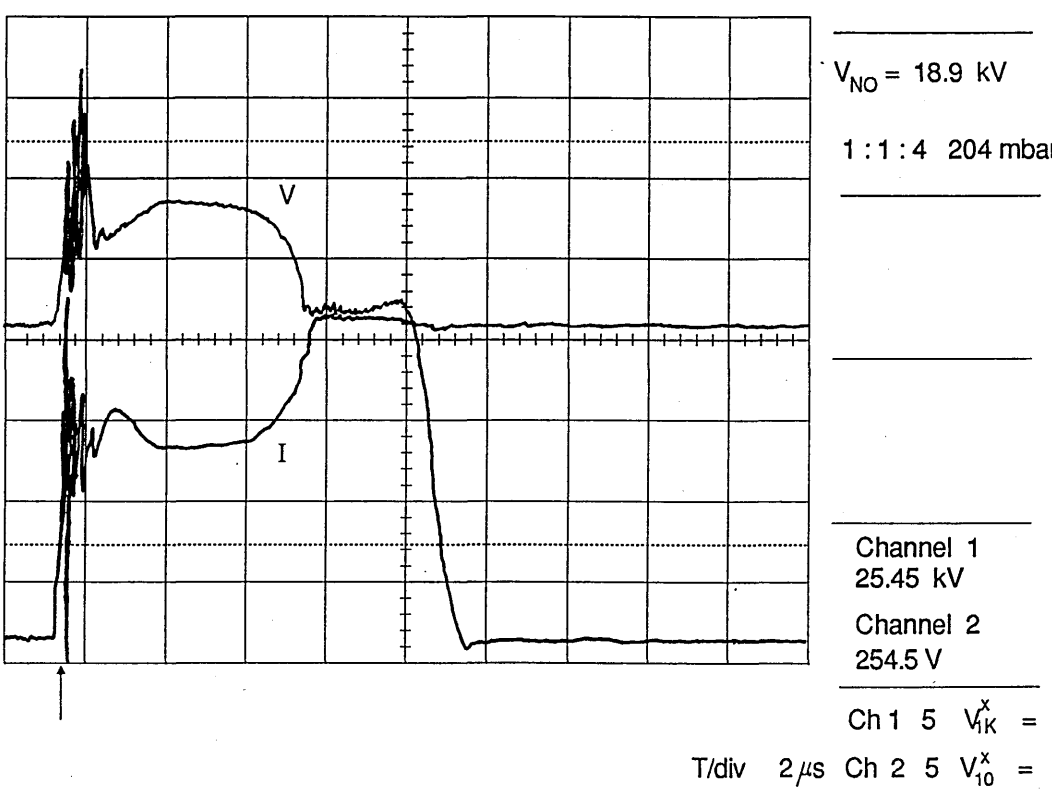

FIGURE 4.66 ARCING IN 1:1:4 MIXTURE P = 204 mbar

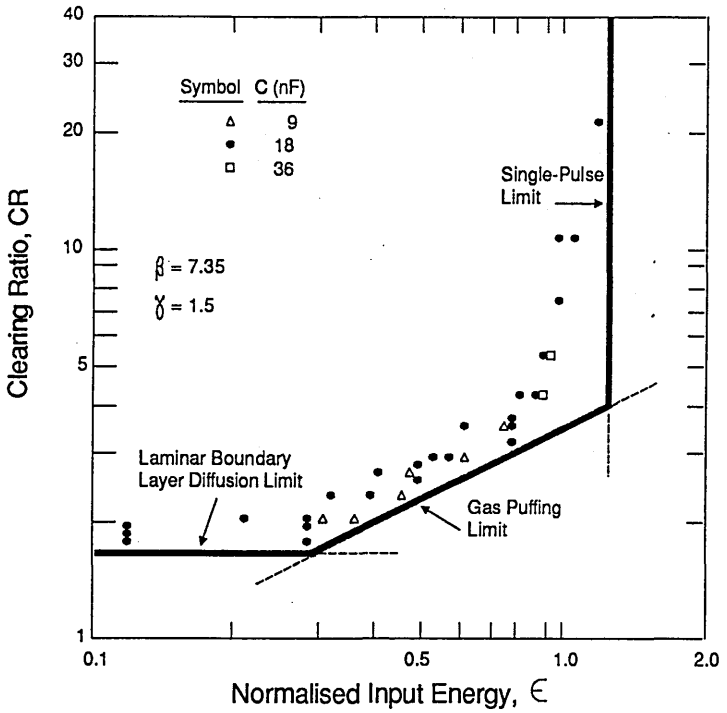

Comparison of predicted and observed clearing ratios.
P_T = 510 Torr: 50 CO_2 : 50 N_2 : 400 He: 10 H_2

FIGURE 4.67 CLEARING RATIO Y's INPUT ENERGY

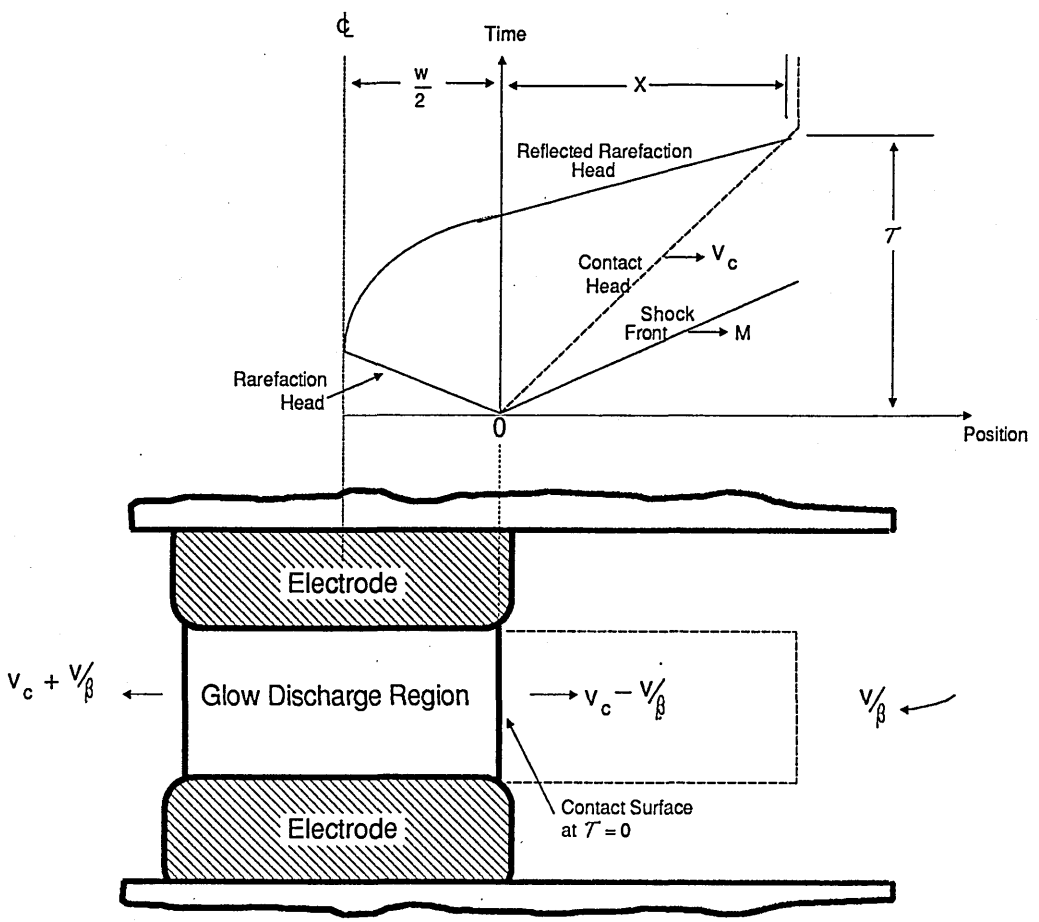

FIGURE 4.68 EXPANSION OF DISCHARGE PRODUCTS

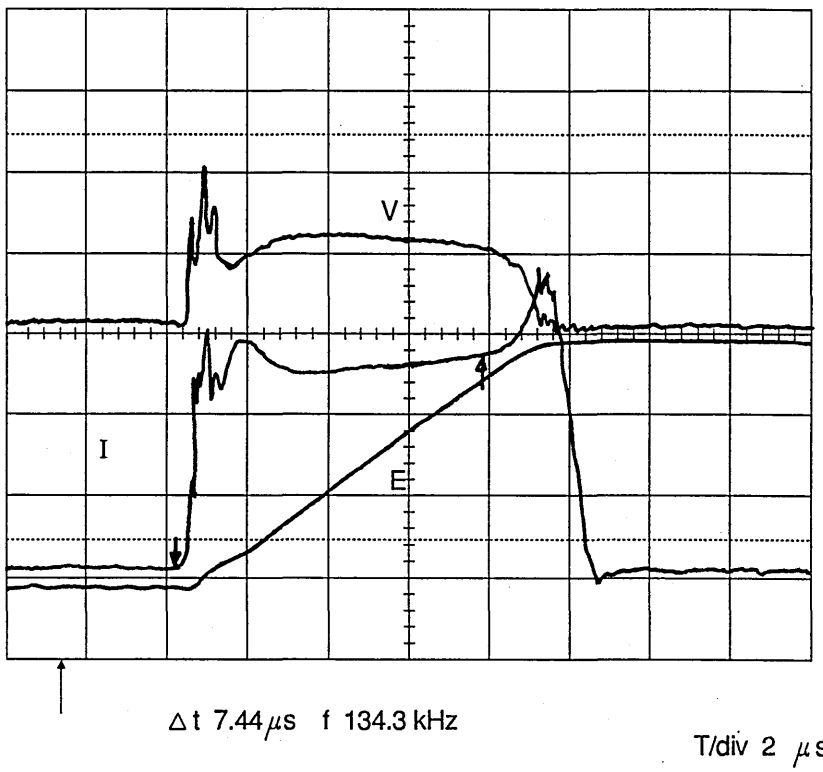

FIGURE 4.69 DISCHARGE VI 1:1:4 156 mbar 80% TAP SETTING

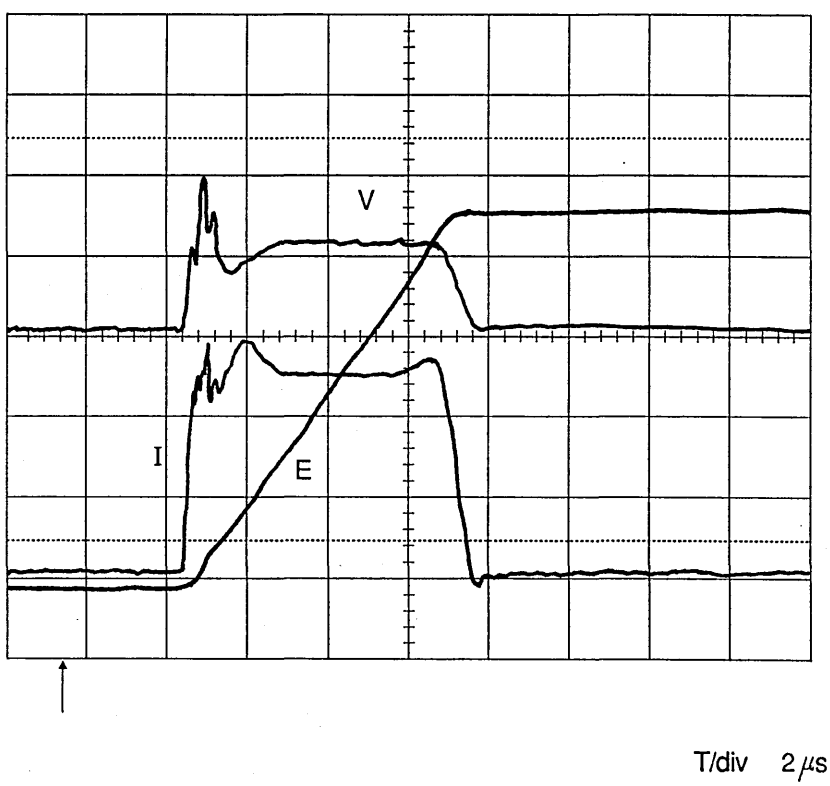

FIGURE 4.70 DISCHARGE V-I 7 μs PULSE DURATION

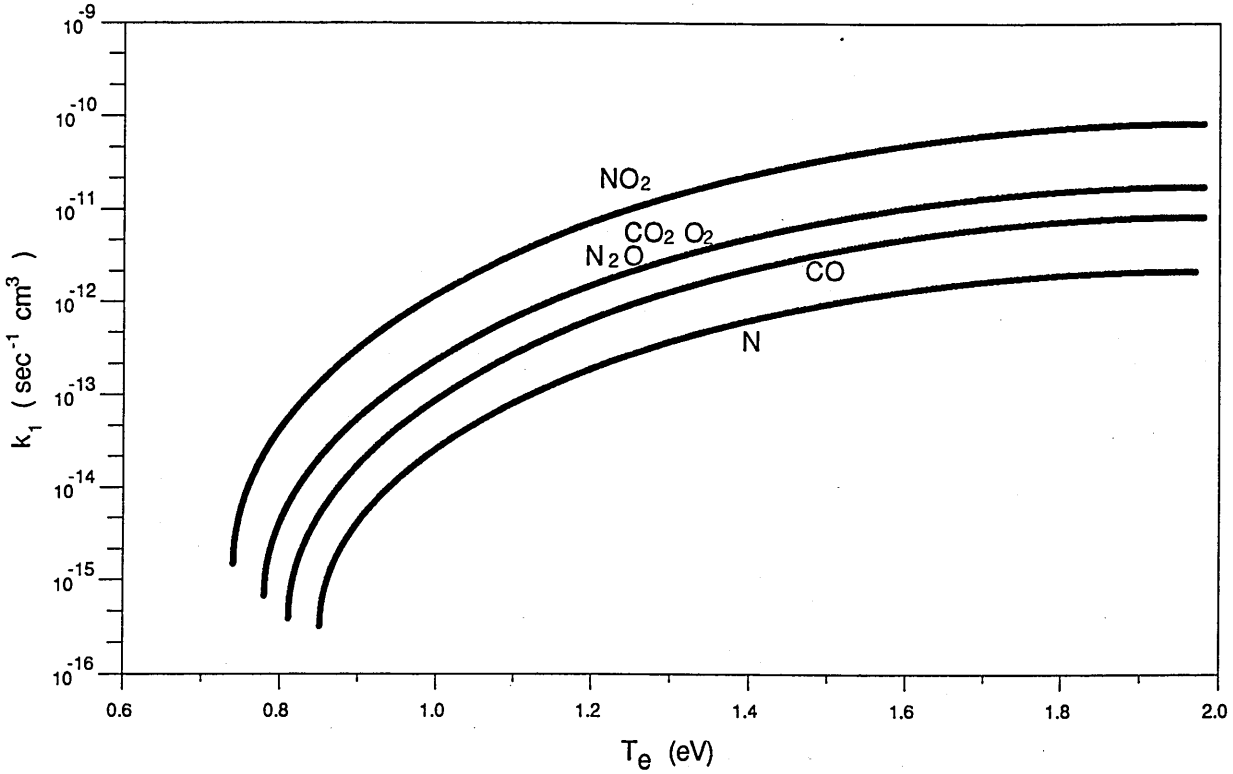

FIGURE 4.71 Electron-molecule ionization coefficients using electron energy distributions for a CO_2-N_2-He mixture in the number density proportions 0.05:0.35:0.60. The rate coefficients for all species other than CO_2 and N_2 are strictly applicable only for these species as minority constituents in a CO_2-N_2-He mixture having the proportions indicated.

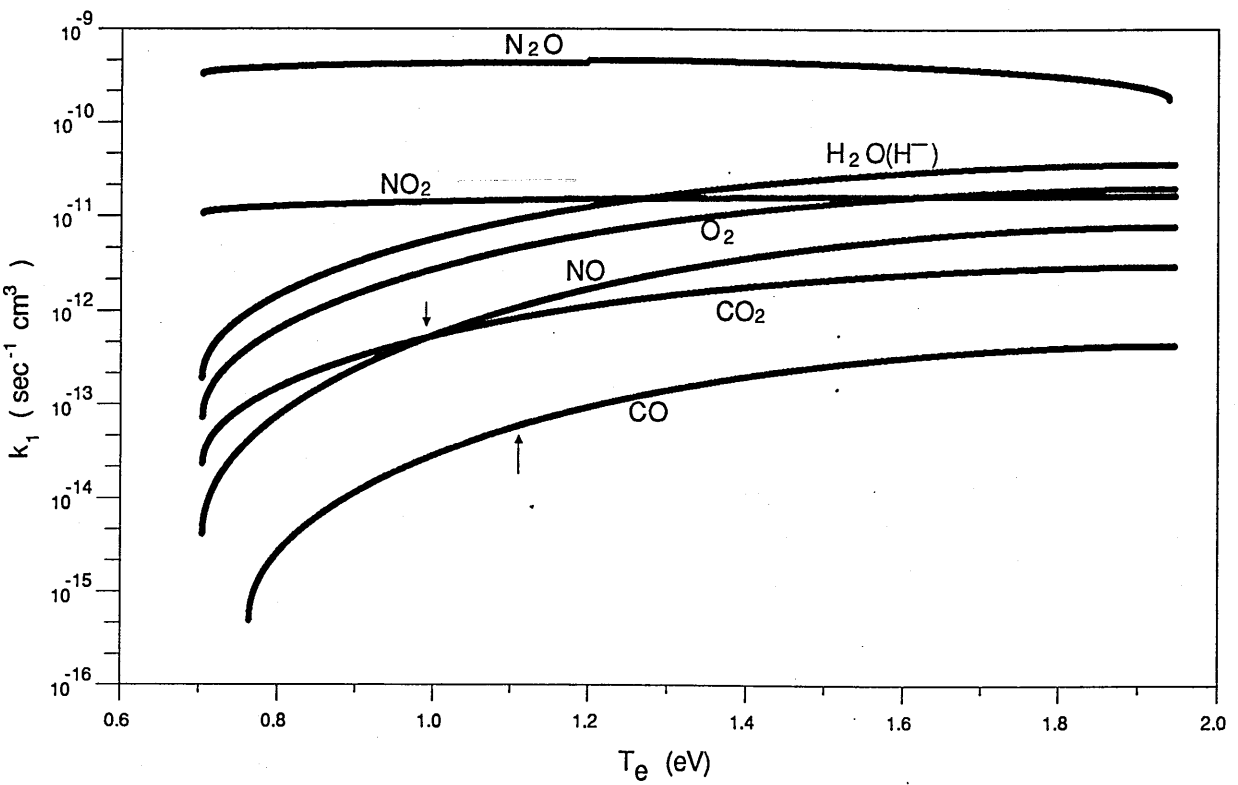

FIGURE 4.72 Electron-molecule rate coefficients for dissociative attachment computed using electron energy distributions for the mixture of the above Figure. The vertical arrows denote the point at which k_i is equal to k_a. For O_2, k_i equals k_a in this mixture for $T_e \sim 2.1$ eV.

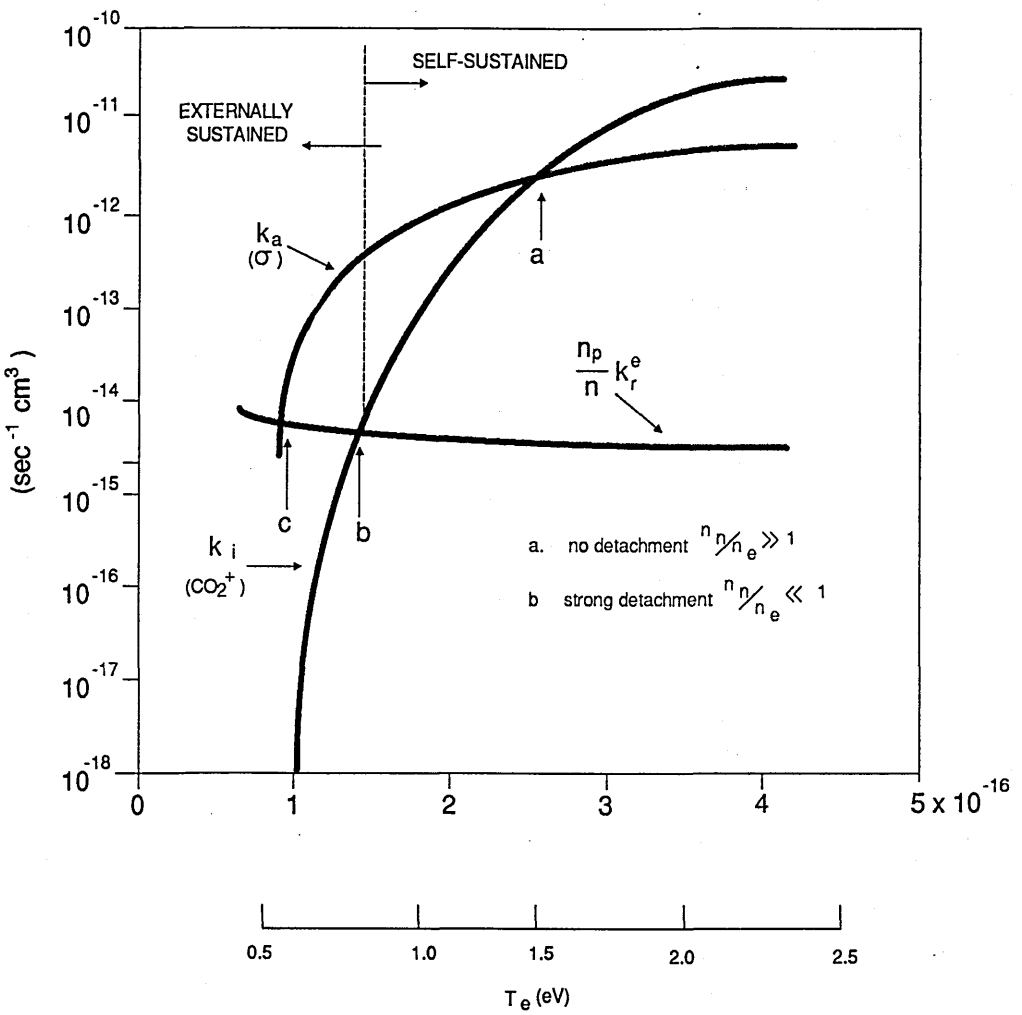

FIGURE 4.73 Illustrative comparison of electron coefficients for ionization, attachment, and recombination for representative discharge conditions for which ionization and attachment processes are dominated by CO_2. The weighted recombination coefficient is typical of a fractional ionization value of approxiamtely 10^{-7}.

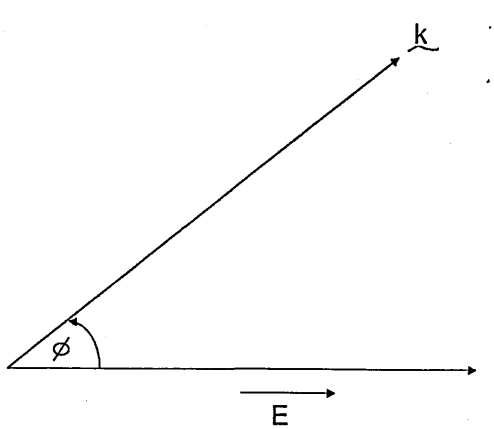

FIGURE 4.74 SPATIAL RELATIONSHIP BETWEEN DIRECTION k, AND $\vec{E}$

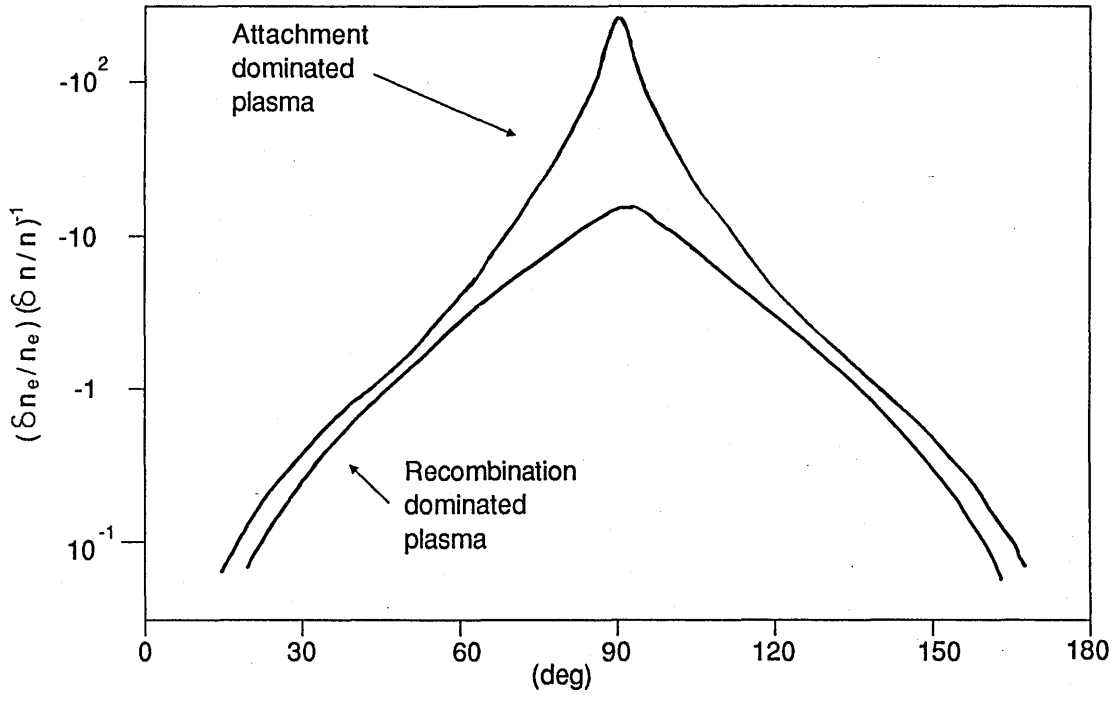

FIGURE 4.75 Fractional response of the electron density to a perturbation in gas density computed for a 20-Torr CO_2 - N_2 - He mixture having the proportions 0.05:0.35:0.60. The electron density was 10^{10} cm^{-3} for both the recombination- and attachment-donimated palsmas.

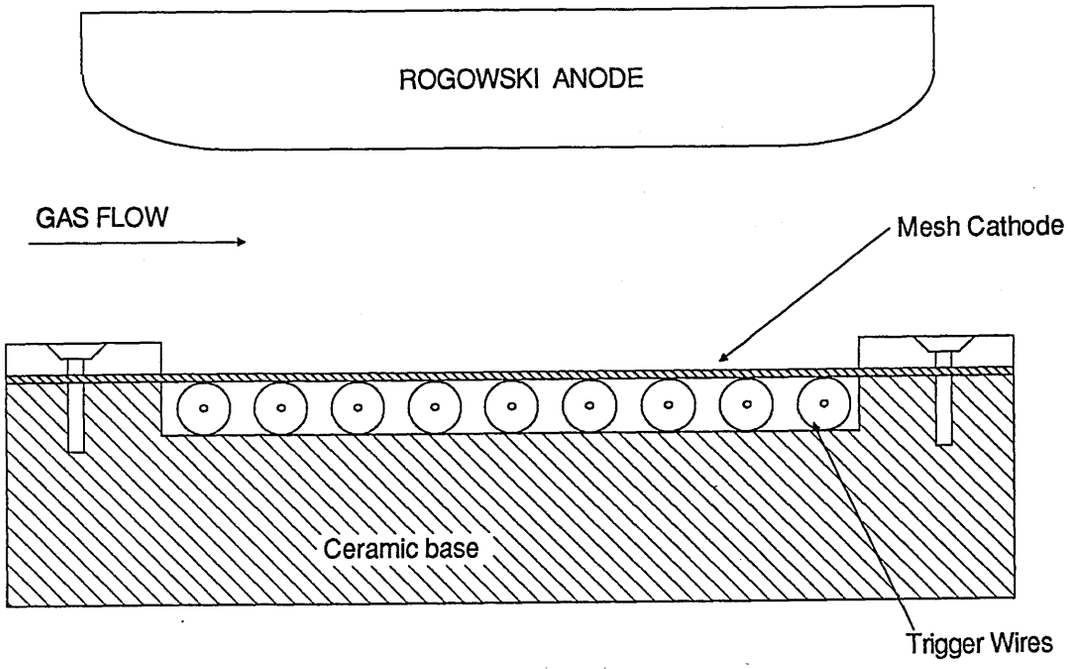

FIGURE 4.76 PROPOSAL FOR CORONA PREIONIZED ELECTRODE SYSTEM

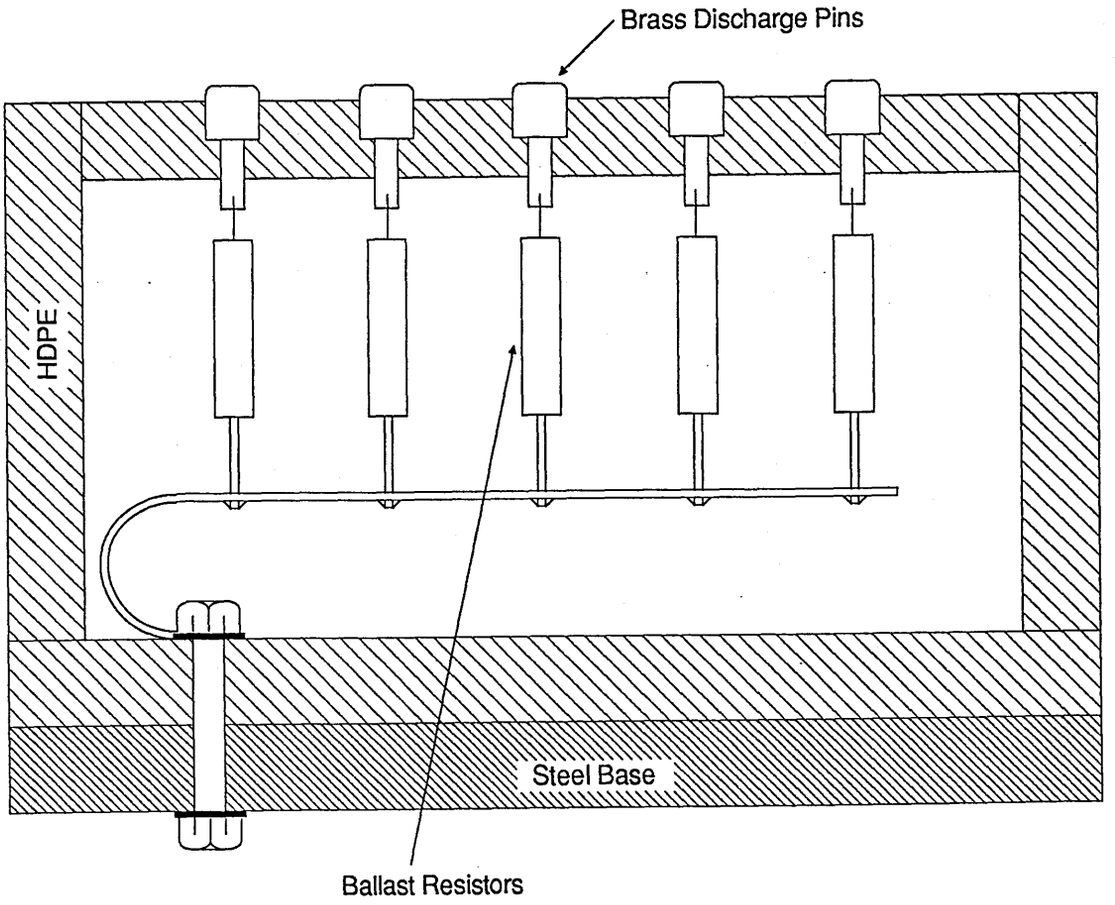

FIGURE 4.77 BALLASTED TEST ELECTRODE

(5.0) LASER OUTPUT PULSE CHARACTERISTICS.

A brief summary of the prelimenary measurements of the laser output pulse characteristics is given. The results are not intended as a complete or thorough analysis of performance, as this will be reported by Watson [5.1] at a later stage. It is sufficient here to draw conclusions regarding the design of the optical resonator and discharge cavity, and to establish the design modifications necessary for performance improvements.

The experimental measurements of the output pulse were obtained with a photon drag monitor (Roffin 7443) with a sensitivity of 6 mV/kW, as quoted by the manufacturer. Due to the low output power levels achieved in these experiments, it was not possible to calibrate the monitor by calometric means. The data on output pulse power is therefore calculated with the above sensitivity value. The output pulse from the monitor was captured by a LeCroy 9400 oscilloscope with the input impedance set to 50 Ω. The input power to the discharge was measured by voltage and current probes (see section 4.3.1) with the waveforms also being captured by the LeCroy 9400. The input and output pulse energies were calculated by integrating the waveforms directly on the oscilloscope. To obtain consistency in the results all measurements were made at a PRF of 100 Hz and the average of 10 readings used. The quoted pulse delay time was measured from the leading edge of the anode current pulse to the peak of the initial spike.

(5.1) 1:1:4 AND 1:1:8 MIXTURE OUTPUT CHARACTERISTICS.

As no measurable laser output was obtained on the first test with the Z resonator, it was decided to examine the performance with a simple single pass resonator as it was very easy to ensure accurate alignment. The single pass resonator was assembled by replacing the plane rear folding mirror with a 20 m radius of curvature mirror alignined to the output window. In this arrangement the beam passed down one side of the electrodes. The rear mirror alignment was set on assembly with no external means of adjustment being provided. For each gas mixture the input power was increased by changing the main transformer tap setting (see section 3.3).

(5.1.1) Single Pass Resonator Performance.

Table (5.1) details the results obtained with a 1:1:4 mixture at a total pressure of 156 mbar. Fig's (5.1) and (5.2) show the recorded output pulses and anode current waveforms at 60% and 70% transformer tap settings. The most important point to note from these results is the extremely low conversion efficiency; a maximum of

0.5% being obtained. The low overall efficiency is due to the low resonator coupling efficiency i.e. power is only obtained from the active region falling within the resonator mode.

Table (5.1) Output pulse characteristics single pass resonator

Tap Settings	E_s (J/cc.torr)	E_{in} (Joules)	E_{out} (nV^2s)	E_{out} (mJ)	η (%)
60	13.06×10^{-6}	4.09	85.6	14.3	0.35
65	15.05×10^{-6}	4.71	96.8	16.1	0.34
70	17.57×10^{-6}	5.50	115.5	18.6	0.33
75	19.23×10^{-6}	6.02	192.0	32.0	0.53

1:1:4 mixture @ 156 mbar $R_f = 85\%$ $R_b = 20$ m $d = 1.3$ m.

Assuming the resonator mode to be TEM_{oo} the beam spot size ω can be calculated from [5.2].

$$\omega_f = \left[\left(\frac{\lambda}{\pi}\right)^2 (R_b - d)\, d \right]^{\frac{1}{4}} \qquad (5.1)$$

$$\omega_b = \left[\left(\frac{\lambda R_b}{\pi}\right)^2 \frac{d}{(R_b - d)} \right]^{\frac{1}{4}} \qquad (5.2)$$

where ω_f and ω_b are respectively the front and rear spot sizes (raduis at 1/e point), R_b is the back mirror raduis of curvature, d is the mirror separation and $\lambda = 10.6$ μm is the wavelength of the emitted light. With $d = 1.4$ m and $R_b = 20$ m the front and rear spot sizes are respectively 4.08 mm and 4.22 mm. The resonator mode volume within the discharge is calculated from the observed discharge length of 980 mm (N.B. this is less then the electrode length). Based on the mean spot diameter the active mode volume is 53 cm^3. As the discharge was also slightly narrower than the full electrode width, the total active discharge volume was estimated to be approximately 2675 cm^3. Thus, on a straight volume basis, the resonator coupling efficiency is approximately 2%. It is not surprising then that the power output is so low.

It is interesting to consider what the output power would be assuming the resonator coupling efficiency to be 100%. For the 75% tap setting this gives a total output pulse energy of 1.6 Joules, which corresponds to an overall conversion efficiency – electrical to optical – of 27%. This is clearly impossible as the predictions of Khahra [5.3] indicate a maximum overall efficiency of 6% at these input power levels.

The above discrepancy raises the question of the validity of calculating resonator coupling efficiency on a volume basis. The conclusion to be drawn is that it is not possible in practice to scale the resonator mode volume to the full discharge volume, without in some way the electrodes clipping the resonator mode. It is generally accepted that the resonator aperture must be approximately two beam diameters for the TEM_{oo} mode to be dominant [5.2]. It would therefore only be possible to scale the single pass resonator to a beam diameter of approximately 20 mm (half of 40 mm electrode gap) before mode clipping reduced the available output power. The corresponding maximum "volumetric" coupling efficiency would be approximately 11%.

It should also be noted that the simulations reported by Khahra [5.3] and Chatwin [5.4] are based on a uniform beam intensity. The equations describing the excitation and relaxation mechanisms and the beam intensity are essentailly solved for an element of volume within the defined cavity. The description does not incorporate the features necessary to describe the transverse resonator mode development. Due to the Gaussian beam characteristics it is to be expected that the actual efficiency, averaged over a given resonator volume, will be less than the efficiency predicted by the simulations. However, the results obtained from the simulations can be assessed qualitatively and important conclusions drawn regarding design of the optical resonator, e.g. spike control. In this respect the simulations are of great utility.

(5.1.2) Z Resonator Performance.

The single pass experiment confirmed that the input powers were sufficient to produce gain in the cavity. The Z resonator was subsequently assembled and experiments conducted with different gases and input powers. Table (5.2) details the results for a 1:1:4 mixture at a total pressure of 156 mbar, with an output window reflectivity R_f = 75%. The specific energy input is calculated from the estimated discharge volume of 2675 cm^3.

Table (5.2) Output pulse characteristics Z resonator.

Tap Settings	E_s (J/cc.torr)	E_{in} (Joules)	E_{out} (nV^2s)	E_{out} (mJ)	η (%)
60	13.32×10^{-6}	4.17	128.0	21.0	0.51
65	15.27×10^{-6}	4.78	196.0	32.6	0.68
70	17.24×10^{-6}	5.40	245.0	41.0	0.76
75	19.36×10^{-6}	6.06	258.4	43.1	0.71

1:1:4 @ 156 mbar R_f = 85% R_r = 20 m d = 7.6 m

Fig. (5.3) shows the output pulse for the 1:1:4 mixture at the 75% tap setting, from which it can be seen that the plateau power is of the order of 5.6 kW. This is a factor of 10 below the design power level (see section 1.1).

Clearly, with this resonator design and specific energy loading, the output power is well below that required. The question is, can the output power be increased by improvements in the design of the optical resonator? It is therefore of value to consider the improvements gained by increasing the number of passes through the discharge in changing from the single pass to the Z configuration. Comparison of the output energies in tables (5.1) and (5.2) reveals that the output energy has approximately doubled. However, the beam spot sizes at the front and rear mirrors have increased to 5.72 mm and 7.30 mm respectively and this together with the increased resonator length gives an active mode volume of 390 cm^3. This compares with the value of 53 cm^3 for the single pass resonator. Thus, a seven−fold increase in mode volume has only produced a two−fold increase in output power.

The poor improvement in coupling efficiency could be due to several factors. Firstly, the Z resonator was more difficult to align with the electrodes, in which case the diffraction losses could have been considerably higher than those of the single pass resonator. Secondly, the active mode volume was calculated assuming three clear passes through the discharge and due to overlap with the diagonal pass, the mode volume may have been over−estimated. Neglecting the diagonal pass reduces the active mode volume to 2/3 of the above value, giving a mode volume of five times the single pass resonator. It can also be shown that the diffraction losses increase with increasing beam diameter [5.5], thus, the output power does not scale linearly with the diameter. In addition to these factors it is possible that the output of the single pass resonator is much higher than expected due to diffusion effects, as described by Cheo [5.6]. At a fixed excitation rate the upper level population is depleted by the radiation field, causing an increase in the lower level population and a decrease in the gain. Diffusion of excited molecules from outside the beam, together with diffusion of lower level molecules out of the beam, replenishes the gain. These effects become less significant as the beam diameter increases, as demonstarated by the increase in gain saturation parameter with decreasing beam diameter typically observed with DC excitaed CO_2 lasers [5.6].

With reference to fig. (5.3) it can be seen that a significant fraction of the pulse energy is contained in the initial spike. A delay of 6.7 μs is also observed between the leading edge of the anode current and the peak of the gain−switched spike. The measured pulse delay time is in good agreement with Chatwin's predictions [5.4]. It was found that the delay time decreased with increasing input energy. For the

conditions of table (5.2) the delay time at 60% tap setting was 8.5 μs. It was also observed that the delay time increased when the resonator was deliberately misaligned by adjusting the output window. Since the output spike grows rapidly when the gain overcomes the cavity losses, it is to be expected that with increased losses it takes longer for the gain to reach the threshold condition. In this respect, the observed delay time gives a qualitative indication of cavity losses. Comparing the output pulses for the single pass and Z resonators, fig's (5.3) and (5.4), it can be seen that the delay time is approximately the same in both cases. As the cavity lengths are different in both cases, and this is known to affect the delay time, it is not possible to conclude that the losess are the same in both resonators, although future simulations could easily confirm this.

Table (5.3) details the results obtained with a 1:1:8 mixture at a total pressure of 160 mbar. As discussed in section (4.3.5), this was the maximum total pressure in terms of discharge stability in the continuous pulse mode. The output pulse recorded at a tap setting of 75% is shown in fig. (5.4). It can be seen that the pulse exhibits a very large spike and the energy falls off almost exponentially. Clearly, this pulse is not suited to materials processing applications due to the absence of a plateau characteristic. Comparing the results of tables (5.2) and (5.3) it can be seen that the 1:1:8 mixture also exhibits a slightly lower overall conversion effficiency at the maximum input power. This is due primarily to the lower specific energy loading i.e. 16.88×10^{-6} as compared to 19.36×10^{-6} J/cc.torr. On the basis of these results alone it would appear the the 1:1:4 mixture offers more potential for high power operation.

Table (5.3) Output pulse characteristics Z resonator.

Tap Settings	E_s (J/cc.torr)	E_{in} (Joules)	E_{out} (nV^2s)	E_{out} (mJ)	η (%)
60	11.81×10^{-6}	3.79	128.0	21.33	0.563
65	13.61×10^{-6}	4.37	146.5	24.42	0.560
70	15.01×10^{-6}	4.82	179.2	29.87	0.622
75	16.88×10^{-6}	5.42	207.9	34.65	0.640

1:1:8 @ 160 mbar R_f = 85% R_b = 20 m d = 7.6 m

(5.2) EFFECT OF GAS COMPOSITION ON LASER OUTPUT.

Some prelimenary tests were conducted on helium free gas mixtures and on the effects of adding helium to a gas mixture with fixed partial pressures of CO_2 and N_2. These tests were conducted as helium free mixtures were found to exhibit good discharge stability at high input energies, provided the total pressure was below 60

mbar.

(5.2.1) Output Pulse Characteristics of Helium Free Mixtures.

Table (5.4) details the results for a 30:30 mbar (CO_2:N_2) mixture as a function of the input energy. The output pulse recorded at the 75% tap setting is shown in fig. (5.5), from which it can be seen that the pulse exhibits a good plateau characteristic, with a plateau power of 5.8 kW and a corresponding total pulse energy of 40.4 mJ. This is only marginally smaller than the pulse energy obtained with the 1:1:4 mixture at a total pressure of 156 mbar.

Table (5.4) Output pulse characteristics Z resonator.

Tap Settings	E_s (J/cc.torr)	E_{in} (Joules)	E_{out} (nV^2s)	E_{out} (mJ)	η (%)
60	$33.3x10^{-6}$	4.01	154.8	25.8	0.64
65	$38.9x10^{-6}$	4.68	205.8	34.3	0.73
70	$43.02x10^{-6}$	5.18	227.0	37.8	0.73
75	$48.0x10^{-6}$	5.78	242.3	40.4	0.70

30:30 mbar (CO_2:N_2) mixture R_f = 85% d = 7.6 m

It can be seen from a comparison of fig's (5.3) and (5.5) that the 1:1:0 mixture pulse plateau is slightly longer than the 1:1:4 mixture plateau, which is beneficial for materials processing. Thus, a 1:1:0 mixture would appear to offer advantages in terms of pulse characteristics, in addition to not requiring helium. However, these tests were conducted at low mean input powers where the thermal capacity of the gas is unimportant. This may not be the case at higher PRF's where each block of gas must handle more than one discharge pulse, in which case, the increased thermal capacity of the 1:1:4 mixture may give better performance.

(5.2.2) Effects of Helium.

With the CO_2 and N_2 partial pressures fixed at 30 mbar as above, the effect of adding helium to the gas mixture was examined. Due to the changing (E/P) and gas pressure, the discharge voltage increased with the addition of helium. Unfortunately, it was not possible to maintain the input pulse power constant as the PFN voltage could not be controlled to the degree required when running continuously. The results, as detailed in table (5.5), therefore also reflect a variation in input power of the order of 10%.

Table (5:5) Output pulse characteristics v's helium pressure.

P_{He} mbar	E_s (J/cc.torr)	E_{in} (Joules)	E_{out} (nV^2s)	E_{out} (mJ)	η (%)
0	42.7×10^{-6}	5.14	184.7	30.8	0.60
20	32.4×10^{-6}	5.20	192.0	32.0	0.61
40	27.2×10^{-6}	5.46	205.8	34.0	0.63
60	22.5×10^{-6}	5.42	193.0	32.0	0.59
80	19.64×10^{-6}	5.52	221.5	36.9	0.67
100	17.69×10^{-6}	5.68	205.9	34.3	0.60

Z resonator $R_f = \approx 5\%$ d = 7.6 m 30:30 mbar $(CO_2:N_2)$

Fig's (5.6) and (5.7) show the output pulses with helium partial pressures of 20 mbar and 80 mbar respectively. It can be seen that the addition of helium increased the amplitude of the gain-switched spike and produces oscillations on the output pulse.

Inspection of the results of table (5.4) reveals that the output pulse energy remains relatively constant throughout the range of helium partial pressures, in spite of a gradual increase in input energy. It can be concluded that the addition of helium to this mixture composition offers no improvement in efficiency or in the temporal characteristics of the pulse. This may not be the case at much higher mean power levels when the thermal capacity of the gas plays a significant role.

(5.3) CONCLUSIONS.

Fig. (5.8) shows a comparison of all the mixtures examined in the prelimenary tests. Of these mixtures, the 1:1:4 gave the highest total pulse energies. However, the output pulse from the helium free mixture was found to give better temporal pulse characteristics, as more power was concentrated in the plateau. These results represent only prelimenary tests and were limited to low mean power levels where the thermal capacity of the gas is not significant. A more detailed experimental/theoretical investigation is therefore required over a wider range of mixture compositions, input powers and resonator configurations, before firm conclusions can be drawn regarding optimum mixture compositions.

The results reported here have highlighted the need for major development of the optical resonator in order to improve the output coupling efficiency. With the Z resonator configuration, the maximum plateau power obtained was 5.6 kW; this is a factor of 10 below that required for the generation of non-conduction limited

processes. On a straight volume basis the resonator coupling efficiency is approximately 15%. With a multi−pass arrangement it should be possible to increase the output coupling efficiency significantly. However, as the volumetric coupling is already above 10% of the discharge volume, the desired increase in output pulse power cannot be obtained with resonator design improvements alone. It will therfore be necessary to increase the discharge power loading as well.

Fig. (5.8) shows the theoretical laser efficiency based on the total laser pulse, as reported by Khahra [5.3]. At the maximum attainable specific energy input for the 1:1:4 mixture i.e. 19.36×10^{-6} J/cc.torr, the theoretical efficiency is 5.4%. Assuming an upper limit on the resonator coupling efficiency of 50% − based on the aperturing constraints for TEM_{00} mode operation − gives a maximum attainable laser efficiency of 2.7% at this specific energy loading. If this could be achieved, the plateau power would be of the order of 40 kW, assuming 80% of the pulse energy to be in the plateau. With the present arrangement, and taking the theoretical efficiency as 5.4%, the actual resonator coupling efficiency for the 1:1:4 mixture is approximately 0.71/0.054 = 13%. This agrees well with the Z resonator coupling efficiency calculated on a volume basis i.e. 15%.

The apparent agreement between the resonator coupling efficiencies as discussed above leads to two important conclusions. Firstly, since the overall efficiency obtained with the single pass resonator is much higher than expected on the basis of resonator output coupling, it is clear that some significant effects are not being accounted for. It is not felt that diffusion effects alone could account for these results. Secondly, with suitable design modifications to the optical resonator, it should be possible to increase the output coupling efficiency to around 50%. This alone will increase the plateau power obtained with a 1:1:4 mixture to above 20 kW.

Assuming the discharge energy loading could be increased to the full 10 Joules, the output pulse power would increase significantly due to the enhancement in efficiency. For instance, 10 J into a 1:1:4 mixture at 120 torr gives a theoretical efficiency of 6.1%. With a resonator coupling efficiency of 50%, the corresponding output energy would be 0.3 J, giving a plateau power in excess of the required 50 kW.

The increased resonator coupling efficiency could be obtained by a multi−pass stable resonator configuration, as shown in fig. (5.10). If properly engineered this would be practicable, although alignment sensitivity would be a major problem. In addition, with a 20 m raduis of curvature rear mirror and such a long mirror separation, the beam spot size would be too large for the present electrode system. Moreover, if $d < R_b$ the resonator would actually become unstable. These problems could be overcome by

continually refocussing the beam on each pass, with concave mirrors being employed for beam folding.

REFERENCES FOR CHAPTER (5)

[5.1] Watson I. A. " Development of a high prf CO_2 laser for materials processing applications." Ph.D thesis, Department of Mech. Eng. Univ. of Glasgow. To be published.

[5.2] Kogelnik H., Li T. " Laser beams and resonators." Proc IEEE, Vol. 54, 1966, pp 1312 – 1329.

[5.3] Khahra J.H., "Optimisation of the output characteristics of a pulsed carbon–dioxide laser for processing of materials." Ph.D. Thesis Univ. Birmingham, Dec 1976.

[5.4] Chatwin C.R., "Thermodynamics of a pulsed carbon–dioxide laser for machining metals." Ph.D. Thesis Univ. Birmingham. U.K. 1979.

[5.5] Kortz H.P., Weber H. "Diffraction losses and mode structure of equivalent TEM_{00} optical resonators." App. Optics Vol 20, No 11, 1981.

[5.6] Cheo P. K. "CO_2 lasers." Marcel Dekker 1971.

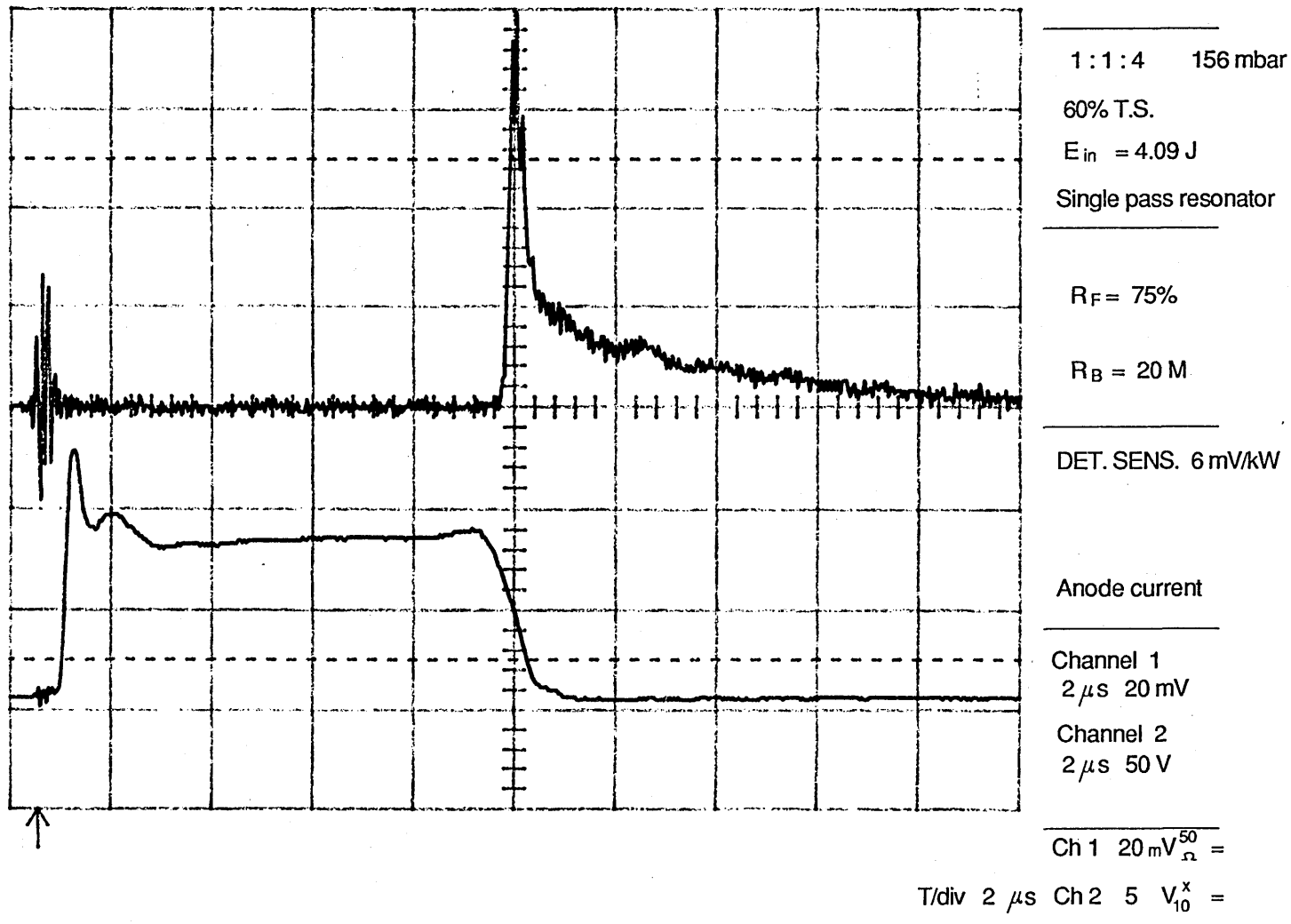

FIGURE 5.1 OUTPUT PULSE SINGLE PASS RESONATOR

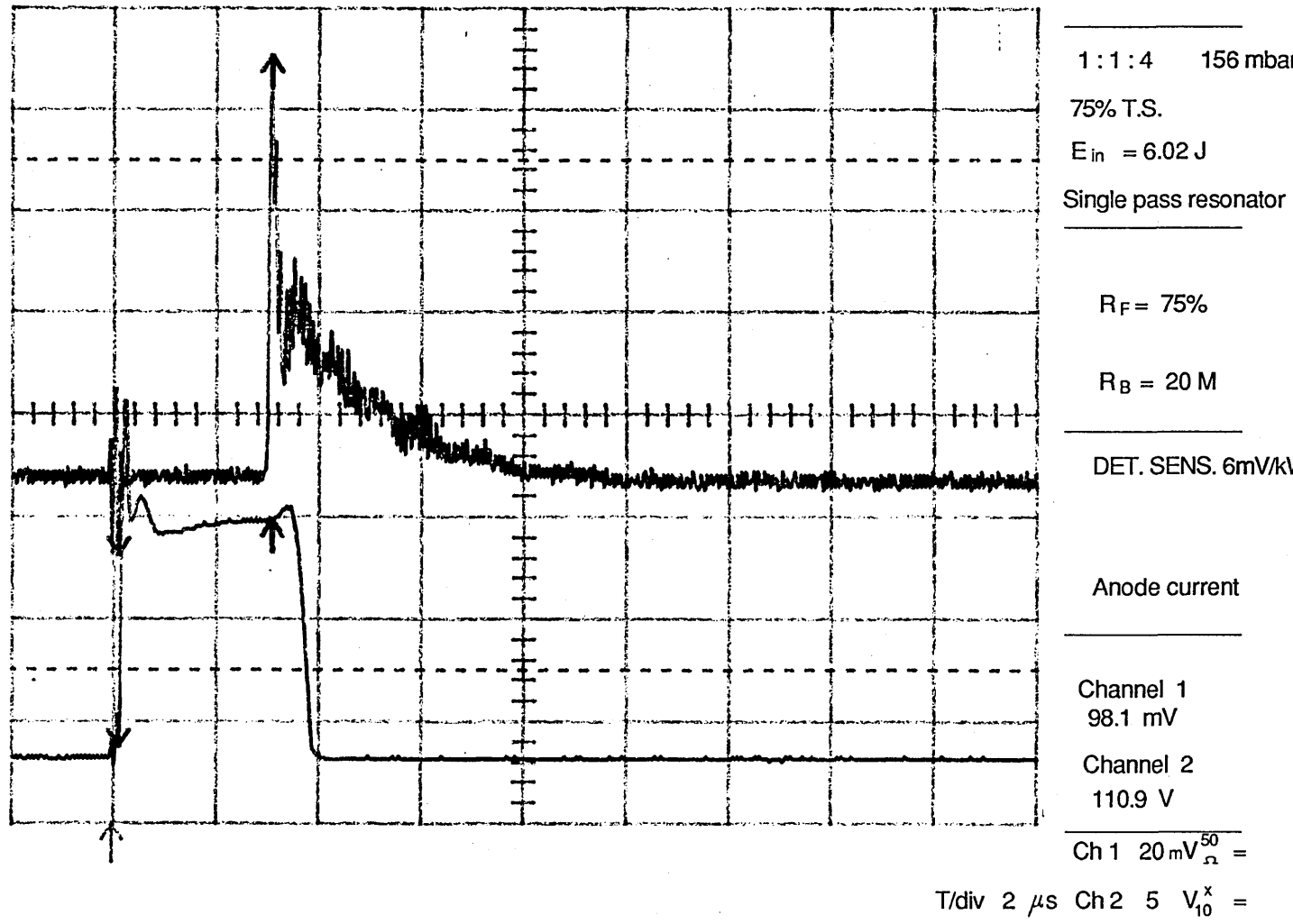

FIGURE 5.2 OUTPUT PULSE SINGLE PASS RESONATOR

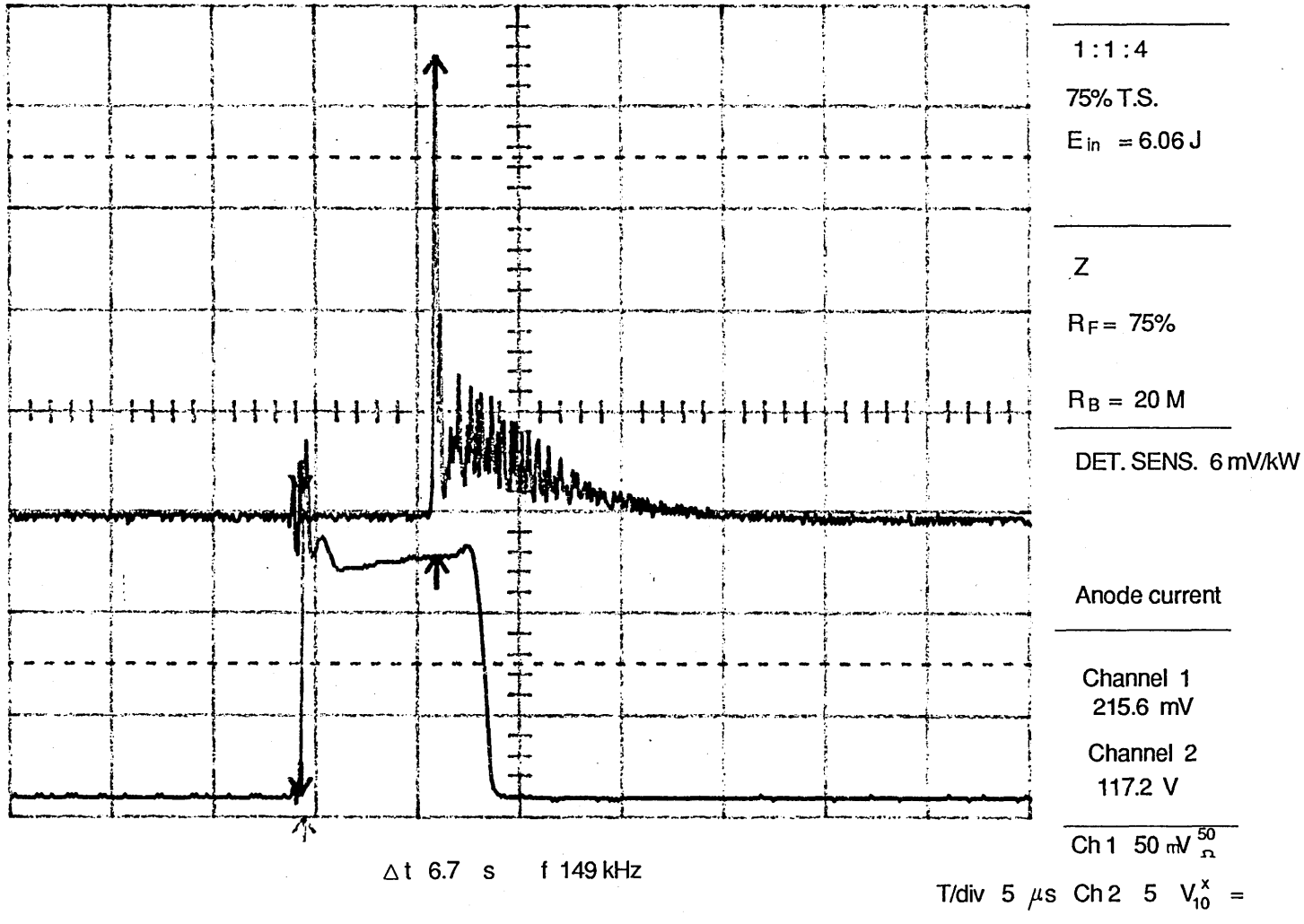

FIGURE 5.3 OUTPUT PULSE Z RESONATOR 1.1.4 MIXTURE

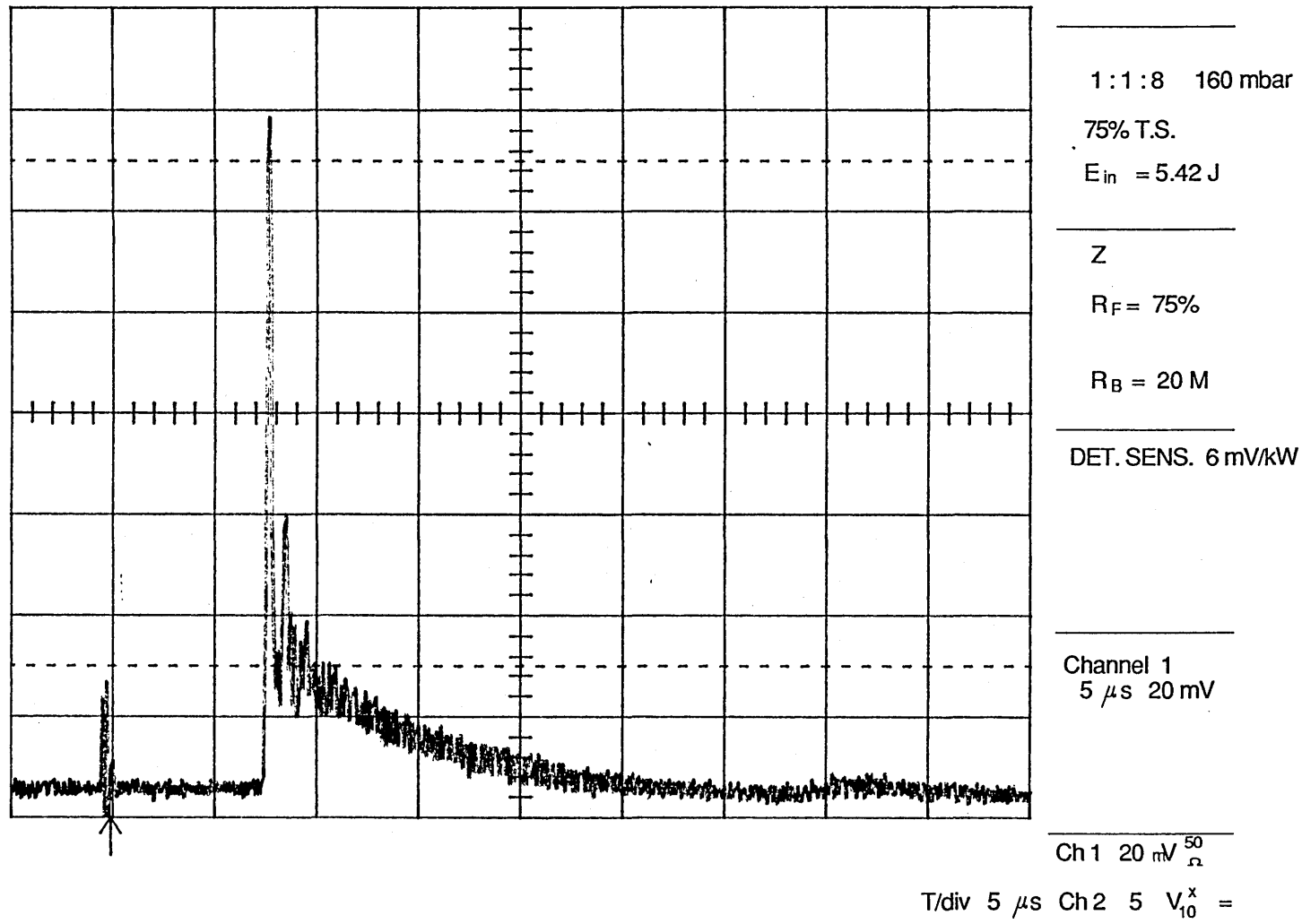

FIGURE 5.4 OUTPUT Z RESONATOR 1:1:8 MIXTURE

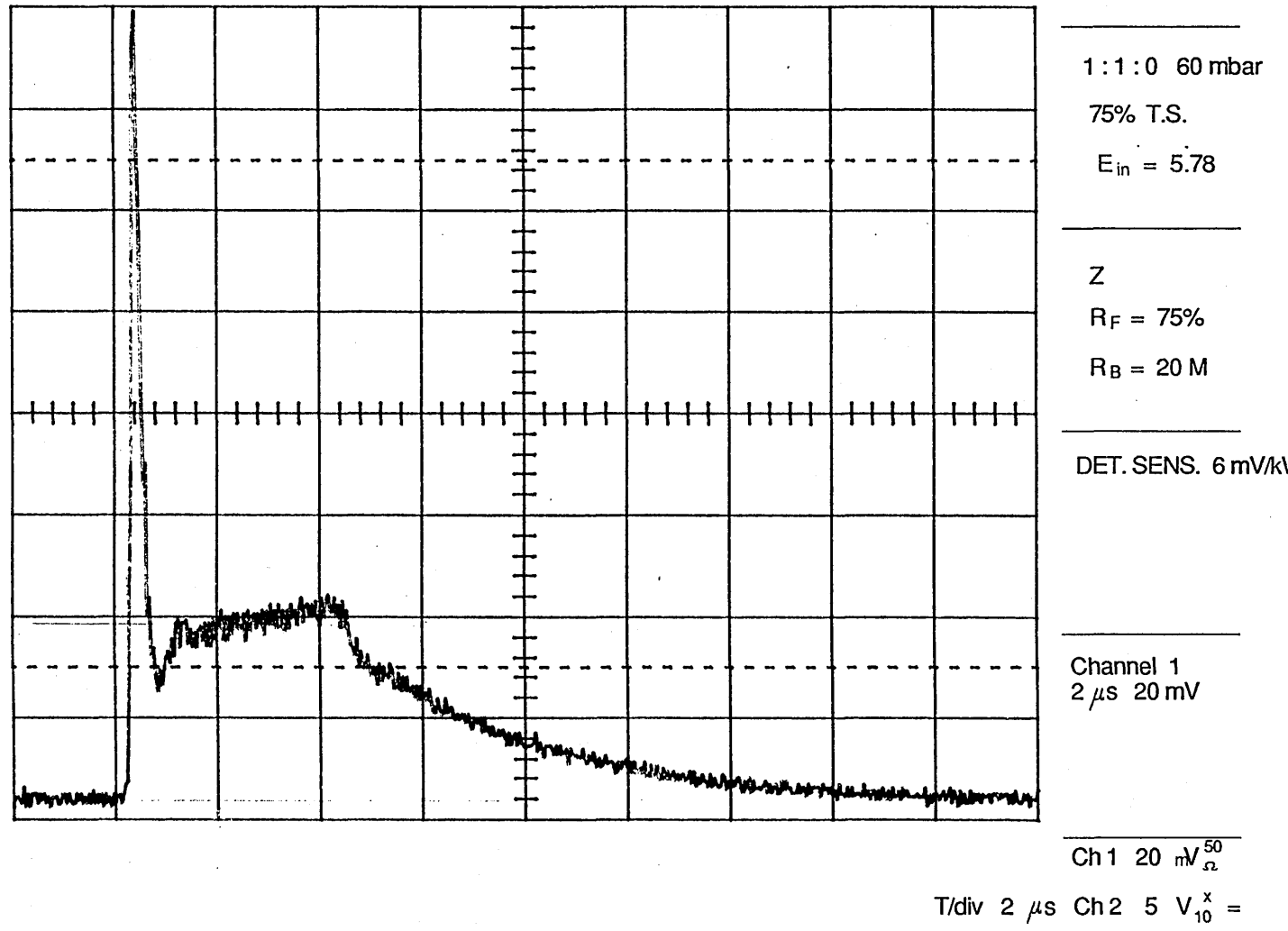

FIGURE 5.5 OUTPUT PULSE Z RESONATOR 1:1 : 0

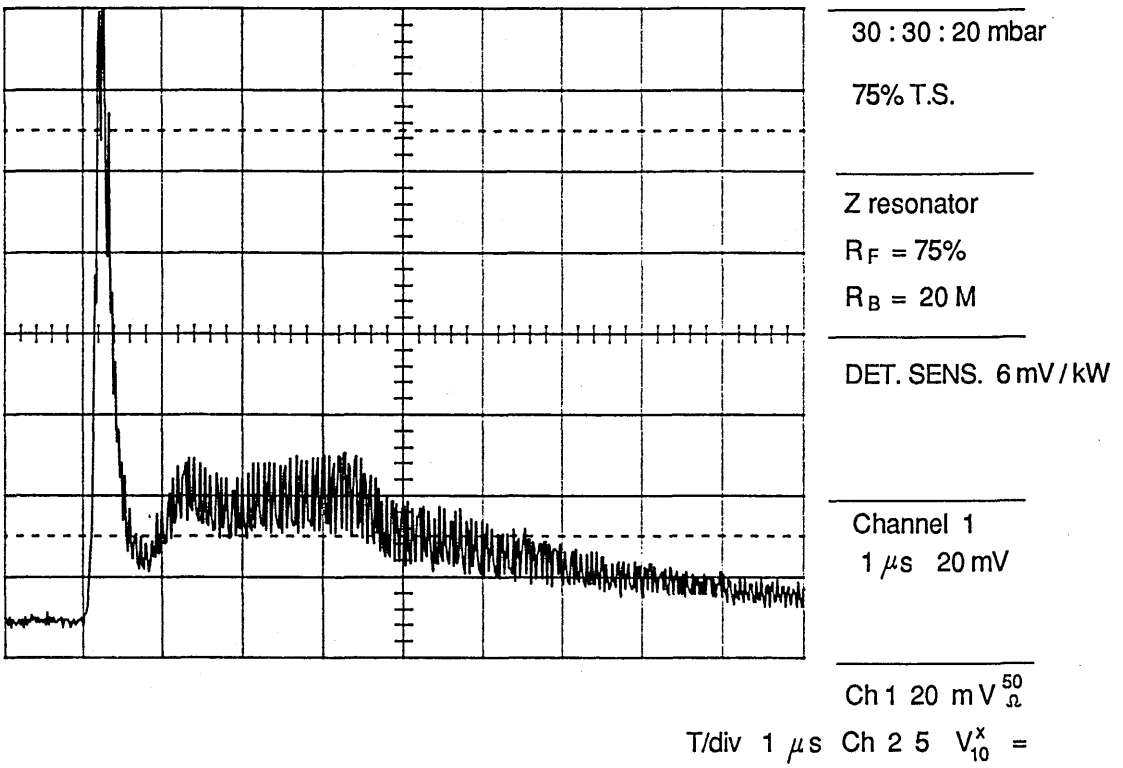

FIGURE 5.6 OUTPUT PULSE 30 : 30 : 20 MIXTURE

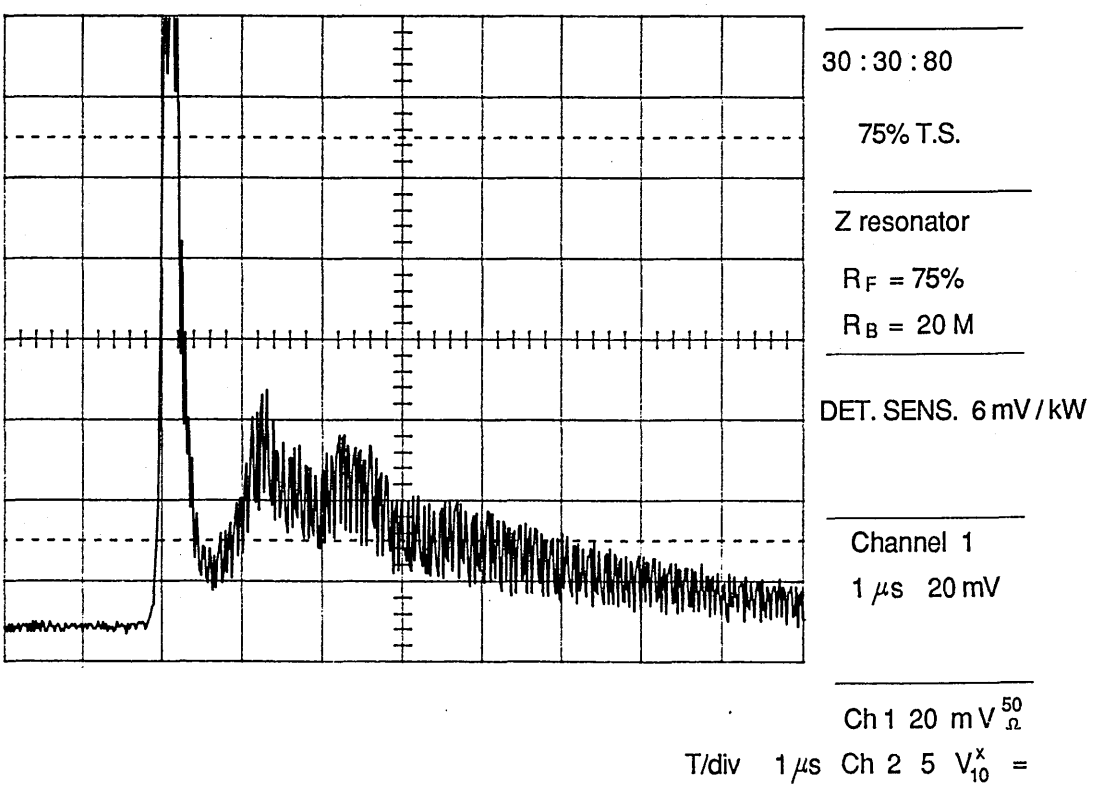

FIGURE 5.7 OUTPUT PULSE 30 : 30 : 100 MIXTURE

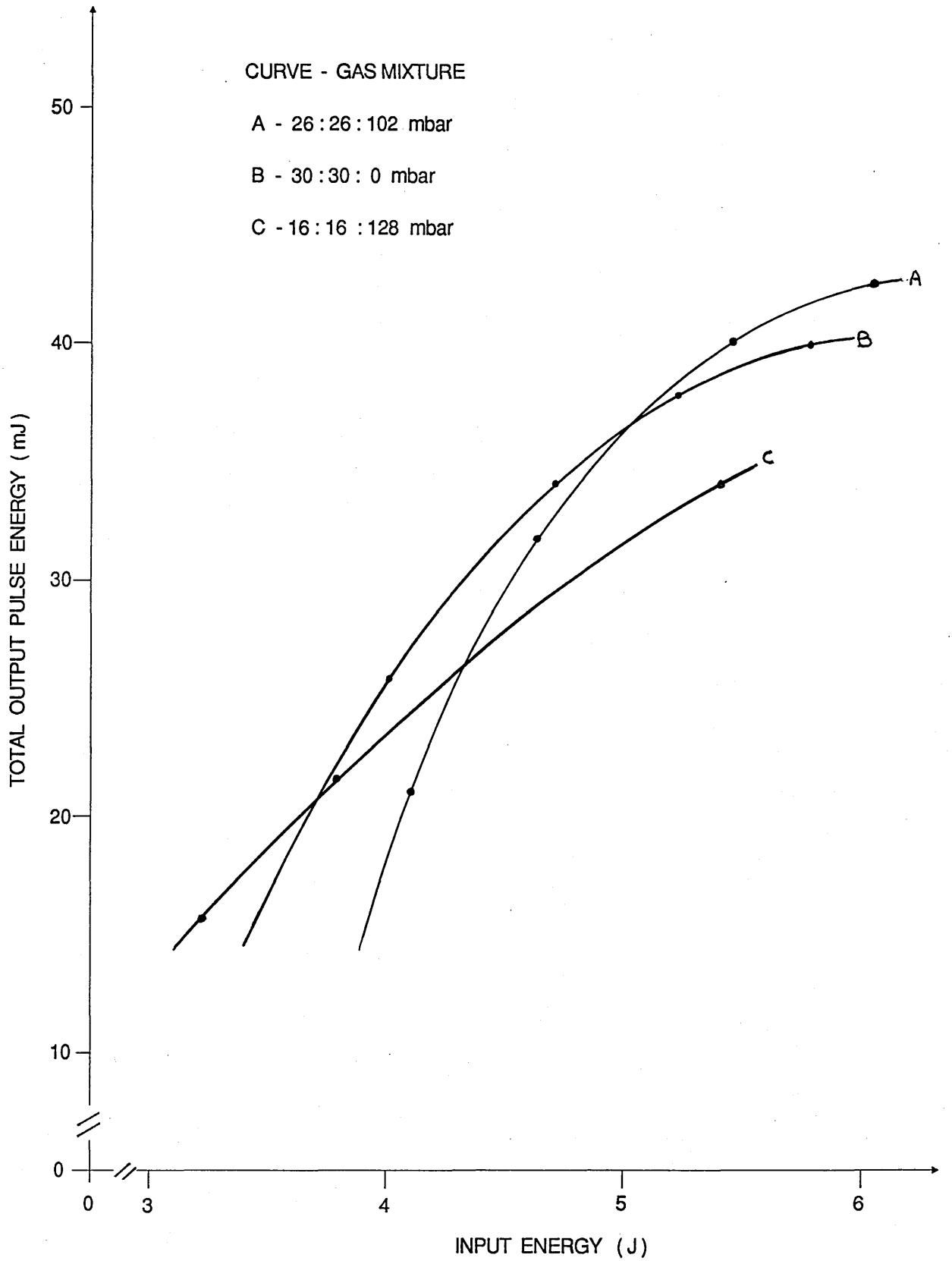

FIGURE 5.8 LASER OUTPUT PULSE ENERGY vs INPUT ENERGY

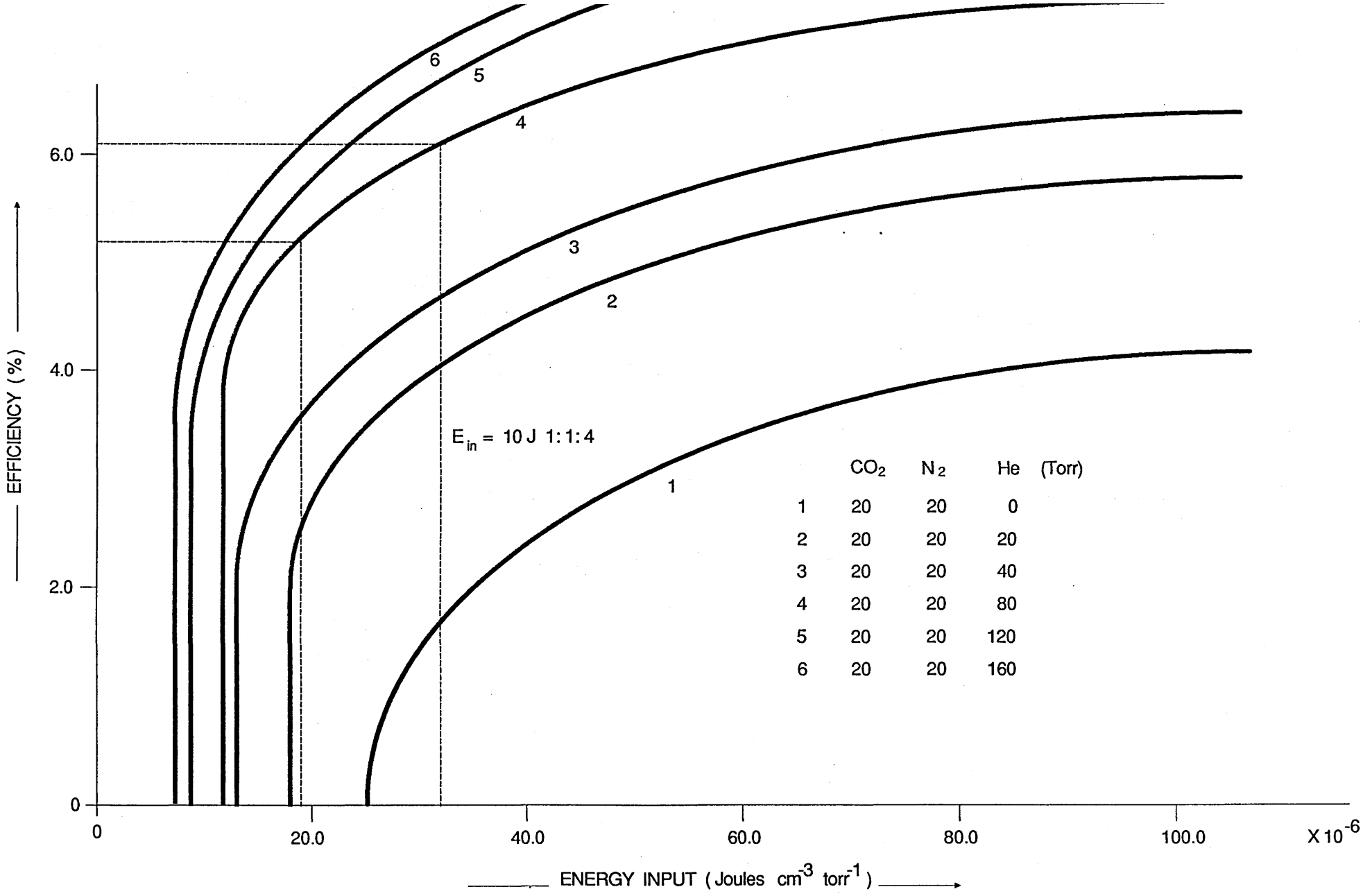

FIGURE 5.9 THEORECTICAL EFFICIENCY vs SPECIFIC ENERGY INPUT

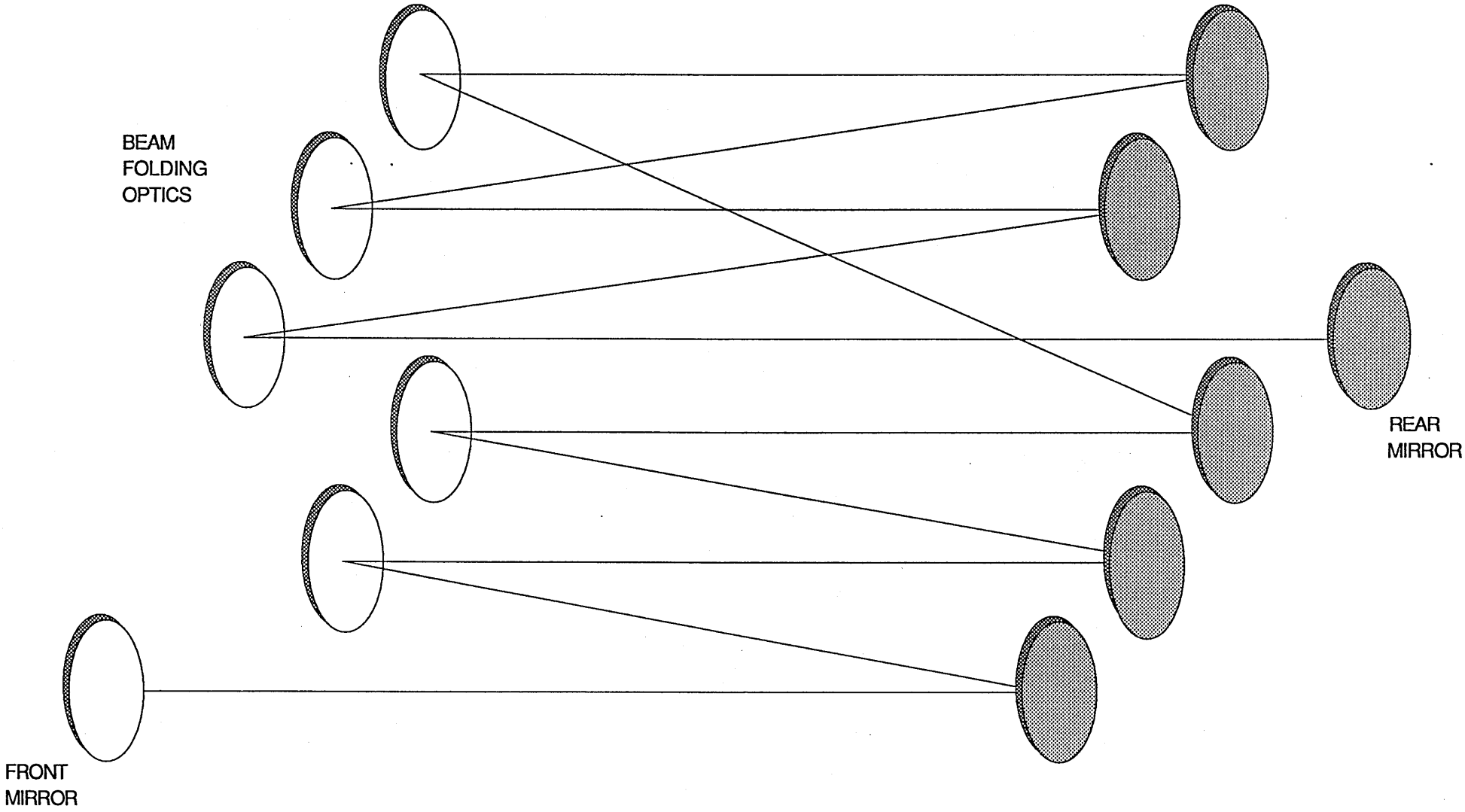

FIGURE 5.10 MULTI-PASS STABLE RESONATOR

(6.0) GENERAL CONCLUSIONS AND RECOMMENDATIONS.

The purpose of the work described was to design and develop a high PRF, pulsed CO_2:N_2 laser, capable of generating the power intensities required for processing refractory metals. The work can split into four main areas.

Gas Circulator Development.

A high flow rate gas recirculator has been designed and built to provide the gas flow required for continuous pulse mode operation of a transverse discharge electrode system. A total gas flow approaching 15000 m^3/hr is provided by two Root's blowers. The circulator was designed and manufactured to vacuum specifications, with a typical leak rate of the order of 1 mbar/hr and a total system pump down time of fifteen minutes. The circulator also includes four gas/water heat exchangers, capable of dissipating in excess of 100 kW and maintaining the cavity gas inlet temperature below 320 K. The off−design performance of the cooling circuit has been modelled, with the conclusion that cooling performance is within specification throughout the range of gas mixture compositions, pressures and flow rates. A gas system is incorporated for automatic control of system initialisation and refresh. The circulator is fully instrumented for thermodynamic analysis.

Pulser Development.

The high frequency line type pulser originally developed by Spall [6.1] has been been modified and tested up to full specification. New thyratron trigger circuits have been developed, together with control circuits and instrumentation. The thyratron trigger units are coupled with fibre−optic links to a main control unit, which provides single shot, burst mode and continuous mode control of the pulser. Circuit fault protection has been substantially improved and integrated with the control and safety circuits.

The main problem experienced during the development of the pulser was the occurence of fire−throughs due to the effect of thyratron grid−anode stray capacitance on the charging thyratron. The resultant coupling between the grid and anode circuits allowed the cathode to be driven positive with respect to the grid during the PFN discharge wave, re−triggering the charging thyratron and causing the pulser to fire−through. This problem was solved by grounding the trigger circuit to the thyratron grid and driving the cathode negative with respect to the grid. This allowed the cathode to be capacitively coupled directly to the grid, thus preventing spurious triggering on the PFN discharge wave. Due to the circuit arrangement, it was only necessary to incorporate this triggering circuit on the charging thyratron; both the

discharge thyratron and the tailbiter employed grounded cathode circuits.

The development of a MOSFET based thyratron trigger circuit was unnsuccessful because of the problems experienced protecting the MOSFET from the thyratron grid spike. The trigger circuits were therefore designed with a small glass envelope thyratron as the main switching element. This design proved to be very robust and offered ideal triggering performance.

Gas Discharge System.

The performance of a transverse electrode discharge cavity has been examined in both single shot and continuous pulse mode operation. It was found that the maximum single shot input energy, as determined by the onset of arcing, was limited to 7.56 Joules for a 1:1:4 mixture at a total pressure of 156 mbar, with a 10 μs excitation pulse length. This was higher than the value obtained by Khahra [6.2] for the same conditions, however, the results reported by Khahra were higher for other mixture compositions, as reported in Tables (4.4) and (4.5). The discrepancy in the results is possibly due to instrumentation errors and the methods employed by Khahra to integrate the V–I waveforms.

In the single shot stability experiments it was observed that arcing occured in the centre of the electrodes, both with a static gas and a flowing gas. In the continuous pulse mode arcs were found to occur first on the downstream edge of the electrodes, moving into the centre with increasing input energy and PRF. It can therefore be concluded that arcing in the continuous pulse mode is related to the gas clearing rate and not the result of misalignment of the electrodes.

Several modifications were made to the electrode system to improve discharge stability. The electrode length weas reduced to the same length as the cavity gas inlet window, in order to improve the gas flow over the end sections. This prevented arcs occuring on the tapered ends. The brass trigger–wire clamps were replaced with PTFE and the trigger wires manufactured in a continuous assembly. It was found that the energy dissipated in the electrode discharge was reduced by the occurrance of arcing in the anode electrical leadthroughs. This problem was overcome by insulating the copper conductor in the leadthrough. Although four leadthroughs are provided, no deterioration in performance was obtained when operating with only one anode connection.

A detailed investigation of preionization and discharge formation was undertaken in order to elucidate the causes of arcing. It was found that the discharge breaks down

in the Townsend regime due to the low applied voltage and low gas pressure. It was also concluded that the trigger–wires do not produce sufficient UV to cause appreciable photoionization ahead of the ionizing wave. The trigger–wires therefore act simply as an electron source at the cathode, with the electrons being liberated from the cathode by field emission. Ionizing wave calculations of discharge formative delay times – based on theoretical ionization coefficients and drift velocities – are in good agreement with experimental observations. Since the discharge breaks down in the Townsend regime, homogeneous discharge formation requires a uniform current density at the cathode during the formative period. It was concluded that the poor discharge stability was principally the result of non–uniform current density due to the position of the trigger–wires within the discharge.

In the continuous pulse mode the maximum attianable PRF was approximately 1kHz, at a gas flow velocity of 41 m/s, corresponding to a clearing ratio of CR $\approx$ 0.6. With reference to Table (4.8), it was found that the maximum PRF decreasd with increasing input pulse energy. It was also found that over a range of pulse energies, the corresponding maximum PRF resulted in an almost constant mean allowable input power to the discharge, as shown in Table (4.8). It has been found that clearing ratios below the accepted minimum of CR $\approx \sqrt{3}$ can be obtained at these low specific energy inputs.

The clearing ratio approaches infinity at the single pulse stability threshold and decreases with decreasing pulse energy. Consequently, if the single pulse stability thereshold can be increased, a significant decrease in clearing ratio can be attained at the lower energy inputs. The single shot discharge stability limits for the electrode system reported here are considearbly less than the results reported by Kline [6.3] for a spark preionized system and the same pulse duration. It can be concluded that the performance obtained by Kline is due to the highly uniform current distribution bestowed by volumetrically preionizing the inter–electrode volume.

Resonator.

The output characteristics from a stable Z configuration resonator have been examined for several gas mixtures. It was found that the laser pulse power was limited by the low resonator coupling efficiency. This was estimated to be of the order of 15% on a straight volume basis, in agreement with the value calculated from the measured output energy and Khhara's theoretical efficiency. A 1:1:4 mixture at a total pressure of 156 mbar was found to give the highest overall output energy, with a plateau power of approximately 6 kW. However, a helium free mixture was found to exhibit excellent pulse characteristics with a total pulse energy very close to that obtained

with the 1:1:4 mixture.

(6.1) GENERAL CONCLUSION.

It is clear that the output pulse powers obtained are almost a factor of 10 lower than required. This is due to the low allowable discharge power and poor resonator coupling efficiency. Considerable development work is therefore still required to establish a new discharge cavity design, capable of continuous operation at the design PRF. A stable optical resonator must also be developed for maximum output coupling efficiency. Recommendations for future development are discussed below.

(6.2) FUTURE WORK

The main factor limiting the stability and convective clearing of the discharge is the present trigger–wire arrangement. It is therefore recommended that the cathode be replaced with a screen mesh and the discharge triggered by corona preionizers positioned behind the cathode, as shown in fig. (4.76). If the trigger–wires are simply capacitively coupled to the anode, this will not produce any volumetric preionization of the discharge volume due to the low applied field. It is recommended that a high voltage spiker circuit be designed to generate the corona current necessary for volumetric preionization.

It is clear that arcing occurs in the continuous pulse mode because of the continual growth of the instabilities over a sequence of pulses. Since it is not practicable to clear the gap at the rate required for 10 kHz operation, a means must be found to decrease the clearing ratio, allowing more pulses to be input into each block of gas. Since any improvements in single pulse stability will be accompanied by a reduction in clearing ratio at lower input powers, it should be possible to extend the stable operational envelope by use of the corona preionized electrode system described above. A further improvement could also be gained by resistively ballasting the anode to stabilize the discharge. Due to the low mean current levels, the penalty on power transfer efficiency may not be to severe. Only minor modifications would be required to the pulser and triggering circuits.

This research has highlighted several areas which are presently poorly understood. The following projects are therefore recommended in addition to the proposals above.

(i) Influence of negative ion processes on the stability of glow discharges. This could be examined theoretically, with data on the electron temperature dependences of the ionization and attachment coefficients being obtained from BOLTZ. Some experimental

work could also be undertaken on the effects of CO addition.

(ii) The processes responsible for the generation of UV in corona discharges is not yet fully understood. A combination of experimentation and theoretical modelling could yield the critical dependance of UV emission on the gas mixture composition and corona parameters.

(iii) UV preionization in CO_2 lasers is found to be predominantly due to low ionization impurities (LIP), with an ionization potential of approximately 10.5 eV. The effects of LIP additives (e.g. propylene) on preionization density and discharge stability could be examined.

(iv) Flow turbulence in the discharge is known to improve stability through the enhancement of diffusion rates and homogenization of the plasma. Tests could be conducted on these effects by generating turbulence upstream of the discharge. Measurements of cavity velocity profiles would also provide valuable information.

(v) Some experimental work is required on the optical resonator in order to determine the maximum possible output coupling efficiency. An optimum beam size and number of passes needs to be determined for the transverse discharge arrangement. The effects of apertures on the resonator mode could also be examined experimentally and theoretically.

(vi) The laser simulations code should be modified to incorporate the calculation of mixture transport properties as described in section (2.2.1). Simulations are required on the total pulse and usable pulse efficiency as a function of specific energy loading, over the full range of gas mixtures.

REFERENCES FOR CHAPTER (6)

[6.1] Spall R. "Pulsed power supply for an unstable resonator." Ph.D thesis, Department of Mech. Eng., Univ. Of Birmingham, 1979.

[6.2] Khahra J.H., "Optimisation of the output characteristics of a pulsed carbon-dioxide laser for processing of materials." Ph.D. Thesis Univ. Birmingham, Dec 1976.

[6.3] Kline L. E., Denes L. J., Perchersky M.J. "Arc suppression in CO_2 laser discharges." App. Phys. Lett., Vol 29, No. 9, 1976.

APPENDIX A1. TRANSPORT PROPERTIES OF CONSTITUENT GASES.

Carbon Dioxide.

Temp (K)	250	300	350	400
Cp (kJ/kgK)	0.791	0.846	0.939	1.041
μ (kg/ms)	12.60×10^{-6}	14.99×10^{-6}	19.49×10^{-6}	23.67×10^{-6}
K (kW/mK)	12.90×10^{-6}	16.61×10^{-6}	24.75×10^{-6}	32.74×10^{-6}

Nitrogen.

Temp (K)	250	300	350	400
Cp (kJ/kgK)	1.0415	1.0410	1.0425	1.0460
μ (kg/ms)	15.53×10^{-6}	17.86×10^{-6}	20.0×10^{-6}	21.99×10^{-6}
K (kW/mK)	22.27×10^{-6}	26.05×10^{-6}	29.69×10^{-6}	33.19×10^{-6}

Helium.

Temp (K)	250	300	350	400
Cp (kJ/kgK)	5.200	5.200	5.200	5.200
μ (kg/ms)	18.40×10^{-6}	20.80×10^{-6}	25.23×10^{-6}	29.30×10^{-6}
K (kW/mK)	134.0×10^{-6}	149.8×10^{-6}	177.9×10^{-6}	202.6×10^{-6}

APPENDIX A2: DESIGN OF CO_2 LASER COOLING SYSTEM.

A(2.1) Design specification

Total laser efficiency $\eta_L = 6\%$

Maximum laser power $P_{max} = 5$ kW

$$\Rightarrow \text{Residual heat} \quad Q = 5\left[\frac{1}{0.06} - 1\right] = 78.3 \text{ kW}$$

say $\underline{Q = 80 \text{ kW}}$

In addition to this heat load there will be an additional load of $Q_b = 18.5$ kW for each blower, giving a total system heat load.

$$\underline{Q_L = 117 \text{ kW}}$$

As the gas flow is split into two parallel circuits, each circuit will have a heat load of 58.5 kW. Since the gas flows are the same, design the cooling system with reference to the flows and heat loads of each circuit as shown in figure 1.

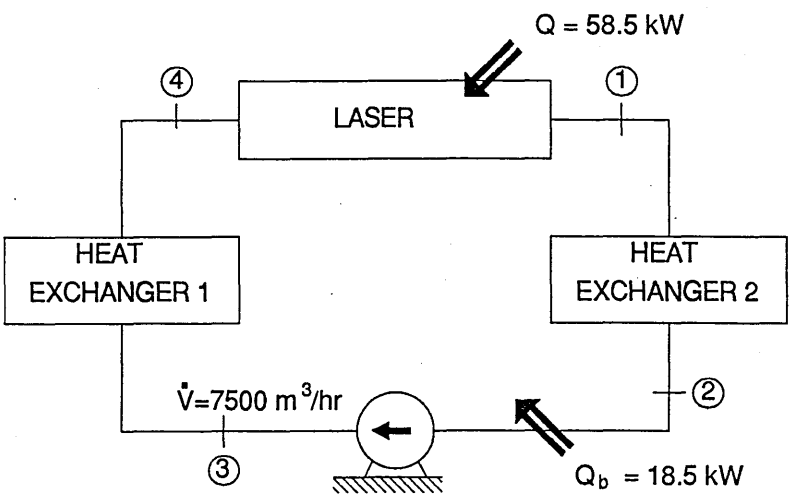

design mixture 1:1:8 200 torr

gas flowrate $\dot{V} = 7500 \text{ m}^3/\text{hr}$

cavity inlet temp. $T_4 = 300\text{K}$ (320K max.)

Assuming $Cp = 4.33$ kJ/kgK @ $T = 300\text{K}$

$R = 799$ kJ/kgK

$$\Rightarrow \text{mass flowrate } \dot{m}g = \frac{7500}{3600} \times \frac{266.66 \times 10^3}{799 \times 300}$$

$$\underline{\dot{m}g = 0.232 \text{ kg/s}}$$

$$\Rightarrow \text{total } \Delta T = \frac{Q_L + Q_b}{\bar{m}g\ Cp} = \frac{58.5}{0.232 \times 4.33} = 58.2°C$$

Since the temperature will be lower than this, use a mean temperature $\bar{T} = 325$ K to evaluate gas properties:

1·1·8 mixture properties T = 325 K

Cp = 4.33 kJ/kgK

R = 799 kJ/kgK

Pr = 0.981 k = 9.0×10^{-5} kW/m²K

μ = 21.3×10^{-6} kg/ms

The above figures can be used for the initial design, however, since the gas flow conditions and mixture compositions will be variable, the performance must be checked at all settings.

A(2.2) Choice of cooling system

One of the main criteria in the design is to ensure full vacuum integrity. It was therefore decided to use the same cooling coils as used by Control Laser Ltd. as these had a proven performance on a similar duty. The coils chosen for this application were modified versions of the CM 1636/37, as supplied by S and P Coil products, Leicester. Figure 2 illustrates the main features of these.

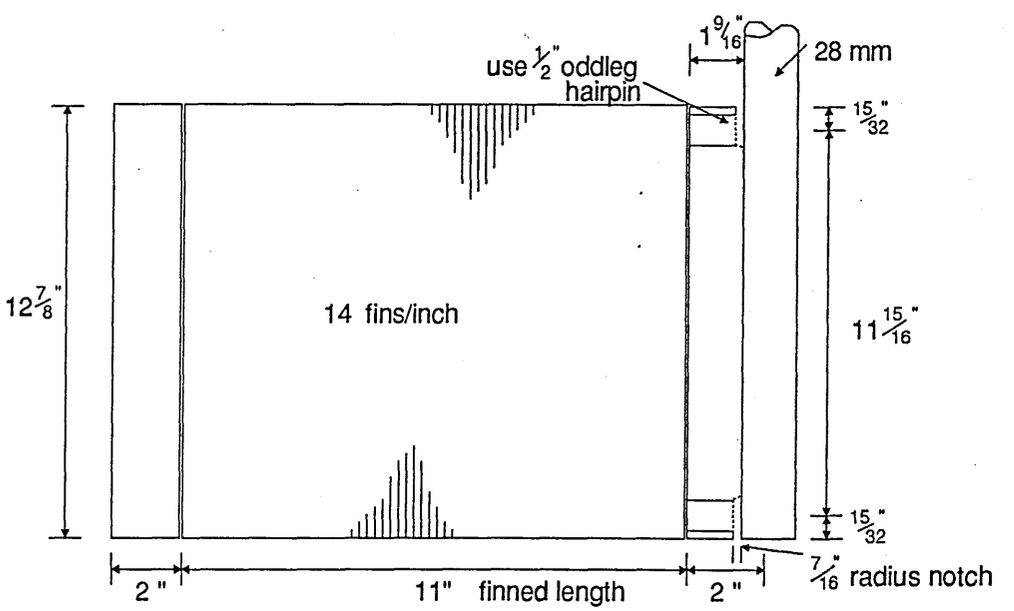

FIGURE 2

The coils were modified to give 4 cross–counterflow tube passes, with eight tubes in each pass.

The performance of the coils are assessed at the above design conditions and the total number of coils required for each exchanger calculated.

A(2.3) Performance of coils

From an initial design study it was decided to use a water flow of 0.5 kg/s to each coil. This will be supplied from a resevoir and pump situated outside the lab.

A(2.3.1) Tubeside heat transfer coefficient

Tube OD $D = {}^{5}/_{8}"$ $\Rightarrow$ ID = 14.96 mm

wall thickness $t = 0.018"$

Flow area/tube $= \frac{\pi}{4} \times (14.96 \times 10^{-3})^2 = \underline{1.758 \times 10^{-4}\ m^2}$

Flow area/pass $= 8 \times 1.758 \times 10^{-4} = 1.41 \times 10^{-3}\ m^2$

mean water velocity $\bar{V} = \frac{\dot{m}}{\rho \cdot A_1} = \frac{0.5}{1000 \times 1.41 \times 10^{-3}}$

$\underline{\bar{V} = 0.35\ m/s}$

Taking water properties at 20°C

$\mu_w = 890 \times 10^{-6}$ kg/ms $\quad K_w = 611 \times 10^{-6}$ kW/mK

$\rho = 997$ kg/m^3 $\quad Pr = 6.09$

Reynolds number

$$Re_{d,m} = \rho \frac{\bar{V}d}{\mu} = \frac{997 \times 0.35 \times 14.96 \times 10^{-3}}{890 \times 10^{-6}}$$

$\underline{Re_{d,m} = 5866}$

The inside heat transfer coefficient can be found from [1]

$$Nu_{d,m} = 0.023\ Re_{d,m}{}^{0.8} Pr_m{}^{1/3}$$

$$Nu_{d,m} = 0.023 \times 5866^{0.8} \times 6.09^{1/3} = 43.44$$

$\Rightarrow$ Waterside coefficient $h_i = \frac{Nu \times kW}{d}$

$$h_i = \frac{43.44 \times 611 \times 10^{-6}}{14.96 \times 10^{-3}} \qquad h_i = \underline{1.77\ kW/m^2K}$$

A(2.3.2) Gas side heat transfer coefficient

The gas side heat transfer coefficient needs to be calculated for both the tube surface and fin surface. These are obtained by the method detailed in reference [2].

Coefficient for plain tubes—

$$Nu = a\ Re^m\ Pr^{0.34}$$

for staggered tubes $a = 0.273$ $L_1 = 1\frac{19}{32}" - D = 24.6$ $L_2 = 24.5$ mm

$m = 0.635$

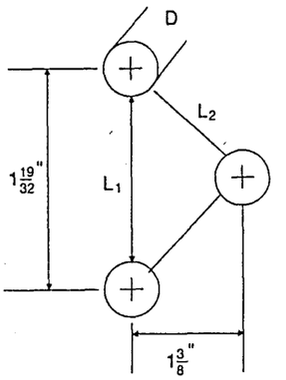

where *Re* is calculated at the minimum cross flow area.

⇒ minimum flow area = 8 tubes per pass

$$A_{min} = 7x + \frac{15"}{32} + \left[11\frac{15"}{16} - 7 \times 1\frac{19"}{32}\right] + \frac{15"}{32}$$

$A_{min} = 200.9$ mm/m width

with a finned width of 11" $A_{min} = 0.056$ m²

with 14 fins/inch = 154 fins x 0.006" thickness

⇒ $A_{min} = 0.056 - 154 \times 0.006 \times (25.4 \times 10^{-3})^2 \times 12\frac{7}{8}$

$= 0.056 - 0.0076$

$\underline{A_{min} = 0.048 \text{ m}^2}$

Gas density $\rho = \frac{P}{RT} = \frac{26.66}{.799 \times 325}$

$\underline{\rho = 0.103 \text{ kg/m}^3}$

$$V_{max} = \frac{\dot{V}}{A_{min}} = \frac{7500}{3600 \times 0.048} \Rightarrow \underline{V_{min} = 43.4 \text{ m/s}}$$

$$Re = \rho\frac{V_{max}}{\mu} Do = \frac{0.103 \times 43.4 \times 15.87 \times 10^{-3}}{21.3 \times 10^{-6}}$$

$\underline{Re = 3330}$

⇒ $Nu = 0.273 \times (3330)^{0.635} \times 0.981^{0.34} = 46.78$

$$h_{ot} = \frac{Nu\ K}{D_0} = \frac{46.78 \times 90 \times 10^{-6}}{15.87 \times 10^{-3}}$$

$\underline{h_{ot} = 0.265 \text{ kW/m}^2\text{K}}$ Outside of tubes

Coefficient for fins –

$$Nu_f = 0.134\ Re^{0.681}\ Pr^{0.33} \left[\frac{y_F}{H_F}\right]^{0.2} \left[\frac{y_F}{\delta_F}\right]^{0.1134}$$

y_F = distance between fins = 1.66 mm

H_F = fin height

Calculate mean area per tube, find equivalent circular diameter D_e and calculate H_F from

$\underline{H_F = (D_e - D_0) = 14.9 \text{ mm}}$

$$\delta_F = 0.006" = 0.152 \text{ mm}$$

$$\Rightarrow \quad Nu_f = 0.134 \times 3330^{0.681} \times 0.981^{0.33} \left[\frac{1.66}{14.9}\right]^{.2} \times \left[\frac{1.66}{.152}\right]^{0.1134}$$

$$Nu_f = 28.2$$

$$\Rightarrow \quad h_{of} = \frac{28.2 \times 90 \times 10^{-6}}{15.87 \times 10^{-3}} \qquad \underline{h_{of} = 0.160 \text{ kW/m}^2\text{K}}$$

Fin effectiveness

From reference [3]

$$\varphi = (1 - A_R - \eta_F A_s)$$

A_R = Root area/m² primary surface

A_s = fin area/m² primary surface

A_{ps} = Area of primary surface

$$A_{ps} = 11" \times 32 \times \pi \times \tfrac{5}{8} \times (25.4 \times 10^{-3})^2 = 0.446 \text{ m}^2$$

and $\underline{A_R = 8.38 \times 10^{-2}}$ $\underline{A_s = 27.53}$

Assuming $\eta_F = 75\%$

$\Rightarrow$ fin effectiveness $\varphi = 1 - 8.38 \times 10^{-2} + 0.75 \times 27.53$

$$\underline{\varphi = 21.56}$$

The average gas side heat transfer coefficient can therefore be calculated from

$$h_o = [h_{oT} (1 - A_R) + h_{of} \eta_F A_s]$$
$$= 0.265 (1 - 8.38 \times 10^{-2}) + 0.16 \times 0.75 \times 27.53$$
$$\underline{h_o = 3.546 \text{ kW/m}^2\text{K}}$$

This is reffered to the primary surface area of the tubes ie. outside are of plain tubes.

A(2.3.3) Overall heat transfer coefficient

$$\frac{1}{u} = \frac{1}{h_o} + \frac{1}{h_i}\frac{D_o}{D_i} + \frac{y_w D_o}{K_c D_T} + R\frac{D_o}{D_i}$$

where

u = overall coefficient referred to primary surface area

y_w = thickness of tubes = 0.018" = 0.45 mm

$$D_w = \frac{D_o - D_i}{\ell n \frac{D_o}{D_i}} = 15.42 \text{ mm}$$

K_c = 398 W/mK copper

R fouling resistance = 0.18×10^{-3} m²K/W

$$\Rightarrow \quad \frac{1}{u} = \frac{1}{3.546} + \frac{1}{1.77}\frac{15.87}{14.96} + \frac{0.457 \times 15.88 \times 10^{-3}}{.398 \times 15.42} + 0.18 \times 10^{-3} \times \frac{15.87}{14.96}$$

$\Rightarrow$ $u = 1.13$ kW/m^{2}K

A(2.3.4) Calculation of coil effectiveness

Since both fluids are "unmixed" the effectiveness of each cross flow pass is given by [3].

$$\epsilon_p = 1 - \exp\left[\frac{\exp(-NCn) - 1}{Cn}\right]$$

where $n = N^{-0.22}$

C = Capacity ratio = $\dot{m}\, C_{pmin} / \dot{m}\, C_{pmax}$

N = No.of transfer units

gas $\quad \dot{m}C_p = 0.214 \times 4.33 = 0.9266 \Rightarrow \underline{C = 0.443}$

water $\quad \dot{m}C_p = 0.5 \times 4.186 = 2.093$

$$N = \frac{uA}{\dot{m}C_{pmin}}$$

with A = primary surface area/pass

$$A = 8 \times (\pi \times 15.87 \times 10^{-3} \times 11 \times 25.4 \times 10^{-3}) = 0.115 \text{ m}^2$$

$$N = \frac{1.13 \times 0.1115}{0.9266} \qquad N = 0.136 \text{ transfer units}$$

$\Rightarrow$ $n = 1.55$

$$\Rightarrow \quad \epsilon_p = 1 - \exp\left[\exp\frac{(-0.136 \times 0.48 \times 1.55) - 1}{0.48 \times 1.55}\right]$$

$$\underline{\epsilon_p = 0.1218}$$

With four cross-flow passes in each coil, the effectiveness of a single coil is [3].

$$\epsilon_c = \frac{\left[\frac{1 - \epsilon_p C}{1 - \epsilon_p}\right]^4 - 1}{\left[\frac{1 - \epsilon_p C}{1 - \epsilon_p}\right] - C} = \frac{\left[\frac{1 - 0.1218 \times 0.443}{1 - 0.1218}\right]^4 - 1}{\left[\frac{1 - 0.1218 \times 0.48}{1 - 0.1218}\right]^4 - 0.443}$$

$$\underline{\epsilon_c = 0.386}$$

This is the effectiveness of each coil at the maximum gas flowrate 7500 m^3/hr and a water flow of 0.5 kg/s. The effectiveness is defined as :-

$$\epsilon = \frac{\text{temperature change of minimum fluid}}{\text{maximum possible temperature change}}$$

Referring to figure (3)

$$\epsilon_c = \frac{T_1 - T_2}{T_1 - t_1}$$

$$\Rightarrow \quad \underline{T_2 = T_1 - \epsilon(T_1 - t_1)}$$

A(2.4) Number of coils required

Heat input by blower will appear as a gradual temperature rise around loop

$$\Delta T_{blowers} = \frac{Q_b}{\dot{m}_g C_p} = \frac{18.5}{0.214 \times 4.33} = 20.0°C$$

Assume 10°C rise across blower and lump remainder with cavity heat load Q_L.

$$Q_L' = 40 + 10 \times 0.214 \times 4.33$$

$$\underline{Q_L' = 49.3 \text{ kW}}$$

Try two coils in each exchanger

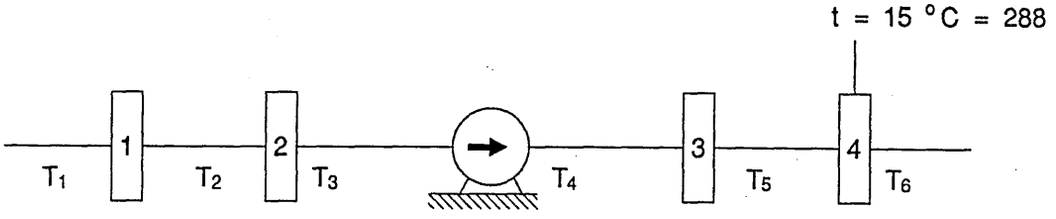

Assume $T_6 = 300$ K initially

$$\Rightarrow \quad T_1 = T_6 + \frac{Q_L'}{\dot{m}_g C_p} = 300 + \frac{49.3}{0.214 \times 4.33} = 353.2$$

$$T_2 = T_1 - \epsilon(T_1 - t_1) = 353.2 - 0.386(353.2 - 288) = 328.0$$

$$T_3 = T_2 - \epsilon(T_2 - t_1) = 312.6 \text{ K}$$

$$T_4 = T_3 + 10 = 322.6 \text{ K}$$

$$T_5 = T_4 - \epsilon(T_4 - t_1) = 309.2 \text{ K}$$

$$\underline{T_6 = T_5 - \epsilon(T_4 - t_1) = 301.0 \text{ K}}$$

This calculation could be interated to find the equilibrium gas inlet temperature at this heat load and gas flowrate; this gives a value $T_6 = 307$ K, which is within the specified design value of 320 K. The design with two coils in each exchanger unit is therefore satisfactory.

APPENDIX A3 – COOLING SYSTEM MODELLING

Referring to figure (2.19) for nomenclature, the following heat balance equations can be derived.

$$Q_L + Q_b = Q_{EX} + M_g C_p \frac{dT_{mean}}{dt} \quad (1)$$

$$Q_{EX} = Q_{EX1} + Q_{EX2} \quad (2)$$

$$Q_{EX1} = m_g C_p (T_1 - T_2) = wC_{pw} (t_{2A} - t_1) \quad (3)$$

$$Q_{EX2} = m_g C_p (T_3 - T_4) = wC_{pw} (t_{2B} - t_1) \quad (4)$$

where Q_L = laser heat load

Q_b = blower heat load

m_g = mass of gas in system

m_w = mass flowrate of water (to each exchanger)

M_w = total mass of water in tank

T and t are respectively the gas and water temperatures at the position indicated by the subscript. It is assumed that the effectiveness of both exchangers is constant.

$$\epsilon = \frac{T_1 - T_2}{T_1 - t_1} = \frac{T_3 - T_4}{T_3 - t_1} \quad (5)$$

The capacity ratio C is defined as

$$C = \frac{m_g C_p}{m_w C_{pw}} \quad (6)$$

this is the capacity ratio based on the total water flow to each exchanger ie. 2 x water flowing to each coil.

Assuming the water in the tank is instantaneously mixed, the following heat balance can be given for the tank

$$M_w C_{pw} \frac{dt_{mean}}{dt} = Q_{EX1} + Q_{EX2} \quad (7)$$

In this case the mean water temperature can be equated to the water inlet temperature t_1

From (3) we have

$$(t_{2A} - t_1) = C(T_1 - T_2) = C\epsilon(T_1 - t_1) \quad (9)$$

Thus

$$Q_{EX1} = m_w C_{pw} C\epsilon(T_1 - t_1) \quad (10)$$

$$Q_{EX2} = m_w C_{pw} C\epsilon(T_3 - t_1) \quad (11)$$

Substituting (10) and (11) into (7) gives

$$\frac{dt_1}{dt} = \frac{m_w C \epsilon}{M_w} \left[(T_1 - t_1) + (T_3 - t_1) \right] \qquad (12)$$

This gives the rate of change of the water inlet temperature in terms of gas temperatures. The solution of this equation therefore required the time dependence of temperatures T_1 and T_3. From equation (1), (2) and (3)

$$Q_\ell + Q_b = Q_{EX1} + Q_{ex2} + M_g C_p \frac{dT_{mean}}{dt} \qquad (13)$$

where T_{mean} is the mean gas temeprature

Thus,

$$Q_\ell + Q_b = m_g C_p (T_1 - T_2) + m_g C_p (T_3 - T_4) + M_g C_p \frac{dT_{mean}}{dt}$$

but $Q_b = m_g C_p (T_3 - T_2)$

$$Q_\ell = m_g C_p (T_1 - T_4) + M_g C_p \frac{dT_{mean}}{dt} \qquad (14)$$

Since approximately half the gas is at temeprature T_4 and half at temperature T_1, we can write

$$T_{mean} = \tfrac{1}{2} (T_1 + T_4)$$

Solution of (14) requires the elimination of one of these variables. From equation (5)

$$T_4 = T_3 - \epsilon(T_3 - t_1) \qquad (15)$$

Also,

$$T_3 = T_2 + \frac{Q_b}{m_g C_p} \qquad \text{and} \quad T_2 = T_1 - \epsilon(T_1 - t_1)$$

Thus,

$$T_3 = T_1 - \epsilon(T_1 - t_1) + \frac{Q_b}{m_g C_p}$$

Substituting this into (15)

$$T_4 = T_1 - \epsilon(T_1 - t_1) + \frac{Q_b}{m_g C_p} - \epsilon\left[T_1 - \epsilon(T_1 - t_1) + \frac{Q_b}{m_g C_p} - t_1\right]$$

and simplifying yields

$$T_4 = T_1(1 - 2\epsilon + \epsilon^2) + \epsilon(2 - \epsilon)t_1 + (1 - \epsilon)\frac{Q_b}{m_g C_p} \qquad (16)$$

Returning to equation (14)

$$Q_\ell = m_g C_p (T_1 - T_4) + \frac{M_g C_p}{2} \frac{dT_1}{dt} + \frac{M_g C_p}{2} \frac{dT_4}{dt} \qquad (17)$$

from (16)

$$\frac{dT_4}{dt} = (1 - 2\epsilon + \epsilon^2)\frac{dT_1}{dt} + \epsilon(2 - \epsilon)\frac{dt_1}{dt} \qquad (18)$$

Substituting (18) into (17)

$$Q_L = m_g\, C_p(T_1 - T_4) + \frac{M_g\, C_p}{2}\frac{dT_1}{dt} + \left[(1 - 2\epsilon + \epsilon^2)\frac{dT_1}{dt} + \epsilon(2 - \epsilon)\frac{dt_1}{dt}\right]\frac{M_g\, C_p}{2}$$

$$Q_L = m_g\, C_p(T_1 - T_4) + \frac{M_g\, C_p}{2}(2 - 2\epsilon + \epsilon^2)\frac{dT_1}{dt} + \frac{\epsilon(2 - \epsilon)}{2} M_g\, C_p \frac{dt_1}{dt}$$

and rearranging

$$\frac{dt_1}{dt} = \frac{2}{M_g\, C_p(2 - 2\epsilon + \epsilon^2)}\left[Q_L - m_g\, C_p(T_1 - T_4) - \frac{\epsilon(2 - \epsilon)}{2} M_g\, C_p \frac{dt_1}{dt}\right] \quad (19)$$

Since dt_1/dt has already been deduced, equation (12), the complete solution only requires the relationship between the two variables T_1 and t_1 and gas temperatures T_3 and T_4. This obtained from

$$T_2 = T_1 - \epsilon(T_1 - t_1) \quad (20)$$

$$T_3 = T_2 + \frac{Q_b}{m_g\, C_p} \quad (21)$$

$$T_4 = T_3 - \epsilon(T_3 - t_1) \quad (22)$$

The complete set of system equations is thus

$$\frac{dt_1}{dt} = \frac{2}{M_g\, C_p(2 - 2\epsilon + \epsilon^2)}\left[Q_L - m_g\, C_p(T_1 - T_4) - \frac{\epsilon(2 - \epsilon)}{2} M_g\, C_p \frac{dt_1}{dt}\right]$$

$$\frac{dt_1}{dt} = \frac{m_w C \epsilon}{M_w}\left[(T_1 - t_1) + (T_3 - t_1)\right]$$

$$T_3 = T_2 + \frac{Q_b}{m_g\, C_p}$$

$$T_2 = T_1 - \epsilon(T_1 - t_1)$$

$$T_4 = T_3 - \epsilon(T_3 - t_1)$$

```
PROGRAM HEATEX

  INITIAL

      ALGORITHM     IALG = 4
      CINTERVAL     CINT = 0.1
      NSTEPS        NSTEP = 1

      CONSTANT MFW=1,MW=6750,QL=25000,CPW=4.187E3
      CONSTANT CPG=3.78E3,TW1IC=15,TG1IC=20,TMAX=30,TMEAN=325
      CONSTANT P=2.666E4,QG=7500,R=562.6,VG=2.4,QB=4000
      CONSTANT DO=15.88E-3,AMIN=0.048,APS=0.1115,KM=7.26E-5
      CONSTANT VIS=2.05E-5,PR=1.07

      RHO=P/R/TMEAN

      MFG=QG*RHO/3600

      C=(MFG*CPG)/(MFW*CPW)

      C2=2*C

      MG=RHO*VG

      VMIN=QG/AMIN/3600

      REN=RHO*VMIN*DO/VIS

      NUT=0.273*(REN**0.635)*(PR**0.34)

      HOT=NUT*KM/DO

      NUF=0.1133*(REN**0.681)*(PR**0.34)

      HOF=NUF*KM/DO

      HOM=0.9162*HOT+20.648*HOF

      U=1/(1/HOM +0.6007)

      NTU=U*1000*APS/MFG/CPG

      N=1/(NTU**0.22)

      DUM=1/EXP(NTU*C2*N)

      EP=1-EXP((DUM-1)/C2/N)

      K4=(1-EP*C2)/(1-EP)

      EC=(K4**4-1)/(K4**4-C2)

      E=EC*(2-EC)

      K1=2/(MG*CPG*(2+2*E+E*E))

      K2=MFW*C*E/MW

      K3=QB/MFG/CPG
```

```
END$"OF INITIAL"

 DYNAMIC

    DERIVATIVE

      TG1=INTEG(K1*(QL-MFG*CPG*(TG1-TG4)-E*(2-E)*DERTW1),TG1IC)

      DERTW1=K2*((TG1-TW1)+(TG3-TW1))

      TG3=TG2+K3

      TG4=TG3-E*(TG3-TW1)

      TG2=TG1*(1-E)+E*TW1

      TW1=INTEG(DERTW1,TW1IC)

      QEX1=MFG*CPG*(TG1-TG2)/1000

      QEX2=MFG*CPG*(TG3-TG4)/1000

      QEX=QEX1+QEX2

      ET=(TG1-TG4)/(TG1-TW1IC)


     TERMT(T.GT.TMAX)

END$"DERIVATIVE"
END$"DYNAMIC"
END$"PROGRAM"
```

APPENDIX B1: DESIGN OF CX1528 TRIGGER CIRCUIT WITH MOSFET OUTPUT STAGE

For 10 kHz PRF at a duty cycle $\delta = 0.1$, the main constant on the CX1528 operating characteristic is the recovery time, which is limited to 10 μs on both the charging switch and the tailbiter. In order to achieve this it will be necessary to limit the grid drive impedance to 100Ω. This is the best compromise which will give a minimum recovery impedance and at the same time allow the trigger pulse to be applied economically.

1. *Trigger circuit design specification*

The following specifications have been selected with reference to the EEV data for CX1528.

Unloaded grid 2 drive pulse	1000 V
grid 2 drive pulse duration	1 μs
loaded grid 2 bias voltage	- 160 V
Impedance of grid 2 drive circuit	100 Ω

2. *Output stage*

The power switching requirements to meet the above specificaition are within the capabilities of power MOSFETS, however, in order to meet the peak pulse voltage, it will be necessary to step the voltage up via a pulse transformer. The main components of the output stage are shown in Figure 1.

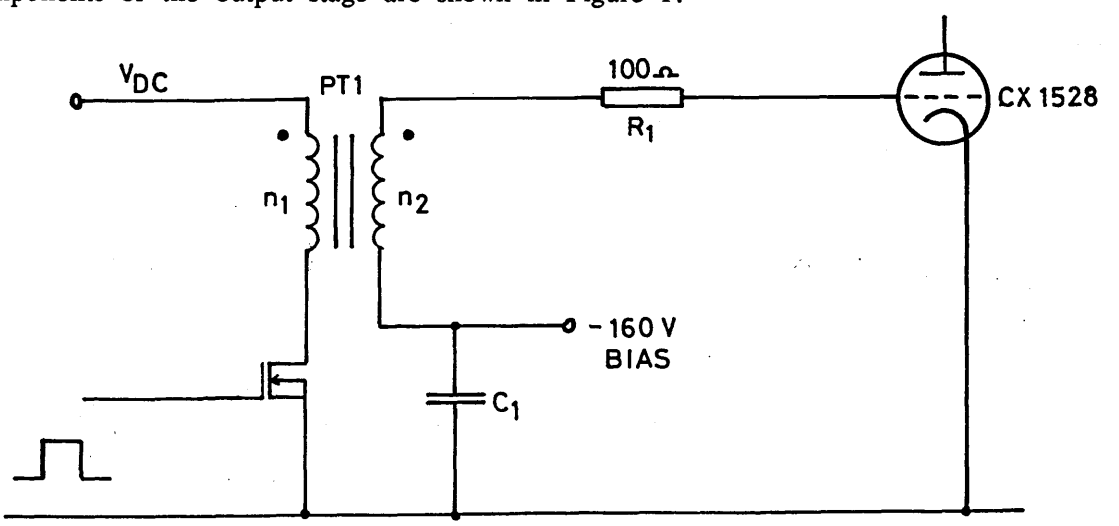

FIGURE 1

The trigger pulse current flows through R_1 and the coupling capacitor C_1, which is connected across the bias supply. With this arrangement the trigger pulses will be superimposed on the bias level of −160 V. Assuming a 240 V rms supply is available to feed the trigger circuits, then the maximum DC voltage is

$$V_{DC} = 1.41 \times 240$$

$$V_{DC} = 340\ V_{DC}$$

Step up ratio

$$r = \frac{1000}{340} = \underline{2.94}$$

The total current switched by the FET will be the sum of the secondary load current referred to the primary and the transformer magnetising current.

$$I_2' = I_2 \cdot r$$

Assuming a CX1528 the grid 2/cathode voltage drop

$$V_{g2} = 25\ V$$

$$\Rightarrow \quad I_2' = \left[\frac{1000 - 160}{100} - 25 \right] = \underline{8.15\ A}$$

Thus,

$$I_2' = 8.15 \times 2.94$$

$$\underline{I_2' = 24\ A}$$

$$I_1 = I_2' - I_{mag}$$

Assuming $I_{mag} = 1.0\ A \Rightarrow \underline{I_1 = 25\ A}$

For 10 kHz running with $\tau = 1\ \mu s$, the duty factor $\delta = 0.01$, the mean drain current is

$$I_D = I_1 \times 0.01 = \underline{250\ mA} \quad @\ 340\ V$$

A suitable power MOSFET to meet these requirements is Phillips BUZ45B, which has the following specification:

$$V_{ds} = 500\ V$$

$$R_{DS(on)} = 0.5\ \Omega$$

$$\hat{I}_s = 30\ A$$

$$P_D = 125\ W$$

3. *Pulse transformer*

The equivalent circuit for the pulse transformer assuming negligible leakage reactance is shown in Figure 2. L_1 is the short inductance ands R_2' is the secondary load referred to the primary. Assuming that the pulse duraton $\tau_p \ll$ time constant L_1/R_{DS}, then

$$L_1 = \frac{340}{1} \times 1 \times 10^{-6}$$

$$L_1 = \underline{0.34 \text{ mH}}$$

Core size: If two ferriteU type cores are used (with an equal air gap in each leg) then the energy assiciated with the magnetising current will be stored in the gap,

$$E_{mag} = \frac{1}{2} L I^2 = \frac{1}{2} \frac{B^2}{\mu_0} \text{Vol}$$

For ferrite $B_{sat} = 0.3\ \tau$, therefore limit peak flux to $0.1\ \tau$

$$\text{Vol} = A\,\ell_a = \frac{\mu_0}{B^2} L I^2 = \frac{4\pi \times 10^{-7} \times 0.34}{0.1^2} \times 10^{-3} \times 1^2$$

$$\underline{\text{Vol} = 4.3 \times 10^{-8} \text{ m}^3}$$

To prevent fringing effects, the ratio of core diameter to air gap must be less than 0.01.

$$\text{Vol} = 2 \cdot \frac{\pi}{4} \cdot D^2\,\ell_a = \frac{\pi}{2} \cdot D^3 \times 0.01 = 4.3 \times 10^{-8}$$

$$\Rightarrow D > \left[\frac{4.3 \times 10^{-8}}{\pi} \times 2000 \right]^{1/3}$$

$$\underline{D > 14 \text{ mm}} \qquad \text{ie} \qquad A > 1.5 \times 10^{-4} \text{ m}^2$$

Use 2 cores NEOSID type number 34−510−25

$$\underline{A = 2.41 \times 10^{-4} \text{ m}^2}$$

Primary turns:

$$L_1 = \frac{\mu_0 N^2}{\ell_a} A$$

Try $N_1 = 20$

$$\Rightarrow \ell_a = \frac{\mu_0 N^2}{4} A = \frac{4\pi \times 10^{-7} \times 20^2}{0.34 \times 10^{-3}} \times 2.41 \times 10^{-4}$$

$$\underline{\ell_a = 0.36 \text{ mm}}$$

Check flux: $B = \left[\frac{\mu_0 L I^2}{A \ell_a} \right] = \underline{0.07 \text{ Tesla}}$

Secondary: $N_2 = r N_1$

$\underline{N_2 = 58}$

Thus actual turns ratio : $r = \frac{58}{20} = \underline{2.9}$

With this turns ratio the corrected trigger pulse characteristics are:

amplitude (relative to cathode) $V = 826$ V

drive current $I_2 = 8.0$ A

4. *340 DC supply baord*

DC power required $= V_{DC} \cdot I_1$

$I_1 = I_{mag} + I_2'$

$= I_{mag} + r \cdot I_2$

$I_1 = 1 + 2.9 \times 8 = \underline{24.2 \text{ A}}$

with duty cycle $\delta = 0.01$ at 10 kHz PRF

$\overline{I}_1 = \underline{242 \text{ mA}}$

$P = 340 \times .242 = \underline{82.3\ \omega}$

Smoothing capacitor : assuming 5% ripple

$\Delta V = 340 \times 0.05 = 17$ V

Assuming all the current is drawn from smoothing capacitor during half cycle of mains

$$C = \frac{I \Delta t}{\Delta V} = \frac{242 \times 10^{-3}}{17} \times 0.01$$

$C = 142\ \mu F$

therefore, use $\underline{C = 200\ \mu F} \implies$ droop < 12 V

$P_{AC} = 1.14\ P_{DC} = 1.14 \times 242 \times 10^{-3} \times 340$

$\underline{P_{AC} = 93.8 \text{ VA}}$

APPENDIX B2: DESIGN OF CX1528 TRIGGER CIRCUIT WITH A THYRATRON OUTPUT STAGE

To overcome the problems associated with the thyratron grid spike it is proposed to use a small glass envelope thyratron to trigger the CX1528. This will provide a circuit which is robust, noise immune and in addition give an output pulse with a very fast rise time. The cost of the modification to the trigger circuit can be reduced if the pulse transformer used in the mosfet circuit is used in the new circuit as a step−down transformer. The trigger pulse specifications are the same as in the mosfet circuit design (see Appendix B1).

1. *Output stage*

The main problem associated with using a thyratron as the trigger switch is the need to reverse bias the tube at the end of the pulse so that the tube recovers before the anode voltage is reapplied. This can be achieved with the inverter circuit shown in Figure 1.

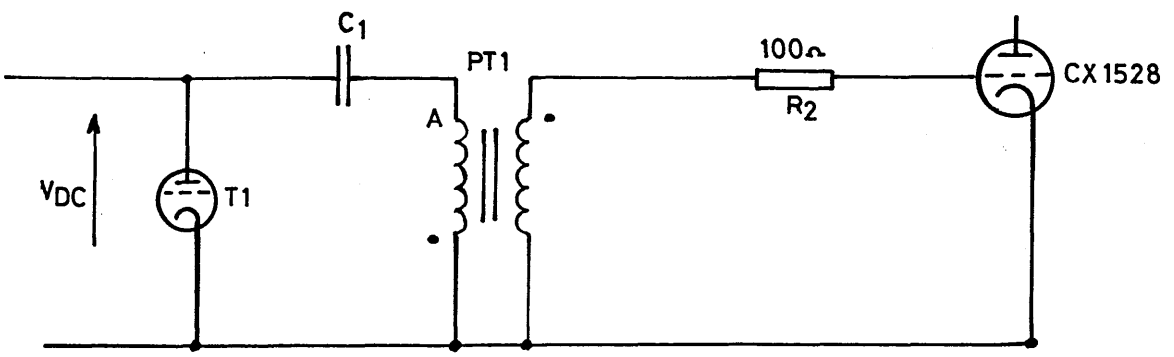

FIGURE 1

If capacitor C_1 is initially charged to a voltage V_0, when T1 fires point A is driven to $-V_0$. The equivalent circuit for this is shown in Figure 2.

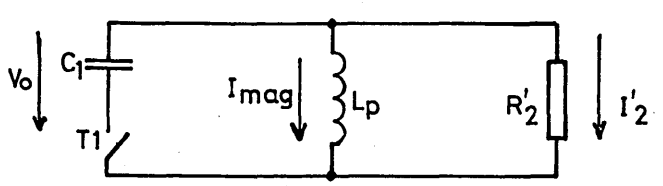

FIGURE 2

$$R_2' = \frac{1}{r^2} \cdot R_2$$

$$r = \left[\frac{20}{58}\right] = 0.345$$

$$R_2' = 900\ \Omega$$

From Appendix B1

$$L_1 = 0.34 \text{ mH} \Rightarrow L_2 = L_1\left[\frac{58}{20}\right]^2$$

Thus $$L_p = 0.34 \times \left[\frac{58}{20}\right]^2 \qquad \underline{L_p = 2.9 \text{ mH}}$$

when T1 fires, C will discharge with a time constant τ determined by C and R_2'. Thus, for an output pulse with a time constant of $1\,\mu s$

$$C = \frac{1 \times 10^{-6}}{900} = 1.1 \times 10^{-9} F$$

Use $\underline{C_1 = 0.001\ \mu F} \qquad \Longrightarrow \qquad \underline{\tau = 0.9\ \mu s}$

A slight current reversal at T1 is required to switch T1 off. This can be achieved by slightly under-damping the system. For the circuit of Figure 2, critical damping is given by:

$$R_2' < \frac{1}{2}\left[\frac{L_p}{C_1}\right]^{\frac{1}{2}}$$

Thus $\underline{L_p > 4\,(R_2')^2\,C_1 = 3.2 \text{ mH}}$

Therefore $L_p = 2.9$ mH should provide sufficient current reversal to switch T1 off.

2. *Thyratron slelection*

$$V_0 = \frac{V_2}{r} = 1000 \times 2.9 \qquad V_0 = 2.9 \text{ kV}$$

Use a slightly higher anode voltage say $V_0 = 3.5$ kV

Peak current $$\hat{I}_1 = V_0\left\{\frac{C}{L}\right\}^{\frac{1}{2}} = 3.5 \times 10^3 \times \left\{\frac{1 \times 10^{-9}}{2.9 \times 10^{-3}}\right\}^{\frac{1}{2}}$$

$$\underline{\hat{I}_1 = 20.A}$$

mean current $$\bar{I} = C\,V_0\,f = 1 \times 10^{-9} \times 3.5 \times 10^3 \times 10^4$$

$$\underline{\bar{I} = 35 \text{ mA}}$$

To meet those switching requirements and give a fast recovery characteristic, it is proposed to use the FX2530 triode. This tube has the following specification:

Peak forward anode voltage	8.0 kV
Peak anode current	85 A
Average anode current	100 mA
Peak inverse anode voltage	8.0 kV

3. *Charging circuit*

Capacitor C_1 needs to be charges to 3.5 kV after each pulse within a timescale of 100 μs for an operating PRF of 10 kHz. This can be achieved by resonant charging via a charging choke L_c and charging diode D1.

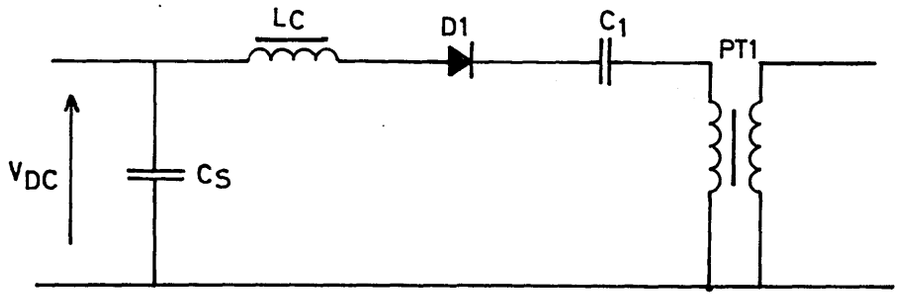

FIGURE 3

For a maximum charging time $T_{max} = 95\ \mu s$

$$T = \pi \sqrt{LC}$$

$$L = \frac{T_c^2}{\pi^2 C} = \frac{(95 \times 10^{-6})^2}{\pi^2 \times 1 \times 10^{-9}} = 0.9\ H$$

Peak charging current

$$\hat{I} = V_{DC} \left\{ \frac{C_1}{L_c} \right\}^{\frac{1}{2}}$$

For resonant charging $V_{DC} = \frac{1}{2}V_0 = 1.75$ kV

$$\hat{I} = 1.75 \times 10^{-3} \left\{ \frac{1 \times 10^{-9}}{0.9} \right\}^{\frac{1}{2}} = \underline{60\ mA}$$

Using two U cores with equal gaps in each leg

$$E_{mag} = \tfrac{1}{2} L \hat{I}^2 = \tfrac{1}{2} \frac{B^2}{\mu_0} \cdot A\ell_a$$

Limit peak flux to 0.1 T

$$A \cdot \ell_a = \frac{L\hat{I}^2}{B^2}\mu_0 = \frac{4\pi \times 10^{-7} \times 0.9 \times (60 \times 10^{-3})^2}{0.1^2}$$

$$A \cdot \ell_a = 4.1 \times 10^{-7} = \frac{\pi}{4} D^2 \ell_a$$

Assuming $\ell_a = 0.01\ D$

$$\Rightarrow \quad D = \left[\frac{4}{\pi} \cdot \frac{4.1 \times 10^{-7}}{0.01}\right]^{1/3} = 37.4 \text{ mm}$$

This is a bit too large: try design with 20 mm core.

NEOSID type no. 34

$$A = 2.41 \times 10^{-4} \text{ m}^2$$

$$\ell_a = \frac{\mu_0 L I^2}{B^2 A} = \frac{4\pi \times 10^{-7} \times 0.9 \times (60 \times 10^{-3})^2}{0.1^2 \times 2.41 \times 10^{-4}}$$

$l_a = 1.7$ mm ie 0.85 each leg

Number of turns

$$N = \left[\frac{\ell_a L_c}{\mu_0 A}\right]$$

$$N = \left[\frac{1.7 \times 10^{-3} \times 0.9}{4\pi \times 10^{-7} \times 2.41 \times 10^{-4}}\right]^{\frac{1}{2}}$$

$N = 2248$ turns

DC smoothing:

Ripple = 5 % of 1.75 kV = 87.6 V

$$C = \frac{\bar{I}t}{V_r} = \frac{35 \times 10^{-3}}{87.5} \times 0.01 \qquad C = 4\ \mu F$$

4. *Trigger circuit protecton*

If any negative residual voltage remains on capacitor C_1 when T1 switches off, this will result in a higher than usual charging voltage. If allowed to continue, the voltage will rise to dangerous levels resulting in flashover of the FX2530. This can be avoided by an inverse diode connected directly across the FX2530 as shown in Figure 4. To limit the peak diode current a 2K7 resistor is connected in series; this gives a discharge time constant of 2.7 μs.

In the event of the FX2530 latching on, the 1.75 kV charging supply must be switched off. This can be achieved by an overcurrent detector situated in the ground line as shown. The maximum anode current for the FX2530 is 100 mA and under normal conditions the load current is 35 mA. Therefore, relays R_7 and R_8 can be selected to give a trip current of 80 mA.

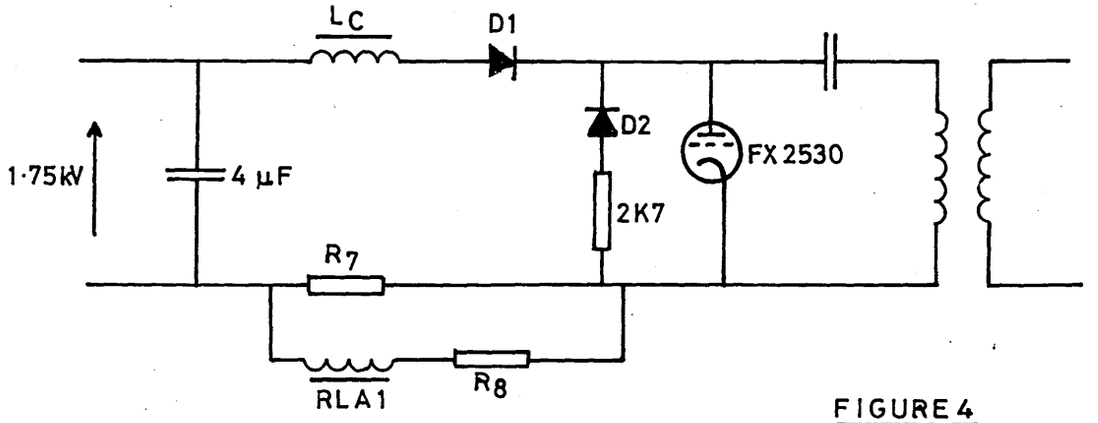

FIGURE 4

5. *FX2530 firing circuit*

FX2530 trigger pulse specification: The following specification has been selected from EEV data for FX2530.

unloaded grid drive pulse amplitude	340 V
unloaded grid pulse length	2.0 µs
rate of rise of grid pulse	350 V/µs
forward impedance of grid drive	470 Ω

The trigger pulse amplitude has been selected as 340 as this will allow the FX2530 to be triggered via a 1:1 pulse transformer. This can be driven by a power mosfet in a similar fashion to the mosfet trigger circuit for the CX1528 thyratron. The essential components of the FX2530 firing circuit are shown in Figure 5.

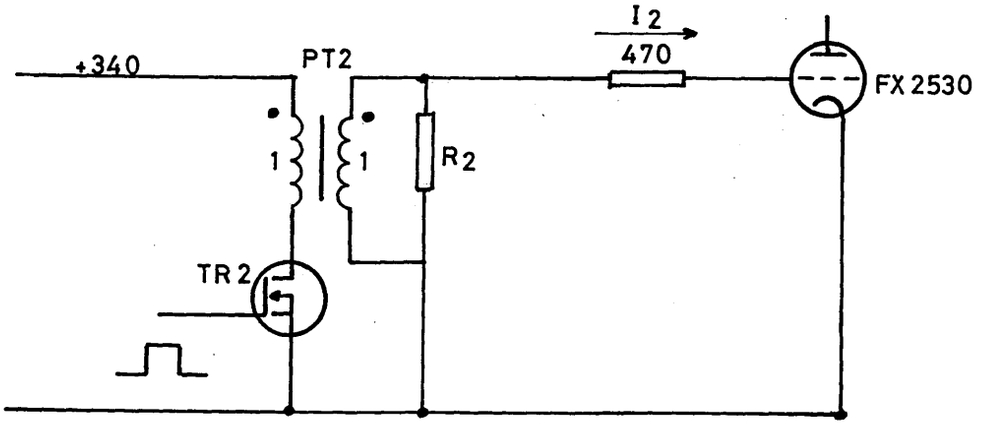

FIGURE 5

For a 1:1 ratio $I_2 = \frac{340}{470} = 0.7$ A

Let $I_{mag} = 0.07$ A @ 1 μs

Therefore, the shunt inductance of PT1 is

$$L_1 = \frac{Vt}{I_{mag}} = \frac{340 \times 10^{-6}}{0.07} = \underline{4.9 \text{ mH}}$$

Limiting maximum flux to 0.1 Tesla. Then the required airgap volume is

$$Vol = A \cdot \ell_a = \frac{\mu_0 L I_2}{B^2}$$

Since $A = \frac{\pi}{4} D^2$ where D = diameter of core and

assuming $\frac{\ell_a}{D} = 0.01$ to avoid fringing

$$\frac{\pi}{4} D^3 \times 0.01 = \frac{\mu_0 L I_2}{B^2}$$

$$D = \left[\frac{400 \times 4\pi \times 10^{-7} \times 4.9 \times 10^{-3} \times 0.07^2}{0.1^2} \right]^{1/3}$$

$$\underline{D = 10.6 \text{ mm}}$$

Use pot core MULLARD type no. FX2243

$$A = 2.9 \times 10^{-4} \text{ m}^2$$

The number of turns required assuming $\ell_a = 0.2$ mm

$$N_1 = \left[\frac{L \ell_a}{\mu_0 A} \right]^{\frac{1}{2}} = \left[4.9 \times \frac{10^{-3} \times 0.2 \times 10^{-3}}{4\pi \times 10^{-7} \times 2.9 \times 10^{-4}} \right]^{\frac{1}{2}}$$

$$N_1 = 52 = N_2$$

FET drain current

$$I_1 = I_{mag} + I_2'$$

$$= 0.07 + 0.7$$

$$\underline{I_1 = 0.77 \text{ A}} \text{ pulse current}$$

Mean FET drain current at 10 kHz

$$\overline{I}_{FET} = 0.77 \times 0.01 = \underline{8 \text{ mA}}$$

This is well within the capabilities of the IRF740 MOSFET which has the following specification:

V_{DS} = 400 V

$\overline{I}_D$ = 10 A

$\hat{I}$ = 40 A

P = 125 W

Protection required:

Need to limit the drain source voltage to 400 V. Therefore, use freeheel diode across the primary of the pulse transformer. In addition put a diode across the source and drain of the mosfet.

APPENDIX B3: AUXILIARY CONTROL CIRCUITS.

The function of the auxiliary control circuits is to provide the excitation and grid signals for the mercury arc rectifier and control the switching sequence of the various DC supply components. This circuitry is interlocked with the overload circuitry of the DC supply and the control/overload circuits of the pulser. The integration of all the circuits is achieved by the power supply control module.

MAR auxiliary control circuit.

This circuitry is housed in the cabinet within the safety enclosure. Details of this circuit are shown on drawing ES−MAR–1 with the associated wiring diagram EWD−MAR–1. This circuit operates as follows:

The auxiliary power is supplied from the main supply panel via the auxiliary control switch S1 and the HRC fuselinks FS−1. On switching on the auxiliary power the fan motor 88FM is energised providing cooling for the six excitron tubes. The phase shifting transformer is connected directly to the auxiliary supply by the HRC fuselinks FS−4. This feeds both the grid and excitation transformers, 508T and 502T via the zig−zag transformer 500T.

The supply to the excitation and grid bias transformer 502T is controlled by the EXCitation contactor EXC, which is energised by push buttons PB−1 (on) and PB−1 (off) on the main supply panel. The DC supply for the excitation contactor is fed through the on /off push buttons, a hold on contact EX−1 of EXC and a N/C contact of the grid tripping relay BB. This contact interlocks the excitation supplies with the grid trip, which is activated to suppress the grid signals in the event of a fault (see later). Thus, provided the grid trip relays have not been activated the excitation can be switched on. In addition to providing the excitation current, transformer 502T also supplies the negative bias of −70V DC to the control grid.

The grid drive transformer 508T is controlled by the Grid Drive Contactor, GDC. In addition to this, the grid AC signal is interlocked with the grid tripping relays BA, BB and BC. These are activated to suppress the grid signals in the event of a fault on the DC supply or the pulser (energise on fault) thus bringing the system under control in approximately one cycle of the mains. The control of the grid tripping relays is executed by the MAR overload unit (see section 3.5.4) in the event of:

(i) HV transformer secondary current exceeding a preset limit.
(ii) External trip signal being applied to MAR O/L unit from main control module

(iii) Failure of cooling Fan.

Specific details of the MAR O/L module can be found in section 3.5.4. For the present discussion it is only necessary to consider what faults result in the grid trip relays being activated.

The grid drive contactor GDC can be switched on or off by the push button PB−3 on the main supply panel or alternatively by PB−4 on the power supply control module inside the lab. This contactor is also interlocked by a N/C contact of one of the grid trip relays so that it is de−energised in the event of a grid trip.

The phasing of the grid signals is controlled by the phase shifting transformer, the output of which depends on the position of the rotor relative to the stator. The position of the rotor is controlled by the phase shifter control unit, which activates the forward/reverse circuit of the rotor drive (drawing ES−MAR−1).This circuit comprises two mechanically interlocked contactors and is housed in the cabinet within the safety enclosure. The controller for this circuit plugs directly into the control bus on the main supply panel, which allows the phase shifter rotor to be positioned remotely. The limit switches provide an automatic cutout when the rotor reaches its limit: a visual indication of this is given on the controller.

The fan motor is monitored by a DC tachograph which gives a voltage proportional to the speed of the fan. As the fan requires time to reach full speed the output from the tachometer falls below the preset value set in the MAR O/L module. Therefore to avoid the grid trip relays being activated during switch on, the supply for the O/L module is fed through a key swithch, mounted on the side of the main supply panel. This must be swithched to the " on" position after the auxiliary power is swithed on, to allow the fan to run up to speed.

Supply panel control circuit

The control circuit for the main supply panel controls the switching sequence of the DC supply components. The circuit details are given on drawing ES−MSP−1 with the associated wiring diagram EWS−MSP−1.

With reference to drawing ES−MSP−1, the main three phase power lines are fed through a 200 amp fuse−isolator unit, a moulded case circuit breaker and a power contactor, before being fed to the main step up transformer. These devices are the main overload protection on the DC supply. The fuse−isolator assembly contains 200 amp HRC fuses, which are only required to protect the power supply in the event of

other overload systems failing (see sections 3.3.4 and 3.5). The main protection on the DC supply is provided by the circuit breaker, which is activated by trip signals from various components on both the DC supply and the pulser in response to certian overload conditions. The trip signals are applied to the breaker by the following circuit components.

(i) MAR grid trip relays: in event of MAR backfire, MAR fan failure or external trip signal from power supply control module.
(ii) Crowbar: in event pulser short circuit (ie a fire through).
(iii) Power supply control module: in event of an emergency stop
(iv) Relay RY−4 main supply panel: in event of phase failure (see below).

When the fuses are inserted in the fuse assembly and the switch closed, the phases are monitored by relays RY−1, RY−2 and RY−3, which confirm that all three phases are live. The contacts of the phase failure relays are connected in series and interlocked with relay RY−4, which is interlocked with the circuit breaker trip circuit. This prevents the circuit breaker being set if one or more of the phases is dead. As the circuit breaker is an energise on fault device, the circuit of RY−4 is supplied from the same DC supply as the circuit breaker and the second contact of RY−4 is interlocked with the contactor coil circuit. This ensures that the contactor cuts out if the supply to the circuit breaker coil fails.

With the circuit breaker set, power is fed through to the contactor, which can then be switched on by push button PB−2 on the supply panel, providing various interlock conditions are satisfied. The " on" button for the contactor is connected in series with a N/C contact of the MAR phase shifter contactor. This prevents the contactor being switched on if the MAR grid drive is on: this being necessary because the MAR has a tendency to backfire if the grid drive is on when the mains feed is switched on. The contactor is also interlocked with a key switch for security and safety purposes. This key switch energises the MAR O/L module, which is also interlocked with the contactor coil circuit. This must be set before the contactor can be switched on, which therefore requires the MAR fan to be running. This condition should be satisfied under normal operation as the contactor and MAR O/L unit are activated by the same key switch. Thus, with the contactor switched on, the DC supply can be controlled from the power supply control module within the lab.

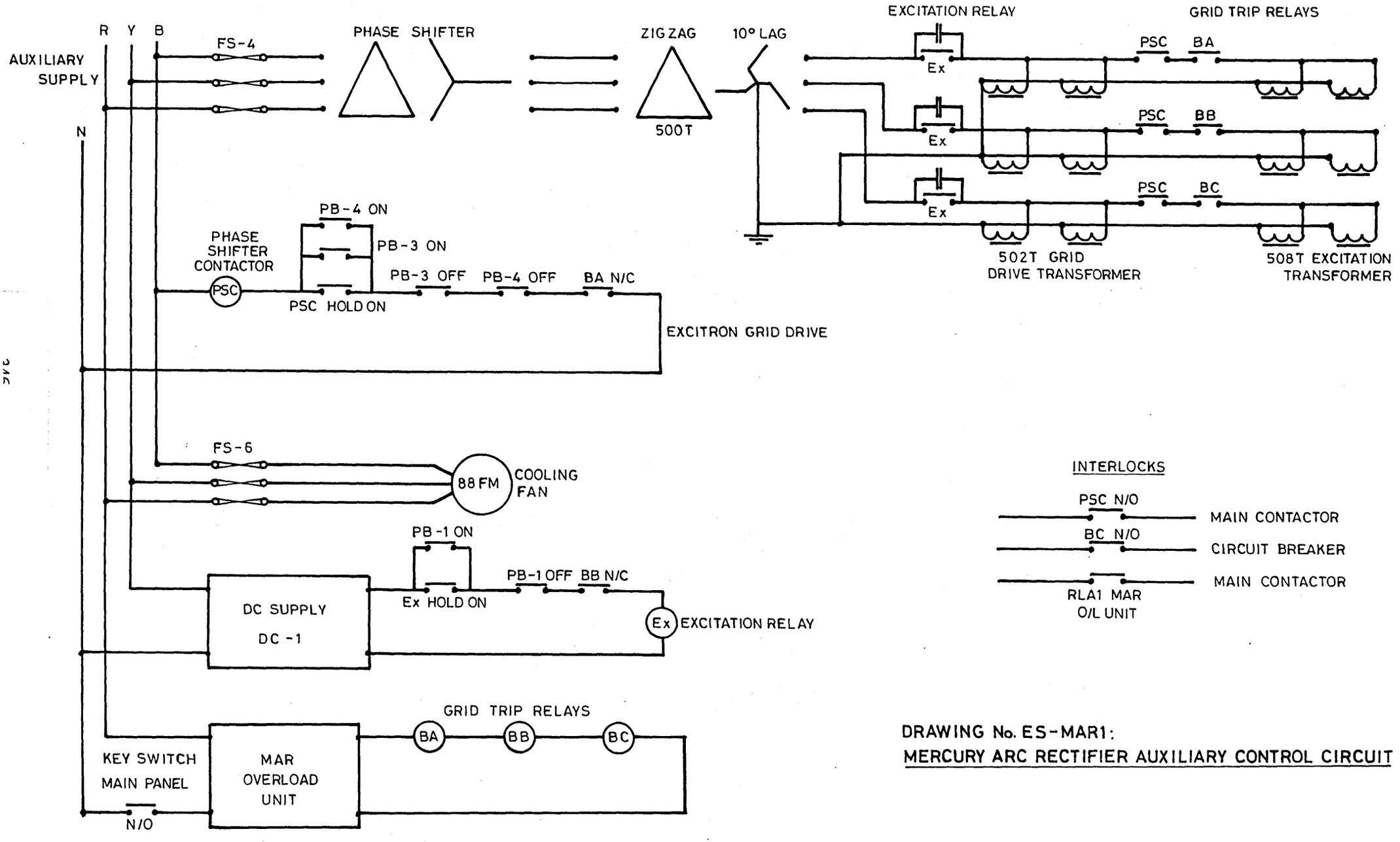

DRAWING No. ES-MAR1:
MERCURY ARC RECTIFIER AUXILIARY CONTROL CIRCUIT

APPENDIX B4 : Calculation of Transformer Phase and Sequence Impedances

Transformer Specifications

Rated Output	133.5	kVA
Secondary Rated Voltage	13.35	kV
Primary Rated Voltage	415.0	kVA
Primary Rated Current	193.5	A
Secondary Rated Current	10.0	A

Manufacturer - Parsons Peebles

Serial No. 1EA3459

Diagram No. QO7B275

Vector Reference Yd11

Reactance and Impedance

1. At 50% rated output:

Impedance $Z_{pu} = 0.0635$

Reactance $X_{pu} = 0.06$

Base quantities : secondary

$MVA_B = 0.1335 \qquad kVA_B = 13.35$

$$Z_{2B} = \frac{kVA_B^2}{MVA_B} = \frac{13.35^2}{0.1335} = \underline{1335\ \Omega}$$

$\Rightarrow Z_2 = 1335 \times 0.0635 \qquad \underline{Z_2 = 84.77\ \Omega}$

$X_2 = 1335 \times 0.06 \qquad \underline{X_2 = 80.10\ \Omega}$

Primary bank :

$$Z_{1B} = \frac{415^2}{0.1335} = 1.29\ \Omega$$

$\Rightarrow$ $Z_1 = 1.29 \times 0.0635$ $\qquad$ $\underline{Z_1 = 0.082\ \Omega}$

$X_1 = 1.29 \times 0.06$ $\qquad$ $\underline{X_1 = 0.077\ \Omega}$

2. At 100% rated output

$Z_{pu} = 0.041$

$X_{pu} = 0.0382$

$\Rightarrow$ $Z_2 = 0.041 \times 1335$ $\qquad$ $\underline{Z_2 = 54.73\ \Omega}$

$X_2 = 0.382 \times 1335$ $\qquad$ $\underline{X_2 = 51.0\ \Omega}$

$Z_1 = 0.041 \times 1.29$ $\qquad$ $\underline{Z_1 = 0.053\ \Omega}$

$X_1 = 0.0382 \times 1.29$ $\qquad$ $\underline{X_1 = 0.05\ \Omega}$

APPENDIX C1 PREIONIZER CIRCUIT DESIGN

1. DESIGN SPECIFICATION

With application of a suitably high voltage to the trigger wires, the gap between the outer surface of the pyrex and the cathode will break down. The effective load seen by the pulse circuit will therefore be a capacitor C_e, figure 1.

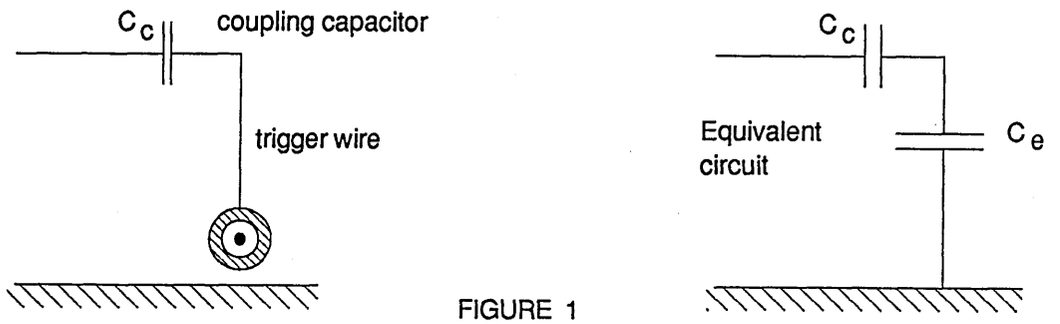

FIGURE 1

Estimate of C_e

$$C = \frac{2\pi\epsilon_0\epsilon_r}{\ell n \frac{D}{d}}$$

$D = 3.5$ mm
$d = 2.0$ mm
$\epsilon_0 = \frac{1}{3\pi}$
$\epsilon_r = 5$

$$=> C = 2\,\frac{\left[\frac{1}{36}\right] \times 10^{-9} \times 5}{\ell n \frac{3.5}{2}}$$

$$\underline{C = 0.5 \times 10^{-9}\ F/m}$$

Trigger wire length $\ell = 130$ mm

104 wires in assembly

$$=> C_e = 0.5^{-9} \times 104 \times 130 \times 10^{-3}$$

$$C_e = 8.45 \times 10^{-9}\ F$$

ie. $\underline{C_e = 8.45\ nF}$

Trigger wire voltage: From figure (4.29), it can be seen that the peak voltage measured across the trigger wires is approximately 6 kV, with a pulse duration of 0.5 μs. For this design it was decided to use a trrgger−wire voltage of 3 kV, and use a design value for C_e = 11nF.

Summary:	effective load capacitance	C_ℓ	= 11.0 nF
	peak output voltage	$\hat{V}_0$	= 3.0 kV
	Pulse duration	τ_p	= 500 nS

2. OUTPUT CIRCUIT DESIGN

As the output load is essentially capacitive, it is proposed to resonantly transfer charge from an intermediate storage capacitor C_1 to the effective trigger wire capacitance C_e as shown in figure 2.

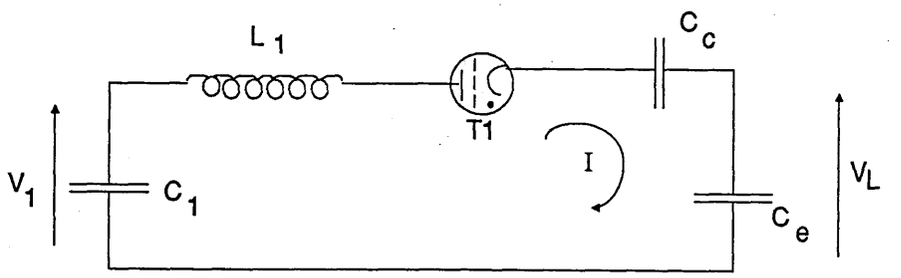

FIGURE 2

Use $C_c = 0.1\ \mu F$ => circuit looks like

$$C_2 = \frac{C_c\ C_e}{C_c + C_e} = \frac{11}{111} \times 100$$

$$\underline{C_2 = 9.9\ nF}$$

To make sure thyratron T_1 switches off and has sufficient time for recovery, make $C_1 < C_2$ to give –ve residual on C_1 at point of current reversal.

$$V_{c2}(t=\tau) = \frac{2V_{c10}\ C_1}{C_1 + C_2}$$

$$V_{c1}(t=\tau) = \frac{(C_1 - C_2)V_{c10}}{C_1 + C_2}$$

$$\tau = \pi \sqrt{(L_1 C)}$$

where $C = \frac{C_1\ C_2}{C_1 + C_2}$

Choose $C_1 = 8.0$ nF

$$\Rightarrow C = \frac{8 \times 9.9}{8 + 9.9} = \underline{4.42 \text{ nF}}$$

$$L_1 = \left[\frac{\tau}{\pi}\right] \frac{1}{C} = \left[\frac{500 \times 10^{-9}}{\pi}\right] \frac{1}{4.42 \times 10^{-9}} \Rightarrow L_1 = 5.70 \mu H$$

For 3 kV output on trigger wire capacitance C_e

$$\Rightarrow \text{voltage on } C_2 = 3 \times \frac{111}{100} = 3.33 \text{ kV}$$

$$\text{voltage on } C_1 : \quad V_{C2} = 2 \frac{V_{C10} C_1}{C_1 + C_2}$$

$$\Rightarrow V_{C10} = 3.33 \times \frac{(8 + 9.9)}{2 \times 8}$$

$$\underline{V_{C10} = 3.73 \text{ kV}}$$

This is the voltage that C_1 must be charged to prior to T1 being fired.

Peak current $\hat{I} = \dfrac{V_{C10}}{\sqrt{\left[\frac{L_1}{C}\right]}}$

$$\hat{I} = 3.73 \times 10^3 \frac{\sqrt{(4.42) \times 10^{-9}}}{5.7 \times 10^{-6}}$$

$$\underline{\hat{I} = 103.9 \text{ A}}$$

Pulse energy $E = \frac{1}{2} C_1 V_{C10}^2 = \frac{1}{2} \times 8 \times 10^{-9} \times (3.73 \times 10^3)^2$

$$\underline{E = 55.7 \text{ mJ}}$$

3. CHARGING CIRCUIT

Design prf = 10 kHz

Design resonant charge circuit for C_1 with $\tau_c = 90$ μs.

$$\tau = \pi\sqrt{(L_c C_1)} \Rightarrow L_c = \left[\frac{\tau}{\pi}\right]^2 \frac{1}{C_1}$$

$$L_c = \left[\frac{90 \times 10^{-6}}{\pi}\right] \times \frac{1}{8 \times 10^{-9}} \Rightarrow \underline{L_c = 0.1 \text{H}}$$

Peak current $\hat{I} = \dfrac{V_{dc}}{\sqrt{\left[\frac{L_c}{C_1}\right]}} = \frac{1}{2} \times 3.73 \times 10^3 \times \dfrac{\sqrt{(8 \times 10^{-9})}}{0.1}$

$$\underline{\hat{I} = 0.53 \text{ A}}$$

Charging choke: Use two Ferrite U cores FX3860 limit peak flux density to 0.15 Tesla.

gap volume $\quad Vol = A.\ell_a = \mu.L\left[\frac{\hat{I}}{B}\right]^2$

$A.\ell_a = 4\pi \times 10^{-7} \times 0.1 \times \left[\frac{0.53}{0.15}\right]^2 = 1560\ mm^2$

$A = 625\ mm^2 \Rightarrow$ gap $\quad \ell_a = \frac{1560}{625} = 2.51$

ie. $\quad \underline{\ell_a = 1.26\ mm}$ each leg

Number of turns $\quad N = \frac{\sqrt{(L\ \ell_a)}}{\mu_0\ A} = \frac{\sqrt{(0.1)} \times 2.51 \times 10^{-3}}{4\pi \times 10^{-7} \times 625 \times 10^{-6}}$

$\underline{N = 565\ turns}$

DC supply:

$V_{dc} = 1.87\ kV$

$I_{dc} = \frac{Q}{T} = C_1\ V_{c10} f = 8 \times 10^{-9} \times 3.73 \times 10^3 \times 10^4$

$\underline{I_{dc} = 0.298\ A}$

$P_{dc} = 0.298 \times 1.87 \times 10^{-3}$ $\qquad \underline{P_{dc} = 558\ W}$

Use FWR circuit $\qquad V_2\ rms = \frac{1.87}{1.4} \times 10^3 = 1335\ V\ rms$

$I_2 = \frac{0.298}{0.62} = 0.481\ A\ rms$

Transformer VA rating $\quad \underline{VA = 641}$

Smoothing: Design for 10% ripple = 187 V

$C_s = \frac{I_{dc}\ \Delta t}{\Delta V} = \frac{0.298 \times 10ms}{187}$

$\underline{C_s = 16\mu F}$

PREIONIZER – CX1191 TRIGGER CIRCUIT

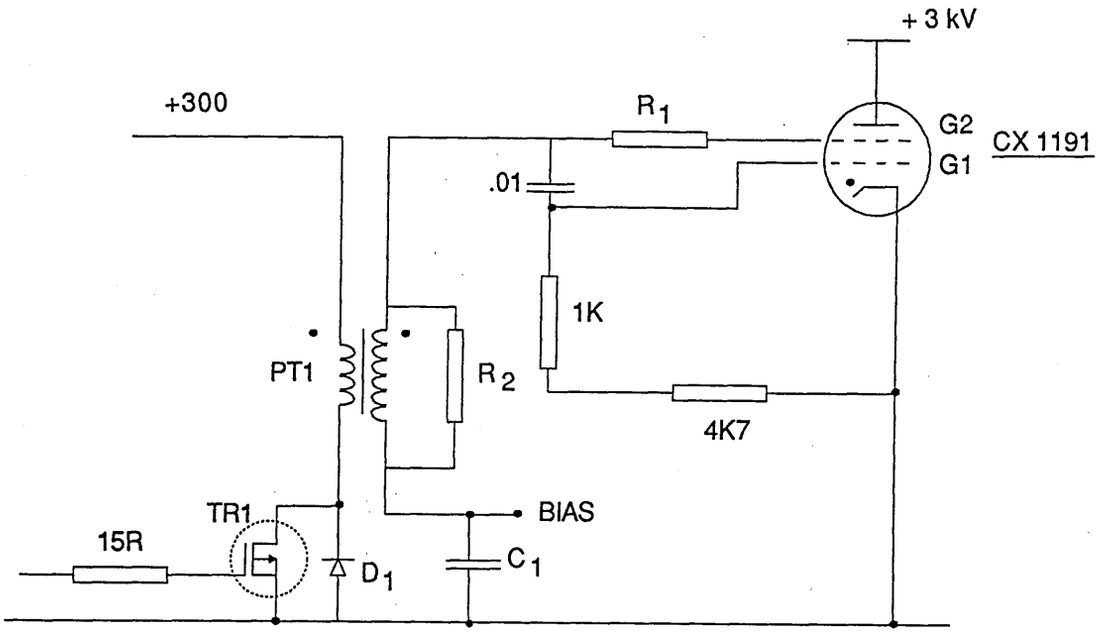

Spec

Unloaded grid 2 pulse amplitude	V	= 400V
pulse duration	τ	= 2μs
G2 impedance	R	< 100Ω
G2 bias		– 100 V DC

Output circuit

Pulse amplitude

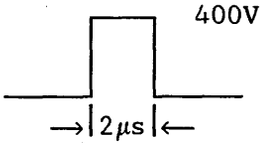

Assuming no voltage drop G2/cathode = $\hat{I}_2 = \frac{400}{100} = 4$

$\bar{I}_2 \approx \frac{4 \times 2}{100} = 80$ mA $\qquad I_2$ rms = 80 mA x 1.2

I_2 rms = 100 mA

$P = I^2_{rms} R = (100 \times 10^{-3})^2 \times 100 = 1$ watt

Transformer

Use pot core FX2243 $A = 2.9 \times 10^{-4}\ m^2$

$I_2 = 4.0\ A$

Let $\hat{I}_{mag} = 1.0\ A$

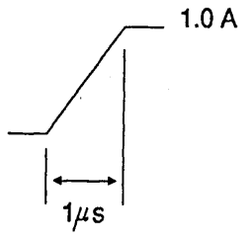

$$V = L\frac{\Delta T}{\Delta t}$$

$$L = \frac{300 \times 1 \times 10^{-6}}{1}$$

$$\underline{L = 0.3\ mH}$$

with $E = \frac{1}{2} L\hat{I}^2 = \frac{1}{2}\frac{B^2}{\mu_0} A.\ell$

$$L_1 = \mu_0 \frac{N^2 A}{\ell_a} \qquad \mu_0 = 4\pi \times 10^{-7}$$

$$B^2 = L\frac{\hat{I}^2}{A\ell}\mu_0 = \frac{0.3 \times 10^{-3} \times 1^2 \times 4\pi \times 10^{-7}}{2.9 \times 10^{-4} \times 0.08 \times 10^{-3}} = 0.016$$

$$\underline{B = 0.13\ \tau}$$

Ferrite saturation flux 0.3τ

$$N_1 = \sqrt{\left[\frac{L\ell}{\mu_0 A}\right]} = \left[\frac{0.3 \times 10^{-3} \times 0.08 \times 10^{-3}}{4\pi \times 10^{-7} \times 2.9 \times 10^{-4}}\right]$$

$$\underline{N_1 = 9\ turns}$$

$$N_2 = \frac{400}{300} N_1 \quad \Rightarrow \quad \underline{N_1 = 12\ turns}$$

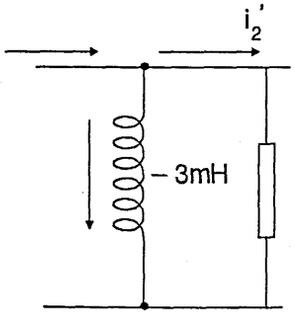

$$R'_2 = 100 \times \left[\frac{300}{400}\right]^2 = 56.3\ \Omega$$

$$\underline{I_p = I_{mag} + i_2'}$$

$$I_p = 1 + 4 \times \left[\frac{400}{300}\right] \qquad \underline{I_p = 6.3\ A}$$

Use IRF 740 to switch this.

Output stage:

$$L_2 = n^2 L_1 = 1.33^2\ 0.3$$

$$\underline{L_2 = 0.53\ \text{mH}}$$

What value for C. Need to make sure most of voltage appears across R.

Use $\underline{C = 5\ \mu\text{F}}$ $\Rightarrow$ $\tau = 50\ \mu\text{s}$

check $Z_C\ @\ \frac{1}{1\mu\text{s}} = \frac{1}{2\pi \times 1 \times 10^6 \times 5 \times 10^{-6}} = 0.03\ \Omega$

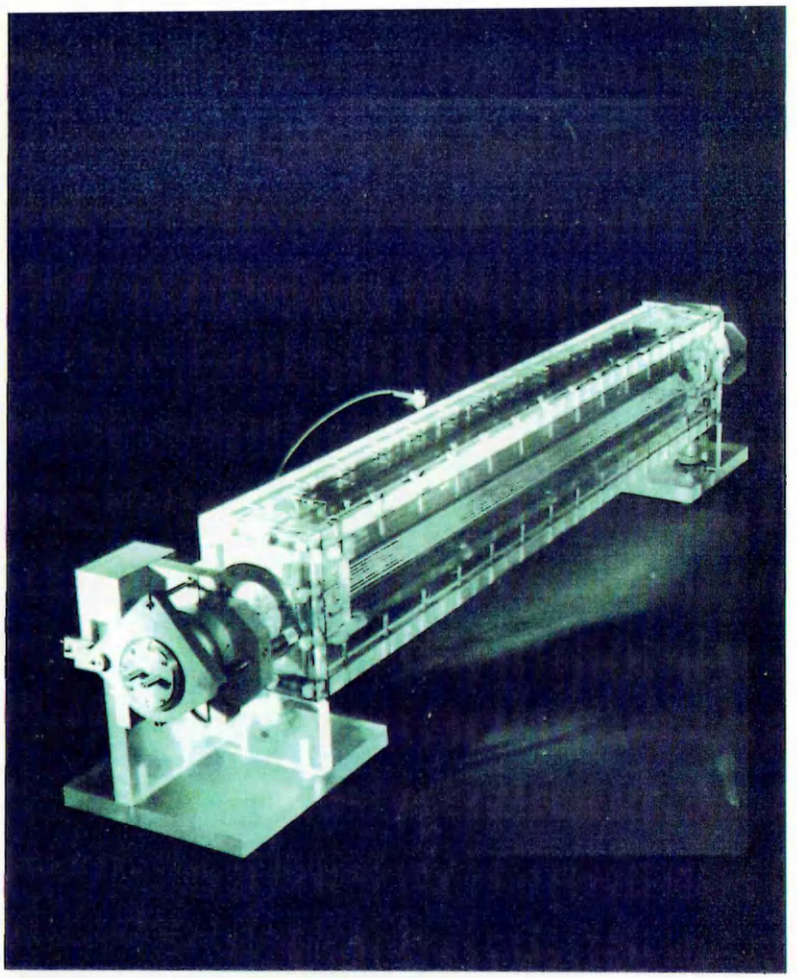

PLATE (1) KHAHRA'S PROTOTYPE DISCHARGE CAVITY.

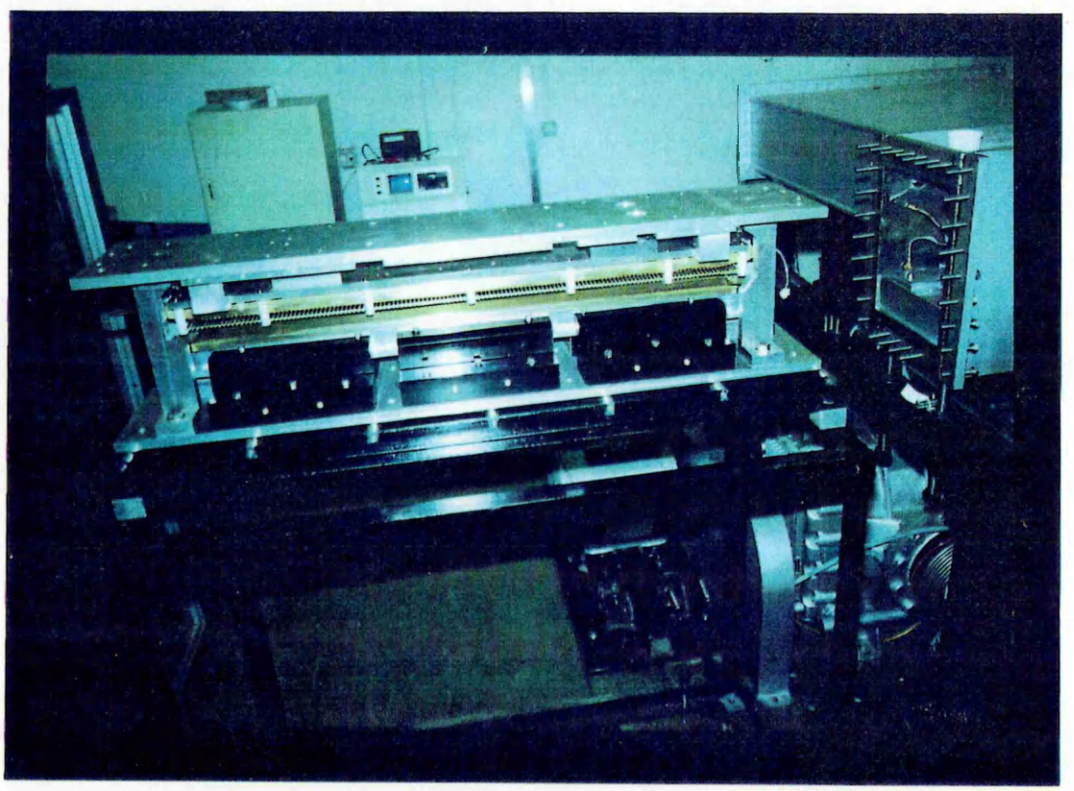

PLATE (2) ELECTRODE ASSEMBLY.

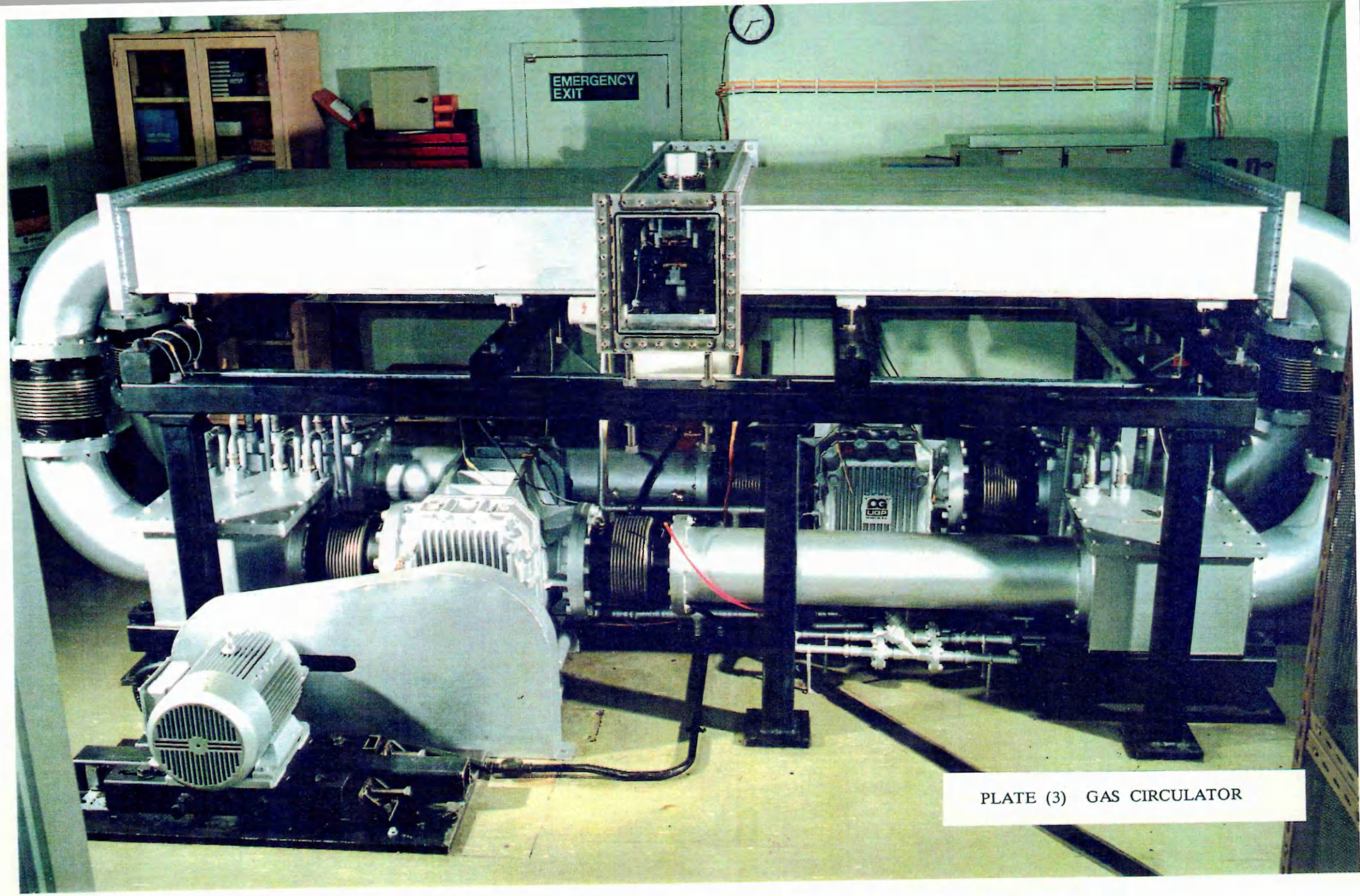

PLATE (3) GAS CIRCULATOR

PLATE (4) HEAT EXCHANGER COOLING COILS.

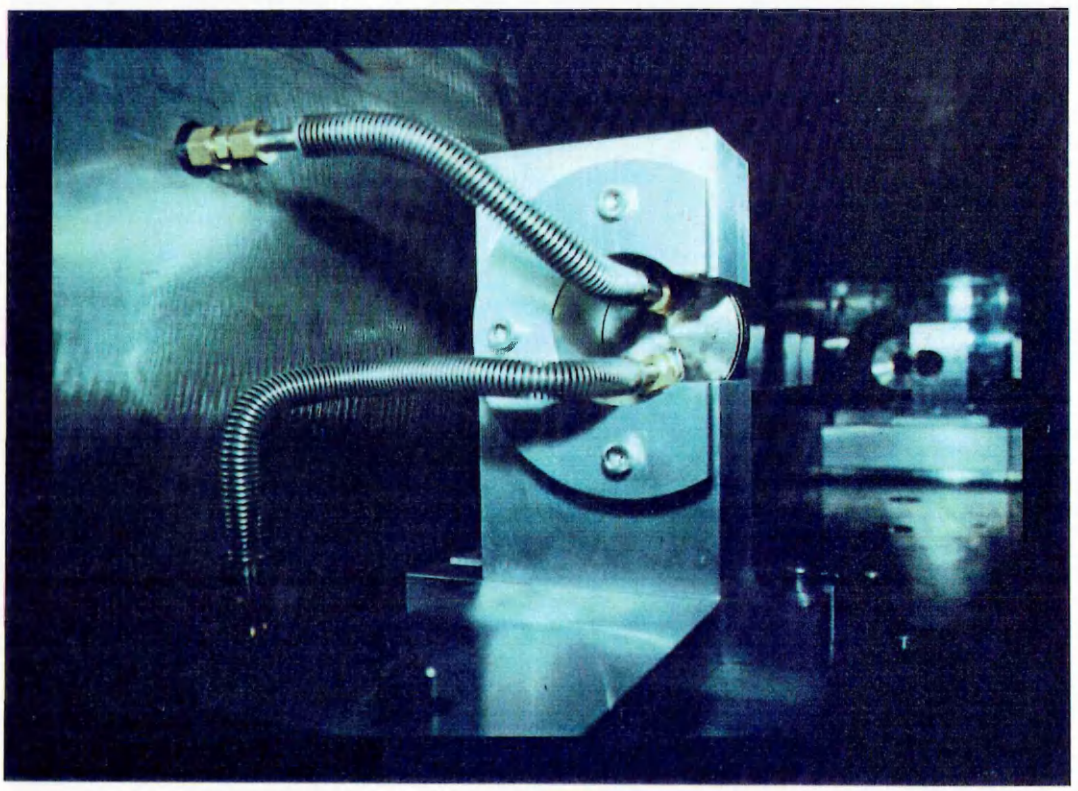

PLATE (5) VIEW OF OPTICAL RESONATOR.

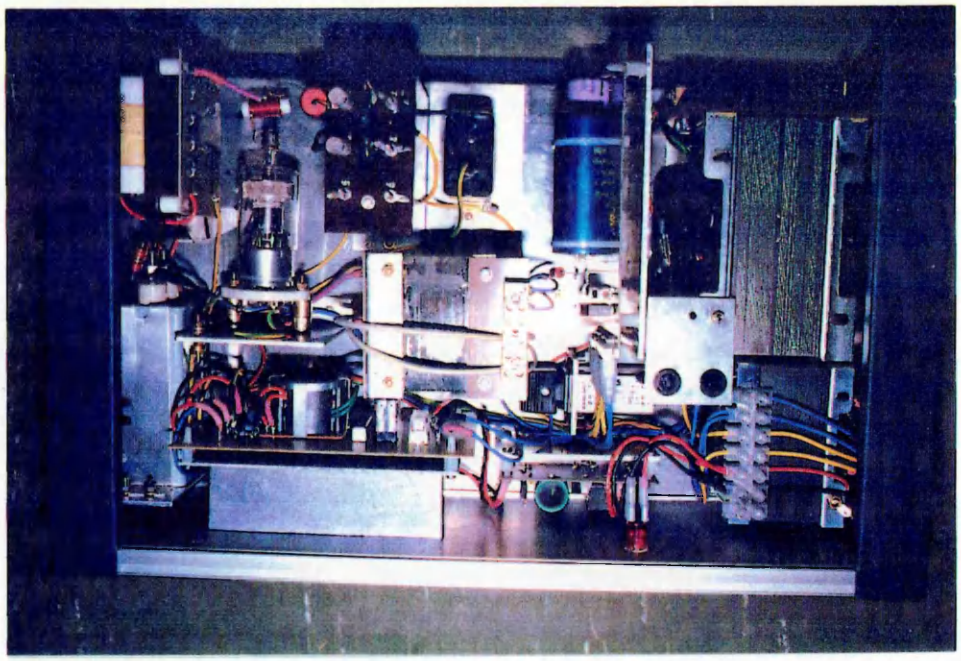

PLATE (6) THYRATRON TRIGGER CIRCUIT.

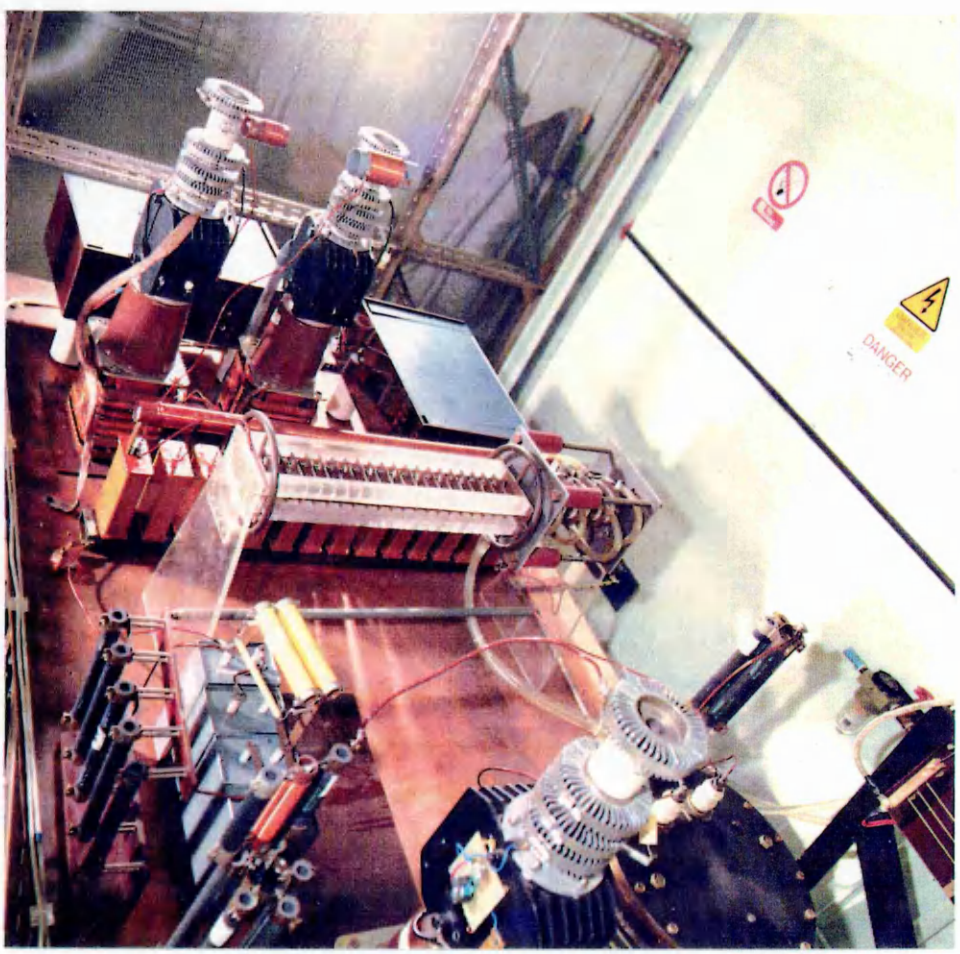

PLATE (7) PULSER CICUIT.

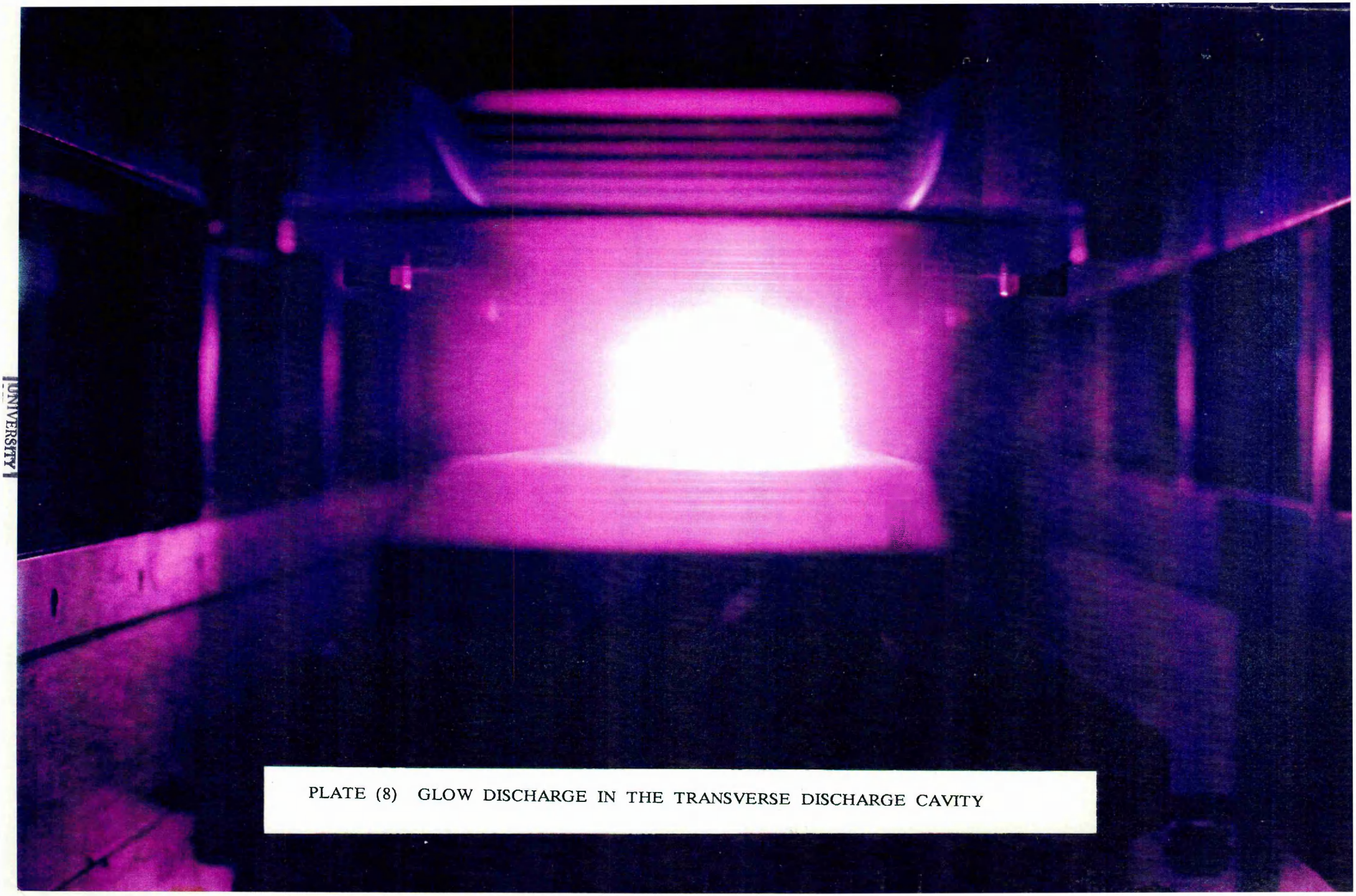

PLATE (8) GLOW DISCHARGE IN THE TRANSVERSE DISCHARGE CAVITY